19TH INTERNATIONAL COSMIC RAY CONFERENCE

LA JOLLA, USA AUGUST 11-23, 1985

NASA-CP-2376-VOL-3
19850026549

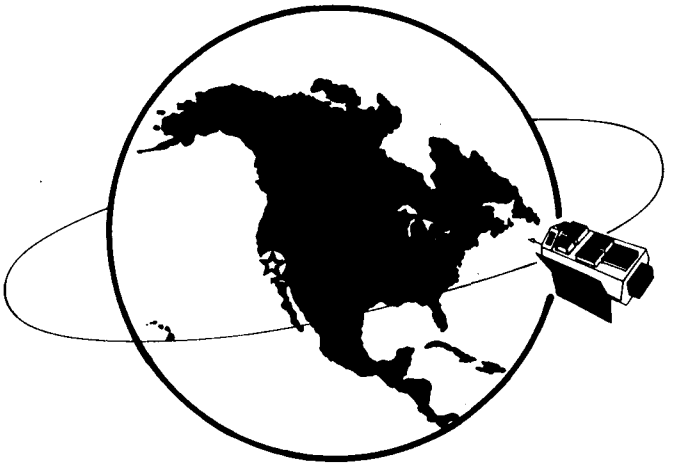

CONFERENCE PROGRAM SESSIONS VOL. 3

19TH INTERNATIONAL COSMIC RAY CONFERENCE

LA JOLLA, USA AUGUST 11-23, 1985

CONFERENCE PAPERS

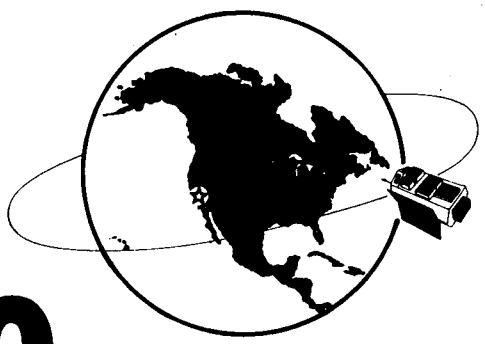

OG

SESSIONS VOL. 3

NASA Conference Publication 2376

Published by
Scientific and Technical Information Branch
National Aeronautics and Space Administration
Washington, D.C. 20546

August 1985

For sale by the National Technical Information Service, Springfield, VA 22151

PREFACE

The 19th International Cosmic Ray Conference, under the auspices of the Cosmic Ray Commission of the International Union of Pure and Applied Physics, is being held on the campus of the University of California, San Diego, on 11 through 23 August 1985. In keeping with the tradition begun in 1971 by the Australian organizers of the 12th ICRC, the Proceedings of this conference are appearing in two sets of volumes. The first set, consisting of volumes 1 through 8, is being distributed to all participants at the beginning of the conference. This set contains the contributed papers. The second set, distributed after the conference, contains invited, rapporteur, and highlight papers. The papers are reproduced here exactly as they were received from the authors, without refereeing.

For the 19th ICRC, the scientific program was organized according to three major divisions-- OG (cosmic rays and gamma rays of Galactic Origin), SH (Solar and Heliosphere), and HE (High Energy). Technical papers are included in each of the three divisions.

This conference depended on funds from several agencies of the United States government, including major financial support from the National Aeronautics and Space Administration and support from the National Science Foundation, the Department of Energy, and the Air Force Geophysics Laboratory. Important financial support also came from the Center for Astrophysics and Space Sciences of the University of California, San Diego, from the California Space Institute of the University of California, from the Department of Physics and Astronomy of the University of Maryland, College park, from the International Union for Pure and Applied Physics, and from several corporate sponsors who will be acknowledged by name in the post-conference volumes.

We appreciate the confidence placed in the conference organizers by the Cosmic Ray Commission, and acknowledge with thanks the role of the Commission members in setting up the rules for the conference and in advising the organizers during its planning.

We are grateful to all of the members of the various organizing committees listed at the front of this volume. The three Program Committees went to great effort to organize a coherent scientific program and to schedule four parallel sessions with a minimum of conflicts. The Local Organizing Committee has worked long and hard to ensure efficient and hospitable accommodations for all the participants, both in the scientific sessions and outside them. The Publications Committee not only took great pains to assemble these volumes but also maintained an orderly data base of papers and authors which was extremely helpful to the program committees. The General Organizing Committee made important contributions of ideas and efforts to make the conference possible; this committee included international representation from all of North America, thus the departure from the traditional name of National Organizing Committee. And the entire effort was coordinated by the dedicated members of the Steering Committee.

Martin H. Israel, Chairman
General Organizing Committee

August, 1985

LETTER FROM THE EDITORS

This conference marks a departure from previous conferences in this series in that the publication of the Conference Papers was carried out an entire continent away from the activities of Local Organizing Committee. This posed some problems but, to the considerable surprise of the Publications Committee members, the one that was expected to be the most trouble turned out not to be significant. The overwhelming majority of those submitting papers and abstracts sent them to the correct address, not to La Jolla as was feared. We wish to thank our many authors for their alertness and commend them for handling a complicated situation so well.

There are eight volumes to be distributed to the conference participants in addition to the Conference Program and Author Index: three volumes for OG, two for SH and three for HE. the detailed makeup of these volumes is described in the prefaces written by the Scientific Program chairmen for their respective volumes. Out of some 1100 abstracts that were accepted by the Scientific Program Committees for inclusion in the conference some 929 papers were finally received in time for inclusion in the Conference Papers. This represents a response of approximately 84 percent, a modest improvement. Even if one excludes the 42 one page papers that should be considered as "confirming abstracts", even though there was no such formal category, the response was somewhat higher than that of recent years. We attribute this to the carrot of a later deadline than before coupled with the stick of there being no printing of post deadline contributed papers. We believe that this decision of the General Organizing Committee was a wise one. Of course invited, rapporteur, and highlight talks will be printed in volumes to be distributed to the participants after the conference as usual.

The Publications Committee had much generous help in performing its duties: from Goddard Space Flight Center we had the help of B. Glasser, L. Harris, E. Schronce, N. Smith, J. Esposito and T. Smith. From the Naval Research Laboratory we were helped by T. Mazzotta, and at the University of Maryland M. L. Snidow and J. Mucha gave much needed assistance. Special thanks are due to Caryl Short, the lone staff member of the Publications Committee. She maintained the computer data base, organized the abstracts as they arrived, and kept track of the papers themselves to see that the finally arrived in the right place at the right time. Without her help the job would have been far more difficult than it was.

PUBLICATIONS COMMITTEE August, 1985

Frank C. Jones, Chm.
Jim Adams
Glen M. Mason

OG SESSIONS
VOLUME III

19th INTERNATIONAL COSMIC RAY CONFERENCE
LA JOLLA, USA
AUGUST 11–23, 1985

INTERNATIONAL UNION OF PURE AND APPLIED PHYSICS
MEMBERS OF THE COMMISSION ON COSMIC RAYS OF IUPAP

A.E. Chudakov, Chm.
F.B. McDonald
G.C. Castagnoli
P.H. Fowler
D. Hovestadt
J. Kota
T.O. Montmerle
H. Morsal
J.R. Prescot
B.V. Sreekantan
K. Suga
J. Wdowczyk

STEERING COMMITTEE

F. McDonald, Chm.
G. Burbage
M. Forman
T. Gaisser
M. Israel
F. Jones
R. Lingenfelter
R. Mewaldt
L. Peterson

GENERAL ORGANIZING COMMITTEE

M. Israel, Chm.
M. Bercovitch
P. Freier
R. Gall
R. Jokipii
L. Jones
V. Jones
S. Krimigis
J. Kurfess
J. Lockwood
P. Meyer
B. Price
R. Ramaty
F. Reines
M. Shapiro
M. Shea
J. Simpson
E. Stone
D. Venkatesan
J. Waddington
S. White

PROGRAM COMMITTEES

OG SESSIONS
R. Mewaldt, Chm.
G. Cassiday
C. Fichtel
A. Harding
J. Matteson
D. Muller
W. Webber

SH SESSIONS
M. Forman, Chm.
H. Hudson
G. Mason
B. McKibben
M. Pomerants

HE SESSIONS
T. Gaisser, Chm.
K. Lande
J. Linsley
E. Loh
G. Yodh

PUBLICATIONS
F. Jones, Chm.
J. Adams
G. Mason

LOCAL ORGANIZING COMMITTEE

L. Peterson,Chm.
G. Burbidge
R. Lingenfelter
R. Rothschild
J. Arnold
W. Baity
A. Buffington
M. Burbidge
W. Fillius
R. Gall
R. Gould
H. Hudson
J. Linsley
K. Marti
G. Masek
J. Matteson
C. McIlwain
R. Mewaldt
O. Piccioni
M. Thiemens
W. Thompson
H. Ticho
R. White

Sponsored by
National Aeronautics and Space Administration
National Science Foundation
Department of Energy
Center for Astrophysics and Space Science, University of California, San Diego
California Space Institute, University of California
Department of Physics and Astronomy, University of Maryland, College Park

Preface to the OG Volumes

The contributed papers presented at the 19th International Cosmic Ray Conference were arranged into three major divisions: OG (for cosmic ray and γ-ray Origin and Galactic phenomena); SH (for Solar and Heliospheric phenomena); and HE (for High Energy phenomena). The OG division encompasses topics related to the origin of galactic cosmic rays and γ-rays, the nature and distribution of their sources, and their interactions with galactic fields and matter. Contributed papers for OG sessions were organized under the following headings:

OG1 γ-ray Bursts
OG2 γ-rays from Point Sources
OG3 Diffuse γ-ray Emission
OG4 Cosmic Ray Nuclei with <1 TeV (Composition, Spectra, and Anisotropy)
OG5 Cosmic Ray Nuclei with >1 TeV (Composition, Spectra, and Anisotropy)
OG6 Electrons, Positrons, and Antiprotons
OG7 Interstellar Propagation and Nuclear Interactions
OG8 Cosmic Ray Sources and Acceleration
OG9 Techniques and Instrumentation

Note that the present OG division is broader than in the past; it includes papers from both the OG and XG divisions at previous International Cosmic Ray Conferences, as well as many papers previously in the T division.

Approximately 400 preliminary abstracts were received under the OG headings listed above. These were organized into 32 contributed paper sessions for purposes of oral presentation. Papers and confirming abstracts for OG papers are contained in Volumes 1, 2, and 3 of these Proceedings. Volume 1 contains papers under headings OG1, OG2, and OG3; Volume 2 contains OG4, OG5, and OG6; while OG7, OG8, and OG9 are contained in Volume 3. Papers on topics of related interest appear in the SH proceedings (Volumes 4 and 5) and the HE proceedings (Volumes 6, 7, and 8).

Four rapporteur speakers were invited to review the OG contributed paper sessions and report on new results and developments, areas of controversy, and future research directions. The written versions of these papers will appear in a later volume of these proceedings, along with other invited papers.

I wish to thank the other members of the OG Program Committee for their help in defining the OG topics, in reading the abstracts and organizing the sessions, and for their advice on the selection of rapporteur, highlight, and invited speakers. Members of the committee include: G. L. Cassiday, Jr. (University of Utah); C. E. Fichtel and A. K. Harding (Goddard Space Flight Center); R. E. Lingenfelter and J. L. Matteson (University of California at San Diego); D. Muller (University of Chicago); and W. R. Webber (University of New Hampshire).

Richard A. Mewaldt
Chairman, OG Program Committee

This conference is the 19th in a series. Previous conferences in this series were held at:

Cracow, Poland	–	1947
Como, Italy	–	1949
Bagneres-de-Bigorre, France	–	1953
Guanjuato, Mexico	–	1955
Varenna, Italy	–	1957
Moscow, USSR	–	1959
Kyoto, Japan	–	1961
Jaipur, India	–	1963
London, UK	–	1965
Calgary, Canada	–	1967
Budapest, Hungary	–	1969
Hobart, Australia	–	1971
Denver, USA	–	1973
Munchen, FRG	–	1975
Plovdiv, Bulgaria	–	1977
Kyoto, Japan	–	1979
Paris, France	–	1981
Bangalore, India	–	1983

OG 7.1
PROPAGTION AND SOURCES OF ULTRA HEAVY NUCLEI

VOLUME 3

OG 7.2
COSMIC-RAY PROPAGATION

OG 8.1
SHOCK ACCELERATION: THEORY AND ASTROPHYSICAL SCENARIOS

VOLUME 3

OG 8.2
COSMIC-RAY SOURCES AND ACCELERATION

OG 8.3
COSMIC-RAY ACCELERATION AND TRANSPORT

OG 9.1
COSMIC-RAY INSTRUMENTS AND TECHNIQUES

OG 9.2
GAMMA-RAY TELESCOPES

OG 9.3
TECHNIQUES IN GAMMA-RAY ASTRONOMY

OG 9.4
NEW AIR-SHOWER ARRAYS

OG 9.5
AIR-SHOWER TECHNIQUES

VARIATIONS IN THE PROPAGATION OF UH-NUCLEI

C. J. Waddington, N. R. Brewster, and M. P. Kertzman

School of Physics and Astronomy, University of Minnesota
116 Church St. S.E., Minneapolis, Minnesota 55455, U.S.A.

Abstract. We have investigated the sensitivity of the predictions of a model of the propagation of UH-nuclei in the interstellar medium on various assumptions.

1. Introduction. At the Paris Conference we reported, Brewster et al. (1981) our initial calculations on the propagation of UH-nuclei, using a leaky box formalism. These results have been discussed in more detail elsewhere, Brewster et al. (1983a). We have since improved this calculation by extending the number of individual nuclides considered, as well as using more recent evaluations of the rigidity dependence of the escape length, the possible source composition, and altered cross sections. We have also considered the effects of using different expressions for the dependence of abundances on first ionization potentials (FIP). In this paper we discuss the sensitivity of the calculated elemental abundances to the various changes made in the propagation assumptions. Details are available in Brewster (1985) and Brewster et al. (1985).

2. Modifications. The number of nuclides considered has been essentially doubled from 580 to 1316 and now includes virtually every one with $26 \leq Z \leq 83$ listed in the "Chart of the Nuclides" (as well as the longest-lived isotopes of Th and U). Those added were all short-lived, and so their production probabilities were included in the cross sections for the production of their final decay products. This has the effect of increasing the partial production cross sections for all the long-lived nuclides, and thus increasing secondary-to-primary abundance ratios.

Another change was in the dependence on rigidity, R, of the mean escape length, λ_{esc}. A recent analysis by Ormes and Protheroe indicates a steeper dependence on rigidity than the $R^{-0.4}$ we used previously. This dependence is expressed as:

$$\lambda_{esc}\ [g/cm^2] = (26.9)[1 + (1.88/R)^2]^{-3/2}\ R^{-0.7}, \quad R < 11.4\ GV$$
$$= (25.8)\ R^{-0.7} \quad R > 11.4\ GV$$

normalized to $\lambda_{esc} = 6.0\ g/cm^2$ at a kinetic energy of T = 5 GeV/nucleon. The constants in front allow for propagation in a hypothetical interstellar medium (ISM) composed of pure hydrogen. As a consequence of making this change we have also used a different injection spectrum, $dJ/dT \sim R^{-2.0}$ rather than $\sim R^{-2.3}$, as is required for consistency with the observed rigidity spectra of $R^{-2.7}$.

Another modification introduced is a change in the assumed solar system source abundances, which is not a change in the propagation model as such. We now use the Anders and Ebihara (1982) abundances, rather than the earlier Cameron (1982) compilation.

Cosmic ray propagation models generally use the semi-empirical formulas of Silberberg and Tsao (1973, 1977) to calculate the partial, $d\sigma$, and total, σ_T, cross sections needed for the model. These $d\sigma$ and σ_T values have been adjusted by "scaling" from the measured $d\sigma$ values of Au-nuclei observed at the Bevalac, Brewster et al. (1983b).

3. Effects of the Modifications. The effects of making these modifications are demonstrated in the Table for the abundances of various selected elements relative to 10^6 Fe-nuclei and several abundance ratios. Column (1) shows the predicted abundances near earth as calculated by Brewster et al. (1983a), based on the Cameron (1982) solar system abundances at the source. Column (2) shows the effect of increasing the number of nuclides while (3) shows the percentage change due to this modification. As expected, using the larger set of nuclides increases the abundances of almost all the elements relative to iron, since all the partial cross sections were increased. The difference is greatest for the most secondary species like Z = 70. In this table we have also defined various ratios of groups of elements. It should be noted that elements with $44 \leq Z \leq 48$, $62 \leq Z \leq 69$, and $70 \leq Z \leq 74$ are presumed to be predominately, although not purely, secondary in origin, whereas the others are mostly primary, originating in the source.

Table: Abundances and abundance ratios (see text)

	Original	All Nuclides	%	A&E	%	Exp FIP	$R^{-0.7}$	%	Step FIP	%	Scaling	%
Z	(1)	(2)	(1)-(2) (3)	(4)	(2)-(4) (5)	(6)	(7)	(4)-(7) (8)	(9)	(4)-(9) (10)	(11)	(7)-(11) (12)
38	27	26	-4%	26	0%	46	46	77%	26	0%	48	4%
46	3.2	4.2	31%	4.0	-5%	4.2	4.1	3%	3.2	-20%	4.9	20%
50	5.5	6.7	22%	6.3	6%	7.1	7.1	13%	5.1	-19%	8.4	18%
52	6.0	6.6	10%	5.2	-21%	4.6	4.6	-12%	2.3	-56%	5.4	17%
56	3.9	4.3	10%	4.0	-7%	7.9	8.0	100%	4.0	0%	9.4	18%
70	.27	.51	89%	.57	12%	.64	.64	12%	.54	5%	1.1	72%
78	.90	.95	6%	.95	0%	.74	.75	-21%	.95	0%	1.0	33%
82	1.5	1.5	0%	1.8	20%	2.0	2.1	17%	1.8	0%	2.4	14%
N_1/N_2												
$\frac{N\ (44\leq Z\leq 48)}{N\ (50\leq Z\leq 58)}$	.56	.59	5%	.61	3%	.57	.56	-8%	.75	23%	.56	0%
$\frac{N\ (62\leq Z\leq 69)}{N\ (75\leq Z\leq 83)}$	.52	.73	40%	.67	-8%	.86	.84	25%	.68	1%	1.1	31%
$\frac{N\ (70\leq Z\leq 74)}{N\ (75\leq Z\leq 83)}$	.24	.35	46%	.31	-11%	.34	.33	6%	.31	0%	.45	36%
$\frac{N\ (80\leq Z\leq 83)}{N\ (75\leq Z\leq 79)}$	.85	.80	-6%	.99	24%	1.3	1.3	31%	.97	-2%	1.1	-15%

The effect of using the Anders and Ebihara (1982) abundances is shown in Column (4) with the resulting percentage changes shown in (5). These changes are entirely due to the differences between the two abundance compilations and while significant are relatively minor.

The application of corrections for the apparent dependence of source abundances on FIP are shown in the next few columns. Column (6) shows the effect of an exponential FIP dependence of the form $f = 9.32 \exp(-0.288I)$, so $f = 1.0$ for a potential, I, of I = 7.75 eV, while (9)

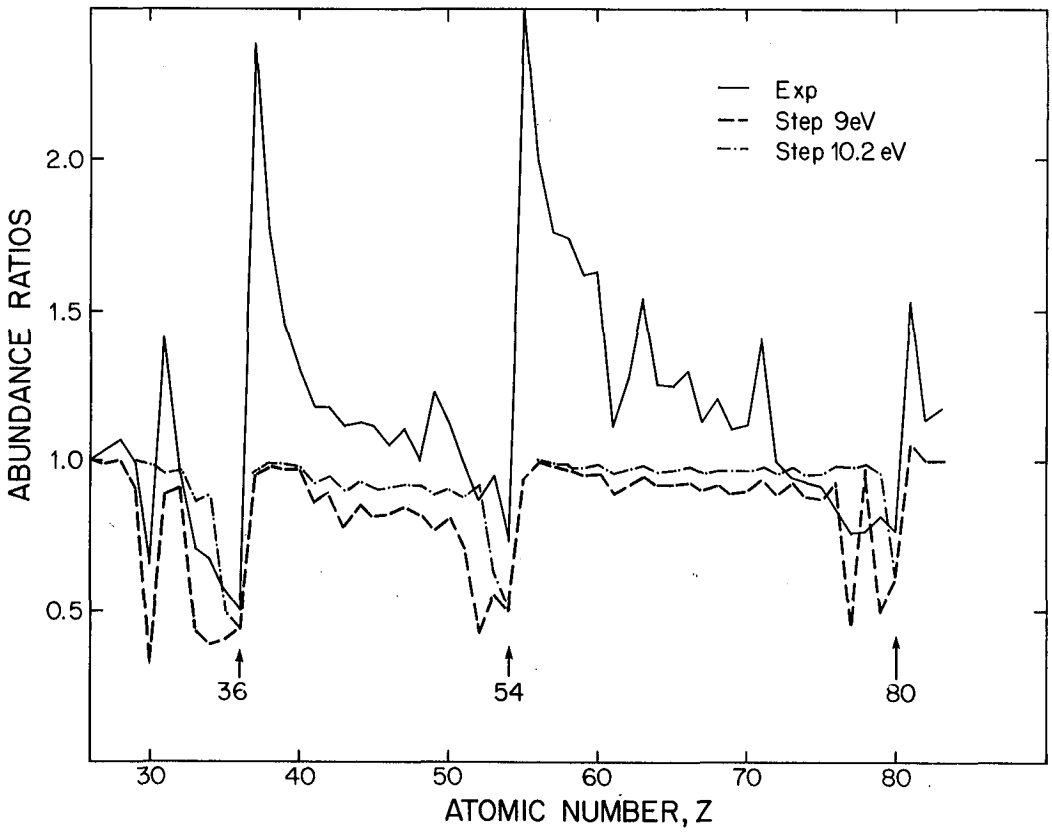

Fig. 1. The ratio of the abundances of a solar system source after propagation, with and without the application of a FIP correction, as a function of the atomic number Z.

shows that of a step dependence with f = 1 for I ≤ 9 eV and f = 0.3 for I > 9 eV. Column (7) shows the very minor effect of changing the rigidity dependence. The differences between no FIP correction and exponential or step FIP dependence are shown in Columns (8) and (10) respectively. There is clearly a strong effect, both on FIP and on which FIP dependence is assumed. This can be more clearly seen in Fig. 1, which shows the Z dependence of the abundance changes and illustrates the fact that a step FIP dependence, unlike the exponential dependence, never increases the abundances significantly, but only depletes them. Figure 1 also shows the effects of a FIP dependence with a step at 10.2 eV, the Lymann H_α, which while not a good fit to the abundance ratios if standard solar abundances are assumed, is reasonable if C2 chondritic meteorite abundances are assumed, Binns et al. (1984). This higher energy step can be seen to still further reduce the effect of applying a FIP correction.

The differences between these various FIP dependencies are large enough that it should be possible to test them by examining data in the $32 \leq Z \leq 42$ and $50 \leq Z \leq 60$ charge ranges. For example, the large relative abundances of ^{38}Sr and ^{56}Ba reported from the HEAO C3 experiment, Binns et al. (1981, 1983), both appear to imply that the exponential FIP dependence is a better representation than the step dependencies unless

the source abundances are quite anomalous.

The effects on the exponential FIP abundances of adjusting the σ_T and $d\sigma$ values, by scaling the predicted values on the basis of those observed for Au-nuclei, Brewster et al. (1983b), are shown in Column (11). The scaling factors used for $d\sigma$ are shown in Fig. 2 as a function

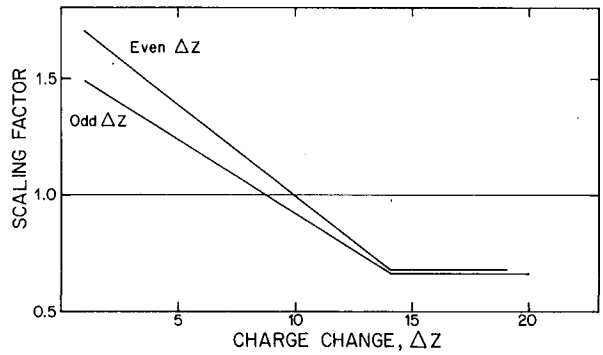

Fig. 2. The scaling factor applied to the predicted cross-sections as a function of ΔZ.

of the charge change, ΔZ, and can be seen to increase $d\sigma$ values for small ΔZ and decrease them for large ΔZ. Column (12) shows the percentage changes between (7) and (11) and can be seen to be always positive, reflecting the greater importance of small charge changes in the propagation process. The recent observations reported elsewhere at this conference, Kertzman et al. (1985; OG 7.2-21), on the interactions of other heavy nuclei show that these scaling factors are strongly Z dependent and hence that the application of the Au-results to other primary nuclei is probably not justified, see e.g. the recent Pb/Pt results also reported at this conference, Waddington et al. (1985; OG 4.4-7).

4. Acknowledgements. This work was supported in part by NASA under grants NGR 24-005-050 and NAG8-500. We are indebted to P. S. Freier for her comments and interest, and to M. H. Israel and E. C. Stone for useful comments.

References

Anders, E., and Ebihara, M. (1982), Geochimica et Cosmochimica Acta, **46**, 2363.
Binns, W. R., et al. (1981), Ap. J. **247**, L115.
Binns, W. R., et al. (1983), Ap. J. **267**, L93.
Binns, W. R., et al. (1984), COSPAR Symposium.
Brewster, N. R. (1985), Ph.D. Thesis, Univ. of Minn.
Brewster, N. R., Freier, P. S., and Waddington, C. J. (1981), 17th ICRC, **Vol. 9**, 126.
_____. (1983a), Ap.J. **264**, 324.
_____. (1985), to be published in Ap.J., July 1.
Brewster, N. R., et. al. (1983b), Proc. 18th ICRC, **9**, 259.
Cameron, A. G. W. (1982), Essays in Nuclear Astrophy., ed. C. A. Barnes, Cambridge U. Press.
Kertzman, M. P., et al. (1985), this conf., Paper OG 7.2-21.
Ormes, J. F., and Protheroe, R. J. (1983), Ap.J. **264**, 324.
Silberberg, R., and Tsao, C. H. (1973), Ap. J. Suppl. **25**, 335.
_____. (1977), Proc. 15th ICRC, **2**, 84.
Waddington, C. J., et al. (1985), this conf., Paper OG 4.4-7.

GERMANIUM AND LEAD : SIGNIFICANT DIFFERENCES BETWEEN METEORITIC AND PHOTOSPHERIC ABUNDANCES ?

Nicolas GREVESSE
Institut d'Astrophysique, Université de Liège, Belgium

Jean-Paul MEYER
Service d'Astrophysique, Centre d'Etudes Nucléaires de Saclay, France

1. Introduction. A key question at present is whether the Galactic Cosmic Ray Source (GCRS) composition is ordered in terms of First Ionization Potential (FIP) (in which case the GCRS composition resembles that of the Solar Corona and of Solar Energetic Particles (SEP)/11,12,31,33,39/, and GCR's have probably been first injected by flaring F to M stars /33/), or in terms of volatility (in which case GCR's must be largely interstellar grain destruction products and their similarity to SEP's is purely fortuitous /10,15,4/).

The problem is that, for most elements, the degree of volatility is (positively) correlated with the value of the FIP, so that it is not easy to distinguish a correlation of GCRS abundances anomalies with FIP from a correlation with volatility. Only a few volatile, though low-FIP, elements that are exceptions to the general rule permit to distinguish between the two kinds of ordering : if they are depleted relative to refractory metals, volatility must be relevant, if not, FIP is relevant /32/. Among them Cu (semi-volatile ; not depleted) and Zn (very volatile; only slightly depleted in accordance with its intermediate FIP) would seem to favour FIP. But among the best indicators are Ge and Pb.

Surprizingly enough, Ge and Pb have recently been found deficient relative to refractory elements with similar FIP /6,7,23,16,8,28,17,18/. Is this observation compelling, in the sense that volatility must indeed be the key parameter ?

The abundance anomalies in GCRS are defined relative to a standard which, for the heavy elements concerned, is commonly taken as C1 Carbonaceous Chondrites. While for most elements C1's are certainly not far from being an unbiased sample of the protosolar nebula (their morphology makes it plausible ; good agreement with photosphere whenever check possible ; continuity of abundances beyond Fe), we do not know precisely to within which accuracy this is the case, especially for volatile elements /1,29, 30,2,14,20,21/. Photospheric abundances, though often less accurately determined, are certainly more directly representative of the protosolar nebula, and hence of ordinary local galactic (LG) matter. (As regards C2 carbonaceous chondrites, which are a mixture of 50% C1-like material, plausibly unfractionated, and of 50% highly fractionated material, there is no reason whatsoever to believe that their bulk composition might have any relevance as a standard /1,29,30,2,14/.)

Here we shall more closely look into the Ge and Pb reference abundance determinations in the Photosphere and in C1 meteorites, and discuss their relevance to the problem of FIP vs. volatility in GCR's.

2. The meteoritic and photospheric abundances of Germanium. The Ge abundance in C1's is very reproducible /14/, and the value for C1's quoted in /2/, Ge = 118 (1.10), should therefore be reliable (fig. 1; see Table 1 for notations).

On the other hand, photospheric abundance measurements have now reached a high degree of accuracy for those elements for which well measurable lines are present in the solar spectrum and accurate atomic data are available. The systematic, model dependent errors, as well as the errors related to departure from LTE, have indeed been reduced to the few % level. With the Holweger-Müller model atmosphere and a microturbulence parameter ~ 0.85 km/s, a high degree of consistency is obtained from a very large number of lines sampling wide ranges of wavelengths, optical depths, and excitation temperatures. In particular, various lines of different ionization states of particular elements, as well as molecular lines, yield very closely consistent abundances. These points are discussed in /20/.

As regards Ge in the photosphere, see /25,35/ for previous studies, and revisions by /5,20/. Five GeI lines can be identified in the solar spectrum : λ3039, 3124, 3269, 4226 and 4685 Å. The λ3124 and 4226 lines are too strongly blended to be of any use. We are thus left with three lines.

In Table 1 we give the measured equivalent widths W_λ . The value for the λ 3039 UV line is based on the spectrum of /35/, which is of good quality. But the line is quite perturbed, partly by an unidentified feature. The λ 3269 line is much less perturbed, and the W_λ value can accordingly be determined much more precisely (see fig. in /35/). Values obtained from older Jungfraujoch spectra, from /35/ and from the atlas of /13/ agree within 4%. As for the blue λ 4685 feature, the atlas of /13/ yields an extremely precise value of $W_\lambda = 5.5 \pm 0.2$ mÅ. But there are two problems. First, the feature is the sum of the Ge I and of a Co I line at about the same wavelength. The Co I contribution to W_λ can be estimated quite reliably to W_λ (Co I) $= 1.5 \pm 0.4$ mÅ based on the accurate transition probabilities of /9/. We are left with W_λ (GeI) $= 4.0 \pm 0.5$ mÅ for the contribution of Ge to the feature. In addition, the λ 4685 feature shows a slight asymmetry on the red side, which implies an unidentified blend. The above value of W_λ is therefore an upper limit to the true W_λ (GeI).

The oscillator strengths log gf given in Table 1 are based on branching ratio measurements by /26/ normalized to beam foil lifetime measurements. They should be accurate to within 20%.

Our adopted photospheric Ge abundance, Ge = 72 (1.38)(Table 1, Fig.1) is lower than the C1 value by a factor of 0.61 (1.40).

3. The meteoritic and photospheric abundances of Lead. The abundance of Pb in C1's is rather well defined : Pb = 3.15 (1.08) /2/ (Table 2, fig.2).

As regards the photosphere, see /36, 25, 19/, and especially /22/ for previous studies. Five Pb I lines can be identified in the solar spectrum : λ 3639, 3683, 3739, 4057 and 7229 Å. The latter two are extremely doubtful. The λ 3639 and λ 3739 lines will be considered, but they are seriously blended with much more intense lines. Only the λ 3683 line is a really good abundance indicator (see fig. in /19/).

In Table 2 we give the equivalent widths W_λ obtained on the atlas of /13/. The λ 3683 value is in excellent agreement with earlier determinations /19/. The other two values are very uncertain, and the previous determinations indeed diverge.

The oscillator strengths log gf given in table 2 are based on lifetime measurements for several Pb I states (to within 5%) combined with branching ratio measurements (to within 8%) by /27/. The overall accuracy is 10%. The validity of the data is confirmed by the relative

oscillator strengths measurements of /34/ which agree within 0.7% with /27/ for the ratio of the gf values for the λ 3683 and 3639 lines.

Our adopted photospheric Pb abundance, Pb = 1.97 (1.12) (Table 2, fig.2) is lower than the C1 value by a factor of 0.63 (1.15).

4. General discussion of photospheric vs. C1 abundances. We have found that the photospheric abundance determinations of both Ge and Pb are lower than their C1 abundance. How does this fit into a more general comparison between C1 and photospheric abundances ? Ge is a moderately volatile element ($T_{cond} \approx 900$ K), and /2/ consider that elements of this class may be on average ~ 25% lower in the Photosphere than in C1's. But the agreement between Photosphere and C1's is generally improved in the updated assessment of /20/. The smoothness of the abundance curve of odd-A (r+s) isotopes vs. mass in the Ga,Ge,As,Se region, as derived from C1 data, tends to support the C1 value for Ge /1,29,2/. The situation is,

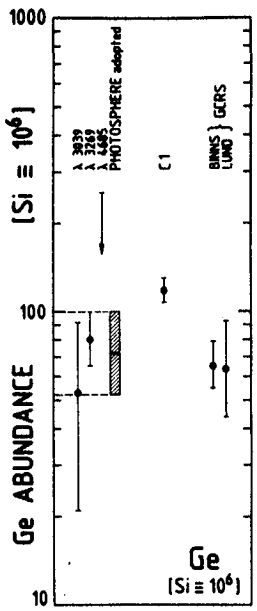

Fig.1

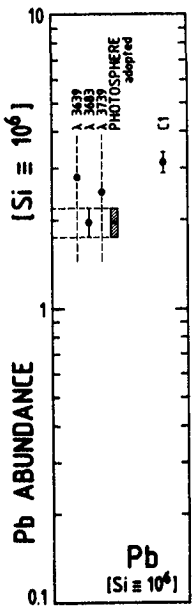

Fig.2

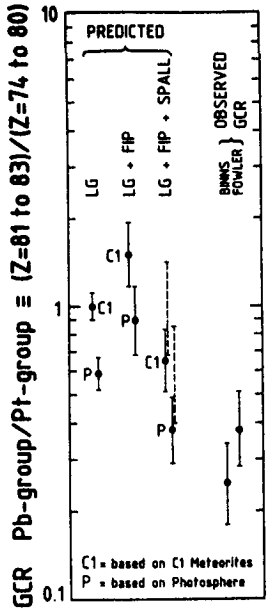

Fig.3

Table 1 - Photospheric and meteoritic abundances of Germanium

Line [Å]	W_λ [mÅ]	log gf	$\log N_{Ge}$ [$\log N_H$=12]	Ge [Si=10^6]
3039	$61.5^{+8.5}_{-11.5}$	0.017 ± 0.080	$3.28^{+0.24}_{-0.40}$	53.(1.74 / 2.51)
3269	43.3 ± 1.3	-0.921 ± 0.080	3.46±0.09	80.(1.23)
4685	< 4.0 ± 0.5	-2.013 ± 0.080	<3.86±0.10	<202.(1.26)
Adopted Photospheric			3.41±0.14	72.(1.38)
Meteoritic C1			3.63±0.04	118.(1.10)

Notations : In parenthesis : error factors ; "log N_{Ge}": scale log N_H= 12; "Ge" : scale Si = 10^6, based on log N_{Si}=7.555 /20/.

Table 2 - Photospheric and meteoritic abundances of Lead

Line [Å]	W_λ [mÅ]	log gf	$\log N_{Pb}$ [$\log N_H$=12]	Pb [Si=10^6]
3639	[6.4]	-0.700±0.040	[2.00]	[2.8]
3683	7.7±0.4	-0.513±0.040	1.85±0.05	1.97 (1.12)
3739	[0.8]	-0.117±0.040	[1.96]	[2.5]
Adopted Photospheric			1.85±0.05	1.97 (1.12)
Meteoritic C1			2.05±0.03	3.15 (1.08)

Notations : see Table 1 ; [ ]: highly doubtful.

however, not simple as regards r and s nucleosynthesis in this range of mass /24/. As regards Pb, it is a highly volatile element ($T_{cond} \approx 400$ K) for which fractionation could easily take place in C1's. For highly volatile elements, the observed C1/photospheric ratios scatter a lot /2,20/. The scatter may be real, or be due to poor photospheric determinations. To muddle up the situation a little more, note also the totally unexpected but probably reliable overabundances of Fe and Ti by ~ 45% and 25% in the photosphere relative to C1's, while the agreement between photospheric and C1 data is very close for all neighbouring elements, both refractory and siderophile /20,21/.

5. Discussion of the Cosmic-Ray Ge and Pb abundances. GCRS abundances of Ge = 66 (1.19) and 64 (1.45) relative to Si = 10^6 have been obtained by /7/ and /28/. It is obvious from fig. 1 that these values, while low with respect to the C1 abundance of Ge, are prefectly consistent with its photospheric abundance relative to Si and other low FIP metals.

As regards Pb, we shall compare the (Pb-group)/(Pt-group) = (Z=81 to 83)/(Z=74 to 80) ratio observed in GCR's to that predicted near earth, starting from LG abundances based on, either meteoritic, or photospheric data. The LG abundances for the Pt-group and the Pb-group are respectively 3.46 (1.07) and 3.47 (1.08) based on meteorites, and 3.88 (1.08) and 2.29 (1.11) based mainly on the photosphere (Si = 10^6) /2,20,21,this paper,3,38/. So the LG Pb-group/Pt-group ratio is 1.00 (1.11) based on meteorites and 0.59 (1.14) based on the Photosphere (fig.3). Applying a bias related to FIP enhances this ratio by a factor of 1.50 (1.25) /33/ (fig.3). Taking into account spallation in the interstellar medium and instrumental effects on the HEAO-C3 data reduces the predicted observable ratio by a factor of ~0.43 /7/ (fig.3). (Pure interstellar spallation calculations by /37/ yield a reduction by a factor of 0.58 to 0.73, depending on the model, the models with the larger reductions being favoured in view of the high fluxes of nuclei in the range Z=61 to 75 ; dashed on fig. 3). The ratios obtained might be compared with the observed ratios 0.25 (1.35) by /7/ and 0.38 (1.33) by /18/. It is clear from fig. 3 that the data are inconsistent with the FIP hypothesis if C1 meteorites are taken as a standard, but are not inconsistent if photospheric values are adopted instead.

6. Conclusion. There is an apparently significant discrepancy between the photospheric and the C1 abundances of Ge and Pb. The Ge and Pb abundances in GCR's are consistent with the ordering in terms of FIP if referred to the photospheric values.

References

1. Anders, E. 1971, GCA,35,516.
2. Anders, E. et al. 1982, GCA 46,2363
3. Beer, H. et al. 1982, Astr.Ap. 105,270
4. Bibring, J.P. et al. 1981, 17th ICRC,Paris,2,289
5. Biémont, E. et al. 1977, Phys. Scripta 16,39
6. Binns, W.R. et al. 1983, 18th ICRC,Bangalore,9,106
7. Binns, W.R. et al. 1984,Adv. Space Res. 4,N°2-3,25
8. Byrnak, B. et al. 1983,18th ICRC,Bangalore, 2, 29
9. Cardon, B.L. et al. 1982, Ap.J. 260, 395
10. Cesarsky, C.J. et al. 1980, IAU Symp.N°94, Origin of Cosmic Rays, G. Setti et al. ed., p.361
11. Cook, W.R. et al. 1980, Ap.J. Letters 238, L97
12. Cook, W.R. et al. 1984, Ap. J. 279, 827
13. Delbouille, L. et al. 1973, Atlas of the Solar Spectrum, Université de Liège
14. Ebihara, M. et al. 1982,GCA 46, 1849
15. Epstein, R.I. 1980, MNRAS 193, 723
16. Fixsen, D.J. et al. 1983, 18th ICRC,Bangalore,9,119
17. Fowler, P.H. et al. 1983, 18th ICRC,Bangalore,9,110
18. Fowler, P.H. et al. 1984, 9th European Cosmic Ray Symp., Kosice
19. Grevesse, N. 1969, Solar Phys. 6, 381
20. Grevesse, N. 1984a, Phys. Scripta T8, 49
21. Grevesse, N. 1984b, in Frontiers of Astr. & Ap.,ed. R. Pallavicini (Florence : Ital. Astr.Soc.), p.71
22. Hauge, O. et al. 1973, Solar Phys. 30, 301
23. Israel, M.H. et al. 1983, 18th ICRC,Bangalore,9,305
24. Kappeler, F. et al. 1982, Ap.J. 257, 821
25. Lambert, D.L. et al. 1969, MNRAS 142, 88
26. Lotrian, J. et al. 1978, J.Phys. B 13,2273
27. Lotrian, J. et al. 1979, JQSRT,21, 143
28. Lund, N. 1984, Adv. Space Res. 4, N°2-3,5
29. Meyer, J.P. 1979a, "Les Eléments et leurs Isotopes dans l'Univers" (U. of Liège Press), p.153
30. Meyer, J.P. 1979b, 16th ICRC, Kyoto, 2, 115
31. Meyer, J.P. 1981a, 17th ICRC, Paris, 2, 265
32. Meyer, J.P. 1981b, 17th ICRC, Paris, 2, 281
33. Meyer, J.P. 1985, Ap.J. Suppl. 57, 173
34. Muradov, V.G. et al. 1982, Opt.Spec.(USSR) 52, 252
35. Ross, J.E. et al. 1974, Solar Phys. 35, 281
36. Ross, J.E. et al. 1968, Proc.Natl.Acad.Sci. 59, 1
37. Tsao, C.H. et al. 1983, 18th ICRC,Bangalore, 2, 225
38. Walter, G. et al. 1983, Astr. Ap. 123, 279
39. Webber, W.R. 1982, Ap.J. 255, 329

LEAD AND URANIUM GROUP ABUNDANCES IN COSMIC RAYS

Yadav, J.S. and Perelygin V.P.*
Tata Institute of Fundamental Research, Bombay 400005,India

*Joint Institute for Nuclear Research, Dubna, Moscow, USSR.

ABSTRACT

In the light of Ariel-VI and HEAO-3 ultra heavy cosmic ray experiment results, the importance of Lead and Uranium group abundances in cosmic rays is discussed in understanding their evolution and propagation. The electronic detectors can provide good charge resolution but poor data statistics. The plastic detectors can provide somewhat better statistics but charge resolution deteriorates. The extraterrestrial crystals can provide good statistics but with poor charge resolution. Recent studies of extraterrestrial crystals regarding their calibration to accelerated Uranium ion beam and track etch kinetics are discussed in this paper and it is hoped that a charge resolution of two charge units can be achieved provided an additional parameter is taken into account. The prospects to study abundances of Lead group, Uranium group and superheavy element in extraterrestrial crystals are discussed, and usefulness of these studies in the light of studies with electronic and plastic detectors is assessed.

1. Introduction. The high energy resolution UH experiments Ariel-VI and HEAO-3 have given the following important conclusions [1,2]: (a) There is no strong evidence for r-process dominance in the cosmic ray source in the charge region $Z < 60$. In this charge region the cosmic ray source composition looks like that of the solar system with a first ionization potential bais or possible some s-process enhancement. (b) The lead group abundance data appear to show r-process dominance in this charge region (Peak at platinum), and (c) The abundances of actinides is much lower than measured in earlier experiments [3,4,5].

The HEAO-3 results of actinide abundances are quite consistent with a source with solar system like composition [1]. However, with the precision of the results based on

one possible actinide event (or three if HEAO-3 and Ariel-VI data is combined) one can not exclude substantial r-process enrichment or deficiency in cosmic ray source. Thus one needs an experiment with larger exposure factor to study actinide abundances. Further, the study of actinide abundances is important as it gives clear indication of r-process contribution. The s-process terminates at Bismuth (z = 83). The main problem in the study of actinide abundance is their very low flux. Following table gives the measured event rate of actinides and superheavy elements for a detector with exposure factor like HEAO-3.

Table 1 : Event Rate in a $5m^2$ sr Detector

	Actinide group	Superheavy elements
From HEAO-3 data	2/ year	-
From extraterrestrial crystal data*	2/ year	10^{-3}/ year**

* These rates are calculated with atleast 10% probability that tracks are completely inside the volume of the crystal revealed successfully. This also takes care of fragmentation of actinides in crystals.

** This is on the basis if observed 3 very long tracks are due to superheavy elements.

It is clear from the above table that one needs a detector with much larger exposure factor than combined HEAO-3 and Ariel-VI detectors to study actinide abundances. Further study of superheavy elements seems to be out of experimental reach at least at present. However, the abundances of actinides and superheavy elements can be studied in extraterrestrial crystals due to their very long exposure time provided their charge resolution is improved. Now we shall describe recent studies regarding track identification in crystals and assess the usefulness of studying UH cosmic ray abundances in extraterrestrial crystals.

2. Results and Discussion. In the recent past, olivine crystal has been exposed to accelerated Uranium beam and the track etch response has been studied[6]. In the further development, track etch kinetics in crystals has been described and the effect of etching time on track etch response and on volume etched track length (VETL) (track identifying parameter) is studied[7]. The VETL variation with etching time is shown in Fig. 1, for Uranium as well as superheavy element tracks.

Above study shows that a charge resolution of two charge unit can be achieved in crystals. However, the exposure of extraterrestrial crystals in adverse environment (not known exactly) will further deteriorate charge resolution [5]. Thus one can expect a charge resolution 3-4 charge units. Let us check the feasibility of extracting useful information regarding UH cosmic ray abundances from studies in extraterrestrial crystals with such charge resolution.

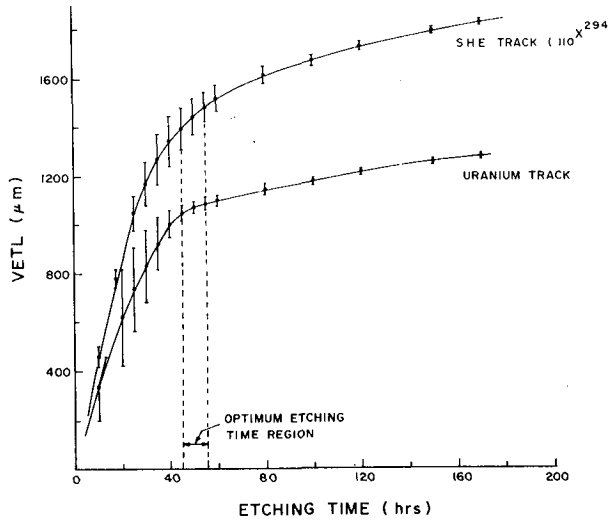

Fig.1 The VETL variation with etching time for Uranium as well as superheavy element tracks.

If we look at the abundances of UH nuclei in cosmic rays there are natural gaps between Lead and Uranium groups and between Uranium group and Superheavy elements. The elements in the charge region $84 < Z < 89$ have half lives that are typically less than a day and hence should be absent in the cosmic rays. Similarly in actinide group only Thorium, Uranium, Plutonium and Curium nuclei have half lines sufficiently large to allow them to survive in cosmic rays. The superheavy nuclei stability island[8] most probably starts at $Z > 110$. Thus it is quite feasible to extract useful informations about abundances of Lead group, Uranium group and Superheavy elements in cosmic rays from UH track studies in extraterrestrial crystals.

Further UH studies in extraterrestrial crystals will provide actinide abundances averaged over millions of years and hence can pin-point any substantial change in actinide abundances over this period. This can indicate continuous r-process in cosmic ray source or solar system like composition of cosmic ray source where r-process is stopped for the last few billions of years.

References

1. Fowler, P.H. et al. (1981), Nature, 291, 45.
2. Israel, M.H., Composition and Origin of Cosmic Rays (1983) Ed. M.M.Shapiro, NATO ASI series, 47.
3. Fowler, P.H. et al. (1977), 15th ICRC, 11, 165.
4. Perelygin, V.P. et al. (1977), Nucl. Track, 1, 199.
5. Shirk, E.K. and Price, P.B., (1978), Astrophys. J., 220, 719.
6. Perron, C.,(1984), Nature, 310, 397.
7. Yadav, J.S. et al. (1985), sent for publiccation in Nucl. Track.
8. Trautmann, N. (1981), Intern. Conf. on 'Actinides 81'.

IMPLICATIONS OF SOURCE ABUNDANCES OF ULTRAHEAVY COSMIC RAYS

W. R. Binns[a], T. L. Garrard[b], M. H. Israel[a], J. Klarmann[a],
S. H. Margolis[a], E. C. Stone[b], C. J. Waddington[c],
[a]Washington University, St. Louis, MO, USA
[b]California Institute of Technology, Pasadena, CA, USA
[c]University of Minnesota, Minneapolis, MN, USA

1. Introduction. In this paper we will examine the ratio of cosmic-ray source abundance to solar-system abundance for individual elements. In particular we will look at correlations of these ratios with first-ionization potential (FIP) and also with the expected mass-to-charge ratio (A/Q) of the elements in a million-degree plasma. We have previously examined the FIP correlation and shown that the correlation is affected by the choice of C2 or C1 chondritic meteorites as the solar-system standard for comparison (Binns, *et al.*, 1984). An A/Q correlation was suggested by Eichler and Hainebach (1981), as a consequence of their model of shock acceleration in the hot interstellar medium, and has been examined by Israel (1985). These correlations are presented in the following four figures.

2. Explanation of Figures. Figure 1 plots the ratio of cosmic-ray source to solar-system abundances, normalized to unity for Fe, as a function of the first ionization potential. Error bars indicate the quadratic sum of the error on the solar-system abundance and that on the cosmic-ray source abundance. The element symbols for the various points have been transferred directly below the point.

Cosmic-ray source abundances in all four figures are derived principally from observations on HEAO-3, except for H and He which come from balloon observations (Webber, 1982; Webber and Lezniak, 1974). Two H points are plotted; H(R) uses H abundances at the same rigidity as the other elements; H(E), at the same energy per nucleon. For $6 \leq Z \leq 27$, and for $Z = 29$ and 31 (Cu and Ga), the results are from the Danish-French experiment on HEAO-3 (Lund, 1984). For $Z = 28$ and 30 (Ni and Zn) and for $Z \geq 32$ the results are from the Heavy Nuclei Experiment (Israel, *et al.*, 1983). In each case experimental results were propagated back to the source in a standard leaky-box model.

In figures 1 and 3 the solar system abundances are from Anders and Ebihara (1982). These abundances are mainly from type C1 meteorites; except H, C, N, and O are from photospheric measurements, He is from the solar wind H/He ratio, Ne is from the solar wind Ne/Ar ratio and from astronomical measurements of extra-solar-system nebulae, and Ar, Kr, and Xe are interpolated from nearby elements. In figures 2 and 4 the C1 meteorite abundances are replaced by C2 meteorite abundances (Mason, 1979) in forming the solar-system values.

Figures 3 and 4 have the same ordinates as figures 1 and 2 respectively, but the abscissa is A/Q_{120}, where A is the atomic weight and Q_{120} is the charge state the element would have after removal of all electrons whose ionization potential is less than 120eV. Thus the abscissa is an estimate of the mass-to-charge ratio which the element would have in a million-degree interstellar gas. (The value 120 eV corresponds to a temperature of 1.4×10^6 K, but the correlation displayed here is insensitive to the precise value of ionization potential selected.)

The implications of these figures will be discussed at the conference.

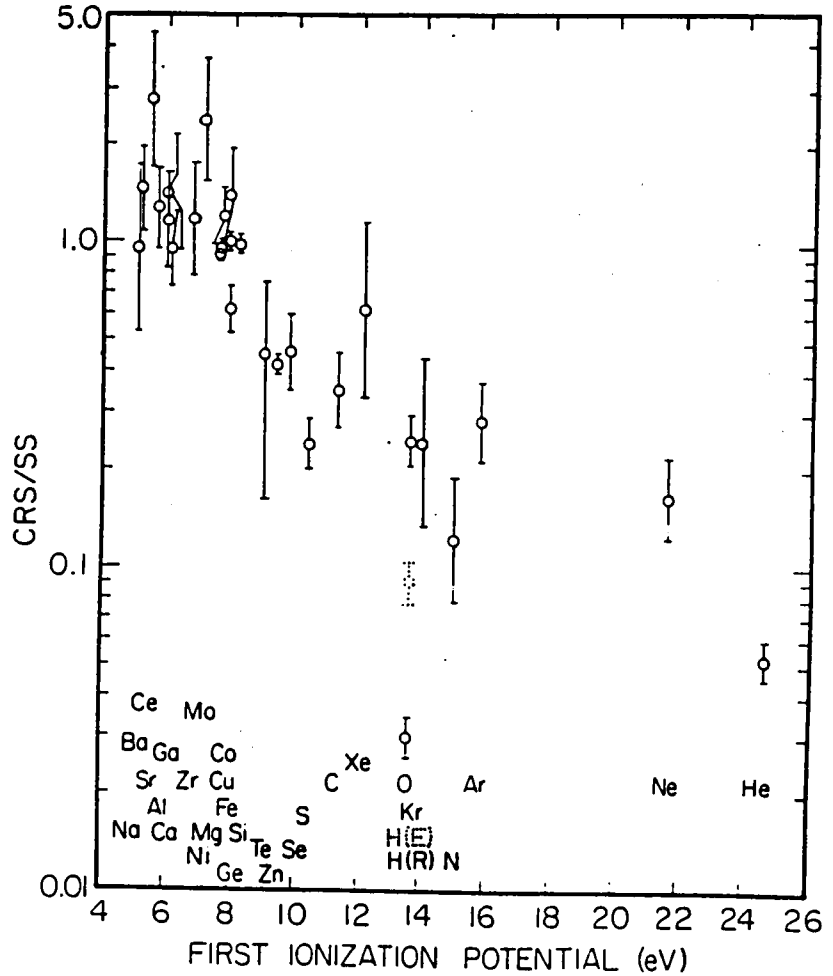

Figure 1

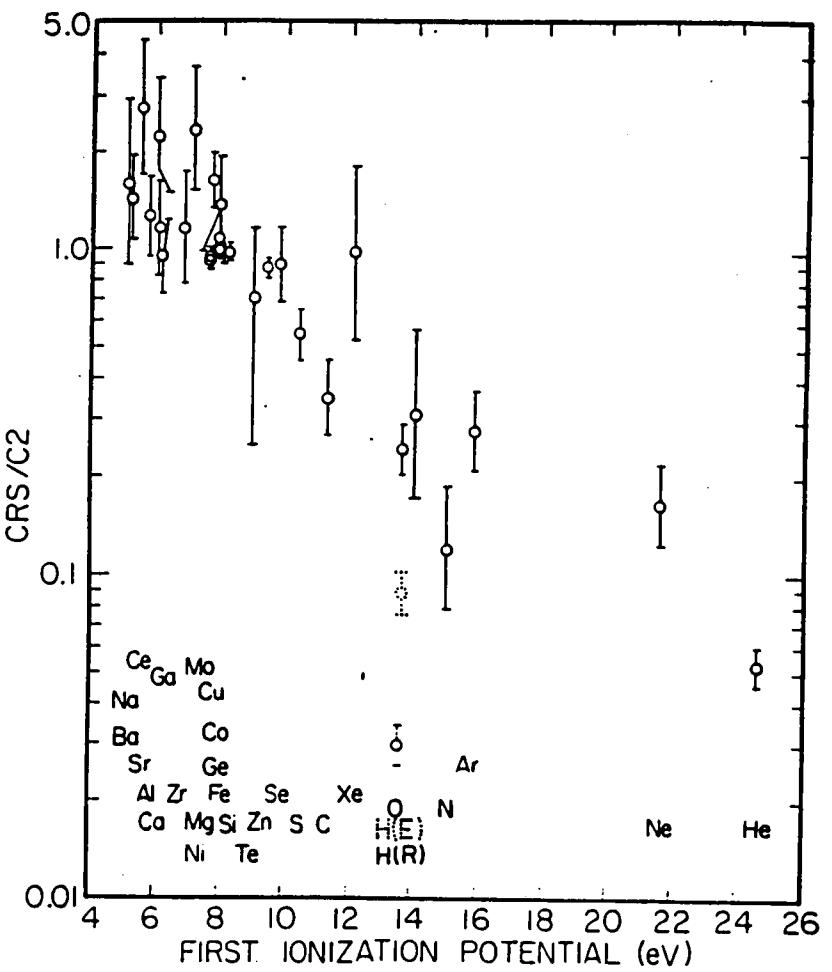

Figure 2

06 7.1-4

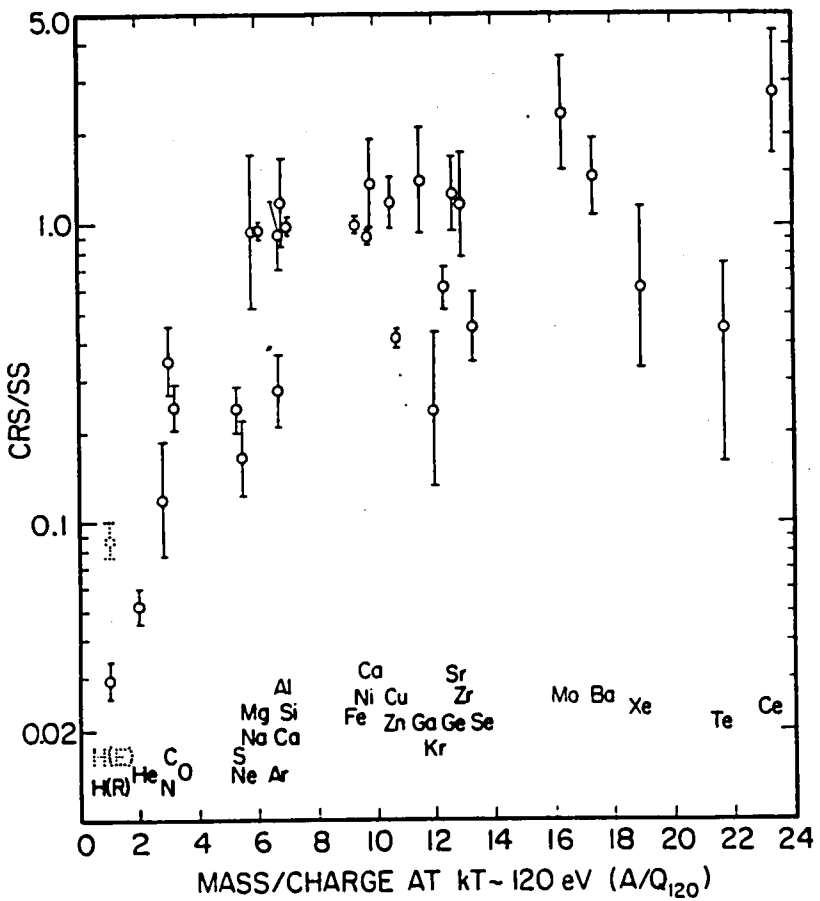

Figure 3

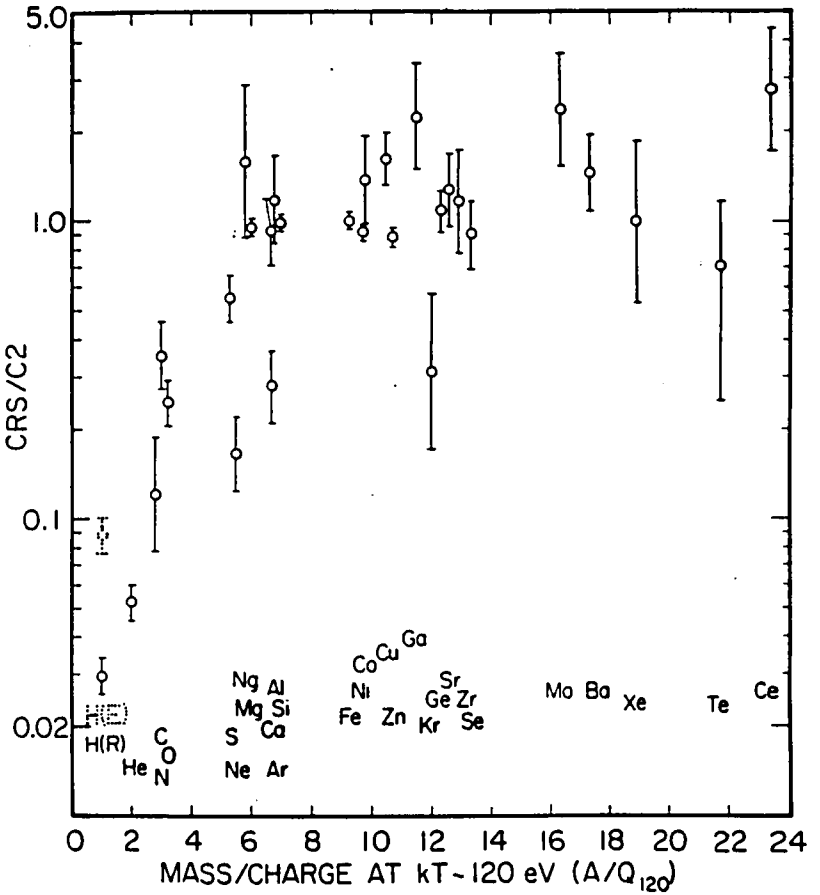

Figure 4

3. References.

Anders, E. and M. Ebihara, 1982, *Geochim. Cosmochim. Acta, 46,*, 2363.
Binns, *et al.*, 1984, *Adv. Space Res. 4*, (no. 2-3), 225.
Eichler, D. and K. Hainebach, 1981, *Phys. Rev. Lett. 47*, 1560.
Israel, M.H., 1985, *12th Texas Symp. Relativistic Astrophys.*, in press.
Israel, *et al.*, 1983, *18th ICRC, 9*, 305.
Lund, N., 1984, *Adv. Space Res. 4*, (no. 2-3), 5.
Mason, B., 1979, Geol. Survey Prof. Paper 440-B-1.
Webber, W.R., 1982, *Ap. J., 255,*, 329.
Webber, W.R. and J.A. Lezniak, 1974, *Ap. Space Sci., 30,*, 361.

OG 7.1-5

PROPAGATION AND NUCLEOSYNTHESIS OF ULTRAHEAVY COSMIC RAYS

M.Giler and T.Wibig
Institute of Physics, University of Łódź
90-236 Łódź, Nowotki 149/153,
Poland

1. Introduction. The observed fluxes of c.r. ultraheavy elements depend on their charge /and mass/ spectrum at the sources and on the propagation effects, namely on the distribution of path lengths traversed by the particles on their way from the sources to the observation point. We shall analyse the effect of different path length distributions /p.l.d./ on the infered source abundances. It seems that it is rather difficult to fit a reasonable p.l.d. so that the obtained source spectrum coincides with the Solar System /SS/ abundances in more detail. It suggests that the nucleosynthesis conditions for c.r. nuclei may differ from that for SS matter. So we shall calculate the nucleosynthesis of ultraheavy elements fitting its parameters to get the c.r. source abundances. We shall see that it is possible to get a very good agreement between the predicted and the "observed" source abundances.

2. Propagation. To analyse the effect of p.l.d. on the obtained source charge spectrum we have used two quite different path distributions - the leaky box one /exponential/ and the distribution obtained for the source located in the Galactic Centre /1/ $f(x) = A \times (x^2 + x_0^2)^{-3/2}$. The parameters A and x_0 have been adjusted so to fit the lower charge /$Z \leq 26$/ c.r. data, and for the leaky box $\bar{x} = 5 g/cm^2$ of H was adopted. The weighted mean fluxes observed by the both ultraheavy experiments Ariel VI /2/ and HEAO 3 /3/ were propagated back to the sources using the Silberberg and Tsao fragmentation cross-sections. The resulting source abundances normalised to Fe are presented on fig.1. The error bars contain the experimental errors, the assumed 50% and 3% uncertainties for the partial and total cross-sections respectively. As the fragmentation process has a stronger effect for the Galactic Centre /G.C./ p.l.d. /more longer paths than shorter ones for $x \lesssim 3 g/cm^2$/ than for the leaky box model, the G.C. abundances are a little less smoothly distributed. The highest Z elements are also more abundant for G.C. model as they are depleted more effectively than iron by longer paths. However the differencies between the two histograms lie mostly within the error bars.

The two assumed p.l.d.'s can, in a sense, be considered as two limiting cases: one /l.b./ corresponding to the sources very close to us, the other - to the sources as far as the Galactic Centre. Comparing both histograms with the Solar System abundances /4/, drawn also on fig.1., it is seen that changing p.l.d. rather drastically does not lead to any better agreement with the SS curve, although the overall shapes are remarkably similar, as has been known

for some time. Even taking into account the first ionisation potential /FIP/ does not help much /e.g./5// as it does for lower elements /$Z \lesssim 28$/, where the c.r. source abundances are rather well explained by SS+FIP /6/. As it is seen / and has been already known/ the c.r. source abundances differ from the SS ones in the following: bigger Pt/Pb ratio / although the experimental errors are large/, overabundance of rare earth elements /$58 \leq Z \leq 72$/, underabundance of $Z > 84$ /although very big errors/, overabundance of Kr /Z=36/ and the $50 \leq Z \leq 54$ elements. In the following we shall investigate whether these discrepancies could be explained by different nucleosynthesis conditions.

3. Nucleosynthesis and results. The shape of the Pt-Pb peak and the presence of $Z \gtrsim 90$ events suggest that the rapid neutron capture process may play an important rôle in the synthesis of the highest Z elements. The neutron densities in the r-process nucleosynthesis region are usualy assumed so high that the A distribution for an element of a given Z, $N(A,Z)$, reaches very quickly an equilibrium state. This is described by the formula /7/

$$\frac{N(A+1,Z)}{N(A,Z)} = \frac{\omega(A+1,Z)}{\omega(A,Z)} \left(\frac{A+1}{A}\right)^{3/2} n_n 2 \left(\frac{2\pi\hbar}{MkT}\right)^{-3/2} \exp\left[\frac{Q(A+1,Z) - Q(A,Z)}{kT}\right] \qquad /i/$$

All isotopes slowly leak out from the given Z value because of the β-decay, so we have

$$\frac{dN(Z)}{dt} = \langle\lambda_\beta\rangle_{Z-1} N(Z-1) - \langle\lambda_\beta\rangle_Z N(Z) + \text{spontaneus fission and other decays} \qquad /ii/$$

where $\langle\lambda_\beta\rangle_Z = \sum_A \lambda_\beta(A,Z) \cdot p(A,Z)$; $p(A,Z)$-determined from /i/. Assuming the initial conditions /only Fe at t=0/ we can solve /ii/ for $N(Z,t)$. Having these we can find $N(A,t)$

$$N(A,t) = \sum_Z N(A,Z,t) \quad , \text{ where } N(A,Z,t) = N(Z,t) \cdot p(A,Z) \qquad /iii/$$

If the synthesis stops at the time t, nuclei come to the stability valley mainly by β-decay, not changing their A, contributing to the lowest $Z(A)$ stable isotope. To get the position of the maxima in the abundance curve coincide with the "experimental" data /particulary the Pt peak/ the temperature $T = 2.75 \cdot 10^9$ K and neutron density $n_n = 10^{30}$ cm^{-3} have been fitted. Any other /T, n_n/ set giving the same $N(A+1,Z)/N(A,Z)$ gives the same results, e.g. $n_n = 10^{29}$ cm^{-3} and $T = 2.32 \cdot 10^9$. Switching the r-process off after any single time will not reproduce the data. So we have assumed a simple form of a continuous time distribution $f(t) \sim e^{-t/t_0}$ for $t > t_1$ and $f(t) = 0$ for $t < t_1$ with $t_0 = 6$s and $t_1 = 3$s. The truncation of short times was necessary to keep down the peak at $Z \simeq 52$ and the width t_0 assures the right abundances of Pb and U. To calculate $S_n \equiv Q(A+1,Z) - Q(A,Z)$ we have used the Myers-Swiatecki /8/ mass law and λ_β were calculated according to /9/. The obtained Z distribution together with the GC source abundances are presented on fig.2. Total amount of Fe nuclei processed by the r-process equals to the $4.3 \cdot 10^{-5}$ fraction of Fe in c.r. sources. We can see that all the abundances for $Z > 60$ can be described by the r-process nucleosynthesis within the error-bar limits.

For lower Z the slow neutron capture process must dominate. This is described by the equation

$$\frac{dN(A)}{d\tau} = \sigma_{A-1}N(A-1) - \sigma_A N(A) + \alpha\text{-decay term for } A > 209 \qquad /iv/$$

where $\tau = \int_0^t n_m(t) v_T dt$ and $v_T = \sqrt{2KT/M}$. The parameter τ describes the total accumulated neutron bombardment per unit area, σ_A are the effective cross-sections for neutron capture at a given temperature /10/. Adopting σ_A for 30 keV we have calculated $N(A,\tau)$, assuming $A=56$ at $\tau=0$. Here again one has to postulate a suitable form of "time" distribution $q(\tau)$ and compare $N(A) = \int_0^\infty N(A,\tau) q(\tau) d\tau$ corresponding to a particular Z with the c.r. data. Allen et al. fitted a power law $q(\tau) \sim \tau^{-4.4}$ for the SS material, with a cut-off for $\tau_{max} = 1.84 \cdot 10^{27}$ n/cm^2. We have assumed the same functional form $\tau^{-4.4}$, but to keep down the synthesis for $Z > 60$, $\tau_{max} = 1.4 \cdot 10^{27}$ n/cm^2 has to be adopted. The result is presented on fig.2. There are rather large discrepancies for Kr /Z=36/, Xe /Z=54/ and Ba /Z=56/. However these can be accounted for applying to the calculated abundances the first ionization potential effect /FIP/. We have applied the form CR/s-process = $9.81 \cdot \exp(-0.218 \cdot I)$ fitted to the c.r. data for $Z \leq 26$. The final result showing the sum of s-process abundances /with FIP/ and these from the r-process is shown on fig.3. Because of large FIP for Kr and Xe /larger than Fe/ and small FIP for Ba /smaller than Fe/ the discrepancies largely disappear, the biggest discrepancy being still for Xe.

4. Discussion. Bearing in mind that the experimental uncertainties are rather large, that the c.r. fluxes of volatile elements /including Xe/ may be suppressed and that the adopted GC path length distribution gives deeper minima and higher maxima in the abundance curve, we find that the agreement between the c.r. data and the predicted abundances is very good. With only a few parameters in our nucleosynthesis model it is quite interesting. Of course, the GC p.l.d. is not crucial here - one would get similar nucleosynthesis parameters adopting the leaky box model.

We have also calculated the superheavy /SH/ elements formed in the r-process. The predicted flux ratio SH/U-group $\simeq 0.005$ may be compared with an experimental results 0.01 ± 0.005 /11/ However Schramm et al. /12/ gets SH/U=0.0014 using a slightly different mass law which shows that the calculations are very sensive to the way of extrapolating the mass formula to the expected stability island at $Z \sim 114$, and our agreement may be coincidental.

The rôle of the r-process in synthetizing cosmic rays is, according to our model, more important than for the SS material, giving all nuclei for $Z > 60$. To determine whether it is true or not, we have probably to wait for precise measurement of even and odd Z fluxes and, what is more desirable but also much more difficult, for measurements of isotopic composition of ultraheavies.

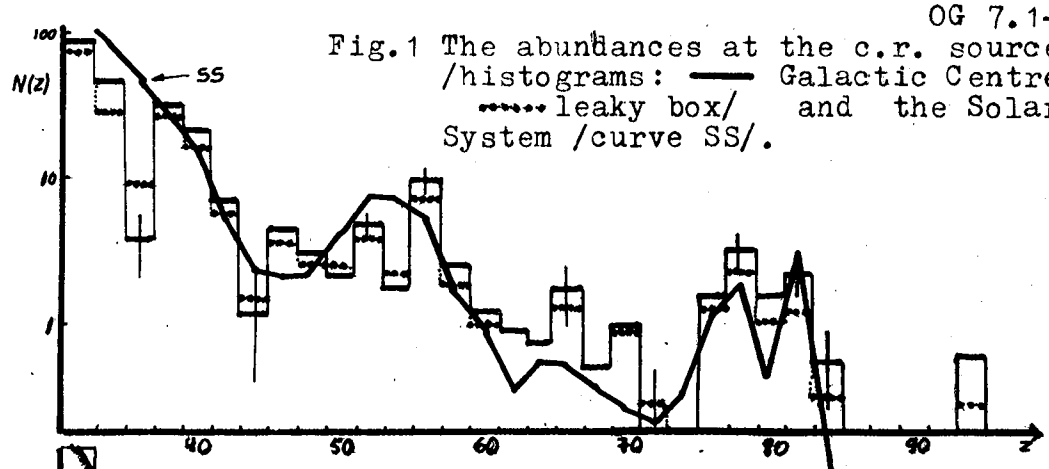

Fig.1 The abundances at the c.r. sources /histograms: —— Galactic Centre, ····· leaky box/ and the Solar System /curve SS/.

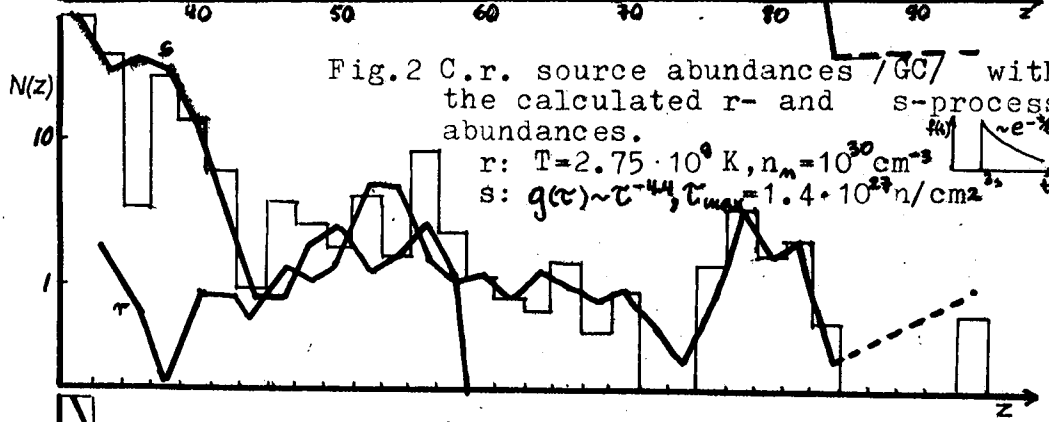

Fig.2 C.r. source abundances /GC/ with the calculated r- and s-process abundances.
r: $T=2.75\cdot10^{9}$ K, $n_n=10^{30}$ cm^{-3}
s: $g(\tau)\sim\tau^{-4.4}$, $\tau_{max}=1.4\cdot10^{27}$ n/cm^2

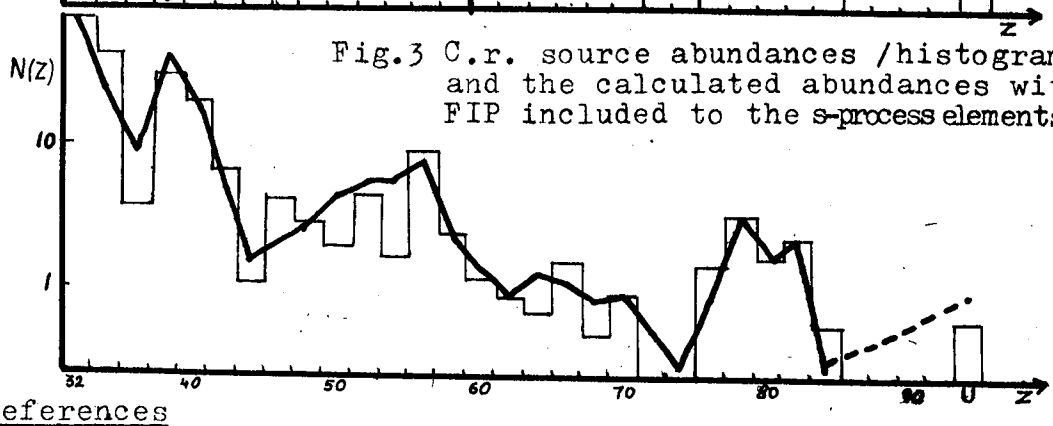

Fig.3 C.r. source abundances /histogram/ and the calculated abundances with FIP included to the s-process elements.

References

1. Giler,M. and Wibig,T., 1983, 18th ICRC/Bangalore/ 9,301
2. Fowler,P.H. et al., 9th Eur. C.R. Symp. Kosice, 1984
3. Binns,W.R. et al., 1983, 18th ICRC /Bangalore/ 9, 106, Fixen,D.J. et al., ib., 119, Stone,E.C. et al.,ib.,115
4. Cameron,A.G.W., in "Essays in Nuclear Astrophysics" ed. C.A.Barnes et al., 1982, Cambr. Univ. Press
5. Giler,M.and Wibig,T.,1984,Acta Univ. Lodz,Folia Physica 7
6. Cassé,M. and Goret,P., 1978, Ap. J., 221, 703
7. Burbidge,E.M. et al., 1957, Rev. Mod. Phys., 29, 547
8. Myers,W.D. and Swiatecki,W.J., 1966, Nucl.Phys., 81, 1
9. Kodama,T. and Takahashi,K., 1975, Nucl. Phys., A239, 489
10. Allen,B.J. et al., 1971, Adv. Nucl. Phys., 4, 205
11. Yadov,J.S. et al., 1983, 18th ICRC /Bangalore/ 2, 38
12. Schramm,D.N. and Fowler,W.A., 1971, Nature, 231, 103

SOURCES OF THE ULTRAHEAVY COSMIC RAYS

STEVEN H. MARGOLIS
McDonnell Center for the Space Sciences
Washington University
St. Louis, MO 63130 USA

and

J. B. BLAKE
Space Sciences Laboratory
The Aerospace Corporation
Los Angeles, CA 90009 USA

ABSTRACT

The suggestions that the source abundances cosmic ray nuclei heavier than Fe differ significantly from Solar System abundances are not well supported by the data without assuming preferential acceleration. The Solar System abundances of Pb and Bi are split into *r*-, standard *s*-, and cyclic *s-process* components; the apparent deficiency of Pb seen in the HEAO-3 HNE data might indicate an absence of Pb from the recycling *s-process*.

1. Introduction. The nuclei substantially heavier than Fe have been measured only relatively recently with electronic detectors (Fowler *et al.* 1983, Binns *et al.* (1984), and these experiments have yielded so far only results on even-Z elements or broad abundance groups in estimated charge. The calculations of Blake and Margolis (1981a) provided a selected set of standard propagations of Solar-like abundances ($26 \leq Z \leq 59$) which could be used to evaluate the experimental results in terms of *r*- and *s-process* contributions and the effects of preferential acceleration with a first ionization potential dependence (hereinafter FIPD). In this paper, propagation calculations of even heavier nuclei ($Z \geq 60$) are discussed in light of the now-published data in this range and other published analyses (Protheroe and Ormes, 1981; Blake and Margolis, 1981b; Brewster, Freier, and Waddington, 1983; Tsao *et al.*, 1983). The analysis presented here demonstrates that the simple picture of Solar abundances propagated according to models inferred from the lower-Z measurements does not account for the structure reported in the higher-Z abundances.

2. Calculations Of Propagated Abundances. The chemical and isotopic abundances of Anders and Ebihara (1982) provide a specific sample of nucleosynthesis in the Galaxy. These were propagated (a full description of the calculation appears in Margolis and Blake, 1985) to generate a set of abundances similar to what might be measured near the Earth, excluding the effects of Solar modulation. Figure 1 compares one such calculation, that for a 7 g cm^{-2} leaky box (shown as a solid line) with a composite data set (shown as isolated circles) assembled from the preliminary results of the HEAO-3 Heavy Nuclei Experiment (Binns *et al.*, 1981, 1984). Both sets of values have been normalized to 10^6 Fe nuclei, and the calculated values have been smeared with a Gaussian profile of width varying with charge in order to join the deconvolved lower charges to the reported resolution of the higher charges. For comparison, the dashed line in that figure displays, with the same normalization and smearing, the source abundances without propagation. In general, the patterns track reasonably well.

The plotting range necessary for displaying Figure 1 makes it an inconvenient form to use for most comparisons with observations, but such a display has a significant advantage over the more usual element group plots. The typical group plot illustrates the changing balance between secondary and primary elements resulting from propagation. One must remember that the comparisons to observation must be made not only in terms of the ratios of widely separated elements. The systematic effects of nucleosynthesis affect both kinds of ratios. The Solar System abundances, a known sample of cosmic matter, provide a definite, global normalization to the value of a single element. In the absence of any isotopic data, this normalization is all the more important. For example, elements near the Te-Ba peak do not change their abundances relative to Fe with propagation, but those at the Pt-Pb peak do. This contrast implies that the group ratio $(50 \leq Z \leq 56)/(Z = 26)$ is not a measure of propagation but of the most basic nucleosynthetic indicator: the abundance of *r*- and *s-process*

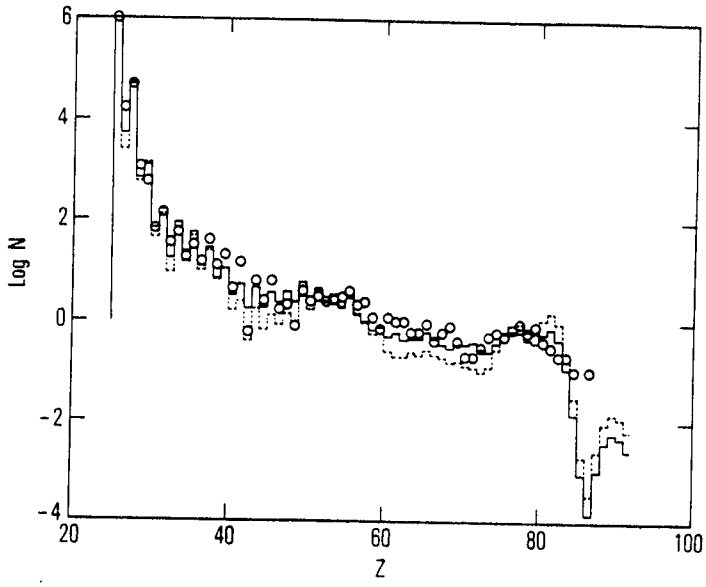

Figure 1. The circles represent a composite of preliminary results from the HEAO-3 Heavy Nuclei Experiment (Binns *et al.*, 1981, 1984). The dashed line shows the Solar abundances of Anders and Ebihara (1982) convolved with a Gaussian profile of varying width. The solid line shows the Solar abundances propagated through a 7 g cm^{-2} leaky box, also smeared.

material relative to that of the iron peak. In this respect, the data indicate that the cosmic ray source is consistent with the solar balance of those nucleosynthesis processes.

Although propagation does affect the observed abundances, removing the effects of a reasonable propagation model is probably sufficient. At least, the available data do not warrant more careful attention to such detail. It is not yet clear that any of the current experiments can recover a global normalization to Fe with the precision reported in a calculation. However, it is clearly worth considerable effort to obtain the best possible global abundance pattern from the experimental data. Important questions can be addressed with only minimal requirements on the charge resolution of an experiment.

3. Preferential Acceleration/Selection Effects. It is now standard procedure to consider selection effects in the cosmic ray chemical abundances based upon atomic properties of the element in question. The parameter usually chosen is the first ionization potential of the atom. A straight-line fit is made to a semi-log plot of the ratio of cosmic ray source abundances (derived from the data) to Solar System abundances *vs.* the ionization potential of the atom in question. This fit is then used to weight the source abundances which are input into a propagation calculation. Binns *et al.* (1984) question this approach, and argue that an equally good fit to their data is obtained with a step function rather than a straight line. They suggest that the discontinuity is an artifact caused by selecting C1 carbonaceous chondrites rather than C2 as the baseline for the Solar System abundances.

This is an interesting suggestion but there is considerable reason for regarding it with suspicion. First, at the sun and in planetary magnetospheres where individual acceleration events can be observed, preferential acceleration is ubiquitous. Second, the plot of the abundance ratio vs. first ionization potential continues to be ordered after exchanging C2 abundances for C1 abundances.

Difference in the ratio of *r*- to *s-process* abundances between cosmic rays and the Solar System can indicate either source differences or preferential acceleration. The question of preferential acceleration in the study of ultraheavy cosmic rays is so vexing because the *r*- and *s*-process peaks also have, on the average, significantly different first ionization potentials. However, selection effects should depend on the overall atomic physics of the atom and not simply the first ionization potential. Margolis and Blake (1983) noted that the influence of the second ionization potential disperses the predictions of preferential acceleration models in a manner consistent with the scatter of the observations about the straight-line fit. Although not perfect, such modifications are certainly the direction for further study. Without more knowledge of the nature of the cosmic ray source, it is difficult to make a meaningful improvement on the presently existing work.

4. Nucleosynthesis Considerations. It is very well known that the nucleosynthesis of the elements with $A > 60$ results largely from neutron capture processes; the *p-process* is responsible only for rare isotopes. In the analysis of ultraheavy cosmic ray data it is traditional to examine the paired abundance peaks which are due to neutron shell closure — Se and Sr, Te and Ba, and Pt and Pb — as an indicator of the relative abundance of the *r-* and *s-process* in the cosmic ray source(s). For (Te, Ba) and (Pt, Pb), the lower mass peak in the pair is largely the result of the *r-process*, and the upper one to the *s-process* nuclei. The heavier nuclei around Sr are mainly *s-process*, but the nuclei around Se show substantial contributions from both processes.

Implicit in these assignments is the assumption that each peak comes from a single nucleosynthetic site, at least once the contribution from the companion process is removed. However, in the case of the *s-process* peak at Pb, this assumption is incorrect. The *s-process* which fits the heavier Solar System isotopes up through ^{204}Pb underproduces the heavier Pb isotopes (Käppeler *et al.*, 1982; Ulrich 1983: although these references are recent and refer to the latest comprehensive work, this fact has been known for a long time.) The *s-process* terminates at ^{209}Bi because the next heavier nucleus, ^{210}Po, decays by emission back to ^{206}Pb. Therefore, with sufficient neutron exposure, all nuclei capture sufficient neutrons to join the quartet consisting of ^{206,207,208}Pb, and ^{209}Bi. The recycling process was described in detail by Clayton and Rassbach (1967). The important point for present purposes is that the site of the intense *s-process* exposure required to cause recycling may well not be the same as that which creates the *s-process* isotopes with $A \leq 204$ (Truran and Iben, 1977; Ulrich, 1983). Therefore, if the cosmic ray source were deficient in *s-process* material only from the recycling site, then the *r-process* and *s-process* nuclei at (Se, Sr) and (Te, Ba) would appear Solar, but at (Pt,Pb), Pb would be deficient.

Nucleus	Total Abundance	Normal *s-process*	Radiogenic *r-process*	Recycling *s-process*
^{206}Pb	0.603	0.180	0.12	0.30
^{207}Pb	0.650	0.176	0.10	0.37
^{208}Pb	1.838	0.402	0.06	1.38
^{209}Bi	0.144	0.016	0.12	0.01

Table 1. The nucleosynthetic origins of the nuclei affected by the cyclic *s-process*. The Total Abundance is taken from Anders and Ebihara (1982), and the Normal *s-process* from Käppeler *et al.*, (1982).

Given here is a zeroth-order decomposition of the Pb peak. The details can be found in Margolis and Blake (1985). It can be seen from the abundance values given in Table 1 that $\approx 65\%$ of the Pb is produced in the recycling *s-process*. Truran and Iben (1977) have suggested stars with $M > 15\ M_\odot$ produce many of the *s-process* isotopes in the mass range $25 < A < 70$, that stars with $2\ M_\odot < M < 8\ M_\odot$ make the bulk of the *s-process* isotopes for $A > 70$, and that stars with $M < 1\ M_\odot$ are responsible for ^{206,207,208}Pb and ^{209}Bi. Thus one possible explanation for the HEAO-3 observation of a deficiency of counts in the Pb region is that the nucleosynthetic contribution of stars with $M < 1\ M_\odot$ is under-represented in the cosmic ray source.

With the contribution of the cyclic *s-process* deleted, the modified Solar System source abundances have been propagated through a 7 g cm^{-2} leaky box for comparison with the measured abundances. A detailed look at the contribution of the terminal *s-process* is visible in Figure 2, which compares the abundances of the nuclei above the Te-Ba peak with (solid line) and without (dashed line) the additional material. Calculations show that about 75% of the difference in source abundances appears as contributions to the elements at lower Z. Such is the relative abundance of Pb that this contribution is significant throughout the illustrated charge region. Despite this change, the measured values in the rare-earth region appear too high. This might indicate a more extreme propagation model, but more probable is that the source abundances in the rare-earth region need further adjustment if the data are correct. The rare-earth elements have nearly the same first ionization potentials, all lower than that of iron, but are refractory to differing degrees. Should that have an effect on the injection process (see above), the variation of injection efficiency across these elements migh provide a useful gauge of the nature of preferential acceleration.

5. Conclusions. The most important conclusion of this work is that the overall composition of the galactic cosmic ray source appears remarkably like that of the Solar System. The abundances above

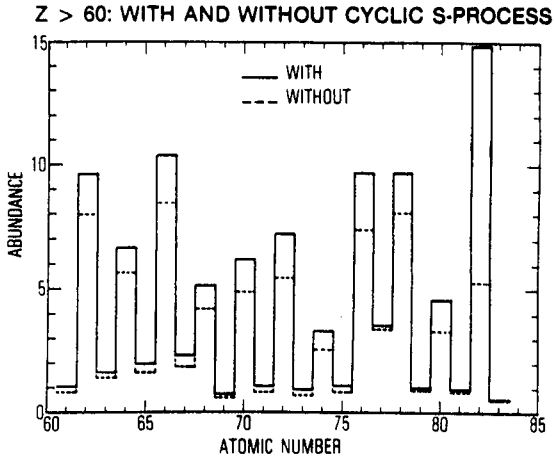

Figure 2. The net contribution to the propagated abundances is illustrated as the difference between the solid line, showing the standard Solar System source, and the dashed line, showing the modified source calculated in this work. Approximately 75% of Pb at the source is incorporated into elements of lower Z. The vertical scale is linear, but the units are arbitrary.

Fe display a very Solar-like balance between several different nucleosynthetic processes. However, if the Pb abundance reported by Binns *et al.* (1984) is correct, it might signify the lack of the products of the terminal or cyclic *s-process*. Such evidence could be used to rule out the appearance of stars with masses $M < 1\ M_{\odot}$ on the roster of cosmic ray sources. Until more precise determinations are available, however, it seems prudent not to consider this abundance as additional confirmation of ever more complex models for selective acceleration.

6. Acknowledgements. The work reported here was supported at Washington University under NASA grant NAG8-448 and McDonnell Center research funds and at the Aerospace Corp. under company-sponsored research funds.

7. References.

Anders, E., and Ebihara, M., 1982. *Geochim. Cosmo. Acta*, **46**, 2263.

Binns, W. R., Fickle, R. K., Garrard, T. L., Israel, M. H., Klarmann, J., Stone, E. C., and Waddington, C. J., 1981. *Ap. J. (Letters)*, **247**, L115.

Binns, W. R., Fixsen, D. J., Garrard, T. L., Israel, M. H., Klarmann, J., Stone, E. C., and Waddington, C. J., 1984. *Adv. Space Res.*, **25**, 4.

Blake, J. B., and Margolis, S. H., 1981a. *Ap. J.*, **251**, 402.

Blake, J. B., and Margolis, S. H., 1981b. *Proc. 17th Int. Cosmic Ray Conf. (Paris)*, **2**, 41.

Brewster, N. R., Freier, P. S., and Waddington, C. J. 1983. *Ap. J.*, **264**, 324.

Clayton, D. D., and Rassbach, M. E., 1967. *Ap. J.*, **143**, 69.

Fowler, P. H., Masheder, M. R. W., Moses, R. T., Walker, R. N. F., and Worley, A., 1983. *Proc. 18th Int. Cosmic Ray Conf. (Bangalore)*, **9**, 110.

Käppeler, F., Beer, H., Wisshak, K., Clayton, D. D., Macklin, R. L., and Ward, R. A., 1981. *Ap. J.*, **257**, 821.

Margolis, S. H., 1983. *Proc. 18th Int. Cosmic Ray Conf. (Bangalore)*, **9**, 267.

Margolis, S. H., and Blake, J. B., 1983. *Proc. 18th Int. Cosmic Ray Conf. (Bangalore)*, **9**, 283.

Margolis, S. H., and Blake, J. B. 1985. *Ap. J.*, (in press).

Protheroe, R. J., and Ormes, J. F., 1981. *Proc. 17th Int. Cosmic Ray Conf. (Paris)*, **9**, 114.

Truran, J. W., and Iben, I., Jr., 1977. *Ap. J.*, **216**, 797.

Tsao, C. H., Silberberg, R., Jr., J. H. Adams,, and Letaw, J. R., 1983. *Proc. 18th Int. Cosmic Ray Conf. (Bangalore)*, **2**, 225.

Ulrich, R. K. 1983. *Essays in Nuclear Astrophysics*, ed. Barnes, C. A., Clayton, D. D. and Schramm, D. N. (Cambridge: Cambridge U. Press), 301.

OG7.1-8

THE COSMIC RAY COMPOSITION AS VIEWED FROM THE CHEMICAL ABUNDANCES OF THE SOLAR SYSTEM

Kunitomo Sakurai

Institute of Physics, Kanagawa University
Rokkakubashi, Yokohama 221, Japan

ABSTRACT

It is shown that the chemical composition of cosmic rays at their sources for the elements up to the atomic number as 80 is quite similar to that of the carbonaceous chondrites, which have been keeping the properties of the proto-solar nebula. In particular, the similarity between these two compositions is significant to the elements classified as refractory and siderphile, in addition to the elements, Ca and Al. These results as cited above suggest that cosmic rays, being currently observed near the earth, may have been accelerated from the matter with the composition similar to that which is found of these chondrites as Allende.

1. Introduction. For many years since 1950's, it has been thought that the sources of cosmic rays are identified with supernova explosions, which seem to happen every ten years or so. However, some questions have recently arisen to the idea on the supernova origin of cosmic rays on the basis of the observations on the chemical composition. Really speaking, the chemical composition of cosmic rays at their sources is different from that which has been theoretically deduced from the r-process associated with supernova explosions, but similar to that of the solar system(1). This difference becomes larger as the charge numbers of nuclei increase, and become more significant to the nuclear species heavier than the medium nuclei as C, N and O(2). This tendency is known as the overabundances of heavy nuclei in the cosmic ray composition as compared to the chemical composition of the solar atmosphere. It is, therefore, urgently necessary to investigate whether the source composition of cosmic rays is similar to the composition of the solar atmosphere and the proto-solar nebula or not. Then, it would become possible to estimate the physical state on the birth place of cosmic rays in the galactic space.

2. Comparison of the Chemical Composition of Cosmic Rays at Their Sources with That of the Solar System. As well known, the chemical composition of the solar system has been mainly derived from the chemical analyses of the earth's crust and meteorites and also from the spectroscopic analysis of the solar atmosphere. Based on these analyses, it is now thought that the chemical composition of carbonaceous chondrites is representative as that of the primordial solar nebula, from which the solar system, both of the sun and its own planets,

may have been originated about 4.6 billion years ago(3).

In order to examine whether the chemical composition of the solar system can be considered as typical to that of cosmic rays at their sources, it is convenient to compare the characteristics of these two compositions. Using the chemical compositions of the solar system and of cosmic rays at their sources currently available(4), the relative abundances have been examined of the elements up to Pb (Z = 82) for these two compositions. The result thus obtained as shown in Fig. 1 clearly shows that the cosmic ray source abundances tend to become relatively higher with the increase of the charge numbers of the elements under consideration.

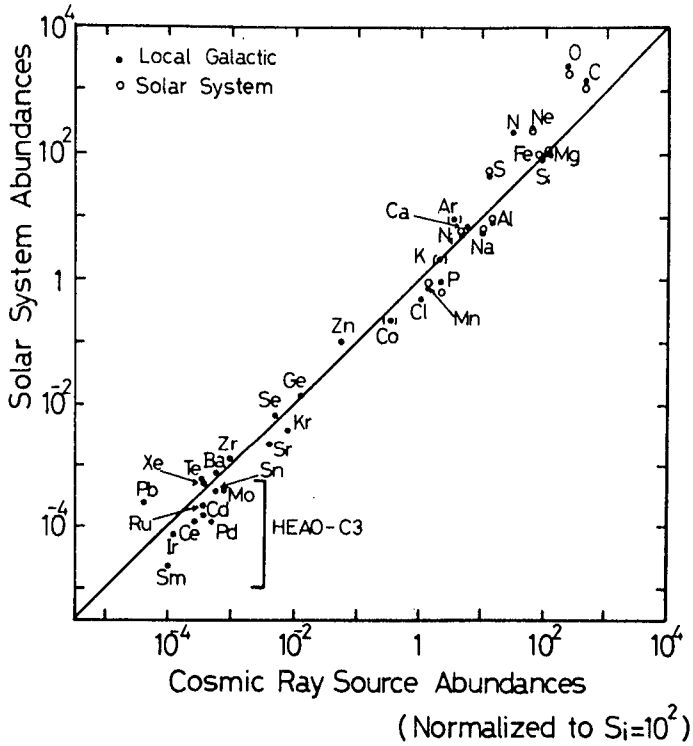

Fig. 1 Comparison between the relative abundances of the solar system and of cosmic ray sources.

Although it is thus clear that, with the increase of the charge numbers of the elements, the chemical composition of the solar atmosphere is relatively less abundant when compared to that of carbonaceous chondrites as the Allende meteorite, Fig. 1 suggests that the chemical composition of cosmic rays at their sources is quite similar to that of the primordial solar nebula. Thus, it can be said that the birth place of cosmic rays in the galactic space may be found in the interstellar clouds whose chemical composition is almost the same as that of the primordial solar nebula.

3. Chemical Composition of Cosmic Rays as Viewed from Their FIP's. In order to see the distinction between the relative abundances of the cosmic ray sources and the solar atmosphere in more detail, the ratio of these abundances for the cosmic ray sources to those of the solar atmosphere have been examined with respect to each element and compared with the first ionization potentials (FIP) of these elements. The relation between the ratios and the potentials for these elements is shown in Fig. 2 without error bars, since we are only interested to see if there is any systematic tendency between these two. Overall relations between these ratios and the FIP's are shown in Fig. 3 as a function of the charge

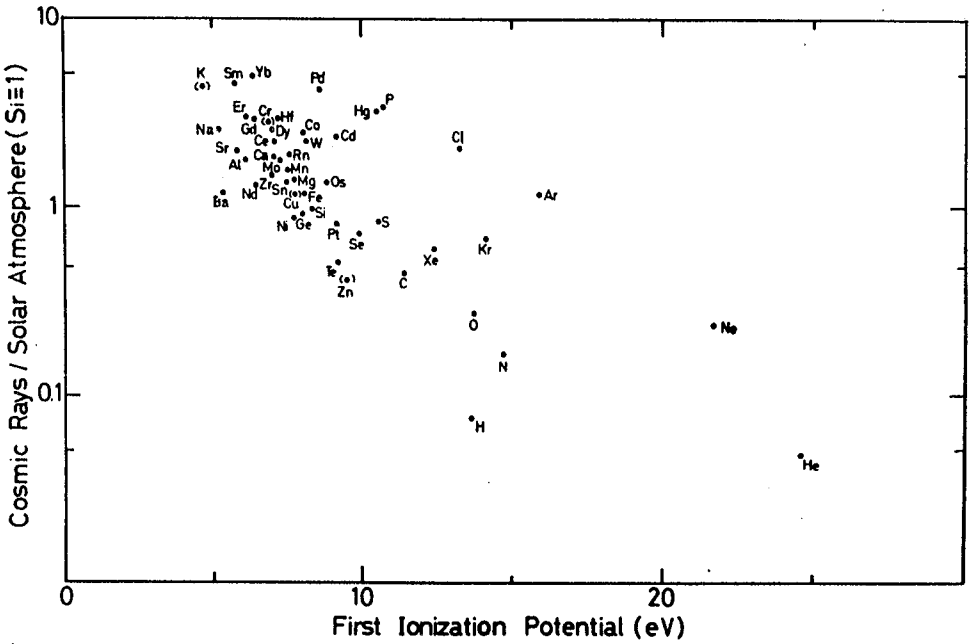

Fig. 2 Relation of the ratios of the chemical composition of cosmic ray sources to that of the solar atmosphere with the first ionization potentials of the nuclei in their atomic states.

number of elements.

The result shown in Fig. 2 indicates that, in addition to the enrichement of Ca and Al nuclei, both refractory and siderophile elements are well overabundant in the source composition of cosmic rays as compared to the chemical composition of the solar atmosphere. This tendency is also clearly seen on the mean chemical composition of the white inclusions, CAI(I) and CAI(II), of the Allende meteorite, a typical example of carbonaceous chondrites(5). As regards lanthanides, their relative abundances in the cosmic ray sources are also similar to those of these inclusions, since the overabundant nature of these elements is very similar between the cosmic ray source composition and the mean composition of these inclusions.

These results as mentioned above seem to indicate that cosmic rays have been accelerated initially from particles in a matter, whose composition is almost the same as that of the primordial solar nebula. Such matters seem to be distributed almost everywhere throughout the galactic space, since they must have been born from the expanding gases associated with supernova explosion. While drifting in this space after cooled down, a part of them may have been later accelerated to cosmic rays by interstellar shocks originated from super-

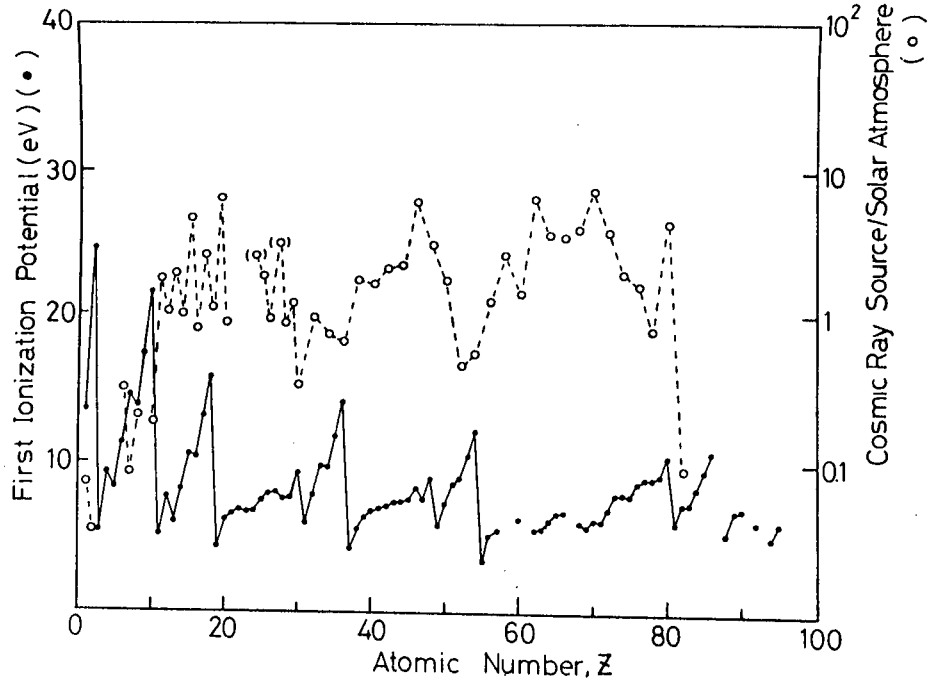

Fig. 3 The same ratios as in Fig. 2 and FIP's as plotted as a function of the nuclear charge numbers.

novae occurred later in the nearby space.

4. Cocluding Remarks. The chemical compositin of cosmic rays at their sources is very similar to that of carbonaceous chondrites which may have been still keeping the properties of the primordial solar nebula or alike. This similarity between these two compositions is clearly seen on the overabundant nature of refractory and siderophile elements as observed in cosmic rays and those chondrites. These results strongly suggest that cosmic rays must have been accelerated from particles ambient in the matter, drifting in the galactic space, whose chemical composition is almost the same as that of carbonaceous chondrites. Furthermore, Fig. 2 suggests that cosmic rays must have been generated in the matter whose temperature is not so high, but is 10^6 K at most as once proposed earlier(2,6).

References

(1) e.g., R.A. Mewaldt (1981) Proc. 17th ICRC, Paris 13, 49 and J.A. Simpson (1983) Ann. Rev. Nuclear Part. Sci. 33, 323.
(2) M. Casse and P. Goret (1978) Ap. J. 221, 703.
(3) e.g., J. Wood (1979) The Solar System, Prentice Hall, New York.
(4) B. Byrnak et al. (1983) Proc. 18th ICRC, Bangalore 2, 29, E. Juliusson (1983) Proc. 18th ICRC, Bangalore 12, 117 and J.B. Blake and S. Margolis (1981) Ap. J. 251,402.
(5) J. Wood (1981) The New Solar System, p. 187, Cambridge. Univ., Cambridge.
(6) K. Sakurai (1981) Proc. 17th ICRC, Paris 2, 277.

Elemental Technetium as a Cosmic-Ray Clock

J. Drach and M.H. Salamon
Physics Department, University of California, Berkeley, CA

1. Introduction. Several radioactive isotopes have been proposed as clocks for the study of the mean cosmic ray confinement time, τ_e. Measurements of ^{10}Be and ^{26}Al [1,2] give a value for τ_e of about 10 Myr when one uses a leaky box cosmic ray propagation model. It is important to obtain additional measurements of τ_e from other radioactive isotopes in order to check whether the confinement is the same throughout the periodic table.

We investigate the possible use of Tc (Z = 43) as a cosmic clock. Since all isotopes of Tc are radioactive, one might be able to group these isotopes and use the elemental abundance as a whole. We were led to this investigation by our involvement with the HNC-LDEF-IB detector [3]. In its original conception, this detector contains 45 trays of plastic track detectors with collecting area A $\Omega \approx 100\ m^2$ sr, to be exposed for ~2.5 years in a 57° orbit. Of the 45 trays, 4 are to be optimized for identification of nuclei with $30 \leq Z \leq 70$ ($\sigma_Z \leq 0.20e$) and 41 are optimized for $Z > 70$ ($\sigma_Z \leq 0.25e$).

The results of our calculations are somewhat inconclusive for two reasons. First, the β^+ decay half-lives of two of the Tc isotopes relevant to our calculation are not known. Second, the dependence of the Tc abundance on the mean confinement time is rather weak when one considers the number of events expected in 4 trays of plastic track detectors. However, a future, finite measurement of the β^+ half-lives and the possible use of the entire collecting area of the HNC to detect Tc nuclei (although with a larger σ_Z) could make the use of Tc as a cosmic-ray clock more attractive.

2. Propagation Calculation. We used a propagation equation of the form:

$$\frac{\partial J_i(E,x)}{\partial x} = -\frac{J_i}{\Lambda_i(E)} + \sum_k \frac{J_k}{\Lambda_{ik}(E)} + \frac{\partial}{\partial E}\left[w_i(E) J_i\right]$$

where Λ_i is the mean free path for losses of species i due to nuclear fragmentation and radioactive decay, Λ_{ik} is the mean free path for gains of species i from species k, and w_i is the absolute value of the ionization loss rate. The solution of this equation is weighted over a path length distribution $P(x,\lambda)$ giving the final flux:

$$J_{Fi}(\lambda) = \int_0^\infty dx\, P(x,\lambda)\, J_i(x)$$

We used the standard leaky box model

$$P(x) = \frac{1}{\lambda} \exp(-\frac{x}{\lambda})$$

with $\lambda = 7.80$ g/cm^2 in a medium consisting of 90% H and 10% He by number. Given the uncertainties in our calculations, we did not it consider appropriate to calculate abundances with other pathlength distributions. For the initial fluxes, we used the Cameron abundances [4] with the following ionization potential correction [5]

exp[-0.27 (7.0)]	($I < 7$ eV)
exp[-0.27 I]	($7 \leq I \leq 13.6$ eV)
exp[-0.27 (13.6)]	($I > 13.6$)

where I is the first ionization potential in eV.

Table 1 shows the Tc isotopes used in the calculation:

Table 1

Isotope	Decay Mode(s) & (half-life in years)
^{95}Tc	E.C. ($\tau_{1/2} = 2.28 \times 10^{-3}$), β^+($\tau_{1/2}$ = unknown)
^{96}Tc	E.C. ($\tau_{1/2} = 1.18 \times 10^{-2}$), β^+($\tau_{1/2}$ = unknown)
^{97}Tc	E.C. ($\tau_{1/2} = 2.60 \times 10^6$)
^{98}Tc	β^- ($\tau_{1/2} = 4.20 \times 10^6$)
^{99}Tc	β^- ($\tau_{1/2} = 2.14 \times 10^5$)

Note: E.C. ≡ electron capture decay. Half-lives for this mode refer to neutral atoms.

Three of the isotopes (^{95}Tc, ^{96}Tc and ^{97}Tc) have electron capture decay modes. We incorporate electron attachment and stripping into the propagation equation using the method described by Letaw, Silberberg and Tsao [6]. Table 1 also shows that the β^+ branching ratios in ^{95}Tc and ^{96}Tc are not known. Positron emission is energetically allowed but it has not yet been observed [7]. We use two extreme values for the β^+ half-lives: a) $\tau_{1/2} = \infty$, i.e., we assume that the isotopes are stable; b) $\tau_{1/2} = 0$, i.e., the isotopes decay as soon as they are created.

3. Results and Discussion. Figures 1 to 3 show relative abundances of Tc with respect to Sn-Ba elements ($Z = 50$ to 56) as a function of mean confinement time τ_e. The results have been integrated over all energies. In Figs. 1 and 2, we see that the abundances of ^{98}Tc and ^{99}Tc are very sensitive to changes in τ_e. These isotopes would be good cosmic clocks if they could be resolved from the other ones. Figure 3 shows the elemental abundance of

Tc. The upper curve corresponds to β^+ decay with $\tau_{1/2} = \infty$. The lower curve corresponds to $\tau_{1/2} = 0$. There are two error bars drawn in Fig. 3. The larger one corresponds to the statistical fluctuations expected if only 4 trays of plastic detectors are used in a 57° inclination orbit (~50 events). The smaller bar corresponds to the statistics expected if all 45 trays of the HNC were used to collect Tc (~550 events). As mentioned earlier, just 4 trays have been optimized for identification of nuclei with $30 \lesssim Z \lesssim 70$. The other 41 trays of detectors are optimized for $Z \gtrsim 70$ and their resolution in the region around $Z = 43$ is not yet known. Even if the Tc abundance measurement were to have negligible errors, we can see that the uncertainty in the β^+ makes it hard to reach any conclusions regarding the mean confinement time.

Only in the most favorable of circumstances (knowing the β^+ decay branching ratios and using the entire collecting power of the HNC) would we be able to use Tc as a cosmic clock in the upcoming HNC-LDEF-IB cosmic ray mission.

References

1. F.A. Hagen, Ph.D. Thesis, University of Maryland, 1976.
2. M.E. Wiedenbeck, Proc. 18th Inter. Cosmic Ray Conf., Bangalore, India, 9, 147, 1983.
3. J. Drach et al., submitted to this Proceedings.
4. A.G.W. Cameron, in Essays in Nuclear Astrophysics, ed. C.A. Barnes, D.N. Schramm and D.D. Clayton, Cambridge University Press, p. 23, 1982.
5. J.R. Letaw et al., Astrophys. J. 279, 144 (1984).
6. J.R. Letaw et al., Astrophys. J. Suppl. 56, 369 (1984).
7. C.M. Lederer and V.S. Shirley, Table of Isotopes, Wiley, New York, 1978.

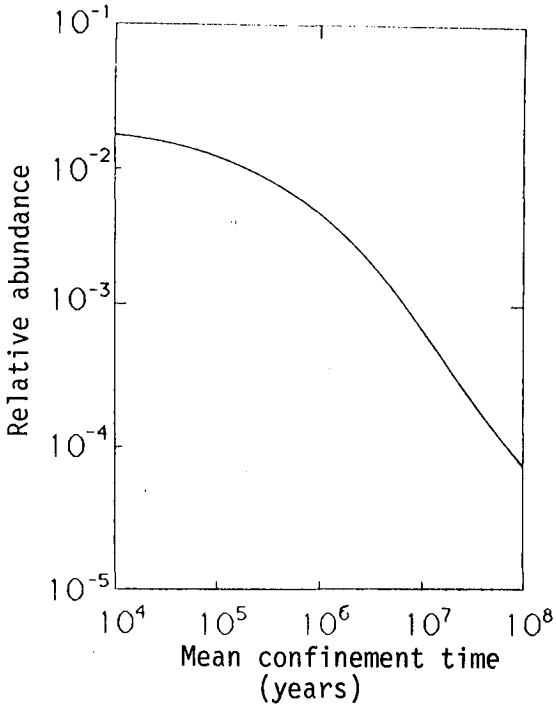

Fig. 1. Relative abundance of ^{98}Tc with respect to the Sn-Ba elements.

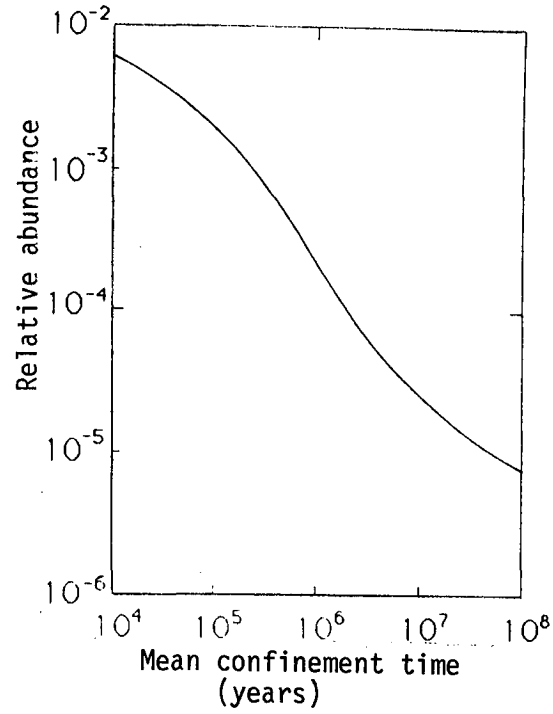

Fig. 2. Relative abundance of ^{99}Tc with respect to the Sn-Ba elements.

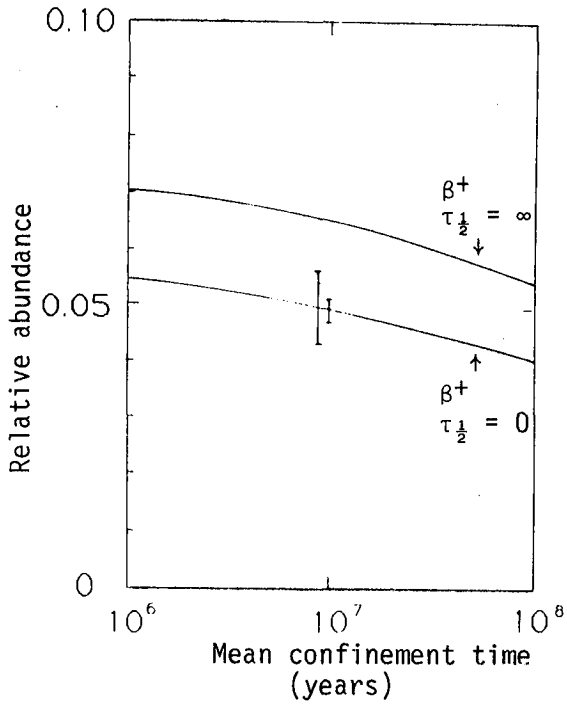

Fig. 3. Relative abundance of elemental Tc with respect to the Sn-Ba elements. The small error bar corresponds to using 100% of the collecting area of the HNC (45 trays). The large error bar corresponds to using ~ 9% (4 trays).

OG: 7.1-10

ELECTRON CAPTURE DECAY OF COSMIC RAYS: A MODEL OF THE INHOMOGENEOUS INTERSTELLAR MEDIUM

John R. Letaw
Severn Communications Corporation, Severna Park, MD 21146

Rein Silberberg and C.H. Tsao
E.C. Hulburt Center for Space Research
Naval Research Laboratory, Washington, DC 20375

1. Introduction. Traditional analyses of cosmic ray composition seek to identify the sources through a determination of the isotopic abundances of these nuclei prior to acceleration. At the same time, it is both necessary and interesting to understand the nature of the medium through which cosmic rays pass before arriving at our detectors. In fact, only within a model of the interstellar medium (ISM) sampled by cosmic rays can a refined estimate of source composition be made. In this paper we explore an elaboration of the traditional model of the ISM used in studying cosmic ray propagation. Inhomogeneity of the ISM is accomodated in this model. We find within this model that the abundances of some electron capture isotopes, specifically ^{44}Ti, ^{91}Nb, ^{93}Mo, ^{167}Tb, are very sensitive to density inhomogeneities which might be expected in the ISM. These nuclei therefore measure the penetration of heavy cosmic rays into interstellar clouds.

2. Model of the Homogeneous Interstellar Medium. McKee and Ostriker (1977) have characterized the ISM as having three components: (1) a hot component maintained by repeated supernova explosions, having a hydrogen number density of about 0.003 cm^{-3}, and filling about 75% of interstellar space, (2) warm clouds with density of 0.25 cm^{-3} filling most of the remaining space and having (3) cold cores with densities on the order of 40.0 cm^{-3}. If cosmic rays are allowed unrestricted access to interstellar clouds, most of the cosmic ray pathlength is accumulated in clouds. These circumstances are suggested by an examination of gamma ray data from molecular clouds (Issa et al., 1981) showing little cosmic ray enhancement or depletion within. Further support for unrestricted access may be based on the cosmic ray pathlength distribution which rules out trapping and escape from multiple cloud systems after acceleration. Compositional measurements proposed here can test the extent of cosmic ray access to interstellar clouds.

We assume that cosmic rays randomly (in time) encounter density fluctuations in the ISM which may be described by the distribution F(n) of interstellar gas number densities n. This function is normalized so that:

$$\int_0^\infty F(n)dn = 1 \qquad (1)$$

F(n) dn is the fraction of time a cosmic ray spends in regions near density n. Equivalently, it is the (spatial) fraction of accessible ISM with density n. If the entire ISM is accessible then models such as that of McKee and Ostriker (1977) may be invoked to estimate the density distribution.

The model is implemented by replacing the differential pathlength, dx, with xf(n)dn in propagation equations. f(n) is the fraction of cosmic ray pathlength over which the interstellar gas density is n. It is related to F(n) by:

$$f(n) = nF(n)/\langle n \rangle \tag{2}$$

where $\langle n \rangle$ is the mean density of the ISM (i.e., the expectation value of n relative to the distribution F(n)). Central to this model is the random association of density with time and accumulated pathlength. Thus this model differs from the extreme types of inhomogeneity proposed by Wiedenbeck (1983) and two-component ISMs which might be constructed from nested leaky box models.

No effect on the composition of most cosmic rays results from the introduction of inhomogeneities according to this model. Fragmentation of cosmic rays is independent of density, i.e.,

$$dJ \propto J\,dx \Longrightarrow Jxf(n)dn \tag{3}$$

so that only the zeroth moment of the density distribution is sampled:

$$\ell n\ J \propto x \int_0^\infty n^0 f(n)\ dn = x \tag{4}$$

The abundances of stable secondaries are sensitive only to the total pathlength. They are independent of density.

Since the beta decay mean free path of radionuclides is inversely proportional to density (see, for example, Letaw et al., 1984), their abundance after passage through the ISM is given by

$$\ell n\ J \propto x \int_0^\infty n^{-1} f(n)\ dn = x/\langle n \rangle \tag{5}$$

where $\langle n \rangle$ is the spatial average of the number density. Radionuclides are therefore sensitive to the average density of the ISM and the total pathlength. The pathlength can be determined from stable secondary abundances, hence radionuclides provide a measurement of the mean interstellar gas density as sampled by cosmic rays. We show below how another moment of the ISM density distribution is sampled by electron capture isotopes.

3. Electron Capture Nuclides. Electron capture decay of cosmic rays is inhibited because most of these nuclei are fully ionized. Thus we

say most electron capture nuclides in cosmic rays are "attachment-limited" because they decay rapidly after an electron is attached. Some decays are held up more by the nuclear decay process than the attachment process; these are called "capture-limited." The distinction between capture-limited and attachment-limited nuclides is dependent on density. The effective mean free path for electron capture decay is:

$$\lambda_{eff} = \lambda_a (1 + kn\tau/\lambda_s) \qquad (6)$$

(Letaw et al., 1985). Here λ_a and λ_s are the attachment and stripping mean free paths respectively, τ is the mean decay time (with an electron attached), and k is the constant relating distance and time. When the first term in Eq. 6 dominates the decay is attachment-limited; when the second term dominates it is capture-limited. The two terms are equal at the transition density (n_T). The effective decay mean free path for ^{44}Ti at 100 MeV/N is shown in Fig. 1.

Eq. 7 shows the moment sampled by electron capture nuclides.

$$\ell n\ J \propto x \int_0^\infty (1 + n/n_T)^{-1} f(n)\ dn \qquad (7)$$

If the density is always below the transition density, only the zeroth moment of the distribution is sampled as in fragmentation (Eq. 4). If the density is always above the transition density, only the mean density is sampled as in the decay of other radionuclides (Eq. 5). The latter case was explored by Raisbeck et al. (1975). We are interested in the intermediate case where new information about F(n) can be found.

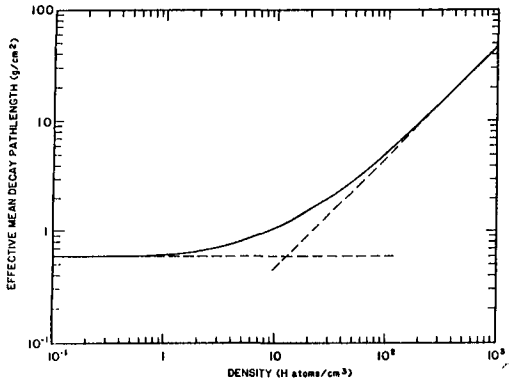

Fig. 1: Effective electron capture decay mean free path of ^{44}Ti at 100 MeV/N versus density.

In an ISM with fixed mean density, maximum decay takes place when the medium is homogeneous. This follows from Fig. 1 where it is evident that the decay mean free path increases rapidly with density above n_T. Using a Dirac delta function for the density distribution in this case, we find the upper limit for Eq. 7 to be

$$x\langle n\rangle/(1 + \langle n\rangle/n_T) \qquad (8)$$

Eq. 7 equals Eq. 8 not only in a homogeneous medium, but also when densities are much greater or much less than the transition density. Only when densities on both sides of the transition density are encountered will slower decay rates and higher surviving fractions be observed.

4. Results and Conclusions. Examples of increased survival fractions are shown in Figs. 2 through 4. The calculations were done for a simple two component medium with a density of 0.003 atoms/cm^3 in rarefied regions. A mean escape time of 10^7 years and rigidity-dependent mean pathlength were used to infer the sizes of clouds of various densities. Electron capture nuclides having interesting transition densities (between 1 and 50 atoms/cm^3) and long effective lifetimes were chosen for study. ^{91}Nb is similar to ^{93}Mo, but is not pictured because its halflife is unknown. We note that ultraheavy nuclides show enhanced survival at median cosmic ray energies. Enhancement of ^{44}Ti at low energies might be obscured by solar modulation.

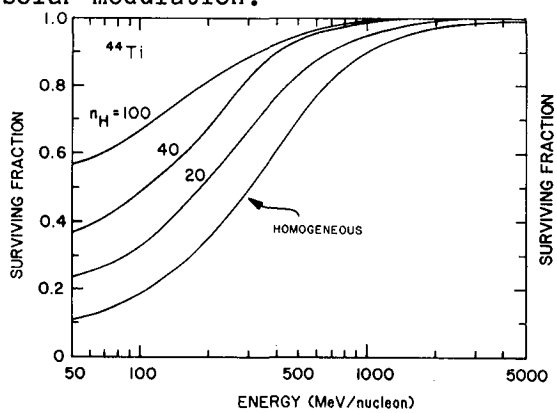

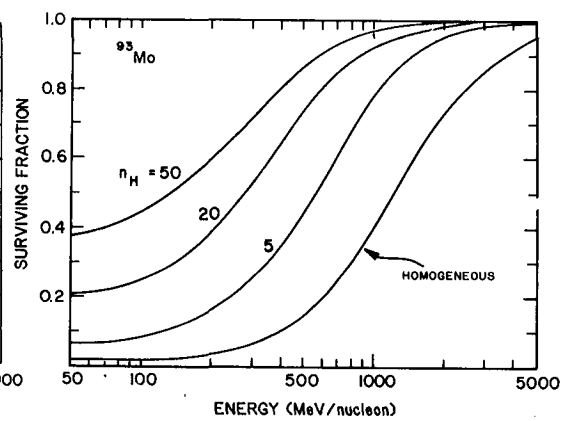

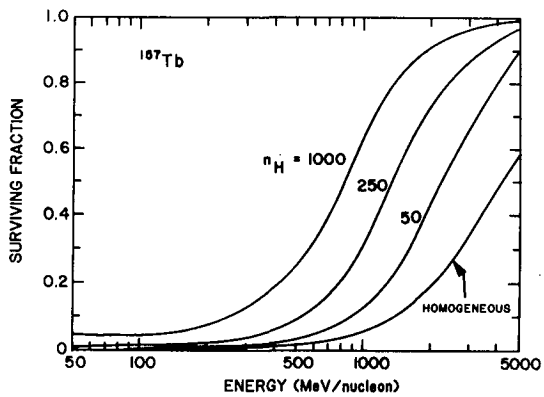

Figs. 2-4: Survival fractions of ^{44}Ti, ^{93}Mo and ^{157}Tb for several ISM density distributions.

References

Issa, M.R., Riley, P.A., Pei, L.T., and Wolfendale, A.W., 1981,17th Int. Cosmic Ray Conf. (Paris), XG 4.3-4.

Letaw, J.R., et al. 1984 Ap. J. Suppl., 56, 369.

Letaw, J.R., et al. 1985, Ast. Sp. Sci., (November).

McKee, C.F. and Ostriker, J.P. 1977, Ap. J., 218, 148.

Raisbeck, G., Comstock, G.M., Perron, C., and Yiou, F. 1975, Proc. 14th Int. Cosmic Ray Conf., 2, 560.

Wiedenbeck, M.E. 1983, 18th ICRC, (Bangalore),OG 2-8.

1 OG 7.1-11

A VERY IMPORTANT PROCESS OF NUCLEOSYNTHESIS IN STARS

Chuanzan Yu Renming Zhou Shijie Zhan
Department of Physics, Yunnan University, Kunming
P.R.C.

ABSTRACT

This is a framework.

At the supernova pre-explosion stage with $M \approx 15\text{--}30M_\odot$, the core with $\bar{\rho} \geq 5*10^{11}$ (g/cm^3), $R \leq 10^7$ cm and $M_1=\frac{4\pi}{3}R^3\bar{\rho} \geq M_\odot$ collapses to a neutron star. The emitted gravitational energy per nucleon $E_n \sim 140$Mev transforms into the radiation energy which prevents material outside $R>10^7$cm from collapsing and causes the explosion of supernova. The γ-radiation is so strong that it makes Fe^{56}--Ni^{60} nuclei of the mass~$0.2M_\odot$ within the inner shell to dissociate and proton-neutron gass with neutron number dencity $n_n \sim 10^{28}\text{--}10^{30}/cm^3$ to be formed. At the same time, the radiation pressure transforms into the kinetic energy of dipersed material, which sets off the shock waves. Thus the local density is $\rho > 10^{12}$ g/cm^3 and neutronization is accelerated, which makes Ca^{56}--Ca^{60} nuclei of $1\text{-}2M_\odot$ mass to collide with each other and to form nuclei with A~112-360. Finally, neutron-rich nuclei (A~140--440, Z~30--82) can be formed by adding a large number of neutrons.

When these nuclei are free from the strong gravitational field, they are unstable and will become stable nuclei by competitions of following processes; (1)neutron-evaporation, (2)spontaneous fission and (3) β^--decay. At the initial stage, (1) and (2) are important and (3) can be ignored.

The qualitative results are as follows;

(1). It seems that nuclei with A>100 come from the spontaneous fission and β^--decay of nutron-evaporated nuclei with A~140--440, which can replace the r-process.

(2). The super-heavy elements with Z=114--126 (A~330--360) can be formed. They can be observed in cosmic rays if they have the halftime $\tau_{\frac{1}{2}} > 10^7$ years.

(3). The peak in the rare-earth elements comes from the symmetric fission of super-heavy elements.

(4). There are more neutron-rich nuclei in the fragments.

(5). The abundances of Z>83 elements in cosmic rays are one order of magnitude higher than that in the solar system.

THE MODEL-INDEPENDENCE OF COSMIC RAY SOURCE DETERMINATIONS

STEVEN H. MARGOLIS
McDonnell Center for the Space Sciences
Washington University
St. Louis, MO 63130 USA

ABSTRACT

The direct inversion method of Margolis (1983) is used to explore the dependence of $Z \leq 28$ source abundance determinations on the choice of the pathlength distribution. The source abundances do not depend strongly on the form of the truncation used, although some truncation at the lower energies (compared to a leaky box) is necessary. The decrease of mean grammage with increasing energy is required by the observations. The effects of errors and the use of other secondary to primary ratios is discussed.

1. Introduction. In the past, discussions of the source abundances of cosmic rays have always been in the context of a particular propagation history (pathlength distribution) and a sequence of calculations designed to correct an initial estimate of the source abundances to match observations. Margolis (1983) showed that the propagation equations of the GCR through the interstellar medium permit a direct inversion. This inversion method is used here to determine the source abundances of the Galactic Cosmic Rays in a model-independent manner. The errors of observation set the criteria for consistency between models. The implications of this method for determining the pathlength distribution (PLD) and the abundances are discussed.

2. The Analytic Procedure. Since the details of the analysis are presented in detail elsewhere, only a brief outline is provided for the reader's convenience. The steady-state diffusion equation governing the propagation of the cosmic rays can be separated into 2 equations, one governing the spatial distribution of the particles, and the other the nuclear physics of fragmentation and decay. This split is frequently referred to as the "weighted slab method." Neglecting energy loss reduces the composition equations to a set of linear equations with energy appearing as a parameter. By expressing the solution in terms of matrix exponentials, Margolis (1983, 1985) showed that the observed abundances and the source abundances could be related for an arbitrary PLD. A graphical analysis of these solutions allows not only the determination of the "best" source abundances from a set of observations, but also the errors associated with the determinations based on those measurements.

3. The Overall Source Abundances. Since cosmic ray observations sample different energies, a separate decomposition can be produced for each energy. Previous determinations have not yielded a single source composition for all energies (Dwyer *et al.*, 1981) nor a single choice of propagation parameters covering all energies (Garcia-Muñoz *et al.*, 1981, 1984; Cesarsky, Koch, and Perron, 1981; Ormes and Protheroe, 1981). Such variations are also seen here. For discussion purposes, consider the truncated exponential distribution of Tsao, Shapiro, and Silberberg (1973), whose shape is that of a linear rise to some grammage Λ_t matched to an exponential tail of scale Λ_e. Simultaneous use of the ratios B/C and (Sc–Mn)/Fe allows the determination of a single decomposition and a single set of source abundances for each energy. For observations, use the 9 energies above 2.54 GeV/nucleon from the HEAO C2 experiment (Engelmann *et al.*, 1983). The resulting plots of Λ_e and Λ_t in Figure 1 show a relatively uniform variation of the escape length and some fluctuations in the truncation length. These results suggest that the truncation is significant but does not vary with energy. Figure 1 also shows an alternate set of tracks, determined by looking at the ratio pair B/C and V/Fe. The escape lengths match reasonably well, but this second set suggests a truncation which decreases with energy. How, then, should these results be compared, and what confidence can be placed on these results?

An advantage of this formulation is the direct calculation of estimated errors from the errors of observation, if reasonable values for these are known. For the data used here, the formal errors at the source are generally smaller than the scatter of the computed values. The true errors are probably somewhat larger. The Silicon measurements, whose average was used to normalize the observations (Engelmann *et al.*, 1983) show a scatter 4 times the size of the formal error of the average. A comparison of the two sets of source abundances described above shows that, at worst, the difference

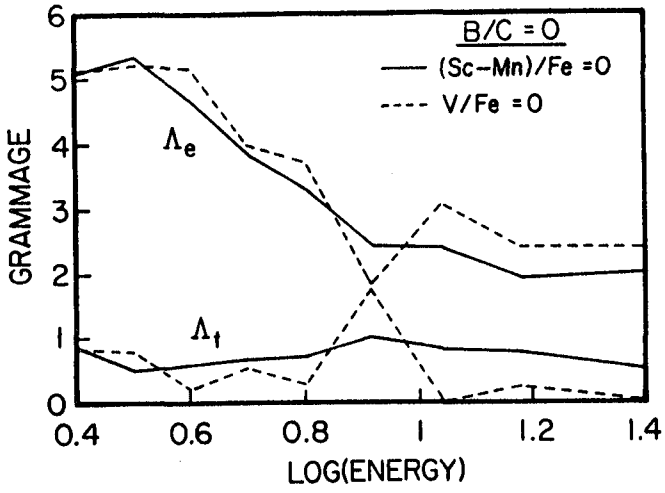

Figure 1. The parameters Λ_e and Λ_t are plotted as functions of energy per nucleon for two different model selection criteria. Note that the decrease of Λ_e is relatively uniform as a function of energy, but that the variation of the truncation Λ_t is quite noisy. Both sets of parameters are determined using the null B/C source ratio. The solid lines are the parameters determined by the null contour of the sub-Fe/Fe source ratio, and the dashed lines were based on the null V/Fe source ratio.

between the separate determinations is only twice the formal error. Given that, it seems reasonable to produce the GCRS abundances shown in Table 1. These were formed from the simple averages of the two sets of 9 decompositions, and the formal errors shown are derived under the assumption of independence. The table also shows the errors derived from the scatter of the individual source abundances, which shall be denoted as the informal errors. These two estimates serve as confidence indicators.

Comparison of the abundances with both the formal and informal errors shows quite clearly the distinction between well- and poorly-determined elements. The formal errors, when compared with the abundances, indicate the significance to which the source abundances are determined within the propagation model. The informal errors, when compared with the formal errors, indicate the variation of the abundances across the separate determinations. The informal error is the better indication of the significance of a source abundance, but as noted above, the intrinsic scatter of the original normalization is about 4 times the formal, statistical error. C ($Z = 6$) and Fe ($Z = 26$), for example, have abundances which stand out quite clearly from the errors. The abundances of F ($Z = 9$) and K ($Z = 19$), though negative, are comparable to the errors. Significant values cannot be determined for those elements whose values are clearly consistent with zero abundance. The difficulty comes in assessing a level of significance relative to the errors. The scatter of the normalization suggests that an abundance is significant only when its value is more than 4 times its associated error. The abundances which are significant under this criterion are marked with an asterisk (*).

4. Discussion. The contrast between the variations in the parameters selected and the abundances calculated can be understood from the complementary variations displayed in Figure 1. The mirroring of changes in the general trends of the escape and truncations lengths imply a well-defined average grammage and a non-pathological PLD underlying the abundances. The observations can be matched approximately by several models. Despite some uncertainty in the PLD, the source abundances vary slowly. This uncertainty suggests two questions. How much error does the choice of a particular PLD introduce? To what extent can the shape of the PLD be investigated using these techniques?

The choice of the form of the PLD need not be a significant source of error. The "no short pathlengths" model employed by Garcia-Muñoz *et al.*, (1984) yields an alternate sequence, with a truncation parameter about half that of the corresponding parameter for the linear rise model; this seems almost intuitive when the linear rise model is viewed as including a triangular distribution with half the area of the rectangle *excluded* by the no short paths model. The more extreme form of the truncation does not significantly change the source abundances estimated here. The abundance values of Table 1 also compare quite well with others derived from the same measurements using other distributions and other methods (Koch-Miramond *et al.*, 1983). (Note again that the errors presented

The Cosmic Ray Source Abundances			
Atomic Number	Abundance Si ≡ 10^3	Formal Error	Informal Error
4	10.2	15.2	51.7
5	1.7	26.2	12.0
6 *	4270.0	43.0	212.0
7 *	374.0	24.5	24.6
8 *	5050.0	44.6	143.0
9	-5.6	3.6	7.1
10 *	660.0	9.7	26.9
11 *	60.8	4.9	9.1
12 *	1050.0	11.7	32.7
13 *	117.0	5.3	8.0
14 *	1000.0	11.1	0.0
15	7.8	2.5	2.1
16 *	143.0	5.5	8.3
17	2.8	2.7	2.7
18 *	15.5	3.6	2.5
19	-1.1	3.5	5.4
20 *	63.7	4.9	5.9
21	-3.2	2.5	3.7
22	-11.8	4.3	8.5
23	0.9	3.1	2.4
24	11.1	4.7	7.8
25 *	20.5	3.8	3.9
26 *	958.0	12.7	34.5
27	3.1	1.0	0.6
28 *	55.1	3.3	4.5

Table 1. The Cosmic Ray Source Abundances determined using the truncated exponential distribution. The asterisks mark those elements with clearly significant abundances. The Formal Errors are those calculated from the errors of the 18 separate energy/model combinations. The Informal Errors represent the scatter of those separate points.

here do *not* include the cross section errors, but are only the measurement errors as modified by the effects of propagation.) There is a well-defined source composition which can be related to the observations by a PLD whose average grammage decreases with increasing energy. Can anything more specific be determined about the form of the PLD?

This method might allow some discrimination between distributions. The internal scatter, the informal error, of the determined abundances differs among distributions. The consistency of a run of abundances with energy is an important measure of the quality of a particular decomposition. The informal errors, examined over all charges, could offer a quantitative reason to select one distribution shape over another. General features of the PLD might be distinguished on a comparative basis; while not truly model-independent, such a procedure does not introduce bias beyond that involved in formulating the propagation problem. The observations used here do not provide sufficient discrimination to distinguish between different forms of truncation, but only to confirm the necessity for some at the lower energies.

Determinations of a variable truncation in a strictly phenomenological way do not explain the propagation of the cosmic ray nuclei. With some decrease in the associated errors, the methods described here should be able to provide a test for quantitative theories such as that of Margolis (1981) and Margolis and Bussard (1983) for the origin of the energy-dependent PLD. They point out that scattering from Alfvén waves generated by the flux of cosmic rays leads naturally to a truncation which decreases with energy and an average grammage which would decrease and then level off with increasing energy. Taking the results of Garcia-Muñoz *et al.* (1984) as evidence for a variable truncation, one must look to the overall variation of grammage with energy as the next key test. The prediction of Margolis and Bussard that the average grammage should level off as energy increases is suggested, but not proved, by the curves of Figure 1. In the future, more sensitive decompositions at

higher energy will resolve this question.

Much of the sensitivity of any decomposition depends on the range of elements through the variation of the total inelastic cross section. Although the various types of distributions lead to different values of precision, the increases in accuracy are comparable for models in the range allowed by the observations. The potential accuracy for the linear rise, truncated exponential models used here is increased by only about 20% if an S/P ratio based on the Te-Ba peak elements is substituted for the sub-Fe/Fe ratio. A ratio based on Pt-Pb group elements might permit a 25% increase compared to the sub-Fe/Fe ratios, all other factors being equal.

Unfortunately, all other factors are not equal. Currently available observations at the higher charges are so much less precise that the overall selectivity is much poorer. The general increase of partial cross sections with atomic number helps a little, but the errors associated with poorly determined cross sections and multiple primary contributions to secondary elements outweigh all such gains. This also limits the utility of the obvious generalization of the two-parameter search to more complex distributions. At present, the search for the GCRS would be aided most by a more reliable normalization of the observed abundances across the dynamic ranges of charge and energy.

5. Summary. The source abundances of the Galactic Cosmic Rays can be calculated by a reasonably model-independent procedure. The decomposition depends on the relations between the production of secondary elements and the relative abundances of the primaries. The analytic nature of the procedure allows the straightforward assignment of errors to the source abundances calculated from the errors associated with the observations. Although a model for the PLD must be used in the procedure, there is no effective restriction on the form of the model, and the dispersion of the source abundances calculated at several energies can be used as a measure of quality to select between distributions. The technique has been demonstrated by calculating the source abundances of the nuclides $Z \leq 28$. The source abundances are consistent with those determined by others using different methods. The average grammage traversed by the cosmic rays decreases with increasing energy. The PLD required by the observations is deficient in short pathlengths at lower energies. There are indications that the truncation decreases with energy, but the errors associated with the observations are a little too large to make a definitive assessment at this time.

6. Acknowledgements. The work reported here was supported by NASA Grant NAG8-448 and by McDonnell Center research funds.

7. References.

Cesarsky, C. J., Koch, L., and Perron, C. 1981. *Proc. 17th Int. Cosmic Ray Conf. (Paris)*, **2**, 22.

Dwyer, R. D., Garcia-Muñoz, M., Guzik, T. G., Meyer, P., Simpson, J. A., and Wefel, J. P. 1981. *Proc. 17th Int. Cosmic Ray Conf. (Paris)*, **9**, 222.

Engelmann, J., Goret, P., Juliusson, E., Koch-Miramond, L., Masse, P., Soutoul, A., Byrnak, B., Lund, N., Peters, B., Rasmussen, I. L., Rotenberg, M., and Westergaard, N. J. 1983. *Proc. 18th Int. Cosmic Ray Conf. (Bangalore)*, **2**, 17.

Garcia-Muñoz, M., Guzik, T. G., Margolis, S. H., Simpson, J. A., and Wefel, J. P. 1981. *Proc. 17th Int. Cosmic Ray Conf. (Paris)*, **9**, 195.

Garcia-Muñoz, M., Guzik, T. G., Simpson, J. A., and Wefel, J. P. 1984. *Ap. J. (Letters)*, **280**, L13.

Koch-Miramond, L., Engelmann, J., Goret, P., Julisson, E., Masse, A P., Soutoul, A., Perron, C., Lund, N., and Rasmussen, I. L. 1983. *(Proc.) 18th Int. Cosmic Ray Conf. (Bangalore)*, **9**, 275.

Margolis, S. H. 1981. *Proc. 17th Int. Cosmic Ray Conf. (Paris)*, **9**, 215.

Margolis, S. H., 1983. *Proc. 18th Int. Cosmic Ray Conf. (Bangalore)*, **9**, 267.

Margolis, S. H. 1985. *Ap. J.*, (in press).

Margolis, S. H., and Bussard, R. W. 1983. *Proc. 18th Int. Cosmic Ray Conf. (Bangalore)*, **9**, 271.

Ormes, J. F., and Protheroe, R. J. 1981. *Proc. 17th Int. Cosmic Ray Conf. (Paris)*, **2**, 31.

Tsao, C. H., Shapiro, M. M., and Silberberg, R. 1973. *Proc. 13th Int. Cosmic Ray Conf. (Denver)*, **1**, 107.

THE EFFECTS OF NEWLY MEASURED CROSS SECTIONS IN HYDROGEN ON THE PRODUCTION OF SECONDARY NUCLEI DURING THE PROPAGATION OF COSMIC RAYS THROUGH INTERSTELLAR H

W. R. Webber & M. Gupta
Space Science Center
University of New Hampshire
Durham, NH 03824

L. Koch-Miramond & P. Masse
Cen Saclay 91191
Gif-sur-Yvette
Cedex, France

1. Introduction. As discussed in papers at this conference and in earlier publications (e.g. Webber & Brautigam, 1982) we have now measured the cross sections of six important cosmic ray source nuclei in hydrogen at several energies between 300 and 1800 MeV/nuc. Significant differences, sometimes exceeding 50%, exist between these new measurements and the earlier semi-empirical predictions, and we are in the process of determining a new set of semi-empirical formulae that better describe this fragmentation (Webber & Hsiung, paper, OG 7.2-24 this conference). We have now obtained enough new cross sections so that the systematics of their effects on cosmic ray propagation through interstellar hydrogen can be examined.

2. Details of Calculation. In this study we have used the propagation program developed by the HEAO-3 experimenters at SACLAY (e.g. Perron and Koch, 1981) as well as a simpler program developed at UNH. For the purposes of this study, for all calculations, we have assumed a source spectrum $\sim P^{-2.3}$ and an exponential distribution of path lengths, $\lambda_e = 22.0\,\beta\,P^{-0.6}$ g/cm^2 of hydrogen above 5.5 GV and $\lambda_e = 8.33\,\beta$ below 5.5 GV. This path length is found to fit a wide variety of cosmic ray abundance data at both high and low energies and for various Z ratios as discussed by Soutoul et al., paper, OG 4.1-3 this conference. No truncation of this path length is considered in these calculations. For the cross sections we have used 1) the earlier semi-empirical formula predictions as updated through 1977 (Tsao and Silberberg, 1979) and 2) revised cross sections as indicated by our new results - including unmeasured cross sections as revised by our updated semi-empirical formulae (Webber and Hsiung, paper, OG 7.2-24 this conference).

3. Results of Calculation. a) Abundance Ratios. In Figures 1, 2 & 3 we show the B/C, Al/Si and K/Fe ratios calculated for secondary production only. (Φ = 600 MV in all cases). The observed ratios (Engelmann et al., 1983) are also shown. In almost every case the new cross sections lead to significantly better fits to the measured individual ratios of mainly secondary nuclei than was the case for the previous semi-empirical cross sections. In order to further illustrate the propagational changes brought about by the new cross sections we examine the situation at one energy only - 1.5GeV/nuc where $\lambda_{esc} = 8.0$g/cm^2. Table I lists the percentage change in secondary production for the various ratios brought about by introducing the new cross sections. It should be pointed out that these percentage changes are at one energy only. They may differ considerably at other energies because of different energy dependances of the cross sections as illustrated in Figure 3. Also note that these differences, which are typically

5-10% or larger, are much greater than the 1-2% abundance ratio errors in the HEAO data base. And finally, the effects of short path length truncation, which are typically ~ 5-10% in the ratio of B/C to the ratio of Z=21-25/Fe, (for example Garcia-Munoz et al., 1984) can be masked by the differences of the same order found for the new cross sections.

b) Source Abundances. The new cross sections allow the secondary abundances of most nuclei to be caluclated to an accuracy ~ 3-5% for a fixed path length. This, coupled with the 1-2% accuracy of the measured charge ratios, allows the source abundance of galactic cosmic ray nuclei to be calculated to a new level of precision, including some charges for which only upper limits existed from previous calculations. This analysis is shown in Table 2. All values refer to 1.5 GeV/nuc and use the propagation parameters already discussed, e.g. λ_e = 8.0g/cm^2, Φ = 600 MV. The caluclated abundance at earth in column one is the secondary abundance only as caluclated from all heavier nuclei -including the revised source abundance from this work. The errors are only those on the cross sections as propagated through the 8.0g/cm^2 of interstellar hydrogen. The observed ratios are the average ratios at 1.5 GeV/nuc from Engelmann et al., 1983. Any differences in the calculated and observed ratios for the mostly secondary nuclei can be directly related to the source abundance of that secondary nucleus. It is seen that for Be, B, Fl, Cl, K, Sc and V this difference is ~ ± 1 σ in the combined errors in the cross sections and the observations. The fact that these differences are almost equally divided between + and - and also show no clear trend with Z shows that 1) the value of 8.0g/cm^2 is consistent to within ± 0.2g/cm^2 and 2) the effects of truncation of short path lengths must be small.

These differences translate into source abundances of a few parts in 1000 to that of Si, with comparable errors. For the remaining nuclei in the table the source abundances are all finite and significant. For the first time it is possible to get meaningful source abundance estimates for the elements P, Ar, Ti and Cr. If the usual plot of the ratio of CRS to LG abundances (≡R_1) versus FIP is made (Figure 4) then a rather abrupt decrease from a value ~ 1 to a value ~ 0.2-0.3 is observed between 8-12V FIP. The elements He, N and Ti and Cr apparently do not fit this simple picture. A very similar behavior occurs when a corresponding plot is made using new and more complete solar particle data from Voyager (Breneman et al., 1985). In Figure 5 we show a plot of the new cosmic ray source data versus the new solar particle abundance data. (≡R_2) Earlier plots of this type suggested ratios R_2 ~ 1 with some notable exceptions. There is now evidence for a structure in this abundance ratio when plotted against FIP. To further examine this we plot in Figure 6 R_1 vs R_2. Seven elements are clustered about one - several of the remaining elements are clustered about R_1 = 0.25 & R_2 = 0.7 suggesting perhaps a difference in the FIP selection process in the sun and in cosmic ray sources for these elements. This selection process or fractionization occurs on the sun between the photosphere and corona and its identification in the cosmic ray sources would be of great importance. It is also possible that all of the elements, except C, lie along a line in R_1 R_2 space as indicated by the line in Figure 6. The further implications of this behavior will be discussed in a separate publication.

4. Acknowledgements. This work was supported by a HEAO Guest Investigator Grant #NAG-8-451, and by a NASA Support Grant #NGR-30-002-052.

5. References.

Breneman, H., et al., paper SP this conference
Engelmann, J. J., et al., *17th ICRC*, 2, 17, 1983
Garcia-Munoz, M., et al., *Ap.J.*, 280, L13, 1984
Perron, C., & Koch, L., *Proc. 17th ICRC*, 2, 27, 81
Soutoul, A., et al., paper OG 4.1-3, this conference

Tsao, C. H., &Silberberg, R., *Proc. 16thICRC*, 2, 202, 1979
Webber,W. R., & Brautigam, D. A., *Ap.J.*, 260, 894, 1982
Webber, W. R., & Hsiung, P., paper OG 7.2-24, this conference

6. Figure Captions.

Figure 1. The observed $^{B}/_{C}$ ratio and that predicted using the new cross sections.
Figure 2. The observed $^{Al}/_{Si}$ ratio and that predicted using the new cross sections. (Secondary production only - no Al in source)
Figure 3. The observed $^{K}/_{Fe}$ ratio and that predicted using the new cross sections - no K in source.
Figure 4. Ratio of cosmic ray source abundance deduced in this analysis to LG abundances vs FIP $\equiv R_1$.
Figure 5. Ratio of new cosmic ray source abundances to new solar cosmic ray abundances vs FIP $\equiv R_2$.
Figure 6. The Ratio R_1 vs. R_2 for elements with $Z \leq 30$.

Table I

Effects of New Cross Sections on Secondary Production Ratios

Ratio	% Change in Secondary Production at 1.5 GeV/nuc*
Be/C	- 3.5
B/C	- 7.3
N/O	+ 5.2
Fl/Ne	≤ 2
Na/Mg	≤ 2
Al/Si	+ 17.0
P/S	+ 10.4
Cl/Fe	- 12.5
Ar/Fe	+ 11.5
K/Fe	- 8.5
Ca/Fe	- 6.1
Sc/Fe	+ 3.0
Ti/Fe	+ 3.2
V/Fe	+ 2.5
Cr/Fe	- 10.2
Mn/Fe	- 16.5
	at 600 MeV/nuc
^{25}Mg	+ 11.5
^{26}Mg	+ 33.0
^{29}Si	
^{30}Si	

* From Tsao & Silberberg, 1977

Table II

Comparison of Calculated & Observed Abundances at 1.5 GeV/nuc - Source Abundances

	Calculated	Observed	Difference	Source Abundance Si = 1000
Be/C	0.109±0.004	0.100±0.005	-0.009±0.007	-8±8
B/C	0.295±0.010	0.305±0.006	0.010±0.012	42±50
C/Si	-	6.76 ±0.12	-	4310±100
N/O	0.303±0.008	0.303±0.003	0.043±0.009	220±50
O/Si	-	6.38 ±0.10	-	4960±80
Fl/Ne	0.133±0.003	0.135±0.003	0.002±0.004	1.3±2.5
Ne/Si	-	1.031±0.010	-	615±15
Na/Mg	0.112±0.010	0.174±0.005	0.062±0.011	66±12
Mg/Si	-	1.305±0.010	-	1075±12
Al/Si	0.158±0.007	0.232±0.005	0.074±0.009	76±9
Si	-	-	-	1000
P/S	0.193±0.009	0.225±0.006	0.033±0.011	45±1.5
S/Si	-	0.203±0.004	-	132±6
Cl/Fe	0.079±0.004	0.076±0.002	-0.003±0.005	-2±5
Ar/Fe	0.110±0.004	0.136±0.003	0.026±0.005	18±5
K/Fe	0.095±0.003	0.099±0.002	0.004±0.004	3±3
Ca/Fe	0.118±0.004	0.220±0.004	0.102±0.006	72±6
Sc/Fe	0.053±0.003	0.051±0.002	-0.002±0.004	-2±4
Ti/Fe	0.140±0.003	0.147±0.003	0.007±0.003	6±3
V/Fe	0.069±0.002	0.073±0.002	0.004±0.003	3±3
Cr/Fe	0.110±0.003	0.146±0.003	0.036±0.005	32±5
Mn/Fe	0.090±0.002	0.097±0.002	0.007±0.0025	6±2.5
Fe/Si	-	0.636±0.013	-	915±15
Co/Ni	0.070±0.007	0.128±0.008	0.058±0.011	2.5±0.5
Ni/Si		0.029±0.0015		45±3

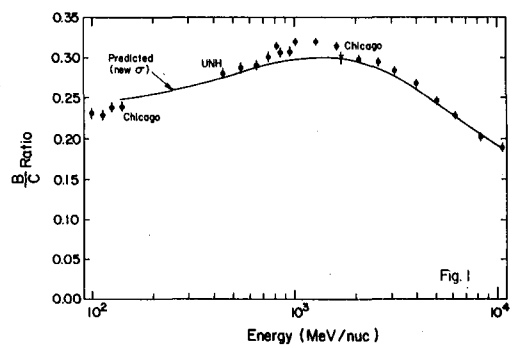

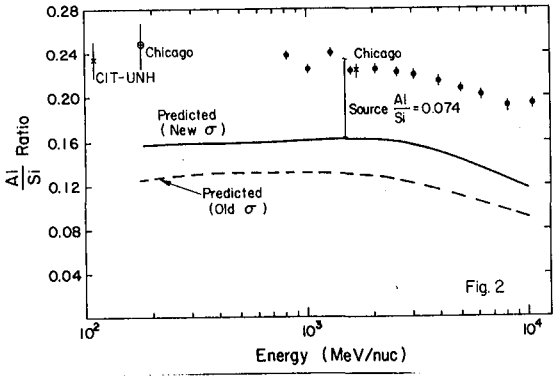

Fig. 2

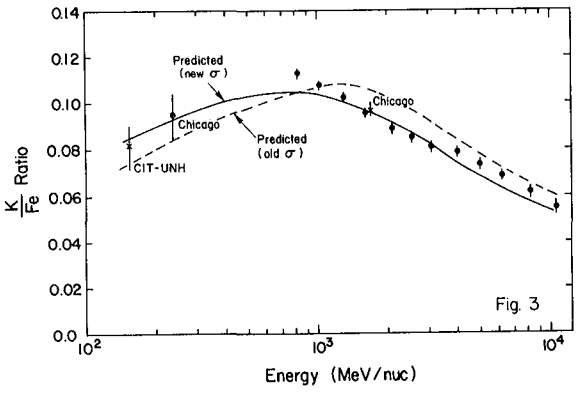

Fig. 3

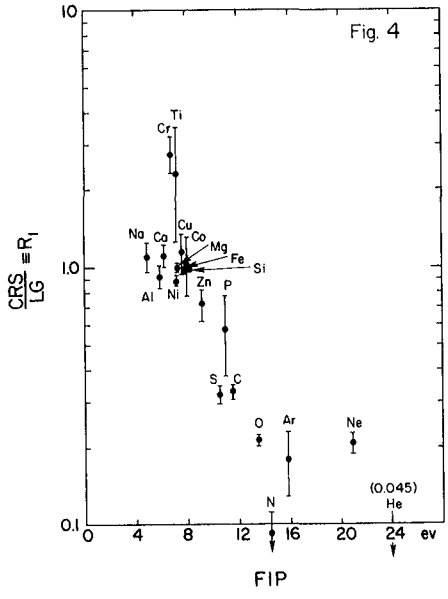

Fig. 4

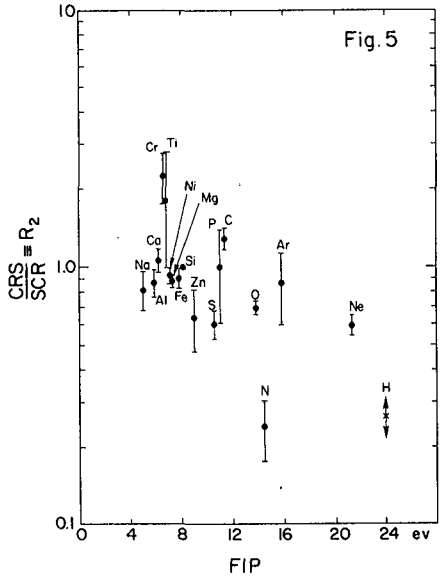

Fig. 5

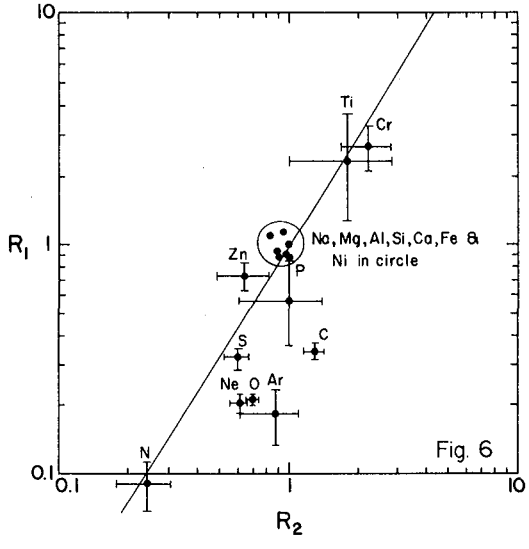

Fig. 6

OG 7.2-3

IMPLICATIONS OF CROSS SECTION ERRORS FOR COSMIC RAY PROPAGATION

John R. Letaw
Severn Communications Corp., P.O. Box 544, Severna Park, MD 21146

Rein Silberberg and C.H. Tsao
Naval Research Laboratory Washington, D.C. 20375

ABSTRACT

Errors in nuclear interaction cross sections are the single most important limitation on the analysis of cosmic ray composition data. In the 18th International Cosmic Ray Conference, Hinshaw and Wiedenbeck (1983) demonstrated the potential importance of correlations in cross section errors in determining cosmic ray source abundances. In this paper we estimate the magnitude of cross section error correlations. Our analysis suggests that cross section errors are essentially uncorrelated for nuclei with $Z < 29$ and that the actual errors may be less than the nominal 35%.

1. Introduction. Uncertainty in nuclear interaction cross sections is the most important limitation on the analysis of cosmic ray composition. Cosmic ray primaries, such as C, O, and Ne, have 5-20% source abundance uncertainties due to errors in estimating the contribution of fragments of heavier nuclei. These errors have a more profound impact as the contribution of secondaries grows. Thus a more detailed understanding of pre-acceleration atomic selection effects awaits improved source abundances for Na, Al, and Ca. Consistency of the N source abundance remains doubtful because of the uncertain O --> N cross sections. Source abundances of K, Ti, V, Cr, and Mn, though possibly not negligible, are entirely obscured by cross section errors.

Hinshaw and Wiedenbeck (1983) analyzed the uncertainties involved in computing cosmic ray source composition from observed abundances. Their analysis included measurement error, total and partial cross section error, and mean pathlength uncertainty. They demonstrated that cross sections are the dominant source of uncertainty. More importantly, they left open the possibility that cross section errors are strongly correlated, meaning only source abundances of pure primaries can be reliably derived from compositional measurements.

In this paper we show that cross section correlations in the semi-empirical formulas (Silberberg and Tsao, 1973 and Silberberg et al., 1985) are essentially negligible in cosmic ray propagation calculations concerning $Z < 29$. Our conclusion is based on the excellent agreement between secondary abundances measured by the French-Danish experiment on HEAO-3 (Engelmann et al., 1983) at 3.99 GeV/N and a primitive propagation model.

2. Method of Calculation. A standard cosmic ray propagation model (Letaw et al., 1984) with exponential pathlength distribution having a rigidity-dependent mean pathlength of $\Lambda R^{-0.6}$ g/cm^2 was used. Initially the source composition was taken as the solar system abundances of Anders and Ebihara (1982). Semi-empirical cross sections were used throughout. Errors of partials were assumed to be 35%.

For fixed values of Λ a propagation was performed iteratively. Primary and secondary contributions were tracked independently. In each iteration, the required fractional increase in the primary arriving abundance needed to match observed abundances was determined. The source elemental abundances were then corrected by these fractions. Isotopic ratios at the source were left unchanged because experience indicates these have little effect on arriving elemental abundances. Eventually the source abundances stabilize. For each element an abundance is given with uncertainty estimated using uncorrelated and correlated cross sections.

To fix the best value of Λ we analyzed the abundances of 9 secondaries (Be, B, F, P, K, Cl, Sc, Ti, V) for several possible choices. These elements should have nearly zero source abundance. Calculated source abundances are shown in Figure 1 as a function of Λ. Note that all values shown are within one standard deviation of zero. Their deviations from zero were divided by the source uncertainties, squared, and summed. This quantity is a measure of the group's proximity to zero and is shown in Figure 2. It is minimized when Λ = 25 (with 70% confidence that it is between 23 and 26.5).

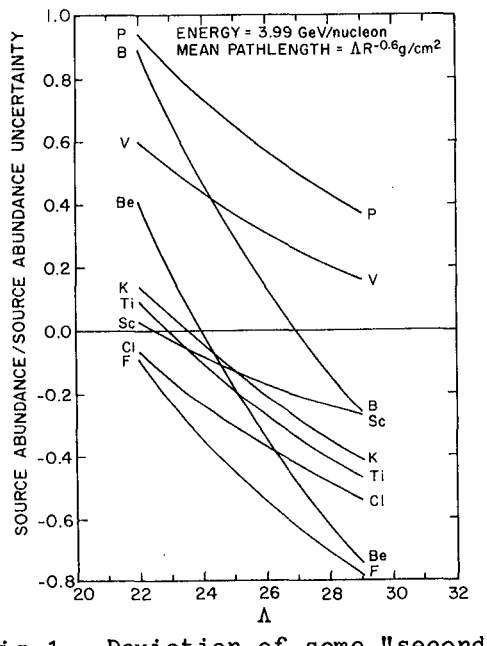

Fig 1. Deviation of some "secondary" source abundances from zero versus pathlength.

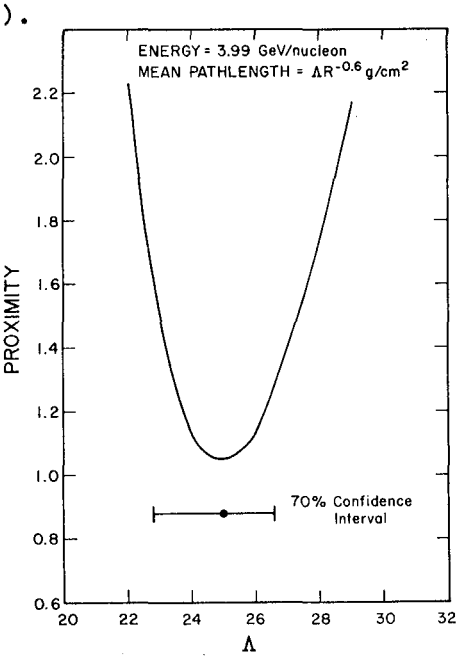

Fig. 2. Proximity of 9 "secondary" source abundances to zero versus pathlength.

There are two important implications of this procedure. First, heavier elements are now allowed to participate in determining the mean pathlength. We believe this approach is advisable when overall source uncertainties of the heavier elements are comparable to those of Li, Be, and B. Second, uncertainty in Λ (i.e., uncertainty in one aspect of the propagation model) should not further increase the computed uncertainties in the source abundances. An indeterminate uncertainty resides in the model. It is not possible to quantify model uncertainties because the model cannot be independently validated.

3. Results. Figure 3 shows some results of the propagation described above. The deviation of computed arriving abundances (with their correlated and uncorrelated uncertainties) from observed arriving abundances of the 9 secondaries are shown. We note first the excellent agreement of this primitive cosmic ray propagation model with the high energy experimental data. Only in one case does the difference amount to more than one standard deviation. This leads us to Conclusion 1: Even simple cosmic ray propagation models provide an excellent representation of the interstellar transport process (with respect to composition).

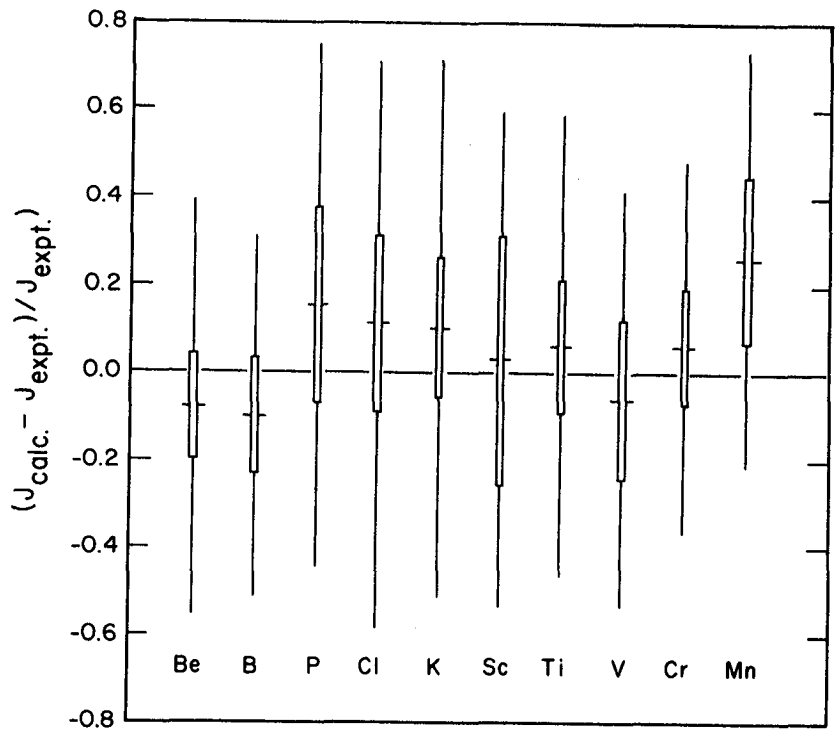

Fig. 3. Comparison of observed and computed source abundances for 9 cosmic ray secondaries. Estimated errors are larger for correlated cross section errors.

A disturbing feature of Figure 3 is that the agreement with experiment is too good. We should expect several of the elemental abundances to differ by more than one sigma. The mean deviation is about 12%. For uncorrelated cross section errors a mean deviation of 18% is expected, while for correlated errors a deviation of 50% is expected. Using the χ^2 test we estimate the probability that agreement with experiment would be so good if uncertainties are properly estimated. In the case of correlated cross section errors (larger uncertainties) the probability appears to be less than 2 in 10^4. For uncorrelated cross sections the probability is about 0.18. Conclusion 2: while we cannot rule out the possibility of error correlations, it appears that cross section error correlations are negligible in cosmic ray propagation. Even with uncorrelated errors the agreement with experiment is improbable suggesting that the nominal 35% cross section uncertainty is too high an estimate for $Z < 29$.

References:

Anders, E. et al. 1982, Geoch. Cosmoch. Acta, 46, 2363.
Engelmann et al. 1983, 18th Int. Cosmic Ray Conf., (Bangalore), OG 1-9.
Hinshaw, G.F. and Wiedenbeck, M.E. 1983, 18th Int. Cosmic Ray Conf. (Bangalore), OG 5.2-7.
Letaw et al. 1984, Ap. J. Suppl., 56, 369.
Silberberg, R. and Tsao, C.H. 1973, Ap. J. Suppl., 28, 315.
Silberberg et al. 1985, to appear in Ap. J. Suppl.

COSMIC RAY SECONDARY NUCLEI AND THE STRUCTURE OF THE GALAXY

G. Morfill, P. Meyer[1], and R. Lüst[2]
Max-Planck-Institut für Extraterrestrische Physik, Garching, FRG

ABSTRACT. We explore the consequences of diffusive acceleration of cosmic rays in supernova shocks propagating through an inhomogeneous interstellar medium. The acceleration takes place in the hot, tenuous, intercloud gas, whilst nuclear collisions, leading to the production of cosmic ray secondaries, predominantly occur in those regions where the supernova shocks collide with interstellar clouds. We use a simple model to calculate the interaction of a (cosmic ray + gas) shock with a cloud, and thus determine the gross topology. Extending this to the whole system, using mean cloud sizes and space densities, allows us to calculate the secondary/primary cosmic ray abundance ratios for light and heavy nuclei.

1. INTRODUCTION. The antiproton/proton abundance ratio in the cosmic rays of a few GeV/n [1] is about 4 times higher than expected on the basis of a model describing the galaxy as a simple leaky box (SLB). The $^3He/^4He$ ratio, also at a few GeV/n, was found to be enhanced by a factor of about 2, using the SLB model [2]. The idea of invoking "thick-target" sources to explain the antiproton observations has recently been introduced [3,4]. In this model a fraction of the cosmic rays sources is assumed to be located in massive, dense, interstellar clouds (i.e. buried supernovae). The clouds essentially absorb the locally produced heavy primaries and secondaries, but allow a significant fraction of light primaries and secondaries to escape. This source thus enhances the secondary/primary ratios for the light particles, provided the mean matter path length in the source region is sufficiently large (of the order $40 g/cm^2$). The remainder of the sources is located in a low density medium, producing cosmic rays that traverse about $6 g/cm^2$ of matter before being lost from the galaxy. This yields the observed secondary/primary ratios of the heavier nuclei. Difficulties with this model arise from galactic gamma-ray observations which imply that embedded sources can not be effective producers of energetic (GeV) cosmic rays [5]. A second problem is the ionization rate inferred for the massive clouds. For $\dot{E}$ ergs/sec injected into massive clouds, of which a fraction η goes into ionizing the gas, and assuming that 10 eV is required for ionization, we compute an ionization rate

$$\xi = 5 \times 10^{-15} \frac{\dot{E}}{\dot{E}_s} \eta \qquad (sec^{-1})$$

This assumes a total cloud mass of $10^9 M_\odot$. $\dot{E}_s$ is the standard cosmic ray energy input rate computed from confinement time measurements ($=10^{41}$ ergs/sec). Thus for an efficiency of ~ 0.2, we still obtain mean ionization rates which exceed the typical observed levels by about two orders of magnitude.

Nevertheless, the idea of "thick-target" sources is very appealing to explain the cosmic ray observations because of its basic simplicity.

We therefore explore whether supernova shocks propagating through an inhomogeneous interstellar medium, interacting with clouds locally and advecting previously accelerated particles into these "absorbers", exhibit some "thick-target" properties. In principle this should be so, the question is of course, "at what price do we obtain quantitative agreement?"

2. THE MODEL. We assume that cosmic rays are accelerated in supernova shocks, when these propagate through the hot ionized intercloud medium [6]. We then calculate in a simplified model how the interaction with an interstellar cloud proceeds. The physical processes considered were:
(1) As long as the cosmic ray energy density exceeds that of the gas, magnetohydrodynamic waves are excited by the streaming instability [7].
(2) Through wave-particle interactions the cosmic ray "gas" can then couple onto the thermal gas and modify its flow.
(3) In the ionized medium wave damping is slow so that this coupling is very close. We then have a mixture of a thermal gas and a relativistic, essentially massless, cosmic ray gas acting as a single fluid.
(4) In the neutral clouds, wave damping by ion-neutral friction is very efficient [8]. As a result, the cosmic rays do not interact with the neutral cloud gas and the two are completely uncoupled, at least parallel to the magnetic field $\underline{B}$.
(5) When the cosmic ray energy density equals that of the gas, wave production by the streaming instability ceases and cosmic rays are no longer tied closely to the interstellar medium. A hydrodynamic treatment then becomes inappropriate; cosmic ray transport is diffusive.
(6) Cosmic rays are, however, absorbed in the cloud by nuclear collisions and ionization losses. Through these processes both energy and momentum are taken out of the cosmic ray gas and deposited inside the cloud.
(7) The cosmic ray energy density is dominated by the most abundant species: the protons. Hence, the dynamics of the system is determined by their fate. Cosmic ray secondaries as well as the heavier primaries have to be discussed within the physical framework set up by this dominant component.

This gives rise to the following picture (Fig. 1):

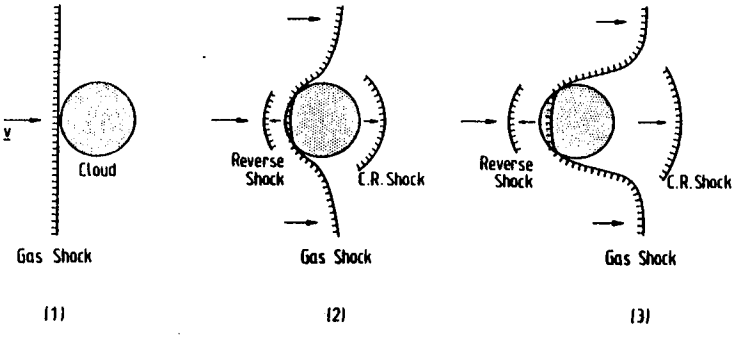

Fig. 1: Illustration of the interaction of a supernova shock, including accelerated cosmic rays, with an interstellar cloud.

The supernova shock with its accelerated cosmic ray component hits the interstellar cloud (1). There is magnetic connection across the cloud, permitting the cosmic rays to enter at essentially the speed of light and to emerge on the other side. The cloud, therefore, acts like a filter, letting cosmic rays through, but not the gas. On the other side, the cosmic rays once again couple onto the tenuous, ionized intercloud gas and produce a cosmic ray pressure driven shock wave (CR) which displaces this gas. The hydrodynamic shock inside the cloud is very slow, and the gas shock begins to envelope the obstacle. There may also be a reverse shock (RS) propagating away from the cloud back into the supernova remnant (2), and cloud evaporation at the contact surface [9]. As time progresses, the gas shock begins to catch up with the (somewhat weaker) cosmic ray shock (3). There may be complicated contact surfaces and reflected shocks, etc. which only a numerical calculation could unravel. For our purposes we shall ignore this and represent the complicated sequence of events with a simple one-dimensional model. By ignoring cloud "crunching" and assuming that evaporation will not be overly significant, we can regard the cloud column density as constant.

3. RESULTS. Figure 2 shows the results of our calculations. We explored a whole range of parameters for the cloud column densities, filling factors, densities, etc. For a full discussion see [10]. Fig. 2 represents the best fit we were able to obtain. As can be seen, the "anomalous" antiprotons and ^{3}He can be explained quite naturally within our theory.

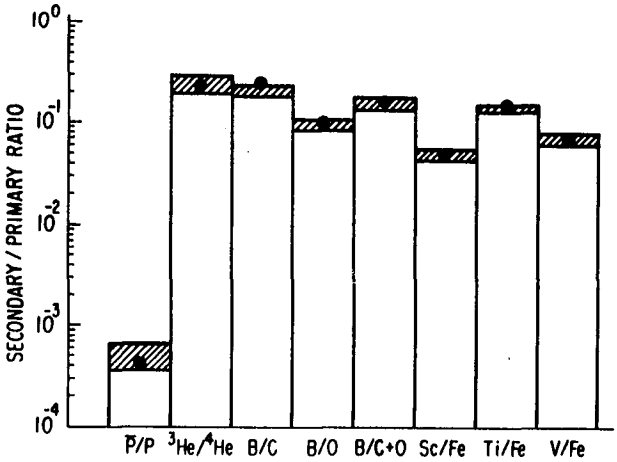

Fig. 2: Comparison between observed (hatched bars which show the measurement uncertainties) and calculated (solid circles) cosmic ray secondary/primary ratios. The model parameters are given in the text.

The structure of the interstellar medium, derived from the fit to the observed secondary/primary ratios, is summarized in Tables I and II.

Table I: Structure of the interstellar medium

Intercloud medium	
density	10^{-2} cm^{-3}
temperature*	4.3×10^5 K
filling factor	0.92
pressure*	0.8 eV/cm^3

Table II: Structure of the interstellar medium Clouds (average properties)	
gas density	$120 cm^{-3}$
column density	$1.1 \times 10^{21} cm^{-2}$
size	3 pc
temperature*	80 K
mass	$94 M_\odot$
spatial density	$2.9 \times 10^{-3} pc^{-3}$
mean separation (line of sight)	40 pc
filling factor	0.08
total mass in galaxy	$1.9 \times 10^{10} M_\odot$

*Not derived from the cosmic ray data, these are input values.

It should be stressed that the measurements pertain to the volume sampled by the cosmic rays, i.e. a region within about 1 kpc of the solar system. Extrapolation to the galaxy as a whole may therefore not be valid. The galactic gamma ray luminosity calculated from this model is 3×10^{38} ergs/sec, in good agreement with measurements [11]. The derived quantities of Tables I and II agree surprisingly well with the interstellar medium structure derived by McKee and Ostriker [12].

No attempt has been made to calculate the secondary spectra, although it is easy to show that the total matter path length traversed by very high energy particles should become progressively smaller, in qualitative agreement with observations.

REFERENCES

1. Golden, R.L., Nunn, S. and Horan, S. 1983, Proc. 18th ICRC 2, 80.
2. Jordan, S.P. and Meyer, P. 1984, P.R. Letters 53, 505.
3. Cowsik, R. and Gaisser, T.K. 1981, Proc. 17th ICRC 2, 218.
4. Cesarsky, C.J. and Montmerle, T.M. 1981, 17th ICRC 9, 207.
5. Morfill, G.E. and Drury, L.O'C. 1981, M.N.R.A.S. 197, 369.
6. Axford, I., Leer, E. and Skadron, G. 1977, Proc. 15th ICRC 11, 132.
7. Lerche, I. 1967, Astrophys. J. 147, 689.
8. Kulsrud, R.M. and Pearce, W. 1969, Astrophys. J. 156, 445.
9. Cowie, L. and McKee, C.F. 1977, Astrophys. J. 211, 135.
10. Morfill, G.E., Meyer, P. and Lust, R. 1985, Astrophys. J., Sept. 15.
11. Strong, A. and Worral, D.W. 1976, J. Phys. A. 9, 823.
12. McKee, C.F. and Ostriker, J.P. 1977, Astrophys. J. 218, 148.

Permanent address:

1) Enrico Fermi Institute and Department of Physics, University of Chicago, Chicago, Illinois USA.
2) Director-General, European Space Agency, Headquarters Paris 15e, France.

OG 7.2-8

WHY DO LEAKY-BOX MODELS WORK SO FINE?

R. Schlickeiser[1], I. Lerche[2]

1) Max-Planck-Institut für Radioastronomie
Auf dem Hügel 69, 5300 Bonn 1, FRG

2) Department of Geology, University of South Carolina
Columbia, SC 29208, USA

ABSTRACT

By introducing the concept of the age distribution of cosmic rays it is possible to decouple the spatial from the momentum transport; and simple leaky-box type equations result. The influence of spatial inhomogeneities, geometries and source distributions enters the spatially homogeneous, infinite (i.e. leaky box) problem through appropriate mean lifetimes. A precise prescription of how to obtain these mean lifetimes: for comparison with data measured in the vicinity of the solar system they have to be calculated from the age distribution at the solar system.

1. Introduction. The propagation of cosmic ray particles in the Galaxy at large momenta, $p > 10$ GeV/c, where spatial diffusion in partially random magnetic fields dominates convection and adiabatic deceleration in the galactic wind, is described by the steady-state transport equation (e.g. Schlickeiser 1983)

$$\nabla \cdot [K(\underset{\sim}{r},p)\,\nabla f] + L_p f + q(\underset{\sim}{r})\,Q(p) = 0 \qquad (1),$$

where f is the particle's phase space density, $K(\underset{\sim}{r},p) = \kappa(p)\,K(\underset{\sim}{r})$ the spatial diffusion tensor, with $\kappa(p)$ chosen dimensionless without loss of generality, and L_p is the momentum operator

$$L_p \equiv p^{-2}\,\frac{d}{dp}\,[p^2\,D(p)\,\frac{d}{dp} - p^2\,\dot{p}_{gain} - p^2\,\dot{p}_{loss}] - \frac{1}{\tau_c} \qquad (2),$$

describing first ($\dot{p}_{gain}$) and second (D(p)) order Fermi acceleration as well as continuous ($\dot{p}_{loss}$) and catastrophic (τ_c) momentum loss processes. $q(\underset{\sim}{r})\,Q(p)$ represents sources and sinks of particles.

2. Decoupling of spatial and momentum transport. If the parameters D(p), $\dot{p}_{gain}$, $\dot{p}_{loss}$ and τ_c do not depend on position ($\underset{\sim}{r}$), equation (1) is solved by the convolution (Lerche and Schlickeiser 1985a)

$$f(p,\underset{\sim}{r}) \equiv \int_0^\infty dy\; G(p,t)\; N(\underset{\sim}{r},y) \qquad (3),$$

with

$$\frac{1}{\kappa(p)}\,L_p\,G(p,y) - \frac{\partial G(p,y)}{\partial y} = 0 \qquad (4)$$

and G(p,y) satisfying given momentum boundary conditions and

$$\lim_{y\to\infty} G(p,y) = 0 \tag{5}$$

$$G(p,y=0) = Q(p)/\kappa(p) \tag{6}.$$

$N(\underset{\sim}{r},y)$ satisfies given spatial boundary conditions, and

$$\underset{\sim}{\nabla}\cdot[K(\underset{\sim}{r})\ \underset{\sim}{\nabla}\ N(\underset{\sim}{r},y)] = \frac{\partial N(\underset{\sim}{r},y)}{\partial y} \tag{7},$$

$$N(\underset{\sim}{r},y=0) = q(\underset{\sim}{r}) \tag{8},$$

and $N(\underset{\sim}{r},y)$ is normalized as

$$\int_0^\infty dy\ N(\underset{\sim}{r},y) = 1 \tag{9}.$$

$N(\underset{\sim}{r},y)$ is commonly referred to as the age distribution of cosmic rays.

The solution of the system of equations (4) - (8) would yield via (3) the particle's momentum spectrum $f(p,\underset{\sim}{r})$ at all positions $\underset{\sim}{r}$ in the Galaxy. However, particle flux measurements can only be obtained at the position of the solar system. In order to compare with these observations we would infer from the general solution $f(p,\underset{\sim}{r})$ the momentum spectrum at the solar system,

$$H(p) \equiv f(p,\underset{\sim}{r}_s) = \int_0^\infty dy\ G(p,y)\ N(\underset{\sim}{r}_s,y) \tag{10}$$

by setting $\underset{\sim}{r} = \underset{\sim}{r}_s$ in (3).

3. Leaky-box equations. However, instead of following this scheme to solve the two partial differential equations (4) and (7), it is much easier to derive from (4) a simpler equation for the momentum spectrum H(p) at the solar system from the known cosmic ray age distribution $N(\underset{\sim}{r}_s,y)$ at the solar system. Integrate equation (4) after multiplying it with $N(\underset{\sim}{r}_s,y)$ to obtain

$$\frac{1}{\kappa(p)} L_p \int_0^\infty dy\ G(p,y)\ N(\underset{\sim}{r}_s,y) = \int_0^\infty dy\ \frac{\partial G(p,y)}{\partial y}\ N(\underset{\sim}{r}_s,y)$$

$$= -\frac{Q(p)\ N(\underset{\sim}{r}_s,y=0)}{\kappa(p)} - \int_0^\infty dy\ G(p,y)\ \frac{\partial N(\underset{\sim}{r}_s,y)}{\partial y} \tag{11},$$

where the right hand side has been integrated by parts taking into account (5) and (6). With (10) equation (11) reads

$$L_p H(p) + \kappa(p) \int_0^\infty dy\ G(p,y)\ \frac{\partial N(\underset{\sim}{r}_s,y)}{\partial y} = -Q(p)\ N(\underset{\sim}{r}_s,y=0) \tag{12}$$

which is an ordinary differential equation in momentum.

If the age distribution at the solar system is a pure exponential,

$$N(\underset{\sim}{r}_s,y) = \frac{1}{\langle T\rangle(\underset{\sim}{r}_s)} \exp\left(-y/\langle T\rangle(\underset{\sim}{r}_s)\right) \qquad (13),$$

one infers $N(\underset{\sim}{r}_s,y=0) = 1/\langle T\rangle(\underset{\sim}{r}_s)$ and $\partial N(\underset{\sim}{r}_s,y)/\partial y = (-1/\langle T\rangle(\underset{\sim}{r}_s))\, N(\underset{\sim}{r}_s,y)$, so that (12) attains the form of a simple leaky-box equation

$$L_p H(p) - \frac{\kappa(p)\, H(p)}{\langle T\rangle(\underset{\sim}{r}_s)} = -\frac{Q(p)}{\langle T\rangle(\underset{\sim}{r}_s)} \qquad (14),$$

where the whole spatial problem enters through the constant parameter $\langle T\rangle(\underset{\sim}{r}_s)$ characterizing the exponential age distribution (13). It has to be emphasized that equation (14) is only valid at the position of the solar system. If for some reason, one wants to calculate the momentum spectrum of particles at some other place in the Galaxy, say $\underset{\sim}{r}_i$, one has to calculate new parameters $\langle T\rangle(\underset{\sim}{r}_i)$ from the respective age distribution $N(\underset{\sim}{r}_i,y)$.

But is the age distribution of cosmic rays arriving at the solar system pure exponential, as assumed in (13) and (14)? As shown by Lerche and Schlickeiser (1985b), in a variety of circumstances the age distribution at the solar system can be expanded in a series of exponentials:

$$N(\underset{\sim}{r}_s,y) = \sum_{m=1}^{\infty} \frac{c_m}{\langle T\rangle_m} \exp\left(-y/\langle T\rangle_m\right) \qquad (15).$$

The convolution of $N(\underset{\sim}{r}_s,y)$ from (15) with equation (4) yields for particle momentum spectrum near the solar system

$$H(p) = \sum_{m=1}^{\infty} c_m\, H_m(p) \qquad (16),$$

where $H_m(p)$ is the solution of equation (14) with $\langle T\rangle_m$ playing the role of $\langle T\rangle(\underset{\sim}{r}_s)$. So in general, H(p) is attained by an (infinite) sum of leaky-box solutions. Very often it suffices to consider only the m = 1 contribution, when the first eigenvalue dominates the behaviour of the age distribution.

4. Conclusions. In studies of the transport and acceleration of cosmic energetic particles the age distribution plays the same role as the escape probability in studies of photon propagation through hot plasma (see e.g. Sunyaev and Titarchuk 1980). The influence of spatial inhomogeneities, geometries and source distributions can be estimated using the solution for the spatially homogeneous infinite problem (leaky-box equation (14)) with the appropriate escape lifetimes $\langle T\rangle$. A precise prescription of how to obtain these escape lifetimes has been given: namely, they have to be calculated from the age distribution at the spatial position of the observer.

References

Lerche, I., Schlickeiser, R., (1985a), Astron. Astrophys., in press
Lerche, I., Schlickeiser, R., (1985b), this conference, OG 8.3-1
Schlickeiser, R., (1983), Proc. 18th Intern. Cosmic Ray Conf. (Bangalore), Vol. 12, 193

Sunyaev, R.A., Titarchuk, L.G., (1980), Astron. Astrophys. 86, 121

ALFVEN WAVE SCATTERING AND THE SECONDARY TO PRIMARY RATIO

G. Larry Bretthorst and Steven H. Margolis
McDonnell Center for the Space Sciences
Washington University
St. Louis, Missouri 63130, U.S.A.

1. Introduction. The cosmic ray abundances have traditionally been used to determine the elemental and isotopic nature of the Galactic Ray Sources and average measures of propagation conditions (1). Detailed studies of the physics of propagation are usually paired with relatively straightforward estimates of the secondary-to-primary (S/P) ratios. In the work reported here, calculations of elemental abundances are paired with a more careful treatment of the propagation process. It is shown that the physics of propagation does indeed leave specific traces of Galactic structure in the Cosmic Ray abundances.

2. Theory. The increasing evidence for an energy-dependent truncation of the pathlength distribution (2,3) led Margolis (4) to suggest that such observations would be the natural result of the low bulk streaming speed of the cosmic rays interacting with self-generated Alfvén waves (5-8). In particular, Skilling (7) showed that the plasma processes could be modeled by a time-dependent, non-linear diffusion equation. Using that equation, Margolis and Bussard (9) demonstrated that the self-scattering phenomenon did lead, not only to an energy-dependent truncation, but also to variations in the S/P ratios consistent with those observed. In that paper, they solved for the pathlength distribution and used the analytic procedure of Margolis (10) to determine the abundances. In the work presented here, the steady-state, non-linear diffusion equation is solved simultaneously with the equations governing spallation to determine the observed cosmic ray abundances directly from the physics.

By neglecting the contribution of the less-abundant heavier nuclei to wave generation and by including fragmentation, the single species equation of Skilling (7) can be written

$$v_A \frac{\partial}{\partial z}\left\{\frac{n_1+\Gamma}{|\partial n_1/\partial z|+T}\frac{\partial n_i}{\partial z}\right\}+\sum_{j=1}^{M}\sigma_{ij}n_j+S_i(z)=0$$

where n_i is the steady-state number density of particles of species i (n_1 represents the protons), σ_{ij} is the net fragmentation/decay cross section for reactions taking species j into i (the diagonal term represents the total inelastic cross section), $S_i(z)$ is the source term for i as a function of position. The single coordinate z represents a relative position along a flux tube; the much smaller transverse diffusion term has been neglected. As will be discussed below, z should not be interpreted directly as either radial position or height in the Galaxy. The other quantities in this equation can be related to parameters describing the interstellar plasma and magnetic field. The Alfvén speed is v_A, Γ is related to the damping rate of the waves, and T is related to the external energy input to the waves. The spatial distribution of the source term in this equation is taken to be a Gaussian with a width subject to adjustment. Symmetry about the origin is assumed. The outer boundary condition is one suggested by Freedman (11) to account for the presence of a Galactic Wind.

In the limit of large Γ and T this model goes into the standard diffusion model. In the limit of small Γ and T this equation goes into a wave equation. In the region of physical interest neither extreme limit applies. This variation in behavior drives the observed features of the energy dependence. The variable truncation results from the changing bulk streaming speed, which forces the relativistic particles to accumulate grammage without the bulk of the particles moving at anywhere near relativistic speeds. This stands in sharp contrast to the image normally associated with, say, the nested leaky box (12), which pictures a source as surrounded by a specific shell of matter.

3. Results. There are seven unknown parameters to be determined from the observed abundances of the cosmic rays. They are: T , Γ, v_A, the source magnitude for hydrogen s_H, a reflection coefficient at the outer boundary r, the full width at half maximum of the source distribution function f_w, and the number density of the interstellar gas with which the cosmic rays interact n_0. These were constrained by matching the abundances from equation (1) to the observed abundances from the French-Danish experiment (13). The distance to the outer boundary z_{max} was fixed at 1.5 Kpc after initial testing showed it was constrained only approximately. The relative source magnitudes were fixed from a calculation by Margolis (14). The hydrogen to heavies ratio and observed spectrum were taken from Webber and Lezniak (15). The errors in the free parameters are estimated to be about 10%. The best values of the free parameters were found to be characteristic of the values given by Spitzer (16) for the cool diffuse clouds (HI regions).

Currently the interstellar medium (ISM) is believed to consist of three types of regions, molecular clouds, HI regions, and hot intercloud regions (17). Classically the cosmic rays were assumed to permeate all types of regions, such that the measured characteristics of the propagation medium were thought to be a weighted average over all regions. Of the three regions, only the HI clouds support significant wave densities. Resonant waves in any region will act to limit the particle bulk streaming velocity to values on the order of the Alfvén velocity. This velocity is low compared to the individual particle velocities; the particles spend a long time in such regions. In the hot intercloud medium, the damping is large (18) so that the waves do not exert a significant influence on the bulk streaming velocity. The molecular clouds seem to have left no imprint on the observed cosmic rays: the particles are either excluded from the clouds (19) or lost by interactions with the dense gas. Interpreting the measurements in terms of wave-particle interactions points only to the HI regions.

This unique signature can be understood simply. Assume that the clouds occupy 1% of the volume of the ISM and the intercloud medium 99% (these figures are estimates of lower and upper bounds, respectively). The cosmic rays will travel through these regions guided along the magnetic field, hence the non-correspondence of the coordinate z to a single direction in space. The Alfvén velocity within the clouds (where the electrons are supplied by the ionization of intersteller carbon) is about 1.9×10^7 cm sec^{-1}: the bulk velocity is held to about 10^{-3} the speed of light. The density within a cloud is about 0.2 atom cm^{-3}, but the density in the intercloud medium is 0.02 atom cm^{-3}. Thus, the cosmic rays accumulate 100 times as much grammage in the clouds as outside them, which explains the singular signature.

The threading of the magnetic field through the different regions does bring to mind the work of Parker (20). The calculations presented here are consistent with Parker's picture of the clouds anchoring the magnetic field in the Galaxy as the cosmic rays inflate the field lines above the plane. This dynamic interaction provides a means for

cosmic ray escape from the Galaxy as well as a complicated topology for the coordinate z. The work presented here indicates that the cosmic rays are injected into the wandering field lines over relatively broad ($f_\omega = 600$ pc) regions (perhaps by interstellar shocks), and that these field lines carry the cosmic rays outside the Galaxy within a distance along the field of 1 or 2 Kpc. Further directions for study would be the understanding of electron propagation in the hope of using radio observations of Galactic halos.

4. Conclusion. The propagation of the cosmic rays and the energy dependence of the secondary to primary ratios can be understood from the interaction of the particles with waves in the interstellar magnetic field. The calculations presented here point to the cool HI clouds as the primary influence on cosmic ray abundances. This work suggests a clear reflection of the structure of the Galaxy in the measurements of Cosmic Rays.

5. Acknowledgements. This work was supported under NASA grant NAG8-448 and McDonnell Center Research funds. One of us (GLB) was supported by a Washington University Graduate Fellowship.

6. References

1. Simpson, J. A. (1983), *Ann. Rev. Nucl. Part. Sci.* **33,** 323.
2. Garcia-Munoz, M., Guzik, T. G., Margolis, S. H., Simpson, J. A., and Wefel, J. P. (1981), *Proc. 17th Int. Cosmic Ray Conf. (Paris)* **9,** 195.
3. Garcia-Munoz, M., Guzik, T. G., Simpson, J. A., and Wefel, J. P. (1984), *Astrophys. J. (Letters)* **280,** L13.
4. Margolis, S. H. (1981), *Proc. 17th Int. Cosmic Ray Conf. (Paris)* **9,** 215.
5. Wentzel, D. G. (1969), *Astrophys. J.* **156,** 303.
6. Kulsrud, R. and Pearce, W. (1969), *Astrophys. J.* **156,** 445.
7. Skilling, J. (1970), *Mon. Not. R. Astr. Soc.* **147,** 1.
8. Skilling, J. (1975), *Mon. Not. R. Astr. Soc.* **173,** 255.
9. Margolis, S. H. and Bussard, R. W. (1983) *Proc. 18th Int. Cosmic Ray Conf. (Bangalore)* **9,** 271.
10. Margolis, S. H. (1983), *Proc. 18th Int. Cosmic Ray Conf. (Bangalore)* **9,** 267.
11. Freedman, I., Giler, M., Kearsey, S., and Osborne, J. L. (1980), *Astron. and Astrophys.* **82** 110.
12. Cowsik, R. and Wilson, L. W. (1975), *Proc. 14th Int. Cosmic Ray Conf. (Munich)* **2,** 659.
13. Engelmann, J. J., Goret, P., Juliusson, E., Koch-Miramond, L., Masse, P., Soutoul, A., Byrnak, B., Lund, N., Peters, B., Rasmussen, I. L., Rotenberg, M., and Westergaard, N. J. (1983), *Proc. 18th Int. Cosmic Ray Conf. (Bangalore),* **2,** 17.
14. Margolis, S. H. (1985), *Astrophys. J.*, (in press).
15. Webber, W. R. and Lezniak, J. A. (1974), *Astrophys. Space Sci.* **30,** 361.
16. Spitzer, L. (1978), *Physical Processes in the Interstellar Medium,* (New York: Wiley-Interscience).
17. McKee, C. and Ostriker, J. P. (1977), *Astrophys. J.* **218,** 148.
18. McIvor, I. (1977), *Mon. Not. R. Astr. Soc.* **178,** 85.
19. Skilling, J. and Strong, A. W. (1976), *Astron. Astrophys.* **53,** 253.
20. Parker, E. N. (1966), *Astrophys. J.* **145,** 811.
21. Garcia-Munoz, Mason, G. M., and Simpson, J. A. (1977), *Astrophys. J.* **217** 859.

OG 7.2-11

On the importance of interstellar Helium for the propagation of heavy Cosmic Rays

P. Ferrando, P. Goret, A. Soutoul
CEN / Saclay - France

The influence of interstellar He on the fragmentation of heavy cosmic rays in the interstellar medium (ISM) has long been a controversial subject. While H-induced cross section data are now available over broad mass and energy ranges, little data for He-induced fragmentation exists (see /1/,/2/ and references therein). With the recent reports of accurate measurements of the secondary/primary ratios in cosmic rays /3/ and of H-induced cross sections /4/,/5/ the problem of including interstellar He in propagation calculations becomes even more critical. As is argued in /6/ the escape lengthes λe deduced from the B/C+O and Sc-Cr/Fe ratios cannot be reconciled within the frame of a simple leaky box model assuming the ISM composed of pure H. It is quite remarkable that the discrepancy is especially large in the GeV region where (i) secondary/primary ratios measured by several groups agree fairly well (see /6/) and (ii) fragmentation cross sections have been recently measured with good accuracy /4/,/5/.

At this stage one may wonder if this is an effect of having neglected the interstellar He in the propagation calculations. Indeed a hint that the ISM He could play a role in the GeV region is indicated in Table 1 which displays the ratios of He-induced and C-induced to H-induced fragmentation and total inelastic cross sections. It is seen that the fragmentation cross sections for Fe secondaries in He-induced reactions do not scale as the total cross section while the effect is much attenuated for C secondaries. The same trend for C-induced cross sections is also indicated in Table 1. It is therefore expected that the escape length calculated from Fe secondaries, which is very sensitive to variations of nuclear cross sections, will be strongly affected while the effect for C+O secondaries will be much less important.

In order to check for the magnitude of the effect concerning the propagation of galactic cosmic rays, a calculation of the escape length λe at 1 GeV/n was performed with the ISM composed of 10% He and 90% H. More specifically the λe(C+O) and λe(Fe) were computed from the B/C+O and Sc-Cr/Fe ratios as measured in the HEAO3-C2 experiment /3/. According to Table 1 the fragmentation cross sections in He were scaled to proton cross sections with factors of 1.8 and 1.0 for C+O and Fe secondaries respectively. The total inelastic cross section in He is computed from $C*(A_t^{1/3}+Ap^{1/3} - 1.25)^2$ mb with C=78 mb up to A =8 /7/ and C=69 mb in the Fe region /10/. The calculations were performed using a new matrix program inspired from /8/ which incorporates a self-consistent treatment of ionization energy losses. It was checked that the λe's computed for a pure H ISM agree with /6/ within a few percent.

The escape length from C+O and Fe secondaries at 1 GeV/n, averaged over 3 energy bins between 0.8 and 1.3 GeV/n are given in Table 2 for both cases of a pure H and a mixed He+H ISM composition. The errors quoted in Table 2 reflect the statistical errors on the measurements of the secondary/primary ratios only. The escape length deduced from Fe secondaries is larger than that from C+O secondaries by 3 sigma's and 4 sigma's for pure H and He+H ISM respectively. These results strongly indicate that the discrepancy at 1 GeV/n

between the λe deduced from the C and Fe secondaries in a simple leaky box model could be even more serious when interstellar He is taken into account. The present analysis reinforces the conclusion drawn in /11/ that the leaky box model with a pure exponential path length distribution is no more able to explain the cosmic ray data as they become more precise. We emphasize that the most important parameters used in the present analysis are measured ones, which increases the reliability of the results. It is also clear that the lack of He-induced fragmentation data becomes more critical as more H-induced cross sections are measured, calling for an effort to perform such measurements.

References

/1/ M.M. Shapiro and R. Silberberg Ann.Rev.Nucl.Sci. Vol 20 1970 p.357
/2/ G.M. Raisbeck and F. Yiou 14th ICRC München 1975 Vol 2 p.502
/3/ J.J. Engelmann et al. 18th ICRC Bengalore 1983 Vol 2p.17
/4/ W.R. Webber and D.A. Brautigam Ap. J. Vol 260 1982 p.894
/5/ W.R. Webber paper presented at the Cosmic Ray Workshop Baton Rouge Oct. 1984
/6/ A. Soutoul et al. this conference OG 4.1-3
/7/ J. Jaros et al. Phys. Rev. Lett. Vol 18 1978 p.2273
/8/ J.R. Letaw et al. Ap. J. Vol 56 1984 p.369
/9/ W.R. Webber unpublished results
/10/G.D. Westfall et al. Phys. Rev. C Vol 19 1979 p.1309
/11/M. Garcia Munoz et al. Ap. J. Vol 280 1984 L13

Table 1 - Ratio of He-induced and C-induced to H-induced cross sections for fragmentation and total inelastic reactions at 1 GeV/n.

Reaction	He-induced	C-induced
C -> Be	1.9 /2/	2.6* /9/
Total	2.0 /7/	3.3 /7/
Fe -> Sc-Cr	1.0 /2/	1.2 /4/
Total	1.6 /10/	2.3 /4/

* at 0.42 GeV/n

Table 2 - The escape length deduced from C+O and Fe secondaries for pure H and He+H ISM composition. The last column gives the ratio $\lambda e(Fe)/\lambda e(C+O)$ with the statistical errors on the secondary/primary measured ratios only.

ISM	λe(C+O) (g/cm²)	λe(Fe) (g/cm²)	ratio
pure H	7.25 ± 0.13	10.39 ± 0.80	1.43 ± 0.15
He(0.1)+H(0.9)	8.94 ± 0.16	20.43 ± 2.50	2.28 ± 0.33

INTERSTELLAR TURBULENCE, RANDOM DENSITY VARIATIONS, AND SCINTILLATION MEASUREMENTS

J. C. Higdon
Jet Propulsion Laboratory, 169-327
California Institute of Technology
Pasadena, CA 91109

1. Introduction. The presence of random electron variations suggests that the ionized interstellar medium is turbulent. In the interstellar plasma the presence of power spectra of such variations extending to spatial scales much less than a Coulomb mean free path, λ_c, is required by analyses of measurements of scintillation and angular broadening of pulsar radio signals (Armstrong et al., 1981). The existence of corresponding variations in magnetic field strength could efficiently scatter cosmic rays and thus constrain cosmic-ray propagation. Unfortunately both the origin of the electron density variations and mechanisms by which these variations couple to fluctuations in magnetic field strength are unknown. In Higdon (1984) I conjectured that the small-scale density variations are generated by the convective distortion of initially large-scale isobaric entropy structures in the turbulent interstellar plasma. The following is an investigation of the spectra of turbulent entropy structures, velocity, and magnetic fields at small spatial scales. The modifier small is employed here to characterize length scales much less than the dimension, L, containing the bulk of the turbulent energy.

2. Isobaric Entropy Structures. Isobaric entropy structures do not propagate and are stationary in the plasma rest frame. Two classes of isobaric entropy structures are identified in magnetogasdynamic fluids: tangential pressure balances and entropy waves (Jeffrey and Taniuti 1964). In the simplest case tangential pressure balances are coupled variations in temperature and density aligned in planes transverse to the direction of local mean magnetic field; $T_t/T_o=-N_t/N_o$, where N_t, N_o, T_t, and T_o are respectively a density variation, mean density, temperature variation, and mean temperature. Tangential pressure balances can possess gradients of wavenumber, K_t, such that $K_t\lambda_c>>1$; entropy waves and propagating magnetoacoustic waves with similar gradients are unstable and disperse on very short time scales (Barnes 1971).

The equation for the evolution of isobaric entropy structures in an electron-proton plasma can be well approximated from Braginskii (1965), for the temperature component, by

$$\partial T/\partial \tau + \underline{u}.\nabla T = DT/D\tau = \kappa_t \nabla_t^2 T + \kappa_p \nabla_p^2 T \qquad (1)$$

where τ is time; $\underline{u}$ is the hydrodynamic velocity; κ_p and κ_t are thermal diffusivities respectively parallel and transverse to the direction of the mean magnetic field, $\underline{Bo}$; and the components of the spatial gradient respectively parallel and transverse to $\underline{Bo}$ are ∇_p and ∇_t. Equation (1) assumes that an arbitrary entropy structure is a mixture of tangential pressure balances and entropy waves. Equation (1) shows that plasma entropy is conserved in the absence of thermal conductivity. Random convection produced by the inertial term of equation (1), $\underline{u}.\nabla T$, distorts the

shape of a fluid volume and consequently leads to a statistical increase in the entropy gradient; the increase in the entropy gradient is halted ultimately at very small scales by the diffusive effect of thermal conductivity (e.g., Batchelor 1959).

When buoyancy forces are small, the reaction of isobaric entropy variations on the turbulent velocity and magnetic fields is negligible. When an additional constraint is met, that the dynamic turbulent components do not generate significant intensities of magnetoacoustic waves, the evolution of the turbulent velocity field as well as the magnetic field can be modeled as solenoidal. These fundamental simplifications can be shown to apply to the small-scale structures of the interstellar flows investigated by Higdon (1984).

3. Solenoidal Velocity Field. The nature of the velocity components that convect the passive entropy structures was investigated by Higdon (1984). At small scales equipartition existed between kinetic and magnetic energies. These solenoidal variations were strongly nonlinear and thus could not be interpreted, as in some models of interstellar turbulence, as weakly-interacting hydromagnetic waves. Small turbulent variations were modeled as statistically homogeneous, stationary, and nonhelical. Three-dimensional isotropy was not assumed; the presence of an approximately uniform mean magnetic field required that the turbulent variations be rotationally isotropic about $\underline{Bo}$ (Montgomery 1982). For such cases I developed a model of anisotropic turbulence, that was applicable at small scales, based on a study of Montgomery (1982) which showed that the presence of a strong mean magnetic field suppressed the generation of variations parallel to $\underline{Bo}$. I employed a model of Fyfe, Joyce and Montgomery (1977) of two-dimensional isotropic magnetohydrodynamic turbulence to approximate the evolution of the dominant transverse velocity components in the inertial range

$$F(K_t) = C_1 \varepsilon^{2/3} / K_t^{5/3} \qquad 1/L \ll K_t \ll K_{du} \tag{2}$$

$$\langle \underline{u}_t^2 \rangle = \int F(K_t) dK_t$$

where $\langle \underline{u}_t^2 \rangle$ is the mean-square turbulent velocity transverse to $\underline{Bo}$, C_1 is a constant of order unity, and ε is the energy transfer rate per unit mass. The inertial range terminates at K_{du} where viscous damping becomes important. In these planes transverse to $\underline{Bo}$ I showed that the viscosity coefficients are dramatically reduced compared to the viscosity found in the absence of mean fields when Braginskii (1965) transport theory is employed. Thus the energy-conserving inertial range extends to spatial scales significantly smaller than a Coulomb mean free path.

4. Spectrum of Entropy Structures. Distortions produced by turbulent convection parallel to the mean field are relatively weak. Employing Braginskii (1965) transport theory to model the anisotropic thermal diffusivities, it can be shown that inertial forces in this direction dominate the diffusive action of thermal conductivity only at large scales in the model flows of Higdon (1984). Only for $KL < 10$, are the entropy flows parallel to $\underline{Bo}$ controlled by inertial forces. Thus at small scales the distorting effect of random turbulent convection acts primarily on the evolution of tangential pressure balances in planes transverse to $\underline{Bo}$.

The evolution of entropy structures at small scales, KL>>10, is straightforward since the turbulent convection of entropy structures parallel to Bo can be disregarded. In this case small-scale entropy structures, as well as velocity fields, can be modeled as superpositions of two-dimensional isotropic structures. These random fields can be decomposed into single-component Fourier spectra, which for tangential pressure balances are,

$$\int G(K_t)dK_t = \langle T_t^2 \rangle, \qquad \int P(K_t)dK_t = (N_o/T_o)^2 \int G(K_t)dK_t = \langle N_t^2 \rangle \tag{3}$$

The statistical increase in the entropy gradient produced by random convection can be interpreted as a transfer among the different Fourier components of the tangential pressure balances; $G(K_t)$ and $P(K_t)$ produced at $K_t \approx 1/L$ are transferred efficiently to large wavenumbers by the action of turbulent convection (e.g. Batchelor 1959). The large-scale entropy structures affect the properties of the small-scale tangential balances primarily through the rate of transfer of random tangential balances, χ. This transfer rate can be determined from the parameters of the large-scale turbulent variations. In the convective range, where dissipation by thermal conductivity and viscosity are negligible, dimensional analysis suggests that $G(K_t)$ can only depend on χ, K_t, and the properties of the small-scale, two-dimensional velocity field. (As shown in equation (2) the velocity field depends only on ε and K_t.) Employing Kolmogorov dimensional arguments,

$$G(K_t) = C_2 \chi / [\varepsilon^{1/3} K_t^{5/3}] \qquad 10/L << K_t << K_{dT} \tag{4}$$

$$P(K_t) = (N_o/T_o)^2 C_2 \chi / [\varepsilon^{1/3} K_t^{5/3}]$$

where C_2 is a dimensionless constant of order unity.

The convective range terminates at K_{dT} where thermal diffusivity becomes important. Employing Braginskii (1965) transport theory for the dispersion of tangential pressure balances, it can be shown that the convective range for these variations extends to spatial scales much smaller than a Coulomb mean free path. This results because thermal conductivity, like viscosity, is dramatically reduced transverse to Bo compared to the conductivity found in the absence of mean magnetic fields.

Figure 1 shows the density spectrum determined by Armstrong et al. (1981) compared to a model density spectrum of tangential pressure balances in which equation (4) was used to calculate the properties of the convective range. The parameters for transport coefficients, magnetic, and velocity fields were taken from Higdon (1984) for model interstellar flows situated in cloud-debris HII regions. The mean-square density of the tangential pressure balances, $\langle N_t^2 \rangle$, was considered to be a free parameter; comparison with the observations required that $\langle N_t^2 \rangle / N_o^2 = 0.16$. Such a random density component is consistent with models of intense turbulent flows in heterogeneous thermal media, if the random entropy component is predominantly tangential pressure balances.

5. Conclusion. A model for the turbulent origin of the random density variations observed in the interstellar medium has been constructed. This model does not employ small-scale magnetoacoustic waves which dissi-

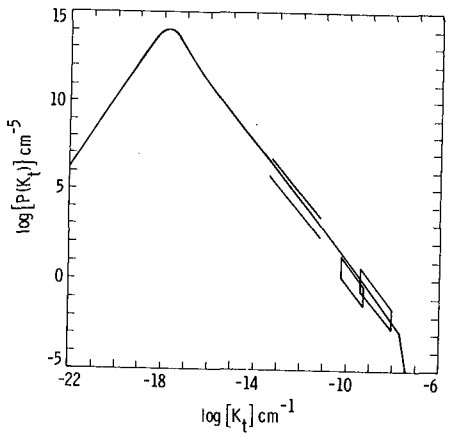

Figure 1. Comparison between the model spectrum (single line) and the spectrum determined from analyses of measurements of scintillation (parallel lines) and angular broadening (boxes) by Armstrong et al (1981).

pate very efficiently in interstellar plasmas. The model has three major components. First random turbulent distortions of initially large-scale isobaric entropy structures generate broad spectra of entropy, temperature and density variations. Second, due to the presence of a strong mean magnetic field, Bo, the small-scale velocity variations are concentrated in planes transverse to the direction of Bo. Third, in these directions the relevant dissipation processes, thermal conductivity and viscosity, are dramatically reduced compared to the values found in the absence of mean fields. Thus transverse to Bo the convective range of the isobaric entropy variations extends to very small spatial scales before the diffusive action of thermal conductivity becomes significant. Work in progress suggests that this model is applicable to analyses of random variations in the interplanetary medium, where fluctuations in density, velocity, and magnetic field, as well as relativistic particle scattering can be measured in detail.

6. Acknowledgements. This research was carried out at the Jet Propulsion Laboratory, California Institute of Technology, under contract with the National Aeronautics and Space Administration. The author is a NAS/NRC Senior Resident Research Associate.

References

Armstrong, J. W. et al. 1981, Nature, 291, 561.
Barnes, A. 1971, J.G.R., 76, 7522.
Batchelor, G. K. 1959, J.F.M., 5, 113.
Braginskii, S. I. 1965, Rev. Plasma Phys., 1, ed. M. A. Leontovich (New York: Consultants Bureau), 205.
Fyfe, D., Joyce, G., and Montgomery, D. 1977, J. Plasma Phys., 17, 317.
Higdon, J. C. 1984, Ap. J., 285, 109.
Jeffrey, A., and Taniuti, T. 1964, Non-Linear Wave Propagation (New York: Academic Press), 176.
Montgomery, D. 1982, Physica Scripta, T2, 83.

ON THE COSMIC RAY DIFFUSION IN A VIOLENT INTERSTELLAR MEDIUM

A.M.Bykov and I.N.Toptygin

M.I.Kalinin Polytechnical Institute, Leningrad 195251, USSR

1. Introduction. A variety of the available observational data on the cosmic ray (CR) spectrum, anisotropy and composition are in good agreement with a suggestion on the diffusion propagation of CR with energy below 10(15) eV in the interstellar medium (see Ginsburg and Ptuskin, 1983). The magnitude of the CR diffusion coefficient and its energy dependence are determined by ISM magnetic field spectra.

Direct observational data on magnetic field spectra are still absent. In this work we present a theoretical model to the turbulence generation in the multiphase ISM. Our model is based on the multiple generation of secondary shocks and concomitant large-scale rarefactions due to supernova shock interactions with interstellar clouds. We derive (also see Bykov and Toptygin, 1985) the distribution function for ISM shocks with account for supernova statistics, diffuse cloud distribution and various shock wave propagation regimes. This allows us to calculate the ISM magnetic field fluctuation spectrum and CR diffusion coefficient for the hot phase of ISM.

2. The ISM turbulence model. Current observational data on the structure of ISM turbulence have been summarized in the review by Armstrong et al.(1981). They have concluded that a variety of data obtained by different methods do not contradict to the assumption on the presence of continuous spectrum of ISM inhomogenuities in a wide scale range. The energy density dependence on wavenumber k takes the form $W(k) \sim k^{-\alpha}$, where $1,4 \leq \alpha \leq 1,8$ for $10(-20) < k < 10(-8)$ cm^{-1} (Armstrong et al., 1981).

The ISM is characterized by a wide variety of phase states, so that the ISM turbulence is highly nonuniform. The possibility of developing an inertial range of weak MHD turbulence produced by energy cascading from long wavelengths to short wavelengths under the ISM conditions has been discussed by McIvor (1977). This discussion is based on the assumption about collisional damping of MHD waves. We remark (Bykov and Toptygin, 1983) that the weak MHD turbulence spectrum can be developed by the energy cascading if only the linear Landau damping of collisionless MHD waves is effectively suppressed. The above suppression can be realized due to the distortion of the thermal plasma distribution function by finite amplitude waves ($\delta B \gtrsim 0,1 B_0$) with scales $l \sim 3 \cdot 10(17)$ cm. If such waves are absent, the energy cascading of weak MHD turbulence seems to be highly unlikely as well as the appearance of some inertial range in the hot ISM.

On the other hand, the fluctuations of ISM magnetic field and electron density may be connected with the presence of strong turbulence. Here we treat the strong turbulence as an ensemble of noncoherent weakly interacting nonlinear

waves. For such a system the energy redistribution between wave-scales are determined by the evolution of nonlinear waves. The strong turbulence of Langmuir solitons has been discussed by Rudakov and Tsytovich (1978).

In the present paper we propose the model for a strong ISM turbulence. The main structural elements of our model are nearly spherical collisionless shock waves with rarefactionsregions in the inner parts of the spheres. Such structures may be formed due to multiple interactions of strong supernova shocks with interstellar clouds. The total energy input to the ISM turbulence in our model can be estimated as 10% from the kinetic energy of large-scale motions produced by supernovae and stellar wind of OB stars (about 10(-27) erg·cm(-3)·s(-1)). Now we obtain the distribution function for ISM shocks of different strengths (also see Bykov and Toptygin, 1985).

3. ISM shock wave distribution function. Theoretical consideration of an average distribution of ISM shocks is important to study the ISM structure (McKee and Ostriker, 1977; Heathcote and Brand, 1983) and CR propagation (Blandford and Ostriker, 1980; Axford, 1981; Ginzburg and Ptuskin,1984). We define the shock strength distribution function $P(M)$ as an average number of passings of shocks with Mach numbers $M, M+dM$ through an arbitrary point of ISM disk per unit time (cf. Blandford and Ostriker, 1980). Supernova explosions with local rate S (~10(-13) pc(-3)/year) produce strong primary shock waves in the ISM. The primary shock evolution is described by selfsimilar spherical solutions with radius

$$R(M) = R_0 M^{-\alpha/3} \qquad (1)$$

where R_0 depends on the energy release and ambient gas parameters. The exponent α is equal to $\alpha = 2$ for the Sedov solution; $\alpha = 4{,}5$ for the McKee and Ostriker solution, and $\alpha = 1{,}2$ for the snow-plow model.

It is known that an average number of passings of primary shocks with Mach numbers $\geq M$ through an arbitrary point of ISM per unit time is given by (see e.g. Blandford and Ostriker, 1980; Axford, 1981)

$$F(M) = S\,\frac{4\pi}{3} R_0^3 M^{-\alpha} \qquad (2)$$

Thus, $P^{(1)}(M) = -dF/dM$. Primary shock propagation through ISM with embedded diffuse clouds will be accompanied by generation of secondary shocks (e.g. see Spitzer, 1982). The number of secondary shocks produced by a primary shock will be about 10(4), provided the cloud number density $n_{cl} \approx$ $\approx 5\cdot10(-4)$ pc(-3), and $R_0 \approx 10(2,3)$ pc. The distribution function of secondary shocks (without account for secondary shock reflection from clouds) takes the form:

$$P^{(2)}(M) = 3 f_{cl} \int_1^\infty dM_1 \int_M^{\sqrt{5}} dM_0\, P^{(1)}(M_1)\, \delta\left(M_1 - \sqrt{\frac{3M_0^2+1}{5-M_0^2}}\right) \frac{(M_0-1)^3}{(M-1)^4}, \qquad (3)$$

where f_{cl} is the diffuse cloud filling factor in the ISM. This formula takes account for shock reflection from dense sphere and the secondary shock propagation regime. For simplicity, we consider a perfect gas with $\gamma = 5/3$ and take into account that secondary shock will be weak (i.e. $M_0 - 1 < 1$) if the primary shock has $M_1 \leq 3$ (for more detailed discussion see Bykov and Toptygin, 1985).

As a result, we derive an approximate distribution function with account for the weak secondary shock contribution:

$$P(M) \approx \alpha S \frac{4\pi}{3} R_0^3 \left[M^{-\alpha-1} + 3 f_{cl} C(3;\alpha)(M-1)^{-4} \right], \quad (4)$$

where $C(3;4,5) \approx 4{,}1 \cdot 10(-3)$. It should be noted the strong dependence of P on M determined by the secondary shock contribution. Among the waves with $M \leq 1{,}2$, secondary shocks are dominant. Multiple interactions of secondary shocks with clouds can be taken into acoount by iterations of eq. (3), i.e. by series expansion of $P(M)$ with respect to f_{cl}.

4. ISM fluctuation spectra. In the discussed model nearly spherical shocks with rarefaction regions in the inner parts of spheres represent well-defined structural cells. The ISM velocity, density and magnetic field fluctuations are determined by noncoherent overlapping of a large number of such structures. For statistically homogeneous and isotropic ensemble of shocks (with strength M) and concomitant rarefaction the spectral energy density takes the form:

$$w(k,M) = (4/\pi) c_s^2 (M-1)^2 k^2 R^3(M) \left[1 + k^2 R^2(M) \right]^{-2} \quad (5)$$

whichis valid for scales $k\delta \ll 1$, where δ is the shock front thickness. For collisionless weak shocks in the hot ISM $\delta \leq$ 10(12) cm. Eq. (5) quite satisfactorily extrapolates the well-known relations at $kR \gg 1$ and $kR \ll 1$ (Bykov and Toptygin,1985).

To evaluate the spectral energy density, W(k), one should average Eq. (5) over an ensemble of shocks with different strengths. This yields $W(k) = W^{(1)}(k) + W^{(2)}(k)$, where

$$W^{(1)}(k) = \int_1^\infty w(k,M) P^{(1)}(M)\, dM, \qquad W^{(2)}(k) =$$

$$= 3 f_{cl} \int_1^\infty dM_1 \int_1^{\sqrt{5}} dM_2 \int_{M_2}^{\sqrt{5}} dM_0 P^{(1)}(M_1) w(k,M_2) \frac{(M_0-1)^3}{(M_2-1)^4} \delta\left(M_1 - \sqrt{\frac{3M_0^2+1}{5-M_0^2}} \right). \quad (6)$$

Let us present the obtained expression for W(k) in the short - wavelength limit ($kR_0 \gg 1$) for the McKee and Ostriker (1977) model ($\alpha > 3$):

$$W(k) = (4\alpha c_s^2 / \pi R_0) \left[1 + 3 f_{cl} C(2;\alpha) \frac{R_0}{R_{cl}} \ln\left(\frac{\sqrt{5}-1}{M_*-1} \right) \right] k^{-2}, \quad (7)$$

R_{cl} being the mean radius of clouds; $(M_*-1) \approx 10(-2)$; $C(2;4,5)$ $\approx 9{,}4 \cdot 10(-3)$. The long-wavelength spectral range has been considered earlier by the authors. The magnetic fluctuation

spectrum appears to be similar to the velocity fluctuation spectrum given by Eqs. (6),(7).

Thus, Eqs. (6) determine the fluctuation spectrum in the model of turbulence produced by shocks from supernova explosions. The main mechanism of energy redistribution over wavelengths is that due to the generation and subsequent self-similar evolution of secondary shocks.

5. The CR diffusion. The magnitude of the CR diffusion coefficient along the field lines $\varkappa_{\parallel}$ and its dependence on the energy E of energetic particles are determined by the magnetic fluctuation spectra (e.g. Toptygin, 1985),

$$\varkappa_{\parallel} = \frac{cG(\nu)}{3}\left(B_0^2/\delta B^2\right)^{(\nu+3)/4}\left(E/eR_0B_0\right)^{2-\nu}R_0, \qquad (8)$$

where the effect of large-scale magnetic fields on the particle scattering at $\vartheta \approx \pi/\lambda$ is taken into account. According to our result (7) for the McKee and Ostriker (1977) model, the spectral turbulence index $\nu = 2$. Hence, it follows from Eq. (8) that the CR diffusion coefficient along the regular magnetic field is energy-independent as long as $E \ll eR_0B_0$. For the above mentioned parameters of the model we have $\varkappa_{\parallel} \approx 5 \cdot 10^{28}$ cm^{2}s^{-1} which is in satisfactory agreement with observational data on CR anisotropy and abundance.

References

Armstrong J.W.,Cordest J.M.,Rickett B.J. Nature,291,561,1981.
Axford W.I. Proc. 17 ICRC, v. 12, p. 155, 1981.
Blandford R.D., Ostriker J.P. Astrophys. J., 237,793,1980.
Bykov A.M.,Toptygin I.N. Proc. 18 ICRC, v.9, p.247, 1983.
Bykov A.M.,Toptygin I.N. Pis'ma Astron. Zh.,11,No.3, p.184, 1985.
Ginzburg V.L.,Ptuskin V.S. In: Soviet scient. reviews, ed. Sunyaev R.A., ser. E, v.4, 1984.
Heathcote S.R., Brand P.W.J.L. MNRAS, 203, 67, 1983.
McIvor I. MNRAS, 178, 85, 1977.
McKee C.F.,Ostriker J.P. Astrophys. J., 218, 148, 1977.
Rudakov L.I.,Tsytovich V.N. Phys. Reports, 40, 1, 1978.
Spitzer L. Astrophys. J., 262, 315, 1982.
Toptygin I.N. Cosmic Rays in Interplanetary Magnetic Fields. Dordrecht, Reidel, 1985.

THE ROLE OF COSMIC RAYS IN MAGNETIC HYDRODYNAMICS OF INTERSTELLAR MEDIUM

V.L.Ginzburg
P.N.Lebedev Physical Institute of the USSR Academy of Sciences, Moscow II7924, USSR

V.S.Ptuskin
Institute of Terrestrial Magnetism, Ionosphere and Radio Wave Propagation, USSR Academy of Sciences, I42092 Troitsk, Moscow Region, USSR

Cosmic ray (CR) propagation in the Galaxy and generally in the cosmic plasma is usually considered in the duffusion approximation. The diffusion is regarded to result from CR scattering due to their interaction with a magnetic and an electric field. In most cases the fields are assumed to be given. Meanwhile, in the Galaxy the CR energy density $w_{cr} \sim I$ eV/cm, i.e. it is comparable with the energy densities of the magnetic field and turbulent motions in the interstellar gas. Therefore, for the Galaxy and for a number of other objects it becomes necessary to take into account the influence of CR on the gas dynamics and on the magnetic fields in this gas; see /I,2/. The simplest way to do this is to use the hydrodynamic approximation, but this is possible only on scales greatly exceeding the CR free path Λ before scattering and only for times larger than $\Lambda/v \approx \Lambda/c$. One should thus obtain corresponding MHD equations and establish the limits of their applicability.

What does the CR pressure affect? The mean force with which CR act on the gas is usually written as $\langle \vec{F} \rangle = -\nabla P_{cr}$, where P_{cr} is the CR pressure. But what is the pressure in our case where particles do not collide? It is clear that the force with which CR act on the background plasma is equal to $\vec{F} = c^{-1}(\vec{j}_g \times \vec{H}_{cr})$, where $\vec{j}_g$ is the current in plasma and $\vec{H}_{cr} \equiv \vec{B}_{cr}$ is a magnetic field created by the CR current $\vec{j}_{cr}$. For quasistationary fields

$$\langle \vec{F} \rangle = -\frac{1}{c}\langle \vec{j}_{cr} \times \vec{H}_g \rangle = -\frac{1}{c}\langle \vec{j}_{cr} \rangle \times \langle \vec{H}_g \rangle - \frac{1}{c}\langle \delta\vec{j}_{cr} \times \delta\vec{H}_g \rangle. \qquad (I)$$

Here we have integrated over an ensemble of random magnetic fields $\vec{H}_g = \langle \vec{H}_g \rangle + \delta\vec{H}_g$, $\langle \delta\vec{H}_g \rangle = 0$ and, accordingly, $\vec{j}_{cr} = \langle \vec{j} \rangle_{cr} + \delta\vec{j}_{cr}$, $\langle \delta\vec{j}_{cr} \rangle = 0$. To calculate $\vec{j}_{cr}$, one should know the CR distribution function $f(t,\vec{r},\vec{p})$. It obeys the equation (we assume that the electric field $\vec{\mathcal{E}} = 0$).

$$\frac{\partial f}{\partial t} + (\vec{v}\nabla)f + \frac{e}{c}(\vec{v} \times \vec{H}_g)\frac{\partial f}{\partial \vec{p}} = 0. \qquad (2)$$

Assuming $f = \langle f \rangle + \delta f$, $\langle \delta f \rangle = 0$ and using the standard procedure of the quasilinear approximation, we find equations for $\langle f \rangle$ and δf. Integrating the equation for δf in the approximation of "nonmagnetized" CR with a charge Ze (this means that in calculation of the interaction between a particle and a single magnetic field inhomogeneity, particle

motion may be considered rectilinear, i.e. the gyroradius $r_H \gg L$, where L is the correlation scale of the field $\delta\vec{H}_g$), we obtain

$$\delta f(t,\vec{r},\vec{p}) = \frac{ze}{c}\int_{-\infty}^{t} dt_0\, \delta\vec{H}_g\left(\vec{r}-\vec{v}(t-t_0)\right)\left(\vec{v}\times\frac{\partial}{\partial\vec{p}}\right)\langle f(t,\vec{r},\vec{p})\rangle. \quad (3)$$

In the diffusion approximation $\langle f\rangle$ has the form (for more details see /3/).

$$\langle f(t,\vec{r},\vec{p})\rangle = f_0 - \frac{3v_i D_{ij}}{v^2}\nabla_j f_0, \quad N = \int d^3p\, f_0, \quad w_{cr} = \int d^3p\, E f_0, \quad (4)$$

where $f_0(t,\vec{r},p)$ is an isotropic part of the function $\langle f\rangle$, N is the total CR concentration, the diffusion tensor is equal to (here $\vec{h} = \langle\vec{H}_g\rangle / \langle H_g\rangle$)

$$D_{ij} = v\Lambda\left[3\left(1+\Lambda^2/r_H^2\right)\right]^{-1}\left[\delta_{ij} + \left(\frac{\Lambda}{r_H}\right)^2 h_i h_j + \frac{z}{|z|}\frac{\Lambda}{r_H}e_{ijm}h_m\right]. \quad (5)$$

The free path along the field $\langle\vec{H}_g\rangle$ is

$$\Lambda = 3c^2p^2\left[2z^2e^2 L \langle\delta H_g^2\rangle \int_0^\infty dy\,\psi(y)\right]^{-1}. \quad (6)$$

We assume that

$$\langle\delta H_i(\vec{r}_1)\cdot\delta H_j(\vec{r}_2)\rangle = \frac{\langle\delta H_g^2\rangle}{3}\left[\psi\left(\frac{x}{L}\right)\delta_{ij} - \psi_1\left(\frac{x}{L}\right)\frac{x_i x_j}{x^2}\right], \quad (7)$$

where $\vec{x} = \vec{x}_1 - \vec{x}_2$, the functions ψ and ψ_1 are related by the condition $\nabla\delta\vec{H}_g = 0$.

Using formulae (2)-(7), we find

$$\langle\vec{F}\rangle = -\nabla P_{cr}, \quad P_{cr} = \frac{1}{3}\int_0^\infty d^3p\, pv\, f_0(t,\vec{r},p), \quad (8)$$

which is the answer to our question. Note that for $\Lambda \gg r_H$ the main contribution into the total force $\langle\vec{F}\rangle$ in the direction longitudinal with respect to the regular field is made by the fluctuation interaction $-\frac{1}{c}\langle\delta\vec{j}_{cr}\times\delta\vec{H}_g\rangle$ /4/, and in the perpendicular direction - by the interaction $-\frac{1}{c}\langle\vec{j}_{cr}\rangle\times\langle\vec{H}_g\rangle$ (more precisely, by its part connected with the Hall current of CR). We have, in fact, extended the problems of momentum exchange between a relativistic charged particle and a "magnetic cloud" (see /5/) to the case of CR propagation in a turbulent medium.

MHD equations for interstellar medium with an account of the action of CR. We proceed from the hydrodynamic description of back-ground plasma motions and from the description of CR by means of the kinetic equation. The equation of background plasma motion in the MHD approximation has the form

$$\rho\frac{d\vec{u}}{dt} = -\nabla P_g + \frac{1}{c}\left(\vec{j}_g\times\vec{H}\right) - ze N\vec{\mathcal{E}}, \quad (9)$$

here $\vec{H} = \vec{H}_g + \vec{H}_{cr}$, $\vec{\mathcal{E}} = -\frac{\vec{u}}{c}\times\vec{H}$ is an electric field in a medium. We assume that in plasma there exists an excessive charge density $-zeN$ which compensates the CR charge.

The averaged kinetic equation for CR now has the form

$$\frac{\partial\langle f\rangle}{\partial t} + (\vec{v}\nabla)\langle f\rangle + ze\left\langle\vec{\mathcal{E}}\frac{\partial f}{\partial\vec{p}}\right\rangle + ze\left(\frac{\vec{v}}{c}\times\langle\vec{H}\rangle\right)\frac{\partial\langle f\rangle}{\partial\vec{p}} + ze\left\langle\left(\frac{\vec{v}}{c}\times\delta H\right)\frac{\partial\delta f}{\partial\vec{p}}\right\rangle = Q(10)$$

In the diffusion approximation with an account of the motion of the medium the distribution function $\langle f \rangle$ differs from (4) by an additional term $-\frac{3(\vec{v}\vec{u})}{v^2} p \frac{\partial f_0}{\partial p}$. Multiplying (IO) by $\vec{p}$ and integrating over d^3p, we have

$$\frac{w_{cr}+P_{cr}}{c^2}\frac{\partial \vec{u}}{\partial t} - \nabla P_{cr} - ze\langle \vec{E}N\rangle - \frac{1}{c}\left(\langle \vec{j}_{cr}\rangle \times \langle \vec{H}\rangle\right) - \frac{1}{c}\langle \delta\vec{j}_{cr} \times \delta\vec{H}\rangle = 0. \quad (II)$$

Here we elimitate terms quadratic in the small parameters u/v, Λ/R (R is the characteristic scale of the change in the CR concentration). The quantities w_{cr} and P_{cr} are defined by formulae (4), (8). Note that in hydrodynamics the density w of the internal gas density and the gas pressure p are defined in the frame of reference moving at a mean mass velocity $\vec{u}$ of the medium. In the case of CR it is more convenient to use a laboratory frame of reference. If the quadratic terms $(u/v)^2$ are neglected, both the definitions of the quantities w and p are equivalent.

Summing up equation (II) and equation (9) averaged over the field fluctuations, we derive

$$\left(\frac{w_{cr}+P_{cr}}{c^2}+\rho\right)\frac{\partial \vec{u}}{\partial t} + \rho(\vec{u}\nabla)\vec{u} = -\nabla P_g - \nabla P_{cr} + \frac{1}{c}\left(\langle \vec{j}_g\rangle + \langle \vec{j}_{cr}\rangle\right)\times\langle \vec{H}\rangle + \quad (12)$$
$$+ \frac{1}{c}\langle(\delta\vec{j}_g + \delta\vec{j}_{cr})\times\delta\vec{H}\rangle.$$

In the quasistationary approximation the regular field $\langle \vec{H}\rangle$ is determined from the equation

$$rot\langle \vec{H}\rangle = \frac{4\pi}{c}\left(\langle \vec{j}_{cr}\rangle + \langle \vec{j}_g\rangle\right). \quad (I3)$$

Substituting (I3) into (12) and neglecting the small terms $\delta H \ll H$, $(w_{cr} + p_{cr}) \ll \rho c^2$, we have

$$\rho\frac{d\vec{u}}{dt} = -\nabla P_g - \nabla P_{cr} + \frac{1}{4\pi}\left(rot\langle \vec{H}\rangle\right)\times\langle \vec{H}\rangle. \quad (I4)$$

We find the equation for w_{cr} by multiplying (IO) by E and integrating over d^3p

$$\frac{\partial w_{cr}}{\partial t} - \nabla\hat{D}\nabla w_{cr} + (\vec{u}\nabla)w_{cr} + (w_{cr}+P_{cr})\nabla\vec{u} = 0. \quad (I5)$$

The same result can be obtained simpler, by using the equation for f_0 in the diffusion approximation: $\frac{\partial f_0}{\partial t} - \nabla_i D_{ij}\nabla_j f_0 + (\vec{u}\nabla)f_0 - \frac{\nabla\vec{u}}{3}p\frac{\partial f_0}{\partial p} = 0$.

The rest of the MHD equation, except (I4), (I5) are obvious:

$$\frac{\partial\rho}{\partial t} + \nabla(\rho\vec{u}) = 0, \quad \frac{\partial\langle \vec{H}\rangle}{\partial t} = rot\left(\vec{u}\times\langle \vec{H}\rangle\right), \quad \nabla\langle \vec{H}\rangle = 0. \quad (I6)$$

Equations (I4)-(I6) form a system of MHD equations for interstellar medium with an account of the action of CR. They must be supplemented with the equation of state for the background plasma and with the relations connecting p_{cr} and w_{cr} (see /6/): For ultrarelativistic CR $p_{cr} = w_{cr}/3$.

In the approximation used here, CR are an additional gas component with a large internal energy, but with a negligible mass density. The small-scale random field $\delta H_g \ll H$, which provides CR scattering, enters only the tensor $\hat{D}$. The field δH_{cr} induced by the fluctuations δf must be small:

$\delta\vec{H}_{cr} << \delta\vec{H}_g$, otherwise CR scattering cannot be considered in the test particle approximation. This condition is fulfilled if (ϑ_{cr} is the degree of CR anisotropy)

$$P_{cr} \cdot \vartheta_{cr} << H^2 / 4\pi . \qquad (17)$$

is is assumed that in the system there are neither kinetic instabilities induced by CR (see /7/) nor a statistical acceleration of particles.

Various dissipative processes may be included into the equations if necessary. Note that CR scattering leads to viscosity and to large-scale conductivity (along the field $<\vec{H}>$)

$$\eta_{cr\parallel} = \frac{2}{15}\int d^3p\, \Delta p\, f_0 \; ; \; \sigma_{cr\parallel} = \frac{4(ze)^2}{3}\int d^3p\, \frac{\Lambda}{p} f_0 . \qquad (18)$$

For examples of the solution of the above MHD equations see /2,8-10/).

REFERENCES

1. Parker E.N. Cosmical magnetic fields. Clarendon Press. 1979.
2. Astrophysics of Cosmic Rays. ed. V.L.Ginzburg, M.: Nauka, 1984.
3. Dorman et al. Ap. Sp. Sci., 1983, 93, 97.
4. Ptuskin V.S. JETP, 1984, 86, 483.
5. Ginzburg V.L., Syrovatskii S.I. Origin of cosmic rays. Pergamon Press, 1964.
6. Ptuskin V.S. Pisma AZ, 1981, 7, 671.
7. McKee J.F., Webb G.M. J. Plasma Phys, 1984, 31, 275.
8. Ptuskin V.S. Ap. Sp. Sci. 1981, 76, 265.
9. Ghosh A., Ptuskin V.S. Ap. Sp. Sci. 1983, 92, 37.
10. Kuznetsov V.D., Ptuskin V.S. Ap. Sp. Sci. 1983, 94, 5.

DIFFUSION OF STRONGLY MAGNETIZED COSMIC RAY PARTICLES IN A TURBULENT MEDIUM

V.S. Ptuskin
Institute of Terrestrial Magnetism, Ionosphere and Radio Wave Propagation, USSR Academy of Sciences, I42092 Troitsk, Moscow Region, USSR

CR propagation in a turbulent medium is usually considered in the diffusion approximation. The methods of the derivation of a corresponding diffusion equation for different cases are proposed, for example, in the reviews /I,2/ and in the literature cited there. Here we obtain the diffusion equation for strongly magnetized particles in the general form and discuss the influence of a large-scale random magnetic field on CR propagation in interstellar medium.

CR diffusion equation. CR are assumed to propagate in a medium with a regular field $\vec{H}$ and an ensemble of random MHD waves. The energy density of waves on scales smaller than the free path l of CR particles is small. We use the collision integral of the general form which describes interaction between relativistic particles and waves in the quasilinear approximation /3/. Wave polarization is described by the polarization density matrix

$$S^{(\alpha)}_{mn}(\vec{k}) = \left(|\mathcal{E}^\alpha_L|^2 + |\mathcal{E}^\alpha_R|^2\right)^{-1} \cdot \begin{pmatrix} |\mathcal{E}^\alpha_L|^2 & \mathcal{E}^\alpha_L \mathcal{E}^{\alpha *}_R \\ \mathcal{E}^\alpha_R \mathcal{E}^{\alpha *}_L & |\mathcal{E}^\alpha_R|^2 \end{pmatrix} = \frac{1}{2} \begin{pmatrix} 1+\mathcal{G}^\alpha & \mathcal{G}^\alpha_1 - i\mathcal{G}^\alpha_2 \\ \mathcal{G}^\alpha_1 + i\mathcal{G}^\alpha_2 & 1-\mathcal{G}^\alpha \end{pmatrix}, \qquad (I)$$

Here $\mathcal{E}^\alpha_{L,R}(\vec{k}) = \mathcal{E}^\alpha_x(\vec{k}) \pm i\,\mathcal{E}^\alpha_y(\vec{k})$ $(k_z>0)$ are the Fourier-components of the electric field of waves, the z-axis is directed along $\vec{H}$; the index α characterizes the type of wave (there exist Alfven, fast and slow magnetosonic waves). Energy densities of a random magnetic field of waves for transverse and longitudinal components with respect to $\vec{H}$ are equal to $M^\alpha_\perp(\vec{k})$ and $M^\alpha_\parallel(\vec{k})$, respectively. The interaction between relativistic particles and waves is of resonant character - particles scatter under the condition

$$\omega^\alpha(\vec{k}) - k_\parallel v_\parallel = s\,\omega_H\,, \quad s = 0, \pm 1, \ldots \qquad (2)$$

Taking into account smallness of the phase velocity of waves as compared with the particle velocities $v \approx c$, it is convenient to introduce the resonant value of the wavenumber

$$k_{res} = \frac{\omega_H}{v_\parallel} = \frac{e|Z|H}{pc|\mu|} = (r_H|\mu|)^{-1}. \qquad (3)$$

Here eZ, p, r_H are charge, momentum and gyroradius of a particle, $\mu = p_z/p$.

The effective frequencies of relativistic particle scattering in a turbulent medium are given by the relations (ψ is the azimuthal angle for $\vec{k}_\perp$):

$$\nu^\alpha_\pm(\vec{k},s) = \frac{4\pi^2}{H^2} k_{res}\omega_H \Big\{ (1-\delta_{s0})\cdot\delta(k_\parallel - s k_{res}) M^\alpha_\perp(\vec{k}) \cdot \Big[J^2_{s+1}\cdot(1+\mathcal{G}^\alpha(\vec{k})\cdot \mathrm{sign}(z\mu)) + J^2_{s-1}\cdot(1-\mathcal{G}^\alpha(\vec{k})\cdot \mathrm{sign}(z\mu)) + 2J_{s+1}\cdot J_{s-1}\cdot \mathcal{G}^\alpha_1(\vec{k})\cdot\cos 2\psi \Big] + \delta_{s0}\cdot\delta\Big(k_\parallel - k_\perp \frac{\sqrt{v_a^2+v_s^2}}{v\cdot|\mu|}\Big)\cdot J^2_1 \frac{M^\alpha_\parallel(\vec{k})}{2}\left(\frac{k_\parallel}{k_\perp}\right)^2 \Big\}, \qquad (4)$$

$J_s \equiv J_s\left(\frac{k_\perp v_\perp}{\omega_H}\right)$ is the Bessel function.

Note that out of the three Stokes parameters ζ, ζ_1, ζ_2 equations (4), (6) involve ζ and ζ_1, whereas for an axially symmetric wave distribution in the k-space they involve only ζ. All the quantities referring to waves are defined in a co-moving reference frame.

In the weak turbulence approximation used here, $\nu_\mu^\alpha \ll \omega_H$. Actually, in interstellar medium for particle energies of I GeV, $\nu_\mu \sim 10^{-6}\omega_H$. The latter inequality means that particles are strongly magnetized and CR diffusion is locally one-dimensional, i.e. it proceeds only along the magnetic field. This fact allows us to pass over to the drift approximation and to average the kinetic equation (including the quasilinear collision integral) over fast particle rotation. The weak inhomogeneity of the regular magnetic field and motion of the medium with a nonrelativistic velocity $\vec{u} = c(\vec{\mathcal{E}}_0 \times \vec{H}) \cdot H^{-2}$ are taken into account in the drift approximation (here $\vec{\mathcal{E}}_0$ is a regular electric field in a laboratory frame of reference, whereas in a co-moving frame of reference, in the approximation of infinite conductivity an electric field is equal to zero).

In the time interval $\Delta t \gg \nu^{-1}$ and on the scale $\Delta z \gg l \sim v\nu^{-1}$ the distribution function is close to isotropic. The isotropic part of the CR distribution function $f(t,\vec{r},p)$ obeys the diffusion equation, which in this case has the form

$$\frac{\partial f}{\partial t} - \nabla_i D_{ij} \nabla_j f + \left(\vec{u} + \frac{1}{3p^2}\frac{\partial}{\partial p}(p^3 \vec{u}_w)\right)\nabla f - \nabla(\vec{u}+\vec{u}_w)\frac{p}{3}\frac{\partial f}{\partial p} - \frac{1}{p^2}\frac{\partial}{\partial p} p^2 D_{pp}\frac{\partial f}{\partial p} = 0. \qquad (5)$$

Here $D_{ij} = D_{\parallel} h_i h_j$, $\vec{u}_w = u_w \vec{h}$, $\vec{h} = \vec{H}/H$, the velocity u_w, the diffusion coefficients along the field $D_{\parallel}$ and by the absolute value of the momentum are given by

$$D_{\parallel} = \frac{v^2}{4}\int_{-1}^{1} d\mu\,(1-\mu^2)\left(\Sigma \nu_\mu^\alpha(\vec{k},s)\right)^{-1};\quad u_w = \frac{3}{4}\int_{-1}^{1} d\mu\,(1-\mu^2)\left(\Sigma v_f^\alpha \nu_\mu^\alpha\right)\left(\Sigma \nu_\mu^\alpha\right)^{-1};$$
$$D_{pp} = p^2 \int_{-1}^{1} d\mu\,\frac{1-\mu^2}{4}\left(\Sigma \nu_\mu^\alpha \left(\frac{v_f^\alpha}{v}\right)^2 - \left(\Sigma \nu_\mu^\alpha\right)\left(\Sigma \frac{v_f^\alpha}{v}\nu_\mu^\alpha\right)\right);\quad v_f^\alpha(\vec{k}) \equiv \frac{W^\alpha(\vec{k})}{K_\parallel},\ \Sigma \equiv \sum_{\alpha,s,\vec{k}}. \qquad (6)$$

The CR diffusion equation in the form (5) was first derived for a simplified collision integral in the paper /4/ (see also /2/).

Diffusion in a medium with a rangom diffusion tensor. The field H has been considered above to be weakly inhomogeneous and regular on the scales of the order of 1. In interstellar medium $\delta H^2/H^2 \lesssim 0.1$ for $l \sim 1$ pc. Strong field fluctuations $\delta H/H \gtrsim 1$ are observed for $L \sim 100$ pc $\gg 1$. On this scale the field $\vec{H}$ should be considered random. There appears the problem of particle diffusion in a medium with a random diffusion tensor.

Assuming the tensor fluctuations $D_{ij}(\vec{r})$ to be weak, one can obtain in the quasilinear approximation the equation for the distribution function $\langle f \rangle$ averaged over the ensemble of fluctuations $\delta D_{ij}(t,\vec{r})$ (we put $u = u_w = 0$):

$$\frac{\partial \langle f\rangle}{\partial t} - \nabla_i \langle D_{ij}\rangle \nabla_j \langle f\rangle + \hat{K}\langle f\rangle = 0, \qquad (7)$$

where $\hat{K}\langle f\rangle = \nabla_i \int \frac{d^3k}{(2\pi)^3} \int_0^\infty d\tau\, U_{ijmn}(\vec{k},\tau)\,[k_j + i\nabla_j]\, e^{-\tau k_\perp k_\beta \langle D_{\perp\beta}\rangle} \cdot [k_m + i\nabla_m]\,\nabla_n \langle f(t-\tau,\vec{r})\rangle$. (8)

The correlator of the Fourier-components of the tensor δD_{ij} is assumed to be

$$\langle \delta\tilde{D}_{ij}(t,\vec{k}_1)\,\delta\tilde{D}_{mn}(t_0,\vec{k}_2)\rangle = (2\pi)^3\delta^3(\vec{k}_1+\vec{k}_2)\,U_{ijmn}(\vec{k},t-t_0) \quad (9)$$

The integral-differential equation (7) is reduced to the diffusion equation if the correlation time for δD is small: $\tau_c \ll \ell^2/\langle D\rangle$. In this case the term $\hat{K}\langle f\rangle$ in eq. (7) can be disregarded, and the effective diffusion tensor for $\langle f\rangle$ is equal to $D_{ij\,eff} = \langle D_{ij}\rangle$.

In the case of static fluctuations, more precisely for $\tau_c \gg \ell^2/\langle D\rangle$, we obtain from (8) in a first approximation

$$D_{in\,eff} = \langle D_{in}\rangle - \int \frac{d^3k}{(2\pi)^3} \frac{k_j k_m V_{ijmn}}{k_\perp k_\beta \langle D_{\perp\beta}\rangle}, \quad \left(U_{ijmn}(\vec{k},0) = V_{ijmn}(\vec{k})\right). \quad (10)$$

The second term in (10) has the order $(\delta D)^2/D$ and is almost always small for $\delta D \ll D$. But for the case $D_{ij} = D_\parallel h_i h_j$ formula (10) leads to a zero diffusion coefficient across the regular homogeneous field $\langle \vec{H}\rangle$:

$$D_{\perp\,eff} = (\delta_{ij} - \langle h_i\rangle\langle h_j\rangle)\cdot\frac{1}{2}\, D_{ij\,eff} = 0. \quad (11)$$

This result apparently suggests a compound diffusion in the system /5,6/, i.e. an imposition of two independent wanderings: that of a magnetic field line and of a particle moving along this line. The summary transverse displacement of particles is here $r_\perp \sim t^{1/4}$ (under a usual diffusion $r_\perp \sim t^{1/2}$). The compound diffusion is violated if the local diffusion coefficient $D_\perp \neq 0$. The standard perturbation theory (10) does not, evidently, give a correct result for an anomalously small $D_\perp \ll D_\parallel$ $(\delta H/H)^4$. This is just the case with CR in interstellar medium, where $D_\perp \sim r_H^2\, v^2/D_\parallel \sim 10^{-12} D_\parallel$, and $\delta H/H \sim 1$. The problem has not yet been strictly solved (see the Discussion in /6-8/). Phenomenologically, diffusion across a regular field occurs due to spreading of random field lines which were initially at a distance r_H from one another /9,10/. If correlation between lines vanishes at a distance s_c, one can use (8) with the correlation function

$$U_{ijmn}(\vec{k},\tau) = V_{ijmn}(\vec{k})\cdot\frac{8}{\pi^2}\cdot\sum_{n=0}^{\infty}(2n+1)^{-2}\exp\left(-(2n+1)^2\,\frac{\pi^2 D_\parallel\cdot|\tau|}{4 s_c^2}\right). \quad (12)$$

For a power-law spectrum of random field inhomogeneities $\delta\tilde{H}^2(k) \sim \kappa^{-4+\varepsilon}$, $(\varepsilon > 0)$ the quantity $s_c(\kappa) \approx L\left(\delta H/H\right)^{-2}(\kappa L)^{1-\varepsilon}$ /11/, which gives

$$D_{\perp\,eff} \sim 0{,}2\left(\frac{\delta H}{H}\right)^4 \cdot D_\parallel. \quad (13)$$

We obtain a different expression if the spectrum has one main scale L, see /IO, II/.

The estimate (I3) with an account of $\delta H/H \sim I$ leads to the conclusion that on the average the CR transport is evidently realized with a diffusion tensor close to an isotropic one.

REFERENCES

I. Jokipii J.R. Rev.Geophys.Space Phys. I97I, 9, 27.
2. Ginzburg V.L., Ptuskin V.S. Astronomy v. 24 (VINITI ANSSSR), I983, p. 94.
3. Kennel C.F., Engelmann F. Phys.Fl., I966, 9, 2377.
4. Skilling J. MNRAS, I975, I72, 557.
5. Getmanzev G.G. AZ, I962, 39, 607.
6. Krommes J.A. Suppl. Prog. Theor. Phys. I978, 64, I37.
7. Horton W. in "Principles of Plasma Physics", Energoatomizdat, I984, p. 362.
8. Barge P. et al., Ap.J. I984, 284, 8I7.
9. Ptuskin V.S. Ap.Sp.Sci I979, 6I, 259.
IO. Rechester A.B., Rosenbluth M.N. Phys.Rev.Lett. I978, 40, 38.
II. Skilling J. et al. MNRAS, I974, I67, 87.

OG 7.2-17

COSMIC-RAY TRANSPORT IN THE GALACTIC MAGNETOSPHERE

Michael Schulz
Space Sciences Laboratory, The Aerospace Corporation
El Segundo, CA 90245
USA

J. G. Luhmann
Institute of Geophysics and Planetary Physics, University of California
Los Angeles, CA 90024
USA

ABSTRACT

It is advantageous to regard cosmic rays as the constituent particles of the Galactic radiation belts and cosmic ray energization as a consequence of inward radial diffusion in the quasi-dipolar Galactic magnetosphere. This process occurs in addition to Fermi acceleration.

1. Introduction. The purpose of this work is to explore a magnetospheric explanation for the elevation of Galactic charged particles to cosmic ray energies. The magnetosphere that is of interest in this context is not a planetary magnetosphere but a galactic magnetosphere entirely analogous to those inferred [1-3] from radio observations [4-6] of distant galaxies. It is the magnetosphere of the Milky Way. Cosmic rays are (by this interpretation) the charged particles that constitute the radiation belts of the Galactic magnetosphere. Thus, the mechanism by which charged particles attain cosmic-ray energies is presumably the mechanism by which radiation-belt particles attain high energies in more familiar magnetospheres, i.e., the radial diffusion associated with magnetic disturbances that contain spectral power resonant with the azimuthal drift of the particles [7].

The existence of galactic radiation belts has been proposed [3] as a means of explaining the similarity of decimetric ($\sim$ 3-GHz) radio-emission patterns from various galaxies to that from Jupiter's magnetosphere [8]. Such radio patterns are believed to result from the synchrotron emissions of relativistic electrons, but it is clear that galaxies might (by analogy with Jupiter) have ionic radiation belts (which would not be remotely observable) as well as electron radiation belts (which are). Indeed, it is logical to identify the Galactic cosmic rays routinely observed in the heliosphere with the constituent ions and electrons of the Galactic radiation belts. This identification is supported (for electrons at least) by comparisons [9,10] between the energy spectrum of cosmic-ray electrons observed at the top of the atmosphere and the frequency spectrum of radio emissions from the disk of the Galaxy.

2. Field Model. An immediate corollary of this line of thought is that cosmic-ray energization must be considered within the context of a specific model for the Galactic magnetic field. A dipolar model [11] is convenient and (in view of the radio observations cited above) at least topologically realistic. The analytical representation of the adopted field model is

$$\underset{\sim}{B}(r,\theta) = \begin{cases} (r_c^3/2r^3)(2\,\hat{\underset{\sim}{r}}\cos\theta + \hat{\underset{\sim}{\theta}}\sin\theta)B_c, & r > r_c \\ \hat{\underset{\sim}{z}}\,B_c = (\hat{\underset{\sim}{r}}\cos\theta - \hat{\underset{\sim}{\theta}}\sin\theta)B_c, & r < r_c \end{cases} \quad (1)$$

where r is the radial coordinate, θ is the colatitude, $z = r\cos\theta$, r_c is the radius of the Galactic core, and B_c (~ 25 nT) is the magnitude of the (ideally uniform) magnetic field within. The emitting electrons in this model [3] reside mainly near the magnetic equator ($\cos\theta = 0$) and not near the magnetic axis ($\sin\theta = 0$), in contrast with the assumption of other investigators [11,12]. It is convenient to define the (dimensionless) magnetic-shell parameter

$$L = \begin{cases} (r/r_c)\csc^2\theta, & r \geq r_c \sim 2 \text{ kpc} \\ (r_c/r)^2\csc^2\theta, & r \leq r_c \sim 2 \text{ kpc} \end{cases} \quad (2)$$

in analogy with the L parameter encountered in the study of planetary magnetospheres. It follows from (2) that $L \geq 1$. A more realistic model of the Galactic $\underset{\sim}{B}$ field would entail a more widely distributed azimuthal current, which in (1) is confined to the sphere $r = r_c$. The dynamo current of a real galaxy would presumably involve the entire core, as well as a major part of the disk. The disk current would tend to distort magnetic shells by analogy with the "magnetodisk" model [13] of Jupiter's outer magnetosphere. This distortion would account for observations [10] that suggest a $\underset{\sim}{B}$ field parallel to the disk itself, while preserving the generally poloidal form [11,14] of the large-scale Galactic magnetic field. Moreover, energy-density considerations [10] suggest that cosmic-ray ions themselves must generate (through gyration and adiabatic charged-particle drifts) a Galactic ring current that significantly distorts magnetic shells from dipolar form even beyond the disk. It is convenient nevertheless to adopt a dipolar model of the Galactic $\underset{\sim}{B}$ field in order to discuss a first approximation of cosmic-ray kinematics and transport in the Galactic magnetosphere, just as it is customary to adopt dipolar models of planetary magnetic fields in order to study radiation belt dynamics for the earth and Jupiter.

3. Kinematics. The adiabatic theory of charged-particle motion therefore provides a kinematical framework for understanding the transport of cosmic-ray ions and electrons in the Galactic magnetosphere, just as it does for radiation-belt particles in planetary magnetospheres. Adiabatic theory is based on quasi-conservation of the three invariant quantities M, J, and Φ, which are proportional (respectively) to the action integrals J_i associated with gyration (i=1), bounce motion (i=2), and azimuthal drift (i=3). The corresponding frequencies $\Omega_i/2\pi$ associated with adiabatic charged-particle motion are supposed to satisfy the inequalities $\Omega_1 \gg \Omega_2 \gg \Omega_3$, and so it follows that the adiabatic theory holds only for particle energies $E \lesssim 10^{18}$ eV/charge on the drift shell ($L = L_\odot \sim 5$; see below) that supplies Galactic cosmic rays to our heliosphere. The bounce period for a very relativistic particle trapped on this drift shell, which has a radius ~ 10 kpc ($\sim 5\,r_c$; see above) is $2\pi/\Omega_2 \sim 10^5$ yr in the dipolar model. Gyration and drift periods are of this order for particle energies $E \sim 7\times 10^{18}$ eV/charge if the Galactic magnetic field has a local magnitude $B \sim 0.1$ nT here, and so the adia-

batic theory of charged-particle motion applies only to particle energies $E \ll 7 \times 10^{18}$ eV/charge in our part of the Galaxy.

4. Transport and Energization. Adiabatic motion impels a charged particle to remain attached to its original magnetic shell, i.e., to retain its original value of L. The usual mechanisms for radial transport of energetic charged particles in planetary magnetospheres involve time-dependent disturbances having azimuthal asymmetry. Such disturbances typically conserve the first two adiabatic invariants M and J while violating the third invariant Φ. The result is a diffusion of the guiding center with respect to L and a corresponding change in the energy of the particle. The change in particle energy for $L \gg 1$ is conveniently expressed by the relationship

$$-3/2 \leq (\partial \ln p/\partial \ln L)_{M,J} \leq -1, \tag{3}$$

where p is the scalar momentum of the particle. The precise value of $(\partial \ln p/\partial \ln L)_{M,J}$ depends upon the L value and equatorial pitch angle α_0 [15], but the limiting values -3/2 and -1 in (3) are attained for $\alpha_0 = \pi/2$ and $\alpha_0 = 0$, respectively.

The observed isotropy of cosmic-ray ion distributions in momentum space [10] is presumably a consequence of anisotropy-destroying plasma instabilities [16-19]. The mean value of $(\partial \ln p/\partial \ln L)_{M,J}$ for a fully isotropic distribution of charged particles trapped in a dipolar magnetic flux tube is found [20] to be

$$\langle(\partial \ln p/\partial \ln L)_{M,J}\rangle \approx -4/3 \tag{4}$$

for $L \gg 1$. This result suggests the utility of a quasi-invariant object

$$\Lambda \equiv (p^2/m_0 B_c)L^{8/3} \tag{5}$$

for the treatment of radial transport in the presence of strong pitch-angle diffusion, in preference to the "invariant" $\tilde{\Lambda} \equiv (p^2/m_0 B_c)L^3$ implicitly proposed by Walt [21] for a similar purpose. Indeed, the appropriate exponent for L in (5) is a function of the anisotropy of the pitch-angle distribution, the values 8/3 and 3 being appropriate to isotropy and to extreme anisotropy ($\alpha_0 = \pi/2$ for all particles), respectively. The essential point is that particles in a galactic radiation belt gain (lose) energy by diffusing inward (outward) in L.

The particle energization implicit in (5) corresponds to the mechanism [22,23] typically invoked for radial transport of the highest-energy particles in the earth's radiation belts. It is separate and distinct from the well-known mechanism of Fermi [24], which requires the violation of J for the energization of particles [25] in a dipolar B field. Both energization mechanisms must rely (in this context) on pitch-angle diffusion (implicitly at nearly fixed p) to maintain the desired pitch-angle isotropy. Both energization mechanisms are multiplicative in the sense that a particle's rate-of-change of p is proportional to p itself, among other factors.

5. Source Distribution. Cosmic rays are presumed to originate in (e.g.,

supernova) events distributed with uniform probability density throughout the core of the Galaxy. In this model the rate-of-production of cosmic rays per unit volume of magnetosphere turns out to be proportional to L^{-4} for $L \gg 1$. However, if the differential energy spectrum is proportional to $p^{-2.6}$ [10], then it follows (assuming immediate isotropization) that the source of phase-space density (differential flux divided by p^2) at fixed Λ varies as $L^{-4}(p^{-2.6}/p^2)$, i.e., as $L^{32/15}$, for $L \gg 1$. This is a monotonically increasing function of L, and so it seems that the net result of radial diffusion in the Galactic magnetosphere can be an inward transport of phase-space density, which corresponds via (5) to a net energization of particles subsequently observed as cosmic rays at $L = L_{\odot} \sim 5$.

6. Acknowledgements. The work of one author (M.S.) was supported by the Aerospace Sponsored Research (ASR) program of The Aerospace Corporation. Both authors thank Prof. F. V. Coroniti for the further suggestion that cosmic rays of energy $E \gtrsim 10^{18}$ eV/charge might (by analogy) be the radiation belt particles trapped in the magnetosphere of the Local Group, i.e., of the cluster of galaxies to which our Galaxy belongs.

References

1. van der Laan, H., (1975), Eos, Trans. AGU, 56, 433.
2. Russell, C.T., (1976), in D.J. Williams (ed.), Physics of Solar Planetary Environments, pp. 526-540, AGU, Washington, D.C.
3. Luhmann, J.G., (1979), Nature, 282, 386.
4. Moffett, A.T., (1966), Ann. Rev. Astron. Astrophys., 4, 145.
5. Rudnick, L., and Owen, F.N., (1976), Astrophys. J., 203, L107.
6. Burch, S.F., (1979), Mon. Not. Roy. Astron. Soc., 186, 293.
7. Fälthammar, C.-G., (1965), J. Geophys. Res., 70, 2503.
8. Berge, G.L., (1966), Astrophys. J., 146, 767.
9. Kraus, J.D., (1966), Radio Astronomy, McGraw-Hill, New York.
10. Longair, M.S., (1981), High Energy Astrophysics, pp. 271, 256, 328, 119, Cambridge Univ. Press, Cambridge, England.
11. Greyber, H.D., (1965), in I. Robinson et al. (eds.), Quasi-Stellar Sources and Gravitational Collapse, pp. 389-390, Univ. of Chicago Press.
12. Alfvén, H., (1981), Cosmic Plasma, p. 57, Reidel, Dordrecht.
13. Hill, T.W., et al., (1974), Geophys. Res. Lett., 1, 3.
14. Yusef-Zadeh, F., et al., (1984), Nature, 310, 557.
15. Schulz, M., and Lanzerotti, L.J., (1974), Particle Diffusion in the Radiation Belts, p. 21, Springer, Heidelberg.
16. Cornwall, J.M., (1965), J. Geophys. Res., 70, 61.
17. Cornwall, J.M., (1966), J. Geophys. Res., 71, 2185.
18. Scarf, F.L., et al., (1967), J. Geophys. Res., 72, 993.
19. Wentzel, D.G., (1968), Astrophys J., 152, 987.
20. Hill, T.W., et al., (1983), in A.J. Dessler (ed.), Physics of the Jovian Magnetosphere, pp. 353-394, Cambridge Univ. Press.
21. Walt, M., (1970), in B.M. McCormac (ed.), Particles and Fields in the Magnetosphere, pp. 410-415, Reidel, Dordrecht.
22. Kellogg, P.J., (1959), Nature, 183, 1295.
23. Parker, E.N., (1960), J. Geophys. Res., 65, 3117.
24. Fermi, E., (1949), Phys. Rev., 75, 1169.
25. Parker, E.N., (1961), J. Geophys. Res., 66, 693.

The Role of Cosmic Rays and Alfvén Waves in the Structure of the Galactic Halo.

M.K. Dougherty and J.F. McKenzie (University of Natal, Durban, R.S.A.) and N.J. Westergaard (Danish Space Research Institute, Lyngby, Denmark)

ABSTRACT

The effect that cosmic rays and the Alfvén waves they generate have on the structure of the plasma distribution perpendicular to the galactic disk is examined. It is shown that the plasma distribution exhibits two length scales and the predicted values of gas density far from the galactic plane indicate that models involving hydrostatic equilibrium should be replaced by those allowing for a galactic wind.

1. Introduction. It is now recognised [1,2,3] that since the energy densities of the interstellar gas, magnetic field and cosmic rays are of the same order (~ 1 eV cm^{-3}) in the interstellar medium, the coupling between these components, which must be taken into account in a self-consistent fashion, leads to important dynamical effects. Here we examine the role of cosmic rays and the Alfvén waves they generate on the distribution of the plasma perpendicular to the galactic plane.

2. General Equations. Hydrostatic equilibrium perpendicular (i.e. along z) requires

$$-\rho g_z = \frac{d}{dz}(p_g + p_m + p_w + p_c) \tag{1}$$

in which ρ = interstellar gas density with pressure p_g, p_c = cosmic ray pressure, p_m = magnetic pressure, p_w = Alfvén wave pressure and g_z is the z component of the galactic gravitational acceleration given by $\frac{-\partial\phi(r,z)}{\partial z}$ where $\phi(r,z)$ is an axisymmetric galactic gravitational potential such as [3]

$$\phi(r,z) = \sum_{i=1}^{2} \frac{G M_i}{[r^2 + (a_i + (z^2 + b_i^2)^{\frac{1}{2}})^2]^{\frac{1}{2}}} \tag{2}$$

a_1, b_1; a_2, b_2 are parameters for the bulge and disk components of the galaxy, M_i is the corresponding mass parameter, G the gravitation constant, and r the radial and z the axial coordinate.
Treating the cosmic rays hydrodynamically, that is, in terms of their pressure and effective diffusion constant κ, the effects of convection and diffusion are described by the cosmic ray transport equations [4]

$$\frac{dF_c}{dz} = V\frac{dp_c}{dz} + Q \tag{3}$$

$$F_c = \left(\frac{\gamma_c}{\gamma_c - 1}\right) V p_c - \left(\frac{\kappa}{\gamma_c - 1}\right) \frac{dp_c}{dz} \tag{4}$$

γ_c = adiabatic index, F_c = cosmic ray enthalpy flux, V = Alfvén wave velocity assumed $\alpha \frac{1}{\sqrt{\rho}}$. The wave energy exchange equation which describes how the wave pressure is generated by the cosmic ray pressure gradient [4,5] is

$$\frac{d}{dz}(V 2p_w) = -V\frac{dp_c}{dz} - L \tag{5}$$

In the absence of additional energy losses or gains, Q = L = 0, (3), (4) and (5) give the total energy flux conservation law as

$$\frac{\gamma_c}{(\gamma_c-1)} Vp_c - \frac{\kappa}{(\gamma_c-1)} \frac{dp_c}{dz} + V2p_w = \text{constant} \qquad (6)$$

3. Results for the cases of strong and weak scattering.

(a) Strong scattering ($\kappa \to 0$) If the cosmic ray diffusive flux is small compared with the cosmic ray enthalpy flux the cosmic ray transport equation (3) integrates immediately to yield the adiabatic form

$$p_c V^{\gamma_c} = \text{constant} \qquad (7a)$$

or $$p_c \propto \rho^{\frac{\gamma_c}{2}} \quad (= \rho^{2/3}, \ \gamma_c = 4/3) \qquad (7b)$$

The total energy equation (6) then tells us how the wave pressure p_w is related to the plasma density, namely

$$p_w = p_{wo} (\rho/\rho_o)^{\frac{1}{2}} + p_{co} \frac{\gamma_c}{2(\gamma_c-1)} (\rho/\rho_o)^{\frac{1}{2}} \left[1-(\rho/\rho_o)^{\frac{\gamma_c-1}{2}}\right] \qquad (8)$$

where the subscript "0" refers to the value of a quantity at some reference level, eg. at the galactic plane. It is often assumed that the magnetic pressure is proportional to the plasma pressure [3,6] which in turn we shall assume is related to the density by some polytropic law of the form

$$\frac{p_g}{p_{go}} = (\rho/\rho_o)^{\gamma_g} \qquad (9)$$

Under these assumptions the magnetic pressure may be simply incorporated into the gas pressure in the form of an effective sound speed also given by

$$a_{so}^2 = \gamma_g \frac{(p_{go} + p_{mo})}{\rho_o} \qquad (10)$$

The above "equations of state" for p_g, p_w and p_c enable us to integrate the hydrostatic pressure balance equation immediately to yield

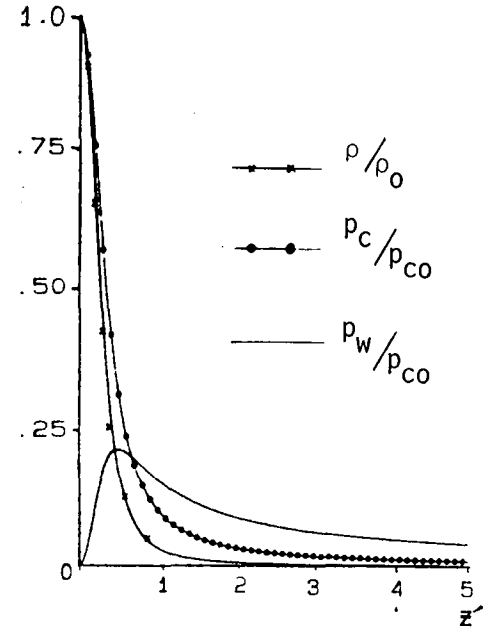

Figure 1 :

Distributions for r = 5kpc,
a_{co} = 13,6 kms^{-1},
a_{so} = 3.8 kms^{-1},
Ve = 500 kms^{-1} ; where $z' = z/b_2$

$$\phi(r,o) - \phi(r,z) = \frac{a_{so}^2}{(\gamma_g-1)}\left[1-(\rho/\rho_o)^{\gamma_g-1}\right] + a_{wo}^2\left[(\rho_o/\rho)^{\frac{1}{2}}-1\right]$$

$$+ \frac{a_{co}^2}{(\gamma_c-1)}(\rho_o/\rho)^{\frac{1}{2}}\left[1-(\rho/\rho_o)^{\frac{\gamma_c-1}{2}}\right] \qquad (11)$$

$$a_{co}^2 = \frac{\gamma_c}{2}\frac{p_w}{\rho_o} \qquad a_{wo}^2 = \frac{p_{wo}}{\rho_o}$$

Thus for a given shape for the galactic gravitational potential (such as equation (2)), equation (11) determines the plasma distribution as a function of r and z. Figure 1 shows the distributions of ρ/ρ_o, p_c/p_{co} and p_w/p_{co} perpendicular to the galactic disk. It is interesting to note the qualitative agreement between the theory and observations [6,7] denoted by crosses. The main point to note is that the model predicts in a natural fashion that the plasma distribution will exhibit two length scales; a fast decay near the galactic plane (determined by the plasma and magnetic pressure)followed by a much slower delay determined by the self-excited Alfvén wave pressure.

(b) Weak Scattering (κ large) If we assume that the cosmic ray enthalpy flux is negligible compared to the diffusive flux in equations (3) and (4) then the wave energy equation may be written

$$\frac{d(V2p_w)}{dz} = \frac{(\gamma_c-1)}{\kappa} VF_o \qquad (12)$$

where F_o is the (constant) diffusive cosmic ray flux.

This equation (with some assumptions for the behaviour of κ) along with hydrostatic pressure balance generalizes the galactic halo model of Ghosh and Ptuskin (GP) to include Alfvén waves generated by the cosmic ray pressure gradient. The GP model and this generalization suffer from the defect that sufficiently far from the galactic plane the density (and therefore the gas and magnetic pressures) and wave pressures begin to increase and the cosmic ray pressure goes negative. This defect in the model arises because it is not consistent to simply assume that the diffusive flux is constant since in fact overall energy flux must be conserved (equation (6)). Thus the wave energy flux can only grow at the expense of the diffusive flux with the implication that the system will eventually drive itself into the strong scattering mode discussed above. We therefore expect that the results for $\kappa \neq 0$ will be similar to those for $\kappa = 0$ with some modifications which will maximize around the point of inflection of the distribution of p_c with z.

Conclusions

The strong scattering limit predicts two length scales describing the gas distribution; the larger one which prevails above the plane arises because the cosmic rays and the waves they generate lift the gas up and stretch it out far beyond the galactic plane, asymptotically approaching a constant value $\rho_\infty \sim \rho_0 (\gamma_c - 1)^2 / (V_e/a_{c0})^4$ (where V_e is the galactic escape speed). Although $\rho_\infty/\rho_0 << 1$ this asymptotic value for the density is nevertheless much greater than typical intergalactic densities ($2.\times10^{-8}\times\rho_0$) with the implication that the hydrostatic model should be replaced with a galactic wind model.

4. References :

1. Ginzburg, V.L. and Ptushkin, V.S. (1976) Rev. Mod. Phys 48, 161
2. Parker, E.N. (1969) Space Sci. Rev. 9, 651
3. Ghosh, A. and Ptushkin, V.S. (1983) Astrophysics and Space Science, 92, 37.
4. O'C Drury, L. (1983) Reports on Progress in Physics, 46, 973.
5. McKenzie, J.F. and Völk, H.J. (1982) Astron. Astrophysics 116, 191
6. Fuchs, B and Thielheim, K.O. (1979) Astrophysical Journal 227, 801.
7. Schmidt, M. (1957) B.A.N. 13, 247.

MEASUREMENTS OF THE FRAGMENTATION OF ^{40}Ar, ^{28}Si AND ^{12}C in CH_2, C AND H TARGETS BETWEEN 300 AND 1500 MEV/NUC AT THE BEVALAC

W. R. Webber & J. C. Kish
Space Science Center
University of New Hampshire
Durham, NH 03824

1. Introduction. In the two years since the last cosmic ray conference we have continued our studies of the fragmentation of various nuclei in CH_2 and C targets with the objective of obtaining cross sections in hydrogen for use in the cosmic ray propagation problem. New measurements include ^{56}Fe, where we now have measurements at 6 energies between 300 and 1700 MeV/nuc, ^{12}C where we also have measurements at six energies, ^{28}Si with measurements at three energies and ^{40}Ar where there are measurements at two energies. The ^{56}Fe data has been summarized in a recent paper (Webber, 1984), in this paper we shall report the new data on ^{12}C, ^{28}Si, and ^{40}Ar nuclei and compare it with the earlier semi-empirical predictions.

2. Experimental Details. a) Charge cross sections. The cross sections in H are obtained using the following procedures. 7.5 cm diameter CH_2 and C targets of varying thickness are placed directly in front of a small Cerenkov x total energy telescope. The thickness of the targets is chosen so that the E loss in each type of target is the same. The CH_2 and C targets are alternated with no target. The H cross sections are obtained by a CH_2 - C subtraction; the no target data is subtracted directly from the individual CH_2 and C runs.

The telescope used is a smaller version of the charge isotope telescope we have used to measure primary cosmic rays. It has been described previously (Webber and Brautigam, 1982). The current telescope is similar but contains several significant improvements. The charge module used in this study contains three thin waveshifted CaF_2 scintillators and a 7940 glass waveshifted fused silica Cerenkov counter. The CaF_2 scintillators have better linearity and resolution than the NE102 scintillators used previously and the 7940 Cerenkov radiator has much better resolution than a comparable thickness of 425 lucite. The analysis procedures used to obtain the total interaction cross sections and the relative charge abundances of the fragments have been described previously (Webber and Brautigam, 1982) and will not be repeated here. In Table I we show some of the parameters of the runs reported here along with the total charge changing cross sections measured. In Table II the various individual charge changing cross sections are given.

b) Isotopic cross sections. To obtain the isotopic composition of the fragments, the events for each charge are treated separately. Additional consistency criteria are placed on the output of all counters in the telescope before the stopping E counter. A matrix of events, C vs stopping E, is made which shows the individual mass lines and from which the mass histograms are constructed. The fraction of events for each charge to be associated with each isotope is obtained by summing the appropriate mass histograms. The typical mass resolution obtained with our recent telescope ranges from σ of about 0.15 AMU for ^{16}O to 0.25 AMU for ^{56}Fe. The isotopic cross sections obtained for ^{12}C, ^{28}Si, and ^{40}Ar for hydrogen targets are shown in Table III.

3. Discussion of Results. a) ^{12}C cross sections. The results for Be and B secondaries are shown in Figure 1, along with the semi-empirical predictions of Tsao and Silberberg (1979). The semi-empirical cross sections appear to be an overestimate at all energies - but particularly - below ~ 1 GeV/nuc where the difference is as great as 30% at energies of a few hundred MeV/nuc. Since the B/C ratio is generally used as a reference to determine the path length traversed by cosmic rays as a function of energy, and since ~ 70% of all Be and B are produced by ^{12}C, these new cross sections will lead to a considerably different interpretation of this energy dependence - particularly below 1-2 GeV/nuc.

The isotope fractions we measure for Be and B are in generally much better agreement with the semi-empirical predictions.

b) ^{28}Si and ^{40}Ar. The main feature of our new cross sections for the production of secondary nuclei by these elements is the large excess in the production of secondaries in the Z = 12-17 range over the semi-empirical predictions. This is illustrated in Figure 2 for an average energy ~ 650 MeV/nuc. In some cases, e.g. the production of Mg and Si from ^{40}Ar, this difference is almost a factor of 2! From a study of the semi-empirical cross sections for nuclei of different Z and different neutron excess, we conclude that the semi-empirical formulae probably considerably underestimate the production of secondary nuclei with Z~12-20 from all primary nuclei with Z~14-22, and that the effect we observe is not just associated with the large neutron excess of ^{40}Ar. This will have a very important effect on the secondary production during interstellar propagation of the rarer elements in this charge range such as Al, P, Cl, Ar and K, which in turn will modify the source abundances of these charges that are deduced. A comparable effect will occur for the neutron rich isotopes - such as ^{26}Mg, ^{29}Si, and ^{30}Si and ^{34}S, possibly significantly altering the source abundances deduced for these isotopes as well.

4. Acknowledgements. This work was supported by a HEAO Guest Investigator Grant #NAG-8-451, and also by a NASA Support Grant #NGR-30-002-052.

5. References.

Tsao, C.H., and Silberberg, R., Proc. 16th ICRC, 2, 202, 1979

Webber, W.R., and Brautigam, D.A., Ap.J., 260, 894, 1982

Webber, W.R., paper presented at Workshop on Cosmic Ray & High Energy γ-ray Experiments for the Space Station Era, LSU, Oct., 1984.

6. Figure Captions.

Figure 1. Cross Sections for ^{12}C fragmenting into Be and B nuclei. Data from this work shown as solid circles.

Figure 2. Ratio of cross sections for ^{40}Ar and ^{28}Si fragmentation measured in this work to the semi-empirical predictions of Tsao and Silberberg (1979).

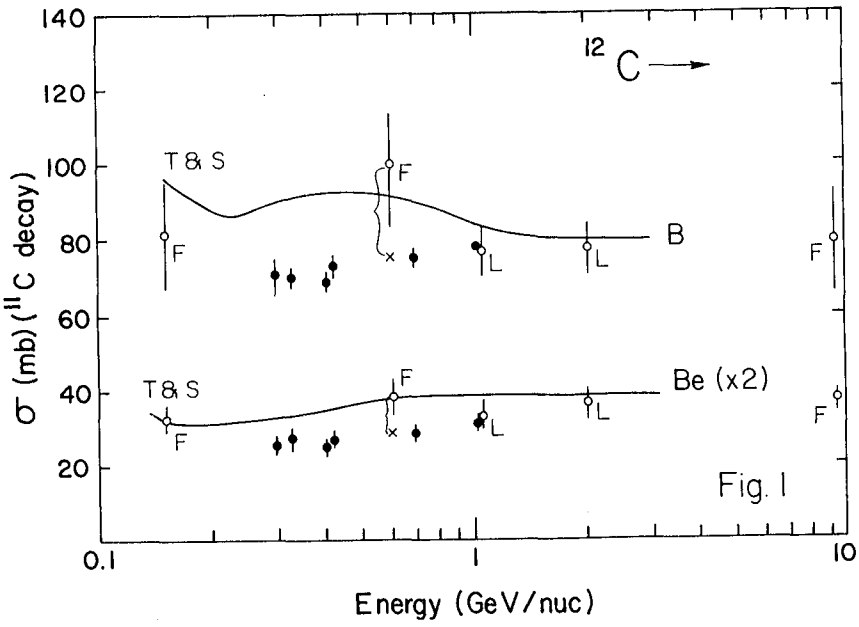

Fig. 1

Table 1

Parameters for BEVALAC Measurements

E (target) (MeV)	Target		(g/cm²)	N_B (x1,000)	N_Z/N_B	(ΔZ Changing) λ(g/cm²)	σ(mb)
				^{12}C beam			
1016	CH_2	=	8.75	417.2	0.6428	19.80	1179
	C	=	10.01	387.8	0.6943	27.44	727
	H	=	-	-	-	7.36	226
693	CH_2	=	8.75	217.3	0.6468	20.08	1163
	C	=	10.01	203.6	0.6962	27.64	721
	H	=	-	-	-	7.53	221
412	CH_2	=	6.01	486.3	0.7635	22.28	1044
	C	=	7.03	465.9	0.7879	29.56	675
	H	=	-	-	-	8.99	185
310	CH_2	=	6.01	235.9	0.7663	22.57	1030
	C	=	7.03	233.9	0.7905	29.89	666
	H	=	-	-	-	9.14	182
				^{28}Si beam			
1296	CH_2	=	6.01	239.0	0.5869	11.44	2037
	C	=	7.03	230.0	0.6452	16.11	1229
	H	=	-	-	-	4.13	403
770	CH_2	=	6.01	491.0	0.5956	11.77	1980
	C	=	7.03	527.1	0.6508	16.44	1215
	H	=	-	-	-	4.32	385
603	CH_2	=	6.01	597.6	0.5911	11.61	2004
	C	=	7.03	594.2	0.6459	16.15	1235
	H	=	-	-	-	4.33	384
				^{40}Ar beam			
792	CH_2	=	6.01	423.7	0.5198	9.19	2532
	C	=	7.03	336.6	0.6014	13.83	1436
	H	=	-	-	-	3.05	544
521	CH_2	=	5.26	295.3	0.5686	9.29	2501
	C	=	6.15	263.0	0.6455	14.05	1419
	H	=	-	-	-	3.08	539

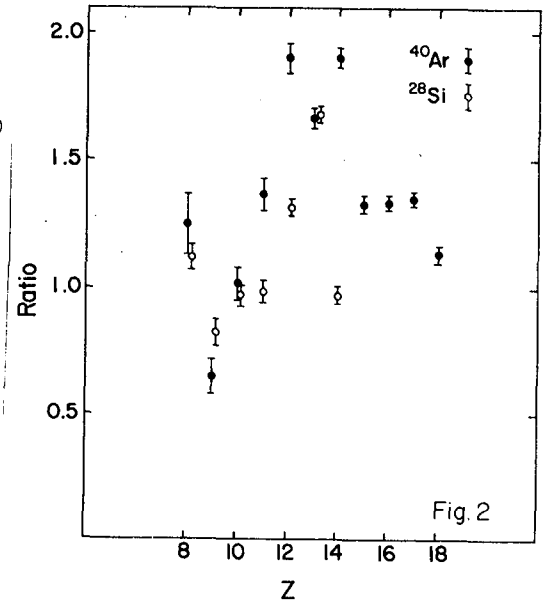

Fig. 2

Table II

Charge Changing Cross Sections In Hydrogen

(σ in mb)

Z	^{12}C			
	1016 MeV/nuc	693 MeV/nuc	403 MeV/nuc	326 MeV/nuc
B	52.9±1.0	51.3±1.1	45.3±1.0	43.6±1.0
Be	15.8±0.8	13.9±0.8	13.0±0.7	13.8±0.8
Li	30.5±2.0	26.6±2.0	24.6±1.8	27.2±2.2

	^{28}Si		
	1296 MeV/nuc	770 MeV/nuc	503 MeV/nuc
Al	84.0±1.5	86.5±1.5	85.3±1.3
Mg	82.7±1.5	84.6±1.5	88.1±1.3
Na	35.6±0.8	38.1±0.8	42.0±0.8
Ne	35.3±0.8	35.0±0.8	37.1±0.7
Fl	17.2±0.7	17.0±0.7	15.9±0.6
O	33.0±1.0	30.5±1.0	33.6±0.9
N	19.6±0.8	18.6±0.8	19.9±0.8
C	31.2±1.0	26.5±1.0	25.7±0.9

	^{40}Ar	
	792 MeV/nuc	521 MeV/nuc
Cl	136.2±1.6	140.3±1.2
S	94.1±1.2	99.6±0.9
P	66.8±1.0	73.5±0.8
Si	74.0±1.0	75.0±0.8
Al	45.6±0.8	47.4±0.6
Mg	41.5±0.8	37.0±0.6
Na	22.1±0.6	20.9±0.5
Ne	15.8±0.5	8.3±0.4
Fl	6.8±0.4	3.3±0.4
O	11.7±0.6	5.1±0.4

Table III

Isotopic Cross Sections
(σ in mb)

	^{12}C 403 MeV/nuc		^{28}Si 770 MeV/nuc		^{40}Ar 521 MeV/nuc		^{40}Ar 521 MeV/nuc
^{11}C	27.6±1.2	^{27}Si	31.3±0.9	^{39}Ar	65.6±1.6	^{32}Si	1.4±0.3
^{10}C	1.0±0.2	^{26}Si	1.4±0.3	^{38}Ar	30.3±0.9	^{31}Si	9.8±0.9
				^{37}Ar	1.7±0.3	^{30}Si	36.2±1.2
^{11}B	30.9±1.2	^{27}Al	53.0±1.2			^{29}Si	22.3±0.9
^{10}B	15.9±1.0	^{26}Al	32.0±1.1	^{39}Cl	31.6±1.0	^{28}Si	5.6±0.5
		^{25}Al	1.6±0.3	^{38}Cl	23.0±0.8		
^{10}Be	1.4±0.3			^{37}Cl	48.2±1.2	^{30}Al	0.7±0.2
^{9}Be	4.8±0.4	^{27}Mg	1.9±0.4	^{36}Cl	27.8±0.9	^{29}Al	7.5±0.8
^{7}Be	7.0±0.7	^{26}Mg	16.3±0.8	^{35}Cl	10.7±1.0	^{28}Al	14.8±0.7
		^{25}Mg	29.0±1.2			^{27}Al	22.5±1.0
		^{24}Mg	35.6±1.3	^{38}S	0.6±0.2	^{26}Al	4.6±0.6
		^{23}Mg	4.1±0.9	^{37}S	3.1±0.4		
				^{36}S	15.9±0.9	^{27}Mg	2.2±0.5
		^{25}Na	0.5±0.2	^{35}S	28.4±1.0	^{26}Mg	14.7±0.9
		^{24}Na	5.2±1.0	^{34}S	43.1±1.2	^{25}Mg	13.8±0.9
		^{23}Na	17.8±0.9	^{33}S	13.9±1.1	^{24}Mg	6.4±0.7
		^{22}Na	11.1±0.8	^{32}S	1.2±0.6		
		^{21}Na	1.0±0.3				
				^{35}P	0.4±0.2		
		^{23}Ne	0.5±0.2	^{34}P	5.1±0.7		
		^{22}Ne	6.1±0.7	^{33}P	21.7±1.0		
		^{21}Ne	12.8±1.1	^{32}P	28.3±1.1		
		^{20}Ne	14.9±1.1	^{31}P	16.4±0.9		
		^{19}Ne	3.0±0.5	^{30}P	1.2±0.5		

Measurements of Fe and Ar Fragmentation Cross Sections

K. H. Lau, R. A. Mewaldt, and E. C. Stone
California Institute of Technology
Pasadena, California 91125 USA

Measurements are reported of the yields of individual isotopes of Cr to Co (Z = 24 to 27) resulting from the fragmentation of ^{56}Fe, and the isotopes of Mg to K (Z = 12 to 19) resulting from the fragmentation of ^{40}Ar.

1. Introduction - Recent advances in the resolution and collecting power of cosmic ray instrumentation, have led to dramatic improvements in the precision of cosmic ray composition measurements, both elemental and isotopic. The interpretation of these measurements is presently limited by uncertainties in the fragmentation cross-sections needed to correct for nuclear interactions with the interstellar gas. Cosmic ray propagation codes now rely mainly on semi-empirical cross-section formulae developed by Silberberg and Tsao (S&T), which have a typical uncertainty of ~25% [1].

We report here relative isotope yields from the fragmentation of ~380 MeV/nucleon ^{56}Fe and ~210 MeV/nucleon ^{40}Ar in CH_2 targets, observed during the calibration of two cosmic ray spectrometers at the Lawrence Berkeley Laboratory Bevalac, and compare these with calculated yields based on the S&T cross-section formulae [1]. Preliminary results from the ^{40}Ar study were reported by Lau, Mewaldt, and Wiedenbeck (LMW) [2].

2. Experimental Setup - The experimental data were obtained during Bevalac runs in April, 1978 (^{56}Fe) and April, 1981 (^{40}Ar). A description of the experimental setup for the ^{40}Ar calibration is given in reference [2]; with additional details in [3]. The setup for the ^{56}Fe run was essentially identical except that the fragmentation products were measured during the calibration of the Caltech Heavy Ion Spectrometer Telescope (HIST) [4], launched on ISEE-3. In the ^{56}Fe run a 587 MeV/nucleon beam was incident on a 5.26 g/cm^2 thick CH_2 target, such that the energy of the interactions ranged from ~100 to 580 MeV/nucleon, with a mean interaction energy of ~380 MeV/nucleon. In the ^{40}Ar runs the beam energy was 287 MeV/nucleon, the CH_2 target thickness 4.1 g/cm^2, and the interaction energy ranged from ~70 to 280 MeV/nucleon with a mean of ~210 MeV/nucleon. We estimate that ~70% (90%) of the analysed interactions occurred in the CH_2 target for the Fe (Ar) runs, the balance taking place in other material including Al and air.

As discussed in LMW, because the experimental setup was designed for calibration purposes, absolute cross-sections could not be measured. In particular, the detectors intercepted only those fragments emitted within ~1° of the beam direction. On the other hand, with the excellent mass resolution achieved, *relative* fragmentation yields can be determined, which are adequate for many cosmic-ray studies (see, e.g., [5]).

3. Data Analysis - For the ^{56}Fe data we use the isotope identification techniques developed for HIST flight data (see, e.g., [6]), where we have restricted the analysis to events stopping in the last four detectors. Figure 1 shows examples of the observed mass distributions, along with Gaussian fits to the data. The excellent mass resolution ($\sigma_m \simeq 0.25$ amu) permits the isotopes ^{53}Fe, ^{54}Fe, and ^{55}Fe to be resolved in the presence of (much more abundant) ^{56}Fe. The relative isotope fractions that we observe for Cr, Mn, and Fe fragments are given in Table 1.

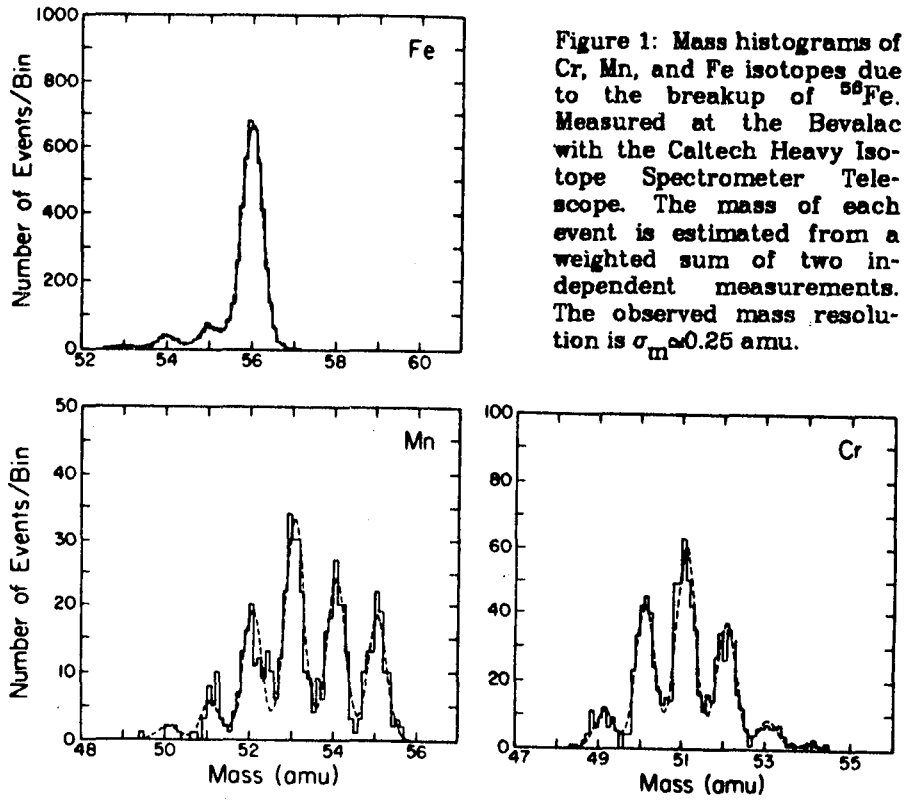

Figure 1: Mass histograms of Cr, Mn, and Fe isotopes due to the breakup of ^{56}Fe. Measured at the Bevalac with the Caltech Heavy Isotope Spectrometer Telescope. The mass of each event is estimated from a weighted sum of two independent measurements. The observed mass resolution is $\sigma_m \approx 0.25$ amu.

The analysis of the ^{40}Ar data set has already been described [2,3]. Table 2 summarizes the fractional yield of isotopes (within each element) for Mg to K fragments ($12 \le Z \le 19$). The $14 \le Z \le 18$ data are essentially the same as those in [2] (with minor differences due to improved statistics and refined corrections), but they are presented in this form for the first time. The Mg and Al data have not been presented before. We find excellent agreement between our isotope fractions and those reported by Viyogi et al. [7], who analyzed the fragmentation of ^{40}Ar in a C target at 213 MeV/nucleon. This suggests that the relative isotope yields do not depend strongly on the target material. Comparing our isotope fractions (Table 2) with those of Viyogi et al. we find no evidence for a mass-dependent bias within an element such as might be introduced by our limited angular coverage.

4. Comparison with Calculated Fragmentation Yields - As described in LMW we have used a Monte Carlo approach developed by M.E. Wiedenbeck to model the experimental setup and calculate the expected yield of each isotope. The calculation takes into account both the energy and target

Table 1 - ^{56}Fe Fragmentation

Isotope	Fraction of Element	
	Observed	Calculated
^{55}Fe	0.669±.010	0.496±.003
^{54}Fe	0.273±.009	0.268±.002
^{53}Fe	0.058±.005	0.236±.002
^{55}Mn	0.215±.007	0.250±.002
^{54}Mn	0.286±.008	0.356±.003
^{53}Mn	0.305±.008	0.220±.002
^{52}Mn	0.146±.006	0.126±.002
^{51}Mn	0.038±.003	0.040±.001
^{50}Mn	0.010±.002	0.008±.001
^{54}Cr	0.026±.003	0.023±.001
^{53}Cr	0.088±.005	0.129±.002
^{52}Cr	0.294±.009	0.375±.002
^{51}Cr	0.315±.009	0.280±.002
^{50}Cr	0.219±.008	0.157±.002
^{49}Cr	0.058±.004	0.036±.001

dependence of the cross-sections [8] for the various materials traversed. Tables 1 and 2 include the calculated isotope fractions for comparison with the observations.

Figure 2 shows a comparison of the measured and calculated isotope yields from ^{56}Fe (normalized to the sum of Cr and Mn). While there is general agreement on the shape of the distributions, there are also significant differences. For example, the calculation predicts Mn/Cr=0.82, while we find Mn/Cr=1.23±0.04, a discrepancy also noted by others [9,10,11] who measured at a variety of energies with C, CH_2, and H targets. Of related astrophysical interest is the result that the radioactive isotope ^{54}Mn fraction is lower than calculated.

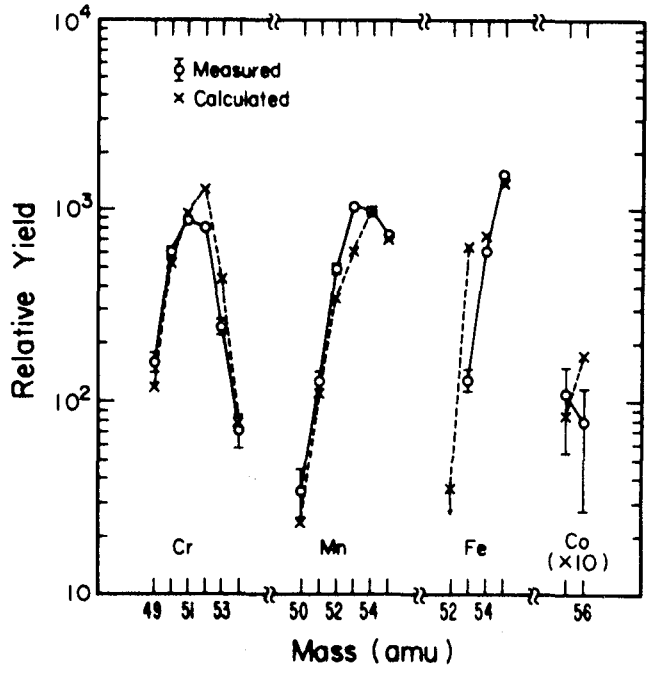

Figure 2: A comparison of measured and calculated yields, normalized to the sum of Mn and Cr.

Table 2 - ^{40}Ar Fragmentation

Isotope	Fraction of Element	
	Observed	Calculated
^{40}K	0.415±.080	0.392±.026
^{39}K	0.585±.080	0.409±.026
^{38}K	<0.03	0.199±.021
^{39}Ar	0.509±.017	0.477±.006
^{38}Ar	0.324±.016	0.357±.006
^{37}Ar	0.125±.011	0.143±.004
^{36}Ar	0.042±.007	0.023±.002
^{39}Cl	0.169±.013	0.130±.004
^{38}Cl	0.146±.012	0.217±.005
^{37}Cl	0.296±.015	0.248±.005
^{36}Cl	0.253±.015	0.273±.005
^{35}Cl	0.115±.011	0.112±.004
^{34}Cl	0.021±.005	0.020±.002
^{38}S	0.009±.003	0.003±.000
^{37}S	0.042±.006	0.027±.001
^{36}S	0.126±.010	0.150±.001
^{35}S	0.218±.012	0.274±.001
^{34}S	0.359±.014	0.377±.002
^{33}S	0.189±.012	0.130±.001
^{32}S	0.057±.007	0.039±.001

Table 2 (continued)

Isotope	Fraction of Element	
	Observed	Calculated
^{35}P	0.027±.006	0.019±.001
^{34}P	0.088±.011	0.088±.001
^{33}P	0.241±.017	0.300±.002
^{32}P	0.341±.019	0.328±.002
^{31}P	0.253±.017	0.211±.002
^{30}P	0.050±.009	0.054±.001
^{32}Si	0.052±.010	0.088±.001
^{31}Si	0.137±.015	0.203±.002
^{30}Si	0.387±.022	0.408±.002
^{29}Si	0.294±.020	0.206±.002
^{28}Si	0.130±.015	0.095±.001
^{30}Al	0.040±.013	0.052±.001
^{29}Al	0.158±.024	0.225±.003
^{28}Al	0.275±.029	0.313±.003
^{27}Al	0.410±.032	0.303±.003
^{26}Al	0.117±.021	0.107±.002
^{27}Mg	0.094±.024	0.145±.002
^{26}Mg	0.306±.038	0.388±.003
^{25}Mg	0.406±.041	0.285±.003
^{24}Mg	0.194±.033	0.182±.003

The two largest discrepancies in either data set are at ^{53}Fe and ^{38}K, both of which are ~6 times less abundant (fraction of element) than calculated. Since both nuclei have 1 less neutron than a "magic number" (n=20-1 for ^{38}K, n=28-1 for ^{53}Fe), their yield may be suppressed if neutron emission is involved. The S&T formulas do not take nuclear shell-structure into account except for a "pairing" correction. Although there are other nuclei with n=19 or n=27 that do not exhibit such a dramatic effect, we suggest that nuclear shell structure should be examined carefully in any attempts to improve semi-empirical cross-sections.

Other significant discrepancies between the observed and calculated fractional yields (e.g., ^{37}Cl, ^{38}Cl, ^{39}Cl, and ^{38}S) involve peripheral reactions, which S&T calculate with special formulae. The agreement for such reactions is better for ^{56}Fe, but these reactions should be less important at the higher energies appropriate to the ^{56}Fe data set.

For both ^{56}Fe and ^{40}Ar fragments the medians of the observed mass distributions are lower than calculated (Figure 2 above and Figure 3 in [2]). There are also differences in the widths of the distributions that are less easily characterized. For both data sets, the ratio of the calculated to measured isotope fractions exhibit rms differences of 25%. Although consistent with the claimed accuracy of the S&T formulae, this demonstrates the need for further cross section measurements if the potential of cosmic ray composition measurements is to be realized.

Acknowledgements: We are grateful to Dr. M. E. Wiedenbeck, who developed the Monte Carlo approach for evaluating the semi-empirical cross-section formulae, for helpful discussions on a number of aspects of this work. Dr. J. D. Spalding was responsible for developing most of the techniques for resolving Fe isotopes in HIST and offered advice on several occasions. We also thank Dr. H. C. Crawford for help with the Bevalac calibrations. This work was supported in part by NASA under grant NGR 05-002-160 and contract NAS5-28449.

References

1. R. Silberberg and C. H. Tsao, *Ap.J. Suppl., 25*, 315, 1973, and *25*, 335, 1973; C.H. Tsao and R. Silberberg, *Proc. 16th Int. Cosmic Ray Conf. 2*, 202, 1979; R. Silberberg, C.H. Tsao, and John R. Letaw, *Composition and Origin of Cosmic Rays*, ed. M.M. Shapiro, Reidel, p. 321, 1983, and references therein.
2. K.H. Lau, R.A. Mewaldt and M.E. Wiedenbeck, *Proc. 18th Int. Cosmic Ray Conf. 9*, 255, 1983.
3. K.H. Lau *Ph.D. Thesis, Caltech, 1985*
4. W.E. Althouse et al., *Geosci. Electronics, GE-16*, 204, 1978.
5. E.C. Stone and M.E. Wiedenbeck *Ap.J., 231*, 95, 1979.
6. R.A. Mewaldt, J.D. Spalding, E.C. Stone and R.E. Vogt, *Ap. J. 235*, L95, 1980.
7. Y.P. Viyogi, et al., *Physical Review Letters 42*, 33, 1978.
8. R. Silberberg and C.H. Tsao, *Proc. 15th Int. Cosmic Ray Conf., 2*, 89, 1977.
9. G.D. Westfall, et al., *Physical Review C, 19*, 1309, 1979.
10. M. Poferl-Kertzman, P.S. Freier and C.J. Waddington, *Proc. 17th Int. Cosmic Ray Conf. 9*, 187, 1981.
11. W.R. Webber and D. Brautigam, *Ap.J. 260*, 894, 1982.

INTERACTIONS OF HEAVY NUCLEI, Kr, Xe AND Ho, IN LIGHT TARGETS

M.P. Kertzman,[1] J. Klarmann,[2] B.J. Newport,[3] E.C. Stone,[3]
C.J. Waddington,[1] W.R. Binns,[2] T.L. Garrard,[3] M.H. Israel[2]

[1]School of Physics and Astronomy, University of Minnesota, Minneapolis, MN 55455
[2]Department of Physics and the McDonnell Center for the Space Sciences, Washington University, St. Louis, MO 63130
[3]George W. Downs Laboratory, California Institute of Technology, Pasadena, CA 91125

1. Introduction. Over the past few years, we have been analyzing the HEAO-3 measurements of the abundances of ultra-heavy cosmic ray nuclei (Z>26) at earth.[1] In order to interpret these abundances in terms of a source composition, allowance must be made for the propagation of the nuclei in the interstellar medium. Vital to any calculation of the propagation is a knowledge of the total and partial interaction cross sections for these heavy nuclei on hydrogen. Until recently, data on such reactions have been scarce, and we have relied on the semi-empirical formalism of Silberberg and Tsao[2] to predict the partial cross sections. However, now that relativistic heavy ion beams are available at the LBL Bevalac, some of the cross sections of interest can be measured at energies close to those of the cosmic ray nuclei being observed.

During a recent calibration at the Bevalac of an array similar to the HEAO-C3 UH-nuclei detector, we exposed targets of graphite (C), polyethylene (CH_2), and aluminum to five heavy ion beams ranging in charge (Z) from 36 to 92. Total and partial charge changing cross sections for the various beam nuclei on hydrogen can be determined from the measured cross sections on C and CH_2, and will be applied to the propagation problem. The cross sections on Al can be used to correct the abundances of UH cosmic rays observed in the HEAO C-3 detector for interactions in the detector itself. Table 1 shows the combinations of beams and targets, as well as the number of events incident on the target for each run. The energies of each beam are also shown. Our preliminary results show that we achieved a charge resolution on the fragments that ranged from 0.21 charge units for Kr on Al to 0.28 c.u. for Au on C, permitting unambiguous resolution of individual fragments. In this paper we report on the total cross sections for Kr on Al, and total and partial cross sections for Xe and Ho on C, CH_2 and H.

Table 1. Number of Events (x 10^3)

Energy (GeV/n):	Kr 1.5	Xe 1.2	Ho 1.1	Au 1.0	U 0.9
Target					
C	--	210	130	260	60
CH_2	--	330	200	400	90
Al	90	160	190	200	--
"Blank"	35	110	120	260	40

2. Experimental Setup. The detector consisted of an array of two front ion chambers, a target space, two rear ion chambers, followed by a Pilot 425 Cherenkov counter. From signals in the front ion chambers, we find

that approximately 10% of the nuclei incident on the detector do not have the nominal charge of the beam, and we eliminate these events from further analysis. Fragments produced in the target as well as beam nuclei surviving through the target are measured in the rear ion chambers and the Cherenkov counter. Scatter plots of the signals in these detectors show well resolved peaks for individual fragments.

3. Total Cross Sections. The interaction mean free path can be found by counting the number of beam nuclei which survive through the target and our detector, and correcting for interactions in the detector itself. This correction is found from a "blank" or no target run. The total interaction cross section per nucleus is related to the mean free path by the following expression:

$$\sigma\ (\text{mb}) = \bar{A}_T/(6.02 \times 10^{-4})\ \lambda\ (\text{g/cm}^2)$$

where $\bar{A}_T$ is the mean mass number of the target. Our results for the total cross sections are given in Table 2, along with values calculated using the formula from Westfall et al.[3] for charge changing cross sections, σ_W. Although this formula was derived from data for nuclei with $Z \leq 26$, it gives values which only slowly deviate from those measured as Z increases, with σ/σ_W = 0.85 for Ho on H.

Table 2. Total Cross-Sections

Beam	Target	λ(g/cm^2)	σ(mb)	σ_W	σ/σ_W
Kr	Al	19.3	2300±100	2460	.95
Xe	C	8.9	2240±80	2460	.91
Xe	CH_2	5.1	1510±50	1670	.91
Xe	H	1.4	1150±90	1270	.90
Ho	C	7.8	2560±70	2760	.93
Ho	CH_2	4.6	1690±40	1910	.89
Ho	H	1.3	1260±75	1490	.85

4. Partial Cross Sections. The numbers of fragments produced in the target are measured in the rear ion chambers and the Cherenkov counter. A histogram of the Cherenkov signal for events consistent with their being fragments is shown in Fig. 1. The charge resolution for this particular run is 0.23 charge units.

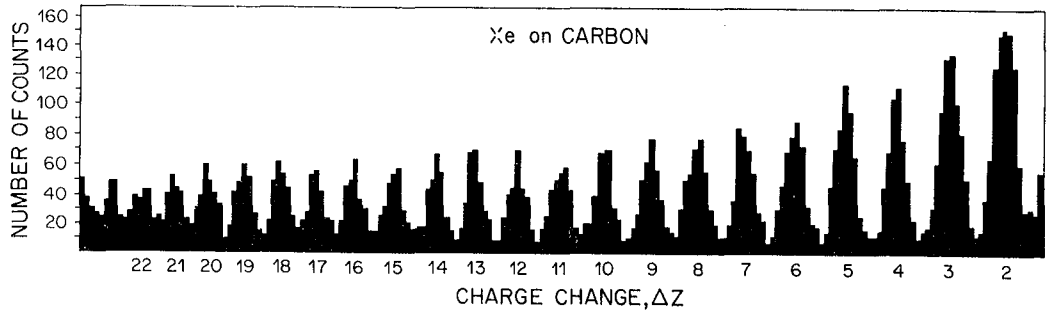

Fig. 1. Cherenkov histogram for Xe nuclei on Carbon.

Several corrections must be applied to the yields obtained from these histograms. First, there is a correction for events observed in the blank run which are also consistent with their being fragments.

These events are due to interactions of the beam in the matter between the Cherenkov counter and the ion chambers. Also, for a given Z, there is a background due to the fragments of charge Z + 1 making a $\Delta Z = 1$ interaction in the Cherenkov counter. Both of these corrections are small, being less than 2%. In addition, there must be a correction for absorption in the detector. We have done this by applying an exponential absorption law, using the Westfall et al.[3] charge changing cross section, scaled to our measurements, to calculate the necessary mean free paths. The numbers resulting from this correction are the numbers of each fragment exiting the target. To obtain the partial cross sections from these numbers we need to correct for multiple interactions in the target. The targets used were approximately 0.25 of a mean free path, and were chosen as a compromise between being thick enough to produce a reasonable number of interactions, yet thin enough so as not to degrade the charge resolution of the Cherenkov due to the energy spread of the fragments. We have used a slab propagation program to do this thick target correction.

Table 3 lists the partial cross sections of Xenon and Holmium on C, CH_2, and H. The hydrogen cross sections are derived from the C and CH_2 cross sections per nucleus by a subtraction procedure:

$$\sigma_H = 1/2\ (3\ \sigma_{CH_2} - \sigma_C)$$

Also given in Table 3 are the values predicted[4] for Xe and Ho on H. Fig. 2 shows the ratios of our values and those predicted, as a function of ΔZ for Xe and Ho. The errors shown are the statistical errors on the target and blank runs, combined with the errors due to the top of detector correction. Also shown is a fit to previously measured ratios reported for Au nuclei,[5] showing distinctively different behavior.

Table 3

ΔZ	Xe on C	Xe on CH_2	Xe on H	S & T	Ho on C	Ho on CH_2	Ho on H	S & T
1	249±21	230±9	220±17	257	343±35	270±26	234±42	267
2	128±5	137±4	141±6	169	138±5	133±4	131±6	257
3	105±4	104±3	104±5	106	103±4	117±3	124±5	166
4	72±4	94±3	105±5	106	81±4	97±3	105±5	114
5	73±4	79±3	82±5	61	73±3	89±3	97±4	95
6	63±3	73±2	77±4	64	67±3	78±2	84±4	81
7	53±3	65±2	71±4	50	60±3	67±2	71±4	66
8	53±3	53±2	53±1	47	53±3	57±2	59±3	71
9	45±3	47±2	48±3	33	45±3	51±2	54±3	53
10	43±3	43±2	43±3	31	46±3	49±2	51±3	51
11	40±2	37±2	35±3	21	43±3	40±2	38±3	34
12	35±2	33±2	32±3	18	34±2	32±2	31±3	32
13	37±2	31±2	28±3	14	38±2	29±2	24±2	18
14	37±2	27±2	23±3	14	33±2	25±1	20±2	14
15	33±2	20±1	14±2	9	33±2	22±1	17±2	12
16	33±2	19±1	12±2	8	32±2	19±1	13±2	8
17	30±2	17±1	10±2	6	34±2	18±1	10±2	7
18	32±2	16±1	7±2	6	32±2	15±1	7±2	5
19	31±2	15±1	6±2	5	27±2	13±1	6±2	5
20	30±2	13±1	5±2	6	25±2	15±1	10±2	5
21	27±2	13±1	6±2	5	--	--	--	--

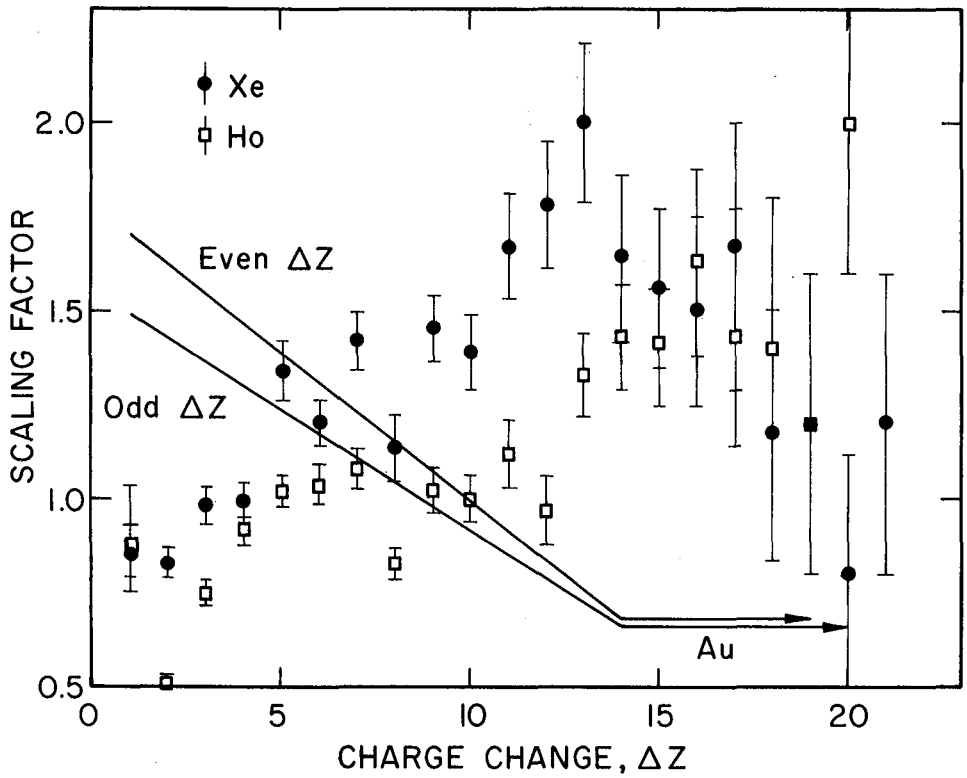

Fig. 2. Ratio of observed to predicted cross-sections as a function of ΔZ.

Examination of these data and of the earlier Au-data from Brewster et al. (1983) shows that they can be well represented by universal curves if expressed as $d\sigma/\sigma_T$ versus ΔZ. We find that for heavy targets, carbon and aluminum, $d\sigma/\sigma_T = a\ (\Delta Z)$ where a and m are closely similar constants for all non-hydrogenous targets and projectiles. Similarly for a hydrogen target, $d\sigma/\sigma_T = b \exp(-n\Delta Z)$, where b and n are closely similar constants for all studied projectiles. The polyethylene targets also show a similar exponential dependence.

4. Acknowledgements. We are grateful to the staff of the LBL Bevalac. This work was supported in part by NASA under grants NAG 8-498, 500, 502, and NGR 05-002-160, 24-005-050, and 26-008-001.

References

[1]Binns, W. R. et al. (1984), Ap. J. 247, L115; (1983) Ap. J. 267, L93.
[2]Silberberg, R. and Tsao, C. H. (1973), Ap. J. Suppl. 25, 335.
[3]Westfall, G. D. et al. (1979), Phys. Rev. C 19, 1309.
[4]Tsao, C. H. and Silberberg, R., (1979), Proc. 16th ICRC (Kyoto), 2, 202.
[5]Brewster, N. R. et al. (1983), Proc. 18th ICRC, 9, 259; (1984) Ph.D. Thesis, Univ. of Minn.

OG 7.2-22

CROSS SECTIONS FOR THE PRODUCTION OF FRAGMENTS WITH Z≥8 BY FRAGMENTATION OF 9≤Z≤26 NUCLEI

W.Heinrich, H.Drechsel, C.Brechtmann, J.Beer

University of Siegen, Physics Department
Adolf-Reichwein-Str., 5900 Siegen, West-Germany

Confirming Abstract:

We investigated charge changing nuclear collisions in plastic nuclear track detectors using a new experimental technique of automatic track measurement for etched tracks in plastic detectors. Partial cross sections for the production of fragments of charge Z≥8 were measured for projectile nuclei of charge 9≤Z≤26 in the detector material CR39 and in silver. For this purpose three independent experiments were performed using Bevalac beams. The first one was an exposure of a stack of CR39 plastic plates to 1.8 GeV/nucl. ^{40}Ar nuclei. The second one was an exposure of another CR39 stack to 1.7 GeV/nucl. ^{56}Fe projectiles. In the third experiment a mixed stack of CR39 plates and silver foils was irradiated with 1.7 GeV/nucl. ^{56}Fe nuclei. Thus the measurement of nuclear cross sections in a light target (CR39 = $C_{12}H_{18}O_7$) and as well in a heavy target (silver) was possible.

The scanning and measuring of the plastic detectors was performed using the Siegen automatic measuring system for nuclear track detectors /1/. The charges of the fragments are determined from the measured areas of the particle tracks in the etched plastic detectors. After the measuring procedure the trajectory of each individual particle is reconstructed from the particle tracks through the whole stack. A nuclear interaction with $\Delta Z \geq 1$ is detected by a change in the measured area of the particle tracks of one trajectory. Altogether more than 33600 charge changing nuclear interactions of beam particles and about 15600 interactions of fragments produced in nuclear collisions were analyzed. Partial cross sections σ_{PT}^{F} for the production of fragments F with 8≤Z≤25 from projectiles P of 9≤Z≤26 in the target T (CR39 and silver) were determined.

Based on the assumption of a factorization of the partial nuclear cross sections /2, 3/ we scaled the semi-empirical formula of Silberberg & Tsao /4/ for cross sections in hydrogen target to heavier targets using the following expression:

$$(1) \qquad \sigma_{PT}^{F} = \gamma_{PT} \cdot \gamma_{H}^{-1} \cdot \sigma_{(ST)}^{F},$$

where $\sigma_{(ST)}^{F}$ is the Silberberg-Tsao cross section, γ_{PT} and γ_{H} are target factors for heavy targets T and hydrogen target respectively.

OG 7.2-22

In figure 1 the ratio R of measured cross sections σ^F_{PT} and calculated Silberberg-Tsao cross sections $\sigma^F_{(ST)}$ are plotted versus the mean fragment mass for Fe-projectiles and for the silver target (□). Taking into account the factorization in the form (1), this ratio R gives the product $\gamma_{PT} \cdot \gamma_H^{-1}$. Since γ_{PT} is a constant in this case, figure 1 shows the dependence of the inverse hydrogen target factor γ_H^{-1} on the fragment mass. There is an increase of this inverse hydrogen target factor for light fragments. For heavier fragments R is constant giving the heavy target factor $\gamma_{P,T=Ag}$, if γ_H^{-1} is set equal to one. The same behaviour has also been reported for the fragmentation of Cu and Ag nuclei /5, 6, 7/. Furthermore for C and O nuclei an increase of γ_H^{-1} for lighter fragments was observed /2/. The dependence of γ_H^{-1} on the fragment mass seen in our data for Fe-projectiles nicely fits between the existing data for lighter and heavier nuclei. The high value of R for Z=25 fragments in silver target is due to the increase of the cross section by the photonuclear effect. For CR39 plastic the partial cross section is a weighted sum over the constituents of the target and can be calculated according to (1) from

$$(2) \qquad \sigma^F_{P,CR39} = \sigma^F_{(ST)} \cdot \left[g_H + \gamma_H^{-1} \left(g_O \cdot \gamma_{P,O} + g_C \cdot \gamma_{P,C} \right) \right] ,$$

where g_H, g_O, g_C are the relative fractions of the three elements H, O, C in CR39. In figure 2 the ratio R as defined above is plotted for CR39 target and Fe-projectiles (Δ, X). From this and from equation (2) we get a similar dependence of γ_H^{-1} on the fragment mass for the CR39 target like for the silver target: an enhancement of light fragments and a constant value for fragments with $\langle A_F \rangle \gtrsim 2/3\ A_P$.

Fragmentation cross sections were measured for the breakup of beam particles Fe and Ar and all their fragments detectable in the plastic. The ratio R as defined above is calculated and summed over all secondary fragments with $\langle A_F \rangle \geq 2/3\ A_P$, where γ_H^{-1} is set to one. These calculated values are plotted versus the projectile nuclear radius for silver (figure 3) and CR39 (figure 4) target. Since γ_H^{-1} is constant in this case, we get from these figures the dependence of the heavy target factor γ_{PT} on the projectile radius. In addition to our measured data (plotting symbols □, Δ, x) values from earlier experiments are shown (plotting symbol X, /2, 3/).

For nuclear fragmentation cross sections, the concepts of "strong" and "weak" factorization have been developed /8/. In the picture of strong factorization the heavy target factor γ_{PT} does not depend on the projectile nucleus, thus giving a constant R in figures 3 and 4. Although the data are, within statistics, consistent with a constant value ($\chi^2 = 54.1$ for 37 degrees of freedom in figure 3, $\chi^2 = 19.7$ for 20 degrees of freedom in figure 4), there is an indication for a slight dependence of

R on the projectile radius in a way, that R is smaller for large projectiles than for medium nuclei. This dependence can be described in the picture of weak factorization /9/.

We are presently developing analytical expressions for γ_{PT} and for γ_H^{-1} that allow the calculation of partial cross sections by scaling the Silberberg-Tsao cross sections for hydrogen target to heavier targets. Without presenting here the final version of the cross section formula, it can already be said, that the distribution of differences between measured and calculated cross sections has a variance of about 25% of the measured cross sections. Since the cross sections for hydrogen target can be calculated within this accuracy, it can be concluded, that no major uncertainties originate from the scaling of these cross sections to heavier targets.

This work was supported by the Bundesminister für Forschung und Technologie, No. 01QV2032, 01QV2130, 01QV3029 and 01QV3127.

We are grateful to the staff of the Bevalac for the assistance at the exposures.

References:

/1/: W.Trakowski et al., Nucl. Instr. Meth. 225, 92 (1984)

/2/: P.J.Lindstrom et al., LBL 3650 (1975)

/3/: G.D.Westfall et al., Rev. C19, 1309 (1979)

/4/: R.Silberberg et al., Ap. J. Suppl. 25, 315 (1973)

/5/: J.B.Cumming et al., Phys. Rev. C10, 739 (1974)

/6/: J.B.Cumming, Phys. Rev. C14, 1554 (1976)

/7/: C.R.Rudy et al., Phys. Lett. 59B, 240 (1975)

/8/: J.Cugnon et al., Phys Rev C21, 2342 (1980)

/9/: D.L.Olson et al., Phys. Rev. C28, 1602 (1983)

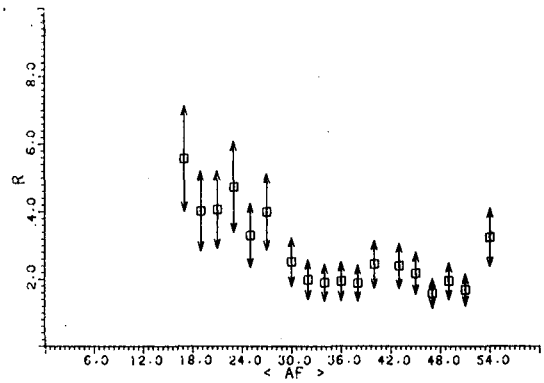

Figure 1: Ratio R of measured cross section σ^F_{PT} and Silberberg-Tsao cross section $\sigma^F_{(ST)}$ for Fe-beam and Ag-target.

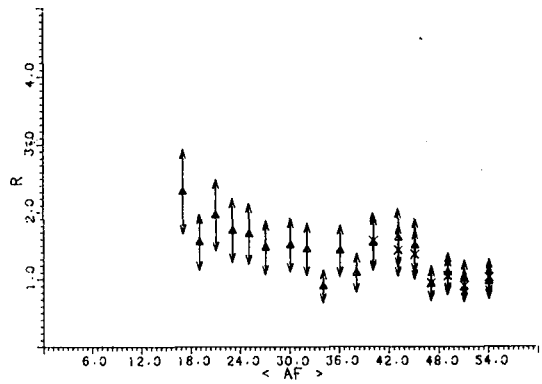

Figure 2: Ratio R of measured cross section σ^F_{PT} and Silberberg-Tsao cross section $\sigma^F_{(ST)}$ for Fe-beam and CR39-target. (Δ: CR39-Ag mixed stack, X pure CR39 stack)

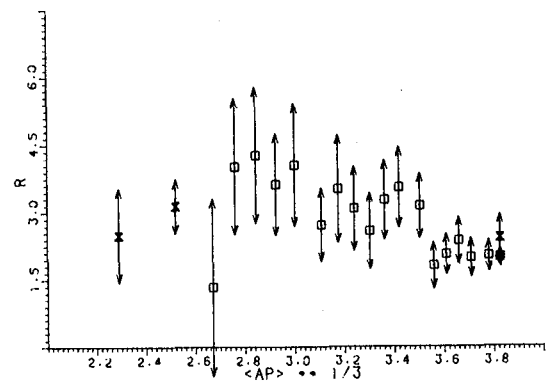

Figure 3: Ratio R of measured cross section σ^F_{PT} and Silberberg-Tsao cross section $\sigma^F_{(ST)}$ summed over all fragments with $\langle A_F \rangle \geq 2/3\ A_P$ for Ag-target (X: data points from refs. 2 and 3)

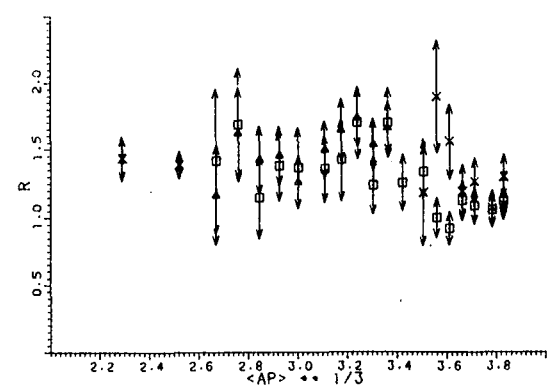

Figure 4: Ratio R of measured cross section σ^F_{PT} and Silberberg-Tsao cross section $\sigma^F_{(ST)}$ summed over all fragments with $\langle A_F \rangle \geq 2/3\ A_P$ for CR39-target (Δ: Ar-beam, □: Fe-beam in CR39-Ag mixed stack, X: Fe-beam in pure CR39 stack, X: data points from refs. 2 and 3)

CALCULATION OF IMPROVED SPALLATION CROSS SECTIONS

TSAO, C.H., and SILBERBERG, R.
E.O. Hulburt Center for Space Research
Naval Research Laboratory
Washington, D.C. 20375-5000
USA

LETAW, J.R.
Severn Communications Corporation
Severna Park, Md. 21146
USA

Several research groups have recently carried out highly precise measurements (to about 10 percent) of high-energy nuclear spallation cross sections. These measurements, above 5 GeV, cover a broad range of elements: V, Fe, Cu, Ag, Ta and Au. Even the small cross sections far off the peak of the isotopic distribution curves have been measured. The semiempirical calculations are compared with the measured values. Preliminary comparisons indicate that the parameters of our spallation relations (Silberberg and Tsao, 1973) for atomic numbers 20 to 83 need modifications, e.g. a reduced slope of the mass yield distribution, broader isotopic distributions, and a shift of the isotopic distribution toward the neutron-deficient side. The required modifications are negligible near Fe and Cu, but increase with increasing target mass.

1. Introduction. Recent highly precise measurements of partial cross sections permit us to explore systematic deviations in our semiempirical partial cross section calculations (Silberberg and Tsao, 1973). In the present paper we confine our investigation to high-energy interactions, $E > 5$ GeV/u, to target nuclei with atomic numbers $Z_t > 20$, and to proton-nucleus reactions. The experimental data are discussed in Section 2. Comparisons with semiempirical calculations are presented in Section 3, as a function of the exponential expressions of the semiempirical equation, in order to explore systematic deviations. Procedures to modify the semiempirical equations are outlined in Section 4.

2. The New Experimental Data. While earlier experimental data were derived from radioactivity measurements after chemical separation of product elements, most of the measurements selected for the present investigation are based on gamma ray line intensity measurements as a function of time. Any systematics introduced by chemical separation are thus avoided.

Table 1 shows the sources of experimental data used in our current analysis. Some of the spallation cross sections are cumulative, i.e. contain the contributions of shorter lived progenitor isotopes. Reactions are omitted in which several isomers are produced, but only one is measured.

Table 1. Sources of Recent High-Energy Experimental Data, $20<Z<80$

Author	Target	Energy (GeV)
Husain and Katcoff (1973)	V	3, 30
Asano et al. (1983)	Ti, Fe, Co, Ni, Cu	12
Cumming et al. (1976)	Cu	25
Hudis et al. (1970)	Cu, Ag, Au	3, 29
Porile et al. (1979)	Ag	300
Chu et al. (1974)	Ta	28
Kaufman et al. (1976)	Au	12, 300

3. Comparison of Data and Calculations. The semiempirical equation for calculating non-peripheral spallation cross sections is of the form

$$\sigma = \sigma_o \exp(-P\Delta A) \exp(-R|Z-SA + TA^2|^{3/2}) \Omega\eta\xi$$

The factors in this equation are defined by Silberberg and Tsao (1973). Systematic deviations from this equation can be explored by comparing the measured and calculated cross sections as a function of $Z-SA+TA^2$ and of ΔA. The former comparison permits a test of systematic deviations as a function of the neutron richness of product isotopes and of the width of the isotopic spread of the products. The latter permits a test of systematic deviations as a function of the target-product mass difference. After these systematics are corrected for we can explore the smaller systematic difference, as a function of the nuclear pairing factor η, which represents the enhancement of even-even product nuclei and the suppression of the odd-odd products.

Fig. 1 shows the ratios of calculated to experimental cross sections of Cu as a function of $Z-SA+TA^2$. A large value of this function implies a small value of A, i.e. a neutron-deficient product. We note a positive slope as a function of $Z-SA+TA^2$. This means that the calculated cross sections of neutron-deficient products, e.g. ^{52}Fe are overestimated, and neutron-rich ones, e.g. ^{47}Ca are underestimated.

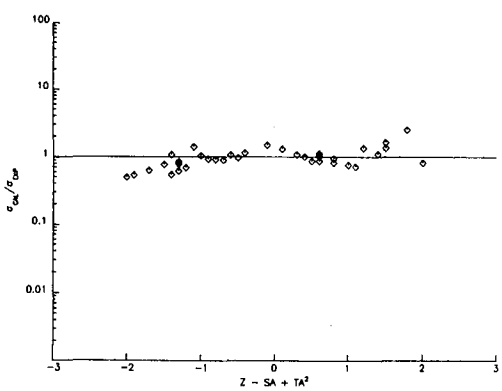

Fig. 1. The ratio of calculated to experimental cross sections of Ta, as a function of $Z-SA+TA^2$, for $E > 3$ GeV.

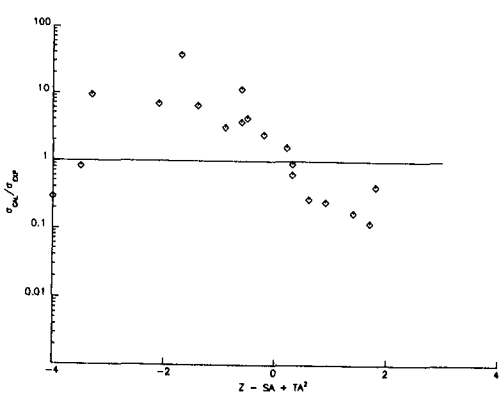

Fig. 2. The ratio of calculated to experimental cross sections of Cu, as a function of $Z-SA+TA^2$, for $E > 6$ GeV.

Fig. 2 shows the corresponding data for tantalum. The large negative slope shows that a significant systematic deviation occurs in the calculated cross sections, however, opposite to that for lighter target nuclei like Cu of Fig. 1. For Ta, the neutron-rich products are overestimated, instead.

Fig. 3 compares the calculated and experimental spallation cross sections of Cu as a function of ΔA. We note that for Cu, the systematic deviations are rather small. The largest and smallest values are those near the extreme values of $Z-SA+TA^2$. After the latter are corrected for, the spread of the ratios about 1 will be very small.

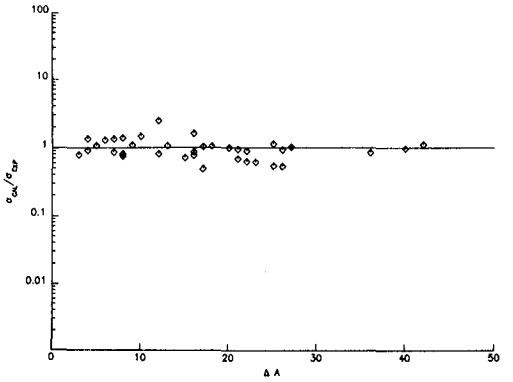

Fig. 3. The ratio of calculated to experimental cross sections of Cu, as a function of ΔA, for $E > 3$ GeV.

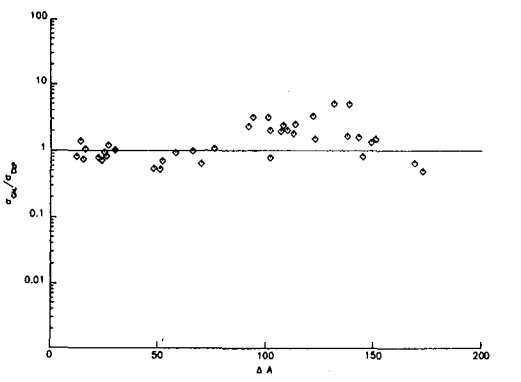

Fig. 4. The ratio of calculated to experimental cross sections of Au, as a function of ΔA, for $E > 6$ GeV. The temporary adjustment factors of Tsao et al. 1983 were applied to the calculations.

Fig. 4 compares the calculated and measured cross sections of Au as a function of ΔA. The agreement of the spallation cross sections (i.e. those with ΔA less than approximately 60) is good. However, this agreement was achieved by special corrections for nuclei with $76 \leq Z_t \leq 83$ we proposed (Tsao et al., 1983). Our aim will be to eliminate such special corrections, and adjust the parameters P, R, S, and T so that the whole region $20 \leq Z_t \leq 83$ can be adequately fitted. We note from Fig. 2, that for Ta (with $Z_t = 73$), the fit to the data is rather poor. A simultaneous fit to Ta and Au is necessary.

4. Procedures to Modify the Semi-Empirical Equations. We noted from Figs. 1 and 2 that one should increase the calculated cross sections of the n-rich products for targets near $Z_t = 30$, while increasing those of the neutron-deficient products near $Z_t = 70$ and 80. This can be accomplished by decreasing S or increasing T in the former case, and by increasing S or decreasing T in the latter case. Since S is associated with A and T with A^2, S is more sensitive for lighter nuclei and T is more sensitive to heavier nuclei. Thus the correction can be accomplished by reducing both S and T, replacing the values 0.486 and 0.00038 given in Table 1D of Silberberg and Tsao by 0.48 and 0.0003 and reducing R to 0.9R. Fig. 5 shows how Fig. 2 is transformed when the above parameters are used and Fig. 6 how Fig. 1 is transformed. A correction for $Z-SA+TA^2 < -2$ is still required.

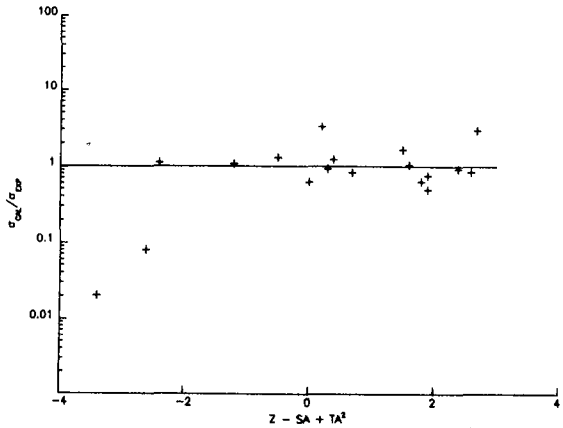

Fig. 5. The ratio of calculated to experimental cross sections of Ta as a function of $Z-SA+TA^2$, with the new values of S and T, for E > 6 GeV.

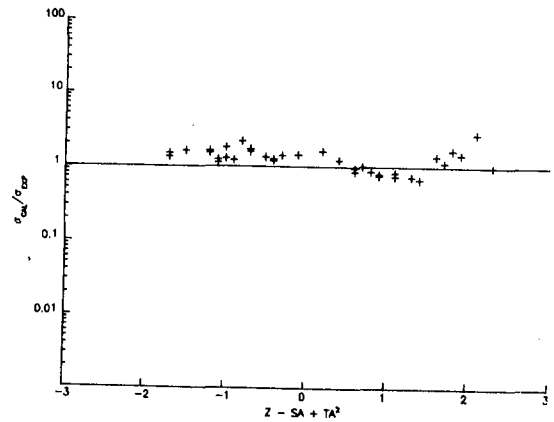

Fig. 6. The ratio of calculated to experimental cross sections of Cu, as a function of $Z-SA+TA^2$, with the values of S and T, for E > 3 GeV.

The modifications we plan to introduce involve special complications, because of multiple feed-back loops. An adjustment of P affects the overall normalization factor σ_o, and the energy dependence of the calculations. Adjustments in S and T affect the calculations of fission and fragmentation cross section, and the parameters f(A) and f(E) of Silberberg and Tsao (1973) must be re-formulated.

5. Conclusions. The recent highly precise experimental data have permitted us to find systematic deviations in the calculated cross sections, and significantly more accurate calculations are possible after optimizing the parameters P, R, S, and T over the range of targets $20 \leq Z_t \leq 83$.

References

Asano, T. et al. 1983, Phys. Rev. C28, 1718.
Chu, Y.Y. et al. 1974, Phys. Rev. C10, 156.
Cumming, J.B. et al. 1976, Phys. Rev. C14, 1554.
Hudis et al. 1970, Phys. Rev. C1, 2019.
Husain, L. and Katcoff, S. 1973, Phys. Rev. C7, 2452.
Kaufman, S.B. 1976, Phys. Rev. C14, 1121.
Porile, N.T. 1979, Phys. Rev. C19, 2288.
Silberberg, R. and Tsao, C.H. 1973, Ap. J. Suppl. 25, 315.
Tsao, C.H. et al. 1981, 18th ICRC (Bangalore) 2, 194.

THE COSMIC-RAY SHOCK STRUCTURE PROBLEM FOR RELATIVISTIC SHOCKS

G. M. Webb
University of Arizona
Department of Planetary Sciences
Tucson, Arizona 85721 U.S.A.

ABSTRACT

The time asymptotic behaviour of a relativistic (parallel) shock wave significantly modified by the diffusive acceleration of cosmic-rays is investigated by means of relativistic hydrodynamical equations for both the cosmic-rays and thermal gas. The form of the shock structure equation and the dispersion relation for both long and short wavelength waves in the system are obtained. The dependence of the shock acceleration efficiency on the upstream fluid speed, long wavelength Mach number and the ratio $N = P_{co}/(P_{co} + P_{go})$ (P_{co} and P_{go} are the upstream cosmic-ray and thermal gas pressures respectively) are studied.

1. Introduction. Nonlinear theories of diffusive shock acceleration of cosmic-rays were initially developed by Axford et al. (1977, 1982), Drury and Völk (1981) (see Drury 1983 for a review and further references). These authors discuss how the efficient acceleration of cosmic-rays in shock waves by the first order Fermi mechanism leads to shock broadening or shock structure due to the interaction between the background thermal gas and cosmic-rays. Previous work on this problem has been restricted to non-relativistic shocks. The purpose of the present paper is to extend these models to relativistic shocks in which the background fluid velocity $\underline{V}$ is an appreciable fraction of the speed of light.

2. Equations. Consider a one dimensional, steady state inviscid, hydrodynamical model of cosmic-ray acceleration in a (parallel) relativistic shock. The basic conservation laws for mass momentum and energy are:

$$\gamma n V = J_n \quad \text{(mass conservation)}, \tag{1}$$

$$(\gamma^2-1)(W_c+W_g)+P_c+P_g+2\gamma^2 V f_c^{40} = P_n \quad \text{(momentum)}, \tag{2}$$

$$\gamma^2 V (W_c+W_g)+(2\gamma^2-1)c^2 f_c^{40} = F_n \quad \text{(energy)}, \tag{3}$$

where J_n, P_n, F_n are the (constant) mass, momentum, and energy fluxes of the system, and

$$W_c = P_c + \rho_c = \gamma_c P_c/(\gamma_c - 1), \tag{4}$$

$$W_g = P_g + \rho_g = \gamma_g P_g/(\gamma_g - 1) + n c^2, \tag{5}$$

are the cosmic-ray and gas enthalpy respectively. P_c, ρ_c, γ_c are the cosmic-ray pressure, energy density and adiabatic index; whereas P_g, ρ_g, γ_g are the corresponding gas quantities; n denotes the gas density, f_c^{40} represents the cosmic-ray energy flux in the scattering frame (or fluid frame) and $\gamma = (1 - V^2/c^2)^{-1/2}$ is the Lorentz factor of the fluid speed V.

Assuming there are no dissipative mechanisms for the gas in the fluid frame, it follows that the thermal gas is compressed adiabatically following the flow (except at gas subshocks) so that $P_g = P_{go}\,(n/n_o)^{\gamma_g}$, where the subscript 'o' denotes the (constant) upstream state. To complete the system we use the cosmic-ray momentum equation (in the scattering frame):

$$-\nu\, T_c'^{10} = \gamma\, dP_c/dx + \left(W_c + 2c^2\, T_c'^{10}/V\right) d\gamma/dx + \gamma V\, dT_c'^{10}/dx, \quad (6)$$

governing the interaction between the cosmic-rays and gas via the scattering frequency ν. (Note the hydrodynamical diffusion coefficient in this development is $K = c^2(\gamma_c - 1)/\nu$.

3. The Shock Structure Equation. The cosmic-ray momentum equation (6) used in conjunction with equations (1) - (5), reduces to the shock structure equation

$$dy/dx = c\,\nu\, y^2 \left(T_c'^{10}/n_o c\right) / \left\{\gamma\left(\left[1 + (a_g/c)^2/(\gamma_g - 1)\right]V^2 - a_g^2\right)\right\} \quad (7)$$

governing the inverse compression ratio $y = n_o/n = \gamma V/\gamma_o V_o$ of the flow. In (7), $T_c'^{10}$ can be expressed solely in terms of y (or V) using (2) and (3), and $a_g = (\gamma_g P_g/n)^{1/2}$ denotes the nonrelativistic thermal gas sound speed.

Note in particular the singularity in the denominator in (7) occurs when the fluid speed matches the short wavelength thermal gas sound speed

$$V_s = a_g \Big/ \left[1 + (a_g/c)^2/(\gamma_g - 1)\right]^{1/2}. \quad (8)$$

For non-relativistic shocks $V_s \to a_g$; also note that there is a strict upper limit to the thermal gas sound speed V_s in the relativistic case with $V_s < (\gamma_g - 1)^{1/2} c$. On the other hand, for a near uniform shock transition we have $T_c'^{10} \simeq 0$ throughout the flow; the solution of $T_c'^{10} = 0$ for the upstream fluid speed V_o then yields the long wavelength sound speed in the system

$$V_{lo} = \left\{\left(a_{co}^2 + a_{go}^2\right) \Big/ \left[1 + (a_{go}/c)^2/(\gamma_g - 1) + (a_{co}/c)^2/(\gamma_c - 1)\right]\right\}^{1/2} \quad (9)$$

where $a_{co}^2 = \gamma_c P_{co}/n_o$.

A further complication that arises in the relativistic theory (as opposed to the non-relativistic theory) is that $T_c'^{10}$ in (7) develops a singularity when the fluid speed $V \to \sqrt{\gamma_c - 1}\, c$ which is the sound speed of the 'effectively massless' cosmic-ray gas (cf. Weinberg, 1972). The occurrence of this singularity is presumably related to the fact that the adiabatic deceleration rate for a fully relativistic cosmic-ray gas is given by

$$\langle \dot{E} \rangle_{ad}/c = \langle \dot{\eta} \rangle_{ad} = \frac{-\eta\,\gamma^2}{3} \frac{d}{dx}\left(\frac{V}{\gamma^2}\right) = \frac{-\eta\,\gamma^2}{3} \frac{dV}{dx}\left(1 - 3\frac{V^2}{c^2}\right), \quad (10)$$

where $\eta = \gamma(x)\, m' c$ and p' and m' represent the individual particle momentum and relativistic mass in the scattering frame. The basic implication of (10) is that cosmic-rays are accelerated in compressive flows with $V < c/\sqrt{3} = \sqrt{\gamma_c - 1}\, c$ but are decelerated in compressive flows with $V > c/\sqrt{3}$ (cf. Webb, 1985).

4. Numerical Results. The nature of the shock transition can be analyzed by a geometrical method employed by Drury and Völk (1981) in their work on non-relativistic hydrodynamical models. This is illustrated in Figure 1 for a shock in which the long wavelength Mach number M = 2, $N = P_{co}/(P_{co} + P_{go}) = 0.3$, $z_0 = V_0/c = 0.5$, $\gamma_c = 4/3$ and $\gamma_g = 5/3$. It shows the Hugoniot, gas adiabat, short wavelength sonic line and $P_c = 0$ curve in the $(P_g, V/c)$ plane. The Hugoniot corresponds to the locus $T'^{*}_{c} = 0$ in the $(P_g, V/c)$ plane, whereas the short wavelength sonic line corresponds to the zero of the denominator in (7). The upstream state (A) and downstream state (C) lie on the Hugoniot. In the initial part of the transition the gas is compressed adiabatically (AB) followed by a subshock to a uniform downstream state (the straight line segment BC). Across the subshock the momentum and energy fluxes of the cosmic-rays and thermal gas are balanced separately. Figure 2 shows the variation of the cosmic-ray shock acceleration efficiency η_s as a function of the upstream fluid velocity V_0 for a range of upstream Mach numbers (M = 2, 4, 5, 10), N = 0.3, $\gamma_c = 4/3$ and $\gamma_g = 5/3$ (η_s is defined as the fraction of flow kinetic energy that is converted to cosmic-ray energy in the transition, i.e., $\eta_s = -\Delta(\gamma^2 V W_c)/\Delta(\gamma \gamma_0 n_0 c^2)$. For $z_0 < \sqrt{\gamma_c - 1} = 0.5773$, there is a weak dependence of η_s on z_0, and η_s increases monotonically with M. At $0.577 < z_0 < 0.9$, there are no solutions and the solutions with $z_0 > 0.9$ are of low efficiency. The negative efficiency solutions at $z_0 > 0.9$ are obtained in expanding flows (V increases initially) followed by a subshock to a downstream state $z_2 = V_2/c < \sqrt{\gamma_c - 1}$. In compressive flows with $V_0 > c(\gamma_c - 1)^{1/2} = 0.577c$, the cosmic-ray pressure decreases as the thermal gas is compressed adiabatically, and the cosmic-ray pressure may eventually become negative; it is then necessary to insert a subshock in the flow while $P_c > 0$; this behaviour is in accord with the result (10). Figure 3 shows the variation of the downstream cosmic-ray pressure P_{c2} as a function of the downstream cosmic-ray adiabatic index γ_{c_2} ($\gamma_{co} = 1.55$, $\gamma_g = 5/3$, M = 5, $z_0 = 0.5$) for a range of N. The dotted curves correspond to smooth transition solutions; whereas solutions with subshocks are given by the full (solid) curves (cf. Achterberg et al. 1984; Heavens 1984 for the non-relativisitc case).

5. Conclusions. The main point to emerge from the present study is that to efficiently accelerate cosmic-rays in relativistic shocks, the upstream fluid speed V_0 needs to be less than $V_{cr} = \sqrt{\gamma_c - 1}\, c$; compressive flows with $V > V_{cr}$ lead to a loss of internal energy to the C.R. gas.

6. Acknowledgements. This work was supported in part under NSF grant ATM-8311241.

7. References.

1. Achterberg, A. et al. (1984), Astron. Astrophys. 132, 97.
2. Axford, W.I. et al. (1977), 15th ICRC, 11, 132.
3. Axford, W.I. et al. (1982), Astron. Astrophys. 111, 317.
4. Drury, L. O'C., (1983), Reports Prog. Phys. 46, 973.
5. Drury, L. O'C. and Volk, H.J., (1981), Astrophys. J. 248, 344.
6. Heavens, A.F., Mon. Not. Roy. Astron. Soc. 210, 813.
7. Webb, G.M., (1985), in preparation.
8. Weinberg, S., (1972), Gravitation and Cosmology, Wiley, N.Y.

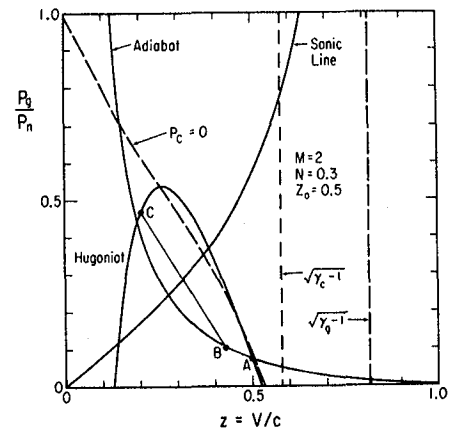

Fig. 1

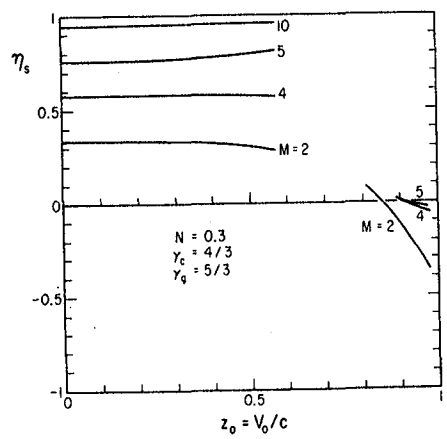

Fig. 2

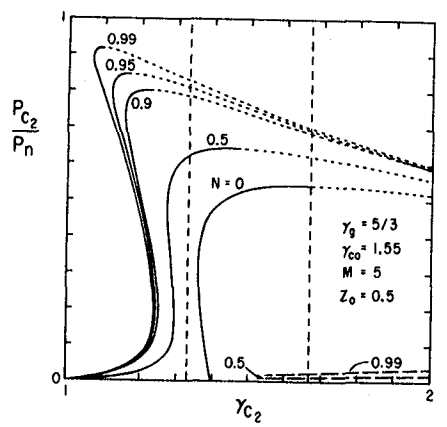

Fig. 3

INSTABILITIES IN DECELERATING SUPERSONIC FLOWS WITH APPLICATIONS TO COSMIC RAY SHOCKS

A.P. Zank and J.F. McKenzie
Dept. of Mathematics and Applied Mathematics
University of Natal, King George V Avenue
Durban (South Africa)

ABSTRACT. We investigate the nature of instabilities in cosmic ray shocks by using two distinct models for the shock wave. For wavelengths which are short relative to the thickness of the shock wave, the shock is treated as a smoothly decelerating flow, and an appropriate JWKB type expansion is used to describe the perturbations to the flow. In this, the short wavelength regime, the presence of "squeezing" and an effective "g" renders strong cosmic ray shocks unstable in a way which is similar to instabilities in other supersonic flows, such as in de Laval nozzle flow or a heat conduction dominated shock wave. In the long wavelength limit, where the shock is treated as a discontinuous transition, we derive a "stability function" which, if negative, corresponds to unstable disturbances growing exponentially in time. In this case, we find that if the cosmic ray fluid is relativistic ($\gamma_c = 4/3$) and the background plasma ideal ($\gamma = 5/3$), then strong shocks are unstable.

1. INTRODUCTION. We examine the stability of cosmic ray shocks (Axford et al [1977], Drury and Völk [1981], Axford et al [1982], Völk [1984], Drury [1984], Dorfi [1984]) in both short and long wavelength regimes. The short wavelength instability in the two-fluid description of a cosmic ray shock may be shown to be similar to the instabilities in other supersonic decelerating flows. Erpenbeck, [1962], established that discontinuous transitions (shocks) are always stable for ideal fluids. We generalize his results, and show that the relativistic two-fluid model considered here is unstable.

2. THE GOVERNING EQUATIONS. The equations which describe the self-consistent interaction between a background thermal plasma and a relativistic cosmic ray fluid are given by

$$\frac{\partial \rho}{\partial t} + \operatorname{div}(\rho \underline{u}) = 0; \qquad \text{(continuity)} \qquad (2.1a)$$

$$\rho \frac{D\underline{u}}{Dt} + \nabla (p + p_c) = 0; \qquad \text{(momentum)} \qquad (2.1b)$$

$$\frac{\partial}{\partial t}\left(\tfrac{1}{2}\rho u + \frac{P}{\gamma-1}\right) + \operatorname{div}\left[\rho \underline{u}\left(\tfrac{1}{2}u^2 + \frac{\gamma}{\gamma-1}\frac{P}{\rho}\right) + \frac{\gamma_c}{\gamma_{c-1}} p_c \underline{u} - \frac{\kappa}{\gamma_{c-1}} \nabla p_c\right] = 0,$$

(energy) (2.1c)

where ρ, p, p_c, and $\underline{u}$ denote gas density, gas pressure, cosmic ray pressure and gas velocity respectively, and κ an effective cosmic ray diffusion coefficient. These equations are supplemented by the cosmic ray energy equation

$$\frac{\partial}{\partial t}\left(\frac{p_c}{\gamma_{c-1}}\right) + \frac{1}{\gamma_{c-1}} \operatorname{div}\left[\gamma_c p_c \underline{u} - \kappa \nabla p_c\right] = \underline{u} \cdot \nabla p_c, \qquad (2.2)$$

which, together with 2.1(a,b), enables 2.1(c) to be expressed in the adiabatic form

$$\frac{D}{Dt}\left(\frac{P}{\rho^{\gamma}}\right) = 0, \qquad (2.3)$$

where $\frac{D}{Dt} = \frac{\partial}{\partial t} + \underline{u}.\nabla$ is the convective derivative. The derivation and discussion of these equations may be found in, for example, Drury, [1983].

A perturbation analysis of (2.1), (2.2) and (2.3) shows that short wavelength perturbations propagate at the plasma sound speed, c, where

$$c = \sqrt{\gamma p/\rho}, \qquad (2.4)$$

and hence decouple from the cosmic ray fluid. Conversely, long wavelength disturbances propagate at the mixed sound speed,

$$\sqrt{a_c^2 + c^2} = \sqrt{(\gamma_c p_c + \gamma_p)/\rho}, \qquad (2.5)$$

Ptsukin, [1981], $a_c \equiv$ cosmic ray fluid sound speed.

A discussion of the shock structure problem may be found in Axford et al, [1982], and Drury and Völk, [1981], McKenzie and Völk [1982], Völk et al [1983].

3. THE SHORT WAVELENGTH INSTABILITY. For the sake of completeness we present a brief modified account of the instability discussed by Drury [1984]. By considering waves whose wavelengths are short relative to the thickness of the shock wave, one may treat the transition as a continuous decelerating flow. If one views the decelerating flow as an "effective gravitational force", the stability problem has the character of a "generalized Rayleigh-Taylor" type problem for a disturbance propagating through the system. The introduction of compressive perturbations $\delta\psi = (\rho, p, p_c, u)$ on the background state $\psi_o = (\rho_o, p_o, p_{co}, u_o)$ enables equations (2.1) and (2.3) to be linearized. We introduce a shock thickness parameter L, related to the decelerating flow u_o, by defining

$$\frac{1}{L} = \frac{-1}{u_o}\frac{du_o}{dx},$$

where $\frac{du_o}{dx}$ is the flow velocity profile. On either side of the shock, u_o is constant, and hence $\frac{1}{L} = 0$. By using the steady state conservation laws (2.1) and (2.3), one can express the gradients of the remaining background variables ρ_o, p_o, p_{co}, as functions of L and the Mach number of the flow. We restrict the analysis to velocity profiles which vary slowly in space, and thus need only consider terms which are $O(\frac{1}{L})$. This is tantamount to performing a WKBJ expansion in space. The use of this expansion, and the search for plane wave solutions whose amplitudes vary harmonically, reduces (2.1) - (2.3) to the following dispersion equation;

$$\omega' + \frac{iu_o}{L} = \frac{k^2(a_c^2 + \frac{ic_o^2}{kL}(M^2-1))}{(\omega' - i\kappa k^2 + \frac{i\gamma_c u_o}{L})} - \frac{iu_o^2(k + \frac{i}{L})}{L(\omega' + \frac{iu_o}{L})} + \frac{c_o^2 k^2 (1 + \frac{i}{kL})}{(\omega' + \frac{i\gamma u_o}{L})}, \tag{3.2}$$

where $\omega' = \omega - u_o k$ in the Doppler shifted frequency, and k the wave number. In the absence of a shock, the dispersion relation reduces to

$$\omega' = 0; \quad \omega' = \pm c_o k. \quad \text{(entropy-vorticity; sound waves)}$$

A perturbation analysis of (3.2), about these frequencies, indicates that in the presence of a decelerating flow,

$$Im\ \omega' = -\frac{u_o}{L}, \tag{3.3}$$

for an entropy wave, and for a sound wave

$$Im\ \omega' = \frac{a_c^2}{2\kappa} - \frac{c_o^2}{2L}[M^2 - (\gamma+1)M - 1], \tag{3.4}$$

which, since we consider solutions of the form $\exp i\omega t$, implies instability for sufficiently large Mach numbers M.

4. THE LONG WAVELENGTH INSTABILITY. In this section we generalize and extend the results of D'Iakov, [1958], Erpenbeck, [1962 a,b], and McKenzie and Westphal, [1968] to include the effect of a cosmic ray fluid. We derive the transmission coefficient of an acoustic wave incident on an oblique shock, and examine the singularities of this transmission function. In the case of a supersonic-subsonic transition it is straightforward to show that, if the shock is perturbed, then three waves diverge from the shock (and thus the problem is well posed). After perturbing the generalized Rankine-Hugoniot boundary conditions

$$[\rho u_n] = 0; \quad \text{(continuity)} \tag{4.1a}$$

$$[p + p_c + \rho u_n] = 0; \quad \text{(normal momentum)} \tag{4.1b}$$

$$[\underline{u}_t] = 0; \quad \text{(tangential momentum)} \tag{4.1c}$$

$$[\tfrac{1}{2}u_n^2 + \frac{\gamma}{\gamma-1}\frac{p}{\rho} + \frac{\gamma_c}{\gamma_c-1}\frac{p_c}{\rho}] = 0, \quad \text{(energy)} \tag{4.1d}$$

where n and t represent directions normal and tangential to the shock, one may derive the transmission coefficient for an acoustic wave,

$$\frac{\delta p_2}{\delta p_1} = \frac{\alpha_3(1 - \frac{u_y k_y}{\omega})N_1 + \beta_3\beta_1 N_2 + \beta_3 N_3}{\alpha_3(1 - \frac{u_y k_y}{\omega})D_1 + \beta_3\beta_2 D_2 - \beta_3 D_3}, \tag{4.2}$$

where (α_i, β_i) denote the cosine and sine of the angle between $\underline{k}$ and the x-axis, and N_i, D_i are suitable generalizations of the functions presented in McKenzie and Westphal, [1968]. The singularities of the function (4.2) correspond to the dispersion equation.

On defining the variables

$$R^2 = 1 + \frac{a_c^2}{c^2}, \quad R^* = 1 + \frac{\gamma-1}{\gamma_{c-1}} \frac{a_c^2}{c^2}, \quad \frac{1}{M^2} = \frac{R^2}{M_s^2}, \quad M_s \equiv \text{gas Mach number},$$

the stability function, F_s, may be written as

$$F_s = \frac{\rho_1}{\rho_2} (1-M_2)(2-(\gamma-1) \frac{M_2 s^2}{R_2 *} (\frac{\rho_2}{\rho_1} -1)) - (1+(\gamma-1)\frac{M_2 s^2}{R_2 *} - (1+(\gamma-1)\frac{R_2}{R_2 *}) M_2^2), \tag{4.3}$$

for waves propagating with the flow, and where the subscript 1(2) indicates ahead (behind) the shock. In the cold plasma approximation, cosmic ray shocks are unstable for all supersonic - subsonic transitions. In the alternate approximation of a tenuous cosmic ray gas ahead of the shock, it may be established that shocks are unstable for all Mach numbers $\gtrsim$ 1,3. The growth rate of these instabilities (for strong shocks) is of the order the compression ratio $(\frac{\rho_2}{\rho_1})$ x ku_1.

References

Axford, W.I., Leer, E., Skadron, G.[1977], Proc. 15th Int.Cosmic Ray Conf. (Plovdiv), 11, 132.

Axford, W.I., Leer, E., McKenzie, J.F.,[1982], Astron.Astrophys. 111, 317

D'Iakov, S.P. [1958], Sov.Phys.JETP 6, 729.

Dorfi, E. [1984], Adv. Space Research 4, No.2-3, 205.

Drury, L.O'C., Volk, H.J. [1981], Astrophys.J. 248, 344.

Drury, L.O'C., [1983], Rep. Prog. Phys. 46, 973.

Drury, L.O'C., [1984], Adv. Space Research 4, No.2-3, 185.

Erpenbeck, J.J. [1962a], Phys. Fluids 5, 604.

Erpenbeck, J.J. [1962b], Phys. Fluids 5, 1181

McKenzie, J.F., Westphal, K.O. [1968], Phys. Fluids 11, 2350.

McKenzie, J.F., Völk, H.J. [1982], Astron. Astrophys. 116, 191.

Ptuskin, V.S. [1981], Astrophys. Space Sci. 76, 265.

Völk, H.J., Drury, L. O'C., McKenzie, J.F. [1984], Astron. Astrophys. 130, 19.

Völk, H.J. [1984], Adv. Space Research 4. No. 2-3, 423.

Time-dependent Nonlinear Cosmic Ray Shocks
Confirming Abstract

E.A. DORFI
Max-Planck-Institut für Kernphysik
Postfach 103980, D-6900 Heidelberg, FRG

1 Introduction

Numerical studies of time dependent cosmic ray shock structures in planar geometry are interesting because analytical time-independent solutions are available which include the non-linear reactions on the plasma flow (1). A feature of these time asymptotic solutions is that for higher Mach numbers ($M \geq 5$) and for a low cosmic ray upstream pressure the solution is not uniquely determined by the usual conservation laws of mass, momentum and energy.

2 Basic physics, initial conditions and method of solution

We start with the time-dependent Euler-equations of hydrodynamics and use an additional equation desribing the cosmic rays in the two-fluid approximation. The mean diffusion coefficient $\bar{\kappa}$ and the adiabatic index γ_C are fixed and we refer for further details to the literature (2,3,4). A shock wave is created by reflection of the flow on a rigid wall ($x = 0$). The gas comes from the left with specified density $\rho = 1$, velocity $u = -1$ and gas and particle pressure P_G and P_C, respectively. A shock wave starts travelling to the right leaving the heated gas at rest behind. The basic parameters characterizing this situation are the diffusion time scale $t_d = \bar{\kappa}/u^2$, the Mach number of the incoming flow $M^2 = \rho u^2/(\gamma_C P_C + \gamma_G P_G)$ and the ratio of the particle pressure to the total pressure in the upstream region, $N = P_C/(P_C+P_G)$, respectively. The system of equations is solved on a fully adaptive grid (5).

3 Results

For low Mach numbers we get weakly modified gas shocks, as expected. The flow in the upstream region is slightly decelerated by the cosmic ray precursor and the main portion of the kinetic energy of the incoming flow is transfered to the gas. In addition to this well known effect one sees a typical time-dependent effect in the downstream region where a particle gradient decreases and the opposite gas gradient pushes the gas towards the shock wave running to the right. The particle gradient occurs because the acceleration process takes some time to increase the particle pressure at the shock; initially the shock is essentially a pure gas shock and only later does the particle pressure become significant. For values $M = 4.4$, $N = 0.5$ and for different times the variables are shown in Figure 1. The transition from a gas dominated shock to a cosmic ray modified shock is clearly shown. Note however that this requires some thirty to forty diffusion time scales.

A shock with higher Mach number $M = 10$ and a lower value of $N = 0.05$ is depicted in Figure 2. The interesting result for this case is again the very long time scale; at $t = 1000$ (in units of the diffusion time scale) the solution still resembles a test particle solution and the particle pressure at the shock is decreasing.

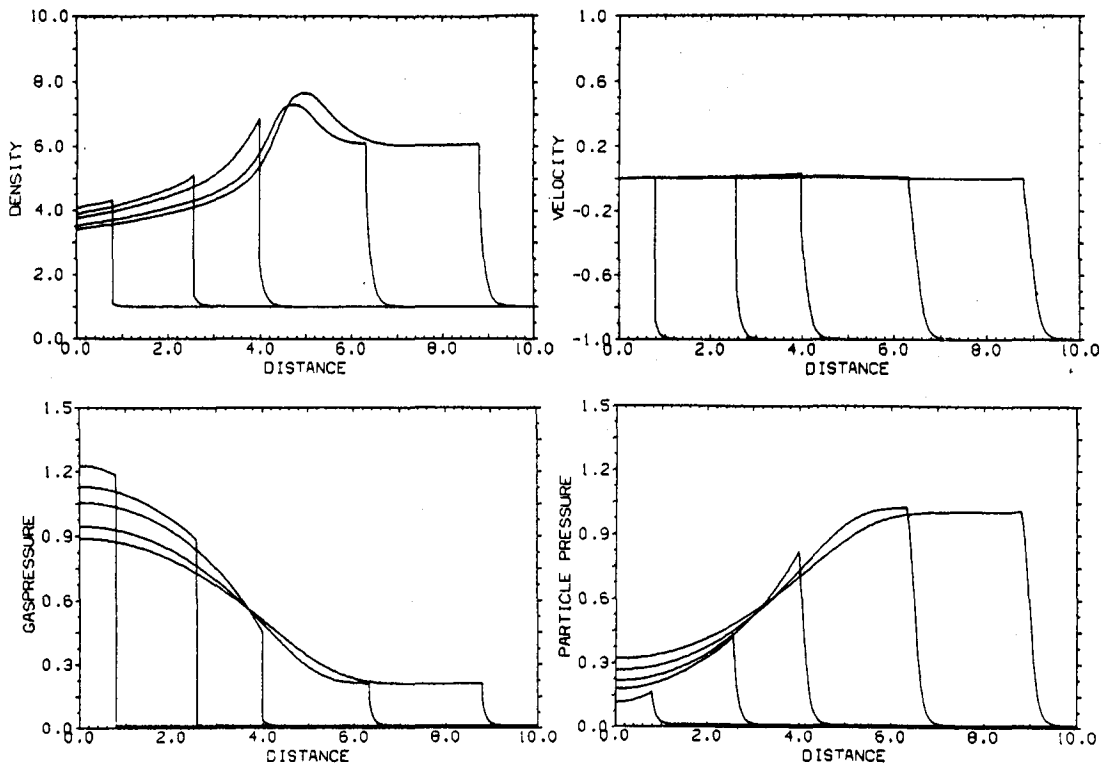

Figure 1:— Evolution of a shock with $M = 4.4$, $N = 0.5$. The curves correspond to times $t = 6, 20, 34, 60, 88$ in units of the diffusion time scale.

Discussion

These numerical solutions clearly indicate that much work needs to be done before we understand shock acceleration as a time dependent process. The slowness of the process is possibly due to the fact that there is a diffusive flux into the downstream region in addition to the usual advective losses. Analytic investigations of this phenomenon are required.

References

1. L.O'C. Drury, H.J. Völk, *Astrophys. J.* **248**, 344 (1981)
2. W.I. Axford, *Proc. IAU/IUPAP Symp. No. 94*, Dordrecht: D. Reidel, pp. 339–358 (1980)
3. L.O'C. Drury, *Rep. Progr. Phys.* **46**, 973 (1983)
4. H.J. Völk, in "High Energy Astrophysics", ed. by J. Tran Thanh Van, éditions Frontières, (1984)
5. E.A. Dorfi, L.O'C. Drury, submitted to *J. Comp. Phys.* (1985)

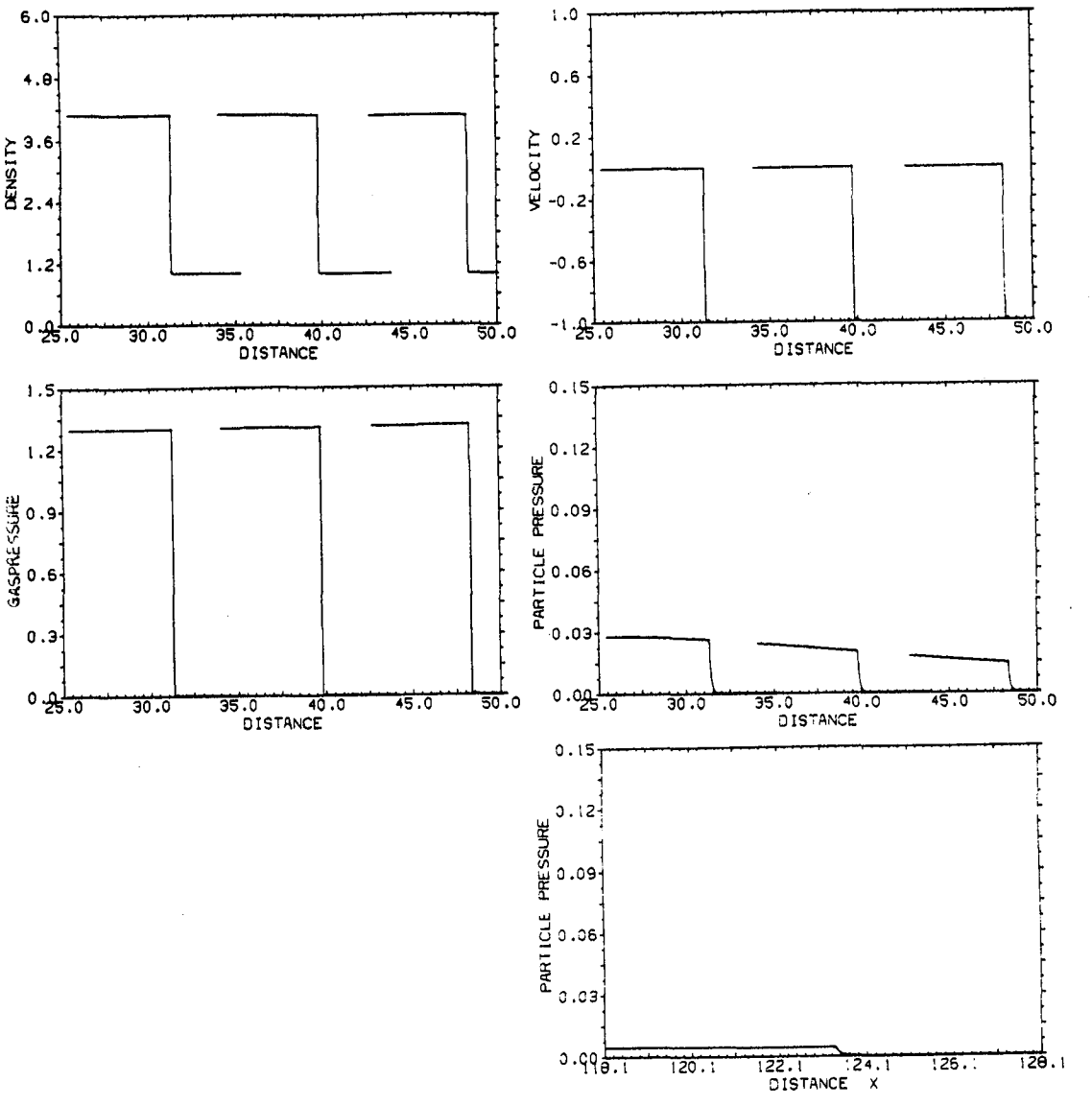

Figure 2:— Evolution of a shock with $M = 10$, $N = 0.05$. The curves correspond to times $t = 440, 560, 660$ in units of the diffusion time scale. The bottom right figure shows the cosmic ray pressure at $t = 1000$.

Selfsimilar Time dependent Shock Structures

R. BECK & L. O'C. DRURY
Max-Planck-Institut für Kernphysik,
Postfach 103980, D-6900 Heidelberg.

1 Introduction

Diffusive shock acceleration as an astrophysical mechanism for accelerating charged particles has the advantage of being highly efficient. This means however that the theory is of necessity nonlinear; the reaction of the accelerated particles on the shock structure and the acceleration process must be self-consistently included in any attempt to develop a complete theory of diffusive shock acceleration. Considerable effort has been invested in attempting, at least partially, to do this and it has become clear that in general either the maximum particle energy must be restricted by introducing additional loss processes into the problem or the acceleration must be treated as a time dependent problem (Drury, 1984).

In stationary modified shock structures where a significant part of the downstream pressure is carried by the energetic particles, because these are in part relativistic and have a softer equation of state than a perfect monatomic gas, the compression ratio of the shock will exceed four and tend towards the limiting value of seven appropriate to a strong shock in a relativistic gas. If, as is almost always the case, the mean free path of an energetic particle and hence the diffusion coefficient increases with particle energy, the diffusion length scale of the particles will be much greater than the thickness of the shock structure above a certain energy. The acceleration of these particles can then be described by test particle theory which applied to a shock of compression greater than four implies a spectrum of accelerated particles flatter than $f(p) \propto p^{-4}$ where p is the particle momentum. Thus without an upper cutoff the energetic particle pressure and energy density will diverge.

We conclude that stationary modified shock structures can only exist for strong shocks if additional loss processes limit the maximum energy a particle can attain. This is certainly possible and if it occurs the energy loss from the shock will lead to much greater shock compressions. It is however equally possible that no such processes exist and we must then ask what sort of nonstationary shock structure develops. The same argument which excludes stationary structures also rules out periodic solutions and indeed any solution where the width of the shock remains bounded. It follows that the width of the shock must increase secularly with time and it is natural to examine the possibility of selfsimilar time dependent solutions.

2 Equations

Our basic idea is that the upper cutoff in the particle energy spectrum is determined through the finite acceleration time scale by the age of the shock. From test-particle theory we know that the cutoff momentum p after time t is given implicitly by (Axford, 1981).

$$t \approx \frac{3}{U_- - U_+} \int_0^p \kappa(p') \left(\frac{1}{U_-} + \frac{1}{U_+} \right) \frac{dp'}{p'}$$

where U_-, U_+ are the upstream and downstream velocities of the plasma relative to the shock and κ is the diffusion coefficient. Thus if the diffusion coefficient has a powerlaw dependence on momentum, $\kappa \propto p^\alpha$ with $\alpha > 0$, the diffusion coefficient of the maximum energy particles is of order $\alpha t U^2$ and increases linearly with time.

If these particles carry significant amounts of energy, as strongly suggested by the high energy divergence of steady solutions, the associated modification of the shock structure will also have a length scale which increases linearly with time. This suggests the possibility of selfsimilar solutions depending on the similarity variable $\xi = x/t$. Indeed on making this ansatz and writing for the effective diffusion coefficient of the high energy particles $\kappa(x,t) = \tilde{\kappa}(\xi)t$ the equations of ideal energetic particle hydrodynamics (see paper OG 8.1-5) reduce to the system of ordinary differential equations,

$$(U-\xi)\frac{\partial \rho}{\partial \xi} + \rho \frac{\partial U}{\partial \xi} = 0,$$

$$(U-\xi)\frac{\partial U}{\partial \xi} + \frac{1}{\rho}\frac{\partial}{\partial \xi}(P_g + P_u) = 0,$$

$$(U-\xi)\frac{\partial P_g}{\partial \xi} + \gamma_g P_g \frac{\partial U}{\partial \xi} = 0,$$

$$(U-\xi)\frac{\partial P_u}{\partial \xi} + \gamma_u P_u \frac{\partial U}{\partial \xi} = \frac{\partial}{\partial \xi}\tilde{\kappa}\frac{\partial P_u}{\partial \xi},$$

where ρ denotes the density, P_g the pressure, U the velocity of the background plasma and P_u the pressure of the ultrarelativistic particles near the upper cutoff. In the related problem for stationary solutions the diffusion coefficient can be eliminated by a change of independent variable but the adiabatic exponent of the energetic particles is uncertain; here $\tilde{\kappa}$ cannot be eliminated, but for the ultrarelativistic particles the adiabatic exponent $\gamma_u = 4/3$.

This system is easily found to have singularities at the points where

$$(U-\xi)\left[(U-\xi)^2 - \frac{\gamma_g P_g}{\rho}\right] = 0,$$

i.e. where the Doppler shifted velocity (note that we have transformed to an expanding coordinate system) is zero or equal to the local sound speed. A major distinction between such time dependent selfsimilar solutions and stationary solutions is that these singularities cannot be avoided; if we start with some asymptotic positive value of U far upstream, $U \to U_-$ as $\xi \to -\infty$, and integrate into the shock U decreases monotonically and ξ increases monotonically so that at some point $U - \xi$ will fall to the local sound speed. Thus selfsimilar shock structures always contain a subshock (whereas in the stationary case the high Mach number solutions are usually smooth).

The matching conditions at this subshock are essentially the same as those in the stationary case, namely that the energetic particle pressure be continuous and that the jump in the energy flux (if any) be positive and result from injection at the subshock,

$$[P_u] = 0, \qquad \left[\frac{\gamma_u}{\gamma_u - 1}P_u(U-\xi) - \frac{\tilde{\kappa}}{\gamma_u - 1}\frac{\partial P_u}{\partial \xi}\right] = Q,$$

where Q is the injection energy flux. The solution downstream from the subshock must be spatially homogeneous, at least as far as the point where $U = \xi$ where a contact discontinuity may occur.

In the stationary case the subshock jump conditions for the plasma properties are simply the ordinary Rankine–Hugoniot conditions applied to a gas with $\gamma_g = 5/3$ and the injection energy flux, though hard to estimate, is probably sufficiently small to be ignored. However in the selfsimilar case the subshock is itself probably modified by the reaction of mildly relativistic particles and the injection flux may be significant.

3 Results

The above system of equations can be integrated in close analogy to the stationary system. In an earlier report on this work (Beck & Drury, 1984) we considered the problem of constructing stationary modified structures for the subshock, but neglected injection. This was found to be possible for moderate Mach numbers, but in general could not be done for shocks with high Mach numbers. The problem is that for strong shocks the subshock, though weaker than the main shock, is still so strong that we return to the problem from which we started; the difficulty of constructing consistent modified structures for stationary shocks. The additional freedom allowed by including the injection flux resolves this problem, but at the expense of an extra unknown parameter (which one can however attempt to estimate using physical arguments based on the concept of selfregulating injection, *cf* Eichler 1981, 1984).

An interesting feature of the timedependent solutions is that the total shock compression is usually large, of order 10 or 20, so that both methods of resolving the divergence problem in strong shocks, the introduction of additional loss mechanisms or the explicit inclusion of secular broadening, lead to the same qualitative conclusion; that strong modified shocks are expected to have large compression ratios. This of course implies that the acceleration is efficient at accelerating particles so that, at least qualitatively, we have a consistent picture.

References

Axford, W. I. 1981 . . . . . *Proc 17th ICRC, Paris*, **12** 155.

Beck, R. and Drury, L. O'C. 1984 . . *Plasma Astrophysics, Varenna, (edited by T. D. Guyenne and J. J. Hunt)*, ESA SP-207 181.

Drury, L. O'C 1984 . . . . . *Adv. Space Res.*, **4** 185.

Eichler, D. 1981 . . . . . *Ap. J.*, **244** 711.

Eichler, D. 1984 . . . . . *Ap. J.*, **277** 429.

A Cosmic Ray driven Instability

E. A. DORFI
Institut für Astronomie der Universität Wien,
Turkenschanzstraße 17, A-1180 Wien.
L. O'C. DRURY
Max-Planck-Institut für Kernphysik,
Postfach 103980, D-6900 Heidelberg.

1 Introduction

The interaction between energetic charged particles and thermal plasma which forms the basis of diffusive shock acceleration leads also to interesting dynamical phenomena. For a compressional mode propagating in a system with homogeneous energetic particle pressure it is well known that 'friction' with the energetic particles leads to damping. The linear theory of this effect has been analyzed in detail by Ptuskin*. Not so obvious is that a non-uniform energetic particle pressure can in addition amplify compressional disturbances. If the pressure gradient is sufficiently steep this growth can dominate the frictional damping and lead to an instability. It is important to note that this effect results from the collective nature of the interaction between the energetic particles and the gas and is not connected with the Parker instability, nor with the resonant amplification of Alfvén waves.

2 Physical description

In diffusing through the thermal plasma the energetic particles produce a reaction force, $-\nabla P_c$, where P_c is the energetic particle pressure. This interaction is mediated by irregularities in the magnetic field, but if their mean motion relative to the thermal plasma is small enough to be ignored the energetic particles can be thought of as exchanging momentum directly with the gas. Consider a small compressional disturbance (which in the absence of energetic particle effects would be simply a sound wave or a magneto-acoustic wave) propagating parallel to the pressure gradient of the energetic particles. For short wavelength disturbances the diffusion timescale of the energetic particles (which decreases quadratically with wavelength) will be much smaller than the dynamical timescale of the disturbance (which decreases linearly) so that the solution of the diffusion equation will approximate a steady solution with constant flux, $\kappa \nabla P_c = \text{const.}$, where κ is the diffusion coefficient. Thus if ρ is the gas density the acceleration resulting from the reaction of the energetic particles is $-\nabla P_c/\rho \propto 1/\rho\kappa$. Clearly small scale density fluctuations will induce acceleration fluctuations (and hence velocity fluctuations which can amplify the density fluctuations) unless $\kappa \propto 1/\rho$.

If the energetic particles were scattered directly by the molecules and ions of the thermal plasma one would indeed expect the mean free path, and hence the diffusion coefficient, to be inversely proportional to the gas density. However there is no reason why the effective diffusion coefficient resulting from collective processes should be inversely proportional to the gas density and in general it will not be. The

* V. S. Ptuskin 1981, *Astrophys. Space Sci.* **76** 265-78.

instability then results from the fact that the energetic particles couple more strongly to regions of higher (or lower) density and push these through the undisturbed gas. This causes the density to increase in the front of the disturbance and decrease at the back so that the original density fluctuation is amplified. The fluctuations in the gas pressure exert restoring forces which oppose this effect; thus we expect the instability to appear most strongly when the gas is cold.

It is not easy to determine the density dependence of the diffusion coefficient, however if the scattering is produced mainly by Alfvén waves of moderate amplitude, quasilinear theory gives

$$\kappa \approx \frac{1}{3} r_g v \left(\frac{B}{\delta B}\right)^2 \cos^2\theta$$

where r_g is the particle gyroradius, v the particle speed, B the magnetic field, δB the amplitude of the field fluctuations and θ the angle between field and gradient. If we compress a small region (but one which is still large compared to the gyroradii of the energetic particles and the wavelengths of the scattering waves) parallel to the gradient θ increases (so that $\cos\theta$ decreases), $B\cos\theta$ is constant, $r_g \propto 1/B$ and $\delta B^2 \propto \rho^{3/2}$ so that for this case $\kappa \propto \rho^{-3/2}\cos\theta$ and decreases at least as fast as $\rho^{-1.5}$. We have ignored the problems associated with wave saturation and cross-field diffusion, however the Alfvén wave excitation through the resonant streaming instability, $v_A \cos\theta \nabla P_c \propto B\rho$ where v_A is the Alfvén speed, is also greater in compressed regions. Thus we expect that the energetic particles will couple more strongly to the compressed regions because the magnetic field, in particular the transverse component, will be larger there and the wave activity will be enhanced.

3 Instability criterion

The ideas outlined above can be put on a firmer footing if we take the equations of ideal energetic particle hydrodynamics,

$$\frac{\partial \rho}{\partial t} + \frac{\partial(\rho U)}{\partial x} = 0,$$

$$\frac{\partial U}{\partial t} + U\frac{\partial U}{\partial x} = -\frac{1}{\rho}\frac{\partial(P_g + P_c)}{\partial x},$$

$$\frac{\partial P_g}{\partial t} + U\frac{\partial P_g}{\partial x} + \gamma_g P_g \frac{\partial U}{\partial x} = 0,$$

$$\frac{\partial P_c}{\partial t} + U\frac{\partial P_c}{\partial x} + \gamma_c P_c \frac{\partial U}{\partial x} = \frac{\partial}{\partial x}\left(\kappa \frac{\partial P_c}{\partial x}\right)$$

(U is the velocity, P_g the gas pressure, γ_g and γ_c the adiabatic exponents of the gas and energetic particles), linearize them and perform a two-scale expansion, *i.e.* look at perturbations of short wavelength and small amplitude on a smoothly varying background. To lowest order the perturbations, denoted by a prefix δ, are simply sound waves with frequency ω and wave number k,

$$\delta u = \pm a_g \frac{\delta\rho}{\rho}, \qquad \delta P_c = 0, \qquad (\omega - kU)^2 = a_g^2 k^2,$$

where $a_g = \sqrt{\gamma_g P_g/\rho}$ is the gas sound speed. To this order and in the short wavelength limit the energetic particles are decoupled from the perturbations in the gas.

The next order is more interesting and gives an equation for the wave amplitude in terms of the wave action density, the wave energy density divided by the Doppler shifted frequency, $A = \rho\delta u^2/(\omega - \underset{\sim}{k}\underset{\sim}{u})$;

$$\frac{\partial A}{\partial t} + \frac{\partial}{\partial x}\left[A(U \pm a_g)\right] = A\left[-\frac{\gamma_c P_c}{\rho\kappa} \pm \frac{1}{\rho a_g}\frac{\partial P_c}{\partial x}\left(1 + \frac{\rho\delta\kappa}{\kappa\delta\rho}\right)\right]$$

In the absence of energetic particle effects the RHS of this equation would be zero and we would have conservation of wave action. The first term on the right is proportional to the energetic particle pressure and represents pure Ptuskin damping. The second term shows the destabilizing effect of an energetic particle pressure gradient; unless $\delta(\rho\kappa) = 0$ waves going in one direction will be amplified.

The condition for the instability to occur is clearly that the second term dominate the first,

$$\left|\frac{1}{\rho a_g}\frac{\partial P_c}{\partial x}\left(1 + \frac{\rho\delta\kappa}{\kappa\delta\rho}\right)\right| > \frac{\gamma_c P_c}{\rho\kappa}$$

or, if $\kappa \propto \rho^\beta$, that the length scale of the energetic particle pressure be less that a critical length scale,

$$\frac{P_c}{|\nabla P_c|} < \frac{|1+\beta|}{\gamma_c}\frac{\kappa}{a_g}.$$

As indicated by the physical discussion the instability occurs when a steep energetic particle gradient is established in a cold gas.

4 Implications

This instability has important consequences for the structure of shocks modified by particle acceleration. The length scale associated with the increase of particle pressure in the shock precursor is κ/U where U is the shock speed whereas the critical length scale is of order κ/a_g; thus we expect the precursor to be unstable for all strong modified shocks. The ratio of the advection time through the precursor to the instability growth time is of order the Mach number of the shock so that any slight density fluctuations in the upstream medium should be strongly amplified in the precursor region.

This probably means that the small-scale structure of the shock is stochastic and irregular. The strongly amplified disturbances we expect to form shocks which contribute to the gas heating and may assist in injecting particles into the diffusive acceleration process. An interesting side effect is that the effective diffusion coefficient in the shock precursor region will be reduced; this will shorten the acceleration time scales and may allow higher particle energies to be reached.

The instability may also be important in determining the structure of the galactic halo and of cooling flows.

RELATIVISTIC COSMIC RAY SPECTRA IN THE FULL NON-LINEAR THEORY OF SHOCK ACCELERATION

David Eichler[1,2] and Donald C. Ellison[1]

[1]Astronomy Program, University of Maryland, College Park, MD 20742
[2]Department of Physics, Ben-Gurion University, Beer Sheva, Israel

1. Introduction. The test particle theory of diffusive shock acceleration predicts a power law cosmic ray (CR) spectrum in momentum of the form

$$N(p) \propto p^{-s}, \quad s = -(r+2)/(r-1), \tag{1}$$

where N(p) is the differential number density of CRs at momentum p and s is determined solely by the compression ratio, $r = u_1/u_2$. Here, the shock is assumed to be planar, of infinite extent, steady state, discontinuous, piece-wise constant, and u_1 (u_2) is the flow velocity (measured in the shock frame) upstream (downstream) of the shock discontinuity (u_1 is the shock velocity in the lab frame)[2,3,4,6].

Since strong, classical hydrodynamic shocks have a compression ratio of 4, the test particle theory predicts a spectral index of -2, in good agreement with the source spectrum of galactic CRs that is inferred from observations. This account of the spectral index is widely viewed as being superior to previous accounts, which required fine-tuning to get the correct spectrum[1].

The non-linear theory, however, which allows for the fact that the CR pressure may be dynamically significant, accordingly allows the compression ratio to be larger than 4. This follows from the facts that (a) much of the post shock pressure can be in relativistic CRs, and, for a relativistic fluid, the classical compression ratio can be as large as 7, and (b) a significant amount of energy can be lost from the shock front in the form of particles that stream away from the shock before being convected downstream of it, and, r may then be arbitrarily large[6].

High production efficiencies (>10%) appear to be as widespread in astrophysical particle acceleration as does a spectral index between -2 and -3, and the possibility that CRs affect the compression ratio needs to be taken seriously. While one could argue that efficiencies of order 10% are marginally consistent with observation without requiring significant non-linear effects, invoking an injection rate that always gives an efficiency ~ 10% in the test particle theory requires a fine-tuning assumption about the injection, which is probably objectionable.

Here we show that the non-linear theory gives rise to spectra that are very close to a p^{-2} power law, over most of the range of astophysically reasonable shock parameters for supernova blast waves in the hot phase of the interstellar medium (HISM), even though r may differ significantly from 4. The universality of the spectrum, in this view, is related to the nature of the non-linear feedback of the CRs on their own acceleration rate, not to the universality of the compression ratio among shocks.

2. The Basic Calculation. The non-linear, steady-state theory includes an explicit description of the waves that couple the particles to the fluid. The full set of equations is

$$\rho u = C_1, \tag{2}$$

$$\rho u^2 + P_e + P_w + P_g = C_2, \tag{3}$$

$$\frac{dT_w}{dx} = u\frac{dP_w}{dx} + v_{ph}\frac{dP_e}{dx} - RP_w, \tag{4}$$

$$RP_w = C_1 T\frac{ds}{dx}, \tag{5}$$

$$T\,ds = dh - \frac{dP_g}{\rho}, \tag{6}$$

$$-\frac{\partial}{\partial x}(u_s F) + \frac{1}{3}\frac{du_s}{dx}\,p\frac{\partial F}{\partial p} + \frac{\partial}{\partial x}D\frac{\partial F}{\partial x} = C_3. \tag{7}$$

Here, ρ is fluid density, u is fluid velocity, u_s is the velocity of the scattering centers, P_e is the pressure in energetic particles, P_w is the wave pressure, P_g is the pressure in gas that has not yet been shocked, T_w is the energy flux due to waves, v_{ph} is the phase velocity of the scattering waves relative to the background medium, i.e. $u-u_s$, R is the damping rate, Tds is the heat per unit mass that enters the fluid via the wave damping, h is the enthalpy per unit mass and C_1, C_2, and C_3 are constant. Equations (2) and (3) express mass and momentum conservation, respectively. Equation (4) is an energy inventory equation for the waves with the terms on the right hand side representing, in order of appearance, amplification of existing waves by compression, growth due to the cyclotron unstable CR gradient, and damping (see 8 and references therein). Equations (5) and (6) describe the energy deposition into the thermal fluid by the wave damping, and (7) is the diffusion equation for $F = 4\pi p^3 f(d\ln p/d\ln E)$, where f(p) is the distribution function and D is the diffusion coefficient. These equations can all be solved using a non-perturbative, non-separable, analytic technique that proves to be extremely accurate in comparison with numerical solutions[5,6]. The numerical solutions referred to are possible only over a limited dynamical energy range. However, the analytic technique exploits the fact that in a real situation there is a very large dynamic energy range - ten decades for galactic CRs - so it should be even more accurate in the latter case than in the comparison with the numerical results.

We have solved the above eqs. for rapid wave damping ($R \to \infty$) and for v_{ph} constant upstream of the shock (v_{ph} is set equal to zero downstream). Results are shown in Fig. 1 where we have plotted partial pressure $\equiv (j/3)EF$, versus energy, E. Here, j = 1 for relativistic and = 2 for non-relativistic particles. Each curve is the partial pressure profile for a locus of (M_1, v_{ph}) values shown in Fig. 2. Each point on a curve in Fig. 2 produces essentially the same profile as seen in Fig. 1. The range in compression ratios from $v_{ph} = 0$ to $M_1 \to \infty$, is as follows: (a) $7.1<r<7.5$, (b) $4.7<r<5.3$, and (c) $3.9<r<4.6$. The dashed lines in Fig. 1 show energy spectral indices of -2 (horizontal) and -2.7, representative of galactic CR source and observed spectra, respectively. Our solutions are approximately power laws, deviating from the horizontal dashed line by at most a factor of 3 over 6 decades of energy. (That they are not perfect power laws results from the slowing of the flow upstream of the shock by CR pressure). It is clear that a small phase velocity, representative of the HISM, allows an extremely wide range in shock strengths, all producing source spectra essentially indistinguishable from that required

to produce the observed CR spectrum. The uncertainties in the CR source spectrum caused by energy dependent leakage exceed the small differences between curves (b), (c), and the horizontal dashed line. Even curve (a) is marginally consistent with the inferred source spectrum.

The ratio of Alfvén to shock velocity is given by, $v_A/u_1 = 2.2\ 10^{11}\ B/(u_1\sqrt{n})$, where B is the magnetic field and n is the number density. For the HISM, we can use B ~ 3μG, n ~ 0.01 per cm^3, and shock velocities ~ 1000 km/s. Therefore, $v_A/u_1 \sim 0.07$, and, as seen in Fig. 2, a very wide range in M_1 will produce spectra similar to those seen in Fig. 1.

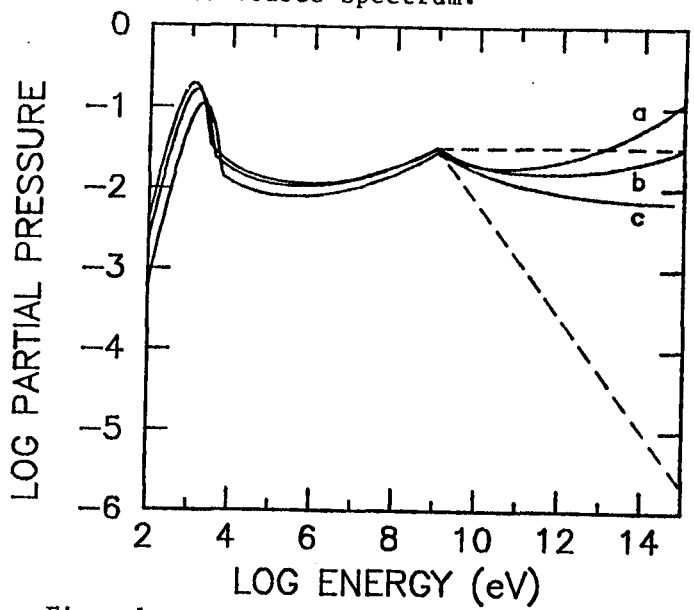

Fig. 1. Postshock partial pressure vs. energy. An energy cutoff = 10^{15}eV has been used. Each label represents a family of curves with a particular $u_1/u(GeV)$.

3. Scaling Laws. The results of the previous section show that the spectrum of relativistic particles is "quasi-universal" in the sense that it depends very weakly on the upstream parameters. The reason for this, we argue, is that the energy content in relativistic particles is a very sensitive function of the spectrum, so that their backpressure on the flow regulates their spectrum very precisely. This principle is illustrated by the fact that the overall compression ratio of the scatterers is always established in a way such that the compression ratio of mildly relativistic particles is virtually independent of the upstream shock parameters. In Fig. 3 the overall compression ratio of the shock is plotted as a function of Mach number for the limiting case of zero phase velocity. It is seen that beyond modest Mach numbers, $r \propto M^{3/4}$, regardless of the fact that the adiabatic index of the post shock gas (i.e. the relative contribution of relativistic and non-relativistic particle pressure) varies substantially over this range in M_1. (The classical result for $\gamma = 4/3$ is shown by the dotted line.) This $M^{3/4}$ law can be derived straightforwardly by merely assuming that the Mach number of the flow when it encounters Gev particles, M(GeV), and the compression ratio at 1 GeV, r(GeV), are ~ constant (we find, for $v_{ph} = 0$ and for $10 < M_1 < 100$ that $3.3 < M(GeV) < 3.6$ and $3.5 < r(GeV) < 3.75$). The result then follows

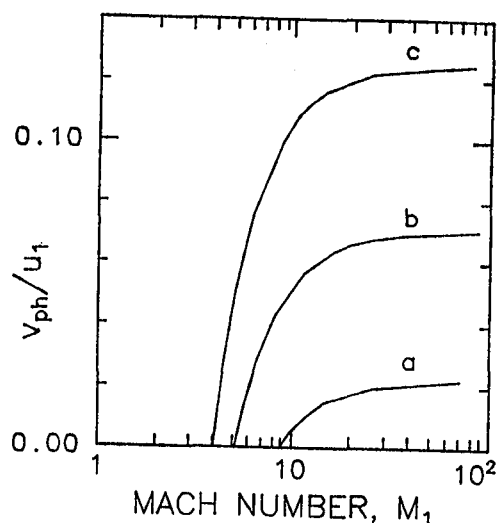

Fig. 2. Labels same as Fig. 1.

from the fact that, because the phase velocity is zero, the upstream fluid behaves adiabatically, i.e. (using eq. [2]),

$$P \propto \rho^{5/3} \Rightarrow [M_1/M(GeV)]^2 = [u_1/u(GeV)]^{8/3}, \qquad (8)$$

Here u(GeV) is the upstream flow velocity felt by GeV particles[6]. Given that M(Gev) and r(GeV) = u(Gev)/u_2 are about constant for $v_{ph} = 0$, r scales as $M^{3/4}$.

As is evident from Fig. 3, the shock compression is dramatically reduced and stabilized by the introduction of even a small v_{ph} for the scattering waves. For an infinite upstream acoustic Mach number, the compression ratio, formally infinite when $v_{ph} = 0$, is reduced to only ~ 7 when $v_{ph}/u_1 \sim 0.03$. This result can be derived analytically to high accuracy; using the same principle invoked to derive the $M^{3/4}$ scaling law when v_{ph} vanishes, one can show that $u_1/u(GeV) \sim 2$ when $v_{ph}/u_1 \sim 1/[2.7\gamma(\gamma-1)M^2(GeV)]$.

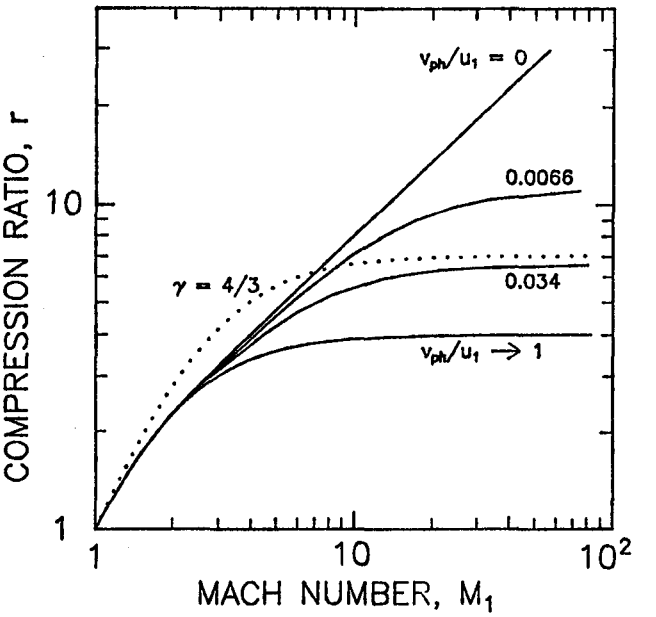

Fig. 3. Dotted line is classical result.

4. Conclusions. The non-linear theory of shock acceleration has been generalized to include wave dynamics. In the limit of rapid wave damping, it is found that a finite wave velocity tempers the acceleration of high Mach number shocks and limits the maximum compression ratio even when energy loss is important. For a given spectrum (see Figs. 1-2), the efficiency of relativistic particle production is essentially independent of v_{ph}. For the three "families" shown in Figs. 1-2, the percentage of kinetic energy flux going into relativistic particles is (a) 72%, (b) 44%, and (c) 26% (this includes the energy lost at the upper energy cuttoff). Even small v_{ph}, typical of the HISM, produce quasi-universal spectra that depend only weakly on the acoustic Mach number. These spectra should be close enough to E^{-2} to satisfy CR source requirements.

References

1. Axford, W.I. 1981, 17th ICRC (Paris), **12**, 155.
2. Axford, W.I. et al. 1977, 15th ICRC (Plovdiv), **11**, 132.
3. Bell, A.R. 1978, MNRAS, **182**, 147.
4. Blandford, R.D. and Ostriker, J.P. 1978, Ap. J. (Let), **221**, L29.
5. Eichler, D. 1985, Ap. J., in press.
6. Ellison, D.C. and Eichler, D. 1984, Ap. J., **286**, 691.
7. Krymsky, G.F. 1977, Dokl.Akad.Nauk SSSR, **234**, 1306.
8. McKenzie, J.F. and Volk, H.J. 1982, Astr. Ap., **116**, 191.

THE CENTRAL ENGINE OF QUASARS AND AGNs: A RELATIVISTIC PROTON RADIATIVE SHOCK

Demosthenes Kazanas and Donald C. Ellison
LHEA, Code 665, NASA/Goddard Space Flight Center, Greenbelt, MD 20771
and
Astronomy Program, University of Maryland, College Park, MD 20742

1. Introduction. Active galactic nuclei (AGNs) and quasars (QSOs) appear to emit roughly equal energy per decade from radio to γ-ray energies (e.g. Ramaty and Lingenfelter 1982). This argues strongly for a non-thermal radiation mechanism (see Rees 1984). In addition, statistical studies have indicated that the spectra of these objects in the IR-UV and 2-50 keV X-ray band, can be fitted very well with power laws of specific indices. These spectral indices do not seem to depend on the luminosity or morphology of the objects (Rothschild et al. 1983; Malkan 1984), and any theory should account for them in a basic and model independent way.

If shocks accelerate relativistic protons via the first-order Fermi mechanism (e.g. Axford 1981), the radiating electrons can be produced as secondaries throughout the source by proton-proton (p-p) collisions and pion decay, thus eliminating Compton losses (Protheroe and Kazanas 1983). As shown by Kazanas (1984), if relativistic electrons are injected at high energies, e^+-e^- pair production results in a steady state electron distribution that is very similar to that observed in AGNs, independent of the details of injection and the dynamics of the source. The conditions required by this mechanism are met in the shock model of Eichler (1984) and Ellison and Eichler (1984) which allows the self-consistent calculation of the shock acceleration efficiency.

2. Model. We assume that a black hole of mass, $M_9 = M/(10^9\ M_\odot)$, accretes gas of density, n, and temperature, T. If the dissipative time scale of the accreting material, τ_{pp}, is longer than the free fall time, τ_{ff}, a steady state radiative shock will develop at $x = R/R_s$, where $R_s = 2GM/c^2$ is the Schwarzschild radius. Inflowing thermal particles with free fall velocity, u, will be shock accelerated and relativistic protons will be produced. These protons will undergo inelastic nuclear collisions to produce pions, i.e., $p + p \rightarrow p + p + \pi^{\pm} + \pi^o$. The pion decay will produce γ-rays, neutrinos, and relativistic electrons which will subsequently produce the observed radiation by synchrotron and inverse Compton emission. Since $\sim$ 50% of the energy flux that goes into relativistic particles is lost to neutrinos (Eichler 1979) and since the shock must form beyond the Schwarzschild radius, the maximum efficiency for this model is considerably less than 1. The maximum luminosity is determined by the ability of the shock accelerated particles to provide sufficient pressure to support the shock against the accreting material. This is determined by the shock dynamics and occurs at ~10% of the Eddington luminosity.

A fraction, Q, of the energy flux crossing the shock is converted into relativistic particles and eventually into radiation. Therefore,

$$L_{tot} = 4\pi R_1^2 \cdot \frac{1}{2} n_1 m_p u_1^3 \cdot Q, \qquad (1)$$

where L_{tot} is the total radiated energy including neutrino losses and the subscript (1) indicates values at the shock. Due to neutrino losses, the

observed luminosity, L, will be $L \sim 0.5\ L_{tot}$. Alternatively, if $\langle E_{rel} \rangle$ is the average energy density in relativistic particles, the total luminosity can be expressed as,

$$L_{tot} \simeq 4\pi R_1^3 \langle E_{rel} \rangle / (3\tau_{pp}), \qquad (2)$$

where $\tau_{pp} \simeq 1/(\langle n_i \rangle \sigma c) \simeq 2.2\ 10^5\ x_1^{3/2}\ M_9^2\ \dot{m}^{-1}$ sec is the p-p interaction time, σ_{pp} is the p-p cross section, x_1 is the shock position in Schwarzschild radii, $\langle n_i \rangle$ is the average density inside the shock, and $\dot{m}$ is the accretion rate in $M_\odot$/yr. Equations (1) and (2) determine the shock position. Assuming mass conservation, i.e., $n \simeq 1.2\ 10^9\ x^{-3/2}\ M_9^2\ \dot{m}/cm^3$, and using $\langle E_{rel} \rangle = 3P_{rel}$, where P_{rel} is the relativistic particle pressure, we have

$$\frac{\dot{m}}{M_9} \simeq 11\ \frac{Q}{\eta}\ , \qquad (3)$$

where $\eta = P_{rel}/(n_1 m_p u_1^2)$. Eq. (3) indicates that $\dot{m}/M_9$ is determined solely by the shock efficiency and cannot have an arbitrary value. The efficiencies Q and η (which to good approximation depend only on the shock Mach number) can be calculated self-consistently using the nonlinear, steady state solution of Eichler (1984) and Ellison and Eichler (1984). This assumes that a magnetic field is present for the formation of the collisionless shock and the elastic scattering of the accelerated particles. We assume, however, that the magnetic field is not dynamically important and that the Alfvén (or phase) velocity is small compared to the shock velocity. We also require that the mean free path of the highest energy particles be no smaller than R_s so they avoid being swallowed by the black hole and hence can provide the pressure to support the standing shock.

Since both Q and η approach 1 for high Mach numbers, there is a maximum value above which no steady state shock solutions of the type described here exist. If $\dot{m}/M_9$ is greater than this limit, the p-p collisions behind the shock occur so rapidly that there is not sufficient relativistic particle pressure to support the radiative shock.

Using the above relations, the observed non-thermal luminosity, L, becomes

$$L \simeq 1.5 \times 10^{47}\ Q^2\ M_9/(\eta\ x_1)\ \ \text{erg/s}. \qquad (4)$$

Defining, $F = L/L_E$, where $L_E = 1.3 \times 10^{47}\ M_9$ erg/s, eq. (4) reads

$$F = L/L_E \simeq 1.2\ Q^2/(\eta\ x_1). \qquad (5)$$

This indicates that the sources should emit at a given fraction of the Eddington luminosity (L_E), which depends only on x_1, Q, and η.

The value of x_1 can be expressed in terms of the Mach number, M_1, and the upstream temperature as,

$$M_1^2 = 3m_p u_1^2/[5k(T_e + T_p)] \simeq 6.5 \times 10^4/(x_1 T_8), \qquad (6)$$

where T_8 is the upstream temperature in units of 10^8 K and is expected to be determined by the balance between X-ray Compton heating and cooling and has been shown to be essentially constant and $\sim 10^8$ K (e.g., Krolik et al. 1981). Consequently, F, depends on only one parameter, M_1 or x_1.

3. Results and Conclusions. By combining eqs. (5) and (6), we can obtain the Eddington efficiency as a function of the shock size or the accretion rate. These relationships are shown in Figs. 1a, and b. A range of upstream temperatures is shown.

The Eddington efficiency drops precipitously with increasing x_1 due to the fact that Q approaches zero as M_1 drops below ~ 4. One therefore expects that there would be an effective upper limit for x_1 (lower limit for M_1) above which the sources are too weak to be seen. At the other extreme, there is a maximum value for F since x_1 can not be arbitrarily small. We have chosen $x_1 \simeq 5$ as a reasonable minimum value of the shock radius. This corresponds to an efficiency, $F \simeq 0.2$.

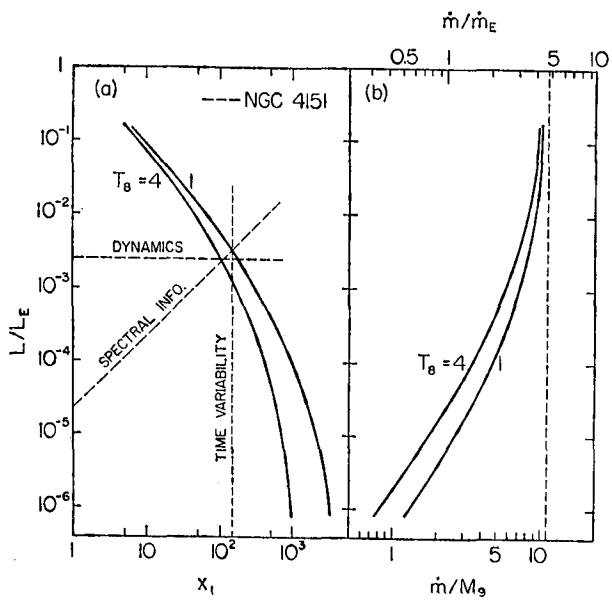

Fig. 1. L/L_E vs. shock position x_1, and accretion rate, $\dot{m}_E = L_E/c^2 = 2.3\ M_9$ solar masses/yr.

We can also express the luminosity as a function of the black hole mass with x_1 as a parameter. Our results can now be directly compared to the correlation between L and M (Fig. 2) found recently by Wandel and Yahil 1985) (W-Y). These authors, by attributing the widths of the H_β line to dynamical motions, and using photoionization arguments to determine the distance of the line emitting clouds, showed that the luminosity of ~ 70 QSOs and Seyfert 1 galaxies is proportional to their mass. In comparing our model, which yields the entire non-thermal luminosity, a bolometric correction raising the points of W-Y by 5-10 should be used. With such a correction, the shock model with $5 \lesssim x_1 \lesssim 150$ reproduces the observations extremely well. The observations indicate that even though the non-thermal radiation from QSOs and AGNs is generally well below the Eddington limit, it is still highly correlated and proportional to the mass. This proportionality is an integral feature of our shock model and results from the fact that $\dot{m} \propto M_9$ (eq. 3). The proportionality constant depends mainly on the p-p strong interaction cross section and results in luminosities well below the Eddington limit in accordance with observations. Also, the fact that no objects in the W-Y compilation are observed to emit much below 0.01 L_E might have an explanation in the sharp decrease in F with $\dot{m}/M_9$ as indicated in Fig. 1b. We consider the straightforward interpretation of this correlation by our model as an indication of the correctness of its basic premises.

The galaxy NGC 4151 affords an additional test of our model. The considerations of W-Y provide an estimate of the mass, $M \simeq 3 \times 10^7\ M_\odot$. This mass along with the observed absolute luminosity, $L \simeq 10^{43}$ erg/s, determine, $F \simeq 2.5 \times 10^{-3}$. This is shown by the horizontal dashed line of Fig. 1a labeled "dynamics". X-ray variability has been established on time scales of $\Delta t \simeq 12$ hours (Mushotzky et al. 1978), indicating a size, $R \simeq c\Delta t \simeq 1.3 \times 10^{15}$ cm. Using the determined mass, this translates into a shock radius, $x_1 \simeq 140$, and is shown in Fig. 1a as "time variability".

Furthermore, measurements of the X-ray spectrum of NGC 4151 (Mushotzky et al. 1978) provide a constraint on the compactness, L/R, within the framework of the non-thermal, e^+-e^- feedback model of AGN spectra (Kazanas and Protheroe 1983; Kazanas 1984); i.e., $L/R \lesssim 10^{28}$ erg/(s-cm). This condition becomes, $F \lesssim 2.3 \times 10^{-5}\ x_1$, and is indicated in Fig. 1a by the line labeled "spectral information". We find the agreement between these independent constraints and our model to be quite remarkable.

In conclusion, we have outlined a model for AGNs and QSOs which is complete in the sense that it simultaneously addresses the source dynamics (i.e. the conversion of accretion energy into radiation) and spectrum (from radio to γ-rays). As shown in Kazanas (1984), the e^+-e^- feedback decouples the spectral signatures from the dynamics, provided that most of the power is injected at energies high enough that the resulting photons are absorbed within the source to produce e^+-e^- pairs. The present model does precisely that, through shock acceleration (Ellison and Eichler 1984). Furthermore, it provides a straightforward physical argument as to why such shocks should occur ($\tau_{pp} > \tau_{ff}$) and also gives estimates of the Eddington efficiencies, F, and sizes, x_1, of these sources. Finally, in its most direct confrontation with observations (Fig. 2), our model provides a natural explanation for the $L \propto M$ correlation. In addition, it also provides the normalization (it is directly related to τ_{pp}) and its value is in remarkable agreement with the data of W-Y.

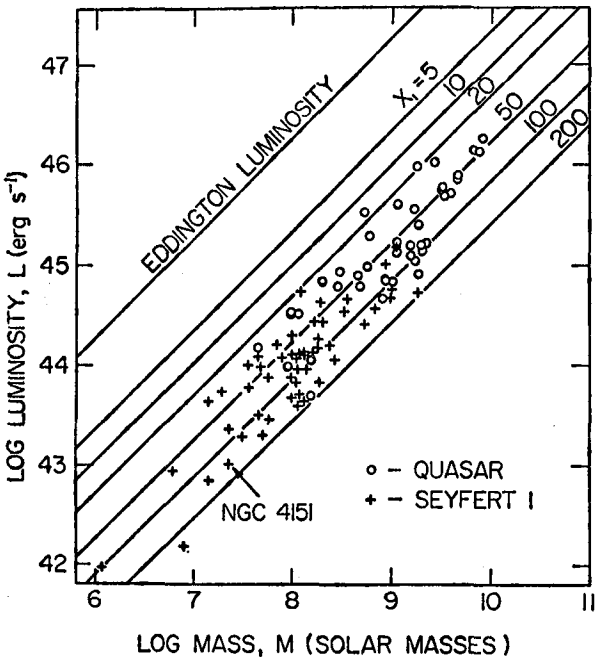

Fig. 2. The lines are from the shock model (using $T_8 = 1$) for shocks which form at various x_1. Points are from Wandel and Yahil.

5. Acknowledgements. We wish to thank C. Dermer, D. Eichler, R. Mushotzky, T. Kalhman, and A. Wandel for helpful discussions.

Axford, W.I., 1981, 17 ICRC (Paris), 12, 155.
Eichler, D., 1979, Ap. J., 232, 106.
Eichler, D., 1984, Ap. J., 277, 429.
Ellison, D.C. and Eichler, D. 1984, Ap. J., 286, 691.
Kazanas, D., 1984, Ap. J., 287, 112.
Kazanas, D. and Protheroe, R.J., 1983, Nature, 302, 228.
Krolik, J.H. et al. 1981, Ap. J., 249, 422.
Malkan, M.A. 1984, "X-Ray and UV Emission from AGNs," eds. Brinkmann and Trumper, p. 121.
Mushotzky, R.F. et al. 1978, Ap. J. (Let.), 225, L115.
Protheroe, R.J. and Kazanas, D., 1983, Ap. J., 265, 620.
Ramaty, R. and Lingenfelter, R.E., 1982, Ann. R. Nucl. Phys., 32, 235.
Rees, M.J., 1984, Ann. R. Astr. Astro., 22, 471.
Rothschild, R.E. et al. 1983, Ap. J., 269, 423.
Wandel, A., and Yahil, A., 1985, Ap. J. (Let.), in press.

A Model for the Origin of High-Energy Cosmic Rays

J. R. Jokipii
University of Arizona, Tucson, Arizona
and
G. E. Morfill
Max-Planck-Institut fur Physik und Astrophysik

Abstract. We suggest that cosmic rays, up to the highest energies observed, originate in the galaxy and are accelerated in astrophysical shock waves. If there is a galactic wind, in analogy with the solar wind, we expect a hierarchy of shocks ranging from supernova shocks to the galactic wind termination shock. This leads to a consistent model in which most cosmic rays, up to perhaps 10^{14} eV energy, are accelerated by supernova shocks, but that particles with energies of 10^{15} eV and higher are accelerated at the termination shock of the galactic wind.

Introduction. It appears that supernova blast waves are the major site for acceleration in the galaxy. While this mechanism is attractive, the energy to which particles can be accelerated is only of the order of 10^{14} eV (Lagage and Cesarsky, 1983). However, the observed cosmic-ray spectrum extends well beyond this cutoff, and one is forced to consider separately the origin of very high energy particles.

Two main factors limit the energy to which particles may be accelerated - their gyroradius (which is related to the mean-free path) and the time available. The time scale for particle acceleration is given by (e.g., Krymsky et al, 1979, Forman and Morfill, 1979, Axford, 1980)

$$t_{acc} = 4\kappa/V_{sh}^2, \qquad (1)$$

where κ is the diffusion coefficient (which is a function of energy) and V_{sh} is the shock velocity. Clearly, since κ increases with energy, at any time there will be an energy above which the energy spectrum cuts off. We set the mean free path a constant of order unity times the gyroradius in the ambient magnetic field. For particles of rigidity R (in electron volts) in a magnetic field of B (gauss) we have

$$t_{acc} \simeq \frac{4cR}{900BV_{sh}^2} \qquad (2)$$

The velocity of a supernova shock wave may be written

$$V_{sh}^2 = \alpha E_{sn}/M_G, \qquad (3)$$

where α 1.33 for a pure blast wave and α 2.5 for evaporative solutions (Mckee and Ostriker, 1977), where E_{sn} is the energy of the explosion and M_G is the mass of gas swept up by the blast.

The value of M_G may be found from the Sedov approximation. For a supernova of age t_5 times 10^5 years, and α 1, the maximum cosmic-ray energy in volts is

$$R(V) = 6.5\times10^{13}\, t_5^{-1/5}\, \eta_{-2}^{-2/5}\, E_{51}^{2/5}\, B_3 \qquad (4)$$

where $\rho_0 = \eta_{-2}\times10^{-2} m_p$, $E_{SN} = E_{51}\times10^{51}$ ergs, and $B = 3\times10^{-6} B_3$ Gauss. See also Lagage and Cesarsky(1983). The possible interaction of cosmic rays with more than one shock does not appreciably alter this limit (Blandford and Ostriker, 1980). The spectrum of cosmic rays accelerated by supernovae, therefore is expected to steepen above a few times 10^{14} eV.

The observed cosmic-ray spectrum displayed in figure 1 shows that, although there is an apparent change in the spectrum in the vicinity of 10^{14} eV, the acceleration process is still quite vigorous above this energy. It remains to find the source of the particles above approximately 10^{14} eV.

Figure 1. Spectrum of cosmic rays presented by Linsley (1980).

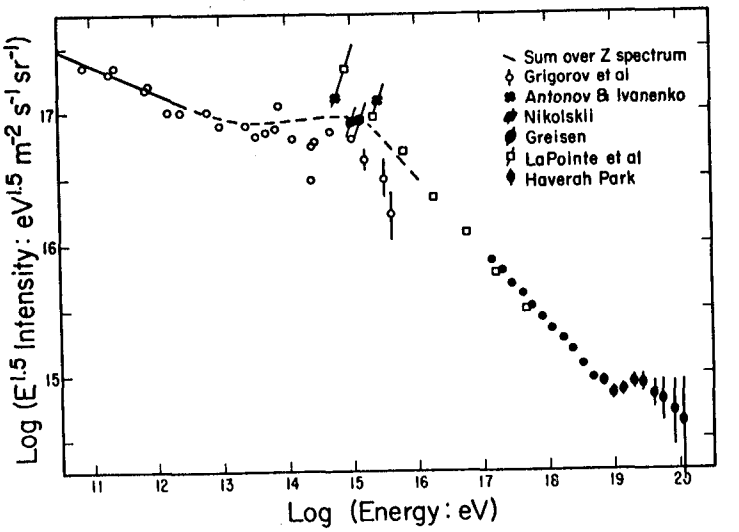

The above discussion indicates roughly that shocks with a greater age and/or greater spatial extent can accelerate particles to a higher energy. Single supernovae shock waves presumably produce most cosmic rays, up to perhaps 10^{14} eV. Supershells, containing the energy of about 100 supernovae, all occurring in a short time, may also contribute. From equation (4) we find that the maximum cosmic-ray energy obtainable in supershells may be expected to increase only by a factor $\sim$ 5 over that of a single supernova.

The largest shock structure associated with our galaxy, and presumably the one with the greatest age, is the termination shock of the galactic wind. Presumably there will also be intermediate-scale shocks resulting from various processes in the galactic wind, similar in nature to those found in the solar wind.

Acceleration at the Galactic Wind Termination Shock. The existence of a galactic wind flowing outward from our galaxy cannot be regarded as established, although it seems likely on the basis of several considerations. A mixture of gas, magnetic field and cosmic rays similar to the hot phase of the interstellar medium is expected to form a supersonic wind (e.g., Johnson and Axford, 1971, Ipavich, 1975, Jokipii,1976, Kopriva and Jokipii, 1983). In addition, the energy dependence of cosmic-ray composition suggests a general outflow from the galactic disk (see, e.g. Jones,1978, Jokipii and Higdon, 1979). We will assume the existence of a galactic wind in which the galactic-halo gas (the intercloud medium) flows outward, and terminates in a shock which can accellerate particles. We can estimate the properties of the galactic wind from some simple considerations. Irrespective of how the wind is driven, the energy source is the supernova explosions. We take a supernova energy input rate into the interstellar medium of

$$\dot{E}_{SN} = 10^{42} \text{ ergs/sec}$$

and assume an energy redistribution between cosmic rays and galactic wind in the ratio 1:1 The energy input rate into cosmic rays, and hence into the galactic wind, is then of order

$$\dot{E}_c = \dot{E}_w = \dot{M}V_w^2/2 = 5\text{x}10^{40} \text{ ergs/sec.}$$

We see immediately that the available time for acceleration at the galactic terminal shock is the lifetime of the galactic wind, which in

turn is T_{gal}, the age of our galaxy, or 1.5×10^{10} years (Hoyle 1961).

Energies of particles accelerated in a galactic wind terminal shock We use our previous estimate for the energy input rate into the wind, $E_W = 5 \times 10^{40}$ ergs/sec. We express the mass loss rate M in units of the present diffuse galactic matter ($5 \times 10^9 M_\odot$) divided by the lifetime, t_{gal} of the galaxy (1.5×10^{10} yrs.). i.e., $M \; 2 \times 10^{25} \times F$ g/sec. where F is a scaling parameter. This yields a wind velocity $V_W \sim 500/\sqrt{F}$ km/sec. A constraint is that $V_W > V_E = 300$ km/sec, the escape velocity. This implies that $F < 4$. In any case, mass loss should not be great, restricting F to perhaps < 1. Thus we do not expect mass balance problems.

Because of galactic rotation, the field lines will be wound up much as in the solar wind. Hence, we use the Parker Archimedean spiral form for the magnetic field and write for the magnetic field B at the shock in terms of that at the reference radius, B_o:

$$B \simeq B_o \left(\frac{R_o}{R_{sh}}\right)^2 \left[1 + \frac{R_{sh}^2 \Omega_{gal}^2}{V_W^2}\right]^{1/2} \qquad (5)$$

where $\Omega_{gal} = 10^{-15}$ sec^{-1} is the galactic rotation rate. Defining $\eta = R_o/R_{sh}$, and substituting for V_W^2 and setting $t_{acc} = T_{gal}$ in equation (2) yields

$$R_{max}(eV) = \frac{450 \, \pi_{gal}}{c} \frac{E_W}{\dot{M} F} B_o \eta^2 \left[1 + \frac{\Omega_{gal}^2 R_o^2 \dot{M} F}{2 E_W \eta^2}\right]^{1/2} \qquad (6)$$

In Table I are displayed R_{max} for various using = 10 kpc, B_o= G, and F = 1. The choice R_o = 10 kpc is in agreement with a lower limit of 4 kpc for the static halo, using I.U.E. observations (Savage and DeBoer, 1981, Pettini and West, 1982).

Table I. Maximum rigidity (and energy of Fe nuclei) of cosmic rays accelerated at the galactic wind termination shock.

	R_{sh}(kpc)	R_{max}(eV)	E_{Fe}(eV)
0.2	50	7×10^{18}	1.8×10^{20}
0.1	100	3.2×10^{18}	$.8 \times 10^{20}$
0.05	200	1.6×10^{18}	$.4 \times 10^{20}$
0.02	500	6.4×10^{17}	$.2 \times 10^{20}$

The distance to the shock, R , should be about half the mean separation of the galaxies in our local cluster, or about 200 kpc.

Finally, we note that particles accelerated at the terminus of the galactic wind will be subject to modulation by the galactic wind. Recent models of the solar problem (see e.g. Jokipii and Kopriva, 1979, Jokipii and Kota, 1983) suggest that the cosmic-ray intensity behaves roughly as if the particles were decelerated in a potential field equal to the electro-static potential difference between the heliospheric pole and equator. Using our standard values and setting $\rho_o \simeq 10^{-3} m_p$ yields a value of 10^{15} eV. This suggests that cosmic-ray particles with energies greater than this value will not be significantly modulated by the galactic wind, whereas lower-energy particles will be modulated. In this picture, galactic cosmic rays with energies less than about 10^{14} eV are primarily accelerated by supernova shocks, whereas those with energies above 10^{15} to perhaps 10^{19} eV are accelerated at the galactic wind termination. Those with intermediate energies may be accelerated by intermediate-scale shocks in the wind, in analogy to blast waves and co-rotating shocks observed in the solar wind.

Further Considerations and summary. The galactic disk cosmic rays represent an average over many super-novae, at different stages (e.g., Bogdan and Volk 1983), whereas the galactic terminal shock is of more constant strength (and probably a higher Mach number), leading to a somewhat different source spectrum.

Since the acceleration process which we propose is quite slow, we must compare it with loss processes. For high-energy nuclei, interaction with the 2.7° K microwave background is the major consideration (Greisen, 1966). Starlight is less important because of the distance from the galaxy. Puget, et al. (1976) showed that photodisintegration is the dominant process. Examination of their figs. 2 and 8 indicates that protons and Fe have a loss time of t_{gal} for energy > $2 \times 10^{19} - 10^{20}$ eV. Therefore, the present mechanism appears capable of accelerating cosmic rays to the highest observed energies. Finally, we suggest that the observed anisotropy in high-energy cosmic rays from north galactic latitudes may be related to the apparent motion of the galaxy, and the pushing of the termination shock closer to the galaxy in that direction.

Hence, a single acceleration process in our galaxy may be responsible for the production of cosmic rays with energies up to 10^{20} eV. The generally uniform spectral characteristics of the cosmic rays over more than ten decades in energy are then easily understood to be a consequence of the same acceleration process - diffusive shock acceleration - and the fact that the shocks all share the same basic energy source - the supernovae explosions in the galactic disk.

Acknowledgements. We are grateful to Prof. P. Meyer for suggesting a relationship to the anisotropy of high energy particles. G. M. wishes to acknowledge the hospitality of the Theoretical Astrophysics Program, and the Depts. of Planetary Sciences and Astronomy, of the University of Arizona. J. R. J. acknowledges support of the National Aeronautics and Space Administration under Grant NsG 7101, and the National Science Foundation under Grant 8317701.

REFERENCES

Axford, W. I., 1980, Proc. IAU/IUPAP Symposium no. 94 (Bologna), 339.
Axford, W. I., Leer E., and Skadron G. 1977, Proc. 15th Internatio nal Cosmic Ray Conference (Plovdiv), 11, 132.
Bell, A. R. 1978a, Mon. Not. R. Astr. Soc., 182, 147.
Bell, A. R. 1978b, Mon. Not. R. Astr. Soc., 182, 443.
Blandford, R. D. and Ostriker, J. P. 1978, Ap. J., 221, L29.
Blandford, R. D. and Ostriker, J. P. 1980, Ap. J., 237, 793.
Bogdan, T. and Volk, H. 1983, Astron. Astrophys., 122, 129.
Forman, M. and Morfill, G. 1979, Proc. 16th Intern Cosmic Ray Conference (Kyoto), 5, 328 (abstract only).
Greisen, K. 1966, Phys. Rev. Lett., 21, 1016.
Hoyle, F. 1961 Proc. Roy. Soc., 260, 201.
Ipavich, F. M. 1975, Ap. J., 196, 107.
Johnson, H. E. and Axford, W. I. 1971, Ap. J., 165, 381.
Jokipii, J. R. 1976, Ap. J., 208, 900.
1983, Space Sci. Rev., 36, 27.
Jokipii, J. R. and Higdon, J. 1979, Ap. J., 228, 293.
Jokipii, J. R. and Kopriva, David A. 1979, 234, 384.
Jones, F. C. 1978, Bull. Am. Phys. Soc., 23, 562 (abstract).
Kopriva, D. and Jokipii, J. R. 1983, Ap. J., 267, 62.
Kota, J. and Jokipii, J. R. 1983, Ap. J., 265, 573.
Krymsky, G. F., Kuzmin A. I., Petukhov S. I. and Turpanov A. A. 1979, Proc. 16th Intern. Cosmic Ray Conference (Kyoto), 2, 39.
Lagage, P. O. and Cesarsky, C. J. 1983, Astron. Astrophys., 118, 223.
Linsley, J. 1980, Proc. I.A.U Symposium #94, p53.
McKee, C. and Ostriker, J. 1977, Ap. J., 218, 148.
Pettini, M. and West, K. A., Ap. J., 260, 561 (1982).
Puget, J. L., Stecker, F. W., and Bredekamp, J. H. 1976, Ap. J., 205, 638.
Savage, B. D. and DeBoer, K. S., Ap. J., 243, 460 (1981).
Volk, H., Drury, L. C. O', and McKenzie, J. 1984, Astron. Astrophys., 130, 19.

Acceleration of Cosmic Rays in Supernova–Remnants

E.A. DORFI AND L.O'C. DRURY
Max-Planck-Institut für Kernphysik,
Postfach 103980, D-6900 Heidelberg, FRG.

1 Introduction

It is commonly accepted that supernova-explosions are the dominant source of cosmic rays up to an energy of 10^{14} eV/nucleon (1). Moreover, these high energy particles provide a major contribution to the energy density of the interstellar medium (ISM) and should therefore be included in calculations of interstellar dynamic phenomena. For the following we will consider the first order Fermi mechanism in shock waves to be the main acceleration mechanism. The influence of this process is twofold; first, if the process is efficient (and in fact this is the case) it will modify the dynamics and evolution of a supernova-remnant (SNR), and secondly, the existence of a significant high energy component changes the overall picture of the ISM. The complexity of the underlying physics has prevented detailed investigations of the full non-linear selfconsistent problem. For example, in the context of the energy balance of the ISM it has not been investigated how much energy of a SN-explosion can be transfered to cosmic rays in a time-dependent selfconsistent model. Nevertheless, a lot of progress has been made on many aspects of the acceleration mechanism and we refer to recent reviews for more details (2,3).

2 Basic physics, initial conditions and method of solution

We apply the usual system of time-dependent hydrodynamical equations to the problem and include an additional cosmic ray pressure term ∇P_C in the momentum equation to describe the reaction on the fluid. The high energy particles are treated in the hydrodynamical approximation as a relativistic gas with adiabatic index $\gamma_C = 4/3$. We note that in this approximation the particle distribution function $f(p)$ is 'averged' out. Hence, it is impossible to determine the mean cosmic ray diffusion coefficient κ and γ_C in a selfconsistent way from $f(p)$. However, the system of equations is closed and consistent if one specifies $\bar{\kappa}$, γ_C and an equation of state for the gas as functions of the other used quantities. For the later we use the ideal gas law with $\gamma_G = 5/3$. Therefore all effects of cooling and heating are ignored. The diffusion coefficient is taken to be constant throughout, $\bar{\kappa} = 10^{27}\mathrm{cm}^2\mathrm{sec}^{-1}$.

For the SN-progenitor star we use a very simple model. The stellar density is taken to be constant at $10^{-11}\mathrm{g\,cm}^{-3}$ out to a radius of $5 \cdot 10^{14}$ cm and decreases than exponentially with a scale length of 10^{14} cm until the density of the external medium is reached, $\rho_{ext} = 5 \cdot 10^{-25}\mathrm{g\,cm}^{-3}$. The SN-energy of 10^{51} ergs is deposited purely as thermal energy within 10^{13} cm. The ejected mass corresponds to 5 $M_\odot$. The external medium is initially at rest and at a temperature $T_{ext} = 8000$ K. The exact details of the progenitor are probably not so critical for the subsequent evolution. More serious is the possibility that a stellar wind from the SN-progenitor star may modify the evolution of the SNR by producing a density structure in the surrounding medium; for this first calculation we have ignored this effect. In the homogeneous external medium the cosmic ray pressure is assumed to be equal to the gas pressure.

The system of equations is discretized and solved numerically on a fully adaptive grid (4). Technically speaking we use a first order upwind conservative implicit scheme thus ensuring the global conservation of mass, momentum and energy. An additional equation for the distribution of grid points is solved simultanously with the physical equations. This procedure enables us to resolve and follow the nonlinear waves over 10 orders of magnitude in radius. The maximum resolution corresponds to 10^8 points and is needed to handle the strong shocks arising in the problem.

3 Results

Between $t = 3 \cdot 10^6$ sec and $t = 10^{11}$ sec the flow structure is characterized by a strong forward shock in the ISM. A contact discontinuity separates the stellar ejecta from the external material and the reverse shock is advected outwards during this phase. The interior background gas cools down adiabatically whereas the cosmic ray pressure stays more or less constant because the adiabatic decompression is compensated by a diffusive flux of particles from the external medium into the remnant. Assuming a mean velocity $v = 10^8 \mathrm{cm\,sec}^{-1}$ the typical length scale of diffusion is $l_d = \frac{\kappa}{v} = 10^{19}$ cm and within this radius diffusion will lead to a flat cosmic ray pressure. Figure 1 depicts the physical variables at time $t = 6.4 \cdot 10^9$ sec and every gridpoint is plotted individually to demonstrate the achieved resolution in this calculation.

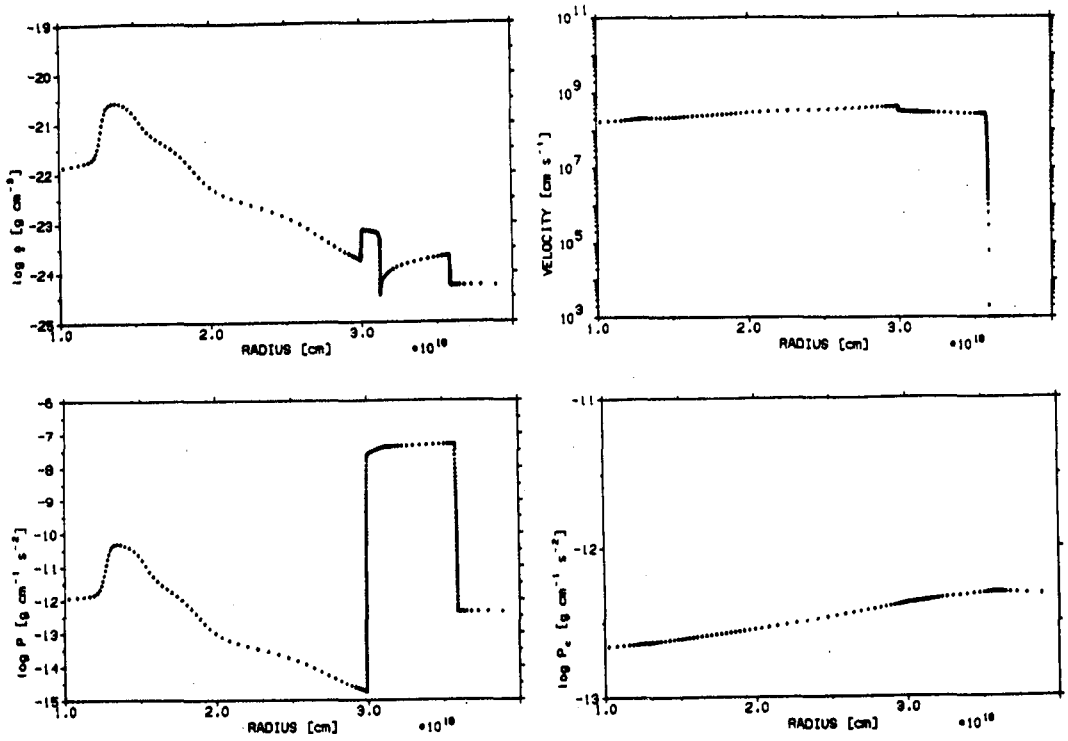

Figure 1:— Physical variables between 10^{14} and $4 \cdot 10^{14}$ cm at time $t = 6.4 \cdot 10^9$ sec. The forward shock, contact discontinuity and reverse shock can be seen.

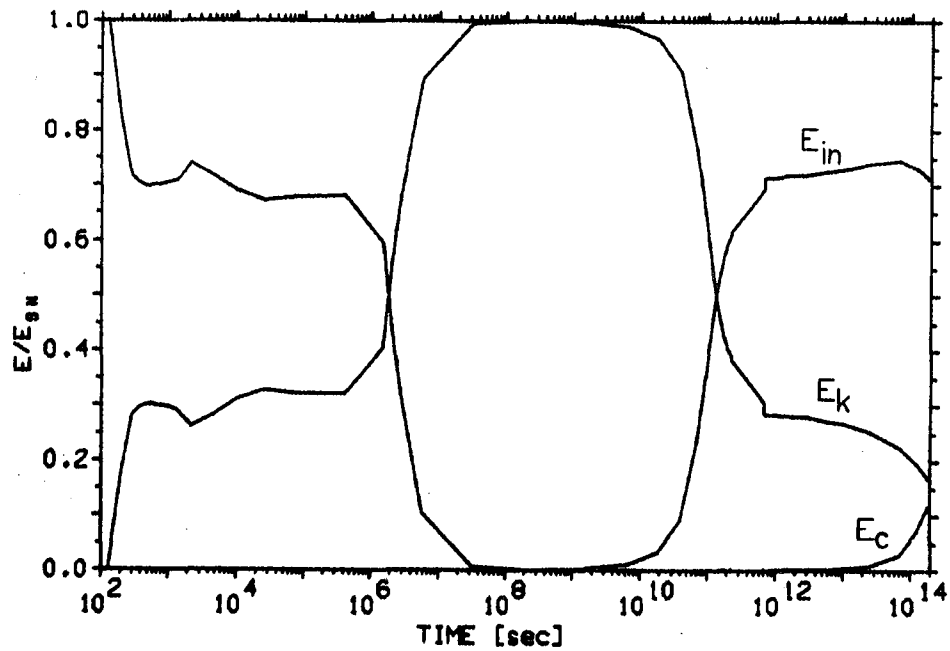

Figure 2:— Energy partition between internal gas energy, $E_{\rm in}$, kinetic energy, $E_{\rm k}$ and cosmic ray energy $E_{\rm c}$ throughout the evolution of the SNR.

At a radius of about $2 \cdot 10^{19}$ cm and at a time $t = 1.3 \cdot 10^{11}$ sec the ejected mass becomes comparable to the swept-up mass. This terminates the phase of free expansion, the flow is decelerated and the reverse shock starts propagating inwards. The ingoing reverse shock accelerates in running down the large density gradient in the interior of the SNR. The strengthening of the reverse shock is further enhanced by the geometrical focusing and the flow velocities become formally superluminal (in this Newtonian formulation). The very low density gas is heated up to extreme temperatures of $T \approx 10^{10}$ K and the dominant force in the interior is now again the gas pressure. The very high Mach-number of 10^6 yields a very high efficiency in accelerating cosmic rays but the small radius 10^{15} cm compared to the actual SNR-radius of $4 \cdot 10^{19}$ cm results in a very small fraction of the total cosmic ray energy being associated with this phenomenon (*c.f.* Fig. 2). A reflecting boundary condition is imposed at an inner radius of 10^{11} cm, and so the inward running shock wave reflects there, propagates outwards and is again reflected at the contact discontinuity. A second somewhat weaker reverse shock compresses and heats up the interior again. During this phase the outer shock continues to expand into the ISM and the interior of the remnant is adiabatically decompressed.

After these events the further evolution corresponds to the Sedov-phase, where an almost homogeneous high pressure bubble expands into the external medium. The Mach-number of the outer shock is moderate, $M = 10 \ldots 1$. The major contribution to the particle acceleration occurs during this phase, $t \geq 6 \cdot 10^{11}$ sec. The time-dependence of the different energy components is shown in Figure 2. Three phases can be distinguished easily, first the shock wave running through the star, secondly

the phase of free expansion with most of the energy stored in kinetic energy and thirdly, after the violence of the ingoing reverse shock waves, the Sedov-phase where the SN-energy is partly given to cosmic rays. As a main physical result we can state that in this selfconsistent model and for the adopted parameter of $\kappa = 10^{27}\,\mathrm{cm^2 sec^{-1}}$ and for times $t = 2 \cdot 10^{14}$ sec about 12% of the SN-energy is transferred to high energy particles.

4 Discussion

The main unknown parameter in this problem is the mean diffusion coefficient κ. In this calculation we have used a constant value of $10^{27}\,\mathrm{cm^2 sec^{-1}}$ whereas in reality κ is expected to be both time- and radius dependent. This value is almost certainly too large so that we have if anything underestimated the particle acceleration efficiency. Unfortunately calculations with smaller values of κ encounter difficulties which we attribute to a cosmic ray driven instability (see paper OG 8.1–5) and which inhibit a detailed description of the further evolution of the remnant. The assumed constancy of the external cosmic ray pressure is another restriction which will influence the net energy gain of cosmic rays. A stellar wind from the progenitor star can decrease the external cosmic ray pressure and in this case the SN will explode in a more or less cosmic ray pressureless environment. Due to our hydrodynamical description of the high energy particles we have not addressed the difficult question of injection of particles at the shock.

5 Conclusions

This numerical investigation demonstrates for the first time that a SN-explosion can transfer a significant part of its energy to cosmic rays. The obtained value of about 12%, probably an underestimate, is in general agreement with current estimates of the efficiency needed to replenish the observed cosmic ray energy density.

References

1. W.I. Axford, *Proc. IAU/IUPAP Symp. No. 94*, Dordrecht: D. Reidel, pp. 339–358 (1980)
2. H.J. Völk, in "High Energy Astrophysics", ed. by J. Tran Thanh Van, éditions Frontières, (1984)
3. L.O'C. Drury, *Rep. Progr. Phys.* **46**, 973 (1983)
4. E.A. Dorfi, L.O'C. Drury, submitted to *J. Comp. Phys.* (1985)

ONION-SHELL MODEL FOR COSMIC RAY ELECTRONS AND RADIO SYNCHROTRON EMISSION IN SUPERNOVA REMNANTS

by

R. Beck, L. O'C. Drury, H. Völk, Max-Planck-Institut für Kernphysik, Postfach 10 39 80, 6900 Heidelberg, W. Germany,

T.J. Bogdan, National Center for Atmospheric Research*, High Altitude Observatory, P.O. Box 3000, Boulder, CO. 80307, USA.

ABSTRACT

The spectrum of cosmic ray electrons, accelerated in the shock front of a supernova remnant (SNR), is calculated in the test-particle approximation using an "onion-shell" model. Particle diffusion within the evolving remnant is explicitly taken into account. The particle spectrum becomes steeper with increasing radius as well as SNR age. Simple models of the magnetic field distribution allow a prediction of the intensity and spectrum of radio synchrotron emission and their radial variation. The agreement with existing observations is satisfactory in several SNR's but fails in other cases. Radiative cooling may be an important effect, especially in SNR's exploding in a dense interstellar medium.

1. Introduction. Diffusive acceleration of relativistic particles in the shock fronts of supernova remnants (SNR's) is thought to be an important mechanism to replenish cosmic rays in the interstellar medium. In case of strong, steady, plane shocks, the particle energy spectrum $N(E) \propto E^{-q}$ becomes a power law with a slope of $q = 2$. In reality, intensity and slope of the spectrum are changed by various effects:
(i) The acceleration time is limited by the SNR age, leading to a high-energy cutoff. (ii) The SNR Mach number decreases with time. (iii) The particle energy decreases due to (adiabatic) expansion. (iv) Radiative cooling sets in below $\sim 10^6$ K temperature. (v) The back-reaction of the accelerated particles modifies strength and structure of the shock. (vi) The accelerated particles excite magnetohydrodynamic waves which produce a shock precursor. (vii) The accelerated particles (particularly the electrons) are subject to energy loss processes due to collisions and radiation.

The full particle transport equation can be solved only for rather special cases (1,2,3), which we cannot use here. Numerical studies of the hydrodynamical version of the time-dependent problem have been started only recently (4), but do not provide information about the particle spectrum. A test-particle model for the cosmic ray production by recurrent passages of SNR shock fronts has been discussed (5). Models for cosmic ray acceleration in a single SNR have been calculated (6,7), in which effects (i), (ii), (iii) and - schematically - (vi) are taken into account. The lifetime of the SNR is

---

* NCAR is sponsored by the NSF

(technically) split into equally spaced intervals corresponding to a series of shells, characterized by the Mach number of the bounding shock. Suprathermal particles with 1 keV energy are continuously injected into the shock front, accelerated up to the cutoff, according to the instantaneous shock Mach number in a shell, and adiabatically expanded with the gas until the gas pressure reaches the external pressure. Particles remain confined within their shell until being released at the end of the SNR evolution. The sum of the particle spectra from all these "onion shells" yields a power-law with q = 2.1-2.3 between 10^6 and several 10^{13} eV, only slightly varying with different choices of the injection energy and the other input parameters. Allowing for energy-dependent subsequent escape from the galaxy, the spectral index of the galactic radio emission is consistent with this model.

2. The Model. We have extended the "onion-shell" model to study the particle spectrum as a function of time and position. Instead of confining the particles to a shell we take account of both the intrinsic width of the acceleration region and of the subsequent diffusion by introducing a smearing length scale λ given by:

$$\lambda^2(t,E) = \left(\frac{\kappa(E)}{\dot{R}(t)}\right)^2 + \kappa(E)\ (t-t_o)$$

Here R(t) is the expansion velocity of the shock front; $(t-t_o)$ is the time since the formation of the shell at the shock. κ is the energy-dependent diffusion coefficient; it roughly increases proportional to particle energy. Due to wave generation by accelerated nucleons κ is taken to be given by the gyroradius limit; for 1 MeV electrons and 3 μG magnetic field strength κ becomes $\sim 10^{19}$ $cm^2 s^{-1}$. At low energies (< 1 GeV) the electrons still remain concentrated in their original shell while at the highest energies (> 1000 GeV) electrons essentially diffuse across the whole SNR.

The SNR is assumed to expand freely until the ejecta have swept up an equal mass of interstellar material. This initial phase is followed by an adiabatic Sedov phase, where $R \propto t^{2/5}$. After passage of the shock each shell expands with the downstream flow (8) until the time of observation t_F. Any point in the spectrum follows from the integral over the contributions from all shells at a fixed observation radius.

Hence it is possible to approximately compute the electron spectrum at any given SNR age and at any given radius.

The accelerated electrons emit synchrotron radio waves in the magnetic field of the SNR. Two extreme field models have been investigated, which bracket the actual situation: (I) constant field strength, (II) field compression $B \propto \varrho$. The distribution of relativistic electrons and of the magnetic field allows a prediction of the radio synchrotron emissivity. For comparison with radio observations, the emission from all shells along the line of sight has to be summed.

3. Results. Models have been calculated for different SNR ages (represented by the Mach number M_F at the time of observation) and for different external gas densities. The explosion was assumed to eject 1 $M_\odot$ with 10 000 km/s velocity. A field strength of 3 μG and a pressure of 1.5 10^{-12} dyne/cm^2 in the interstellar medium has been adopted.

Particles with low energies (< 1 GeV) are supplied by all shells created at different SNR ages. High-energy particles, however, are produced only during the early stages of the SNR evolution when the Mach number is high. This result still holds after extensive adiabatic expansion, i.e. for old adiabatic SNR's. Therefore, a steepening of the particle spectrum with increasing distance from the center is expected, except for the highest energies where diffusion dominates.

The spectral index for the electron energy spectrum between 10^6 and 10^{12} eV varies varies with radius. In young SNR's (final Mach number $M_F \geq 3$) almost no variation occurs. A spectral steepening occurs in the outer region of old adiabatic SNR's ($M_F \leq 2$). The corresponding radio spectral index between 100 MHz and 10 GHz frequency for $B \propto \text{const}$ (Fig. 1) refers to the emission along the line of slight radius R so that variations with R are somewhat smoothed out. The assumption B = const does not change the curves of Fig. 1 significantly. The spectral index of the integral radio emission varies with SNR age, from $\alpha \cong 0.60$ in young SNR ($M_F > 5$) to $\alpha \cong 0.65$ in old SNR ($M_F < 1.5$), which is consistent with the result given (6).

These general conclusions hold if the SNR remains adiabatic during its evolution. In fact, for an external hot interstellar medium gas density of $3 \times 10^{-3} cm^{-3}$ radiative cooling of the outer shell becomes important only in the latest phases ($M_F \leq 1.1$) when the downstream

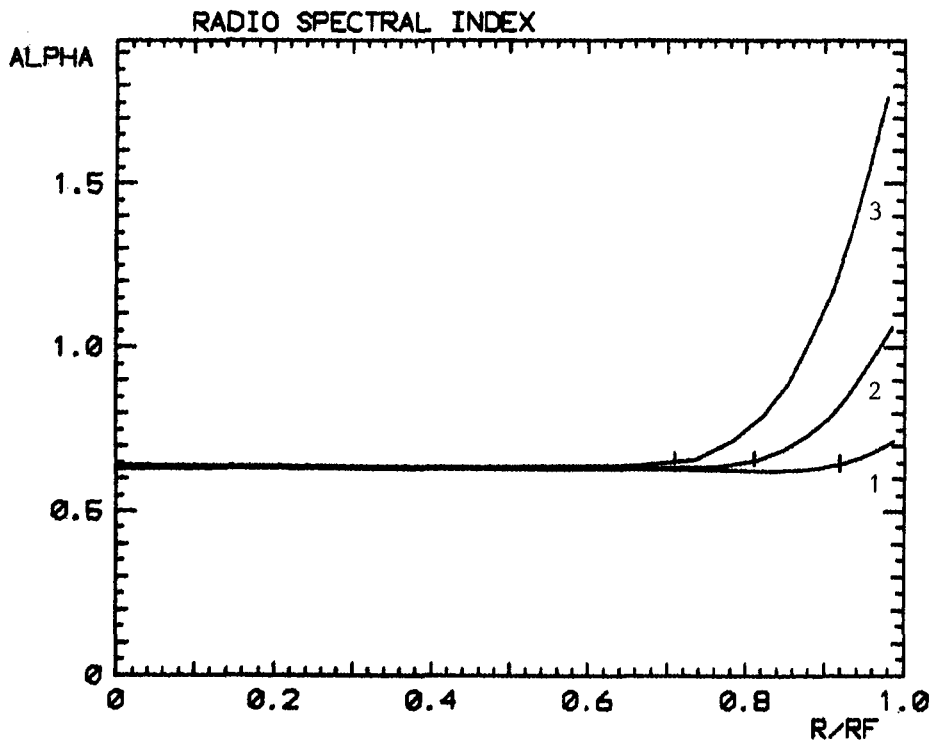

Fig. 1: The variation of radio synchrotron spectral index α with radius relative to the final radius R_F of the shock front for three models:
(1) Final Mach number $M_F = 3$ ($R_F = 90$ pc), (2) $M_F = 2$ ($R_F = 117$ pc),
(3) $M_F = 1.5$ ($R_F = 142$ pc). The maximum radio intensity is marked. At fixed external pressure the curves are independent of the external density.

temperature drops to 10^6 K. For larger densities, say $n \sim 3 \times 10^{-2} cm^{-3}$, shell cooling sets in earlier ($M_F \lesssim 3$). Then the outer shock tends to become isothermal. The increased compression ratio then yields a harder spectrum, at least for high energies, leading to a radial decrease of the spectral index. Although this effect is not explicitly treated here, it is an obvious diagnostic possibility regarding the evolutionary state of a given SNR, with radial increase (decrease) indicating an adiabatic (radiative) phase of the compressed outer shell.

4. Comparison with observations. The mean spectral index of SNR's, including also flat-spectrum (Crab-type) SNRs, is $\alpha = 0.45 \pm 0.15$ (9) which is not inconsistent with the prediction of the "onion-shell" model. The same data do not indicate a correlation between SNR spectral index and diameter(10), while in a more recent catalogue (11) a statistically weak flattening with increasing diameter is visible. Since the diameter depends mainly on the initial velocity and the external gas density and is far from being a unique measure of SNR age, these observations do not conflict with our model.

The determination of radio spectral index within a SNR requires an accurate subtraction of the background emission which is difficult especially for large SNRs in the galactic plane. The remnant of Tycho's supernova is a favourite object because it is small and radio-bright. The spectral index of the integrated emission is $\alpha = 0.61 \pm 0.03$ without a significant variation across the remnant (12).This agrees with the prediction of our model for young SNR's. The large, probably old, SNR G65.2+5.7 in Cygnus reveals a spectral steepening from $\alpha \cong 0.4$ in the inner part to $\alpha \cong 0.6$ in the main shell of emission, followed by an increase to $\alpha \cong 1.0$ beyond, (13), as expected in view of our model.

A larger sample of SNRs with radial spectra has now become available (Fürst, private communication). In most cases, no spectral index variation across the SNR is detected. In some sources, however, the spectrum seems to flatten with radius, indicating the limits of the model presented here.

References

1. Drury, L. O'C., Axford, W.I., Summers, D.: 1982, MNRAS 198, 833.
2. Bogdan, T.J., Lerche, I: 1985, MNRAS 212, 413.
3. Webb, G.M., Bogdan, T.J., Lee, M.A., Lerche, I.: 1985, MNRAS (submitted).
4. Dorfi, E.: 1984, Adv. Space Res. 4, No. 2-3, 205.
5. Blandford, R.D., Ostriker, J.P.: 1980, Astrophys.J. 237, 793.
6. Bogdan, T.J., Völk, H.J.: 1983, Astron.Astrophys. 122, 129.
7. Moraal, H., Axford, W.I.: 1983, Astron.Astrophys. 125, 204.
8. Kahn, F.D.: 1975, Proc. 14th Int. Cosmic Ray Conf., München, Vol. 11, 3566.
9. Clark, D.H., Caswell, J.L.: 1976, MNRAS 174, 267.
10. Lerche, I.: 1980, Astron.Astrophys. 85, 141.
11. Green, D.A.: 1984, MNRAS 209, 449.
12. Klein, U., Emerson, D.T., Haslam, C.G.T., Salter, C.J.: 1979, Astron.Astrophys. 76, 120.
13. Reich, W., Berkhuijsen, E.M., Sofue, Y.: 1979, Astron.Astrophys. 72, 270.

THREE DIMENSIONAL CALCULATION OF FLUX OF LOW ENERGY ATMOSPHERIC NEUTRINOS

H. Lee‡ and S. A. Bludman‡
Department of Physics, University of Pennsylvania, Philadelphia, PA19104

Abstract; Results of three-dimensional Monte Carlo calculation of low energy flux of atmospheric neutrinos are presented and compared with earlier one-dimensional calculations [1,2] valid at higher neutrino energies. These low energy neutrinos are the atmospheric background in searching for neutrinos from astrophysical sources. Primary cosmic rays produce the neutrino flux peaking at near $E_\nu = 40$ MeV and neutrino intensity peaking near $E_\nu = 100$ MeV. Because such neutrinos typically deviate by $20^0 \sim 30^0$ from the primary cosmic ray direction, three-dimensional effects are important for the search of atmospheric neutrinos. Nevertheless, the background of these atmospheric neutrinos is negligible for the detection of solar and supernova neutrinos.

1. Introduction

Recently one-demensional Monte Carlo calculations of cosmic ray production of neutrinos in the Earth's atmosphere, including geomagnetic and solar modulation effects, were reported [1,2]. These calculations agree well with the flux and angular distribution of neutrinos of energy $E_\nu > 200$ MeV observed in underground detectors. But these earlier one-dimensional cascade calculations are inapplicable to neutrinos of lower energy $E_\nu < 50$ MeV important in neutrino astronomy. In fact, we shall see (Fig. 3) that the mean angular deviation between the primary cosmic rays and neutrinos is appreciable even for neutrinos of several hundred MeV. The flux of low-energy atmospheric neutrinos we obtain (Fig. 2) in the present three-dimensional calculation is negligible compared with the known flux of solar or supernova neutrinos, but maybe significant in the case of other sources of astrophysical neutrinos.

The three-dimensional atmospheric neutrino flux is

$$dN_\nu(E_\nu, \theta_\nu, \phi_\nu)/dE_\nu = \int y_\nu \Omega(E_p, \theta_p, \phi_p, \lambda)(dN_p/dE_p) dE_p d\omega_p,$$

where $y_\nu(E_\nu, \theta_\nu, \phi_\nu, E_p, \theta_p)$ is the yield of neutrinos of energy E_ν, zenith angle θ_ν and azimuth angle ϕ_ν by primary cosmic rays of energy E_p and zenith angle ϕ_p. dN_p/dE_p is the primary cosmic ray spectrum, and $\Omega(E_p, \theta_p, \phi_p)$ is the geomagnetic cut-off. This geomagnetic cut-off depends on geomagnetic latitude λ and magnetic rigidity $R = pc/e$ where p is the primary cosmic ray's momentum.

2. Calculational details

We modified the Gaisser-Protheroe-Stanev one-dimensional hadron interaction model [5] by assigning to secondary particles the transverse momentum distribution.

‡ Work supported by U.S. Department of Energy

$$W(a, x_t) = (a + 1)(a + 2)x_t(1 + x_t)^a.$$

Here $a = 2p/\langle p_t \rangle - 3$ for $p > 1.5\langle p_t \rangle$, a = 0 for $p < 1.5\langle p_t \rangle$, $x_t = p_t/p$ and p is the incident hadron's momentum. At high p, $W \sim p_t exp(-ap_t)$. The angular deviation of secondary hadrons from the incident hadron direction produced by the above formula affects our results insignificantly.

In our computer program analytic formulae are used for the energy distribution of decay particles. For those energies, a microcanonical ensemble average is taken; total energy is conserved in each individual decay. The secondary directions are, however, assigned according to a canonical ensemble; the total momentum is conserved on average but not in individual decays. Interaction cases are treated similarly. We use energy-independent energy loss rates for charged particles by air ionization in a simple isothermal atmosphere to determine the decay height and energy, and energy-dependent formulae to determine the interaction height and energy. Our results are insensitive to these parameters.

For the comparison with the earlier one-dimensional calculation we calculated the yield function

$$Y_\nu(E_\nu, E_p, \theta_p) \equiv \int y_\nu(E_\nu, \theta_\nu, \phi_\nu, E_p, \theta_p) d\omega_\nu,$$

integrated over appropriate neutrino directions.

3. Results and Conclusions

Fig. 1 shows the yield Y_ν of vertically incident protons of several energies E_p, integrated over the downward 2π solid angle of neutrino's directions. Because low-energy neutrinos are made mainly from low-enrgy pions and muons at rest, for all primary cosmic ray energies the peak flux occurs near 40 MeV and the peak intensity near 100 MeV. Because most muons decay at rest and $\langle E_{\nu_e} \rangle = 0.3E_\mu$, $\langle E_{\nu_\mu} \rangle = 0.35E_\mu$, the atmospheric neutrino flux peaks near 40 MeV.

Fig. 2 shows the downward neutrino flux produced by vertically incident primaries at high geomagnetic latitude, where

$$dN_\nu/dE_\nu \cong \int Y_\nu \Omega (dN_p/dE_p) dE_p.$$

While this expression is not exact for a three-dimensional cascade, it compares simply with the one-dimensional calculations. The near-vertical neutrino flux is also insensitive to zenith angle. Because, if not supressed by geomagnetic cut-off, the primary cosmic rays have a steep power-law spectrum, the main contribution to the low-energy neutrino flux is from primary cosmic rays just above the pion-production threshold energy. The total flux is therefore very sensitive to geomagnetic cut-off [6].

For neutrinos above $E_\nu = 200$ MeV, this three-dimensional calculation agrees with earlier one-dimensional calculations [1,2]. At lower energies ($E_\nu < 50$ MeV), however, we now obtain neutrino fluxes significantly lower than those one-dimensional calculations would give.

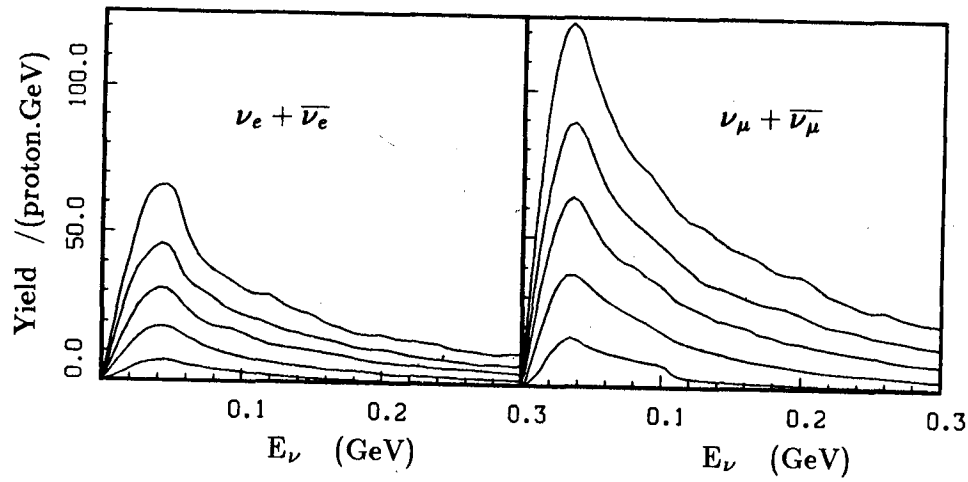

Fig. 1. Integrated neutrino yields from vertically incident protons. 2 5 10 20 50 GeV cases from bottom to top.

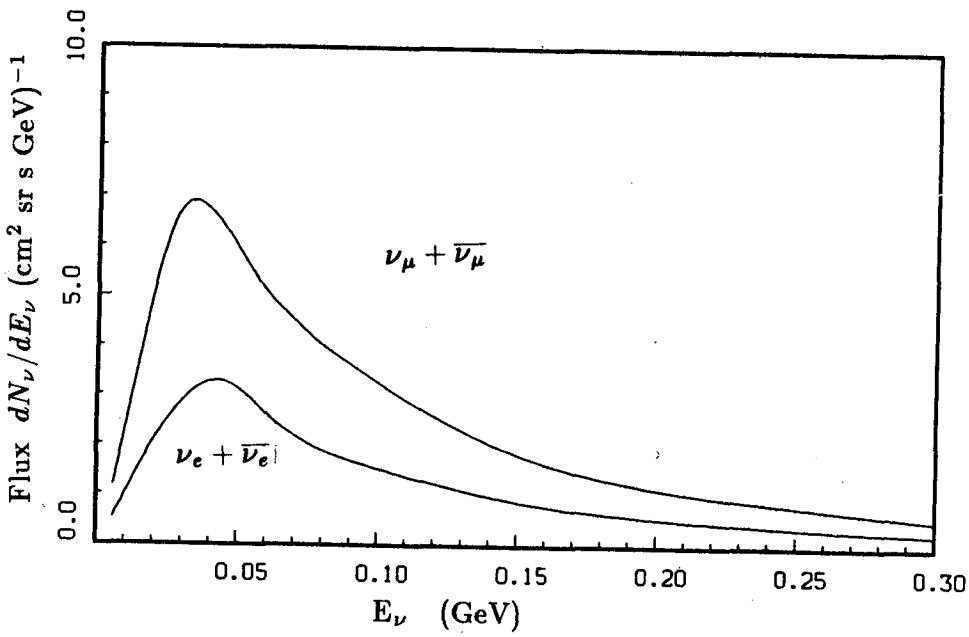

Fig. 2. Calculated downward neutrino flux at high geomagnetic latitude

This atmospheric neutrino background is totally negligible compared to the solar neutrino flux and the flux of neutrinos expected from supernova at any reasonable distance ($< 10^3$ Mpc).

Fig. 3 shows the average angular deviation of down-going ν_es of energy E_ν produced by vertically incident protons of energy E_p = 2, 10, 50 GeV. Other neutrino types have similar spectra. While average angular deviation is $20^0 \sim 30^0$, neutrino direction at neutrino energy below 50 MeV is near isotropic and a long tail of more energetic neutrinos deviating by $5^0 \sim 10^0$ is produced at $E_\nu > 200$ MeV.

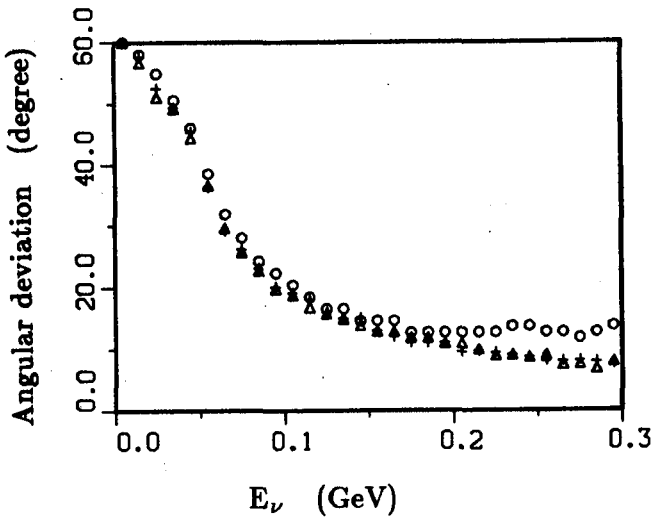

Fig. 3. ν_e angular deviation from primary proton.
2 GeV (○), 10 GeV (△), 50 GeV (+) cases.

Acknowledgements; We thank to T. K. Gaisser and Todor Stanev for useful discussions.

References

[1] T. K. Gaisser, Todor. Stanev, S. A. Bludman and H. Lee, Phys. Rev. Lett 51, 223(1983) and Fourth Workshop on Grand Unification (FWOGU), U. of Pennsylvania, (Birkhauser, Boston, ed. A. Weldon, P. Langacker, P. J. Steinhart, p. 87 (1983)).

[2] T. K. Gaisser and Todor Stanev, to appear in Proc. ICOBAN '84, Park City, Utah, Jan. 1984.

[3] Private communication with T. K. Gaisser and Todor Stanev, also *see* , T. K. Gaisser and Todor Stanev, to appear in Proc. Neutrino '84 conference, Dortmund, June 1984.

[4] D. J. Cooke, Phys. Rev. Lett. 51, 320 (1983).

[5] T. K. Gaisser, R. J. Protheroe and Todor Stanev, Proc. 18th ICRC (Bangalore) 5, 174 (1983)

[6] H. Lee and S. A. Bludman, exact 3-dimensional expression of neutrino flux and angular dependence is in preparation.

APPROXIMATE SUPERNOVA REMNANT DYNAMICS WITH COSMIC RAY PRODUCTION

by

H.J. Völk, L. O'C. Drury, Max-Planck-Institut für Kernphysik, Postfach 10 39 80, 6900 Heidelberg, W. Germany, and E. Dorfi, Institut für Astronomie, Universitäts-Sternwarte, Wien, Austria.

Introduction: Supernova explosions are the most violent and energetic events in the galaxy and have long been considered probable sources of Cosmic Rays (1). Recent shock acceleration models (2,3), treating the Cosmic Rays (CR's) as test particles in a prescribed Supernova Remnant (SNR) evolution, indeed indicate an approximate power law momentum distribution $f_{source}(p) \sim p^{-a}$ for the particles ultimately injected into the Interstellar Medium (ISM). This spectrum extends almost to the momentum $p = 10^6$ GeV/c, where the break in the observed spectrum occurs. The calculated power law index $a \simeq 4.2$ agrees with that inferred for the galactic CR sources. The absolute CR intensity can however not be well determined in such a test particle approximation.

It is important to know the intensity which results if the CR's are selfconsitently included in the dynamics of the SNR, and whether the predicted spectral characteristics are approximately conserved in such a nonlinear treatment. In the average ISM the CR energy density is comparable to the thermal and magnetic energy densities. Thus, in their sources the CR's must also be a significant dynamical element that manifests itself through its pressure as well as its high energy current (4,5). In fact the usual estimates for the observationally required CR production efficiency of SNR sources are too low by about a factor 4 which raises the overall production efficiency from the traditional 2 to 4 percent of the average SNR energy input rate to about 8 to 16 percent. The reason is simply that not the observed intensity

$$f_{obs}(p) \sim p^{-4.75}$$

but the source intensity f_{source}, obtained from f_{obs} by correction for rigidity dependent escape $\tau_e(p) \sim p^{-\varepsilon}$ must be replenished after a CR lifetime $\tau_e(p \simeq 1$ GeV/c) of about $2 \cdot 10^7$yrs. Taking $\varepsilon = 0{,}55$ (6,7,8) and a cutoff momentum of 10^6 GeV/c, the additional input rate corresponding to the hatched region in Fig. 1 is about a factor of 2.75 larger than the one corresponding to f_{obs}, leading to a factor $(4.75-4)/(4.75-4-\varepsilon) = 3.75$ increase in the overall efficiency requirement. According to the test particle models, most of the acceleration must take place prior to the phase in which the SNR radius is about a factor 4 below

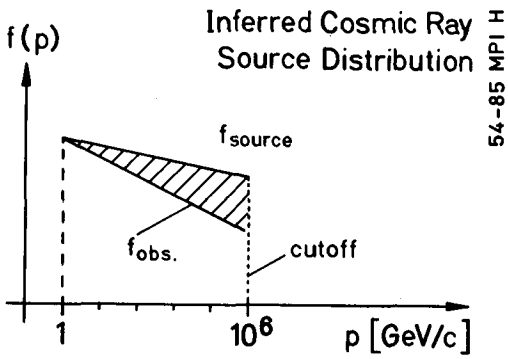

Fig. 1: The inferred source distribution f_{source} for rigidity dependent escape from the galaxy up to the cutoff imposed by the finite acceleration time in SNR's.

its radius at particle release. Therefore the instantaneous early conversion efficiency must be about 4 times higher than the required average acceleration efficiency and correspond to 32 to 64 percent of the total energy input rate per supernova. Thus one must expect an extensive CR reaction on SNR dynamics. This is not only of interest for CR origin but also for the overall structure of the ISM in galaxies.

This paper discusses simplified models for SNR evolution with CR's. Although ultimately this must be calculated numerically, such models are needed to clarify the numerical results. They are important for parameter studies and provide a first iteration and rough guidance for the interpretation of observations. Since the present theory only calculates macroscopic CR quantities we do not get spectral information about the particle distribution, but information on the most important unknown, the overall efficiency of the acceleration process.

2. Phases of SNR evolution: In the initial phase of a SNR the cooling ejecta sweep up external interstellar material until a reverse shock runs into the interior and heats it to high temperatures. Even though the reverse shock will certainly accelerate particles from the ejecta and may in fact push the maximum particle energy from a disk SNR easily to 10^6 GeV with interesting consequences for the chemical and isotopic composition in this energy range, it is not included in the model presented here. We consider the subsequent phases where the outer shock is driven by a uniform hot interior generating a uniform dense shell with a thickness ΔR that is small compared to the remnant radius R(t) (Fig. 2). The local physical variables in the shell are assumed to have their postshock values.

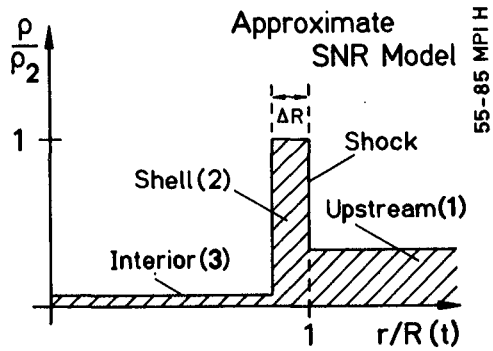

Fig. 2: Density field in a 2-shell model for a SNR, where upstream ISM, shell, and interior parameters are denoted by the suffices 1,2, and 3 respectively. All mass is concentrated in the shell, all internal energy in the interior.

Such an approximation is by no means new. For the adiabatic phase it has been used e.g. by Chernyi (9) and it is standard for the so-called pressure modified snowplow phase after the onset of shell cooling. We apply it here for particle acceleration and backreaction on the gas dynamics in a hydrodynamic approximation for the CR, or High Energy Component as the energy containing part of the CR spectrum below 10^6 GeV/c might be more appropriately called (10).

Mass balance is then given by

$$\frac{d}{dt}(M_s) = \frac{d}{dt}(M_3) + 4\pi R^2 \cdot \rho_1 \cdot \frac{dR}{dt} \qquad (1)$$

, where the total mass M_s is assumed to be concentrated in the shell and $dM_3/dt \sim T_3^{5/2}$ denotes the mass evaporation rate from cold clouds in the hot interior with temperature T_3. Momentum balance is that of the shell

$$\frac{d}{dt}\,(M_s \cdot v_2) = 4\pi R^2 \cdot (p_3 - p_1) \qquad (2)$$

where v_2 is the postshock mass velocity, and the total pressure $p = p_g + p_c$ is the sum of gas pressure p_g and CR pressure p_c. In the adiabatic phase where gas cooling is unimportant overall energy conservation - neglecting any other CR energy losses than adiabatic ones - reads as

$$\frac{d}{dt}\left\{\frac{1}{2} M_s v_2^2 + \frac{4\pi}{3}R^3 \cdot \frac{p_{g3}}{(\gamma-1)} + \frac{4\pi}{3}R^3 \cdot \frac{p_{c3}}{(\gamma_c-1)}\right\} = 4\pi R^2 \cdot \frac{dR}{dt} \cdot \left\{\frac{p_{g1}}{(\gamma-1)} + \frac{p_{c1}}{(\gamma_c-1)}\right\} \qquad (3)$$

Here $\gamma = 5/3$, and $4/3 < \gamma_c < 5/3$ are the effective adiabatic indices of thermal gas, and CR's, respectively. CR energy balance can be written as

$$\frac{d}{dt}\left\{\frac{4\pi}{3} R^3 \cdot \frac{p_{c3}}{(\gamma_c-1)}\right\} = 4\pi R^2 \cdot v_2 \cdot (p_{c2} - p_{c3}) - 4\pi R^2 \cdot \left\{F_{c2} - \frac{dR}{dt} \cdot \frac{p_{c2}}{(\gamma_c-1)}\right\} \qquad (4)$$

, where $F_c = v \cdot p_c \cdot \gamma_c/(\gamma_c-1) - (\partial p_c/\partial r) \cdot \bar{\kappa}/(\gamma_c-1)$ is the local CR energy flux density, $\bar{\kappa}$ the mean CR diffusion coefficient (10), and we have assumed $v(r,t) = v_2(t) \cdot r/R(t)$ in rough correspondence to the selfsimilar Sedov solution.

For the particle acceleration at the shock (Fig. 2) we assume a quasi-stationary state, i.e. steady fluxes of mass, momentum and total energy in the shock frame plus local Energetic Particle Hydrodynamics (11). Due to the finite acceleration time this is a far reaching assumption indeed. However, adiabatic cooling in the expanding SNR introduces a finite postshock gradient in CR pressure which couples the acceleration at the shock to the interior dynamics. Among other effects this is equivalent to an instantaneous cutoff of the accelerated spectrum at that particle momentum where the acceleration time becomes equal to the SNR lifetime.

Radiative cooling of the shock heated gas sets in for $T \lesssim 10^6$K. Unless cloud evaporation were so efficient that cooling set in first in the interior (12), cooling leads to a dense shell and an adiabatic interior: $p_{g3} \sim R^{-5}$ and $v_2 \simeq dR/dt$. Of course the CR's do not cool radiatively. Due to the now lower shock speed some of the highest energy particles escape, but the rest still continues to be accelerated, driving the remnant. The higher energy particles should then be accelerated across the dense shell where they are scatterfree due to ion-neutral damping of hydromagnetic waves (13). Neglecting $p_{g2} - p_{g3}$ across the thin shell, continuity of mass and momentum flux allows one to simply determine the pressure p_{c2} of accelerated particles

$$p_{c2} = \rho_1 \cdot (dR/dt)^2 + p_{c1} + (p_{g1} - p_{g3}) \qquad (5)$$

in terms of the shock velocity and overall gas pressure contrast.

3. Preliminary conclusions: (i) the CR's take away internal energy from the gas with earlier onset of cooling, while on the other hand (ii) the CR's cool much less due to their softer equation of state so that they can push the shell from the interior longer than the gas (iii) coupling with the interior introduces an effective time dependence of acceleration through a cutoff in the spectrum (iv) disregard of the sweep-up phase makes the model somewhat inconclusive regarding the relative contribution of gas and CR pressure during the earliest phases (v) After cooling the effective shock compression ratio increases, leading possibly to harder momentum spectra for older shocks with intriguing consequences for the radial (synchrotron) spectral index variation in SNR's.

References

1. Ginzburg, V.L., Syrovatsky, S.I.: 1964, "The Origin of Cosmic Rays (transl. H.S.M. Massey, ed. D. ter Haar), Macmillan Co., New York.
2. Bogdan, T.J., and Völk, H.J.: 1983, Astron.Astrophys. 122, 129.
3. Moraal, H., and Axford, W.I.: 1983, Astron.Astrophys. 125, 204.
4. Axford, W.I.: 1981, Proc. 17th Intl. Cosmic Ray Conf. 12, 155.
5. Drury, L. O'C.: 1983, Rep.Progr.Phys. 46, 973.
6. Juliusson, E., et al., 1972, Phys.Rev. Letters, 29, 445.
7. Koch-Miramond, L.: 1984, in "High Energy Astrophysics", Proc. 19th Rencontre de Moriond Astrophysics Meeting (J. Tran Thanh Van, ed.), Editions Frontieres, p. 265.
8. Simon, M., and Mathis, K.D., 1983, Proc. 18th Intl. Cosmic Ray Conf. 2, 215.
9. Chernyi, G.G., 1957, Dokl.Akad.Nauk SSSR 112, 213.
10. Völk, H.J.: 1984, in "High Energy Astrophysics", Proc. 19th Rencontre de Moriond Astrophysics Meeting (J. Tran Thanh Van, ed.), Editions Frontieres, p. 281.
11. Drury, L.O'C., and Völk, H.J.: 1981, Astrophys. J. 248, 344.
12. Cowie, L.L., McKee, C.F., Ostriker, J.P.: 1981, Astrophys.J. 247, 908.
13. Kulsrud, R.M., and Pearce, W.: 1969, Astrophys.J. 156, 445.

EFFICIENCY OF REGULAR ACCELERATION OF PARTICLES BY A SHOCK WAVE AT DIFFERENT INJECTION REGIMES

E.G.Berezhko, V.K.Yelshin, G.F.Krymsky, A.A.Turpanov

Institute of Cosmophysical Research & Aeronomy,
Lenin Ave., 31, 677891 Yakutsk, USSR

1. Introduction. A significant fraction of the inflowing plasma energy in the collisionless shock vicinity might be transferred to the particles accelerated by a regular acceleration mechanism [1,2], [3-6]. The accelerated particles back pressure modifies an infinite planar shock structure so that a profile of the plasma flow velocity $u(x)$ in the shock frame has two characteristic length scales as it is seen in Fig.1.

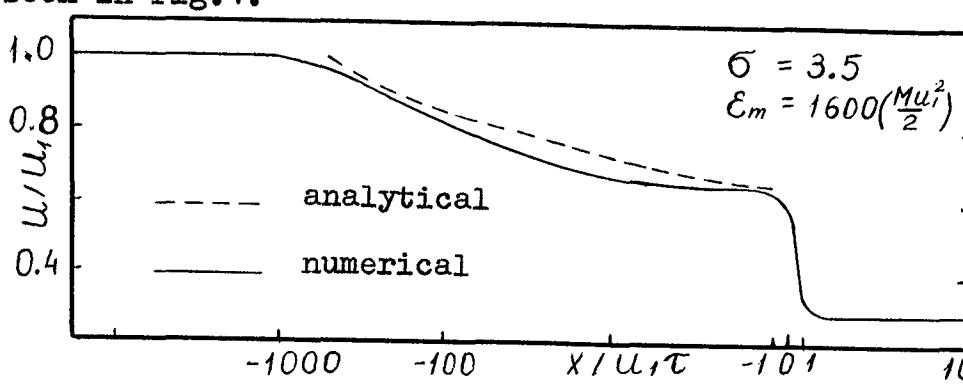

Fig.1.

The smooth velocity transition $u_1 \leq u \leq u_s$ within the scale $L \simeq \varkappa(\varepsilon_m)/u_1$ (the precursor) is due to the accelerated particles pressure; the abrupt decrease from u_s to u_2 within the scale $\ell \simeq \lambda_T$ (the subshock) is caused by the thermal particles. Here λ_T is the mean free path of the thermal particles, $\varkappa$ - the energetic particles diffusion coefficient, ε_m - the maximum (or cutoff) particle energy.

The parameter $\beta = (u_1 - u_s)/u_1$ is introduced to express quantitatively the modification level. If the magnetic field dynamics within the precursor is neglected, β might be related to the fractional pressure P_c of the accelerated particles at the subshock. For nonrelativistic particles $P_c = \beta \rho_1 u_1^2 = \rho_2 \beta \sigma/(\sigma-1)$, where ρ_1 is the upstream ($x=-\infty$) plasma mass density, σ -the total compression ratio, P_2 -the postshock plasma pressure. The interrelation between $P_c, \beta, \varepsilon_m$ and the rate of the thermal particles injection to the acceleration process is an important but poorly investigated question.

2. Method and Results. It follows from the transport equation for the accelerated particles under certain approximations [3,4] that within the precursor

$$\ln \frac{\varepsilon_m}{\varepsilon_s} = \int_{u_s}^{u_1} \frac{du}{u_1} \left(\frac{\rho_1 u_1^2}{\rho} \right), \qquad (1)$$

where the partial pressure $p = dP/d\ln\varepsilon$ is related to the plasma flow velocity by

$$\frac{p}{\rho_1 u_1^2} = \frac{u-u_2}{u_1} + \frac{3}{2\sigma}\ln\frac{u-u_2}{u_1} + C \quad . \qquad (2)$$

The constant C should be determined by matching $p(\varepsilon)$ to the thermal spectrum at some energy ε_s, which separates thermal particles from the accelerated ones. Assume the injection energy ε_s be equal to $Mu_1^2/2$ (M - the particle mass). Assume also that the accelerated particles with the mean free path larger than ℓ do not interact with the subshock. In such a case p_{inj} should be a function of the subshock compression ratio $\sigma_s = u_s/u_2$ only. Since determination of the injection function $p_{inj}(u_s/u_2)$ is a complicated problem itself, we assumed it to be constant.

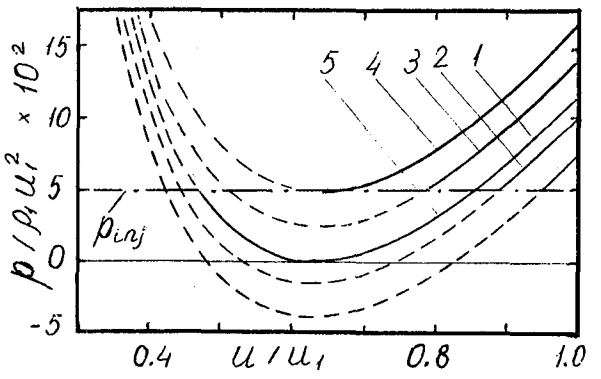

Fig.2.

1 - $\varepsilon_m = 2.5\,\varepsilon_s$

2 - $\varepsilon_m = 4.8\,\varepsilon_s$

3 - $\varepsilon_m = 15.0\,\varepsilon_s$

4 - $\varepsilon_m = 178.0\,\varepsilon_s$

5 - $\varepsilon_m = \infty$

Fig.2 represents a family of curves $p(u)$ vs. u for a set of parameters C corresponding to different u_s and ε_m. Solid lines indicate a physically reasonable range $u_s \le u \le u_1$ at $p_{inj} \le 5\cdot10^{-2}\rho_1 u_1^2$ for $\sigma = 4$. It follows from (1) and (2) that if $u_s < \frac{5}{2\sigma}u_1$

$$u_s \simeq \left[\frac{5}{2\sigma} - \sqrt{\frac{3p_{inj}}{\sigma\rho_1 u_1^2} - \left(\frac{3\pi}{\sigma\ln(\varepsilon_m/\varepsilon_s)}\right)^2}\right]u_1 . \qquad (3)$$

If $u_s > \frac{5}{2\sigma}u_1$ (curves 1-3) this relationship is :

$$u_s \simeq \left[1 - \frac{2(\sigma-1)}{2\sigma-5}\frac{p_{inj}}{\rho_1 u_1^2}\left(\left(\frac{\varepsilon_m}{\varepsilon_s}\right)^{\frac{2\sigma-5}{2(\sigma-1)}} - 1\right)\right]u_1 . \qquad (4)$$

It is seen from this expression that the modification level is limited by $\beta_{max} = \frac{2\sigma-5}{2\sigma} + \sqrt{\frac{3p_{inj}}{\sigma\rho_1 u_1^2}}$ corresponding to the highest attainable pressure of the accelerated particles $P_c/P_2 = \frac{2\sigma-5}{2(\sigma-1)} + \frac{\sigma}{\sigma-1}\sqrt{\frac{3p_{inj}}{\sigma\rho_1 u_1^2}}$ which is reached at $\varepsilon_m = \infty$ (curve 5). The above conclusion differs from that one derived in the hydrodynamical approach [7].

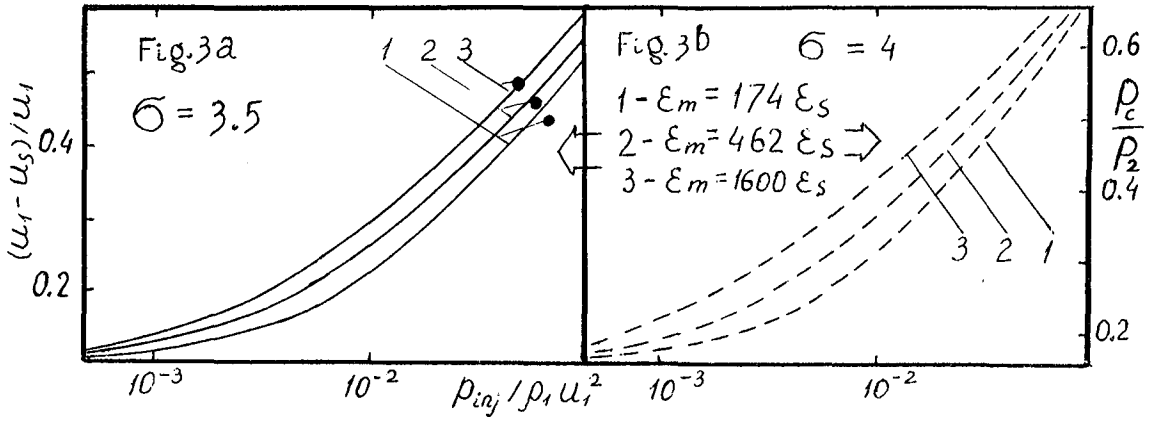

The existence of the significant dependence of the modification level and the acceleration efficiency on the injection rate is illustrated by Fig.3 representing β and P_c vs. ρ_{inj} at different ε_m for $\sigma = 3.5$ (solid lines) and $\sigma = 4$ (dashed lines). Circles are results of the numerical shock structure simulation via the Boltzmann equation [6] with $\sigma = 3.5$ and $\varepsilon_m/\varepsilon_s$ = 174, 462, 1600.

After the constant C in (1) has been determined for $\rho_{inj} = 0.05\rho_1 u_1^2$ that corresponds to a numerical simulation, the equation (1), with ε_s and u_s replaced with ε and u respectively, yields u as a function of ε which, in turn, is related to x by $x = \mathcal{X}(\varepsilon)/u(\varepsilon)$ and $\mathcal{X}(\varepsilon) = 2\varepsilon\tau/3M$ (τ =const). The analytical and numerical solutions for velocity profiles at $\sigma = 3.5$ and ε_m = 1600 ε_s are compared in Fig.1.

The results of the analytical and numerical solutions represented in Figs.1,3 are in a reasonable agreement confirming the adequacy of the approximations used while deriving (1) and (2). The analogous conclusion was drawn in [8] published when the present paper was in preparation.

3. Summary. Thus, the above analysis leads to the following conclusions:

The acceleration efficiency, the modification level and the precursor structure are well fitted by the analytical approximation [3,4], provided that the injection function $\rho_{inj}(u_s/u_2)$ is known. The modification level and the acceleration efficiency are in the considerable dependence on ρ_{inj}. The fractional energy of the accelerated particles (i.e. the acceleration efficiency) and the shock modification level increase as the cutoff energy ε_m increases. However, for an arbitrarily large Mach numbers there exist the finite limiting values of the acceleration efficiency and modification level corresponding to $\varepsilon_m \to \infty$. When taken into account the energy flux, carried away by particles escaping through q might slightly modify the above results. But conclusion on the injection rate role should remain valid. Thus, the investigation of the thermalization process of the particles at the shock seems to be the important problem for the shock acceleration theory.

References.

1. Krymsky, G.F., (1977), Dokl.AN SSSR, 234, № 6, 1306.
2. Axford, W.I., et al., (1977), Proc.15-th ICRC, Plovdiv, 11, 132.
3. Eichler, D., (1979), Astrophys.J., 229, 419.
4. Krymsky, G.F., (1981), Izv.AN SSSR, Ser.fiz., 45, 461.
5. Ellison, D.C., (1984), Ph.D.Thesis, Catholic Univ., Washington, D.C.
6. Berezhko, E.G., et al., (1983), Proc.18-th ICRC, Bangalore, 2, 259.
7. Völk, H.J., (1984), Paper Presented at the 4-th Moriond Astrophys.Meeting "Cosmic Rays and Elementary Particles",

La Plagne.
8. Ellison, D.C., Eichler, D., (1984), Astrophys.J., 286, 691.
9. Eichler, D., (1984), Astrophys.J., 277, 429.

A NUMERICAL STUDY OF DIFFUSIVE SHOCK ACCELERATION OF COSMIC RAYS IN SUPERNOVA SHOCKS

C. M. Ko
J. R. Jokipii
University of Arizona
Tucson, Arizona 85721 U.S.A.

Abstract. The evolution of the energy spectrum of cosmic rays accelerated by the first order Fermi mechanism, by a supernova remnant shock wave, including adiabatic deceleration effects behind the front, is carried out by means of a time-dependent numerical code. The calculations apply to the adiabatic stage (or Sedov stage) of the supernova explosion, and the energetic particle spectrum is calculated in the test particle limit (i.e., the back reaction of the cosmic rays on the flow is not included). The particles are injected mono-energetically at the shock. We show the radial distribution, and the spectrum of the accelerated and decelerated particles.

I. Introduction. Diffusive acceleration of cosmic rays at collisionless astrophysical shock waves, where the particles pass (diffuse) across a plane shock repeatedly is a promising candidate for the origin of cosmic rays (Axford, Leer and Skadron, 1977; Krymskii, 1977; Bell, 1978; Blandford and Ostriker, 1978).

Supernova explosions have long been supposed to be the origin of cosmic rays, primarily because of the energy they liberate. The diffusive shock acceleration mechanism has been applied to spherically symmetric supernova shocks (Krymskii and Petukhov, 1980, Prishchep and Ptuskin, 1981; Drury, 1983) and analytical solutions can be obtained with the assumption that $K/R\dot{R}$ is a constant (see also Blandford and Ostriker, 1980 Bogdan and Völk, 1983; Moraal and Axford, 1983).

In this paper, we solve the time dependent problem of cosmic rays diffusively accelerated in a spherical shock by numerical integration.

II. The Model. Under the assumption that there is sufficient scattering that the pitch-angle distribution is nearly isotropic (diffusion limit) the cosmic ray transport equation (Parker, 1965) may be written (for spherical symmetry) as:

$$\frac{\partial f}{\partial t} = \frac{1}{r^2}\frac{\partial}{\partial r}\left(Kr^2\frac{\partial f}{\partial r}\right) - U\frac{\partial f}{\partial r} + \frac{1}{3}\left(\frac{1}{r^2}\frac{\partial}{\partial r}(r^2U)\right)p\frac{\partial f}{\partial p} + S \quad , \qquad (1)$$

where $f(t,\vec{r},\vec{p})$ is the phase space distribution function, U is the flow velocity, and S is the source.

If there is a shock at radius R, we require f to be continuous at the shock (Toptygin, 1980), and the jump in streaming flux can be obtained by integrating (1) across the shock. Subscript 1 corresponds to the region outside the shock (upstream region), while subscript 2 corresponds to the region inside the shock (downstream region), the boundary conditions at the shock are:

$$f_1 = f_2 \quad \text{and} \quad \left[K\frac{\partial f}{\partial r} + \frac{Up}{3}\frac{\partial f}{\partial p}\right]_2^1 = -\lim_{\epsilon \downarrow 0}\int_{R-\epsilon}^{R+\epsilon} S\, dr \quad . \qquad (2)$$

III Supernova Shock If the shock front is moving, i.e., R = R(t), then it is useful to use the following dimensionless quantities:

$$\xi = r/R(t) \quad , \quad \tau = K_0 t/R^2(t) \quad \text{and} \quad q = \ln(p/p_0) \quad , \qquad (3)$$

where K_0 and p_0 are constants to be defined later. This transformation breaks down if $2t\dot{R}/R = 1$ because the Jacobian of the transformation is then zero. Note that if K is constant and so is $R\dot{R}/K$, then $R \propto t^{1/2}$.

Assume a velocity profile $U = \dot{R}V(\xi)\theta(1-\xi)$ (e.g. Sedov's blast wave; Sedov, 1959) and consider particle injection at the shock, i.e.,

$$S = Q\delta(r-R)\delta(p-p_0) = \frac{Q}{Rp_0}\delta(\xi-1)\delta(q_\xi) \quad , \tag{4}$$

where the units of Q are #/sec/length^2/momentum^2. If $V(\xi)$ goes to zero faster than ξ^k , $k > 1$ (which is true for Sedov's blast wave approximation), then $V(0)=0$ and $\partial(\xi^2 V)/\partial\xi|_0 = 0$ (i.e., the boundary condition at $\xi=0$ is $\partial f/\partial\xi = 0$). If we assume self-similar solutions to the shock, $R = At^\alpha$, then by equation (3) we have:

$$\tau = \frac{K_0}{A^2}t^{(1-2\alpha)} \quad , \quad R = A\left(\frac{A^2\tau}{K_0}\right)^{\alpha/(1-2\alpha)} \quad \text{and} \quad R_\tau/R = \frac{1}{\tau}\left(\frac{\alpha}{1-2\alpha}\right) \tag{5}$$

Substituting (3), (4) and (5), together with $K = K_2 e^{a_2 q} - (K_2 e^{a_2 q} - K_1 e^{a_1 q})\theta(\xi-1)$ into (1) and (2), the equations for the transport of cosmic rays in a moving spherical shock can be obtained. In order to have a forward in time equation, α has to be smaller than 1/2 (e.g. Sedov's blast wave, $\alpha = 2/5$).

IV. Results and Discussion. We employ a finite differencing scheme implicit in the spatial variable but explicit in the momentum variable; it is also second order in spatial variable and first order in the momentum variable. To satisfy causality, we use downstream differencing for momentum except at the shock, where we use upstream differencing. We replace $\delta(q_\xi)$ by a Gaussian with a spread of the order of the step size in q during computation.

In the case of a moving spherical shock, we use the supernova shock as an example. We concentrate on the adiabatic stage (or Sedov's stage) of a supernova explosion only.

The self-similar solution (Sedov, 1959) to the blast wave equations is $R = At^\alpha$ where $A = (E/\rho_1)^{1/5}$ and $\alpha = 2/5$. The energy, E, is proportional to the explosion energy, E_0. If $\gamma = 5/3$, then $E = 2.02\,E_0$. ρ_1 is the density of the undisturbed (i.e. upstream) gas. The velocity $V(\xi)$ is given by $V(\xi) = 5/2\,\xi\,v(\xi)$ where $v(\xi)$ is a complicated but monotonically increasing function and $0.24 \le v(\xi) \le 0.3$.

The adiabatic stage of a supernova remnant begins roughly when the mass of interstellar gas swept by the shock is equal to the expelled mass of the supernova (e.g. Spitzer, 1978). At the beginning of this stage the shock radius is:

$$R_\lambda = \left(\frac{3\beta M_\odot}{4\pi\rho_1}\right)^{1/3} \tag{6}$$

where β is the expelled mass in solar mass units ($M_\odot$). Substituting (4) and $R_\lambda = At_\lambda^\alpha$ into (6), we get:

$$\tau_\lambda = K_0\left(\frac{\rho_1}{E}\right)^{1/2}\left(\frac{3\beta M_\odot}{4\pi\rho_1}\right)^{1/6} \tag{7}$$

The adiabatic stage will last roughly until the temperature behind the shock drops below the recombination temperature (i.e. the shock becomes radiative) (e.g. Spitzer, 1978). Let subscript f represent this. The relation between upstream and downstream temperature for a strong shock is (e.g. Landau and Lifshitz, 1959):

$$\frac{T_2}{T_1} = \frac{2\gamma(\gamma-1)}{(\gamma+1)^2}\mathcal{M}^2 = \frac{2\gamma(\gamma-1)}{(\gamma+1)^2}\frac{\rho_1\dot{R}^2}{\gamma P_1} \tag{8}$$

Assume an ideal gas law in the undisturbed (upstream) region $P_1/\rho_1 = kT_1/\mu$ where μ is mean molecular weight. This, together with $R_f = \alpha\, t_f^{(\alpha-1)}$ and $T_2 = T_r$ (the recombination temperature), gives:

$$\tau_f = K_0\left(\frac{\rho_1}{E}\right)^{1/3}\left(\frac{8}{25}\frac{(\gamma-1)}{(\gamma+1)^2}\frac{\mu}{kT_r}\right)^{1/6} \tag{9}$$

Both τ_λ and τ_f of the adiabatic stage are proportional to $K_0\rho_1^{1/3}$. We have studied cases with $\gamma = 5/3$ (which gives $E = 2.02\,E_0$(Sedov, 1959)) and the ratio of the density of helium to that of hydrogen, ρ_{He}/ρ_H , $= 0.4$.

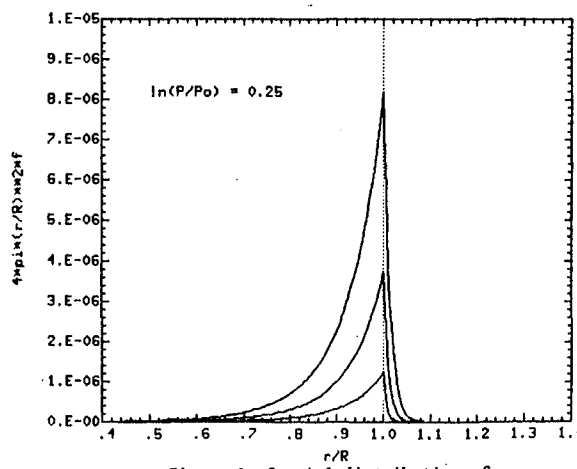

Figure 1. Spatial distribution of particles accelerated by a moving spherical shock. Particles are injected at the shock.

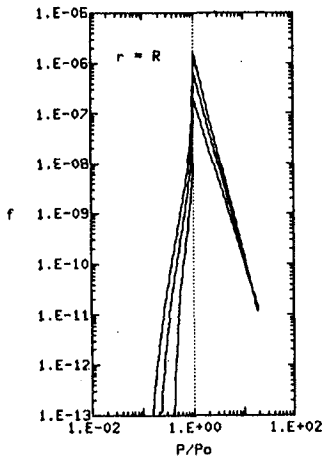

Figure 2. Spectrum of particles accelerated by a moving spherical shock. RR/K is large.

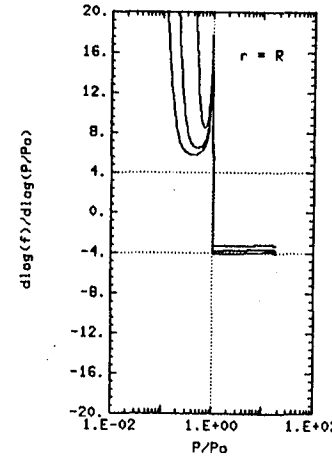

Figure 3. The spectral index with small τ_k and τ_ϕ.

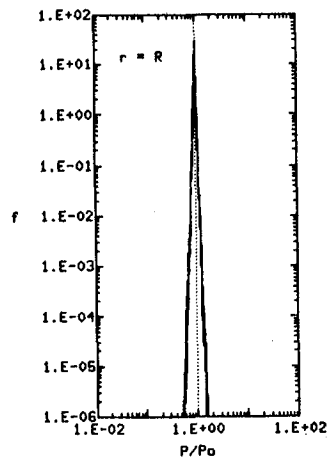

Figure 4. Spectrum of particles accelerated by a moving spherical shock. RR/K is small.

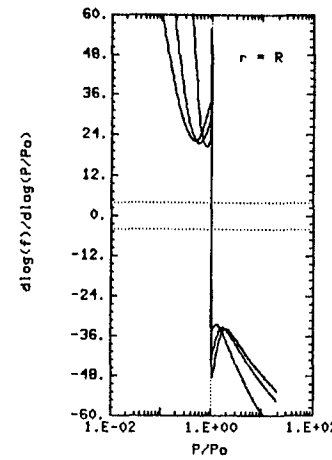

Figure 5. The spectral index with large τ_k and τ_ϕ.

In Figure 1 to 3 we used $E_0 = 3 \times 10^{50}$ erg, $\beta = 0.3$, $K_1 = K_2 = K_0 = 10^{26}$ $cm^2\ sec^{-1}$, $a_1 = a_2 = 0$, $Tr = 10^{26}$ K (the recombination temperature of proton and electron) and the number density of hydrogen $n_H = 3 \times 10^{-3}$ cm^{-3} (hot interstellar medium); i.e., $\tau_i = 1.78 \times 10^{-3}$ and $\tau_f = 5.56 \times 10^{-3}$. An absorbing boundary is set up at a radius 2R.

By studying Figure 1, we see that only a very small portion of particle (high or low energies) stays outside the shock, the absorbing boundary can be considered as being at infinity where the particle distribution, f, is supposed to be zero. This can be understood by the fact that there is no convection outside the shock and the diffusion time scale (R^2/K_0) is much larger than the accelerating time scale (K_0/U^2); and the adiabatic stage ends before the steady state is attained.

The low energy spectrum is very steep and process a cut-off (see Figures 2 and 3), which indicates the adiabatic deceleration is not very effective. The spectral index for accelerated particles ($p > p_0$) starts from values larger than -4 and then relaxes to pass -4 (see Figure 3).

In Figures 4 to 5 we used $E_0 = 3 \times 10^{50}$ erg and $\beta = 0.3$, $K_1 = K_2 = K_0 = 10^{28}$ $cm^2 sec^{-1}$, $a_1 = a_2 = 0$, and $T_r = 10^6$ K, $n_H = 0.1 cm^{-3}$; i.e. $\tau_i = 0.572$ and $\tau_f = 1.79$. The absorbing boundary is at a radius 5R. The spectrum (see Figures 4 to 5) is very steep due to the large curvature of the shock and the escape of particles out of the system.

We have studied the case of momentum dependent diffusion coefficient. The basic features are the same; some detailed changes are consistent with results of a steady state plane shock.

V. Conclusion. The results discussed above may be understood as a consequence of the length scale or time scale involved (e.g. Prishchep and Ptuskin, 1980). There are three time scales involved: diffusion time scale R^2/K, convection time scale $R/\dot{R}$ and acceleration time scale $K/\dot{R}^2$. If the radius of curvature parameter $R\dot{R}/K$ is large, then the acceleration is very efficient and the spectrum will approach that from plane shock and vice versa.

Acknowledgements.

This work was supported in part by NASA under grant NsG7101. The authors are grateful to Garry Webb for helpful discussions.

References

Axford, W.I., Leer, E. and Skadron, G.: 1977, Proc. 15th International Cosmic Ray Conference, Plovdiv, 2, 273.
Bell, A.R.: 1978, M.N.R.A.S., 182, 147.
Blandford, R.D. and Ostriker, J.P.: 1978, Ap. J. (Letters), 221, 129.
Blandford, R.D. and Ostriker, J.P.: 1980, Ap. J., 237, 793.
Bogdan, T.J. and Völk, H.J.: 1983, Astron. Astrophys., 122, 129.
Drury, L. O'C.: 1983, Rep. Prog. Phys., 46, 973.
Krymskii, G.F.: 1977, Dokl. Akad. Nauk. SSSR, 234, 1306 [1977, Sov. Phys. Dokl., 22(6), 327].
Krymskii, G.F. and Petukhov, S.I.: 1980, Pisma Astron. zh., 6, 227 [1980, Sov. Astron. Lett., 6(2), 124].
Landau, L.D. and Lifshitz, E.M.: 1959, Course of Theoretical Physics, Vol. 6: Fluid Mechanics (Pergamon Press).
Moraal, H. and Axford, W.I.: 1983, 125, 204.
Parker, E.N.: 1965, Planet. Space Sci., 13, 9.
Prishchep, V.L. and Ptuskin, V.S.: 1981, Astron. Zh., 58, 779 [1981, Sov. Astron., 25 (4), 446].
Sedov, L.I.: 1959, Similarity and Dimensional Methods in Mechanics (Academic Press).
Spitzer, L. Jr.: 1978, Physical Processes in the Interstellar Medium (John Wiley and Sons).
Toptygin, I.N.: 1980, Space Sci. Rev., 26, 157.

SCALING FROM JUPITER TO PULSARS AND THE ACCELERATION OF COSMIC RAY PARTICLES BY PULSARS, III

C. Y. Fan
Department of Physics, University of Arizona, Tucson, AZ 85721, USA

1. Introduction. In our first paper on this subject (Fan and Wu, 1981), we derived an expression for the rate of energy generation by a pulsar and estimated the contribution from all the pulsars in our galaxy to the observed cosmic ray intensity. The theory was then developed to an expanded version, and observational facts supporting the theory were cited (Fan et al., 1982; Fan and Hang, 1983). In this paper we supplement additional evidences.

2. Brief Review. The theory is based on two propositions:

(1) The rate of the energy generation by a spinning pulsar is given by

$$\frac{dT}{dt} = K \frac{M^2\omega^2}{Rc^2} \quad , \tag{1}$$

where M, R, and ω are respectively the magnetic dipole moment, the radius, and the angular velocity of the pulsar; c is the velocity of light, and K is a characteristic constant of the surrounding medium. This expression should be viewed as Ohm's Law in cosmological scale in which the EMF is generated by the spinning magnetized celestial body and K is a measurement of conductivity of the medium.

(2) The magnetic dipole moment of the pulsar, M, is related to its angular momentum L by the following expression:

$$M = \alpha L \quad , \tag{2}$$

where α is a "form factor," a characteristic constant of the interior of the pulsar. It is an extrapolation of so-called "Bode's Law" of planetary magnetism. The relationship seems to hold approximately true for all celestial bodies whose magnetic diple moments and angular momenta have been estimated or measured. They are over 15 orders of magnitude with Mercury, Venus, and Mars at the lower end and 24 Babcock magnetic stars at the upper end of the ladder, including a neutron star in the middle. The physical reason behind this fundamental relation is not known.

By combining (1) and (2), we have for the rate of energy generation as

$$\frac{dT}{dt} = \frac{K\alpha^2}{c^2} \frac{L^2\omega^2}{R} = \frac{K\alpha^2}{c^2} \frac{I^2\omega^4}{R} \quad , \tag{3}$$

where I is the moment of inertia of the pulsar. Since $T = 1/2\ I\omega^2$, we have finally

$$-\frac{2}{\omega^3} \frac{d\omega}{dt} = \frac{2K\alpha^2}{c^2} \frac{I}{R} \tag{4}$$

The values of K and α were determined from the observation on Jupiter; they are 2×10^{-2}/sec and 2×10^{-16} gauss cm.s.g^{-1}, respectively. The scaling constant $k\alpha^2$ is then 8×10^{-34} cm.s^{-1}.g^{-1}. Equation (4) allowed us to use measured values of ω and $d\omega/dt$ of a pulsar to calculate its I/R, and then, by invoking neutron star models, we determined the mass m, the moment of inertia I, and the radius R of the pulsar and calculated the value of dT/dt.

3. Additional Evidences. An integration of Eq. (4) yields

$$\frac{1}{\omega^2} - \frac{1}{\omega_0^2} = \gamma t \quad , \quad \gamma = \frac{2K\alpha^2}{c^2}\,\frac{I}{R} \quad , \tag{5}$$

where ω_0 is the initial angular velocity of the pulsar. Assume that $\omega_0 >> \omega$, then

$$\frac{1}{\omega^2} = \gamma t \quad . \tag{6}$$

Figure 1 is a plot of $\log(2/\omega^3)$ $(-d\omega/dt)$ against $\log\omega$ for 202 pulsars (Fan et al., 1982). The pulsars at the left lower corner of the figure appear to be on a straight line given by Eq. (6) with t as a parameter. We interpret the line as the age limit of all pulsars. Using 8×10^{-34} cm.$s^{-1}g^{-1}$ for the value of $K\alpha^2$, we find $t \sim 6\times10^{15}$ sec (0.5 billion years). Consider the fact that the scaling constant could be off by a factor of 10, the time limit seems to be reasonable.

The low-energy charged particle (LECP) on Voyager 1 and 2 also detected a flux of hot plasma escaping from the Saturnian magnetosphere, just like in the case of Jupiter (Krimigis et al., 1981). Although the dynamics of the Saturnian magnetoshpere may be complicated by the existence of the rings, the energetic particles escaping from the system can be used to make an order-of-magnitude check of the prediction of Eq. (1). Estimating from their published figures, the escaping flux of 53-85 keV ions from the Saturn appears to be a factor of 100 lower than that from the Jupiter. The prediction of Eq. (1) is 1000.

Refererences

Fan, C. Y. and Wu Jiping, 17th ICRC, Conf. paper 1, 58 (1981).

Fan, C. Y., et al., Astrophys. J. 260, 353 (1982).

Fan, C. Y. and H. R. Hang, 18th ICRC Conf. paper 2, 287 (1983).

Krimigis, S. M., et al., Science 212, 225 (1981).

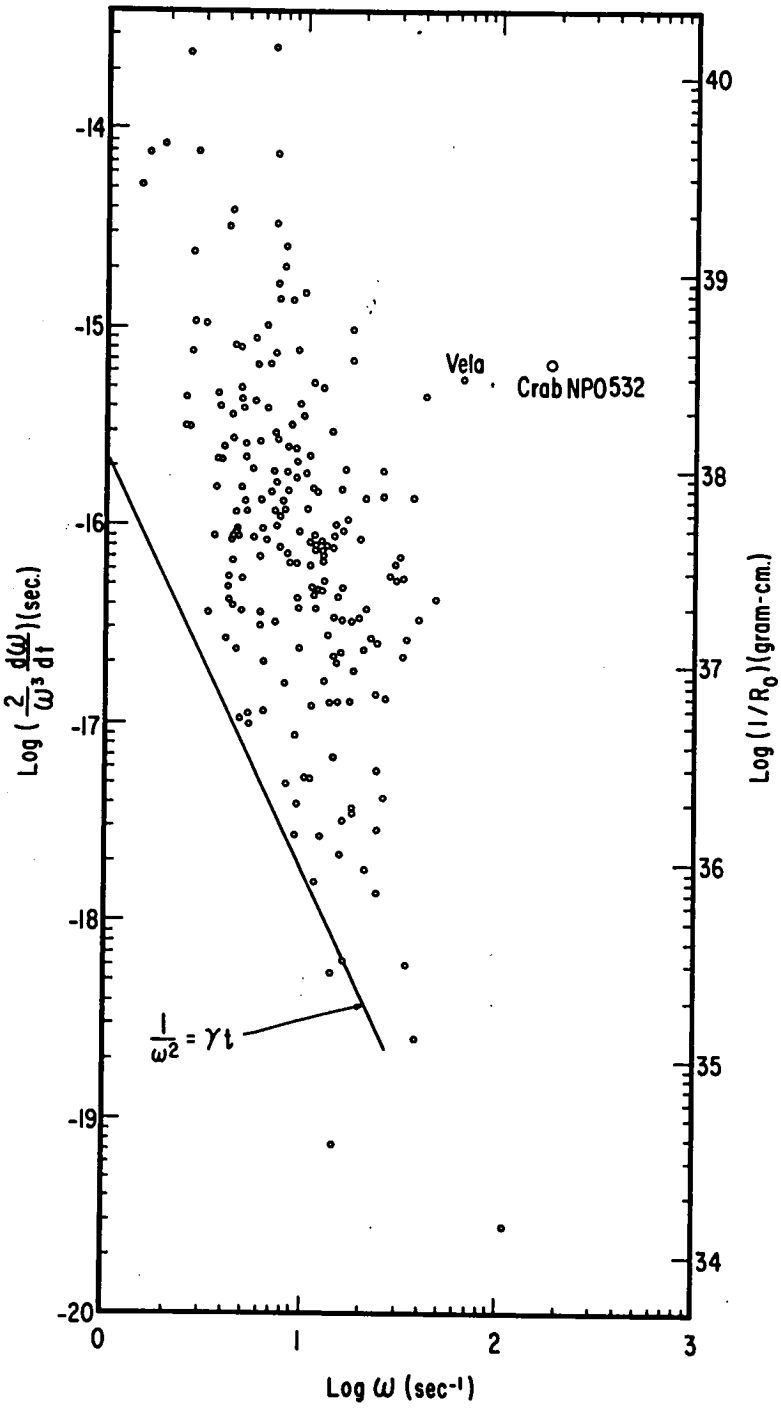

Fig. 1. A plot of $\log(2/\omega^3)$ $(-d\omega/dt)$ against $\log\omega$.

OG 8.2-5

DO SUPERNOVAE OF TYPE I PLAY A ROLE IN COSMIC-RAY PRODUCTION?

Maurice M. Shapiro
Max Planck Institut für Astrophysik*
8046 Garching, West Germany

ABSTRACT

A model of cosmic-ray origin is suggested which aims to account for some salient features of the composition. Relative to solar abundances, the Galactic cosmic rays (GCR) are deficient in hydrogen and helim (H and He) by an order of magnitude when the two compositions are normalized at iron. Our conjectural model implicates supernovae of Type I (SN-I) as sources of some of the GCR. SN-I occur approximately as often as SN-II, though their genesis is thought to be different. Recent studies of nucleosynthesis in SN-I based on accreting white dwarfs, find that the elements from Si to Fe are produced copiously (1). On the other hand, SN-I are virtually devoid of hydrogen, and upper limits deduced for He are low. If SN-I contribute significantly to the pool of GCR by injecting energetic particles into the interstellar medium (ISM), then this could explain why the resulting GCR is relatively deficient in H and He. A test of the model is proposed, and difficulties are discussed.

1. Introduction. A puzzling feature of cosmic-ray composition is the enhancement of many heavy primary nuclei (HPN) among the particles arriving in the vicinity of the earth (2). Compared to solar composition or the local galactic abundances, this ten-fold enrichment in peak elements like Mg, Si, and Fe can also be described as a relative deficiency of H and He. However it may be characterized, this order-of-magnitude discrepancy, unlike other anomalies in composition, cannot be explained by fragmentation in the interstellar medium or by selection effects that depend on the first ionization potential. Any viable theory of cosmic-ray genesis must account for this anomaly.

It is noteworthy that the source energy spectra of H and He also differ from those of the HPN; the latter are somewhat steeper (3). Taken together, the dearth of H and He, and the difference in their energy spectra from those of the HPN, raise the question whether these two components have had different histories. On the other hand, the fact that their production spectra are not very different suggests that a common acceleration mechanism may be working for both.

2. Supernovae and Cosmic Rays. Some three decades ago, supernovae and their remnants were invoked as self-contained sites of cosmic-ray

*Current address: 205 Yoakum Parkway,#1720, Alexandria,VA 22304, USA

origin, i.e., as energy sources, material sources, and regions of acceleration. In trying to explain the source composition, the massive precursors of Type II supernovae (SN-II) were favored as sites of nucleosynthesis for the material destined to become cosmic rays. Recent calculations of SN-II explosions show, however, that it would be difficult to eject sufficient Fe, since the iron is left in the core of the residual neutron star. Moreover, it is doubtful that a sufficient flux of heavy nuclei could escape from the SN-II explosion through the surrounding red-giant envelope.

3. Supernovae of Type I as Injectors of HPN. We propose a conjectural model for the genesis of GCR in which the pool of cosmic-ray nuclei is a mixture of two components:

(A) the bulk of cosmic-ray hydrogen and helium, and a minor portion of HPN, with an overall composition resembling that of the solar system or the ISM; and
(B) the bulk of the HPN (some 90 per cent?) originating predominantly in supernova outbursts of Type I.

With this model we hope to account for the relative deficit of H and He in the cosmic rays.

First we recall some distinguishing features of SN-I and SN-II. While the two types of explosions occur with comparable frequency, their precursors are quite different according to currently favored theories. A Type II supernova results from the evolution of a single massive star; an SN-I, on the other hand, evolves from an accreting white dwarf in a binary system. Among the observational differences are the following. An SN-II has a thick hydrogen envelope, whereas in SN-I light spectra, the lack of H lines implies the absence of a substantial hydrogen envelope. The same SN-I spectra have been used to deduce very low upper limits to the He abundance. The precursors of SN-I are old stars of low mass. The two types of supernovae have different light curves. SN-I are considered to have steep density gradients and to generate strong shocks.

Referring to the two components (A and B) of the GCR postulated above, we envisage the following scenarios for their injection and acceleration: (A) The arriving ("primary") H and He nuclei, and a small fraction of the HPN are injected, e.g., from flares in main-sequence F-to-M stars; other source-injectors are not excluded. They are then accelerated at expanding shock fronts in the ISM, energized mainly by supernova outbursts. (B) Nearly all of the HPN are injected--with modest energies-- from SN-I explosions, and then accelerated in the ISM by the same shock waves as component (A).

4. Nucleosynthesis in SN-I. Since the SN-II seem incapable, by themselves, of yielding a solar-type composition, attention has turned to SN-I models that might produce a plausible mix of metals, especially to carbon-deflagration models (1, 4, 5). These involve a rapidly accreting white dwarf in a close binary system. The evolution of the progenitor system is calculated from the start of accretion to the complete disruption of the white dwarf. From this outburst one gets ~ 0.5 M of ^{56}Ni which decays to cobalt, then to iron. The radioactivities generate the

observed light curves. From a sequence of nuclear burnings in the white dwarf, one obtains a copious supply of the intermediate elements, from Co to Ca. Based on this calculated output, it has been possible to construct synthetic profiles of line spectra; these are consistent with the spectra observed near maximum brightness (6). Certain of the carbon deflagration models seem to work well. There is a whole class of such models which depend on the choice of certain parameters. The products of these modeled SN-I events are complementary to those of nucleosynthesis in SN-II, giving an ISM composition in reasonable accord with observations.

5. Test of the Cosmic-Ray Model. Our prescription for a critical test, dealing mainly with component (B), starts with the calculated output of nuclides from SN-I using a promising model of nucleosynthesis, e.g., one like "W7" of Nomoto, Thielemann and Yokoi. A fraction of the ejected material is assumed to be boosted in energy to, say, tens of MeV or higher, and injected into the ISM. The initial ensemble of sub-relativistic nuclei is then "propagated" through the ISM with an appropriate distribution of path lengths. This can be done with available computational programs utilizing the latest cross sections for fragmentation. The calculated residual distribution of nuclides arriving locally can be compared with observations of metal abundances in the solar system (taking account of solar modulation at sub-GeV energies). Finally, one tries to construct a plausible mix of components (A) and (B) so as to get a reasonable fit to the observed, arriving composition.

6. Discussion. It would be fortuitous if the initial attempts at fitting were to succeed in accounting for the cosmic-ray composition as well as the composition of (thermal) solar material. In the SN-I models, the main uncertainties at the burning fronts reside in the hydrodynamics rather than in the nuclear physics (7). The quasi-convective mixing length is unknown, and must be selected rather arbitrarily (8). Yet the final deflagration yields depend decisively on this choice.

Apart from uncertainties in models of nucleosynthesis, one may ask whether particle injection by SN-I will work. A conceivable obstacle is the energy loss during the adiabatic expansion. It seems, however, that while such loss may prevent acceleration at or near the source up to relativistic energies, it would not preclude injection into the ISM at modest energies. The steep density gradients and strong shocks occurring in SN-I could provide the limited boost in energy that is required.

It should be emphasized that we are concerned here mainly with particle energies $\lesssim 10^{12}$ eV/amu, a domain comprising, by far, most of the cosmic rays, and for which the composition is rather well known.

A different explanation of HPN enhancement has been proposed by D. Eichler et al. (9,10). They argue that shocks in the ISM preferentially accelerate partially ionized heavy elements over protons. Their model may provide an attractive alternative to the one presented here.

7. Conclusions. If SN-I contribute significantly to the Galactic pool of cosmic rays by injecting enough HPN into the ISM, then this would

solve a major cosmic-ray problem--we would understand why the GCR is relatively deficient in H and He. From our model one could expect some difference in the energy spectra of components (A) and (B). On the other hand, because the main acceleration of the HPN is accomplished by the same mechanism that energizes the H and He, it is understandable that the spectral difference between the two components is not great.

8. Acknowledgments. Invaluable discussions with W. Hillebrandt, K. Nomoto, F. Thielemann, and E. Müller are gratefully acknowledged. I am also indebted to Professors R. Kippenhahn, W. Hillebrandt and their colleagues for the hospitality and stimulating atmosphere of the Max Planck Institut für Astrophysik in Garching. I thank Beth Kessler for her timely assistance.

References

1. Nomoto, K., F.K. Thielemann, and K. Yokoi (1984), Ap.J. 286, 644.
2. Shapiro, M. and R.Silberberg (1975), Phil Trans. Royal Soc.London, A 277, 319.
3. Engelmann, J. J. et al. (1981), 17th ICRC, Paris, 9, 97.
4. Woosley, S. et al. (1984), in Proc. Erice Workshop on Stellar Nucleosynthesis, Reidel Publ. Co., Dordrecht.
5. Nomoto, K.,F.K. Thielemann, and J. C. Wheeler (1984), Ap.J. 279:L 23
6. Branch, D., et al. (1982), Astroph. J. 252, L61.
7. Arnett, D.,(1985), remarks at Moriond Symposium on Nucleosynthesis, Les Arcs, France.
8. Thielemann, F. K. and Nomoto, K., private communications.
9. Eichler, D. and K. Hainebach, (1981), Phys. Rev. Ltrs. 47, 1560.
10. Ellison, D.C., F.C. Jones, and D. Eichler (1981), J. Geophys. 50,110.

OG 8.2-6

NEUTRON-RICH NUCLEI IN COSMIC RAYS AND WOLF-RAYET STARS

N.Prantzos[1],M.Arnould[2],J.P.Arcoragi[3] and M.Cassé[1]

1.Service d'Astrophysique,Institut de Recherche Fondamentale, CEN Saclay,France.
2.Institut d'Astronomie et d'Astrophysique Université Libre de Bruxelles,Belgique.
3.Département de Physique,Université de Montréal,Canada.

1.Introduction Wolf-Rayet stars figure prominently in astrophysical research (see e.g.Humphreys and Davidson, 1984).As a bonus,they seem to offer,in the same way as supernovae and supernova remnants in the recent past,an interesting connection between classical astronomy and high energy astrophysics due to their unusual composition and their huge mechanical power (Cassé and Paul,1981,1982, Maeder,1983,1984,Prantzos and Arnould 1983,Prantzos 1984a,b Arnould 1984,Audouze 1984,Meyer 1985,Prantzos et al 1985). The material flowing from WC stars (carbon-rich WR stars) contains gas which has been processed through core-helium burning,i.e. considerably enriched into ^{12}C, ^{16}O, ^{22}Ne,and $^{25,26}Mg$.This composition is reminiscent of the cosmic ray source anomalies (e.g.Simpson 1983,Meyer 1985b).Encouraging agreement is obtained with observation in the mass range $12 \lesssim A \lesssim 26$ assuming acceleration of wind particles at the shock that delineates the WR cavity (Cassé and Paul,1980),and adequate dilution with "normal" cosmic rays,but silicon poses a problem (e.g.Prantzos,1984 a,b and Prantzos et al,1985). If massive stars contribute significantly to the $^{25,26}Mg$ excess at the CR sources,they should also enhance other neutron-rich isotopes since the production of ^{25}Mg releases a copious amount of neutrons.These neutrons,in turn react with preexisting nuclei,producing a host of neutron-rich isotopes,of which a few are of interest for CR physics (Prantzos,Arnould and Cassé 1983,Blake and Dearborn 1984, Prantzos et al 1985).Detailed models of WR stars have been developed (de Loore et al 1985,Prantzos et al 1985b)delivering physical conditions (initial composition,temperature and density versus space and time coordinates) relevant to a consistent s-process calculation.

2.Results The stellar model developed within the Brussels-Saclay collaboration,coupled to a full s-process network, allows to follow the abundance of all nuclear species of interest,both in the stellar core and at the stellar surface. 4 different cases (50,60,80 and 100 $M_\odot$ on the zero age main sequence) have been studied (for details see Prantzos et al, 1985).In all the cases considered only n-rich isotopes in the range $20 \lesssim A \lesssim 90$ are substantially enhanced at the end of helium burning (with a few exceptions however),due to the rather low neutron fluence ($\sim 8.10^{26}$ n cm^{-2}),in agreement with Lamb et al,1977.
The global enhancement of a given isotope in the wind of

WC stars (60 % of all WR stars) relative to its solar system abundance will be denoted, in the following by $E_i^{WC} = \langle X_i^{WC} \rangle / X_{i,\odot}$, $X_{i,\odot}$ is its solar mass fraction and the bracketed symbol stands for the double average of this mass fraction of this isotope over the duration of the WC phase and over the mass spectrum of its stellar progenitors (IMF).

More specifically:

$$X_i^{WC}(M) = \int_{WC} X_i^{(s)}(t,M)\ \dot{M}_{WC}\ dt \ / \ \Delta M_{WC}$$

where $X_i^{(s)}$ is the instantaneaus surface abundance of i,

$\dot{M}_{WC}$, the mass loss rate ($3.10^{-5}\ M_\odot yr^{-1}$)

and $\Delta M_{WC} = \int_{WC} \dot{M}_{WC}\ dt$ is the total mass ejected during the WC phase.

$$\langle X_i^{WC} \rangle = \int_{50}^{100} \phi(M)\, \Delta M_{WC}(M)\ X_i^{WC}(M)\ dM \Big/ \int_{50}^{100} \phi(M)\, \Delta M_{WC}(M)\ dM$$

where $\phi(m)dM$ is the initial mass function (IMF).

Now, the enhancement of species i at the sources is

$$E_i^{CRS} = [1 + (1/f)\ \langle E_i^{WR} \rangle] / [(1/f) + 1] \quad \text{(Maeder, 1983)}$$

with $\langle E_i^{WR} \rangle = 0.4\ \langle E_i^{WN} \rangle + 0.6\ \langle E_i^{WC} \rangle$,

1/f denotes the fraction of CR particles coming from WR stars. The dilution factor f is obtained by adjusting the calculated overabundance of ^{22}Ne relative to ^{20}Ne (about 100, irrespective of the WR mass) to that at the CR sources (about 4).
We get f~35 : 1 CR particle out of 35 should originate from WR stars.

We predict the following correlated CR excesses E_i^{CRS} (selecting those $\gtrsim 1.2$):

$^{12}C(2.4)$, $^{16}O(1.6)$, $^{21}Ne(2.0)$, $^{22}Ne(4.1)$, $^{23}Na(1.4)$, $^{25}Mg(1.7)$, $^{26}Mg(1.7)$, $^{36}S(1.6)$, $^{37}Cl(1.4)$, $^{40}K(3.2)$, $^{58}Fe(1.8)$, $^{59}Co(1.4)$, $^{61}Ni(1.4)$, $^{63}Cu(1.4)$, $^{65}Cu(1.6)$, $^{67}Zn(1.2)$, $^{69}Ga(1.2)$, $^{71}Ga(1.2)$, $^{70}Ge(1.2)$, $^{80}Kr(1.4)$, $^{82}Kr(1.2)$, $^{86}Sr(1.2)$, $^{152}Gd(1.4)$ and $^{202}Hg(1.2)$.

Among these species only a few are of practical interest for present CR research (table 1), the others being so rare that they are overwhelmed by spallation of heavier nuclei en route (e.g. Adams et al, 1981).

Element	CRS/SEP(1)	CRS/LG(1)	E_i^{CRS}
C	~3		2.4
O	~1.5		1.6
Na		0.8(2.0)	1.4
Co		1.3(1.6)	1.4
Cu		1.1(1.6)	1.4
Ga		1.5(1.5)	1.2

Table 1. Predictions of WR models confronted to observations.

SEP=Solar energetic particles, LG=Local galactic abundances.
(1) Meyer (1985a,b) except for Ga (Anders and Ebihara, 1982).
CRS abundances are those derived from the HEAO 3 data (Koch-Miramond et al, 1983, Engelmann, 1984 and Lund, 1984).
(x)=within a factor of x).
C and O, having a high first ionisation potential are affected by selective filtering in the cosmic ray reservoir, both in SEP and Galactic CR sources. The CRS/SEP ratio is therefore sensitive to any deviation of Galactic CR sources from the standard (LG), irrespective to atomic discrimination, (Meyer 1985b)
The other elements, due to their uniformally low FIP are not affected by discriminating atomic effects.

Predicted enhancements are all within experimental uncertainties.

As concerns isotopes, we predict a definite enhancement of ^{58}Fe (by a factor close to 2), Which is not far of reach of the present technology. We thus confirm our previous estimate (Prantzos, Arnould and Cassé, 1983, Prantzos, 1984a,b, Prantzos et al, 1985) and agree with Blake and Dearborn, 1984, at least qualitatively.

3. Conclusion Enhancement factors of a series of neutron-rich isotopes in CR sources, due to WR contamination, have been estimated. The predicted overabundances are all within observational uncertainties.
There is at least no contradiction with present observations. The best prospect to test the WR scenario is to measure the

$^{58}Fe/^{56}Fe$ with an accuracy of about 20 %.

Aknowledgements: We thank all our colleagues of the Brussels-Saclay collaboration for constant help and support. We are indebted to C.Ryter and A.Raviart for generous allocation of computer time.

References:

Anders,E. and Ebihara M.,1982,Geochim. Cosmochim. Acta 46,2363.
Arnould,M.,1984,Adv. Space Res.,4,45.
Audouze,J,1984,Moriond Symposium:"High Energy Cosmic Rays" p.325.
Blake,J.B. and Dearborn,D.S.P.,1984,Adv. Space Res.,4,89.
Cassé,M; and Paul,J.A.,1980,Ap.J.,237,236.
Cassé,M. and Paul,J.A.,1981,17th Int. Cosmic Ray Conf.13,111.
Cassé,M. and Paul J.A.,1982,Ap.J.,258,860.
de Loore,C.,Prantzos,N.,Arnould,M. and Doom,C.,1985,Moriond Symposium:"Nucleosynthesis and its applications on nuclear and particule physics",in press.
Engelmann,J.,1984,European Cosmic Ray Symposium,Kosice.
Humphreys,R.M. and Davidson,K.,1984,Science,223,243.
Lamb,S.A.,Howard,W.M.,Truran,J.W. and Iben,I.Jr,1977, Ap.J.,217,213.
Lund,N.,1984,Adv. Space Res.,4,5.
Koch-Miramond,L.,Engelmann,J.,Goret,P.,Juliusson,E.,Masse,P., Soutoul,A.,Perron,c;,Lund,N. and Rasmussen,I.L.,1983,9,275. 18th Int.Cosmic Ray Conf.,9,275.
Maeder,A.,1983,Astron. Astrophys.,120,130.
Maeder,A.,1984,Adv. Space Res.,4,55.
Meyer,J.P.,1985,Ap.J. Suppl.,57,151.
Meyer,J.P.,1985,Ap.J. Suppl.,57,173.
Prantzos,N.,1984a,Adv. Space Res.,4,109.
Prantzos,N.,1984b,Moriond Symposium:"High Energy Cosmic Rays",p.341.
Prantzos,N. and Arnould,M.,1983,in "Wolf-Rayet stars: Progenitors of Supernovae?",Observatoire de Paris-Meudon,pII.33.
Prantzos,N.,Arnould,M. and Cassé M.,1983,18th Cosmic Ray Conf.,9,155.
Prantzos,N.,Arcoragi,J.P. and Arnould,M.,1985,Moriond Symposium "Nucleosynthesis and its applications on nuclear and particle physics",in press.
Prantzos,N.,de Loore,C.,Doom,C. and Arnould,M.,1985, Moriond Symposium.

BURSTING STAR FORMATION AND THE OVERABUNDANCE OF WOLF-RAYET STARS

G. Bodifee and C. de Loore

Astrophysical Institute
Vrije Universiteit Brussel
Brussels, Belgium

Abstract

The ratio of the number of WR-stars to their OB progenitors appears to be significantly higher in some extragalactic systems than in our Galaxy. This overabundance of WR-stars can be explained as a consequence of a recent burst of star formation. It is suggested that this burst is the manifestation of a long period nonlinear oscillation in the star formation process, produced by positive feedback effects between young stars and the interstellar medium. Star burst galaxies with large numbers of WR-stars must generate γ - fluxes but due to the distance, all of them are beyond the reach of present-day γ ray detectors, except probably 30 Dor.

1. Introduction. Supersonic stellar winds from luminous early-type stars create shocks in the interstellar medium that could be agents of cosmic ray acceleration. The Wolf-Rayet phase in the evolution of massive stars is especially important because of the extremely high mass loss rates and wind terminal velocities. O-stars are the exciting sources for the ionized gas in which the particles are trapped. γ rays are generated by the interaction of the relativistic particles with the interstellar medium. It is generally accepted that the ratio of WR-stars to blue supergiants in the solar neighborhood is close to 0.1. Assuming a Conti WR formation scenario, described in section 2, for all single stars of more than 20 $M_\odot$, this ratio corresponds with a continuous star formation rate. However, higher ratios are found in some external galaxies, especially in giant HII regions and blue compact galaxies.

It is argued in this paper, that a local overabundance of WR-stars can be explained by a recent burst of star formation in that location. The interaction of the local CR fluxes provoked by WR stars in these bursting galaxies with molecular clouds surrounding the star-formation region could then be a source of γ rays.

2. The Wolf-Rayet production scenario. WR-stars can originate from massive stars through mass loss during the main sequence phase (Conti, 1975) or during the red supergiant phase (Maeder, 1981,1982) or through Roche lobe overflow in close binary systems (de Loore, 1980). According

to the Conti scenario single O-stars evolve into Of-stars, that are further transformed into WN7-stars, normal WN-stars and possibly into WC-stars. The lifetime of the WR stage is short. According to the evolutionary computations for massive stars ($M>50M_\odot$) that include mass loss, extended mixing and a detailed nucleosynthesis network (de Loore et al. 1985, Prantzos et al. 1985) the duration of the WR stage including all subtypes, is approximately $4\ 10^5$ years, i.e. about 10 % (for a 100 $M_\odot$ star) to 8 % (for a 60 $M_\odot$ star) of the total stellar lifetime.

The minimum initial mass of a WR-progenitor is difficult to estimate but should be approximately between 20 and 40 $M_\odot$ (Schild and Maeder, 1984; Conti et al. 1983) in our Galaxy. However, in low-metallicity regions, such as the Magellanic Clouds and blue compact galaxies, the production efficiency of single WR-stars through radiation driven mass loss may be considerably lower, leading to a much higher minimum initial mass within these systems (Pylyser et al. 1984).

3. Nonlinearities in the star formation process system. Assuming a production scenario, the number of WR-stars in a region depends on the star formation rate and the initial mass function. Large variations in the star formation rate could lead then, with a time delay of the order of the main O-star lifetime, to considerable deviations in the WR/O ratio. Rapid changes in the star formation rate can occur as a consequence of positive feedback effects operating in the process system of a star formation region.

Triggered star formation by the emissions of previously formed young stars (e.g. Elmegreen and Lada, 1977) is a kind of autocatalysis that destabilizes the star formation process system. Another positive feedback may operate as a consequence of molecular cooling and shielding from UV radiation in molecular clouds, leading to low cloud temperatures. Hence, collapse of these clouds can occur, so that more molecules are produced through the increased density in the cloud.

Bodifee and de Loore (1985) have shown by model calculations of a star formation region, that nonlinear oscillations may occur under certain circumstances. Under the influence of the different timescales of the processes involved, various behavioral regimes of the star formation system may occur. Within certain ranges of the relevant parameter values the stationary state is unstable and develops limit cycle oscillations. For large values of the efficiency coefficient of triggered star formation, limit cycles are produced, exhibiting long quiescent periods, interrupted by short and violent bursts of star formation.

Star formation events that are observed in some low-metallicity dwarf galaxies, and in the nuclei of some emission-line galaxies may be manifestations of this bursting mode.

4. Star formation bursts and abnormal WR abundances. The sudden variations in the star formation rate that are inherent to a burst can lead to abnormal WR/O ratios. Shortly after the start of the burst, when massive O-stars are formed, but not yet enough time has elapsed to let them evolve into WR-stars, abnormal low values may be expected. On the other hand, after the burst, the O-star number decreases but the production of WR-stars still goes on for some time, so that high values may be attained. The figure shows the WR/O ratio for a time t-T after a burst of duration T, based on calculations that assume only the Conti-scenario as a way for WR production. More diversified scenarios can alter the numbers somewhat, but the conclusion remains quantitatively the same: shortly after a burst there is an overabundance of WR stars with respect to the WR/O ratio in our Galaxy. Although the results of the figure should not be overinterpreted in a quantitative sense, it is interesting to relate them to the high HeII emission lines that are observed in some blue compact galaxies and giant extragalactic HII regions. Kunth and Sargent (1981) observed a large I(4686)/I(Hβ) in Tololo 3. If the strong HeII emission feature in this galaxy is ascribed to a population of WN4-5 stars, the number of WR-stars can be estimated at 150.

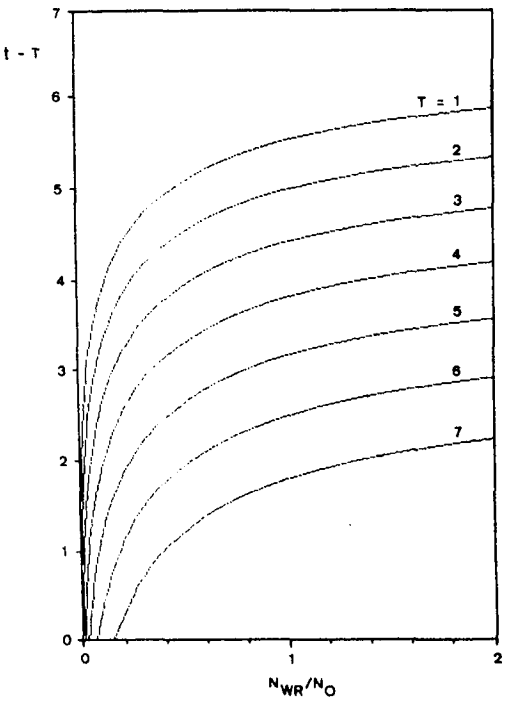

Assuming that only O-stars ionize the gas, they derive the presence of 375 O9-4 stars from the Hβ flux. The number ratio of about 1/2 could indicate the end of a short burst, 5-6 million years ago. High I(4686)/Hβ values are observed in some other star burst regions, such as IZw36 (Viallefond and Thuan, 1983), IZw18 (Bergeron, 1979; Kinman and Davidson, 1981), He2-10 (Allen et al. 1976; Hutsemekers and Surdej, 1984), IIZw70 (Lequeux et al. 1979), NGC604 (D'Odorico and Rosa, 1981; D'Odorico et al. 1983) and in some HII regions of NGC300 (D'Odorico et al. 1983).

5. Star burst regions as γ-sources. In the galactic Carina OB association (distance 2.5 kpc), three WR-stars are present, and the HII mass is determined at 10^5 $M_\odot$ (Dorland et al. 1985). COS-B observed a flux of 1.3 10^{-6} photons cm^{-2} s^{-1} from this region (Bignami and Hermsen, 1983). The flux of a region can be put proportional to the number of WR-stars, and to the HII mass within the region (from Montmerle

and Cesarsky, 1981), where the HII mass is a function of the age of the cluster. The γ intensities of the galaxies mentioned in the previous paragraph can then be roughly estimated. It turns out that all these sources are far too weak to have been observed as individual sources by COS-B (In fact, only one extragalactic object has been observed, the 3C273 quasar).

6. Conclusion. A star formation region may undergo repetitive bursts as a consequence of the intrinsic nonlinear dynamics of the star formation process system. The interaction of the energetic outflows of massive young stars with the interstellar medium make a star formation region a site of CR acceleration and γ sources. The high energy phenomena will happen especially during a short time after a burst, when the region is unusually rich in WR-stars. Only 30Dor, however, is within the reach of γ satellites to be launched in the near future.

References

Allen, D.A., Wright, A.E. Goss, W.M., 1975, Month.Not.R. Astron.Soc., 77,91
Bergeron, J., 1977, Astroph.J. 211,62
Bignami, G.F., Hermsen, W., 1983, Ann.Rev.Astron.Astroph.21,67
Bodifee, G., de Loore, C., 1985, Astron.Astroph.,142,297
Conti, P.S., 1975, Mem.Soc.Roy.Sci.Liege, IX,193
de Loore, C.,1980, in "Effects of Mass Loss on Stellar Evolution, IAU Coll. 59, C. Chiosi and R.Stalio eds.,p 405
de Loore, C., 1985, Prantzos, N., Arnould, M., Doom, C., 1985 5th Moriond Astroph.Meeting, J.Audouze, J. Tran Thanh Van,eds.
D'Odorico, S., Rosa, M., 1981 Astroph.J., 248,1015
D'Odorico, S., Rosa, M., Wampler, E.J., 1983, Astron.Astroph. Suppl. 53, 97.
Dorland, H., Montmerle, T. Doom, C., 1985, Astron. Astroph. in press.
Elmegreen, B.G., Lada, C.J., 1977, Astroph. J., 214,725
Hutsemekers, D., Surdej, J., 1984 Astron.Astroph., 133,209
Kinman, T.D., Davidson, K., 1981, Astroph.J., 243,127
Kunth, D., Sargent, W.L.W., 1981, Astron.Astroph., 101,L5
Lequeux, J., Peimbert, M., Rayo, J.F., Serrano, A., Torres-Peimbert, S., 1977, Astron. Astroph.,80,155
Maeder, A., 1981, Astron.Astroph., 99,97
Maeder, A., 1982, Astron.Astroph., 105,149
Montmerle, T., Cesarsky, C.J., 1981, Proc.Int. School and Workshop and Plasma Astroph., Varenna, ESA SP-161,319
Prantzos, N., de Loore, C., Doom, C., Arnould, M., 1985, in 5th Moriond Astroph. meeting, J.Audouze, J.Tran Thanh Van,eds
Pylyser, E., de Loore, C., Doom, C., 1984, Proceedings of the Coll. Birth and Evolution of massive stars and stellar systems, W. Boland, H. Van Woerden, eds.
Schild, H., Maeder,A., 1984, Astron.Astroph., 136,237
Viallefond, F., Thuan, T.X., 1983, Astroph.J. 269, 444
Walborn, N.R., 1983, Proc. of the IAU Symposium 108, Reidel, Dordrecht

OG 8.2-12

INTERSTELLAR ^{22}Na AS A POSSIBLE SOURCE OF THE EXCESS ^{22}Ne IN THE GALACTIC COSMIC RAY

S. Yanagita

Department of Earth Sciences
Ibaraki University
Bunkyo 2-chome, Mito 310, Japan

ABSTRACT

We propose a selective injection mechanism of cosmic ray seed nuclei due to nuclear decay effects. It is shown that ^{22}Na ejected by novae explosion can explain the excess ^{22}Ne in the galactic cosmic ray source by invoking energization and ionization during its beta-decay process in interstellar space.

1. Introduction. Recent investigations on the cosmic ray charge and isotopic composition have revealed many remarkable features to understand the origin of the galactic cosmic ray (GCR). Among of these are;the organization by the first ionization potential(FIP) of the elemental abundance in GCR source relative to the local galactic abundance(1,2); the excess abundance of several neutron rich isotopes at GCR source(1,3). The most significant and well-established fact is that ^{22}Ne is overabundant in GCR source by a factor of $\sim$3.5 with respect to the solar system value(1).

In this contribution, we want to propose a new mechanism to explain this peculiar imprint bearing the nature of GCR source, and also want to discuss the origin of the source material relating with the recent observational result of galactic gamma-ray lines(4,5).

2. Mechanism producing the excess ^{22}Ne in GCR source. It has been suggested that the elemental abundance pattern of GCR source relative to the local galactic abundance is well organized by FIP and that this pattern is reproduced by an exponential distribution of temperature at GCR source, with an average temperature $T_0 \simeq 7000$ K(6). Accordingly, a dramatic increase in the relative abundance might be expected for species which attain a significantly higher speed than that of thermal particles, if the particles are injected and accelerated from the tail of a Maxwellian distribution. An example of this kind of preferential heating is proposed to explain ^{3}He-rich solar flare events(7).

Along the similar lines of thought, we want to propose here a new mechanism of selective heating and subsequent preferential injection due to nuclear decay effects which is applicable in principle to any isotopes which have radioactive progenitors. Specificall, we consider here the case of ^{22}Na. This isotope decays to ^{22}Ne via beta-decay with a half life of $\sim$2.6 yr and with a maximum beta-decay energy of

~0.55 MeV. The ^{22}Ne produced by this decay will attain an energy $E_r \simeq 10$ eV owing to the nuclear recoil effect. The temperature corresponding to this energy is $\sim 1.2 \times 10^5$K and is significantly higher than the average temperature at GCR source, ~7000 K(6). In addition to this heating, ^{22}Ne will be ionized by the "shakeoff" process during the beta-decay(8), even if the parent ^{22}Na is neutral. This ionization effect might be significant, because neon is virtually neutral at a temperature of ~7000 K. Because of these energization and ionization effects, it is expected that the ^{22}Ne population originated from ^{22}Na may be selectively picked up as cosmic ray seeds and be subjected to subsequent acceleration processes. Certainly, to show this mechanism actually does work, we must investigate if the thermalization and recombination timescales of recoiled ^{22}Ne are long enough so that the nucleus has a chance to be accelerated. But, here, we want to restrict our discussion only to pointing out the possibility of the preferential injection mechanism due to the nuclear decay effects as shown above. Instead, in following, we want to compare quantitatively the rate of ^{22}Na supply into interstellar medium(ISM) with the production rate of ^{22}Ne in GCRs.

3. Estimation of production rates. The excess isotopic abundance of ^{22}Ne in GCR source to be explained is

$$\Delta n_{22} = (^{22}Ne/^{20}Ne)_{GCR} - 1.6 \times (^{22}Ne/^{20}Ne) \simeq 0.2$$

where $(^{22}Ne/^{20}Ne)_{GCR}$ and $(^{22}Ne/^{20}Ne)$ are the neon isotopic ratios in GCR source (~0.4) and in the solar system (~0.12), respectively(1,3).Here we assume the excess ^{22}Ne up to ~1.6 times of the solar system value is explained by the super metalicity hypothesis(9)(although our conclusion is not affected whether the factor of 1.6 is taken into account or not). Then the production rate of the excess ^{22}Ne in the whole galaxy is estimated as follows,

$$\Delta \dot{N}_{22} \simeq \dot{N}_{CR} \times (n_{20}/n_{CR}) \times \Delta n_{22} \simeq 3 \times 10^{38} \text{particles/sec}$$

where $\dot{N}_{CR}$, $\sim 3 \times 10^{42}$ particles/sec, is the production rate of GCR in the whole galaxy and is estimated from the localcosmic ray density $\sim 10^{-10}/cm^3$, the volume of the galaxy $\sim 10^{67} cm^3$ and the life time of GCRs, $\sim 10^7$yr(10). (n_{20}/n_{CR}) is the relative abundance of ^{20}Ne in the cosmic ray, $\sim 5 \times 10^{-4}$(2). From our point of view, it is necessary that sufficient amount of ^{22}Na exists in interstellar space to maintain ^{22}Ne abundance in GCR. In other words, the rate of ^{22}Na supply should be higher than the production rate of the excess ^{22}Ne in GCR. Explosive nucleosynthesis in novae is expected to produce ^{22}Na and ^{26}Al (11). The gamma-ray spectroscopy experiment has detected the line with an energy of 1.8 MeV, consistent with the decay of $\sim 3\ M_\odot$ of ^{26}Al in the interstellar space(5). The source of the observed ^{26}Al has been attributed to galactic novae, not supernovae(5). We can estimate the total amount of ^{22}Na of

novae origin, M_{22}, from the observed amount of ^{26}Al, $M_{26} \simeq 3\ M_{\odot}$, by using the simple model for the chemical evolution of the galaxy(12) as following,

$$M_{22} = M_{26} \times (X_{22}/X_{26})$$

$$\simeq M_{26} \times (P_{22}/P_{26}) \times (T_{22}/T_{26})$$

where, (X_{22}/X_{26}) is the abundance ratio of ^{22}Na and ^{26}Al in the present interstellar space; (P_{22}/P_{26}) is the average isotopic production ratio of ^{22}Na and ^{26}Al for explosive process in novae and is $\sim 10^{-3}$ (13); (T_{22}/T_{26}) is the ratio of half lives, $\sim 3.6 \times 10^{-6}$. From this analysis the amount of ^{22}Na in the interstellar space is estimated as $\sim 2.2 \times 10^{25}$g or 5.9×10^{47}atoms. If the decay and production are in equilibrium, the rate of supply of ^{22}Na is estimated as $\sim 5 \times 10^{39}$atoms/sec (approximately the same value is also obtained from the occurance of novae in the galaxy $\sim$40/yr (14), the average mass of matter ejected by a nova explosion $\sim 10^{-4} M_{\odot}$ and the concentration of ^{22}Na in the ejecta $(2 \sim 10) \times 10^{-7}$g/g (13)). This value of the production rate(or the decay rate) of ^{22}Na, Q_{22}, is not inconsistent with the upper limit $\sim 4.4 \times 10^{42}$ atoms/sec obtained by HEAO3 observation of the diffuse galactic gamma-ray lines(4) and is higher than $\Delta \dot{N}_{22} \simeq 3 \times 10^{38}$ atoms/sec, the production rate of the excess ^{22}Ne in GCR source. The ratio of $\Delta \dot{N}_{22}$ to Q_{22} is $\sim$6%. This means that the probability of ^{22}Na ejected by novae to become a cosmic ray ^{22}Ne is 6%. Therefore, novae can supply the seeds of excess ^{22}Ne in GCRs, in principle. ^{22}Na ejected by novae explosion might be preferentially injected as cosmic ray seeds owing to the effects shown above.

4. Discussion and conclusion. Although the amount of ^{22}Na ejected by novae explosion is enough to account the excess ^{22}Ne, the probability of 6% seems to be rather high. So it is interesting here to estimate the probability for the bulk GCRs and enhancement factor of ^{22}Ne to be realized by our selective injection model. It has been suggested by the shock acceleration model for cosmic ray production that energetic particles are drawn directly from a thermal pool (15). If this view is correct, we can estimate the average efficiency of interstellar medium(ISM) to become cosmic rays. The ISM is undergoing continual change on a time scale of $\sim$Gyr (16). If our galaxy is in a steady state (or if the amount of ISM is constant) during the last several Gyr, the rate of supply of ISM from stars is estimated as $\sim 3 \times 10^{51}$ atoms/sec by dividing the amount of ISM with 10^{9}yr. So the efficiency of ISM is $\dot{N}_{CR}/(3 \times 10^{51}) = 10^{-9}$. Consequently, the efficiency of ^{22}Na is $\sim 6 \times 10^{7}$ times higher than that of the general ISM. On the other hand, the enhancement factor of $\exp(E_r/kT_0) = 2.8 \times 10^{7}$ is expected by our selective injection mechanism for ^{22}Ne due to the nuclear decay effects if the average temperature of the thermal pool of GCR source is $\sim$7000 K as suggested by the ionic model for GCR source(6).

This value is not different so much to the required enhancement factor $\sim 6 \times 10^7$. Furthermore, the requirement may be weekened if there is any source of ^{22}Na other than novae.

Finally, we should comment on a question, that is, why the excess is seen only for ^{22}Ne. The answer is that the selective injection mechanism due to the nuclear decay effects does not work fully for isotopes other than ^{22}Na, because they are either too short-lived or have been locked up into grains. Only ^{22}Na has an appropriate half life and remains in gas phase because Na is expected to behave as a volatile in space.

In conclusion, it may be possible to explain the origin of the observed ^{22}Ne excess in GCR source as due to interstellar ^{22}Na selectively injected by the nuclear recoil and shakeoff effects.

References

1. Simpson, J.A., 1983, Ann. Rev. Nucl. Part. Sci., 33, 323.
2. Meyer, J.P., 1985, Ap. J. Suppl., 57, 151.
3. Koch-Miramond, L., 1981, Proc. 17th Int. Cosmic Ray Conf., Paris, 12, 21.
4. Mahoney, W.A. et al., 1982, Ap. J., 262, 742.
5. Mahoney, W.A. et al., 1984, Ap. J., 286, 578.
6. Arnaud, M. and Casse, M., 1985, Astr. Ap., 144, 64.
7. Fisk, L.A., 1978, Ap. J., 224, 1048.
8. Freedman, M.S., 1974, Ann. Rev. Nucl. Sci., 24, 209.
9. Woosley, S.E. and Weaver, T.A., 1981, Ap. J., 243, 651.
10. Garcia-Munoz, M. et al., 1981, Proc. 17th Int. Cosmic Ray Conf., Paris, 2, 72.
11. Clayton, D.D. and Hoyle, F., 1974, Ap. J., 187, L101.
12. Clayton, D.D., 1984, Ap. J., 280, 144.
13. Hillebrandt, W. and Thielmann, F.K., 1982, Ap. J., 255, 617.
14. Allen, C.W., 1976, "Astrophysical Quantities" (London; Athlone).
15. Eichler, D., 1979, Ap. J., 229, 419.
16. Salpeter, E.E., 1977, Ann. Rev. Astr. Ap., 15, 267.

ON MAGNETIC PAIR PRODUCTION ABOVE FAST PULSAR POLAR CAPS

Shuyuan An
Physics Department, Beijing Teachers College
China

ABSTRACT

Magnetic pair production is one of high-energy electromagnetic conversion processes important to the development of pair-photon cascades in pulsars. On the basis of current polar cap models, this paper is concerned with the properties of magnetic pair production in fast pulsars. Suppose there is a roughly dipole magnetic field at the stellar surface, the author estimate the effects of non-zero curvature of magnetic field lines upon curvature radiation from primary particles and pair production rate near the surface of pulsars.

INTRODUCTION

In current pulsar theories[1,2], primary particles accelarated to extreme relativistic energies by the electric field component along the magnetic field near the polar cap emit curvature radiation, the photons of which, with sufficient energies, will convert into electron-positron pairs, and the processes will further develop into pair-photon cascade. The secondary pairs resulting from the cascade (Lorentz factor $\gamma \sim 10^2$-10^3) then produce radio or optical emission via a conherent process, and the surviving curvature photons constitute the observable high energy radiation from pulsars. It is believed that magnetic pair production is a very important attenuation mechanism governing the hard γ-ray emission from pulsars. The main aim of this paper is to estimate the effect of non-zero curvature of magnetic field lines in fast pulsars on the magnetic pair production and the curvature radiation from primary particles.

CURVATURE RADIATION AND MAGNETIC PAIR PRODUCTION

In the calculation concerned with pair-photon cascade above polar

cap, it is usually thought that primary particles move along curved magnetic field lines with vanishing pitch angle, and that most of the curvature radiation from primaries is emitted into a forward cone of half-angle $\sim 1/\gamma$, the power of which, according to the current estimate, is

$$P_{curv} \doteq 2\gamma^4 e^2 c/3R_{mc}^2 , \tag{1}$$

where R_{mc} denotes the curvature radius of field lines. Theoretically, a high-energy photon can be absorbed in an external magnetic field to create $e^{\pm}$ pair only if the following kinematic condition holds, i.e.,[3]

$$\hbar\omega \sin\theta \geq 2mc^2, \tag{2}$$

where $\hbar\omega$ is the photon energy, and θ the angle at which the photon propagates to the magnetic field. According to this view, at the moment when the photon is just emitted by a primary particle the threshold condition (2) will not be satisfied because $\theta = 0$. Thus, the pair can not be produced until θ grows to exceed the threshold condition with the propagating of the photon in the curved and rotating dipole magnetic field.

This point of view, however, would be partially corrected, if the effects of non-zero curvature of magnetic field lines on motion of charged particles are taken into account. Within the framework of the classical theory the associated calculation (see another conference paper by the author, OG 6.2-11) shows that the primary particle with a longitudinal initial velocity parallel to a field line possesses in fact non-zero pitch angle ψ for which one can approximately write

$$\psi \doteq \beta c/\omega_b R_{mc} \doteq 1.7\times 10^3 \gamma/B_p R_{mc} \ll 1, \tag{3}$$

where $\beta = v/c$, $\omega_b = eB_p/\gamma mc$ is the relativistic cyclotron frequency, and B_p the magnetic field intensity at the pole of pulsar. The curvature radius of the particle orbit R_{oc} is then

$$R_{oc} \doteq R_{mc}/2\left|\sin(\omega_b t/2)\right|, \tag{4}$$

which differs from the curvature radius of the field line R_{mc}. This implies that the radiation from primaries is of the synchro-curvature radiation, whose power (averaged over a cyclotron period) can be easily found with a direct calculation:

$$\bar{P}_{synch-curv} = \frac{1}{2\pi}\int_0^{2\pi} \frac{2}{3}\gamma^4 (e^2 c/R_{oc}^2) d(\omega_b t) \doteq \frac{4}{3}\gamma^4 (e^2 c/R_{mc}^2), \tag{5}$$

which is just twice that of the net curvature radiation. Bearing in mind that the power of synchrotron radiation, arising from the helical motion of a relativistic particle with the pitch angle ψ and Lorentz factor γ in a constant uniform magnetic field, may be put into the form[4]

$$P_{synch} = \frac{2}{3}(e^4/m^2c^3)(\gamma^2-1)B_p^2\sin^2\psi \doteq \frac{2}{3}\gamma^4(e^2c/R_{mc}^2)$$

which is formally identical with (1), it is immediately evident that in the case represented by (3) both the synchrotron radiation and the curvature radiation would make roughly the same contributions to the total power. A direct consequence is that one can establish a quantitative criterion for estimating the components of synchro-curvature radiation from a relativistic electron with various possible initial conditions, that is, the curvature radiation becomes significant only when the pitch angle of the electron does not increase beyond the value given by (3), otherwise the synchrotron radiation will be dominant.

On the other hand, it is possible that at the moment when the photon is just emitted by the primary the threshold condition (2) with $\theta=\theta_0=\psi$ might be satisfied due to $\psi\neq 0$, so the pair could be created. In particular, in the cases where $\theta_0=\psi\gg 1/\gamma$, the curvature photon could nearly satisfy even a much more severe condition imposed by dynamics of magnetic pair production,[3,5] i.e.,

$$\hbar\omega\sin\theta \gtrsim 0.2(B_{cr}/B_p)mc^2, \tag{6}$$

where

$$B_{cr} = m^2c^3/e\hbar \doteq 4.414\times 10^{13}\ \text{G}.$$

Under this condition one would anticipate for a considerable pair conversion rate.

IN APPLICATION TO FAST PULSARS

Fast pulsars possess usually shorter period, and sometimes weaker magnetic field. Most spectacular and extreme is the millisecond pulsars such as PSR 1937+214 for which the period P=1.558ms and field intensity $B_p \doteq 3\times 10^8$ G.[6] Suppose there is a dipole magnetic field at the stellar surface, and take the stellar radius $R\doteq 10^6$cm, one readily finds the curvature radius of field lines in the polar cap

$$R_{mc} \doteq (CRP/2\pi)^{1/2} = 2.7\times 10^6\text{cm} \tag{7}$$

and the Lorentz factor of primary particles

$$\gamma \doteq 3.1\times10^{6}(R_{mc}/10^{6}\text{cm})^{4/7}(P/1\text{s})^{-1/7}(B_p/10^{12}\text{G})^{-1/7} \doteq 4.4\times10^{7} \quad (8)$$

for PSR 1937+214. Inserting (7) and (8) into (3) we obtain the pitch angle of primary particles

$$\psi \doteq 1.7\times10^{3}\gamma/B_pR_{mc} \doteq 10^{-4} \gg 1/\gamma. \quad (9)$$

It is easy to see from (4) and (5) that considerable radiations occur only at about $R_{oc}=R_{mc}/2$, and so the critical energy of the curvature photon can be written, approximately,

$$\hbar\omega_{cr} = 3\hbar c\gamma^{3}/2R_{oc} \doteq 3\hbar c\gamma^{3}/R_{mc} \doteq 1.8\times10^{12}\text{ev}. \quad (10)$$

By using (9) and (10) we have

$$\hbar\omega_{cr}\sin\theta_0 \doteq \hbar\omega_{cr}\psi \doteq 370mc^{2} \gg 2mc^{2} \quad (11)$$

for $B_p \doteq 3\times10^{8}$G. This representation shows clearly that at the moment when the curvature photon is just emitted by the primary the threshold condition (2) is already exceeded greatly.

Datta[7] has recently placed an upper limit on B_p of 10^{7}G for PSR 1937+214 based on rotating neutron star models and realistic equations of state. If so, one would yield

$$\hbar\omega_{cr}\sin\theta_0 \doteq 6.7\times10^{4}\ mc^{2} \quad (12)$$

which is closer to the value imposed by the dynamic condition (6) than (11).

CONCLUSION

Our results point out that, when the effects of non-zero curvature of magnetic field lines on the motion of an electron with initial velocity exactly parallel to field lines (such as the primary particle in pulsars) are taken into account, the radiation power would be stronger than that given by current curvature radiation theories, and the curvature photons would convert into pairs more readily. One would expect that these results would affect to a certain extent the theoretical estimate for high-energy radiations from the millisecond pulsars.

ACKNOWLEDGEMENT

The author is grateful to Prof. Liaofu Luo for useful discussions.

REFERENCES

1. Ruderman, M. A. et. al., (1975), Astrophys. J. 196, P51.
2. Arons, J. et. al., (1979), Astrophys. J. 231, P854.
3. Daugherty, J. K. et. al., (1983), Astrophys. J. 273, P761.
4. Sutherland, P. G., (1979), Fund. Cos. Phys. 4, P95.
5. Sturrock, P. A., (1971), Astrophys. J. 164, P529.
6. Alpar, M. A. et. al., (1982), Nature 300, P728.
7. Datta, B., (1984), Nature 308, P338.

THE ELECTROMAGNETIC RAM ACTION OF THE PLASMA FOCUS AS A PARADIGM FOR THE GENERATION OF COSMIC RAYS AND THE GIGANTIC JETS IN ACTIVE GALAXIES.

W. H. Bostick, and V. Nardi
Stevens Institute of Technology
Hoboken, N.J. 07030, USA

ABSTRACT

Recent measurements(1) of the energy spectrum of the plasma-focus-generated deuteron beam yield a spectrum of the form $N(E) \sim E^{-2.7}$ for 1MeV<E<13MeV. Other measurements(2) show that the $\beta \to 1$ electron beam which is generated simultaneously with the deuteron beam is interrupted into segments of spacing 25ps and duration ~4ps. A stuttering-electromagnetic-ram (ser) model of the plasma focus is proposed which is similar to Raudorf's electronic ram(3) which produces a similar spectrum for an electron beam for 1Mev<E<10MeV. It is proposed that the cosmic ray spectrum and the gigantic galactic jets are both generated by ser action near the centers of active galaxies.

Raudorf(3) has shown experimentally and explained theoretically that a 20keV, rotating, electron beam traveling in an axial magnetic field will, upon running into a magnetic mirror, generate a stuttering electron beam (at the mirror) with energies up to 14 MeV, with an energy spectrum of $N(E) \sim E^{-3}$. Raudorf has called it an electronic ram. The plasma focus machine which is a discharge of a capacitor between two coaxial electrodes in a chamber filled with deuterium gas at 3 torr produces a current sheath which travels axially down the annular region of the coax as it conducts current from the center conductor to the outer conductor. Near the end of the center conductor the current sheath collapses radially to form what is loosely called a "pinch". In a typical small (5kJ) plasma focus machine, 45μf charged to 15kV produces a peak current at the time of the pinch of about 0.5MA in 1.3μs. This current of 0.5MA in the column of the pinch far exceeds the Alfven limit of $17000\beta\gamma$Amperes, but the current sheath automatically constructs itself into pairs of Beltrami-like, force-free, minimum-free-energy vortex filaments where the current density vector $\vec{J}$, magnetic field $\vec{B}$, mass flow velocity $\vec{V}$, and vorticity $\vec{\omega}$ are all parallel or antiparallel. The filaments are thus Lorentz and Magnus force free, with electrons everywhere flowing parallel to a local magnetic field, and the Alfven limit does not hold. But as the column "pinches", by its self-magnetic forces, down to a diameter of about 5mm it executes an action which is functionally similar to Raudorf's electronic ram: With a hollow center electrode a relativistic electron beam is generated which passes back (180°) through the hollow center electrode. The energy spectrum of the hard x-rays generated by this beam as it strikes metallic targets indicates an electron energy (up to a few Mev) spectrum of the form $N(E) \sim E^{-3}$. Measurements by the Darmstadt plasma focus group(2) show that the electron beam is segmented with segments of about 4ps duration and 25ps spacing. A deuteron beam is generated in the forward direction (0°) whose energy spectrum has been measured by the Stevens group(1) with both magnetic deflection and time of flight to have an overall shape of $N(E) \sim E^{-2.7}$ for 1 MeV<E<13MeV with mild peaks at 50keV, 300keV and 1.5Mev. Pinhole camera "photos" of the deuteron beam recorded on CR39 etchable plastic (nuclear particle track detectors) indicate a

diameter of the beam source of $\leq$ 0.5mm. X-ray (0.8keV-5keV) pinhole photos at 80° of the dense accelerating region (bremsstrahlung of electrons on deuterium) indicate dense electron beams and dense plasma of densities 10^{19} to $10^{21}/cm^3$ and dimension as low as 30μm in diameter and 100μm in length. dI/dt signals show a violent interruption of the column current.

Image-converter photos and time-resolved Mach Zender interferograms show that a rupturing of the Beltrami-like filaments occurs rapidly around the circumference of the column, probably on a picosecond time scale, and the well-organized current flow structure has been chopped in two, as if with a meat cleaver. In this cloven region the conduction current carried by the electrons can no longer flow because of the magnetic insulating effect which is produced by the displacement current in the cloven region. The inductive energy stored by the 0.5MA in the plasma column and the coaxial structure will not permit the net current to change with infinite abruptness, so the displacement current flows and charges up the plasma capacitor. However, the magnetic field of the displacement current is zero at the geometrical center of the column and it is here that a beam can flow and its electrons and deuterons can be accelerated by the voltage existing across the "capacitor". As the beam current approaches the Alfven limit it must organize itself into paired Beltrami-like filaments if its electron current is to continue, and this the beam very likely does and then ruptures itself again, and so on through a number of cycles. Fig. 1 is an attempt to construct on paper this series of cycles, which we call a stuttering electromagnetic ram. This process of increase of voltage across the "plasma capacitor" is adorned, in the profession, with the nomenclature of "anomalous resistance". The power, V^2/R, delivered to this resistance takes the form of accelerating the beams of electrons and deuterons to high energies.

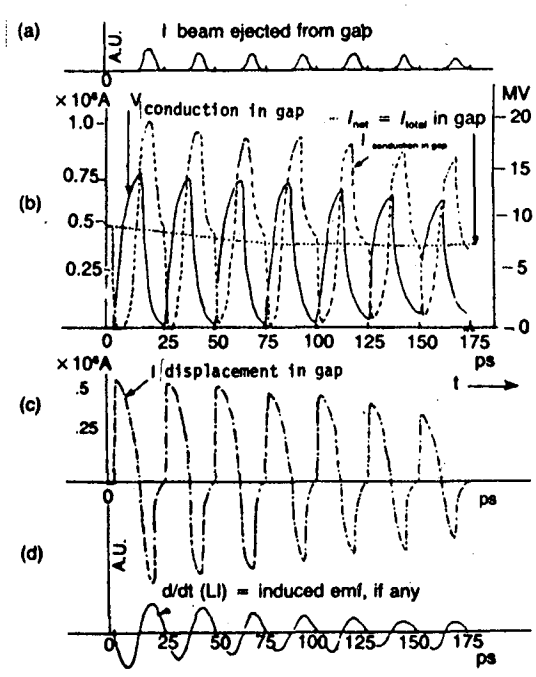

Fig. 1. Estimated wave forms produced by plasma focus as a stuttering electromagnetic ram. AU = arbitrary units.

In the portion of the cycle where the displacement current reverses direction the V_{cap} would be expected to approximate $V \sim e^{-t/RC}$ which would give a spectrum for the electron and ion beams of $N(E) \sim E^{\gamma}$ where $\gamma=-1$. However, if it is recognized that the increase of magnitude of the reversed I_{displ} also will increase the radius r of the electron and ion beams, and that the resistance $R \sim 1/r^2$, it can then be argued that the energy spectrum should be approximated by $N(E) \sim E^{\gamma}$ where $\gamma \tilde{=} -3$. This electronmagnetic ram effect represents only one of several morphological varieties of ion and electron acceleration by explosive magnetic field reconnection. The Stevens plasma focus machine has produced (5) for

example a "contact print" on CR-39 track-detector plastic of a filamentary "barber pole" structure with dimensions of ∿1cm. This "fossil" imprint of a plasmoid as it died in its encounter with the track-detector plate was engraved by deuterons whose energy (≧ 2.4MeV) was imparted to each of them locally as they delineated the print. It has been recognized at least as early as 1966 that the plasma focus was the laboratory-produced paradigm (b) of the solar flare phenomenon.

The stage has now been irresistibly set for this text to advance the hypothesis that the ser action of the plasma focus is the laboratory-produced paradigm for the generation of the primary cosmic ray spectrum. To identify the sources in the Universe where this ser action might be occuring this text recollects the galactic-genesis paradigms that were accidentally discovered by one of the authors when, in 1955, he projected plasma jets at one another across a magnetic field in the presence of an ionized background gas(7): Barred-spiral galactic morphology (see Fig. 2) was displayed with high fidelity and led to a model of galactic genesis and evolution in which the "bar" is the armature of a homopolar generator whose currents flow perpendicularly outward from each side of the center of the galactic disc, through force free filaments in a pattern in the halo which sustain and increase the overall dipole field of the galaxy, and return via the arms of the spiral. There is a nexus (an ser site) for these currents on each side of the center of the galactic disc. Here the cosmic ray primaries (the protons and heavier ions, and electrons) are accelerated by ser action which also can be conveniently responsible for the gigantic segmented jets in active galaxies(8).

Fig. 2. Kerr-cell (time-resolved, 0.1μsec exposure) photos of barred-spiral configurations generated by firing two plasma guns at one another across a magnetic field. Pressure of background gas in the chamber is indicated in microns; magnetic field in gauss.

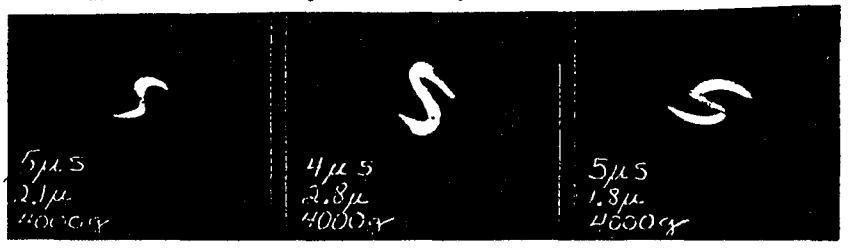

(+) This implies that the current carrier flow and the self-magnetic field lines in a filament are not exactly collinear. More appropriately, a quasi-force free rather than a force-free configuration should be used to describe the internal structure of a filament.

Acknowledgements: Work supported in part by AFOSR, Washington, D.C., and ONR, Arlington, VA.

References:

1. C. Powell, 1985, An Experimental Investigation of High Energy Ion Beam Production in the Plasma Focus, H. Kilic, Ph.D. Theses, Stevens Inst. of Technology, University Microfilms, Ann Arbor, Mich., 1985.
V. Nardi: et al. 1984 IAEA Conf. Aachen.
2. G. Herziger, et al. 1983 Radiation and Particle Emission from a 1.6Kj Plasma Focus, Plasma Focus Workshop, Stuttgart, (Sept).
3. W. Raudorf 1951, July, An Electronic Ram, Wireless Engineer:215.

References:

1. C. Powell, 1985, Ph.D. Thesis, Stevens Institute of Technology: An Experimental Investigation of High Energy Ion Beam Production in the Plasma Focus, H. Kilic, 1984, Ph.D. Thesis, Stevens Inst. of Technology, University Microfilms, Ann Arbor, Mich. V. Nardi: et al. 1983, XI European Fusion Conf., Aachen, p.483, Vol. 7D, part I.
2. G. Herziger, et al. 1983 Radiation and Particle Emission from a 1.6 kJ Plasma Focus, Plasma Focus Workshop, Stuttgart, (Sept. 1983).
3. W. Raudorf, An Electronic Ram, Wireless Engineer: 28, 215 (1951) and Proceedings of First International Conference on Energy Storage, Compression, and Switching (New York, Plenum), p. 381 (1976).
4. W. H. Bostick, 1985, (Jan.), Int. Journal of Fusion Energy, Vol. 3, No. 1, p, 74.
5. V. Nardi, et al., 1983 Second Int. Conf. on Energy Storage, Compression and Switching, Venice 1978 (New York: Plenum) p. 449. 1980 Phys. Rev. A, 22 (5):2211.
6. W. H. Bostick, et al. Phys. Fl. 9, 2079 (1966).
7. W. H. Bostick, 1956, Phys. Rev.104:292. Ibid. 1957, 106:404. 1956, Dec. 12, New York Times, p.1. Experimental Study of Plasmoids, Electromagnetic Phenomena in Cosmical Physics. IAU Symposium No.6, Stockholm (Cambridge Univ. Press). Rev. Mod. Phys., 1958,July, Vol. 30, No. 3: 1090 A. Peratt, et al. 1980 June, Phys. Rev. Lett. 44:1767.
8. J. O. Burns and R. M. Price, Centaurus A: The Nearest Active Galaxy, Scientific American, Nov. 1983, Vol.249, No. 5, p. 56.

THE ORIGINS OF COSMIC RAYS AND QUANTUM EFFECTS ON GRAVITY*

Yukio Tomozawa

Randall Laboratory of Physics
University of Michigan
Ann Arbor, Michigan 48109

Abstract

The energy spectrum of primary cosmic rays is explained by particles emitted during a thermal expansion of explosive objects inside and near the galaxy, remnants of which may be supernova and/or active galaxies, or even stars or galaxies that disappeared from our sight after the explosion. A power law energy spectrum for cosmic rays, $E^{-\alpha-1}$, is obtained from an expansion rate $t \propto R^{\alpha}$. Using the solution of the Einstein equation, we obtain a spectrum which agrees very well with experimental data. The implication of an inflationary early universe on the cosmic ray spectrum is also discussed. It is also suggested that the conflict between this model and the singularity theorem in classical general relativity may be eliminated by quantum effects.

*Paper submitted to the 19th International Cosmic Ray Conference, 1985

Since the discovery of cosmic rays early this century, an impressive amount of experimental data has been accumulated. Yet, the origin of cosmic rays defies the understanding of physicists. Several important questions are: What is the fraction of galactic and extragalactic components of primary cosmic rays? How can one understand the power law energy spectrum ($\sim E^{-2.5}$ - E^{-3} for the energy range 10^9 eV < E < 10^{20} eV)? How do they attain such high energies? Despite various attempts in the past to answer these questions, we are still left in the dark.[1] In this article, we present a model which explains some of the features of cosmic rays described above.

The following are the assumptions which we propose to make:

(a) The sources of primary cosmic rays are supernova, galaxies and/or clusters of galaxies which have exploded in the past, after the gravitational contraction. Active galaxies such as radio- or X-ray galaxies, Seifert galaxies, or QSO's may be the remnants of such an explosion. Or some of them might have disappeared completely from our sight after the explosion.

(b) The explosion of such an object is a replica of the expansion of the universe at a smaller scale. It goes from expansion in a radiation dominated era at extremely high temperature to that in a matter dominated era at lower temperature. It may even undergo a phase like that of an inflationary early universe.

(c) In the course of expansion, high energy particles of various kinds are emitted because of nonequilibrium processes. The energy distribution of the emitted particles reflects the black body radiation law at the temperature T at which the particles are emitted. The number of such

particles is not large and the system is approximately in equilibrium at each instant since the collision time is much smaller than the expansion time.

Under the assumptions, the number of particles of type x emitted with energy E is given by

$$f_x(E) = \frac{(2s+1)}{2\pi^2} \int \eta_x(E/kT) \frac{E^2 V_S dt}{e^{E/kT - \mu/kT} \pm 1}, \quad (1)$$

where V_S is the effective volume around the surface of the system which emits the particles, $\eta_x(E/kT)dt$ is the fraction of particles x emitted in time interval dt and μ and s are the chemical potential (zero) and the spin for fermions (bosons) of type x. The +(-) sign in the denominator is for fermions (bosons). The volume V_S is taken to be

$$V_S = 4\pi R^2 d = 4\pi \frac{a^2}{(kT)^3} \quad (2)$$

since the surface of the particle distribution is defined with uncertainty $\Delta x = d = 1/kT$, where a is a constant defined by $R = a/kT$. For an expanding system

$$t = bR^{\alpha}, \quad (3)$$

where b is constant and[2]

$\alpha=2$ for the radiation dominated era (4a)

and

$\alpha=3/2$ for the matter dominated era (the Einstein-deSitter flat space) (4b)

The function $\eta_x(E/kT)$ is unknown, but is assumed to scale as a function of E/kT. The result is essentially the same if the E (or T) dependence of $\eta_x(E/kT, E \text{ (or } T))$ is slowly varying except in E/kT. The chemical potential for fermions is obtained by the condition

$$\frac{N}{V} = \frac{(2s+1)}{2\pi^2} (kT)^3 \int_0^\infty \frac{x^2 dx}{e^{x - \mu/kT} + 1} \tag{5}$$

or equivalently

$$\mu_o \equiv \mu/kT = g\left(\frac{N}{V(kT)^3} \frac{2\pi^2}{(2s+1)}\right), \tag{6}$$

where N is the total number of particles in the system and V is the volume given by

$$V = \frac{4\pi}{3} R^3 = \frac{4\pi}{3} \frac{a^3}{(kT)^3} \tag{7}$$

(At high temperature, $g(x) = \ell n(x/2)$.) Obviously, μ_o is independent of temperature since VT^3 is constant during the course of the expansion. ($\mu_o=0$ for bosons, as was stated earlier.) Using eqs.(1)-(4), we obtain

$$f_x(E) = \frac{A_{x,\alpha}}{E^{\alpha+1}} , \tag{8}$$

where

$$A_{x,\alpha} = \frac{2(2s+1)\alpha b(a)^{2+\alpha}}{\pi} \int_0^\infty \frac{n_x(s) s^{\alpha+2} ds}{e^{s-\mu_o} \pm 1} \tag{9}$$

is a constant. Then, the total energy spectrum is given by

$$f(E) = \frac{A_\alpha}{E^{\alpha+1}} \tag{10}$$

where

$$A_\alpha = \sum_x A_{x,\alpha} . \tag{11}$$

The power law energy spectrum (8) and (10) with the values of α in eq.(4), is

EVALUATION OF PARAMETERS FOR PARTICLES ACCELERATION BY THE ZERO-POINT FIELD OF QUANTUM ELECTRODYNAMICS

A. Rueda
Department of Physics
University of Puerto Rico at Humacao
College Station, Humacao, Puerto Rico 00661

1. Preliminaries. That particles may be accelerated by vacuum effects in quantum field theory has been repeatedly proposed in the last few years[1-10]. A natural upshot of this is a mechanism for cosmic rays (CR) primaries acceleration[2-3,7-12]. We have been concerned with a mechanism for acceleration by the zero-point field (ZPF) when the ZPF is taken in a realistic sense (in opposition to a virtual field)[2,3,7,8,11,12]. Originally the idea was developed within a semiclassical context[2,3]. We used the classical Einstein-Hopf model (EHM) to show that free isolated electromagnetically interacting particles performed a random walk in phase space and more importantly in momentum space when submitted to the perennial action of the so called classical electromagnetic ZPF.[1] The Einstein-Hopf drag force provided the counteracting dissipation which vanished because of the ZPF Lorentz-invariance. The model could be applied to polarizable particles like protons and nucleii. For monopolar particles like electrons it could be shown that there would be a quenching of the acceleration due to a time dilation effect associated to the ultrarelativistic oscillation of the center of charge of the particle around the center of mass. This was reminiscent of zitterbewegung but in the context not of an intrinsic but of a vacuum effect.[6] Energy spectra of the accelerated particles could be derived assuming several presumably extant dissipation mechanisms in intergalactic space (IGS) like interparticle collisions,bremsstrahlung, inverse-Compton collisions and cosmic expansion (CE) [2,3,7]. IGS particle densities were taken at 10^{-5}- 10^{-7} cm^{-3}. The cut-off in the energy spectrum imposed by CE could be avoided if there was enough magnetic confinement within the magnetic cavities of superclusters so that particles would not be adiabatically cooled [7] by CE.

2. Quantum Version of the Einstein-Hopf Model. In order to check if the ZPF acceleration, originally predicted semiclassically, also occurs within ordinary Quantum Electrodynamics (QED), one should develop a quantum version of the EHM[8,12]. The original EHM considered a linear dipolar oscillator, constrained to vibrate parallel to the z-axis, mounted on a particle restricted to move unidimensionally along the x-axis[13,14]. Such a model was only good for discussing matters of principle[1,13,14]. We had to extend the model to three dimensions in the vibrations and three dimensions in the translations[2]. The linearity assumption could be relaxed[15]. Recently we have developed a quantum version[8,12] of the EHM by means of the Abraham-Lorentz operator equation proposed by Moniz and Sharp[16] in their nonrelataivistic approach to QED. Among several desirable features this approach has the advantage of being nonperturbative in its approximations, a real advantage when dealing with the divergent energy spectrum of the ZPF.

3. Acceleration in the Time Symmetric Zero-Point Field. With the quantum model above we show that if the ZPF is represented as a time symmetric background random field, there is acceleration[12]. The time symmetry of the ZPF suggests itself naturally if one is willing to preserve the time constancy of Planck's constant $\hbar$ in an expanding Universe where the ZPF is a background field tied to particles, i.e., if the ZPF is not a free field but if it is generated by the motion of charges in the Universe as is usually assumed in Stochastic Electrodynamics[17]. So, one constructs the ZPF by superimposing half-advanced

and half-retarded plane wave operators as follows from simple second quantization of Wheeler and Feynman's radiant absorver theory[18]. The resulting average translational energy growth per proton is given by[12,8]

$$\left\langle \frac{dE}{dt} \right\rangle = \frac{15\alpha}{4\pi^3} \int_0^\infty d\omega \left(\frac{\hbar\omega}{Mc^2} \right)^2 \left(\Gamma_M \omega \right) \left(\hbar\omega \right) |g|^2 \qquad (1)$$

where α is the fine structure cosntant, e and M are the proton charge and mass respectively, $\Gamma_M = 2e^2 / 3Mc^3$ is the associated Abraham-Lorentz time parameter, and

$$g \equiv \left[\delta + i\sigma \right]^{-1} \qquad (2)$$

with

$$\delta \equiv \frac{m}{M} \left[\left(\left(\frac{\omega}{\omega} \right)^2 - \frac{m}{M} \right)^{-1} - 1 \right] . \qquad (3)$$

$$\sigma \equiv \left(\frac{\Gamma_m \omega}{3} \right) \sum_{s=0}^{\infty} \frac{(8s + 9)}{(s + 1)(2s + 3)} \frac{(4s + 1)!!}{(2s)!} \left(\frac{\omega}{\omega_c} \right)^{2s} \qquad (4)$$

where $\Gamma_m = \Gamma_M (M/m)$, m is the equivalent mass of the entity that oscillates inside the proton[19]. The summation results from going to the point particle limit[16] and $\omega_c = mc^2/\hbar$ is the corresponding Compton frequency. In practice one may take mc^2 to be approximately equal to a few MeV (H. Leutwyler, personal communication), and in principle m cannot be smaller than the quark's rest mass[19].

4. No Acceleration in the Time-Asymmetric Zero-Point Field. If the ZPF is represented as a time asymmetric (retarded) expansion of plane waves, it can be rigorously shown[12] at least up to the first iteration in the quantum EHM, that no acceleration takes place and $< dE/dt > = 0$. This result is to be expected if internal thermodynamic consistency of QED is demanded but one has to pay the price of not having a clear origin for the ZPF and of giving up interesting vacuum effects.

5. Evaluation of Parameters. When a Fokker-Planck equation is established for a dilute (10^{-5} - 10^{-7} cm^3)gas of protons under the influence of the ZPF plus a thermal background it can be numerically shown[12] that the ensueing very long relaxation time (much longer than the age of the Universe) implies that the mechanism of Section 3 works efficiently up to inelastic inverse Compton collisions energies (10^{18} eV, pair production) implying that other dissipation mechanisms like those mentioned above should be invoked to establish the energy spectrum of particles. The correspondance between the semiclassical $< dE/dt >$ and the quantum $< dE/dt >$ of Section 3 is quantitatively very good. All the previously proposed preliminary propagation models[2,7] may then easily be adapted to the quantum case[12]. Numerical evaluation of $< dE/dt >$ has been performed for a wide range of values of m/M (or ω_c). The fitting of the model to times consistent to expected CR propagation times taking care of the mentioned Greisen-Zatsepin effect is easily done for a rather wide margin of values of ω_c (or m/M)[20]. Unfortunately there is a paucity of data and of theoretical numerically tractable results on the proton polarizability response at the ultrahigh ZPF induced excitations frequencies that are expected[21,7].

6. SUMMARY. The acceleration mechanism was originally established semiclassically using the EHM in a classical stochastic version of the ZPF[2,3,6,7,11]. The acceleration was an

upshot of the Lorentz-invariance of the ZPF spectral energy density. By a quantum version of the EHM we have shown within QED that acceleration occurs for the time-symmetric version of the ZPF[7,12] but not for the time-asymmetric (retarded) version[12]. We hope this opens the way to an important new class of candidates for sources of acceleration of particles in the IGS, namely vacuum effects in quantum field theory.

7. Postcript. This postcript is written for the theoretically minded reader. We have performed the second quantization of the one half-advanced plus one half-retarded radiation in the Wheeler-Feynman absorver theory.[18] No attempt however has been made at a full quantization of an action at a distance theory which because of troublesome boundary conditions is not easily quantizable as is well known[22].

8. Acknowledgements. This work was sponsored by the Resource Center for Sciences and Engineering at the UPR in Rio Piedras. The author acknowledges the sponsorship of Professors M. Gómez, J. Arce de Sanabia and J.F. Nieves.

References

1. Boyer, T.H., Phys. Rev. 182, 1374 (1969) and 186, 1304 (1969).

2. Rueda, A., Nuovo Cimento 48A, 155 (1978).

3. Rueda, A., Phys. Rev. A 23, 2020 (1981).

4. Marshall, T.W., Phys. Rev D 24, 1509 (1981).

5. Cavalleri, G., Phys. Rev D 23, 363 (1981).

6. Rueda, A. and Cavalleri, G., Nuovo Cimento C 6, 239 (1983).

7. Rueda, A., Nuovo Cimento C 6, 523 (1983).

8. Rueda, A., Phys. Rev. A 30, 2221 (1984).

9. Namsrai, Kh., Found. Phys. 15, 129 (1985).

10. Sinha, M. and Roy, S. "Stochastic Space Time and the primary energy spectrum of cosmic rays at $E \geq 10^{19}$eV", preprint, Indian Statistical Institute (Calcutta, India, 1985).

11. Rueda, A., Proceedings 17th ICRC 2, 361 (Paris, 1981) and Proceedings 18th ICRC 1, 31 (Bangalore, India, 1983).

12. Rueda, A., UPR Preprint, in preparation (1985).

13. Einstein, A. and Hopf, L., Annalen der Physik 33, 1105 (1910).

14. Bergia, S. et al., Ann. Fond. L. de Broglie 4, 295 (1979).

15. Diaz-Salamanca, C. and Rueda, A., Phys. Rev. D 29, 648 (1984).

16. Moniz, E.J. and Sharp, D.H., Phys. Rev. D 15, 2850 (1977).

17. See, e.g. De la Peña, L. in Stochastic Processes in Physics and Related Fields Gómez B. et al, (editors) (World Scientific, Singapore 1983).

18. Wheeler, J.A. and Feynman, R.P., Rev. Mod. Phys. 17, 157 (1945).

19. See, e.g. Gasser, J. and Leutwyler, H. "Quark Masses" preprint (University of Bern, 1982).

20. Arenas L. and Rueda A., UPR preprint, in preparation (1985).

21. See, e.g., Gasser J. and Leutwyler H., Quark Masses (U. of Bern, 1982) preprint;

Leutwyler H., On the Status of QCD (U. of Bern, 1982) preprint; for a more detailed exposition see Flamm D. and Schöberl F., Introduction to the Quark Model of Elementary Particles (Gordon and Breach, New York, 1982).

22. See, e.g., Barut A.O., Electrodynamics and Classical Theory of Fields and Particles (Dover, New York 1964,1980); Coleman S., Classical Electron Theory from a Modern Standpoint preprint (Rand Corp., Santa Mónica Ca. U.S.A., 1961); Davies P.C.W., The Physics of Time Assymmetry (U. of California Press, Berkeley Ca., 1974); Hoyle F. and Narlikar J.V., Ann. Phys. 54, 207 (1969).

GIANT MOLECULAR CLOUDS AS REGIONS OF PARTICLE ACCELERATION

Dogiel V.A., Gurevich A.V., Istomin Ya.N., Zybin K.A.
P.N.Lebedev Physical Institute of the USSR Academy of Sciences, Moscow, USSR.

One of the most interesting results of investigations carried out on the satellites SAS-II and COS-B is the discovery of unidentified discrete gamma-sources. Possibly a considerable part of them may well be giant molecular clouds /I/. Gamma-emission from clouds is caused by the processes with participation of cosmic rays /2/. The estimation of the cosmic-ray density in clouds has shown that for the energy E ~ I GeV their density can 10-10^3 times exceed the one in intercloud space /3,4/. We have made an attempt to determine the mechanism which could lead to the increase in the cosmic-ray density in clouds.

The main results of these studies are as follows: I. In clouds there may occur particle acceleration. 2. The density of protons ejected by clouds in interstellar (intercloud) space is equal to I-I0% of the observed one. 3. Such a mechanism of acceleration, if it is realistic, necessitates a change in the existing concept of the formation of the chemical composition of cosmic rays in the Galaxy. 4. In its characteristics the intensity of non-thermal (synchrotron) emission from clouds is similar to the emission from H II-regions. This allows us to suppose that a part of radioemission, which was considered earlier to be thermal is acutally a non-thermal emission from molecular clouds.

In our estimations we have used the following parameters of the molecular clouds: dimension R = 10 pc. hydrogen mass $M = 10^5 M_\odot$, neutral gas density $N_n = 10^3$ cm^{-3}, degree of ionization $N_i / N_n = 10^{-6}$.

The crucial moment in our model is that the neutral gas of molecular clouds is turbulized. According to observations, the turbulence spectrum has the form /5/: $u(L)^{km/sec} \simeq I.I\, L^{\alpha}$ (pc) for $0.I < L < I00$ pc. Here u is velocity, L is scale, the parameter $\alpha \simeq 0.38$. Below we discuss how the energy of the neutral gas can be transformed into the energy of accelerated particles.

The spectrum of magnetic field fluctuations. According to the condition $\nu_{ei} > \nu_{en},\ {}^{m}/_{m_e}\nu_{in}$ the equations for the velocity of the ionized plasma component and for the magnetic field $\bar{B}$ have the form

$$\frac{d\bar{V}}{dt} = -\nabla P/\rho - [\bar{B}\cdot curl\,\bar{B}]/4\pi\rho - \nu_{in}(\bar{V}-\bar{u}) + \eta_i \nabla^2 \bar{V}$$

$$\frac{\partial \bar{B}}{\partial t} = curl[\bar{V}\bar{B}], \qquad \frac{\partial \rho}{\partial t} = -div(\rho \bar{V}), \qquad div\,\bar{B} = 0 \qquad (I)$$

Here i, e, n stand for the ion, electron, and neutral plasma components; ν is collision frequency of corresponding particles, η_i is ion viscosity which is the largest for the assumed parameters.

The frequency interval for motions of the ionized component is as follows $\nu_{ni} < \omega = 2\pi V(u)/L \ll \nu_{in}$. According to the

first inequality, we can neglect the influence of the ionized component on the neutral one. According to the second inequality ($\omega/\nu_{in} \ll 1$), we obtain $v(L) \simeq u(L)$ from the first equation of the system (I). Note that the interval of L values is determined by the relation $L_0 > L > L_{min}$, $L_{min} = L_0 Re^{-1/(1+\alpha)}$, $Re = u_0 L_0/\eta_i$ ($u_0 = 10^6$cm/sec, $L_0 = 10^{19}$ cm, $L_{min} = 10^{13}$cm). The eigenvalues ω of the system (I) are imaginary, $\omega = iV_A^2/(\nu_{in}L)^2$, and hence the magnetic field on the scale $L > L_{min}$ is excited only under the action of an inducing force (friction between charged and neutral components) on the scale L_{min}. Then the spectrum of magnetic field fluctuations has the form/7/: $B^2(L) = B_m^2 \cdot (L/L_{min})^{-5}$ for $L > L_{min}$. The estimations give $B_m \simeq 10^{-5} - 10^{-6}$oe.

Equations of motion for particles in random electromagnetic fields. In a magnetic field $B \sim 10^{-5}$ oe protons with energies $E_p \simeq 3$-30 GeV and electrons with energies $E_e \simeq 10^2 - 10^3$ GeV turn out to be magnetized, i.e. $\gamma < \omega_H \tau_c$ (here ω_H is cyclotron frequency, γ is gamma-factor of particles, τ_c is correlation time $\tau_c = L_{min}/c$). For magnetized particles one can derive (see /8/) the equation for the distribution function f :

$$\frac{\partial f}{\partial t} = \nabla(A_x \nabla f) + \frac{\partial}{\partial \gamma}\left(\gamma A_\gamma \frac{\partial}{\partial \gamma}(\gamma f) + p f\right) \qquad (2)$$

Here A_x and A_γ are diffusion coefficients in the coordinate and energy spaces, p is the function describing energy losses of particles.

$$A_x \simeq \frac{\pi c L_{min}}{6}, \quad A_\gamma \simeq \frac{\pi u_0^2}{3 c L_{min}} \qquad (3)$$

The equation of motion for nonmagnetized particles has the form

$$\frac{\partial f}{\partial t} = \gamma^2 \mathcal{D}_x \nabla^2 f + \frac{\partial}{\partial \gamma}\left(\gamma^2 \mathcal{D}_\gamma \frac{\partial}{\partial \gamma}\left(\frac{f}{\gamma^2}\right)\right) \qquad (4)$$

$$\mathcal{D}_x = \frac{m^2 c^4}{6 \nu_0}, \quad \nu_0 = e^2 \int_0^\infty \langle B^2 \rangle_{\tau, v\tau} d\tau, \quad \mathcal{D}_\gamma = \frac{2}{3} \frac{e^2}{m^2 c^4} \int_0^\infty \langle v^2 \rangle_{\tau, v\tau} \langle B^2 \rangle_{\tau, v\tau} d\tau \qquad (5)$$

Cosmic-ray density in a cloud. Let us assume the distribution function f of particles inside a cloud or radius R to be described by equations (2) and (4) and let outside the cloud the equation have the form

$$\frac{\partial f}{\partial t} = \nabla(\mathcal{D}_0 \nabla f) \qquad (6)$$

where $\mathcal{D}_0$ is the spatial diffusion coefficient in interstellar space, $\mathcal{D}_0 = 10^{28}$ cm^2 /see/2//. We obtain from the expressions (3) that inside a cloud the spatial diffusion coefficient is much smaller, $A_x \simeq 10^{23}$cm^2/sec. and the value $A_\gamma \simeq 10^{-11}$ sec^{-1}. At infinity ($r \to \infty$) we set up the cosmic-ray spectrum in intercloud space, f_∞ , and assume it to be similar to the one observed near the Earth ($f_\infty = K E^{-\lambda}, \lambda \simeq 3$). Then inside the cloud ($r < R$) there holds the following solution for magnetized particles ($\omega_H \tau_c > \gamma \gg 1$)

$$f = \frac{2 N_\infty}{\varkappa} \lambda \frac{R}{r} \sin\left(\pi \frac{r}{R}\right) \cdot \gamma^{-\left(1+\pi \frac{\lambda}{\varkappa}\right)} \qquad (7)$$

Here $N_\infty = \int_0^\infty f_\infty d\gamma$, the quantity $\varkappa = \lambda\sqrt{A_\gamma R^2/A_x}$. Thus, a statistic acceleration in random electric fields ($\bar{\mathcal{E}}(L) = -\frac{1}{c}\cdot[\bar{v}\bar{\beta}]$) of a cloud leads to generation of hard spectra. The spectrum of non-magnetized particles ($\gamma \gg \omega_H \tau_c$) has the form

$$f = C\gamma^{3/2} K_{1/4}[(\pi^2 \mathcal{D}_x/(R^2\mathcal{D}_\gamma)\gamma^2/2] \quad (8)$$

Here C is the constant determined from the conditions of joining of the solutions (7) and (8), $K_\nu(x)$ is a McDonald function. The solution (8) falls exponentially in the energy range $\gamma \gg \omega_H \tau_c$.

If we take as f_∞ the proton spectrum observed near the Earth, we obtain that the proton density inside a cloud can exceed more than by an order of magnitude the proton density in intercloud space for proton energies $E \simeq 1$ GeV.

Not let us pass over to astrophysical applications of this model.

I. Gamma-emission from molecular clouds and determination of the cosmic-ray gradient from the background emission in the Galaxy. The total gamma-emission flux ($E_\gamma > 100$ MeV) from a molecular cloud makes up about 10^{35} erg/sec. Assuming that in the Galaxy there exist several thousands of such clouds, we come to the conclusion that the considerable part of gamma-emission from the galactic disk consists of emission from molecular clouds. It is thus clear that inside the solar circle, where a large amount of molecular hydrogen is concentrated, we cannot determine the gradient of cosmic-rays which is due to cosmic ray leakage from the Galaxy. The cosmic ray gradient calculated there from the diffusion gamma-emission of the galactic disk will simply reflect the mean density of cosmic rays accelerated in the clouds. This cosmic-ray density must, in turn, be proportional to the nonuniform distribution of molecular hydrogen in the galactic disk.

In connection with what has been said it is important to measure the spectral index of gamma-sources and of the diffusion gamma-emission of the galactic disk where the main part of gas is concluded in the clouds. If acceleration does take place in the clouds, the gamma-radiation intensity for $E \gg 100$ MeV has the following dependence: $I_\gamma \propto E_\gamma^{-1}$. If not, then $I_\gamma \propto E_\gamma^{-2.75}$.

2. Molecular clouds as antiproton sources in the Galaxy. As the estimates show, the antiproton density inside clouds can be of the order of 10^{-12} $(cm^3 GeV)^{-1}$ for energies $E_{\bar{p}} \simeq 1$ GeV. Calculating the antiproton flux from the clouds we obtain that the antiproton density in intercloud medium must be $n_{\bar{p}}(E_{\bar{p}} \simeq 1\,GeV) \simeq 10^{-14}$ $(cm^3 GeV)^{-1}$. This value corresponds to the antiproton density observed near the Earth. According to our calculations, the antiproton density must fall like $n_{\bar{p}} \propto E_{\bar{p}}^{-1.4}$ in the relativistic energy range. In the nonrelativistic region (30 MeV $< E_{\bar{p}} <$ 1 GeV) the antiproton density weakly depends on the particle energy ($n_{\bar{p}} \propto E^{-0.5}$). Thus, the origin of galactic antiprotons (see ref./9/) can be explained in the framework of our model.

3. Molecular clouds and secondary nuclei in the composition of galactic cosmic rays. There exists a problem of the origin of light secondary nuclei in the Galaxy. The calculations of the grammage passed by cosmic rays before the formation of secondary nuclei give the following results: for antiprotons ($E_{\bar{p}} > 1$ GeV) $x \simeq 21$ gr/cm^2 /10/, for deuterium $x \simeq 15$ gr/cm^2 /11/, for He^3 $x \simeq 15$ gr/cm^2 /12/. For heavier nuclei, beginning with the group Li, Be, B, the calculations of X give approximately the same value: $X \simeq 5$ gr/cm /2/. All these calculations are made in the assumption diffusion or leaky-box models.

As our estimates show, light nuclei (P, D, He^3) can be effectively accelerated in the clouds since their acceleration time ($\sim 1/\Lambda_{\delta}$) is much less than the characteristic lifetime of particles (through the nuclear collisions). For heavier nuclei with an atomic number $A \gtrsim 10$ the situation is quite opposite, and therefore their acceleration in clouds is not effective. From this we can assume that the P, D, and He^3 nuclei are formed in molecular clouds, and heavier secondary nuclei in interstellar (intercloud) medium in the process of propagation diffusion of primary cosmic rays.

4. Molecular clouds and positrons in the composition of cosmic rays. As the estimates show, for the energies $E \simeq 1$ GeV their density of positrons $n_{e^+} \simeq 10^{-12}$ (cm^3 GeV)$^{-1}$ and the dependence of the density on the particle energy E_e is as follows: $n_e(E>1\,\mathrm{GeV}) \propto E_e^{-1}$. The estimates show that the density of positrons ejected by the clouds in intercloud space is equal to the one observed near the Earth for $E \simeq 1$ GeV. In the diffusion model the positrons ejected from the clouds into intercloud space must have the spectrum $I_{e^+} \propto E_{e^+}^{-1.7}$ for $E_{e^+} > 1$ GeV. If there is no acceleration in the clouds, the positron spectrum must have the form $I_{e^+} \propto E_{e^+}^{-3.4}$ /2/.

The observations /12/ just show an anomalously high positron intensity for energies $E_{e^+} \sim 10$ GeV near the Earth that is in accordance with our model.

5. Radioemission of molecular clouds. According to the above characteristics of the electron spectrum in the clouds, the intensity J_ν of radioemission from the clouds does not depend (or depends weakly) on the frequency ν: $J_\nu \simeq$ const. The flux of radioemission from a cloud can be of the order of $\Phi_\nu \simeq 10^{21} - 10^{22}$ erg/sec for all frequencies up to $\nu < 10^{12}$–10^{16} Hz where the spectrum of radioemission from the cloud suddely falls.

1. Wolfendale A.W. - Quart.J.Ray.Astron.Soc., 24, 226, 1983.
2. Berezinsky V.S., Bulanov S.V., Ginzburg V.L., Dogiel V.A., Ptuskin V.S.-Cosmic Ray Astrophysics, Moscow, Nauka, 1984.
3. Issa M.R., Wolfendale A.W.-Nature, 292, 420, 1981.
4. Morfill G.E., Forman M., Bignami C.F. - Ap.J., 284, 656, 1984. 5. Larson R.B. - MNRAS, 194, 809, 1981. 6. Gurevich A.V. - Nonlinear Phenomena in the Ionosphere, Springer, 1978. 7. Graichnan R.H., Nagarajan S.-Phys.of Fluids, 10, 859, 1967. 8. Gurevich A.V., Zybin K.P., Istomin Ya.N.-JETF, 84, 86, 1983. 9. Juliusson E.-18 ICRC, 12, 117, 1983.
10. Golden R.L., Nunn S., Horan S.-18ICRC, 2, 80, 1983.
11. Webber W.D., Yushak S.M.-Ap.J., 275, 391, 1983. 12. Jordan S.P. Meyer P.-Phys.Rev.Let., 53, 505, 1984. 13. Protheroe J. Ap.J.

THE NUCLEOSYNTHESIS OF DEUTERIUM AND HELIUM-3

Lavrukhina A.K., and Kuznetsova R.I.

V.I.Vernadsky Institute of Geochemistry and Analytical Chemistry, USSR Academy of Sciences, Moscow, USSR

We have supposed a new model of the creation of D and ^{3}He in supernova of the first generation. It is based on the idea that a supernova event leads simultaneously to acceleration of particles in the shock wave front and to their interactions with supernova atmosphere matter. The D, ^{3}He, Li, Be, B and by-passed isotopes are created in these interactions. The cosmic abundances of the by-passed isotopes with $A \geq 113$ allowed to determine the integral proton flux - $I_p(E_p > 25\ MeV)=5\times10^{21}$ cm^{-2}, the spectral index - $\gamma = 3$. The calculations of the D and ^{3}He yields in various nuclear reactions at these irradiation conditions show that only the ^{4}He(p,d)^{3}He reaction leads to cosmic abundances of these isotopes on the assumption that all matter has been exposed.

1. Introduction

The nucleosynthesis of D and ^{3}He is possible: (1) during expansion of the hot and dense Universe, (2)in spallation reactions of interstellar matter with galactic cosmic rays, (3)in high-energy ion reactions in shock wave front during explosions of supermassive objects and supernovae of Type II, (4)during momentary processes in active galactic nuclei, and (5)in reactions of interaction of neutrino from collapsing nucleous of supernova. The theoretical models of the expanding Universe explain the main observations of cosmological significance: (1)the red-shifts of distant galaxies, (2)the isotropic distribution of galaxies, (3) the homogeneous distribution of nearby galaxies, (4) the distribution of distant galaxies and radio sources, (5)the microwave background, (6)the X-ray background, and (7)the chemical and isotopic compositions of the initial matter. The D, ^{3}He, ^{4}He, and ^{7}Li cosmological abundances and the microwave background properties are the most informative characteristics for investigation of the physical conditions in the early Universe. The observated tendency of the decreasing of the initial component parts of $Y_p(^4He) \approx 0.22-0.245$, $D/H \approx (2 + 0.5)\times 10^{-5}$, $^3He/H=(1-2)\times10^{-5}$ and $^7Li/H=1\times10^{-9}$ /1/ leads to serious difficulties of the cosmological models. Even the standard isotropic and homogeneous models with the zero lepton number /1,2/ do not allow to obtain the cosmic abundances of ^{4}He and deuterium at anyone ent-

ropy value. Therefore the investigation of a possibility of the galactic nucleosynthesis of deuterium is important for the problem of an initial nucleosynthesis in the early Universe.

A few possible classes of objects may be responsible for most of the galactic nucleosynthesis of deuterium. These are: (1)the explosion of supermassive objects, (2)supernovae of Type II, (3)the active galactic nuclei and quasars, and (4)interstellar gas.Two main processes have led to the formation of deuterium. One of them is the spallation in supernova shocks /3, 4/. The propagation of the supernova explosion shock wave in the density gradient of the stellar envelope results in a shock of increasing strength. The acceleration of matter by the shock wave has previously been associated with the formation of cosmic rays. In the peculiar very low density conditions of a presumed red-giant envelope, a strong shock wave, ~10 MeV per nucleon in 10^{-3} to 10^{-4} stellar mass fraction, can result in the nearly complete spallation of He plus heaviers to free neutrons and protons. The neutron capture on the protons has led to creation of deuterium.The other group of processes includes the spallation reactions with galactic cosmic rays in the interstellar gas /5,6/.

We have examined a possibility of the creation of deuterium and helium-3 in a massive supernova of the first generation. Our model is based on the idea that a supernova event leads simultaneously to explosive nuclei burning, to acceleration of particles in the front of a shock wave and their interactions with the atoms in supernova atmosphere /7,8/.

2. Nuclear reactions of the synthesis of deuterium and helium-3

We have examined the following nuclear reactions: $H(p,\beta^+)D$, $^4He(p,d)^3He$, $^4He(p,2p)^3H$, $^4He(p,pn)^3He$, $^4He(p,pd)D$, and $^4He(p,2pn)D$ with the threshold energies of ~300, 18.32, 19.81, 20.55, 23.75, and 25.97 MeV, respectively. The second reaction is the most probable. Its function dependence of $d\sigma/d\Omega$ from θ has been only determined at the proton energies of 31.5 MeV /10/, 55 MeV /11/, and 93 MeV /12/. Using the method of graphic interpolation on the energy regions of < 30 MeV and >100 MeV we have obtained the excitation function for the $^4He(p,d)^3He$ reaction (see Figure, curve 1). The excitation function of the $H(p,\beta^+)D$ reaction has been obtained in accordance with the experimental data /12, 13/ (see Figure, curve II).

The experimental data for the cross sections of the break up reactions of $^4He(p,2p)^3H$, $^4He(p,pn)^3He$, $^4He(p,pd)D$, and $^4He(p,2pn)D$ are absent. However, it was possible to make a comparison of the total cross section of the break up reactions at E_p=55 MeV with

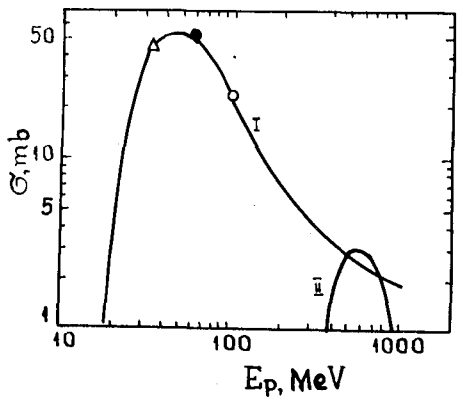

Figure. The excitation functions: I -the $^4He(p,d)^3He$ reaction from /10-12/, II - the $H(p,\beta^+)D$ - reaction from /12,13/. 1-from /10/, 2-from /11/, and 3-from /12/.

corresponding value for the $^4He(p,D)^3He$ reaction /11/. They are equal to 50-80 mb and 40 mb respectively. Hence, the contribution from the break up reactions doubles the yields of deuterium and helium-3. The observed and calculated abundances of deuterium and helium-3 are given in the Table. The calculations have been made at the following parameters: (1)the cosmic abundances of the seed nuclei /9/, (2)$I_p(E_p \geq 25MeV) = 5 \times 10^{21}$ cm^{-2}, (3)the spectral index of $\gamma = 2.5$. The cross-section of each reaction was averaged according to the energetic spectrum of galactic cosmic rays, as well as averaged according to the isotopic elemental compositions of the irradiated matter.

TABLE. The calculated and observed abundances of deuterium and helium-3(atoms/10^6atoms Si)

Target	Isotope	$\bar{\sigma}$, cm^{-2}	N calculated	N observed
^4He	^3He	38.5×10^{-27}	4.2×10^5	3.7×10^5
^4He	D	38.5×10^{-27}	4.2×10^5	5.2×10^5
H	D	1.4×10^{-30}	2.2×10^2	

These data show that the created in the $^4He(p,D)^3He$ reaction amounts of deuterium and helium-3 are comparable with the cosmic abundances of these isotopes on the assumption that all matter has been exposed. However, if we take into consideration the contribution of the break up reactions then the amount of irradiated matter will decrease up to ~50 per cent.

3.Conclusions

The nucleosynthesis of D and ^3He in supernova of the first generation puts a hard limitation in temperature and chemical composition of the envelopes where it had taken place. The temperatures of the C and O envelopes are high ($T \geq 10^7 K$) and the D, ^3He, Li, Be, B isotopes, created by spallation reactions with the CNO nuclei, are destroied. Therefore, the D and ^3He creation had taken place only in the atmospheres of the

first generation supernova and in interstellar gas which have cosmological composition (hydrogen and helium). The nucleosynthesis of the Li, Be and B isctopes had taken place in nuclear reactions during supernova events of the second generation stars /14/. These data lead to the conclusion that the matter, thrown of the supernova of the first generation, are not exposed to an intensive irradiation in interstellar space. This puts a limitation on models of the galactic structure formation and their evolution.

The D nucleosynthesis in the first generation supernovae not agree with the model of the Galaxy formation in a process of protogalaxy collapse. This model leads to an overproduction of Li, Be and B. To avoid the excess of these elements we examine a model of a homogeneous matter fragmentation with the formation of fragments of $M \sim (10^6 \div 10^8) M_\odot$. The collapse of latter led to formation of massive stars ($M > 100 M_\odot$) of the first generation which have simultaneously evolved. However, these stars have large mass-loss rates and expose the products of nuclear burning at the surface relatively early in their life. This material ejected in the stellar wind can mix with a nearby interstellar gas (and dust) prior to the supernova event. It also leads to an overproduction of Li, Be and B. This problem requires a detailed study.

REFERENSES

1. Audouze, J. (1982). In: Pontifical Academie Scienciarum Scripta Varia., 1981, p.48.
2. Olive, K.A. et al., (1981), Astrophys.J. 241, 557.
3. Colgate, S.A. (1974), Astrophys.J. 187, p.321.
4. Hoyle, F. and Fowler, W.A. (1973), Nature, 241, p.384.
5. Reeves, H.E. et al., (1973), Astrophys.J. 179, p. 909.
6. Audouze, J. et al., (1978). In: Spallation nuclear reaction and their applications, D.Reidel, Dordrecht, p.113.
7. Lavrukhina, A.K. and Kuznetsova, R.I. (1979). In: Origin and Distribution of the Elements, Pergamon Press, Oxford and New York, p.3.
8. Lavrukhina, A.K. and Kuznetsova, R.I. (1980), Geochimia (Russian), p.3.
9. Cameron, A.G.W. (1973), Space Sci.Rev. 15, p.121.
10. Benveniste, J. and Cork, B. (1953), Phys.Rev. 89, p.422.
11. Hayanowa, S. et al., (1964), J.Phys.Soc. of Japan, 19, p.2004.
12. Selove, W. and Teem, J.M.(1958),Phys.Rev.112,p.1658.
13. Overseth, O.E. et al., (1964), Phys.Rev.Lett., 13, p.59.
14. Kuznetsova, R.I. and Lavrukhina, A.K. (1982), Geochimia (Russian) p.307.

OG 8.2-I9

NUCLEAR REACTIONS IN SHOCK WAVE FRONT DURING SUPERNOVA EVENTS.

A.K.Lavrukhina

V.I.Vernadsky Institute of Geochemistry and Analytical Chemistry, USSR Academy of Sciences, Moscow, USSR

The new unique isotopic anomalous component of Xe(XeX) was found in the carbonaceous chondrites. It is enriched in light shielded isotopes (^{124}Xe and ^{126}Xe) and in heavy nonshielded isotopes (^{134}Xe and ^{136}Xe). We suppose that all characteristics of Xe-X can be explained by a model of nucleosynthesis of the Xe isotopes in shock wave front passed through the He envelope during supernova events. The light isotopes are created by p-process and the heavy isotopes are created by n-procese ("slow" r-process). They were captured with high-temperature carbon grains condensing by supernova shock waves.

1. Introduction

The shock waves from supermassive object explosions pass through an environment of low density (outer envelopes of supernovae) and form a compressed nonequilibrium phase where the high-energy (~10 MeV/nucleon) ion reactions take place. In according to this theoretical model the interactions of protons with the helium nuclei with formation of D and free nucleons, the nuclear reactions with the CNO nuclei and the $\alpha+\alpha$ interactions with the formation of the Li, Be and B isotopes were examined /1,2/. The main difficulty of this model is conditioned by temperature limitation because all these isotopes are destroyed at $T \sim 10^7$K. In region of heavy elements this limitation is not essential and the high-energy ion reactions can lead to nucleosynthesis of some rare isotopes, for example, of the bypassed isotopes by p-process /3/. The (n,γ)-reactions can simultaneously take place because the neutron flux is increased in shock wave front both in fragmentation reactions and in the $^{13}C\ (p,n)^{13}N$ reaction.

Detailed investigations of isotopic composition of some elements (C,N,O,Ne,Mg,Si,Ar,Ca,Ti,Kr,Ag,Te,Xe,Ba, Nd,Sm,U) in mineral phases of carbonaceous chondrites led to the conclusion about presence the relicts of nucleogenetic origin /4,5/. We believe that one of them is a relict of nuclear reactions in shock wave front during supernova events. It is unique isotopic anomalous component of Xe (XeX). It is present in the carbonaceous chondrites which are nonchanged substance of protoplanetic nebula and contain some relicts of interstellar grains.

2. Results.

The totality of the experimental data /6/ allows to make the following conclusion about the characteristics of XeX. (1)The isotopic composition of Xe-X is characterised by the excesses of light shielded isotopes ^{124}Xe and ^{126}Xe ($^{124}Xe \gg {}^{126}Xe$) and heavy nonshielded isotopes ^{134}Xe and ^{136}Xe ($^{136}Xe \gg {}^{134}Xe$) (Fig.1). (2)This component realizes only after long action of various oxidizing reagents on meteorite matter. These reagents dissolve all phases enriched in another componets of Xe (solar and planetary Xe).

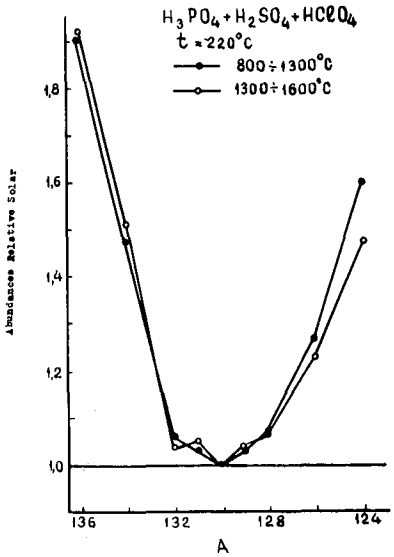

Fig.1.The isotopic composition of XeX ($^{130}Xe=1$) in acid-insoluble residue of the carbonaceous chondrite Efremovka CV, etched by H_3PO_4, H_2SO_4 and $HClO_4$ at t= 220°C.

(3)XeX is characterized by the correlations for the isotopic ratios $^{124}Xe/^{130}Xe$-$^{136}Xe/^{130}Xe$ and $^{136}Xe/^{130}Xe$-$^{134}Xe/^{130}Xe$ ($r \geqslant 0.9$). (4)The host phase of XeX is a fine-grained carbon matter of unknown nature. Its content is $\ll 1\%$ of the total carbon content in meteorite. It is very stable to the action of oxidizing reagents. (5)The maximum of the XeX realization as an indivisible component corresponds to 900-1000°C (Fig.2).

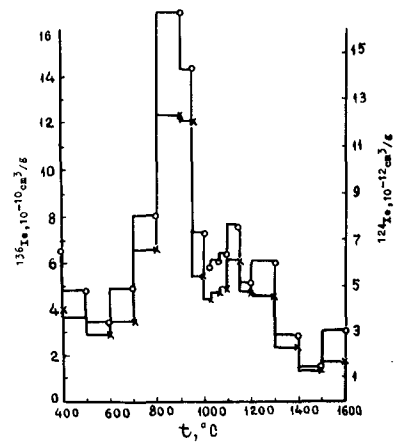

Fig.2. The histograms of realization of ^{124}Xe (1) and ^{136}Xe (2) at temperature annealing of the acid-insoluble residue of the carbonaceous chondrite Kainsaz CO, etched by conc. HNO_3 /7/.

(6)The XeX quantitaty is equal of $\ll 1\%$ of the total Xe in meteorite: it does not correlate with the trapped Xe content. (7)XeX is accompanied by the main quanti-

ties of the trapped He and Ne, and by the excesses of heavy nonshilded isotopes ^{84}Kr and ^{86}Kr (not by light isotope ^{78}Kr). (8)XeX is not accompanied by excesses of the heavy isotopes Ba,Nd,Sm and also radiogenic ^{129}Xe and by-passed isotope ^{1840}s.

In this paper it has made an attempt to show that all these reliable observations may be understanded only in the terms of a nucleogenetic origin of XeX. The unique isotopic composition of XeX and its very low abundances withness about exotic process of nucleosynthesis. According to the classical theory of nucleosynthesis /8/ the Xe isotopes can be created in the following nuclear reactions: s-process in the He envelope of massive stars at the stage of red giant (^{128}Xe, ^{129}Xe,^{130}Xe,^{131}Xe,^{132}Xe), r-process at the stage of explosive carbon (oxygen) burning (^{129}I,^{131}Xe,^{132}Xe, ^{134}Xe,^{136}Xe) and in inner envelopes, enriched in ^{56}Fe (the heavy element isotopes), p-process in outer envelopes, enriched in hydrogen, at high parameters ($T \sim 10^9 K$ and $\rho \sim 10^4$ g.cm^{-3}) (^{124}Xe,^{126}Xe), spallation process with high-energy particles accelerated in front of supernova shock waves /9/ (^{124}Xe,^{126}Xe), radicactive decay of ^{129}I(^{129}Xe) and spontaneous fission of ^{244}Pu,^{248}Cm and other (^{131}Xe,^{132}Xe,^{134}Xe,^{136}Xe).

The observed differences of the isotopic ratio values for XeX and solar Xe: ($^{124}Xe/^{126}Xe$) XeX/ ($^{124}Xe/^{126}Xe$) solar = 1.245 and ($^{136}Xe/^{134}Xe$) XeX/ ($^{136}Xe/^{134}Xe$) solar=1.293 (see Fig.1) withness about the XeX nucleosynthesis in the processes which are differ from those for solar Xe. For the understanding of a nature of these processes two facts have a significance. (1)As it was shown by us /9/, the cosmic abundances of ^{124}Xe and ^{126}Xe ($^{124}Xe \cong ^{126}Xe$) can be explained by their creation in spallation reaction with the high-energy particles accelerated in front of supernova shock waves at $I_p(E_p > 25\ MeV) = 5 \times 10^{21} cm^{-2}$ and $\gamma = 2.5$. (2)The XeX isotopic ratio value $^{124}Xe/^{126}Xe > 1$ (see Fig.1) is typical only for the by-passed isotopes with $A \leq 114$ which by p-process have been created /9/. Hence, ^{124}Xe and ^{126}Xe in that exotic component of Xe have been created also by p-process. One of the real astrophysical objects, in which the condition for p-process can be realized, is the shock wave front (waves of unloading) crossed through the He envelope of supernova. The ^4He fragmentation leads to an increasing of the n_p values and consequently to an increasing of the amounts of the (p,γ)-reaction products on seed nuclei formed in s-process in the He envelope.

The sumultaneous increasing of neutron flux (n_n) leads to fast (n,γ)-reactions. However, the parameters of r-process in shock wave front are essentially different from those of the classical r-process and mainly at the experence of lower n_n value. It leads to a increasing of the τ_n value and to a partial contri-

butions of β^--decay in r-process. This is a slow r-process or n-process /10/. This process is characterized a change of the peak position on the mass curve up to A > 130 /11/. The isotopic structure of the heavy isotopes of Xe corresponds to the curve of yields of nuclides in n-process /10/. The maximum yield has ^{136}Xe(N=82) which lies on the decay ladder at N=82 and is the first stable nucleus encountered by the ladder. At high parameters of classical r-process the nuclear structure has not influence on the yields of nuclides. Therefore, just the fact that ^{136}Xe has the maximum yields in XeX withnesses about a presence of n-process simultaneously with p-process in the shock wave front during supernova events. The products of these processes were captured as an indivisible component with high-temperature carbon grains condensing by supernova shock waves.

3. Conclusion

All above-mentioned properties of XeX may be explained by the model of its isotopes formation in the shock wave front during supernova events, the chemical and isotopic compositions of presupernova He envelope, and the property of high-temperature grains "survive" at the conditions which during all stages of supernova remnant evolution have taken place. These grains can be exposed by the action of intensive cosmic ray irradiation, mutual collisions, shock waves, turbulent magnetic fields and other. Thus, isotopic anomalous XeX is a relict of new nonstuded processes of nucleosynthesis, which in the shock wave front during outbursts of supernova or another cosmic objects have taken place.

References

1. Hoyle F. and Fowler, W.A., (1973), Nature, 241, p.384.
2. Colgate, S.A., (1974), Astrophys.J., 187, p.321.
3. Audouze, J. and Truran, J.W., (1975), Astrophys.J. 202, p.204.
4. Podosek, F.A., (1978), Annu.Rev.Astron. and Astrophys., 16, p.293.
5. Lavrukhina, A.K., (1980), Nukleonika, 25, p.1495.
6. Lavrukhina, A.K., (1985), Geochimia (in Russian), in press.
7. Shukolyukov, Ju.A. et al., (1985), Meteoritica (in Russian), in press.
8. Trimple, V., (1975). Rev.Mod.Phys., 47, p.877.
9. Lavrukhina, A.K. and Kuznetsova, R.I., (1980), Geochimia (in Russian), p.3.
10. Blake, J.B. and Schramn, D.N., (1976). Astrophys.J., 209, p.846.
11. Black, D.C., (1975), Nature, 253, p.417.

BREAKDOWN OF HELIUM NUCLEI IN MATTER PROCESSED NEAR BLACK HOLES

Robert J. Gould
Physics Department B-019
Univ. of Calif., San Diego
La Jolla, CA 92093 USA

ABSTRACT

The rate of breakup of helium nuclei by particle-induced reactions is computed. It is shown that the rate is determined by the endothermic reaction $p + {}^4He \rightarrow {}^3He + d$, becoming effective at $kT \gtrsim$ few MeV. It is suggested that matter having been processed to these temperatures will be depleted in helium and in the elements C, N, O, and Ne.

1. Introduction. In recent years considerable interest has developed in relativistic plasmas in which the electron gas is highly relativistic ($\Theta = kT/mc^2 \sim 10$). At these temperatures the ions would be non-relativistic but capable of undergoing endothermic reactions. In a recent paper [1] devoted to nuclear-force effects in p-p scattering, it was suggested that helium nuclei will break down in the following series of endothermic reactions:

$$p + {}^4He + 18.353 \text{ MeV} \rightarrow {}^3He + d \tag{1}$$

$$p + {}^3He + 5.493 \text{ MeV} \rightarrow d + p + p \tag{2}$$

$$p + d + 2.225 \text{ MeV} \rightarrow p + p + n \tag{3}$$

Because of its significantly larger threshold, the reaction (1) would be the slowest and therefore determine the rate of the overall helium-destruction process. Once the helium is broken down to hydrogen, any subsequent buildup would be very slow because of the small cross section for the fundamental p-p reaction $p + p \rightarrow d + e^+ + \nu_e$. The plasma would then remain essentially pure hydrogen. Other elements would also be broken down (see [1]), such as the abundant medium-weight C, N, O, Ne, although large Coulomb barriers are involved, since the threshold energies for the breakup reactions are much larger than in reaction (1).

The most elementary estimate of the characteristic breakdown temperature is obtained [1] by setting $kT \sim 0.1E_b$, where E_b is the binding energy difference (18,353 MeV) in reaction (1). The factor 0.1 arises since the equation for the breakdown temperature will be of the form, characteristic of ionization and dissociation phenomena,

$$e^{E_b/kT} \sim N = \text{large number} . \tag{4}$$

The logarithm of any large number is ~ 10, and this yields for the breakdown temperature:

$$\Theta_b(He) \sim 4 . \tag{5}$$

2. Calculation of Breakup Reaction. The calculation of the character-

istic breakdown temperature is really a non-equilibrium problem requiring a knowledge of the density (n_p) of the plasma and the available time (τ). If $r = dN/dVdt$ is the number of reaction (1) per unit volume per unit time, the breakdown temperature will be computed from

$$r\tau = n_p \ . \tag{6}$$

The rate r will be proportional to n_p^2 and an integral over the reaction cross section:

$$r = \frac{1}{2} n_p^2 < v_r > \ , \tag{7}$$

where v_r is the relative velocity of the reacting protons.

The problem is in the correct use of the reaction cross section σ and in the extrapolation of its experimental values to low energies. For in this case of a reaction with a threshold energy and reactants with a Maxwellian velocity distribution, the main contribution to $< \sigma v_r >$ will come from c.m. energies just above threshold. However, then the Coulomb effects in the cross section will be very important, especially for the outgoing particles in the reaction. To include these effects the experimental cross section [2] has been fit to a form

$$\sigma = \sigma_{nuc} \ C^2 C'^2 \ , \tag{8}$$

where σ_{nuc} is a "nuclear part" and C^2 and C'^2 are (incoming and outgoing) Coulomb factors of the form [3]

$$C^2 = 2\pi\eta/(e^{2\pi\eta}-1) \tag{9}$$

for the incoming and outgoing particles. Here $\eta = z_1 z_2 (Ry_\mu/E)^{1/2}$, in terms of the charges $z_1 e$ and $z_2 e$ of the particles involved and $Ry_\mu = (\mu/m)Ry$ is the Rydberg energy corresponding to the reduced mass of the pair of nuclei. In terms of the c.m. energy (before reacting) and the threshold energy E_t for reaction (1), σ_{nuc} is found to have the form

$$\sigma_{nuc} = \sigma_{nuc-t} \ [1 - a_s(E-E_t)/E_t] \tag{10}$$

with $\sigma_{nuc-t} = 93\text{mb}$ and $a_s = 0.148$.

Due primarily to the Coulomb factor C'^2 for the outgoing particles, the integrand in $< \sigma v_r >$ is found to have a "Gamow peak" where most of the contribution is centered. An asymptotic evaluation of the integral yields the following set of breakdown temperatures for given values of τn_p:

Θ_b(He)	2	3	4	5	6	7	8
τn_p(yr cm^{-3})	1.4×10^{15}	3.8×10^{12}	2.1×10^{11}	3.8×10^{10}	1.2×10^{10}	5.4×10^{9}	3.0×10^{9}

That is, the original estimate [1] $\Theta_b(\text{He}) \sim 4$ is reasonable, although the result does depend logarithmically on τn_p.

Although no details were given of the method of calculation, Aharonian and Sunyaev [4] have also computed the rate of reaction (1) in the high-temperature range. Their lowest T corresponds to the highest value in the above table and the results agree. However the domain

$\Theta < 5$ is probably most relevant, since it is especially important to know when the process begins to be effective as the temperature rises. Further details of the calculations described in the present work may be found in a separate paper [5]. For example, competing reactions have been investigated, such as

$$p + {}^4He + 20.578\ MeV \rightarrow {}^3He + p + n$$
$$p + {}^4He + 19.814\ MeV \rightarrow {}^3H + p + p \qquad (11)$$

These are found to contribute only about 1% as much as reaction (1), due essentially to the smaller cross sections for the reactions (11) at low energies (just above threshold); this is a phase space effect.

3. Discussion. In a strong gravitational potential, say, $\Phi \sim 0.1\ c^2$, it can be expected that a temperature $kT \sim 0.1\ Mc^2 \sim 100$ MeV can be attained (M = nucleon mass). This potential (and temperatures) could occur in regions around black holes, for example, and is well beyond that necessary to break up He and other nuclei. Matter that has attained this temperature can then be expected to be pure hydrogen. However, it might not be observed until after it has cooled. We would then see a recombination-cascade spectrum with only hydrogen lines after cooling to $\sim 10^5$K. While at $\sim 10^7$K there would be a pure bremsstrahlung x-ray spectrum without x-ray lines from excitations of one- and two-electron ions from the K-shell.

4. Acknowledgement. This research was supported by NASA through Grant NGR 05 005 004.

References

[1] R. J. Gould, Astrophys. J. 263, 879 (1982).

[2] J. P. Meyer, Astron. Astrophys. Suppl. 7, 417 (1972).

[3] N. F. Mott and H. S. W. Massey, Theory of Atomic Collisions, 3rd Ed. (Oxford: Oxford Univ. Press, 1965).

[4] F. A. Aharonian and R. A. Sunyaev, Mon. Not. Roy. Astron. Soc. 210, 257 (1984).

[5] R. J. Gould, Breakup of Helium Nuclei in High-Temperature Plasmas (Sub. to Nucl. Phys.)

oG 8.2-21

PULSARS AS COSMIC RAY PARTICLE ACCELERATORS: PROTON ORBITS

K.O. Thielheim
Institut für Kernphysik
Abteilung Mathematische Physik
Universität Kiel
(23) Kiel, West Germany

ABSTRACT

Proton orbits are calculated in the electromagnetic vacuum field of a magnetic point dipole rotating with its angular velocity $\vec{\omega}$ perpendicular to its dipole moment $\vec{\mu}$ by numerical integration of the Lorentz-Dirac equation. Trajectories are shown and discussed for various initial conditions. A critical surface is shown seperating initial positions of protons which finally hit the pulsar in the polar region from those which finally recede to infinity.

1. Introduction. In this paper proton orbits will be shown which I obtained with one of my students (Laue and Thielheim, 1985 a and b) by numerical integration of the Lorentz-Dirac-equation in the electromagnetic vacuum field of a magnetic point dipole rotating with its angular velocity $\vec{\omega}$ perpendicular to its dipole moment μ. Parameter values (model 1) are $\mu = 10^{30}$ G cm^3 and $\omega = 20\,\pi$ s^{-1}. The corresponding magnetic field strength in the polar region of a spere of radius $R_0 = 10$ km is about $2 \cdot 10^{12}$ G. The resulting light radius is $R_L = 4.775$ km. The procedures of numerical integration are described elsewhere (Marotzke and Thielheim, 1985).

The initial velocity of protons is zero, which is a reasonable specification since it turns out that particles very rapidly gain ultrarelativistic energies such that their orbit depends very little on their initial velocities as long as these are sufficiently small (i.e. nonrelativistic). The orbits under consideration, therefore, depend only on their initial positions. In a certain set of orbits these initial positions are defined by a given value of radius ($R_0 = 10$, 2.2 and 1.8 in units of R_L), equidistant values of latitude ($\theta_0 = 10^o$, 25^o, 40^o, 55^o, 70^o and 85^o against the vector of angular velocity $\vec{\omega}$) and equidistant values of longitude ($\phi_0 = 0^o$, 15^o, ..., 345^o against the x-axis, which corresponds to the direction of the dipole moment $\vec{\mu}$ for zero phase $\omega t - r/R_L = 0$). These initial positions are shown in figure 1.

2. Symmetry Properties. In the given field configuration the magnetic vector is symmetric, while the electric vector is antisymmetric under point reflection. In view of the symmetry properties of the equation of motion, therefore, protons starting from point symmetric initial positions with opposite initial moments move on point symmetric orbits. For this reason one may restrict calculations to initial positions on one of the two hemispheres.

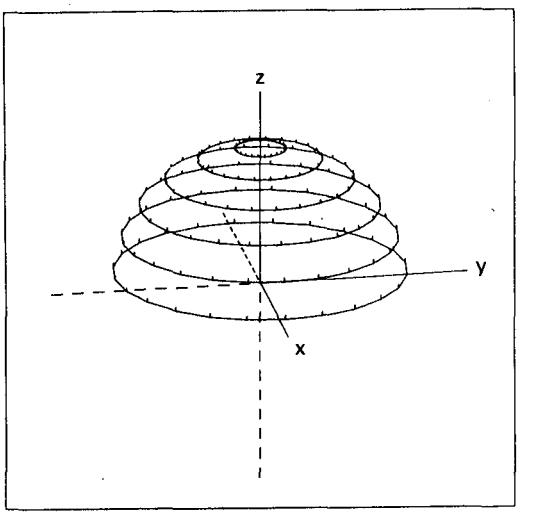

Definition of initial conditions

figure 1

3. Particle Drift in the Equatorial Plane. In the field configuration considered here the electric vector is perpendicular to the equatorial plane z = o, while the magnetic vector in this plane is parallel to the z-axis, i.e. $(\mathcal{E}, \mathcal{B}) = o$. Thus, in the equatorial plane, there is no acceleration along the magnetic field lines. Still there is an $[\mathcal{E}, \mathcal{B}]$-drift within the plane. This is illustrated by figure 2, the arrows indicating the drift velocity. Asteriks mark regions, where $E^2 > B^2$ and thus protons are torn out of the equatorial plane by the dominating electric field. (In this diagram, the arrows at the outer edge correspond to initial positions with $R_o = 3$).

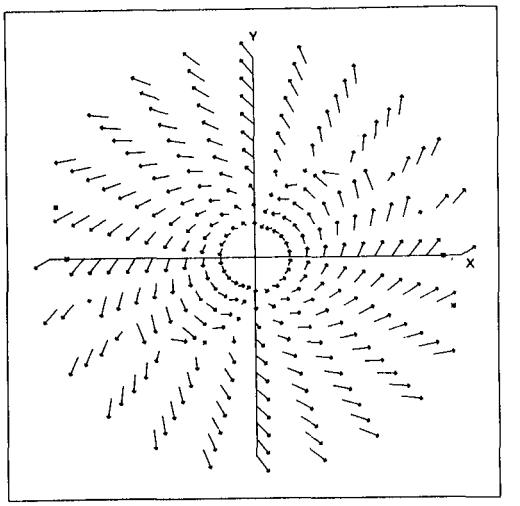

E×B-Drift velocity of protons originating from the equatorial plane

figure 2

4. Protons starting in the Distant Zone. Orbits of protons starting from initial radius $R_o = 10$ and latitude $\Theta_o = 25^o$ (with the radial coordinate r given in the logarithmic scale log (r/rmin)) are shown in figure 3 for $\Delta t = 90$ units of time. These protons move practically in the radial direction forming a narrow bundle slightly deflected towards the electric vector (broken line). An analogous diagram for $\Theta_o = 70^o$ is shown in figure 4 exhibiting a wider bundle of orbits.

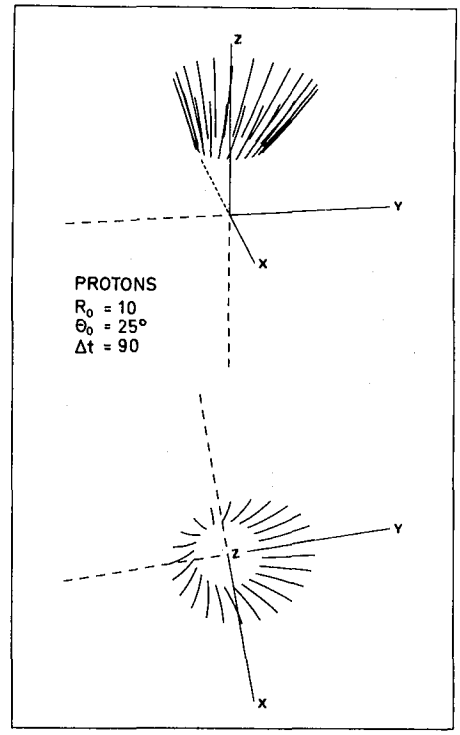

figure 3

5. Protons starting in the Near-Zone. The topography of orbits is quite different for small values of initial radius R_o, as is shown for $R_o = 1$, $\Theta_o = 7o^o$ and $\Delta t = 2$ (with linear scale) in figure 5. Here, trajectories originating from a certain range of ϕ_o do not eventually recede but finally hit the pulsar surface in one of the two polar regions (protons originating from corresponding initial positions of the other hemisphere would eventually reach the opposite polar region).

6. Critical Surface. Obviously, for each pair of given initial latitude Θ_o and longitude ϕ_o there is a critical initial radius $R_c = R_c(\Theta_o, \phi_o)$, which is the minimum of all initial radii $R_o \geq R_c$ such that tra-

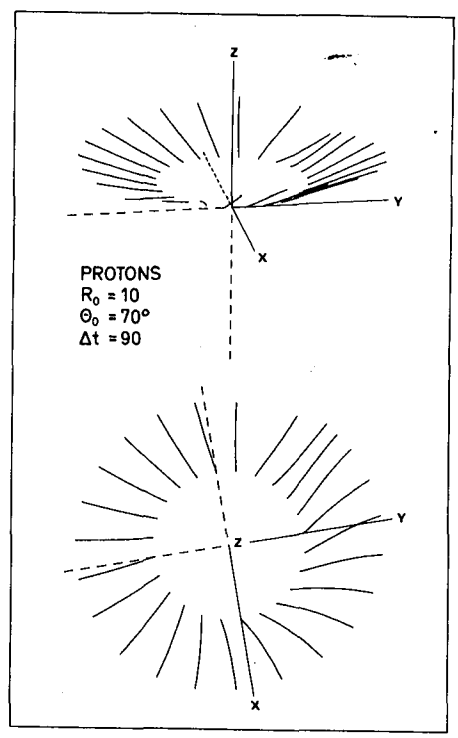

figure 4

jectories starting from (R_o, Θ_o, ϕ_o) run to infinity. Thereby a critical surface is defined (for parameter values as specified in model 1) which is illustrated by figure 6 in a perspective view (The largest radius is about $R_c = 2$).

References. H.Laue, K.O.Thielheim: Kleinheubacher Berichte No. 28(1985).Astrophys.Space Sci.(1985),submitted for publication.

J.Marotzke,K.O.Thielheim:unpublished(1985).

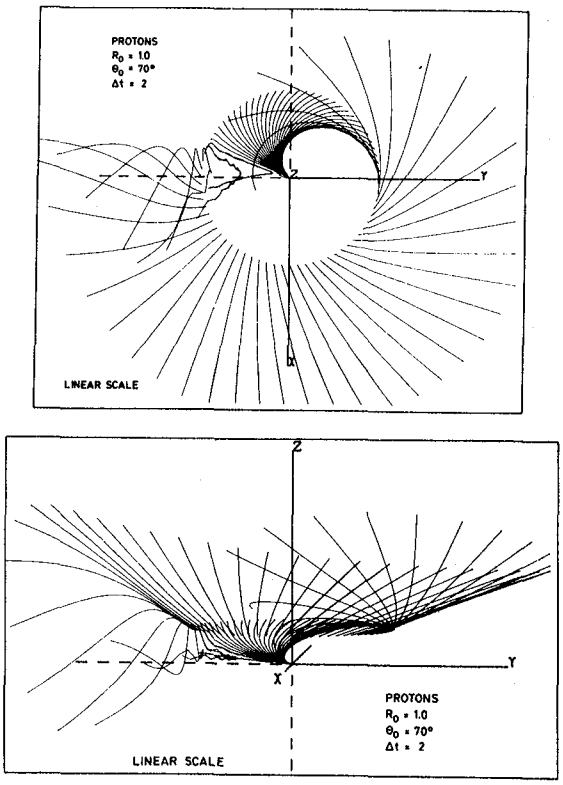

figure 5

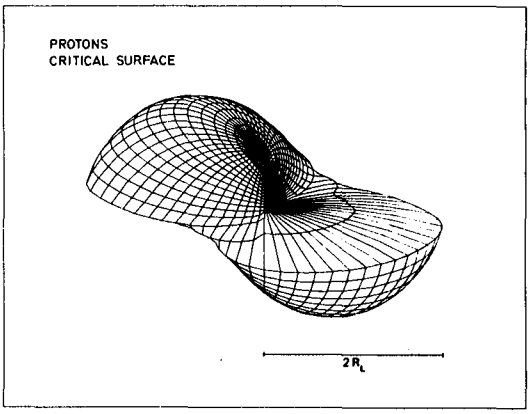

figure 6

oG 8.2-22

PULSARS AS COSMIC RAY ACCELERATORS: ENERGY DEVELOPMENT OF PROTONS

K.O. Thielheim
Institut für Kernphysik
Abteilung Mathematische Physik
Universität Kiel
(23) Kiel, West Germany

ABSTRACT

Results of numerical integrations of the Lorentz-Dirac-equation with Landau-approximation for protons in the electromagnetic vacuum field of a magnetic dipole rotating with its angular velocity $\vec{\omega}$ perpendicular to its magnetic moment $\vec{\mu}$ will be discussed with special attention to the energy development of protons.

1. Introduction. Numerical data on the orbital motion of protons discussed in the proceeding paper also give information on the development of proton energy and may therefore be helpful in discussions about pulsars as possibly accelerators of high energy cosmic ray particles. Present results were obtained under the specifications of our model 1 and are intended to illustrate some of the general features observed in particle acceleration by rotating magnetic dipoles.

2. Maximum Energy of Protons originating from the Distant Zone. As I have shown before, protons starting from $R_o = 1o$ (in units of light radius) move outwardly more or less in radial direction. Still the maximum value of energy they achieve during the first 9o units of time (corresponding to 14.3 revolutions of the magnetic dipole) depends strongly on both, the initial latitude θ_o as well as the initial longitude ϕ_o. This can be seen from figure 1 showing the maximum value of energy (precisely: the maximum value of the Lorentz factor γ in a logarithmic scale) within the time interval under consideration for various values of initial latitude ($\theta_o = 1o^o$, 25^o, $4o^o$, 55^o, $7o^o$ and 85^o) as a function of initial longitude ϕ_o. It should be noted that not always the final energy equals the maximum energy. Protons starting near the axis of ration (e.g. from $\theta_o = 1o^o$) practically all have the same maximum energy (which under the assumptions of model 1 is about $1o^{5.2}$ times their rest energy). In contrast to this behaviour, protons starting near the equator of rotation (e.g. from $\theta_o = 85^o$) obtain maximum values of energy, which may differ by a factor up to about 1oo depending on their initial value of longitude

ϕ_o. Largest values of maximum energy correspond to initial positions of maximum (electric as well as magnetic) field strength for t = o. This is already an indication to the fact that particles in general experience a very strong acceleration in their earliest stages of orbital motion which thereby become decisive also for what the final energy of the particles will be.

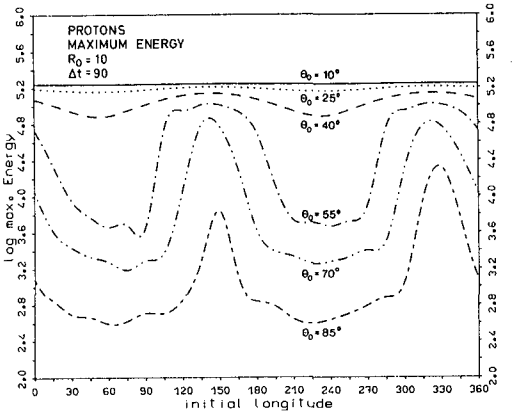

figure 1

3. Development of Energy of Protons originating from the Distant Zone.

This is further illustrated by figure 2 showing the energy development of protons starting from R_o = lo as a function of time (On a log (1 + t) scale) for four orbits starting near the equator of rotation ($\Theta_o = 85^o$) at various values of initial longitude (ϕ_o = o^o, 165^o, 135^o and 330^o). On any of these orbits a Lorentz-factor of about loo is reached already within the first very small fraction of a unit of time (ω^{-1}). But otherwise there are different features visible in these orbits: Two of them (ϕ_o = o^o and 165^o) exhibit a considerable oscillation of energy before the latter ap - proaches what appears to be a limiting value. Particle motion in these cases obviously is drift dominated and the energy

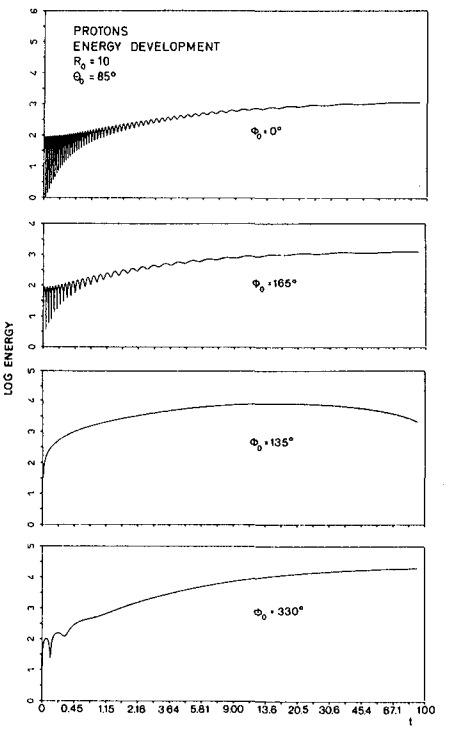

figure 2

oscillations reflect particle gyrations in a region of field where the electric and magnetic field vectors to a very good degree are perpendicular to eachother. The characteristics of the other two orbits are different. For $\phi_o = 135^o$ e.g. energy increases monotonically during the first stages of orbital motion. This can be explained by the presence of a considerable component of the electric vector parallel to the magnetic field vector on this part of the orbit under consideration.

4. Maximum Energy of Protons originating from the Transition Zone.

The maximum value of energy reached during the first 3o units of time (corresponding to 4.8 revolutions of the dipole) by protons originating from $R_o = 2.2$ at various values of initial latitude ($\theta_o = 1o^o, 25^o, 4o^o, 55^o, 7o^o$ and 85^o) is shown as a function of initial longitude ϕ_o in figure 3. Again the maximum value of energy is practically the same for all protons starting near the axis of rotation (e.g. $\theta_o = 1o^o$) amounting to about $1o^{5.9}$ times proton rest energy. But otherwise maximum energy of protons starting nearer to the equator of rotation (e.g. $\theta_o = 85^o$) strongly depends on the initial value of longitude ϕ_o.

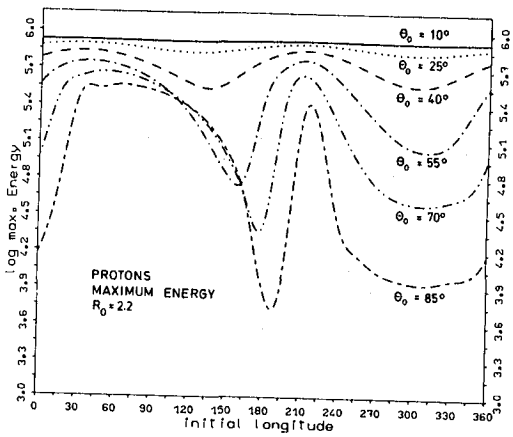

figure 3

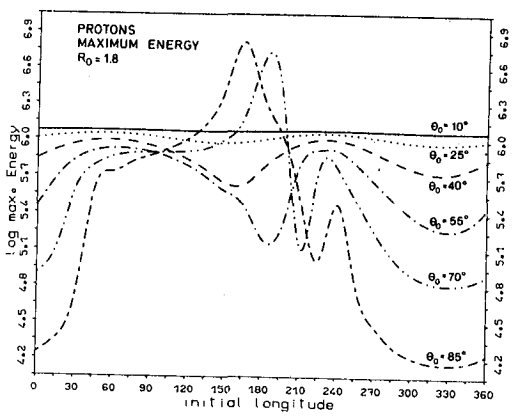

figure 4

The asymmetry in the maximum - minimum structure of the dependence of these curves from initial longitude ϕ_o certainly indicates an increasing influence of the near-field contributions as one approaches the dipole.

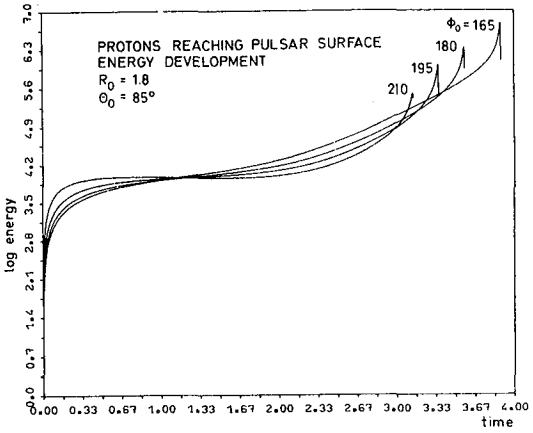

figure 5

5. Energy of Protons originating from the Near-Zone. Maximum energy of protons starting from R_o = 1.8 within the first 3o units of time (or else before their radial distance from the dipole becomes smaller than lo km) is shown in figure 4 for different values of initial latitude Θ_o as a function of initial longitude ϕ_o. Protons starting near the axis of rotation (e.g. at Θ_o = lo^o), which as has been shown receed from the dipole region more or less in radial direction, attain energy values of about $lo^{6.1}$ times their rest energy. Protons starting near the equator of rotation (e.g. at Θ_o = 85^o) within a certain region of initial longitude (around ϕ_o = $16o^o$) which ultimately reach the lo km limit attain much higher energies about $lo^{6.8}$ times their rest energies. As I have demonstrated earlier, these protons are focussed to one of the polar regions.
The development of energy with time on these orbits some of which are shown in figure 5, is obviously quite different from the one discussed before. A very strong acceleration during the very first stages of orbital motion and the slow increase of energy in the succeeding stages are followed by a second regime of strong acceleration during which the energy again increases by a factor up to loo or even 1.ooo. Ultimately, before the protons reach the lo km limit, their energy decreases sharply as they invade the polar region of extremely strong magnetic field strength (about lo^{12}G).

oG 8.2-23

PULSARS AS COSMIC RAY PARTICLE ACCELERATORS: Dynamics of Electrons

K.O. Thielheim
Institut für Kernphysik
Abteilung Mathematische Physik
Universität Kiel
(23) Kiel, West Germany

ABSTRACT

The Lorentz-Dirac-equation with Landau-approximation has been solved numerically for electrons in the electromagnetic field of a magnetic dipole rotating with the angular velocity $\vec{\omega}$ perpendicular to its magnetic moment $\vec{\mu}$. Results are discussed with respect to electron orbits and energy development.

1. Introduction. Initial conditions are as in my preceding papers (Thielheim 1985 a,b). In the case of the perpendicular rotator, considered here, there is an additional symmetry for particles with opposite electric charge and equal rest mass. Although, of course, the rest mass of electrons and protons is different, this symmetry, nevertheless, may be helpful for comparisons between electron and proton orbits. By this symmetry, namely, corresponding orbits of particles with opposite charge and equal rest mass become identical through rotation of 180° around the axis of rotation (z-axis). The difference in rest mass between electrons and protons becomes irrelevant in the ultra relativistic regime as long as radiation reaction is negligible. In this context it is important to note that under the premises of model 1 and with the initial conditions applied here electrons as well as protons very rapidly become ultrarelativistic. Therefore in many cases corresponding electron and proton orbits respectively are quite similar in the initial stages of orbital motion. But then radiation reaction is, of course, much more important for electrons than for protons.

2. Electrons starting in the Distant Zone. The orbits of electrons starting in the distant zone are quite similar to the corresponding orbits of protons as can be seen from figure 1 showing electron orbits of initial radius $R_o = 3$ and initial latitude $\theta_o = 7^{\circ}$. The maximum energy of electrons originating from this initial radius $R_o = 3$ and different values of initial latitude ($\theta_o = 1^{\circ}, 2^{\circ}, 3^{\circ}, 4^{\circ}, 5^{\circ}, 6^{\circ}, 7^{\circ}$ and 8°) is shown as a function of initial longitude ϕ_o in figure 2. Electrons starting near the equator

of rotation (e.g. for $\theta_o = 70^o$ corresponding to the orbits in figure 1) show a larger maximum near $\phi_o = 180^o$ and a smaller maximum near $\phi_o = 45^o$. This asymmetry between the two maxima is much more pronounced in electron orbits than in proton orbits. Maximum energy may exceed 10^8 times the rest energy of electrons giving rise to spectecular radiation reaction effects when accelerating forces perpendicular to the velocity vector become important. This is illustrated clearly by figure 3 in which the energy development on some electron orbits with $R_o=3$ and $\theta_o = 50^o$ is shown as a function of time. On any of these orbits there is a very strong increase of electron energy with time in the early stages of orbital motion. But then in certain ranges of initial longitude (e.g. for $\phi_o = 40^o, 120^o$ and 160^o) electron energy continues to increase further monotonically, while in other ranges of initial longitude (e.g. for $\phi_o = 300^o$ and 320^o) electron energy may even decrease depending of the field configurations these particles run into.

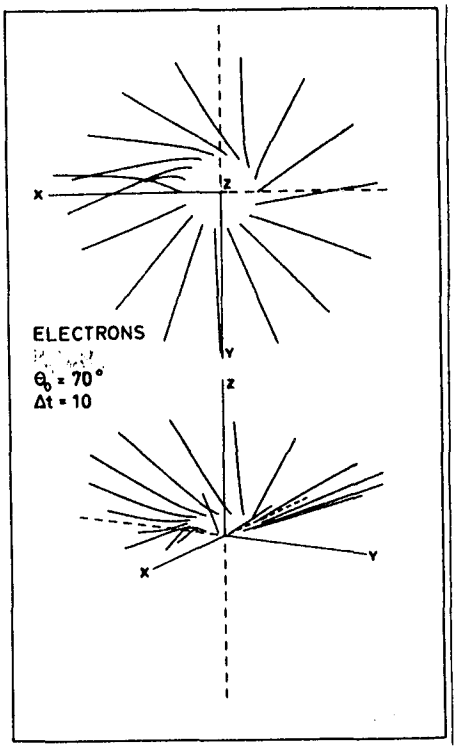

figure 1

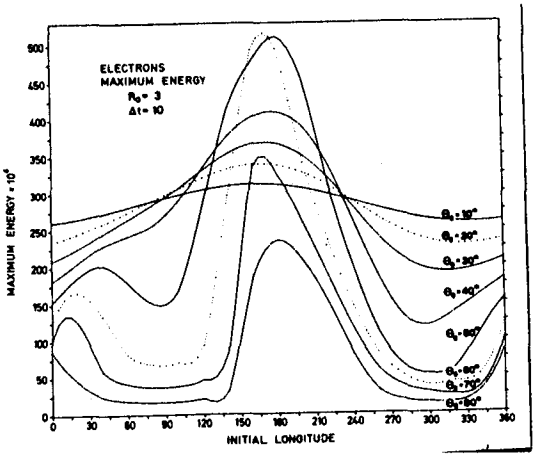

figure 2

3. Electrons starting in the Near Zone. The critical surface (separating initial points of orbits leading to the surface R_p=10km from

those leading to infinity) does not seen to be very different for electrons than for protons (after rotation by 180° around the z-axis, of course). Maximum energy R_o=2.2 and R_o=1.8 leads to values well above 10 times the rest energy. In those examples for particles starting in the equatorial zone (with respect to rotation) there is a larger maximum around ϕ_o =27° and a smaller maximum around ϕ_o =7°. For R_o=1.8 there are electrons running inwardly as can be seen for Θ_o=7° in figure 6. These orbits appear to be more curled than the corresponding ones of protons. The double maximum structure of electron energy resembling the double maximum structure observed in pulsar radiation appears to be an interesting feature of the pre - sent calculations. Finally it should be mentioned that considerably higher particle energies can be expected for other parameters concerning the rotating dipole.

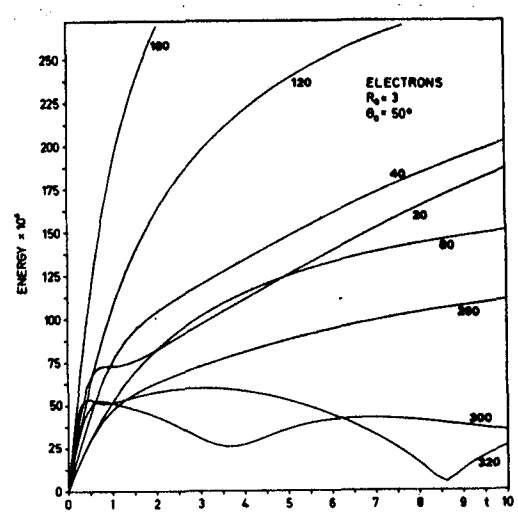

figure 3

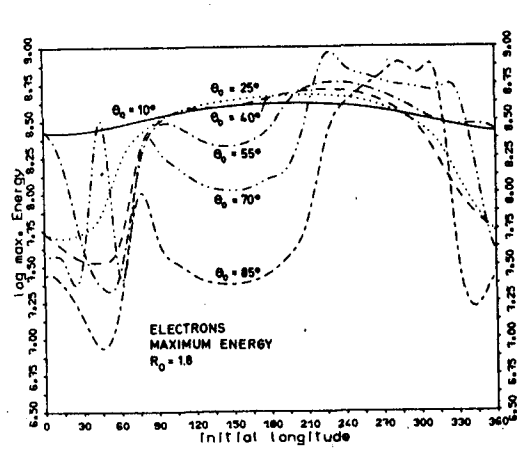

figure 4

References.
K.O.Thielheim (1985a) oG 8.2-21 this conference. (1985b) oG 8.2-22 this conference.

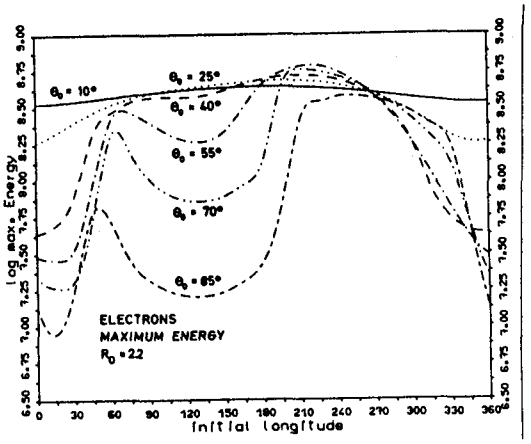

figure 5

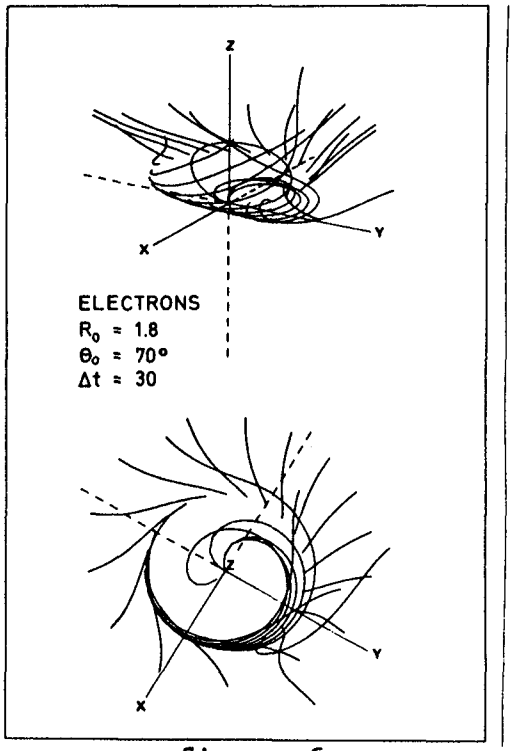

figure 6

INFLUENCE OF THE SOURCE DISTRIBUTION ON THE AGE DISTRIBUTION OF GALACTIC COSMIC RAYS

I. Lerche[1], R. Schlickeiser[2]

1) Department of Geology, University of South Carolina
Columbia, SC 29208, USA

2) Max-Planck-Institut für Radioastronomie
Auf dem Hügel 69, 5300 Bonn 1, FRG

ABSTRACT

The age distribution of galactic cosmic rays in the diffusion approximation is calculated. The influence of the scale height of the spatial source distribution on the mean age of particles arriving at the solar system is discussed. The broader the source distribution with respect to the galactic plane, the longer the mean age. This result provides a natural explanation for the shorter mean age of secondary cosmic rays compared to primary cosmic rays necessary for the understanding of the observed secondary/primary ratio.

1. Introduction. The concept of the age distribution of cosmic ray particles at the solar system allows to reduce the solution of the full cosmic ray transport equation to the simpler leaky-box equation (Schlickeiser and Lerche 1985, OG 7.2-8). Here we consider the influence of the spatial source distribution on the resulting age distribution and mean arrival time at the solar system.

2. Age Distribution in the Diffusion Approximation. At large momenta spatial diffusion in partially stochastic magnetic fields dominates particle's escape by convection in a galactic wind. Because of the highly flattened shape of the Galaxy we may neglect spatial gradients in the galactic plane compared to gradients perpendicular (z-coordinate) to the galactic plane. For simplicity and ease of exposition, we also assume a constant diffusion coefficient throughout the Galaxy, $K(r) = K_o$. The cosmic ray age distribution can then be derived from the solution of the diffusion equation (see Schlickeiser and Lerche 1985, OG 7.2-8, equations (7) - (9)).

$$K_o \frac{\partial^2 N(z,y)}{\partial z^2} = \frac{\partial N(z,y)}{dy} \qquad (1),$$

$$N(z,y=0) = q(z) \qquad (2).$$

As boundary condition we use the free escape boundary condition

$$N_{z=+L} = N_{z=-L} = 0 \qquad (3)$$

which in cases, where the majority of particle sources do not concentrate on the disk boundary, is appropriate. We also demand symmetry of the solution relative to the galactic plane

$$N(z,y) = N(-z,y) \qquad (4).$$

The solution of equations (1) - (4) is

$$N(z,y) = \frac{1}{L} \sum_{m=1}^{\infty} c_m \sin\left[(2m-1)\,\pi\,\frac{z+L}{2L}\right] \exp\left(-\lambda_m^{\,2} y\right) \tag{5}$$

belonging to the eigenvalues (m = 1, 2, 3, ...)

$$\lambda_m^{\,2} = \frac{\pi^2 K_o}{4L^2}\,(2m-1)^2 \tag{6}.$$

As can be seen from (6) the set of eigenvalues $\lambda_m^{\,2}$ form a monotonously increasing sequence $0 < \lambda_1^{\,2} < \lambda_2^{\,2} < \lambda_3^{\,2} < \ldots$, so that for times $y >> \lambda_1^{-2} = 4L^2/(\pi^2 K_o)$ the tail of the age distribution is pure exponentially, $N(z,y) \propto \exp(-\lambda_1^{\,2} y)$. After these times the cosmic ray particles have been scattered so often that they "forget" their original source distribution.

Throughout this work we consider a step-like source distribution

$$q(z) = \begin{cases} 1 & \text{for } |z| < B < L \\ 0 & \text{otherwise} \end{cases} \tag{7}$$

where B is the scale height of the sources. The expansion coefficients c_m in (5) are then determined via the initial condition (2) as

$$c_m = \frac{1}{L} \int_{-L}^{+L} dz\, q(z) \sin\left[(2m-1)\,\pi\,\frac{z+L}{2L}\right] = \frac{4(-1)^{m-1}}{\pi(2m-1)} \sin\frac{\pi(2m-1)B}{2L} \tag{8}.$$

Using (8) in (5) and normalizing N(z,y) yields the age distribution

$$P(z,y) \equiv \frac{N(z,y)}{\int_0^{\infty} dy\, N(z,y)}$$

$$= \sum_{m=0}^{\infty} \frac{(-1)^m}{(2m+1)}\, e^{-\frac{\pi^2 K_o (2m+1)^2 y}{4L^2}} \left[\left[\cos\frac{\pi(2m+1)(L+z-B)}{2L}\right.\right.$$

$$\left.\left. - \cos\frac{\pi(2m+1)(L+z+B)}{2L}\right]\right] \cdot \begin{cases} \dfrac{4K_o}{\pi(2BL-B^2-z^2)} & \text{for } |z| \leq B < L \\ \dfrac{2K_o}{\pi B(L-|z|)} & \text{for } B \leq |z| \leq L \end{cases} \tag{9}.$$

The mean age at position z is determined from (9) as

$$\langle T \rangle(z) \equiv \int_0^{\infty} dy\; y\; P(z,y) =$$

$$= \begin{cases} \frac{1}{12K_o}\left[\left[5B(2L-B)-z^2 + \frac{4B(2L^3+4LB^2-5BL^2-B^3)}{B(2L-B)-z^2}\right]\right] & \text{for } |z| \leq B \\ \frac{2L^2+2L|z|-z^2-B^2}{6K_o} & \text{for } B \leq |z| \leq L \end{cases} \quad (10).$$

Equations (9) and (10) generalize results of Owens (1976) who has only considered the cases B = 0 and B = L. For B = L equation (10a) coincides with Owens' equation (16a); in the case B = 0 Owens' expression (16c) differs ours (10b).

3. Mean Age of Cosmic Rays Arriving at the Solar System. The solar system is located very near to the galactic plane $z_s \cong 0$. For small values of $|z| << \sqrt{B(2L-B)}$ (10) reduces to

$$\langle T\rangle(z\cong 0) \cong \frac{L^2}{3K_o}\left(1 + \frac{1}{2}\frac{B}{L} - \frac{1}{4}\left(\frac{B}{L}\right)^2\right) \quad (11)$$

which is shown in Figure 1. It can be seen that the mean age of cosmic rays arriving at the solar system depends significantly on the scale height of cosmic sources: the broader the source distribution with respect to the galactic plane, the longer the mean age.

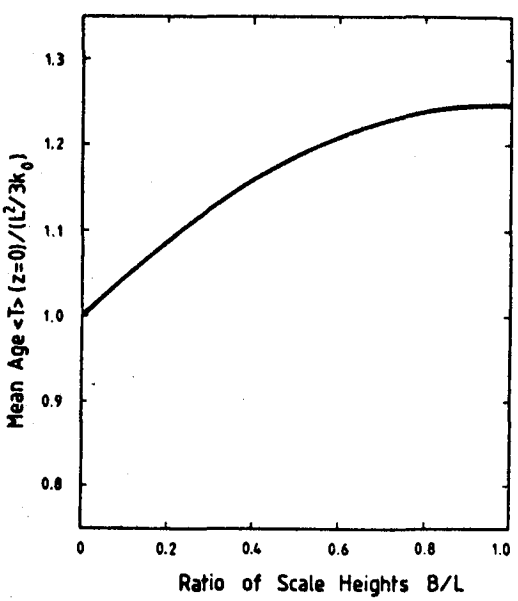

Fig. 1: Mean age of cosmic rays arriving at the solar system $\langle T\rangle(z=0)$ in units of $L^2/(3K_o)$ as a function of B/L. K_o is the value of the spatial diffusion coefficient, L the half-thickness of the cosmic ray confinement volume, and B the scale height of the cosmic ray source distribution. The larger the value of B, the larger the mean age.

This important result offers a natural explanation for the shorter mean age of secondaries compared to primaries necessary for the understanding of the observed secondary/primary ratio (see Lerche and Schlickeiser 1985, OG 8.3-2). Primary cosmic rays are continuously accelerated from the thermal background plasma which has a scale height of $B_F = 5\ T_6$ Kpc, if associated with the hot coronal gas (McKee and Ostriker 1977) where T_6 is the gas temperature in units of 10^6 K. Secondaries are mainly produced in dense molecular clouds where primary cosmic rays fragment

in interactions with gas atoms, so their source scale height is given by the scale height of galactic molecular clouds, $B_S \cong 60$ pc (Burton 1976). For the ratio of lifetimes we then find

$$\Omega = \frac{\langle T \rangle_S (z=0)}{\langle T \rangle_F (z=0)} = \frac{4L^2 + 2B_S L - B_S^2}{4L^2 + 2B_F L - B_F^2} \qquad (12)$$

which equals $\Omega = 0.87$ for $T_6 = 0.4$ and $L = 5$ kpc, and $\Omega = 0.97$ for $T_6 = 0.04$ and $L = 2$ kpc. As can be seen from (12) the smallest value of Ω is $\Omega_{min} = 0.8$ for $B_S \cong 0$, $B_F = L$.

References

Burton, W.B., (1976), Ann. Rev. Astron. Astrophys. 14, 275
Lerche, I., Schlickeiser, R., (1985), this conference, OG 8.3-2
McKee, C.F., Ostriker, J.P., (1977), Astrophys. J. 218, 148
Owens, A.J., (1976), Astrophys. Space Sci. 40, 357
Schlickeiser, R., Lerche, I., (1985), this conference, OG 7.2-8

EXPLANATION OF THE SECONDARY TO PRIMARY RATIO WITHIN THE CONTINUOUS FERMI ACCELERATION MODEL

I. Lerche[1], R. Schlickeiser[2]

1) Department of Geology, University of South Carolina
Columbia, SC 29208, USA

2) Max-Planck-Institut für Radioastronomie
Auf dem Hügel 69, 5300 Bonn 1, FRG

ABSTRACT

The secondary to primary ratio in galactic cosmic radiation at relativistic momenta is calculated in a model, where the primaries are continuously accelerated from the thermal galactic background medium by 1st and 2nd order Fermi acceleration. It is shown that the measured decrease with momentum does not exclude that cosmic rays are accelerated in the interstellar medium as a whole, as claimed by Cowsik (1980) and Eichler (1980). Once a momentum dependence of the mean lifetime and the different spatial source distributions are adequately taken into account, the measured decreasing ratio can be explained.

1. Introduction. Hayakawa (1969), Eichler (1980) and Cowsik (1980) claimed that the measured ratio of secondary to primary cosmic rays rules out continuous acceleration of cosmic rays in the interstellar medium as a whole. Here we show that their predicted logarithmically increasing ratio is a sole consequence of the assumed equality of the secondaries and primaries reciprocal sum of fragmentation and mean lifetime. If the momentum dependence of the mean lifetimes and the different source distributions of primary and secondary nuclei are adequately taken into account, the measured decreasing secondary/primary ratio can be successfully explained in the framework of continuous acceleration in the whole interstellar medium.

2. Basic Equations. The steady-state momentum (hereinafter momentum stands for momentum per nucleon) equilibrium spectrum of primary (F) and secondary (S) cosmic rays at the solar system is controlled by two leaky-box type equations

$$p^{-2}\frac{d}{dp}\left[D(p)\,p^2\frac{dF}{dp}\right] - p^{-2}\frac{d}{dp}\left[p^2\,(\dot{p}_{Gain}+\dot{p}_{Loss})\,F(p)\right]$$

$$-n\,v\,\sigma_o\,A_F^{2/3}\,F - \frac{F}{T_F}\cdot\left(\frac{p}{p_1}\right)^b + q_o\,\delta(p-p_i) = 0 \qquad (1),$$

$$p^{-2}\frac{d}{dp}\left[D(p)\,p^2\frac{dS}{dp}\right] - p^{-2}\frac{d}{dp}\left[p^2\,(\dot{p}_{Gain}+\dot{p}_{Loss})\,S(p)\right]$$

$$-n\,v\,\sigma_o\,A_S^{2/3}\,S - \frac{S}{T_S}\cdot\left(\frac{p}{p_1}\right)^b + \xi\,F(p,p_i) = 0 \qquad (2),$$

where the mean lifetimes T_F and T_S have to be calculated from the respec-

tive age distributions at the solar system (compare Schlickeiser and Lerche 1985, OG 7.2-8, equations (14), (2)).

Equations (1) and (2) are based on the physical model, that primary cosmic rays are continuously accelerated from the hot interstellar medium ($p_i << m_p c$) by resonant wave scattering (D(p)) and shock wave acceleration ($\dot{p}_{Gain}$), whereas secondaries result from fragmentation of primaries. Fully ionized particles heavier than protons at the same momentum per nucleon have the same stochastic ($D(p) = a_2\ p^{2-\eta}$) and first-order Fermi ($\dot{p}_{Gain} = a_1\ p^{1-\eta}$) acceleration rates as well as the same continuous momentum loss term ($\dot{p}_{Loss} = -\theta p$, $\theta = 1/3$ div $\vec{V}_w$, due to adiabatic cooling in the galactic wind).

Differences occur in the catastrophic fragmentation loss term where the total cross section varies proportional to the number of nucleons, $\sigma_F = \sigma_0\ A_F^{2/3}$, $\sigma_S = \sigma_0\ A_S^{2/3}$ (Silberberg and Tsao 1973). Likewise the sources of primaries and secondaries are different: whereas primaries are accelerated according to our model out of the thermal pool ($p_i << m_p c$), secondaries result solely from spallation of primaries, so that their source momentum spectrum is $\xi F(p,p_i)$ where $\xi = n\,v\,\sigma_{F\to S}$ depends on the gas density of the interstellar medium (n) and the partial spallation cross section $\sigma_{F\to S}$. Also, the spatial distribution of primary and secondary sources may be different: primaries probably are accelerated in the hot coronal phase of the interstellar medium which has a broad distribution with respect to the galactic plane. Secondaries are mainly produced in dense molecular clouds where the interstellar gas is clumped, so that their source scale height is given by the scale height of galactic molecular clouds, $B_S \cong 60$ pc (Burton 1976), which is much smaller than the scale height of the hot coronal gas, $B_F = 500\ (T/10^5\ K)$ pc, T: temperature of coronal gas (McKee and Ostriker 1977). This difference in the spatial distribution of their respective sources determines the age distributions of particles at the solar system (Lerche and Schlickeiser 1985a, OG 8.3-1). As a result (see Figure 1, OG 8.3-1), secondaries arriving at the solar system on average are younger than primaries, $T_S < T_F$, since their sources on average are closer to the solar system than the primary sources, and, as shown in Schlickeiser and Lerche (1985), these lifetimes enter the leaky-box equations. According to equation (12) of OG 8.3-1, T_S is 13 percent smaller than T_F, if a confinement volume size of L = 5 kpc, B_S = 60 pc, and $B_F = 2$ kpc are taken. This difference in the mean ages of particles arriving at the solar system is the physical reason why the secondary to primary ratio decreases with momentum at momenta larger than 10 GeV/(c.nucl.), as we will demonstrate now.

3. Secondary/Primary-Ratio at Relativistic Momenta. Introducing the secondary to primary ratio $R(p) \equiv S(p)/F(p)$ we find from (1) and (2) at relativistic momenta (Lerche and Schlickeiser 1985b)

$$p^{2-\eta}\frac{d^2R}{dp^2} + [2\,p^{2-\eta}\Delta(p) + (4-a-\eta)\,p^{1-\eta} + \beta p]\frac{dR}{dp}$$

$$+ [(\lambda_F - \lambda_S)\,(\frac{p}{p_1})^b + \xi_0\,(A_F^{2/3} - A_S^{2/3})]\,R \cong -\frac{\xi}{a_2} \qquad (3)$$

with $\beta = \theta/a_2$, $\lambda_F = (a_2 T_F)^{-1}$, $\lambda_S = (a_2 T_S)^{-1}$, $\xi_0 = n\,v\,\sigma_0/a_2$, $\Delta(p) =$

$[F(p)]^{-1}(dF/dp)$. A decreasing ratio R(p) is observed in the momentum range 10 GeV/(c.nucl.) - 10^5 GeV/(c.nucl.) where the primary momentum spectrum is a straight power law $F(p) \propto p^{-\chi}$, χ = const., so that $\Delta(p) = -\chi/p$.

We consider the behaviour of R(p) as $p \to \infty$ to demonstrate under what conditions the secondary to primary ratio R(p) is decreasing with momentum. Table 1 summarizes the results for various combinations of η (momentum dependence of acceleration rates) and b (momentum dependence of mean lifetime). If the spatial transport is diffusion along the magnetic field, $\eta = b$.

From Table 1 we see that:

(i) a logarithmically increasing ratio R(p) is a sole consequence of the assumed equality of the secondaries and primaries reciprocal sum of fragmentation and escape lifetime, i.e. $\lambda_S(p/p_1)^b + \xi_0 A_S^{2/3} = \lambda_F(p/p_1)^b + \xi_0 A_F^{2/3}$. This logarithmic dependence is a highly isolated and artificial solution to the problem which even for equal escape lifetimes ($\lambda_S = \lambda_F$) does not hold due to the well-established mass dependence of the total fragmentation cross sections. And it was this isolated solution which Cowsik (1980) used to rule out continuous acceleration of cosmic rays in the Galaxy as a whole.

(ii) For equal primary and secondary escape lifetimes ($\lambda_F = \lambda_S$) we find a decreasing power law solution in case $\eta > 0$ whose spectral index is determined by the ratio of catastrophic fragmentation losses to continuous momentum losses, which, however, for $p \to \infty$ approaches a negative constant.

(iii) Agreement with observations is reached once a momentum dependence of secondaries and primaries escape lifetimes, which have the same momentum shape but different absolute values ($T_{(F)}(p) = T_F(p/p_1)^{-b}$, $T_{(S)}(p) = T_S(p/p_1)^{-b}$, $b > 0$, p_1 = const., $T_S < T_F$, is allowed. For this case the secondary/primary ratio at large momenta approaches

$$R(p) \to \frac{\xi(p/p_1)^{-b}}{a_2\,(\lambda_S - \lambda_F)} = \frac{nc\,\sigma_{F\to S}}{\frac{1}{T_S} - \frac{1}{T_F}} \left(\frac{p}{p_1}\right)^{-b} .$$

These results indicate that the measured secondary to primary ratio of galactic cosmic radiation can be explained in the framework of continuous acceleration models in the general interstellar medium, once the momentum dependence of the mean lifetimes at the highest momenta and the different source distributions are adequately taken into account. So the strongest argument in the past against continuous acceleration of cosmic rays (see e.g. Cowsik 1980) has been invalidated.

References

Burton, W.B., (1976), Ann. Rev. Astron. Astrophys. 14, 270
Cowsik, R., (1980), Astrophys. J. 241, 1195
Eichler, D., (1980), Astrophys. J. 237, 809
Hayakawa, S., (1969), Cosmic Ray Physics, Wiley, New York, p. 551 ff
Lerche, I., Schlickeiser, R., (1985a), this conference, OG 8.3-1
Lerche, I., Schlickeiser, R., (1985b), Astron. Astrophys., in press
McKee, C.F., Ostriker, J.P., (1977), Astrophys. J. 218, 148

Schlickeiser, R., Lerche, I., (1985), this conference, OG 7.2-8
Silberberg, R., Tsao, C.H., (1973), Astrophys. J. Suppl. 25, 315

Table 1: Secondary/Primary - Ratio R(p) at Large Momenta for $\Delta = -\chi/p$

Case	$\lambda_S (\frac{P}{p_1})^b + \xi_o A_S^{2/3} = \lambda_F (\frac{P}{p_1})^b + \xi_o A_F^{2/3}$ Cowsik's case	$\lambda_S = \lambda_F$	$\lambda_S + \xi_o A_S^{2/3} > \lambda_F + \xi_o A_F^{2/3}$	$\lambda_S + \xi_o A_S^{2/3} < \lambda_F + \xi_o A_F^{2/3}$
$\eta = b = 0$	$\frac{\xi \ln p}{a_2 (2\chi+a-\beta-3)}$ + const.	$R \propto p^{\Gamma}$, $\Gamma > 0$ if $(2\chi+a-\beta-3) > 0$ $R + \frac{-\xi}{a_2 \xi_o (A_F^{2/3} - A_S^{2/3})}$ if $(2\chi+a-\beta-3) < 0$	$\frac{\xi}{a_2[\lambda_S - \lambda_F + \xi_o (A_S^{2/3} - A_F^{2/3})]}$	$R \propto p^{\Gamma}$, $\Gamma > 0$ if $(2\chi+a-\beta-3) > 0$ $R + \frac{-\xi}{a_2[\lambda_F + \lambda_S + \xi_o (A_F^{2/3} - A_S^{2/3})]}$ if $(2\chi+a-\beta-3) < 0$
$0 = b < \eta$	$-\frac{\xi}{a_2 \beta}$ const. + ln p	$-\frac{\xi_o}{\beta} (A_F^{2/3} - A_S^{2/3})$ $R \propto p$ $R(p=\infty) < 0$	$\frac{\xi}{a_2[\lambda_S - \lambda_F + \xi_o (A_S^{2/3} - A_F^{2/3})]}$	$-\frac{1}{\beta}[\lambda_F - \lambda_S + \xi_o (A_F^{2/3} - A_S^{2/3})]$ $R \propto p$ $R(p=\infty) < 0$
$b > 0, \eta > 0$	$-\frac{\xi}{a_2 \beta}$ const. + ln p	$-\frac{\xi_o}{\beta} (A_F^{2/3} - A_S^{2/3})$ $R \propto p$ $R(p=\infty) < 0$	$\frac{\xi}{a_2(\lambda_S - \lambda_F)} (\frac{P}{p_1})^{-b}$	$\frac{\xi}{a_2(\lambda_S - \lambda_F)} (\frac{P}{p_1})^{-b}$

PROPAGATION OF INJECTED COSMIC RAYS UNDER DISTRIBUTED REACCELERATION

M. Simon, W. Heinrich, K.D. Mathis
University of Siegen, Physics Department
Adolf-Reichwein-Str., 5900 Siegen, West Germany

Abstract:

We here present a calculation in which we allow cosmic ray sources but also allow for reacceleration of propagating particles. It is shown that such a model can be accomodated with the data but it requires a modification of the path-length distribution.

1.) Introduction

The cosmic ray acceleration model in which the particles gain continuously energy from stochastic processes in the interstellar space by encountering shocks leads to a logarithmic increase in the secondary-to-primary ratios with energy, which is inconsistent with observations (1). The observed decrease of the secondary-to-primary ratios may therefore suggest that a considerable part of the acceleration has taken place rapidly at the sources. Astronomical observations on the other hand indicate that shocks from supernovae do exist in the galaxy and observations in the interplanetary space show clear evidence that shock-acceleration works. Therefore we here present and discuss a concept in which we combine both ideas:

a) Cosmic rays are preaccelerated at their sources.
b) During propagation the particles are moderately reaccelerated.

2.) The astrophysical assumptions

Our model has the following astrophysical assumptions:

a) Cosmic rays are injected by discrete sources. All injected nuclei show a power law spectrum in rigidity, providing the same spectral index.
b) Particles encounter exponential age - or pathlength distribution.
c) Particles undergo nuclear collisions leading to secondary spallation products.
d) Particles, secondaries and primaries, gain rigidity when they encounter expanding supernova remnants during their propagation.

We assumed that the reacceleration is predominantly controlled by supernova remnants in a developed stage. Encounters with expanding supernova remnants in its early stage with high shock speed are very unlikely since they fill only a very small portion of the volume of the galaxy. The reacceleration by old supernova remnants on the other hand is also limited since the shock speed becomes too small to account for significant reacceleration. Thus we estimated a reacceleration around every 10^6 years and allowed a

rigidity gain of typically 10 % to 30 % per encounter.

3.) The Monte Carlo Propagation Program

A particle on its way can change its energy, its mean pathlength $\bar{\lambda}_{esc}(E)$ and the fragmentation cross sections several times. In order to describe this complex situation mathematically we developed a Monte Carlo propagation program. It is capable of following each particle through space, considering interaction, escape and reacceleration. The pathlengths, the position of interaction and the fragmentation chanels were treated as random variables with appropriate distribution functions. No ionization losses were considered so that the results are restricted to higher energies. The cross sections were derived from the semi-empirical formulae given in (2) and we used a source composition as given by (3).

4.) Results

We used the $\bar{\lambda}_{esc}(R)$-values as derived from observations by various groups under the Leaky Box approximation and adapted the following fit to these data

$$\bar{\lambda}_{esc} = x_0(g/cm^2) \text{ with } x_0 = 8.0 \text{ for } R \leq 6(GV)$$
$$\bar{\lambda}_{esc} = x_0(R/6)^{-\alpha} \text{ with } x_0 = 8.0 \text{ and } \alpha = 0.5 \text{ for } R > 6(GV) \quad (1)$$

and allowed for reacceleration.

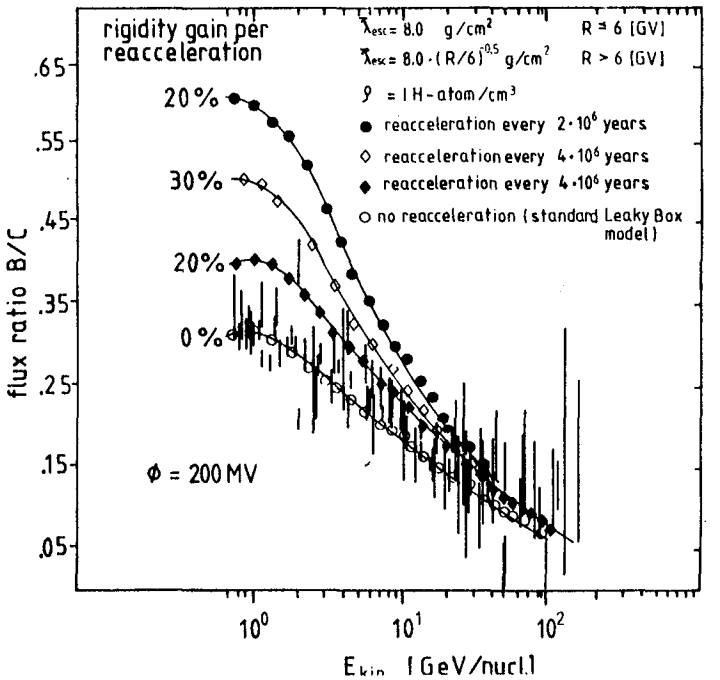

Fig.1: The calculated B/C-flux ratio under different reacceleration conditions.

The result is shown in Fig.1. The Leaky Box approximation is in good agreement with the data. However by allowing for reacceleration the calculated B/C-flux ratio increases considerably and falls well above the experimental data. The ratio at lower energies is more effected than at higher energies. High energy particles stay too short in the galaxy to be effectively reaccelerated. There are different reasons for the increase in the secondary-to-primary ratio.

1) The energy dependence of the fragmentation cross sections, (4). More secondaries at low energies can be produced which then after reacceleration show up at higher energies. But this effect does not necessarily lead to an enhanced production of secondaries because the cross sections do not always increase with decreasing energy.
2) Reacceleration always shovels particles of lower energies to higher energies and the longer a particle stays in the galaxy the higher is the probability to obtain more energy. There are only a few particles with long residence times since the age-distribution decreases exponentially. But these few particles, which contribute after reacceleration to higher energies, have to be weighted by the steep falling injection spectrum. Particles which have encountered a number of reaccelerations are those out of the tail of the exponential pathlength distribution. A large amount of traversed matter translates to more secondaries. This effect always results in an enhanced secondary-to-primary ratio.

5.) Discussions

The more effective production of secondaries can be compensated by reducing the mean traversed matter. Results of such a calculation are shown in Fig. 2. The propagation parameters are given in the figure. Under these conditions we found that the mean traversed matter around 1 GeV/n is closer to 4 g/cm^2 instead of 8 g/cm^2 and the energy dependence of $\bar{\lambda}_{esc}(E)$ is more like $\bar{\lambda}_{esc} \sim R^{-0,3}$ instead of $\bar{\lambda}_{esc} \sim R^{-0,5}$. The calculations show the following trends. The stronger the reacceleration is (more frequent and/or higher rigidity gain) the less traversed matter with an even flatter energy dependence is required in order to fit the data. The weaker the reacceleration is the closer it reflects the standard Leaky Box situation. Measurements on the energy dependent decrease of the secondary-to-primary ratios beyond 100 GeV/n may place limits on the reacceleration conditions if one assumes that the weaker energy dependence of $\bar{\lambda}_{esc}(E)$ extends to higher energies, Fig. 3.

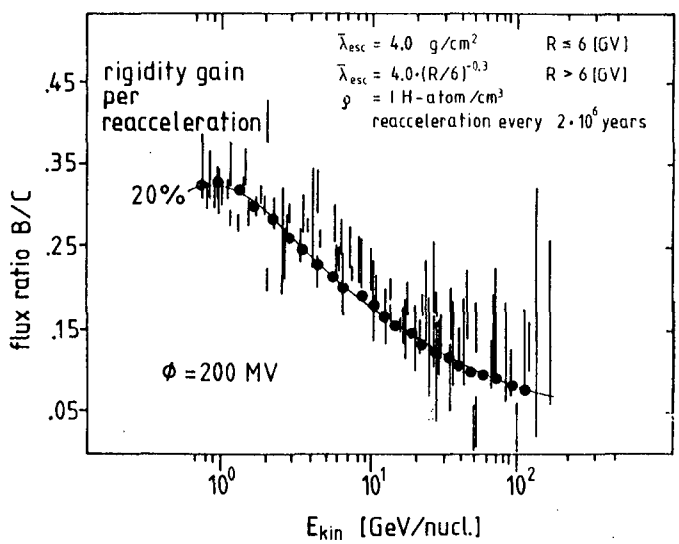

Fig.2: The B/C-flux ratio under reacceleration conditions, calculated with a modified pathlength distribution.

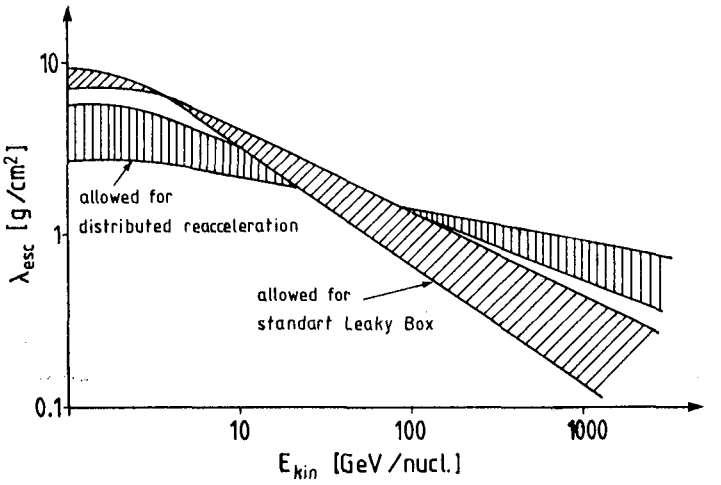

Fig.3: Schematic drawing of the energy dependence of $\lambda_{esc}(E)$ as predicted by the standard Leaky Box and the distributed reacceleration model.

6.) Conclusions

Reacceleration has also an impact on the surviving fraction of radioactive cosmic ray nuclei. In the Leaky Box model the surviving fraction is solely a function of the interstellar gas density. By allowing for distributed reacceleration the mean Lorentz factor is less than that determined by the arriving energy. This leads to a more frequent decay and causes an underestimation of the gas density by interpreting the data in the framework of the Leaky Box model.

Good data on the Be10/Be9-flux ratio are available around 100 MeV/n but this is an energy range where we are not capable of making meaningful calculations since our computer program at the present state does not take ionization losses into account. But in general, reacceleration works towards a shorter cosmic ray age due to less amount of traversed matter and a smaller mean Lorentz factor. When reacceleration is allowed we are probably closer to 10^6 years than to 10^7 years. The flux ratios in the energy regime around 100 MeV/n may be very much affected by cross section variations which occur below 100 MeV/n. It is observed that some cross sections show resonance-like increases below 100 MeV/n. B10 and B11-production for instance from the p-016-interaction is 4 times higher around 60 MeV/n than around 200 MeV/n. Under reacceleration condition the high production rate of these particles should influence the result also above 100 MeV/n. The effect may be somewhat washed out by ionization losses but measurements in this low energy regime should open new possibilities to check on the validity of reacceleration processes.

References

(1) Cowsik, R. 1980, Ap.J. 241, 1195
(2) Silberberg, R., Tsao, C.H. 1973, Ap.J. 25,315
and 15th ICRC, Plovdiv 2, 89, 1977
(3) Cameron, A.G.W. 1973, Space Sci.Rev. 15, 121
(4) Silberberg et al. 1983, Phys.Rev.Lett. 51,1217

OG 8.3-4

SECONDARY TO PRIMARY RATIO AND THE CONTINUOUS ACCELERATION

M.Giler[1], B.Szabelska[2], J.Wdowczyk[2] and A.W.Wolfendale[3]

1 Institute of Physics, University of Łódź
90-236 Łódź, Nowotki 149 153, Poland

2 Institute of Nuclear Studies
90-950 Łódź 1, box 447, Poland

3 University of Durham, Durham DH1 3LE, England

1.Introduction. It is well known that the ratio of secondary to primary nuclei in the cosmic radiation is a decreasing function of energy for $E \gtrsim 2$ GeV/n. This fact has to be interpreted in terms of c.r. propagation and acceleration model. An important problem is whether these two processes are separated in time (and in space) or can occur simultaneously. Assuming the leaky box model, Cowsik[1] showed that the decreasing sec/prim ratio is in a strong disagreement with an effective acceleration taking place in the ISM, predicting an increasing sec/prim ratio with energy. However it seems that there is still some confusion whether this conclusion is applicable to other models of c.r. propagation[2] or it is true for the leaky box model only.

In this paper we give a general formula for the sec/prim ratio, independently of any details of the propagation and acceleration model. In the limit of equal fragmentation paths for primaries and secondaries, this ratio at a given momentum nucleon is proportional only to the mean path of the observed primaries at that momentum. We shall show (basing partly on this formula) that it is unlikely to get a decreasing sec/prim ratio with energy if an acceleration process takes place during particle propagation in the ISM.

2.General formula. Let us denote by $f(p,t)$ the vacuum time distribution of primaries observed at the Earth with the momentum/nucleon p. The number of the observed primaries is of course $n_1(p)=\int_0^\infty f(p,t)e^{-t/T_1}dt$, where T is their mean life time against fragmentation. (We shall keep in mind that "time" means "path length" in g/cm^2). Particles arriving with age t have produced secondaries, which must propagate and be accelerated in the same way as their parent particles, if we adopt a reasonable assumption that these processes depend on p only (which is not changed by fragmentation). So they come to the observation point with the same momentum/n and their number is

$$n_{2,t}(p)=\int_0^t f(p,t)e^{-t'/T_1}k\,dt'e^{-(t-t')/T_2}=k\left(\frac{1}{T_1}-\frac{1}{T_2}\right)^{-1}\left(e^{-t/T_2}-e^{-t/T_1}\right)\cdot f(p,t)\rightarrow \quad (1)$$

$$\rightarrow kte^{-t/T_1}f(p,t) \quad \text{for } T_2\rightarrow T_1$$

The total number of secondaries is $n_2(p)=\int_0^\infty n_{2,t}(p)\,dt$ and for the sec/prim ratio we have

$$r(p)\equiv\frac{n_2(p)}{n_1(p)}=k\Delta\left(\frac{\int_0^\infty f(p,t)e^{-t/T_2}dt}{\int_0^\infty f(p,t)e^{-t/T_1}dt}-1\right) \quad \text{where } \Delta\equiv\left(\frac{1}{T_1}-\frac{1}{T_2}\right)^{-1} \quad (2)$$

Of course it has been well known for a long time that the sec/prim ratio depends on the path length distribution but we would like to stress here that eq. (2) holds for any model of the Galaxy and for any assumptions about the acceleration or deceleration processes (provided they depend on p only). For $0 < (T_2 - T_1)/T_1 \ll 1$ eq. (2) gives

$$r(p) \simeq k[\bar{t}(p) + \tfrac{1}{2} \cdot \bar{t}^2(p) \cdot (T_2 - T_1)/T_1^2 + \ldots] \qquad (3)$$

where $\bar{t}(p) = \int_0^\infty t f(p,t) e^{-t/T_1} dt \,/\, \int_0^\infty f(p,t) e^{-t/T_1} dt$ (and similarly for $\bar{t}$ (p)) is the mean time (path length) of the observed primary particles at a given p. Thus the sec/prim energy dependence is practically equivalent to the energy dependence of the mean propagation time of the observed particles (for $T_2 - T_1 \ll \bar{t}$ and $\overline{t^2} \sim \bar{t}^2$), but not of the mean vacuum time.

3. Examples. First we shall consider a situation when p is a unique function of t. This could occur if, for example, c.r. were produced with a constant p and then accelerated according to $dp/dt = h(p) > 0$. Then f(p,t) is reduced to F(t) where $n_1(p)dp = F[t(p)]dt(p)e^{-t(p)/T_1}$. For the sec/prim ratio we have from (1) $r(p) = k\Delta(e^{t(p)/\Delta} - 1)$ with $t(p) = \int_{p_0}^{p} du/h(u)$ (4) so n_2/n_1 is a growing function of p. For the first order Fermi process, when $dp/dt = \beta p$ ($\beta > 0$), we get

$$r(p) = k\Delta[(p/p_0)^{1/\beta\Delta} - 1] \xrightarrow[T_2 \to T_1]{} \frac{k}{\beta} \ln p/p_0 \qquad (5)$$

If particles are produced with a distribution of primary momentum p then $f(p,t)dt = f(p',t')dt'$ where $t' = t + \tau$ with $\tau = \int_p^{p'} du/h(u)$ and

$$r(p') + 1 = \int_0^\infty f(p,t) e^{-(t+\tau)/T_2} dt \,/\, \int_0^\infty f(p,t) e^{-(t+\tau)/T_1} dt \qquad (6)$$

so $r(p') + 1 = [r(p) + 1] e^{\tau q/\Delta}$; hence $r(p') > r(p)$. (7)

Here τ is independent of t but it is not a necessary condition for r(p) to grow. r(p) will also grow if f(p,t) for higher p' is effectively shifted to longer times so that, for example, $f(p,t)dt = f(p',t')dt'$ with $t = t + \tau(p,p',t)$ and $\tau > 0$. One would expect that to be rather natural when the acceleration takes place. Growing of r(p) is seen from (6) since $e^{\tau/T_2} > e^{\tau/T_1}$ for any t for $T_2 > T_1$, which is the case for secondaries being lighter.

Let us next consider a second order Fermi acceleration - when p is not a unique function of time. In particular we shall assume that its behaviour with time corresponds to a uniform diffusion along the log p axis. Moreover we adopt a 1-dim. model of the Galaxy, the dimension x being perpendicular to the Galactic plane. C.r. nuclei are produced in the region $0 < x < l$ at a constant rate q (per unit length) with a single momentum p_0. They diffuse, are accelerated and fragment at the same time, leaking out of the Galaxy at x = 0 and x = l. First we shall consider a case of a constant spatial diffusion coefficient D. For that case it is easy to find the function f(p,t):

$$f(p,t)dp = (4\pi Kt)^{-1/2} \exp[-\ln^2(p/p_0)/4Kt] \frac{dp}{p} \cdot \frac{4q}{\pi} \sum_{1,3,\ldots} \frac{1}{m} \sin\frac{m\pi x}{l} \cdot \exp[-(\tfrac{m\pi}{l})^2 Dt] \qquad (8)$$

since particles with age t have a gaussian distribution of $y = \ln(p/p_0)$. Denoting $\int_0^\infty f(p,t) e^{-t/T_i} \equiv I_i$ we find

$$I_i = \frac{2q_i}{\pi\sqrt{K}} \frac{1}{p} \sum_{1,3,..} \frac{1}{m} \sin\left(\frac{m\pi x}{l}\right) \left[\frac{1}{T_i} + \left(\frac{m\pi}{l}\right)^2 D\right]^{-1/2} \cdot \left(p/p_0\right)^{-\frac{1}{4K}\left[1/T_i + \left(\frac{m\pi}{l}\right)^2 D\right]} \quad (9)$$

It is evident that r(p) increases with momentum for $T_2 > T_1$. In the limit $p \to \infty$, when the first term in the series dominates, we get

$$\tau(p) \to \left(p/p_0\right)^{\frac{1}{4K\Delta}} - 1 \quad (10)$$

4.Other solutions. It is sometimes difficult to find analytically f(p,t). In particular one would be interested in finding f(p,t) in the above described model if the spatial diffusion depends on p but this does not seem to be an easy task. So we shall treat this problem considering the equilibrium equations. We assume a second order acceleration occuring, for example, as a result of particle collisions with Alfven waves in the ISM. This corresponds to a particle diffusion in the 3-dimensional momentum space with a momentum dependent coefficient K(p). The equation for primary particle density in the phase space ($F_1(x,p) \cdot 4\pi p^2 dp dx = dn_1(x,p)$) is

$$\frac{1}{p^2}\frac{\partial}{\partial p}\left(K(p)p^2\frac{\partial F_1}{\partial p}\right) + D(p)\frac{\partial^2 F_1}{\partial x^2} - \frac{F_1}{T_1(x)} + q_i\delta(p-p_0) = 0 \quad (11)$$

Let us first neglect the term with fragmentation $F_1/T_1(x)$. As it is usually done we look for solutions in the form $F_1(x,p) = F'(p)\cdot F''(x)$. Assuming further $K(p) = B\cdot p^{\eta}$ and $D(p) = A\cdot p^{\alpha}$ we get for $p > p_0$

$$p^{\eta}\frac{\partial^2 F'}{\partial p^2} + (\eta+2)p^{\eta-1}\frac{\partial F'}{\partial p} - \frac{\lambda A}{B}p^{\alpha}F' = 0 \quad (12)$$

We shall look for power law spectra and this implies that $\eta = 2 + \alpha$. (However, for a consistent picture of acceleration and spatial diffusion due to Alfven waves both diffusion coefficients are related by $K(p)\cdot D(p) \sim p^2$ for relativistic particles, but this does not lead to experimentally observed power law spectra). With $F'(p) \sim p^{-\gamma}$ we have from (12)

$$\gamma_{\pm}(\lambda) = \frac{1}{2}\left(3+\alpha \pm \sqrt{(3+\alpha)^2 + 4\lambda A/B}\right) \quad (13)$$

where $F'(p) \sim p^{-\gamma_+}$ for $p > p_0$ and $F'(p) \sim p^{-\gamma_-}$ for $p < p_0$. $F''(x) \sim \sin(\sqrt{\lambda}x)$, with $\lambda = (n\pi/l)^2$ and $n = 1,3,5,..$; hence

$$F_1(x,p) = \sum_{1,3,} G_n \sin\left(\frac{n\pi x}{l}\right)\cdot\left[\left(p/p_0\right)^{-\gamma_n^-}\Theta(p_0-p) + \left(p/p_0\right)^{-\gamma_n^+}\Theta(p-p_0)\right] \quad (14)$$

where $\Theta(p - p_0)$ is a step function. Substituting (14) to (11) (with no fragmentation) we get

$$G_n = 2q\cdot\left[n\pi B p_0^{1+\alpha}(\gamma_n^+ - \gamma_n^-)\right]^{-1} \quad (15)$$

At high p the momentum spectrum behaves as $p^{-\gamma_+}\cdot 4\pi p^2$, so independently of the spatial distribution of the sources which influences only G_n.

We shall find now the secondary particle spectrum. Let $F_2(x_0,x,p)$ denote the phase space density of secondaries observed at x with p, produced at x_0. Then we have

$$F_2(x_0,x,p) = k\varrho(x_0)\int_{p_{thr}}^{\infty} F_1(x_0,p')\cdot F_{1p'}(x_0,x,p)\,dp' \quad (16)$$

where $F_{1p'}(x_0,x,p)$ is the solution to the eq. (11) ($T_1 \to \infty$) with the last term $q\delta(p-p_0)$ substituted by $q\delta(x-x_0)\cdot\delta(p-p_0)$. This solution differs from (14) only by different coeffi-

cients $G_n(x_o)$, the p dependence being the same. Solving (16) we get for $p > p_o$ $F_2(x_o, x, p) = I_1 + I_2$ where

$$I_1 = \frac{k\,\varrho(x_o)}{p_o^{1+2\alpha}} \sum_n G_n \sin\left(\frac{n\pi x_o}{L}\right) \left\{ \sum_m G_m(x_o) \sin\left(\frac{m\pi x}{L}\right) (\gamma_n^+ - \gamma_m^+ + \alpha)^{-1} \left[(p/p_o)^{-\gamma_m^+} - (p/p_o)^{-(\gamma_n^+ + \alpha)} \right] \right\}$$

and (17)

$$I_2 = \frac{k\,\varrho(x_o)}{p_o^{1+2\alpha}} \sum_n G_n \sin\left(\frac{n\pi x_o}{L}\right) \left[\sum_m G_m(x_o) \sin\left(\frac{m\pi x}{L}\right) (\gamma_n^+ - \gamma_m^- + \alpha)^{-1} (p/p_o)^{-(\gamma_n^+ + \alpha)} \right]$$

For simplicity we have put $p_{inv} = p_o$. I_1 (I_2) corresponds to the secondaries that have been produced with momenta smaller (larger) than p. To find $F_2(x,p)$ we have to integrate $\int_0^L F_2(x_o, x, p)\, dx_o$ but its momentum dependence is already seen from (17). The terms with $p^{-\gamma_n^+}$ and $p^{-(\gamma_n^+ + \alpha)}$ dominate for $p \gg p_o$, so the sec/prim ratio increases with p as $1 - (p/p_o)^{-\alpha}$, practically independently of the gas density distribution $\varrho(x)$. For $\varrho(x)$ = const. and $\alpha = 0.6$ F_2/F_1 (for $p/p_o = 10$) reaches ~80% of its maximum value.

Taking now into account the fragmentation term in (11) we look, as before, for solutions in the form $F_1(x,p) = F'(p)F''(x)$, if $T_1(x)$ = const. For $F'(p) \sim p^{-\gamma}$ we get

$$[\gamma(\gamma+1) - \gamma(\eta+2)]\, p^{\eta-2} - (\lambda A/B)\, p^{\alpha} - 1/BT_1 = 0 \qquad (18)$$

This can only be fulfilled at $p \to \infty$ and it can be seen that then the fragmentation term does not play any rôle. In particular, if $\eta - 2 = \alpha$, γ has the same form as in (13). If we assume that the secondary spectrum has a form $\sim p^{-\Gamma}$ for $p \to \infty$ then we get

$$[\Gamma(\Gamma+1) - \Gamma(\eta+2)]\, p^{\eta-2} - (\lambda A/B)\, p^{\alpha} - 1/BT_2 + k\, p^{\Gamma-\gamma} = 0 \qquad (19)$$

This can only be fulfilled at high momenta if $\Gamma = \gamma$. So at $p \to \infty$ the sec/prim ratio $\to$ const. even if we take into account fragmentation.

5. Conclusions. We conclude that, contrary to some suggestions, a simultaneous acceleration and propagation in the ISM would lead to the sec/prim ratio increasing with momentum (tending in some cases to a constant for $p \to \infty$). That is in a strong discrepancy with observation. The logarithmic rise, stressed by Cowsik [1], is obtained for some particular cases only. Moreover the shape of the particle spectra at $p \to \infty$ does not depend on the spatial distribution of their sources.

References

1. Cowsik, R., (1979), Ap.J. 227, 856
(1980), Ap.J. 241, 1195
(1981), in "Origin of Cosmic Rays", IAU Symp. no. 94, Bologna
2. Schlickeiser, R., (1984), lectures given at Int. School of C.R. Astrophysics, Erice

PROPAGATION OF COSMIC RAYS AND NEW EVIDENCE FOR DISTRIBUTED ACCELERATION

R. Silberberg, C. H. Tsao, E. O. Hulburt Center for Space Research, Naval Research Laboratory, Washington, D. C. 20375-5000 USA
J. R. Letaw, Severn Communications Corporation, Severna Park, MD 21146
M. M. Shapiro, Max Planck Institute for Astrophysics, Munich, Germany

We explore the origin and propagation of cosmic rays in terms of conventional as well as supplementary newer assumptions. Cosmic rays are considered to be accelerated by supernova shock waves (possibly after injection by stellar flares) and to traverse clouds in the source region. After rigidity-dependent escape from these clouds into interstellar space, cosmic rays are further accelerated by the weakened shocks of old supernova remnants and then pass through additional material. The distributed acceleration hypothesis is discussed with emphasis on recent data on the abundances of cosmic-ray isotopes of N above 1 GeV/u and of He near 6 GeV/u. The isotopic abundance of He at 1 GeV/u would provide another test between this hypothesis and the scenario generally assumed hitherto. Measurement of the production cross sections, of the nuclides A = 14 and 15 from oxygen at E = 75 to 100 MeV per amu is also considered essential.

1. Introduction. A theory of cosmic ray propagation must satisfy numerous experimental as well as theoretical constraints. We discuss some of these constraints in the next Section. Thereafter we describe a propagation scenario that takes into account these constraints. Finally we shall propose additional tests for distributed acceleration.

2. Experimental and Theoretical Constraints. Acceleration and nuclear spallation do not occur at the same time, nor even intermittently in a series of equally strong acceleration processes, otherwise the secondary spectra would be flatter than those of the parent nuclei (Eichler, 1980, Cowsik, 1980, Fransson and Epstein, 1980). On the other hand, cosmic rays encounter a large number (about 100) shock waves during their galactic residence time (Axford, 1981). The seeming contradiction is resolved if cosmic rays are subject to a strong, early acceleration energized by a relatively young ($\geq 10^4$ years) supernova remnant, e.g. by shock waves with a high compression ratio (3 to 4), and subsequent weak accelerations with a compression ratio ≤ 2.5, which will not flatten the secondary energy spectra, (Axford 1981).

While the observed spectra of various cosmic-ray components (except at low energies) are similar in shape, the source spectra, after correction for rigidity-dependent depletion by fragmentation are flatter for protons and helium then for heavier nuclei (Engelmann et al. 1984). This is consistent with acceleration of protons and helium by very strong shock waves at even younger supernova remnants ($\leq 10^4$ years). The absence of heavier nuclei with such spectra is explicable by postulating confinement in clouds near these supernova remnants in

which heavier nuclei break up while $\bar{p}$ and e^+ are produced, mainly in cosmic ray proton interactions.

Another observation that propagation models must satisfy is the near-constancy of the anisotropy below 10^5 GeV. From the review of Linsley (1983) we see that the amplitude of the anisotropy increases only a factor of about 3 between 10 and 10^5 GeV. The anisotropy is nearly constant also after correcting for the Compton-Getting anisotropy, since the latter is opposite in direction to the observed anisotropy. The effect of correction for the Compton-Getting anisotropy is shown in Fig. 4 of Hillas (1983). The small energy dependence of the anisotropy (much smaller than that of the secondary to primary abundance ratios) is readily explained in terms of the nested leaky box models of Cowsik and Wilson (1973, 1975), the multiple cloud model of Silberberg et al. (1983a) and the somewhat similar recent model of Morfill et al. (1985).

We shall now explore some constraints on the regions of cosmic ray acceleration and the injection process. Issa et al. (1981) explored the density of cosmic rays in various clouds and found that the density is about 4 times higher at O-B associations and about 4 times lower in other clouds such as those near T-Tauri associations. In O-B associations (with massive young stars) one can expect frequent supernovae; such regions were proposed as cosmic ray sources by Montmerle (1979).

The relationship between the cosmic ray abundances and the first ionization potential implies injection near 10^4 °K. Such injection conditions occur in solar and stellar flares (J.-P. Meyer, 1985). Also the warm, fluffy regions around interstellar clouds have such temperatures, but a large fraction of non-volatile material is in grains in these regions; while the contribution of material from grains at cosmic ray sources has been explored, quantitative predictions are still inadequate. J.-P. Meyer (1985) has also shown that due to electron attachment and reduced ionization losses of heavy nuclei, injection energies of $\geq$ 1 MeV are consistent with cosmic ray abundances. While H and $\overline{\text{He}}$ abundances in cosmic rays are low, they may be low already at the injection stage, just as in solar flares there are effects of heavy ion enhancement.

3. Origin and Propagation. The following scenario is consistent with the above constraints: Flare particles are injected and accelerated by supernova shock waves in O-B stellar associations with an energy gain by a factor of about 100. From the earliest phase, when the clouds are least broken up, only protons and helium and their secondaries survive; the source spectra of protons and helium are flatter due to acceleration during the young phase of supernova remnants ($\sim 10^4$ years old) . Some time thereafter, when the clouds are broken up to some extent, heavy nuclei and their secondaries also survive after acceleration and propagation in clouds. The rigidity dependence of secondary-to-primary ratios is associated with rigidity-dependent leakage from the clouds of the source regions. Subsequent leakage from the galaxy has a small rigidity dependence-such as that of the anisotropy.

In interstellar space (Axford, 1981) cosmic rays encounter about a 100 weak shocks with small (< 2.5) compression ratios, which accelerate cosmic ray particles without flattening their spectra, consistent with our model of distributed acceleration (Silberberg et al. 1983b).

4. Further Tests for Distributed Acceleration. Jordan and P. Meyer (1984) have recently measured the ratio $^3He/^4He = 0.24 \pm 0.05$ at 6 GeV/u. This value is higher by a factor of two than those measured at 200 to 300 MeV per amu, 0.114 ± 0.015 at 200 MeV per amu (Badhwar et al. 1967 and Webber and Yushak 1983) and 0.11 ± 0.03 at 300 MeV per amu (O'Dell et al. 1965). J.-P. Meyer (1971, 1974) has calculated the energy dependence of the $^3He/^4He$ ratio, assuming an exponential path length distribution and a mean path of 7 g/cm^2. More recent data permit the calculation of the energy dependence of the mean path length traversed by cosmic rays (Ormes and Protheroe 1983). In Fig. 1 we display the above experimental data, and the calculated abundance ratio, including the energy dependence of the mean path length. The solid line represents the case of distributed acceleration, with an energy gain of 4 after fragmentation, and the dashed curve represents the standard propagation calculation. We note that with distributed acceleration, the peak value of the ratio $^3He/^4He$ is shifted to ~ 4 GeV/u, and agrees with the measured value within 1.4 standard deviations, or 1.0 standard deviations if a weaker rigidity dependence of the path length $\propto R^{-0.5}$, (that is also in common use), is adopted. The uncertainty in solar modulation does not permit an adequate determination of the path length for E < 500 MeV per amu. Fig. 1 is based on the cross sections used by J.-P. Meyer (1971, 1974) and the modulation parameters of Webber and Yushak (1983). A considerably longer path length fits the low-energy data, if one uses the modulation parameters of Jordan and P. Meyer (1984). Thus, with distributed acceleration, the $^3He/^4He$ data near 6 GeV/u are consistent with the standard path length of ~7 g/cm^2 at these energies. Without distributed acceleration, the dashed line of Fig. 1 shows the significant disagreement between the high energy measurement of $^3He/^4He$ and the standard propagation model.

Jordan and Meyer (1984) have interpreted the data in terms of a long path length, ~ 15 g/cm^2 possibly associated with regions where cosmic-ray $\bar{p}$ production takes place. In terms of this model, the $^3He/^4He$ ratio near 1 GeV/u should be high, probably near 0.3. With distributed acceleration, it is expected to be between 0.15 and 0.20.

Another test for distributed acceleration is provided by the $^{15}N/^{14}N$ ratio between 0.1 and 0.4 GeV/u, and the cross sections $\sigma_1[O\ (\Delta A = 1)]$ and $\sigma_2\ [O\ (\Delta A = 2)]$ at energies between 75 and 100 MeV/u. The ratio σ_1/σ_2 at the latter energies should be smaller than the value at 225 MeV/u of Guzik et al. (1985) and at 700 to 900 MeV/u of Webber et al. (1983). This would account for the discrepancy between the data of $^{14}N/N$ at 2.5 GeV/u of 0.55 ± 0.04 (Byrnak et al. 1983 and Goret et al. 1983) and the lower value of 0.45 ± 0.04 at 100 to 400 MeV/u, (Mewaldt 1981 and references therein).

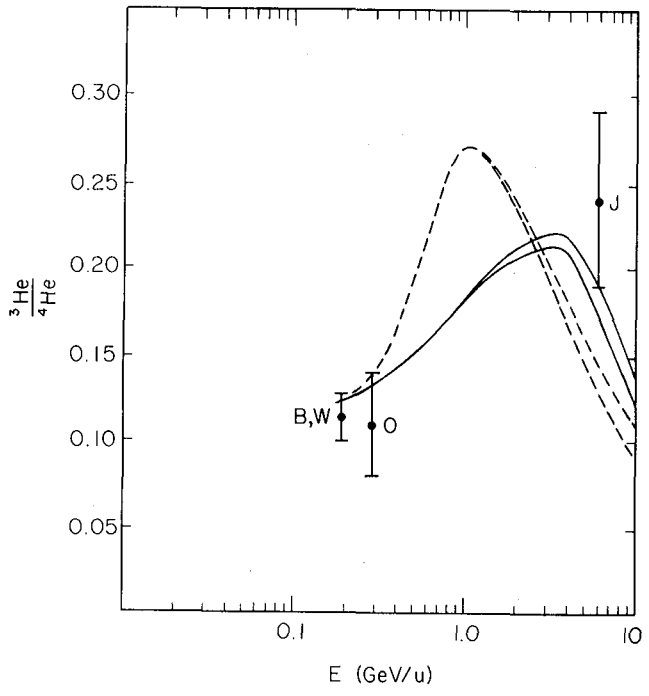

Figure 1: The experimental and calculated ratios of $^3He/^4He$. The solid curve is based on distributed acceleration and the dashed curve on the standard propagation model.

References:

1. Axford, W. I. (1981), 17th ICRC (Paris) 12, 155.
2. Badhwar, G. D. et al. (1967) Phys. Rev. 163. 1327.
3. Byrnak, B. et al. (1983) 18th ICRC, (Bangalore) 9,135.
4. Cowsik, R. (1980) Ap. J. 241, 1195.
5. Cowsik, R. and Wilson, L. W., (1973), 13th ICRC (Denver), 1, 500.
6. Cowsik, R. and Wilson, L. W., (1975), 14th ICRC (Munich), 2, 659.
7. Eichler, D. (1980), Ap. J. 237, 809.
8. Engelmann, J. et al. (1984), Proc. XXV Cospar Conf.
9. Fransson, C. and Epstein, R. I., (1980), Ap. J. 242, 411.
10. Goret, P. et al. (1983), 18th ICRC (Bangalore), 9, 139.
11. Guzik, T. G. et al. (1985), Bull. Am. Phys. Soc. 30, 762.
12. Hillas, A. M., (1983) Comp. and Origin of Cosmic Rays, p. 125, Reidel Publ. Co.
13. Issa, M. R. et al. (1981), 17th ICRC (Paris), 1, 150.
14. Jordan, S. P. and Meyer, P., (1984), Phys. Rev. Letters, 53, 505.
15. Linsley, J., (1983), 18th ICRC (Bangalore), 12, 135.
16. Meyer, J.-P., (1971) Lyngby Conf. on Isotopic Composition of Cosmic Rays and (1974) Thesis.
17. Meyer, J.-P., (1985), Ap. J., Suppl. 57,, 173.
18. Mewaldt, R. A., (1981), 17th ICRC (Paris) 13, 49.
19. Montmerle, T., (1979), Ap. J. 231, 95.
20. Morfill, G. E., Meyer, P. and Lust, R.,(1985), to be publ. in Ap. J.
21. O'Dell, F. W., et al. (1965), 9th ICRC (London), 1, 412.
22. Ormes, J.F. and Protheroe, R. J. 1983, Ap. J. 272, 756.
23. Silberberg, R. et al., (1983a) 18th ICRC (Bangalore), 2, 179.
24. Silberberg, R. et al., (1983b), Phys. Rev. Letters, 51, 1217.
25. Webber, W. R. and Yushak, S. M. (1983), Ap. J. 275, 391.
26. Webber, W. R. et al. (1983), 18th ICRC (Bangalore), 2, 202.

EXACT SOLUTIONS FOR SPORADIC ACCELERATION OF COSMIC RAYS

R. Cowsik
Tata Institute of Fundamental Research, Bombay 400005, India

ABSTRACT

The steady state spectra of cosmic rays subject to a sporadic acceleration process, wherein the gain in energy in each encounter is a finite fraction of the particle energy, are derived on the basis of a simple mathematical model which includes the possibility of energy dependent leakage of cosmic rays from the galaxy. Comparison with observations allows limits to be placed on the frequency and efficiency of such encounters.

1. Comparison of Fermi-process and Sporadic Acceleration. Among the various processes of cosmic-ray acceleration the possibility suggested by Fermi [1] that the particles, above a minimum threshold energy, gain energy statistically in encounters with moving magnetised interstellar clouds, has been studied most extensively [2-6]. In the mathematical formulation of such a model one assumes that the average change in energy in each encounter is small fraction of the original energy so that in the Taylor-expansion of the Boltzmann collision integral one retains only the first two, convective and diffusive, terms. Exact analytic solutions upto the second order, keeping the leakage from the galaxy constant at all energies, are given in references [5-6]. Learche and Schlickeiser have investigated extensively the problem including energy dependent leakage [7] and one can find an extensive list of references in their paper.

2. A Mathematical Model of Sporadic Acceleration. When in a single encounter the energy of the cosmic ray increases by a large factor we can not treat the transport under the diffusion approximation; the fluctuations in the number of encounters become critically important in determining the spectra of primaries and secondaries. In the mathematical formulation of the problem, to keep it tractable and simple, it is assumed here that the energy of the particle E is multiplied by a factor α after each encounter and the spread in α is taken to be negligible. Let the probability of such an encounter per unit time be A, the leakage probability B(E) and s be the spallation rate. If the injection with the spectral form I(E) started at time t=0, then the spectrum of particles which have suffered exclusively n encounters at time t is given by

$$M(n,E,t) = \int_0^\infty \int_0^t M(n-1, E', t')\, A\ (E-\alpha E') \times \exp - [A+B(E)+s]\,(t-t')\, dt'\, dE' \qquad (1)$$

with

$$M(o,E,t) = \int_0^t I(E,t') \exp - [A+B(E)+s]\,(t-t')\, dt' \qquad (2)$$

Assuming that the cosmic rays are in steady state the spectrum is given by

$$M(E) = \lim_{t \longrightarrow \infty} \sum_{n=0}^{\infty} M(n,E,t) \qquad (3)$$

It is straight forward to derive the result

$$M(E) = \sum_{n=0}^{\infty} I\ (E/\alpha^n)\ \frac{\alpha}{A} \prod_{k=0}^{n} A/\alpha\ [A+B(E/\alpha^k) + s] \qquad (4)$$

The spectra of secondaries L(E) is obtained by substituting s M(E) for I(E) in equation (4). Writing $P_n(E)$ for the product one gets

$$L(E) = \sum_{n=0}^{\infty} s\ M(E/\alpha^n)\ \frac{\alpha}{A}\ P_n(E) \qquad (5)$$

Now various cosmic-ray models can be investigated by specifying I, A, B and α. For example for $I = I_o\ E^{-\beta}$, $B = B_o$ independent of energy eqation (4) converges for

$$A\ \alpha^{\beta-1}\ (A + B_o + s)^{-1} < 1 \qquad (6)$$

Or keeping in mind the currently popular models of acceleration by shocks in the interstellar medium [8-11] it is appropriate to choose

$$I = I_o\ [E_o + E]^{\delta-\beta}\ ;\quad B = B_o E^{\delta} + h \qquad (7)$$

with E_o = 1 GeV/nucleon, $h = 10^{-7} yr^{-1}$, $\beta = 2.7$ and $\delta = 0.5$.

3. Comparison with Observations and Results. In figure 1 the ratio L(E)/M(E) is shown for two values of the acceleration parameter $\alpha = 1.26, 1.6$ with the maximum probability of encounter at low energies $A B_o^{-1} = 1, 3$ and 6 respectively. These theoretical expectations are compared with the observations [12-14] of the ratio of boron to carbon in cosmic rays at various energies. The theoretical results allow upward or downward scaling to approximately represent change in the spallation rate s due to different choice of the interstellar density.

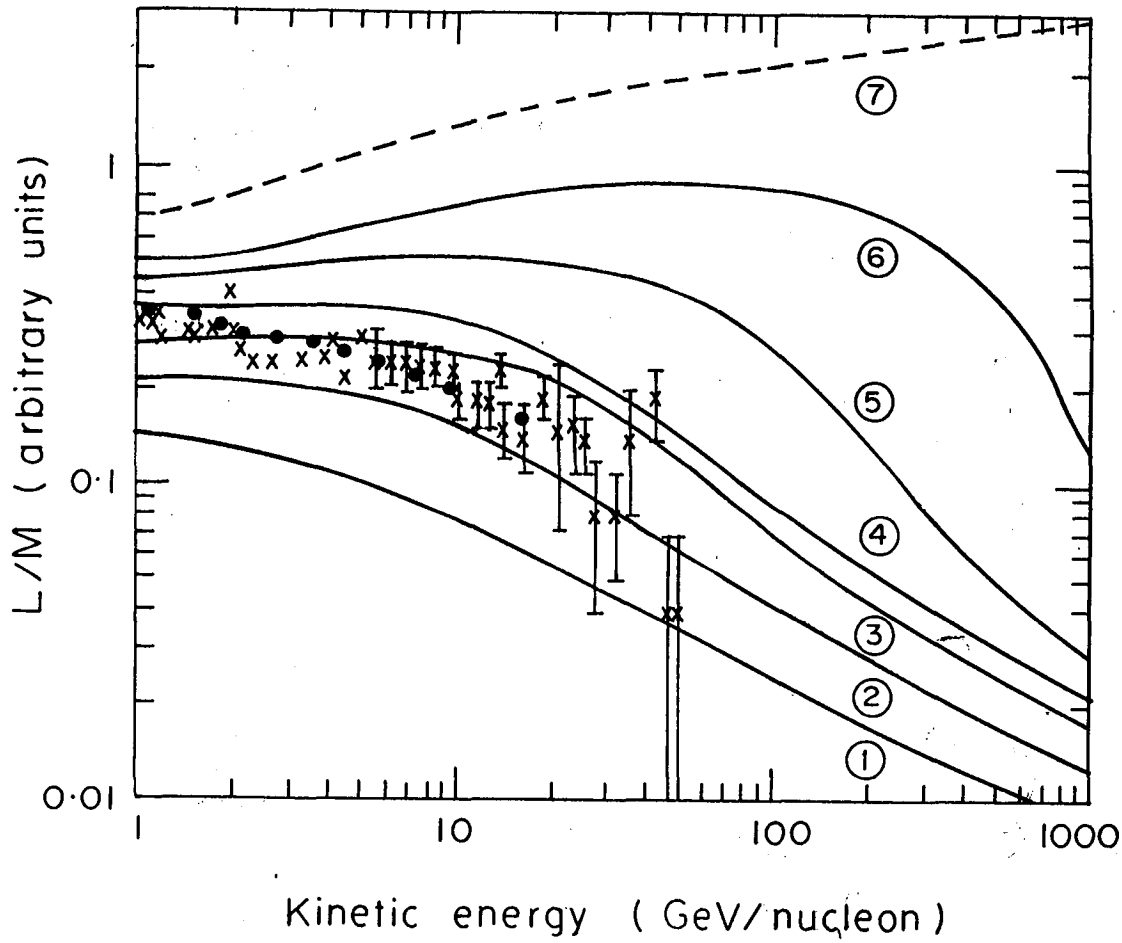

Fig. 1. Theoretical ratios of secondary to primary cosmic rays for $(\alpha, AB_o^{-1}) = (1.26, 1), (1.26, 3), (1.26, 6), (1.6, 1), (1.6, 3)$, are labelled 1-6 and the standard Fermi-process [6] is labelled 7. The observed boron/carbon ratios are from references [12-14].

One can draw several conclusions : (a) All curves tend to $\sim E^{-\delta}$ at high energies as expected, (b) As the rate of acceleration increases L/M ratios increase in magnitude and also become flatter thereby losing the $E^{-\delta}$ behaviour upto progressively higher energies, (c) Thus $\alpha = 1.6$ and $AB_0^{-1} = 3$ is the maximum acceleration rate in the interstellar medium, corresponding to a mean increase of $(1.6)^3 \approx 4$ in the energy of the low energy cosmic rays. As energy increases $P_n(E)$ decreases rapidly so that the expected net acceleration decreases also rapidly to negligible levels even at > 10 GeV/nucleon. On the basis of this analysis and the earlier work on Fermi-process [1-6] it appears that cosmic rays suffer negligible reacceleration in the interstellar medium after they emerge from their sources.

References

1. Fermi, E., (1949), Phys. Rev., 75, 399.
2. Fermi, E., (1954), Ap. J., 119, 1.
3. Hayakawa, S. (1969), in Cosmic Ray Physics (Wiley Interscience).
4. Eichler, D. (1980), Ap.J., 237, 809 (Instantaneous generation of power-law spectra after each collision is discussed here).
5. Cowsik, R. (1979), Ap.J., 227, 856.
6. Cowsik, R. (1980), Ap.J., 241, 1195.
7. Lerche, I. and Schlickeiser, R. (1985), to appear in Astronomy and Astrophysics.
8. Axford, W.I. et al. (1977), Proc. ICRC, 2, 273.
9. Bell, A.R. (1978), MNRAS, 182, 147.
10 Blandford, R.D. and Ostriker, J.P. (1978), Ap.J., 237, 793.
11 Volk, H.J. et al. (1979), Proc. ICRC, 2, 38.
12 Engelman, J.J., et al (1981), Proc. ICRC, 9, 97
13. Boufford, M. et al. (1982), Ap. and Sp.Sci., 84, 3.
14 Ormes, J.F. and Prothoroe, R.J. (1983), ICRC Proc. 2, 221.

RELATIVISTIC TRANSPORT THEORY FOR COSMIC-RAYS

G. M. Webb
University of Arizona
Department of Planetary Sciences
Tucson, Arizona 85721 U.S.A.

ABSTRACT

We discuss various aspects of the transport of cosmic-rays in a relativistically moving magnetized plasma supporting a spectrum of hydromagnetic waves that scatter the cosmic-rays. A local Lorentz frame (the co-moving frame) moving with the waves or turbulence scattering the cosmic-rays is used to specify the individual particle momentum. Since the co-moving frame is in general a non-inertial frame in which the observer's volume element is expanding (contracting) and shearing, geometric energy change terms appear in the cosmic-ray transport equation which consist of the relativistic generalization of the adiabatic deceleration term obtained in previous analyses, and a further term involving the acceleration vector of the scatterers (this term may be thought of as a gravitational redshift effect). We also present a relativistic version of the pitch angle evolution equation, including the effects of adiabatic focussing, pitch angle scattering, and energy changes.

1. Introduction. The transport equations for cosmic-rays in a bulk plasma flow (such as the solar wind) were originally obtained by Parker (1965), and later by Dolginov and Toptygin (1966), Gleeson and Axford (1967), Skilling (1975) and Webb and Gleeson (1979). These developments assumed that background plasma flow was non-relativistic; whereas the present work is concerned with obtaining equations that also apply in relativistic flows. Our derivation relies mainly on relativistic transport theory for Liouville's equation (or the Boltzmann equation) as developed by Lindquist (1966).

2. The Equations. The development of a relativistic transport theory for the Boltzmann (or Liouville equation) for charged particle propagation in electromagnetic fields starts with the equation of motion for the individual particle:

$$m_o \, dx^a/d\tau = p^a \, , \tag{1}$$

$$m_o \, dp^a/d\tau = -\Gamma^a_{bc} \, p^b p^c + q \, F^a{}_b \, p^b \, , \tag{2}$$

where Γ^a_{bc} are the affine connection coefficients (the term involving Γ^a_{bc} represents non-inertial forces). The electromagnetic ($\underline{E}$ and $\underline{B}$) forces are contained in the last term in (2) involving the Faraday Tensor $F^a{}_b$; q denotes the particle charge; $\{p^a\}$ a = 0,1,2,3 is the momentum four vector, m_o is the particle rest mass, and τ is the proper time. As a consequence of (1) and (2), the 1-particle phase space distribution function satisfies the relativistic Liouville equation

$$L(F) = p^a \partial F/\partial x^a - \Gamma^a_{bc}\, p^b p^c \frac{\partial F}{\partial p^a} + q\, F^a_{\ b}\, p^b \frac{\partial F}{\partial p^a} = 0 . \qquad (3)$$

For the case of stochastic electromagnetic fields we set

$$F^a_{\ b} = \langle F^a_{\ b} \rangle + \delta F^a_{\ b} , \quad F = \langle F \rangle + \delta F , \qquad (4)$$

and applying quasilinear theory we obtain the Boltzmann equation

$$\langle L \rangle (f) = (p^0/c)(\delta F/\delta t)_c = q^2 p^b \frac{\partial}{\partial p^i} \left\langle \delta F^i_{\ b} \langle L \rangle^{-1} \left(\delta F^j_{\ c}\, p^c \frac{\partial f}{\partial p^j} \right) \right\rangle \qquad (5)$$

where the angular brackets denote ensemble averages $f = \langle F \rangle$, and δF and $\delta F^a_{\ b}$ denote the random components of F and $F^a_{\ b}$. The operator $\langle L \rangle$ in (5) is the particle propagator in the average background field, and $\langle L \rangle^{-1}$ its inverse.

Taking moments of (5) with respect to directions of the particle momentum leads to moment equations for cosmic-ray transport. It is convenient to use a local Lorentz frame moving with the scatterers Σ' to specify the individual particle momentum p'. In the special case where the observer's frame is a global Lorentz frame (the more general case is considered in Webb, 1985), the cosmic-ray continuity equation, or zeroth order moment of (5) with respect to momentum directions of p' is:

$$\begin{aligned} &\partial/\partial t \left[\gamma (n'^0 + \underline{V}\cdot \underline{J}'/c^2) \right] + \partial/\partial \underline{x} \cdot \left[\gamma \underline{V} n'^0 + \underline{J}' + (\gamma - 1) \underline{V}\, \underline{V}\cdot \underline{J}'/V^2 \right] \\ &+ \partial/\partial p' \left[(q\underline{E}' - m'\underline{a}')\cdot \underline{J}'/v' - \tfrac{1}{3} p' n'^0 \left(\partial\gamma/\partial t + \underline{\nabla}\cdot(\gamma \underline{V}) \right) \right] = 0, \end{aligned} \qquad (6)$$

where

$$\underline{J}' = - \underline{\underline{K}} \cdot \left[\partial n'^0/\partial \underline{x}' + p' m' (q\underline{E}' - m'\underline{a}')\, \partial (n'^0/p'^2)/\partial p' \right] , \qquad (7)$$

is the particle current in the co-moving frame;

$$\underline{a}' = \gamma^2 \left\{ d\underline{V}/dt + \underline{V} (d\gamma/dt) \; / \left[\gamma (\gamma + 1) \right] \right\} \qquad (8)$$

is the acceleration vector of the scatterers; n'^0 is the particle number density ($n'^0 = 4\pi p'^2 f_0$ where f_0 is the isotropic part of the distribution function in Σ'); $\gamma = (1 - V^2/c^2)^{-1/2}$ is the Lorentz factor corresponding to V, with $\underline{V}$ the velocity of the scattering frame relative to the observer's frame. $\underline{\underline{K}}$ is the cosmic-ray diffusion tensor, $\underline{E}'$ is the mean electric field in Σ' (which is negligible for a highly conducting plasma); m', v' denote the relativistic particle mass and speed in Σ' ($p' = m'v'$), and the time derivative

$$\frac{d}{dt} = \frac{\partial}{\partial t} + \underline{V}\cdot \frac{\partial}{\partial \underline{x}} , \qquad (9)$$

occurring in (8) is the Lagrangian derivative moving with the scatterers. The effects of second order Fermi acceleration have been omitted in (6), but can be included in the analysis if necessary.

The term $- m'\underline{a}'\cdot \underline{J}'/v'$ in (6) involving the acceleration vector of the scatterers may be thought of as a gravitational redshift effect: it arises because the scattering frame is in general an accelerating frame and it is then necessary to introduce non-inertial forces to properly

describe the particle motion in Σ'. The form of this term is similar to that of the Joule heating term $\underline{J}'\cdot(q\underline{E}')/v'$ but with $q\underline{E}'$ replaced by $-m'\underline{a}'$. The second momentum change term in (6)

$$\langle \dot{p}' \rangle^* = -\tfrac{1}{3} p' \left[\frac{\partial \gamma}{\partial t} + \underline{\nabla} \cdot (\gamma \underline{V}) \right] , \qquad (10)$$

may be thought of as the relativistic generalization of adiabatic deceleration. However, care is required in its interpretation; it is intimately connected with the fact that the co-moving frame is a non-inertial frame. More generally one can show that

$$\langle \dot{p}' \rangle^* = -\tfrac{1}{3} p' c \, \Gamma'^{\alpha}_{0\alpha} = -\tfrac{1}{3} p' c \, U^{\alpha}{}_{;\alpha} , \qquad (11)$$

where in (11) we have used the summation convention on the index α (α = 0,1,2,3) and $\underline{U}$ denotes the four velocity of the scattering frame. Thus (11) shows that $\langle \dot{p}' \rangle^*$ is associated with the affine connection coefficients in the co-moving frame. The streaming equation (7) follows from the first moment of the Boltzmann equation (5) with respect to directions of $\underline{p}'$. In the derivation of (6) and (7) the diffusion approximation has been used (the distribution function is assumed to be near isotropic with respect to $\underline{p}'$) and the cosmic-ray inertia in Σ' has been neglected in the derivation of (7)).

An alternative basis for deriving cosmic-ray transport equations is to use the drift approximation in which the particle gyrofrequency is assumed to be large compared to the scattering frequency ν, so that to a first approximation the distribution function is independent of gyrophase. By averaging the Liouville equation (5) over gyrophase in Σ' one obtains the pitch angle scattering equation:

$$\begin{aligned} &\gamma\left(1+\mu' v' \underline{n}\cdot\underline{V}/c^2\right)\partial F/\partial t + \left[\underline{V} + (\mu'/\gamma)\left(v'\underline{n} + (\gamma-1)\, v'\underline{n}\cdot\underline{V}\,\underline{V}/V^2\right)\right]\cdot\underline{\nabla} F \\ &+ p'\,\partial F/\partial p' \left\{ \tfrac{1}{2}(1-3\mu'^2)(\gamma+1)\,\underline{n}\cdot\partial/\partial x'_3\left(\gamma\underline{V}/(\gamma+1)\right)\right. \\ &\quad \left. -\tfrac{1}{2}(1-\mu'^2)\, c\, U^{a}{}_{;a} - (\mu'/v')\,\underline{n}\cdot\underline{a}' \right\} \\ &+ \tfrac{1}{2}(1-\mu'^2)\,\partial F/\partial\mu' \left\{ v'\,\underline{\nabla}'\cdot\underline{n} + \mu'\left[c\, U^{a}{}_{;a} - 3(\gamma+1)\,\underline{n}\cdot\partial/\partial x'_3\left(\gamma\underline{V}/(\gamma+1)\right)\right]\right. \\ &\quad \left. - \frac{2}{v'}\,\underline{n}\cdot\underline{a}' \right\} = \frac{\partial}{\partial\mu'}\left[\tfrac{1}{2}(1-\mu'^2)\,\nu\,\frac{\partial F}{\partial\mu'}\right] , \end{aligned} \qquad (12)$$

where $\mu' = \cos\theta'$ with θ' the particle pitch angle,

$$\frac{\partial}{\partial x'_3} = \gamma\,\frac{\underline{n}\cdot\underline{V}}{c^2}\,\frac{\partial}{\partial t} + \underline{n}\cdot\underline{\nabla} + (\gamma-1)\,\underline{n}\cdot\frac{\underline{V}(\underline{V}\cdot\underline{\nabla})}{V^2} , \qquad (13)$$

and $\underline{n} = \underline{e}'_3 = \underline{B}'/B'$. The electric field in Σ' has been assumed to be zero in the derivation of (12). Equation (12) is the special relativistic generalization of the pitch scattering equation used by Skilling (1975) to derive the cosmic-ray transport equations. It also contains for example the adiabatic focussing term used in solar cosmic-ray propagation theory.

3. Conclusions. The development presented here has concentrated on deriving kinetic equations for cosmic-ray transport in special relativistic flows; in addition, hydrodynamical forms of the equations can be obtained.

These equations are being used to study cosmic-ray acceleration in relativistic shocks.

4. Acknowledgements. This work was supported in part under NSF grant ATM-8311241.

References

1. Dolginov, A.Z. and Toptygin, I.N., (1966), Bull. Acad. Sci. USSR, Phys. Ser. 30, 1852.
2. Gleeson, L.J. and Axford, W.I., (1967), Astrophys. J. Lett., 149, L115.
3. Lindquist, R.W., (1966), Ann. Phys. 37, 487.
4. Parker, E.N., (1965), Planet. Space Sci. 13, 9.
5. Skilling, J., (1975), Mon. Not. Roy. Astr. Soc., 172, 557.
6. Webb, G.M. and Gleeson, L.J., (1979), Astrophys. Space Sci., 60, 335.
7. Webb, G.M., (1985), Astrophys. J. (to appear).

OG 8.3-9

STOCHASTIC PARTICLE ACCELERATION IN FLARING STARS

T.J. Bogdan[1], R. Schlickeiser[2]

1) High Altitude Observatory, National Center for Atmospheric Research, P.O. Box 3000, Boulder, CO 80303, USA*

2) Max-Planck-Institut für Radioastronomie Auf dem Hügel 69, 5300 Bonn 1, FRG

ABSTRACT

We consider the acceleration of electrons by the Fermi-Parker mechanism in a quasi-stationary turbulent plasma of dimension ℓ, mean magnetic field strength B, and mean number density n. The electrons suffer radiative and ionization losses ($\dot{p} = -\alpha p^2 - \gamma$) and have a scattering mean free path that increases linearly with their momentum. We give exact analytic solutions for the steady-state electron energy spectra. The spectra are characterized by an exponential cutoff above a given momentum determined by the synchrotron or the confinement time, depending on the physical characteristics (ℓ, B, n) of the accelerating region.

1. Introduction. Direct acceleration of electrons from a thermal pool to relativistic energies is problematic for two reasons both, in diffusive shock wave acceleration, and in resonant Alfvén wave scattering. First, because of their small Larmor radii electrons do not see a shock wave as a discontinuity, unless their momentum becomes very large. Secondly, electrons only fulfil the resonance condition with Alfvén waves if their momentum is larger than $p_t = m_p v_A = 20$ keV/c $(B/3 \cdot 10^{-6}$ G$)$ $(n/1$ cm$^{-3})^{-1/2}$ (Achterberg and Norman 1980). One solution to this problem is to find injectors of energetic electrons in space which preaccelerate these particles to moderately large momenta $p > p_t$. Viable injector candidates are (i) secondary electron production in inelastic nuclear collisions of cosmic ray nucleons with interstellar gas atoms and molecules (e.g. Schlickeiser 1982), and (ii) electron acceleration in the flares on M and K type stars (Lovell 1974). Here we discuss the acceleration of energetic electrons by the second-order Fermi, or stochastic acceleration, mechanism in flare stars in more detail.

2. Acceleration in Flare Stars. We consider the acceleration of relativistic electrons by the Fermi mechanism in a quasi-stationary turbulent plasma of dimension ℓ, mean magnetic field B, and mean number density n. Additionally, we allow the electrons to suffer simultaneously radiation and ionization losses,

$$\dot{p} = -\alpha p^2 - \gamma \qquad (1a),$$

with

$$\alpha = 1.2 \cdot 10^{-11} (B/B_2)^2 \text{ (eV/c)}^{-1} \text{ s}^{-1} \qquad (1b),$$

*The National Center for Atmospheric Research is sponsored by the National Science Foundation

$$\gamma = 5.2 \cdot 10^2 \ (n/n_9) \ (eV/c) \ s^{-1} \qquad (1c),$$

where (B/B_2) is the magnetic field strength in units of 100 Gauss, (n/n_9) the plasma density in units of 10^9 cm^{-3}. The electrons may also escape from the acceleration region with a mean free path that increases linearly with momentum, so that the escape time is

$$T = \ell^2 / K_{\parallel}(p) = 1 / (Ap) \qquad (2a)$$

with

$$A = 5.8 \cdot 10^{-9} \ (\frac{\lambda}{\lambda_7}) \ (\frac{\ell_{10}}{\ell})^2 \ (eV/c)^{-1} \ s^{-1} \qquad (2b),$$

where ℓ/ℓ_{10} is the dimension of the acceleration region in units of 10^{10} cm, and λ/λ_7 the scattering mean free path ($\lambda = 3 K_{\parallel}/v$) in units of 10^7 cm at $p = m_e c$. The second-order Fermi diffusion coefficient then is (Skilling 1975)

$$D_{pp} = \frac{V_A^2 \ p^2}{9 \ K_{\parallel}(p)} = D \ p \qquad (3a)$$

with

$$D = (2.7 \cdot 10^5) \ (B/B_2)^2 \ (\lambda_7/\lambda) \ (n_9/n) \ (eV/c) \ s^{-1} \qquad (3b).$$

The equilibrium phase space density of electrons resulting from the combined effect of acceleration, radiation loss, ionization loss and escape is given by the solution of (Schlickeiser 1985)

$$\frac{\partial f}{\partial t} = \frac{1}{p^2} \frac{\partial}{\partial p} [p^2 \ (D_{pp} \frac{\partial f}{\partial p} - \dot{p} f)] - \frac{1}{T} f + S(p,t) \qquad (4),$$

where $S(p,t)$ denotes the source term.

We define the dimensionless momentum $x = p/p_c$, where

$$p_c = (D/\alpha)^{1/2} = 1.5 \cdot 10^8 \ (\frac{\lambda_7}{\lambda})^{1/2} \ (\frac{n_9}{n})^{1/2} \ (eV/c) \qquad (5)$$

and the parameters

$$a \equiv \gamma/D = 1.9 \cdot 10^{-3} \ (n/n_9)^2 (\lambda/\lambda_7)(B/B_2)^{-2} = \frac{\tau_F(p)}{\tau_I(p)} \qquad (6)$$

$$b \equiv A/\alpha = 4.8 \cdot 10^2 \ (\ell/\ell_{10})^{-2} \ (\lambda/\lambda_7) \ (B/B_2)^{-2} = \frac{\tau_R(p)}{T(p)} \qquad (7).$$

p_c is that momentum where the Fermi acceleration time ($\tau_R = p/D$) exactly equals the radiation loss time ($\tau_R = (\alpha p)^{-1}$). a is the momentum-independent ratio of Fermi acceleration time ($\tau_F = p/D$) to ionization loss time ($\tau_I = p/\gamma$). b is the momentum-independent ratio of radiation loss time ($\tau_R = (\alpha p)^{-1}$) to escape time ($T = (Ap)^{-1}$).

3. Results and Discussion. ($x_o = p_o/p_c$) We consider the delta-function source term

$$S(x) \equiv \frac{N_o}{\tau_S} \cdot \frac{1}{4\pi p_c^3} x_o^{-2} \delta(x-x_o) \qquad (8),$$

where p_o is some characteristic injection momentum and N_o/τ_S is the rate at which electrons are supplied to the acceleration region. The steady-state solution of equation (4) then is (Bogdan and Schlickeiser 1985)

$$f_\infty(p) = \frac{N_o}{16\pi p_c^3 \tau_S (\alpha D)^{1/2}} \frac{2^{a/2}\,\Gamma(b/2)}{\Gamma(2-(a/2))} x_o^{-2} x^{-a} \exp(-x^2/2)$$

$$\cdot \begin{cases} U(b/2, 2-(a/2), x_o^2/2)\, M(b/2, 2-(a/2), x^2/2) & \text{for } x \leq x_o \\ M(b/2, 2-(a/2), x_o^2/2)\, U(b/2, 2-(a/2), x^2/2) & \text{for } x \geq x_o \end{cases} \qquad (9)$$

in terms of confluent hypergeometric functions.

Figure 1 illustrates the behaviour of $p^2 f_\infty(p)$ in different parameter regions deduced from the asymptotic forms of the confluent hypergeometric functions. At the very lowest ($p < p_o$) momentum [$p^2 f_\infty(p) \propto p^{2-a}$] and the very highest ($p \gg p_c$) momentum [$p^2 f_\infty(p) \propto p^{2-a-b} \exp(-p^2/(2p_c^2))$] the spectrum is rather independent of the values of a and b. At intermediate momenta, the spectrum is determined by b, the ratio of radiation loss time (τ_R) to escape time (T). If $b \leq 1$, i.e. $\tau_R < T$, the p^{2-a} power law extends up to the injection momentum p_o, and a constant spectrum ($a \leq 2$)

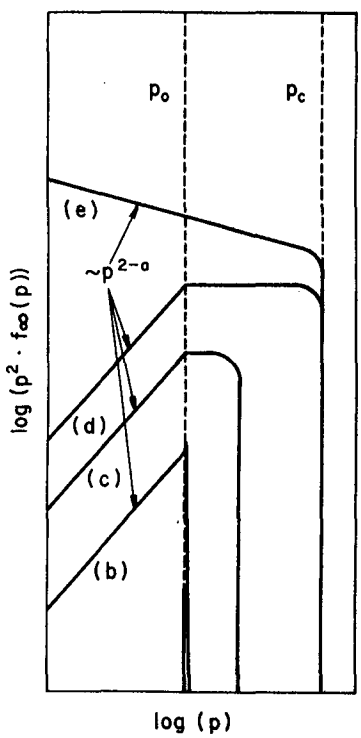

Fig. 1: Schematic illustration of some representative steady-state electron spectra $p^2 f_\infty(p)$ from (9). The relative normalizations of the spectra are arbitrary. The injection momentum (p_o), and the critical momentum p_c [Eq. (5)] are indicated by dotted lines. For spectrum (b) $b \gtrsim (p_c/p_o)^2$, $a < 2$; (c) $1 \ll b \ll (p_c/p_o)^2$, $a < 2$; (d) $b \lesssim 1$, $a < 2$; and (e) $b \lesssim 1$, $2 < a < 4$.

or $p^{2-a}(2 \leq a < 4)$ power law extends up from the injection momentum to the critical momentum p_c. In this case, the escape time is large and the spectrum is determined by the interplay between acceleration and radiation losses. If $b \gtrsim 1$, i.e. $T < \tau_R$, the spectrum develops an $\exp(-b^{1/2}p/p_c)$ shoulder before the $\exp(-p^2/(2p_c^2))$ fall off for $p < p_c$. Finally when $b >> 1$, and the escape time decreases still further, the spectrum develops a pronounced spike at the injection momentum. In this case, the particles escape from the acceleration region so quickly that they have little chance to interact with the magnetized plasma. Summarizing: electrons can be accelerated efficiently in flare stars if in the acceleration region the parameter b (equation (7)) is smaller than unity. The maximum momentum then is given by p_c in equation (5) which is that momentum where the Fermi acceleration time ($\tau_F = p/D$) exactly equals the radiation loss time ($\tau_R = 1/(\alpha p)$).

Another important point to note is, that the upper cutoff in the momentum spectrum (9) is due to synchrotron losses only in cases where $b \leq 1$. In the opposite situation $b \gtrsim 1$, the escape of energetic electrons from the acceleration region causes the cutoff. This should be kept in mind when interpreting the peak microwave emission of flares from RS CVn stars. Misidentifying the physical mechanism for the cutoff may yield wrong constraints on the physical conditions in the flare site, n, ℓ, λ and B.

References

Achterberg, A., Norman, C.A., (1980), Astron. Astrophys. 89, 353
Bogdan, T.J., Schlickeiser, R., (1985), Astron. Astrophys. 143, 23
Lovell, B., (1974), Phil. Trans. Royal Soc. London A.277, 489
Schlickeiser, R., (1982), Astron. Astrophys. 106, L5
Schlickeiser, R., (1985), in: Cosmic Radiation in Contemporary Astrophysics, ed. M.M. Shapiro, Reidel, Dordrecht, in press

THE DESIGN OF AN EXPERIMENT TO DETECT LOW ENERGY ANTIPROTONS

J. Lloyd-Evans*, B. S. Acharya+, V. K. Balasubrahmanyan
J. F. Ormes, R. E. Streitmatter, and S. A. Stephens≠
NASA/Goddard Space Flight Center, Greenbelt, MD 20771, U.S.A.

ABSTRACT

The techniques to be used in a balloon-borne experiment ("APEX") to detect < 220 MeV antiprotons are described, paying particular attention to potential sources of background. Event time history is shown to be very effective in eliminating this background. Results of laboratory tests on the timing resolution which may be achieved are presented. The limiting experimental sensitivity of this experiment is $\bar{p}/p < 10^{-5}$.

1. Introduction. The conceptual design of a balloon-borne experiment to detect low energy antiprotons in the cosmic ray flux has been described by Balasubrahmanyan et al [1]. The serious revision of ideas concerning the origin and transport of galactic cosmic ray protons seemingly required by the high $\bar{p}$ flux reported by Buffington et al [2] makes such an independent measurement at solar minimum an urgent requirement.

Referring to Figure 1, the trigger criterion of:

S1(> 1.6 min.)* S2(> 1.6 min.)* $\overline{C1}$ (prompt)* C2 permits the unambiguous identification of antiprotons if (a) $\bar{p}/p > 10^{-5}$ and (b) event time history in OS ('outershield') can be measured to 0.5ns. We have previously considered [1] the importance of vetoing protons > 220 MeV because of the rapid rise in the π° production cross section above this energy [3]

Here we consider other backgrounds in detail (Section 2), and show how the timing history is effective in eliminating all but the neutral high energy background. Schemes to achieve the timing resolution are discussed in Section 3, and the results of laboratory tests reported in Section 4.

2. Background Elimination. The flux, coincidence rate, and method of elimination for each type of background are summarized in Table 1. These are:

(a) π° production by protons > 220 MeV--the elimination of this background has been discussed in reference [1].

(b) An out-of-geometry relativistic charged particle interacting in the Pb glass calorimeter (C2) and depositing an energy ≃ annihilation energy in time coincidence with a slow (< 220 MeV) proton within the geometry. This is the most serious background, amounting to ~ 75% of the $\bar{p}/p$ ratio at 2×10^{-4}. The time history (OS precedes C2 by 3ns) is to be compared to that for a genuine $\bar{p}$ event (C2 precedes OS by 3ns) so that this background can be eliminated (to $\bar{p}/p < 10^{-5}$) if (1)

* Also University of Maryland, Department of Physics and Astronomy College Park, MD 20742, U.S.A.
+ NAS/NRC Research Associate
≠ Tata Institute of Fundamental Research, Bombay, INDIA

minimum ionizing particle detection efficiency is > 99% and (2) the relative times in S1, C2, and OS can be measured to $\sigma(\Delta t) \approx 0.5$ ns. Such timing resolution (nominally a '12σ' rejection factor) is deliberately conservative in recognition of the existence of non-Gaussian tails in scintillator timing distributions.

(c) OS is ineffective if the out-of-geometry particle in (b) is an atmospheric neutron. Calculations have been performed including the measured neutron flux [4], the expected directional distribution at 2-5 gm cm^{-2} of residual atmosphere, the interaction cross section, and experimental geometry factor. We determine that the spurious $\bar{p}$ events induced by atmospheric neutrons correspond to a $\bar{p}/p$ ratio $< 2 \times 10^{-6}$. Since this background cannot readily be eliminated, it determines the $\bar{p}/p$ sensitivity of a calorimetric balloon-borne detector in this energy range.

Table 1. Summary of APEX Backgrounds

Text Ref.	Particle	Flux/cm^2sr.s.	Ref.	Background s^{-1}	Elimination
(a)	L.E. p	0.2-0.3 GeV: $< 2\times10^{-2}$	[8]	<30	S1.S2.$\overline{C1}$
(b)	H.E. p	> 6 GeV: $< 6\times10^{-2}$	[9]	2×10^{-3}	Timing
(c)	n	> 2GeV: $< 3\times10^{-3}$	[4]	8×10^{-6}	--
		> 1GeV: $\sim 5\times10^{-3}$	[4]	2×10^{-5}	--
(d)	e^-	> 0.1 GeV: 1×10^{-2}	[10]	3×10^{-4}	Timing
(e)	γ	> 0.1 GeV: $< 6\times10^{-5}$	[10]	2×10^{-6}	--
(f)	$\mu\rightarrow e$	< 50MeV: $< 10^4$	[11]	$< 4\times10^{-4}$	C2 Threshold

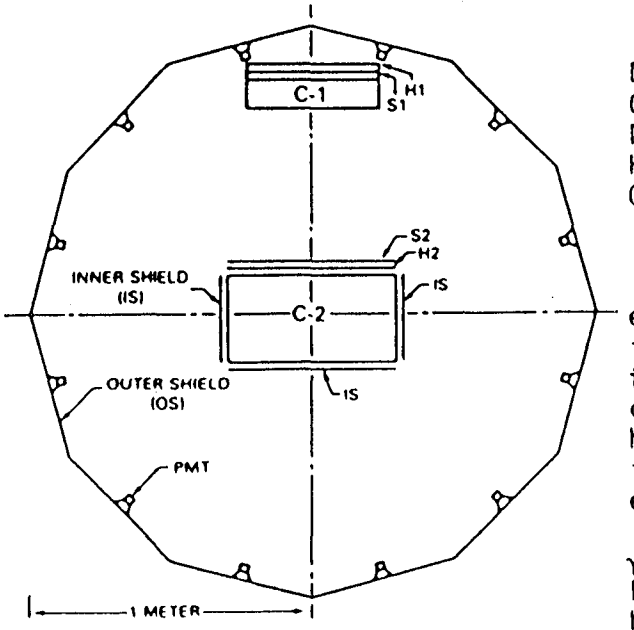

Figure 1. (left) APEX Design. C1, C2: Crown Glass, Lead Glass Cherenkov Detectors. H1, H2: Hodoscopes. S1, S2, IS, OS: Scintillator

(d) Out-of-geometry electrons > 100 MeV, again in time coincidence, result in a cascade in C2 which could simulate an annihilation. This background is eliminated by timing as efficiently as (b)

(e) Atmospheric γ-rays (> 100 MeV) cannot be rejected efficiently by OS, and can simulate an annihilation as in (d). Fortunately, the flux of atmospheric γ-rays is low, resulting in a < 2% contribution to $\bar{p}/p$ at 10^{-5}.

(f) A low energy (< 50 MeV) atmospheric muon (satisfying the within-geometry criteria) can decay in C2. although the rate is high, the resulting cascade is low energy. Simulations have shown that ~ 95%

of the resulting C2 signals are below 98% of the $\bar{p}$ signals, so a suitable C2 threshold can effectively eliminate this background.

Summarizing, the time history eliminates all but the neutral backgrounds, resulting in a sensitivity of $\bar{p}/p \simeq 10^{-5}$. An experiment above the atmosphere would achieve much better sensitivity because of the virtual absence of the atmospheric n, γ background.

3. Timing Resolution. To achieve the high detection efficiency and good timing resolution, we consider using a 1 cm thick segmented scintillator sphere of 1.2m radius completely surrounding C2. Two possibilities are considered.

(1) Approximately 250 x 2" PMT's in optical contact with the scintillator. A large number is required to satisfy the conflicting requirements of redundancy (each signal seen by > 2 PMT's) and a high order of scintillator segmentation. For a background event, the signal in some of the OS PMT's consists of that of the interaction progenitor followed (in a barely resolvable time) by that of the interaction products. Positional information is therefore difficult to extract. The segmentation area (each PMT viewing $\sim$ 0.1 m^2) is thus dictated by the acceptable time dispersion due to light propagation (at C/2) across the whole scintillator segment.

(2) Segmentation can be relaxed by viewing the scintillator face-on. Simulations have shown that a sphere of $\sim$ 50 x 5" PMT's, looking in towards OS provide sufficient redundancy, photoelectron efficiency (> 10 p.e.) and minimum time dispersion. This sphere is located $\sim$ 40 cm outside OS so that direct Cherenkov emission in any one PMT does not provide a false veto, which would reduce the genuine $\bar{p}$ detection efficiency.

Design (2) is to be preferred on the basis of cost-effectiveness, if 5" PMT's can be demonstrated to have the required timing stability.

4. Timing Results. Preliminary tests on RCA 8575 (2") and 4522 (5") have been performed with a small (5cm x 5cm x 0.5cm) scintillator and Sr^{90} source. The resulting signal distribution is not dissimilar in amplitude (threshold of $\sim$ 10 p.e.) or, more importantly, dynamic range ($\sim$ 100:1) to that expected in practice. The standard start-stop, low-high technique has been employed with two PMT's viewing the scintillator. Application of an unconventional timing technique [5] allows the measurement of both time and amplitude in a single commercial ADC module (LeCroy 2249A). Excellent resolution ($\sigma(\Delta t) < 30$ ps) and linearity (integral non-linearity over a dynamic range of 50:1 of < 0.5% full scale) for the recording electronics is in agreement with the findings of Venema [5].

Figure 2 shows a comparison of the timing resolution achieved ($\sigma(\Delta t) \simeq \sqrt{2} \times \sigma(t_i)$) for the 2" and 5" PMT's, for leading edge and constant fraction discriminators (Ortec 453) as a function of the fraction of the low to high discrimination levels. The leading edge resolution is inadequate without time-walk corrections. In agreement with D'Agostini et al. [6], we find that an individual time correction to each PMT of the form $\Delta t_i = K_i/(\text{amplitude})^{1/2}$ minimizes the time dispersion, and that the corrected resolution is comparable to that of the constant fraction discriminator.

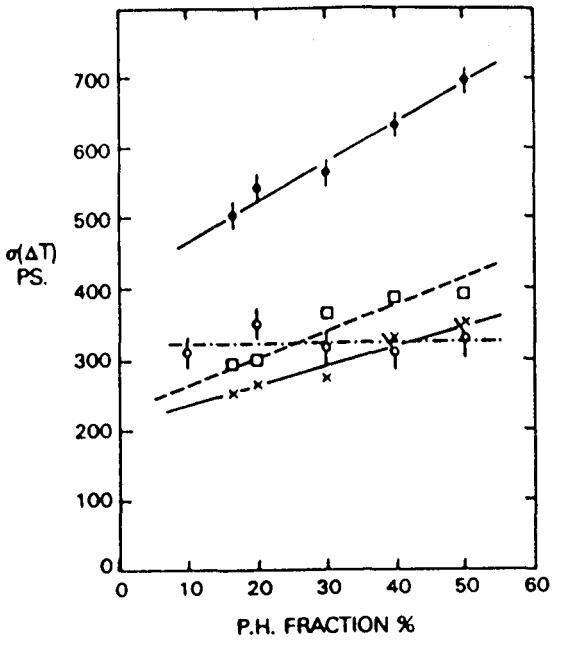

Figure 2. (left) Time Resolution for leading edge discrimination without walk correction (● 2" PMT); with walk correction (x 2" PMT, □ 5" PMT); and constant fraction (o 2" PMT).

The resolution achieved for the 2" PMT does not rival other reports (in particular, reference [6]) but, for both 2" and 5" PMT's, it is sufficient for the purposes outlined in Section 3.

5. Conclusions. The background limitations for APEX have been described. Severe demands are made on the time resolution of a large area scintillator shield in order to eliminate this background. Preliminary tests on small scintillators show that this resolution can be achieved with 2" or 5" PMT's. We are currently investigating much larger area scintillators. As an alternative, we are also investigating the possibility of using large area PSC's [7] as shields. These detectors have unprecedented time resolution (< 50 ps), offer the possibility of particle track identification, and (because of the localization of discharge) are sensitive multihit devices.

6. Acknowledgements. We thank J. Linsley for pointing out the timing characteristics of PSC's.

References

1. Balasubrahmanyan, V. K., et al. (1983), 18th ICRC, Bangalore, Special Session on "$\bar{p}$ and other antiparticles".
2. Buffington, A., et al. (1981), Ap. J. 248, 1179.
3. Stephens, S. A., (1981), 17th ICRC, Paris, 9, 60.
4. Hess, W. N. et al. (1961), J. Geo. Research, 66, 665.
5. Venema, W. Z., (1984), NIM, 219, 257.
6. D'Agostini, G., et al. (1981), NIM, 185, 49.
7. Atwood, W. B., et al. (1983), NIM, 206, 99.
8. Balasubrahmanyan, V. K., et al. (1966), J. Geophys. Res, 71, 1771.
9. Ginzburg, V. L. and Syrovatskii, S. I. (1964), "The Origin of Cosmic Rays" (McMillan).
10. Daniel R. R., Stephens, S. A.(1974), Revs. Geophys. Space Phys., 12, 233.
11. Stephens, S. A. (1981), 17th ICRC, Paris, 4, 282.

An Experiment to Measure the Energy Spectrum of Cosmic Ray Antiprotons from 100 to 1000 MeV

M.H. Salamon, P.B. Price, S.W. Barwick, and D.M. Lowder
Physics Department, University of California, Berkeley, CA

S.P. Ahlen
Physics Department, Indiana University, Bloomington, IN

1. Introduction. Since the 1981 measurement by Buffington et al. [1] of a finite, low energy (~0.1-0.3 GeV) flux of cosmic ray antiprotons ($\bar{p}$), there has been a growing excitement over its possibly profound implications, since the observed flux ($\bar{p}/p \sim 2 \times 10^{-4}$) is orders of magnitude larger than that predicted by standard propagation models [2]. Apart from the possibility that this single measurement is in error, numerous production models have been developed, the confirmation of any one of which would have significant or even profound astrophysical impact. These include radical modifications of propagation models [3,4], $\bar{p}$ injection from neighboring domains of antimatter [5], $\bar{p}$ production by evaporating primordial black holes [6,7], and most recently, cosmic ray $\bar{p}$'s as annihilation products of supersymmetry particles (photinos [8-10] or higgsinos [10]) that might make up the "dark"dynamical mass of the Galaxy. It is possible that $\bar{p}$'s originating from supersymmetric parents might have distinct spectral features that would survive solar modulation; in one model [10], higgsino annihilation proceeds through the $b\bar{b}$ quark-antiquark channel, producing a spectral bump at ~0.3 GeV in the $\bar{p}$ spectrum.

2. The Detector. Because of the exciting potential signatures within the $\bar{p}$ spectrum, we are at present designing a detector that will measure the cosmic ray $\bar{p}$ spectrum between 0.1 and 1.0 GeV (energies at the instrument). With a payload weight of ~1000 kg and ~100 cm^2-sr acceptance, a 2-day balloon flight over northern Canada will yield ~250 $\bar{p}$'s, given the Buffington et al. flux.

Unlike calorimeter detectors, our PB (p-bar) detector identifies $\bar{p}$'s by directly visualizing their trajectory within a magnetic field. Figure 1 is a schematic of the PB detector. A multilayer array of high resolution drift tubes is placed within the dipole field volume of a permanent magnet. Momentum analysis of the trajectory gives particle energy and sign of charge. An aerogel Cerenkov radiator of index $n \approx 1.10$ acts as a high-energy veto that eliminates much of the background, and a time-of-flight scintillator pair discriminates against albedo protons and provides a measurement of the charge magnitude.

The PB instrument makes use of advances both in drift-tube technology and in permanent magnet technology. The drift tubes to be used are based on those recently incorporated into the MAC detector at PEP, as part of a high

resolution vertex chamber [11]. They consist of 0.7 cm diameter tubes of aluminized mylar, with a wall thickness of 0.01 cm, operated at high pressure (4 atm) and high voltage (~4 kV). With a heavily quenched gas, such as 50% Ar/50% ethane, a limited streamer mode is achieved. In this mode essentially the first electron to reach the anode wire produces the entire pulse height. This has been shown to provide optimal spatial resolution [12], and reduces amplifier and cross-talk requirements as well. Measurements at SLAC found the tube resolution to be ~25 μm. In the analysis of PB, we assume a tube resolution of 30 μm (optimal) to 50μm (conservative). The drift tube array in PB will consist of ~17 layers (close-packed) of tubes with cylinder axes along the direction of the magnetic field (y-direction); these will give the projected trajectory information in the xz plane needed for curvature analysis. Two additional layer pairs with cylinder axes along the x-direction, placed above and below the main array, will provide a value for the less critical y-component of momentum.

The permanent magnet in which the drift tube array is imbedded is based on recent advances in permanent magnet materials and design. Figure 2 shows the toroidal geometry of the magnet, whose novel segmented design [13] provides a dipole field in a direction perpendicular to the opening angle of the magnet. The magnet material, neodymium-iron-boron, is a new rare-earth material with an extraordinarily high remnant field strength of ~12 kG. Computer calculations have produced a magnet design giving an interior dipole field strength of ~10 kG, with a total weight of ~225 kg. Once constructed, there are none of the failure modes that can plague a superconducting magnet system. However, as the rare earth materials are brittle, and as the mechanical forces between magnet elements are quite strong, extreme care has to be taken during its construction.

The Cerenkov radiator is a thermally sintered aerogel of refractive index n = 1.10, which will veto protons of energy >1.3 GeV, and will also eliminate the e^-, μ^-, and π^- background, as those particles which do not generate a Cerenkov signal will have a measured momentum below our cutoff corresponding to a 0.1 GeV proton, as shown in Fig. 3. A total thickness of ~5 g/cm^2 gives ~42 photoelectrons from a muon with $\beta = 1$ [14], of which <5% is from scintillation within the accompanying light diffusion box. Species of lower mass (except kaons) with momenta above the lower limit of 0.45 GeV/c will therefore produce signals of such high statistical significance, compared to veto threshold, that $\bar{p}$ contamination will be negligible.

Finally, a TOF scintillator pair, separated by 50-100 cm, will screen against albedo protons, which in going backward through the detector also have the "negative" curvature which identifies the antiproton. To minimize $\bar{p}$ energy loss and background production, the individual scintillators will be <2 cm thick, giving a TOF resolution of ~300 psec, more than adequate to detect albedo protons with $E < 1.3$ GeV.

3. Resolution and Background. As discussed above, potential backgrounds from low-energy e^-, μ^-, π^-s are eliminated by the Cerenkov radiator in

concert with a low-momentum cutoff. Because of its high mass the K^- cannot be similarly screened, and in fact creates an irreducible background that must be calculated and subtracted from the $\bar{p}$ signal. All of the K^- background is produced within our instrument upstream of the Cerenkov radiator. Using K^- multiplicity data from the CERN ISR collider [15], along with subthreshold production data from LBL's Bevalac [16], we estimate a low-energy background $K^-/p < 10^{-5}$. More accurate calculations are in progress.

The major factors degrading resolution and possibly contributing to background are large-angle single Coulomb scattering (SCS), multiple Coulomb scattering (MCS), and δ-ray production. Our minimum field strength of 10 kgauss has been chosen to eliminate both SCS and MCS as a source of serious contamination. We have calculated that MCS is a minor factor in resolution degradation and is not able to generate any $\bar{p}$ background. SCS is a more serious problem: a subthreshold proton scattered in the "negative curvature" direction must be screened with high statistical confidence. Estimated confidence levels for discriminating against a proton that has been scattered at an optimal angle for masquerading as a $\bar{p}$, combined with the SCS probability distribution, indicate that contamination of $\bar{p}$'s from this process should be negligibly small. A Monte Carlo program is now being developed to accurately determine momentum resolution as a function of energy when MCS, SCS and δ-ray production are fully taken into account.

References

1. A. Buffington, S.M. Schindler and C.R. Pennypacker, Ap. J. 248, 1179 (1981).
2. T.K. Gaisser and R.H. Mauger, Phys. Rev. Lett. 30, 1264 (1973); T.K. Gaisser and B.G. Maurer, Ap. J. 252, L57 (1982).
3. L.C. Tan and N.K. Ng, Ap. J. 269, 751 (1983); L.C. Tan and N.K. Ng, Proc. 18th Inter. Cosmic Ray Conf, (Bangalore) 2, 90 (1983).
4. S.A. Stephens and B.G. Mauger, to be published in Astrophys. Sp. Sci.
5. F.W. Stecker, Nucl. Phys. B (1984), and references there.in.
6. P. Kiraly, J. Szabelski, J. Wdowczyk and A.W. Wolfendale, Nature 293, 120 (1981).
7. M.S. Turner, Nature 297, 379 (1982).
8. J. Silk and M. Srednicki, Phys. Rev. Lell. 53, 624 (1984).
9. F. Steck, personal communication.
10. J.S. Hagelin and G.L. Kane, to be published.
11. E. Fernandez et al., SLAC PUB 3390, August, 1984.
12. J. Va'vra, SLAC-PUB 3131, June, 1983.
13. K. Halbach, LBL Report No. 8906, March, 1979.
14. S.M. Schindler, personal communication.
15. A. Antinucci et al., Lett. Nuovo Cim. 6, 121 (1973).
16. A Shor et al., Phys. Rev. Lett. 48, 1597 (1982).

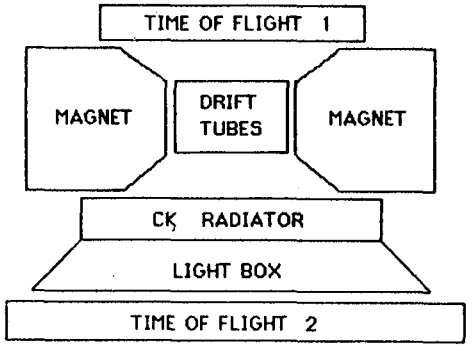

Fig. 1. Schematic showing detector elements of PB (not to scale).

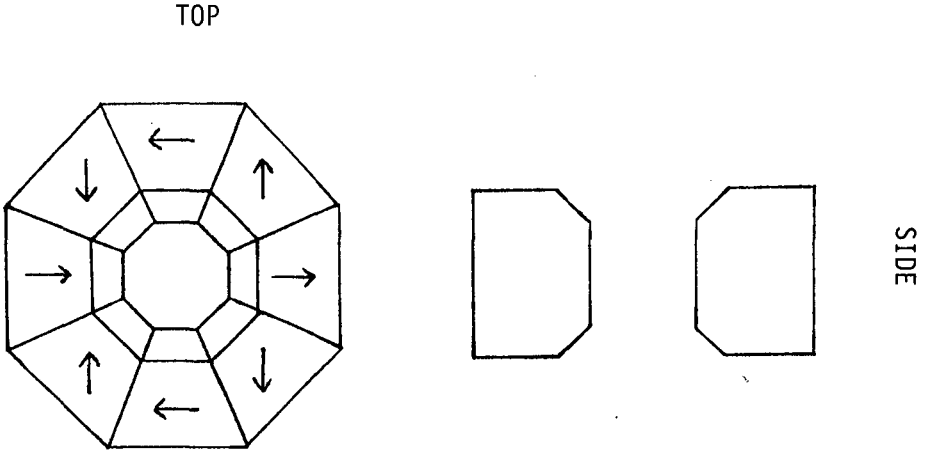

Fig. 2. Permanent magnet geometry (not to scale). Arrows within each segment show magnetization direction, with the summed field giving a dipole field in the central volume.

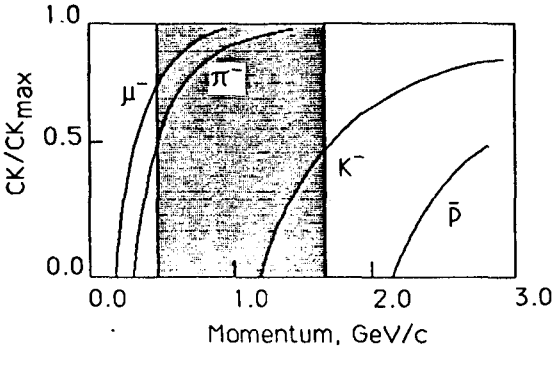

Fig. 3. Cerenkov emission from radiator as a function of particle species and momentum. Events are accepted only within the shaded interval.

HIGH RESOLUTION CHERENKOV DETECTORS FOR COSMIC RAY ISOTOPE EXPERIMENT

B. S. Acharya*, V. K. Balasubrahmanyan, J. A. Esposito**,
J. Lloyd-Evans**, J. F. Ormes and R. E. Streitmatter
NASA/Goddard Space Flight Center, Greenbelt, MD 20771, U.S.A.

ABSTRACT

Cherenkov detectors can be used to measure the velocity of particles in a variety of configurations designed to study the isotopic composition of galactic cosmic rays. In order to achieve the highest possible resolution it is necessary to understand the geometrical properties of the detector in detail. We have carried out Monte-Carlo simulations of propagation of photons in a diffusive detector to help to achieve that understanding. We have also measured the scattering properties of diffusively reflecting white paint and of surface treatments for the radiator material. We find that the absorption of light in the radiator is an important light loss mechanism. We also use these simulations to find optimal mapping techniques and data reduction strategies. The application of these techniques will be discussed with respect to the ALICE Cherenkov detector[1].

1. Introduction. The use of the Cherenkov detector in balloon-borne cosmic ray experiments was first introduced by Webber and McDonald[2]. Ever since, these detectors have become an indispensable tool in experiments where the velocity of an incident particle of known charge is measured. However, the resolution of these detectors often causes a severe limitation in the resolution of ultimate physical parameters measured in an experiment. For example, in experiments designed for isotopic mass measurement using the Cherenkov versus range technique, the resolution in mass number depends critically on the resolution of Cherenkov detectors.

The resolution of a Cherenkov detector depends upon the total light collection efficiency as well as spatial uniformity. The highly directional nature of Cherenkov emission leads to further complications of dependency of light collection efficiency on the energy and incident angle of the projectile. Besides, background signals from δ-electrons above Cherenkov threshold, residual scintillation in the radiator, Cherenkov emission from white paint (usually used in the integration chamber) etc., limit the ultimate resolution of the detector. Though the resolution is limited primarily by photo electron statistics, other effects may become significant either at large pulse heights or in detectors with high detection efficiency as the resolution scales with the number of photo electrons as $n_{pc}^{-1/2}$. Requirements on a large area of these detectors further increases the importance of spatial uniformity.

* NAS/NRC Research Associate on leave from the Tata Institute of Fundamental Research, Bombay, INDIA
** Also, Univ. of Maryland, Dept. of Physics, College Park, MD 20742

High resolution is usually achieved by processes such as selecting a radiator of high photon yield per cm., by placing the radiator material in a white diffusion box with a high photo cathode to total area ratio, by frosting the surfaces of the radiator to eliminate specular reflections, by resolution quality control of the selected Photomultiplier (PM) tubes, etc.

In this paper we shall discuss the Monte-Carlo simulations carried out to study the nonuniformity in the Cherenkov response due to the geometry of the set up. Also discussed are the results of laboratory tests on the various surface treatments for the radiator. All the results refer in general to a detector of square geometry and in particular to a Cherenkov detector to be employed in the large area isotopic composition experiment ALICE[1].

2. Properties of the Cherenkov Detector. The response of a Cherenkov detector is determined by Monte-Carlo simulations. The actual geometry of a Cherenkov detector to be used in ALICE is adopted in the simulations. Briefly, the Cherenkov radiator consists of 113.7 x 113.7 x 2.25 cm^3 Pilot 425, a plastic with an index of refraction of 1.5. The radiator is housed in a chamber having dimensions 114.3 x 114.3 x 20 cm^3. The chamber interiors are coated with a diffusely reflecting $BaSO_4$ paint[3] which has a reflectivity of 95 percent in the visible light region. The detector configuration utilizes 24 RCA S83006 photomultiplier tubes of 5" diameter, forming an effective detection area of 3354 cm^2. The PM tube has a maximum quantum efficiency of ~ 30 percent at a wavelength of ~ 400 nm.

The required percentage spatial uniformity in the response of this Cherenkov detector is shown against resolution in mass number for the ALICE detector assembly in Figure (1). It is seen that less than a percent nonuniformity is required to achieve a mass resolution of ~ 0.3 A.M.U. Usually, Cherenkov detector responses are mapped[4,5] using accelerator beams.

However, it is unwieldly to map large area detectors using accelerators. Alternatively, one can simulate the Cherenkov chamber response map and map the detector using cosmic ray muons or flight data.

Two extreme cases of surfacing of the radiator, namely, 'perfectly polished' and 'ideal frosted' are considered in our simulation. In the case of 'polished' surface, light is required to follow Snell's law at the boundary while an isotropic angular distribution is assumed for the 'frosted' surface whenever photons pass the boundary of the radiator. Each photon is followed until it is either absorbed by the radiator or the white paint coated wall or detected by PM tubes. A photon is considered to be absorbed if it is surviving even after 50 reflections either in the walls or in the radiator. A five percent probability for absorption of photons is assumed for the white paint coated wall and a uniform angular distribution for the scattered photon off the wall. The individual PM tube responses are assumed to differ only in parameters describing the relative positions of impact point and center of the photo cathode.

The simulated response of the detector for a particle passing through with different incident angles is shown in Figure (2) for 'polished' surface, 'polished' and 'frosted' surfaces of a radiator doped with waveshifter. Frosting of the surface reduces the nonuniformity as expected.

Laboratory tests were carried out to study the angular distribution of outgoing light for different surface treatments. Four samples of lucite of thickness 5 mm are chosen. One side of each sample is polished while the other side is either polished, machined with a fly-cut technique, sandblasted or sandpaper treated using 80 grit sandpaper. A He-Ne laser beam (λ = 6320 Å) is made to impinge on the polished surface of the samples at right angles and the angular distribution of the forward component of light is measured at the other side. The angular distributions are shown in Figure (3) for all samples along with an angular distribution obtained for a surface coated with a white paint of $BaSO_4$ base. It is seen that for all test samples, the transmitted light is far from isotropic.

It was also observed that the contamination of the surface due to the sandblasting process is higher than the rest. Samples are kept inside a light diffusion box mounted with a green Light Emitting Diode (LED), (λ = 5700 Å) and a photomultiplier. A significant absorption of light due to contamination of the surface is observed in the case of sandblasted samples. However, this absorption may be reduced if one uses AlO_2 for blasting the surface instead of sand.

The nonuniformity due to a geometric dependent variation in the response of the Cherenkov detector is studied through Monte-Carlo simulations. Particles are made to impact at different positions in the detector, and the Cherenkov response is mapped. The percentage of detected photons is plotted in Figure (4) against the distance along the diagonal for two attenuation mean free paths of 1 m and 10 m.

3. Conclusions. A sandpaper treated surface looks good for our purpose. Radiators doped with waveshifting materials and having a long attenuation length tend to make the detector response uniform over the area besides yielding higher light output. Further simulations are being carried out and the results will be compared with the mapped response of the Cherenkov detector, obtained using cosmic ray muons. Also simulations are currently being extended for a detector of circular geometry[6].

4. Acknowledgement. We thank Dr. Walter Viehmann for results on scattering experiments.

References

1. Esposito J. A., et al., This Conference, OG-9.1-9.
2. Webber, W. R. and McDonald, F. B., 1955, Phys. Rev., 100, 1460.
3. Schult, J. B., and Shai, C. M., 1971, NASA/GSFC X-762-71-266.
4. Ahlen, S. P. et al., 1976, Nucl. Inst. Methods., 136, 229.
5. Rasmussen, I. L., et al., 1983, Proc. 18th ICRC, Bangalore, 8, 77.
6. Streitmatter, R. E., et al., 1981, Proc. 17th ICRC, Paris, 8, 54.

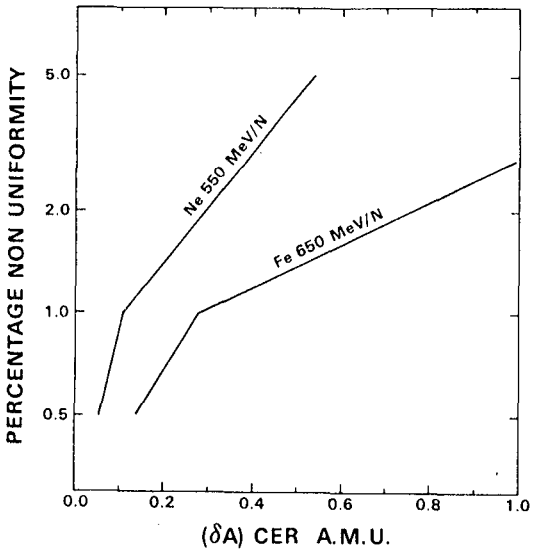

Figure 1.

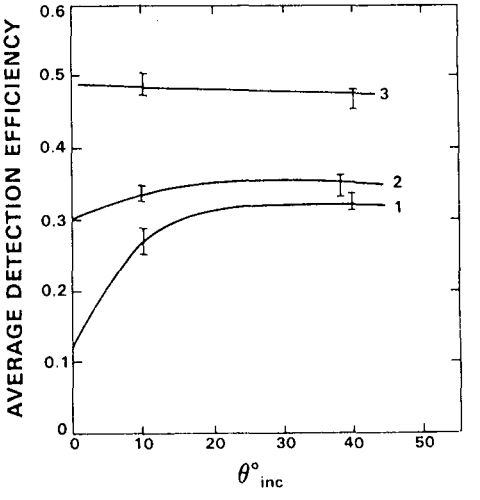

Figure 2.
1. Polished surface
2. Polished surface of a radiator doped with wave-shifter.
3. Frosted surface of a radiator doped with wave-shifter

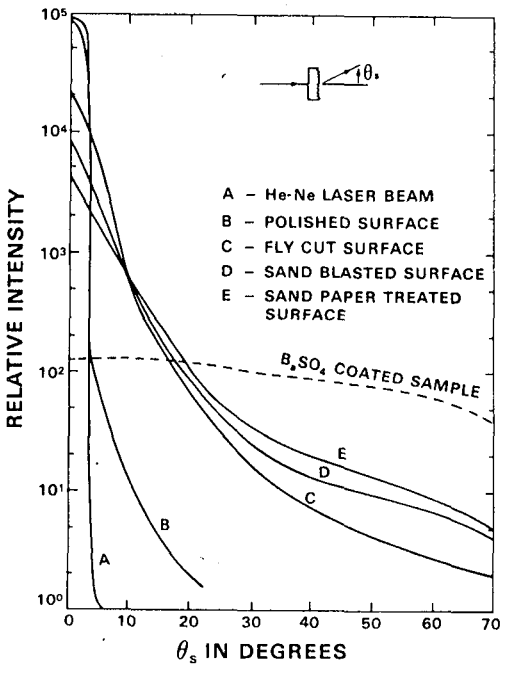

Figure 3.

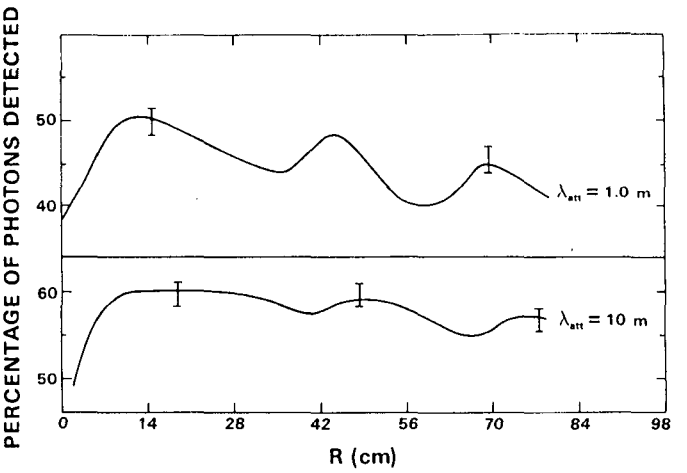

Figure 4.

CERENKOV COUNTERS FOR HIGH ENERGY NUCLEI: SOME NEW DEVELOPMENTS*

S.P. Swordy and D. Muller+

Enrico Fermi Institute, University of Chicago
Chicago, Illinois 60637 USA

In this report we discuss a method to determine with gas Cerenkov counters the Lorentz factor, $\gamma = E/mc^2$, of cosmic ray nuclei with high accuracy ($\sim$1% for iron) over the range $\gamma \sim$ 20-100.

Conventional integrating gas Cerenkov counters in cosmic ray instruments measure the total flux of light produced by an incoming particle. The accuracy of such a measurement is statistically limited to $1/\sqrt{N}$, (where N is the number of collected photoelectrons), but has a fixed minimum value due to systematic contributions from residual gas scintillation, Cerenkov light from paint, light from delta-rays, etc. For gases with high Cerenkov thresholds, ($\gamma > 20$), the Cerenkov light levels of such integrating counters become extremely low, comparable to these sources of background. Thus, the energy resolution is quite poor, even for counters with large pathlengths and with a very large number of photomultipliers.

As an alternative, we consider the measurement of the Cerenkov emission angle θ, by use of a suitable imaging system. The resolution of such a system is $\Delta\theta/\theta \times 1/\sqrt{N}$, where $\Delta\theta$ is the accuracy of determination of the Cerenkov angle from imaging <u>one</u> collected photoelectron. If it is possible to construct a device with $\Delta\theta/\theta \ll 1$, one would achieve far better resolution than with an integrating counter for the same N. In addition, the sources of background mentioned above are greatly suppressed by an imaging system.

Imaging counters, known as ring imaging Cerenkov counters (RICH), have been recently developed for use on accelerators. In these devices a spherical mirror is used to focus the Cerenkov light, from a particle travelling along the optical axis, into a circular ring on a gas filled, position sensitive, detector for UV photons.

The application of a RICH to cosmic ray studies is not straightforward, because the isotropic nature of the particles precludes aligning the optical axis of the system with a "beam" of particles. Clearly, we must examine the image of off-axis particles to determine the amount of image distortion as a function of the direction of the incoming nucleus. We may then define an acceptance solid angle, relative to the optical axis, within which the nucleus produces an image with an acceptable level of distortion. By computer simulations, we have studied the properties of the image, which becomes elliptical, for off-axis particles. The dominant problem in the reconstruction is associated with

---

+also Department of Physics

*work supported by NASA grants NGL-14-001-258 and NSG-7464

the thickness of the detecting device, which must be $\gtrsim$ 10cm to provide a reasonable quantum efficiency. Ring images for on-axis particles may be reconstructed by measuring the coordinates, x and y, of photoelectrons in a plane perpendicular to the optical axis. However, for off-axis particles, the third coordinate z, corresponding to the depth in the detector, must also be measured. We show that with this information an accurate reconstruction of the elliptical ring image is possible for a rather large acceptance solid angle.

For example, a 3m cylindrical RICH, having a 1.4m diameter detector, would be capable of measuring the energy of an iron nucleus to $\sim$1% at γ=50, with an acceptance aperture of $\sim 0.24 m^2$ str. Such an energy measurement could be combined with the proposed superconducting magnet spectrometer facility on the Space Station to determine isotopic abundances at energies far beyond those covered in present experiments.

A High Resolution Gas Cerenkov Detector for the Superconducting Magnet Facility

P. Goret
CEN - Saclay - France

R.L. Golden
New-Mexico State University

ABSTRACT
A high resolution gas Cerenkov imaging detector for Cosmic Ray heavy ions is described. The performances of this detector are evaluated in view of its association with a Superconducting Magnet.

1 - Introduction

The project of implementing a Superconducting Magnet Facility (SCMF) in orbit, with its associated tracking hodoscope, is currently considered by NASA for the future Space Station /1/. Such an instrument, performing accurate rigidity measurements in the range from a few tens to several hundreds of GV, is likely to open a new field in Cosmic Ray research. Measurements of electron and positron spectra could be extended over the 100 GeV region where synchrotron losses in galactic magnetic fields dominate /2/. Long exposures in orbit would enable an extensive search for antinuclei heavier than Hydrogen. The measurement of the antiproton/proton ratio in the 30-500 GeV range would surely help unravel the controversial situation brought up by the few existing data at lower energy. The isotopic composition of Cosmic Rays around 100 GeV/n is also of utmost interest. A refined study of the decrease of the escape length with increasing energy could be performed over the whole charge range from H to Fe. Primaries could be searched more accurately for source isotopic anomalies since the secondary component is expected to be less important than at lower energy because of the escape length shortening. For those anomalies already discovered at lower energy (Ne22, Mg25+26) the question is whether they still show up at 100 GeV/n or more.

However these goals could be met only if, in addition to an accurate rigidity measurement, the particle momenta are also measured with a good resolution. In the following we describe a high resolution gas Cerenkov detector which can perform this measurement with a few percent accuracy over extended charge and energy ranges. We also evaluate the performances of an assembly composed of this detector associated to a SCMF.

2 - The Gas Cerenkov Imaging Detector

Gas Cerenkov detectors have been used in several space experiments either as a threshold device to discriminate between electrons and pions or protons /3/ or to effectively measure the momentum of Cosmic Ray nuclei /4/,/5/. These experiments essentially recorded the number of Cerenkov photons collected by pho-

tomultipliers with using either a diffusing light box or a focussing mirror arrangement. This technique however is plagued by a rather poor momentum resolution especially at the highest energies of interest here. With Cerenkov gases appropriate to the SCMF energy range the number of photoelectrons is hardly in excess of a few units for a Z=1,ß=1 particle so that statistical errors are overwhelming. In addition background light originating either from Cerenkov radiation in the material on the particle path or from delta-ray electrons contribute to further degrade the resolution.

Here we propose to rather measure the particle momenta by the angle of Cerenkov emission Ø which is related to the particle velocity ß=v/c and the gas index of refraction n through cos Ø = 1/ßn.

The Cerenkov light radiated by the charged particles in the radiator gas is focussed by a spherical mirror onto a position sensitive photon detector at the focal plane. In the absence of optical distortions, the Cerenkov photoelectrons are distributed along a circle with radius r. Let f be the focal length of the mirror, then the Cerenkov angle Ø is inferred from the measurement of r through Ø=atan(r/f). In addition the position of the circle center gives a measurement of the arrival direction of the primary particle. Accelerator experiments were successful at recording Cerenkov ring images with using various types of position sensitive photon detectors (see /6/ for a review).

In the next section we discuss the performances of a gas Cerenkov having the characteristics given in Table 1.

3 - The detector performances

The momentum resolution of a gas Cerenkov imaging detector depends primarily on the following factors:

(i) the granularity of the focal detector: a reasonable tradeoff between spatial resolution and the number of readout channels leads to a pixel pitch of a few mm i.e. an angular resolution of less than a milliradian for individual photons.

(ii) the dispersion of the gas refractive index: for Ar it is of the order of the pixel resolution in the VUV range while being negligible in the visible.

(iii) the optical distortions arising from the large aperture of the optical system and the fact that Cerenkov photons travel at relatively large angles to the optical axis.

In practice effect (iii) is the most severe as far as the momentum resolution is concerned. The Cerenkov images are no more circles but rather ellipses which greatly complicates the analysis.

The resolution of the detector having the characteristics given in Table 1 was investigated by a Monte-Carlo simulation. The Cerenkov images of Cosmic Ray charged particles impinging randomly on the telescope at an angle up to 5° to the axis were first generated. The adopted value for the average number of photoelectrons generated by a Z=1,ß=1 particle was 3 per meter of Argon, a figure valid in the VUV but probably pessimistic for the visible range. Then a second computer program was designed to analyze each image and assign the most likely energy to the primary particle. Optical distortions could be successfully handled by the program as is shown in figure 1 where the expected resolution for H and He nuclei is displayed as a function of momentum/nucleon. The particle trajectories through the gas radiator are also fitted to an accuracy of the order of 0.1 mrad.

A great advantage of the imaging technique is that background photon hits can be removed as being not part of the well defined Cerenkov image. Although the present study was restricted to Ar at STP as the radiator gas, with an energy threshold of 35 GeV/n, the energy range can be adjusted by varying the gas pressure. Finally we note that the energy resolution should improve for higher Z nuclei since more photoelectrons are available.

In the next section we estimate the performances of a SCMF fitted with a gas Cerenkov imaging detector.

4 - The imaging gas Cerenkov coupled to the SCMF

The rigidity resolution of the SCMF can be roughly estimated from the Maximum Detectable Rigidity (MDR), with the r.m.s error $\sigma(R)$ on a rigidity measurement R being given by:

$$\sigma(R)/R \simeq R/MDR \qquad \text{eq. (1)}$$

In order to estimate the isotopic resolution of a gas Cerenkov+SCMF association we simulated the response of both instruments to a Cosmic Ray beam containing equal amounts of He3 and He4. The rigidity R of the particles was sampled according to eq.(1) while the momentum/nucleon p was assigned as described in the preceding section. The observed mass A of He isotopes, computed from A=R/2p, is displayed in fig.2a and 2b for a MDR value of 1500 and 5000 GV respectively. It is clear that the factor limiting the isotopic resolution is the MDR rather than the momentum resolution. This is quite important for the design of the future SCMF which should have a high MDR value. Concerning the e/p separation it is seen from fig.1 that the gas Cerenkov has the capability of discriminating protons from electrons with equal rigidities up to at least 200 GeV/c. The e/p mass difference is so large that the difficulty in identifying $\overline{p}$'s and e+'s is not with the MDR but rather with the spillover of p's and e-'s due to a wrong magnetic deflection measurement. The evaluation of this effect requires careful simulations and possibly calibrations of the SCMF alone.

5 - Conclusions

The performances of a gas Cerenkov imaging detector are well matched to the high rigidity resolution expected for the SCMF. Accurate isotopic measurements in the 50-100 GeV/n range and e+/e-/$\overline{p}$ measurements up to 200 GeV/c can be achieved with combining these instruments. The Cerenkov imaging technique is actively developed at Saclay in a joint effort with particle physicists at CERN. Prototypes of multineedle detectors and multianode photomultipliers, with a granularity of a few mm, are currently under testing together with a compact low power readout electronics. Such detectors, suited for long exposures in space environment,are likely to become available within a few years.

References

/1/ Proceedings of the Workshop On Cosmic Ray and High Energy Gamma Ray Experiment for the Space Station Era
Baton Rouge 1984 in the press
/2/ W.R. Webber
in Composition and Origin of Cosmic Rays M.M. Shapiro ed. D. Reidel 1984
/3/ R.L. Golden et al.
NIM Vol 148 (1978) p.179
/4/ R.E. Streimatter et al.
Proc. of the 17th ICRC Paris 1981 Vol 8 p.54
/5/ S.P. Jordan and P. Meyer
Phys. Rev. Lett. Vol 53 n°5 (1984) p.505
/6/ G. B. Coutrakon
IEEE Trans. Nucl. Sci. NS-31 (1984) P.27-31

Mirror:
spherical
focal length 2.4 m
diameter 1.2 m
Radiator:
Argon at STP
maximum Cerenkov angle 1.5°
energy threshold 35 GeV/n
Focal detector:
45 cm diameter
full field of view 10.7°
cell size 3x3 mm²
number of cells 18,000

Table 1 - Physical parameters of the Cerenkov imaging telescope.

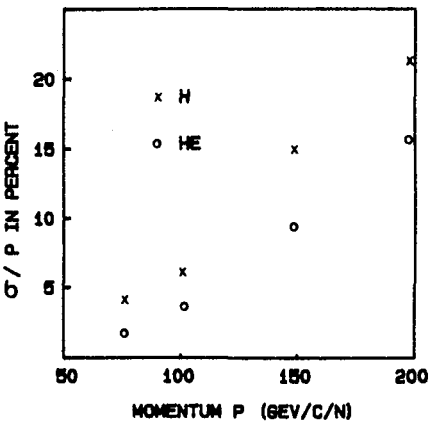

Figure 1- Momentum resolution of the telescope.

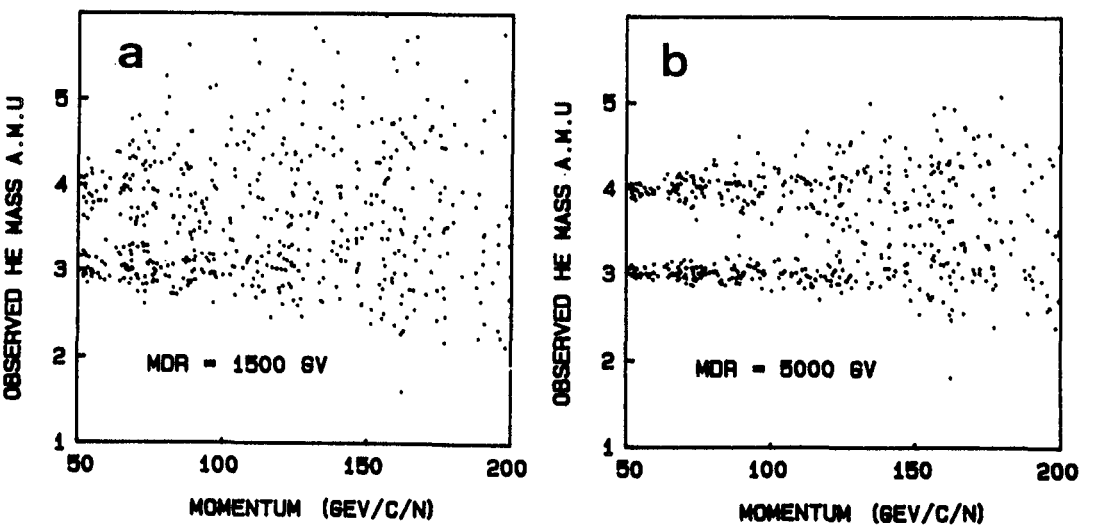

Figure 2 - The separation of He isotopes as determined from a simulation which takes into account the resolution of both the Cerenkov and the SCMF ; a) MDR=1500GV ; b) MDR=5000GV.

BEVALAC CALIBRATION OF THE SOFIE RANGE AND HODOSCOPE DETECTORS

W. R. Binns, J. J. Connell, M. H. Israel, and J. Klarmann
Department of Physics
and the McDonnell Center for the Space Sciences,
Washington University, St.Louis, MO 63130

1. Introduction. The Scintillating Optical Fiber Isotope Experiment (SOFIE) is a Cherenkov-dE/dx-Range experiment being developed initially for balloon flight to study the isotopic composition of cosmic rays in the iron region. The electronic range and hodoscope detectors in this experiment use scintillating optical fibers to image the tracks of stopping charged particles and to determine their trajectory. From this information the particle range can be determined and used together with a Cherenkov measurement to determine the mass of the stopping particle. This paper describes preliminary results of a Bevalac calibration performed in August, 1984 with a prototype of the balloon flight instrument, for the purpose of studying the measurement precision in range and trajectory which could be attained with this detector.

2. Experiment. Figure 1 shows a cross-section of the instrument exposed at the Bevalac. Incident particles pass through two thin plastic scintillator counters which provide a coincidence signal after which a Cherenkov measurement is obtained in a 2.5 cm thick Pilot 425 counter. Particles exiting the Cherenkov counter pass through a 0.794 cm thick steel passive absorber. This thickness was chosen so that particles stopping in the range detector would be above threshold in the Cherenkov counter. The range detector consists of a bundle of scintillating optical fibers which are proximity focused onto the face of a fiber optic reducer which was coupled to an image intensified video camera system consisting of a G.E. TN-2505 camera and an ITT-4144, dual microchannel plate image intensifier tube (Binns *et al.*, 1983a and b). The CID sensor in the camera is a rectangular array of 244x388 pixels, with each pixel having dimensions 23x27 microns^2. The fiber bundle which is coupled onto this array consists of about 7×10^4 fibers with length 30 cm and a 100 micron square cross-section joined together into a solid rod with cross-section 2.7×2.7 cm^2. The fiber bundle was constructed by first making a boule with plastic scintillator core material (KSTI-415) and acrylic cladding. Fibers with 1.5 mm square cross-section were then drawn and 225 of these were fused into a "multifiber boule" which was then drawn again into fibers with a 1.5 mm square cross-section. These multifibers were then fused into solid rods with cross-section 1.4 cm square. Four of these rods were then joined together and coupled to the intensified camera to form the detector. When a coincidence signal occurred, the image intensifier was gated off and a video frame was then processed along with Cherenkov, dE/dx, and penetration counter pulse heights.

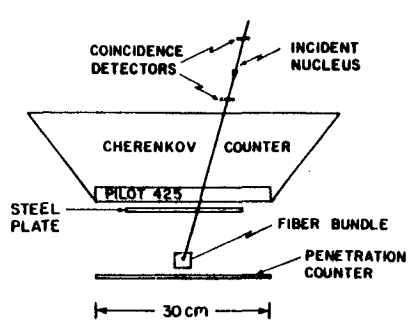

Figure. 1
Experiment cross-section

3. Range Detector Results. Iron-56 nuclei stopping in the fiber bundle produced tracks with a breadth of about 10 fibers (full width half maximum) near the end of the particle range. The energy deposition in plastic scintillator should, however, extend over a range of less than 1 fiber width. This track broadening is believed to be predominately the result of coupling between fibers due to incomplete conversion of ultraviolet photons within the fiber in which they were produced. Imperfections in the fibers may also contribute to cross talk. Curve a) in Figure 2 is a plot of light output from the fiber bundle versus residual particle range where the light output is obtained by summing the light intensity along pixel columns which are nearly perpendicular to the tracks. A running sum of three pixel columns is then taken to smooth the data. The theoretical energy loss versus particle range is also plotted (curve b) and has been smeared in one dimension by a gaussian with a sigma of 400 microns to simulate the track broadening due to fiber cross talk and broadening within the intensified camera system. These curves have been arbitrarily normalized using a "best eyes fit" so that the energy loss and light output match for the entry end of the track. Qualitatively these curves are similar. However in detail it is evident that there are fluctuations in light output along the track, and these fluctuations occur roughly on the scale of a single multifiber (about 1.5 mm). These fluctuations are believed to be the result of nonuniformities within the fiber bundle. In addition there is evident saturation in the scintillator output as the particle slows down and stops.

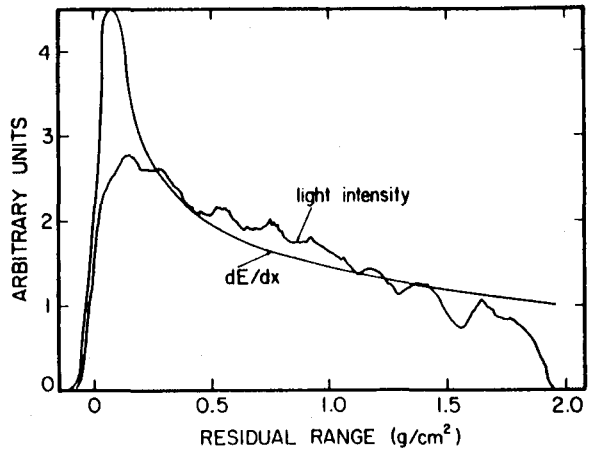

Figure 2
Curve a) is a plot of the light intensity from the fibers vs. residual range and curve
b) is the calculated dE/dx (Henke and Benton, 1966) vs. residual range spread by a gaussian function with σ = 400 microns.

Figure 3 shows the distributions in range that we obtained for iron-56 nuclei with beam energies 473 and 529 MeV/amu and having an incidence angle of 10 degrees with respect to the normal to the fiber bundle entry side. These nuclei were selected to have a low penetration counter signal, and they have had a first order mapping correction applied to account for variations in the flatness of the entry window into the fiber bundle. The range algorithm searches from the end of the track until it finds the maximum in light intensity as shown in figure 2. The half maximum intensity point is then taken to be the end point of the track. From Figure 3 we obtain a sigma in the range distributions of 260 and 280 microns for the beam energies 473 and 529 MeV/amu respectively. (The sigma was obtained from the full width half maxima of the distributions.) The 529 MeV/amu distribution appears to have non-gaussian wings which we hope to reduce by further data analysis. Calculations show that the combination of multiple coulomb scattering, range straggling, and the finite fiber size

will result in a range uncertainty of about 150 microns sigma. The additional broadening which we observe in our measurements is believed to be the result of imperfections in our fiber bundle. We have calculated that for a range measurement uncertainty of 300 microns and using a Cherenkov counter similar to that developed by Webber and Kish, (1983) appropriate hodoscopes, and an Aluminum passive absorber, a mass resolution of better than 0.25 amu can be obtained for incident angles less than 30 degrees and better than 0.30 amu for most particles with incident angle less than 55 degrees. We expect to be able to improve the quality of our fiber bundles which should result in improved range measurement precision.

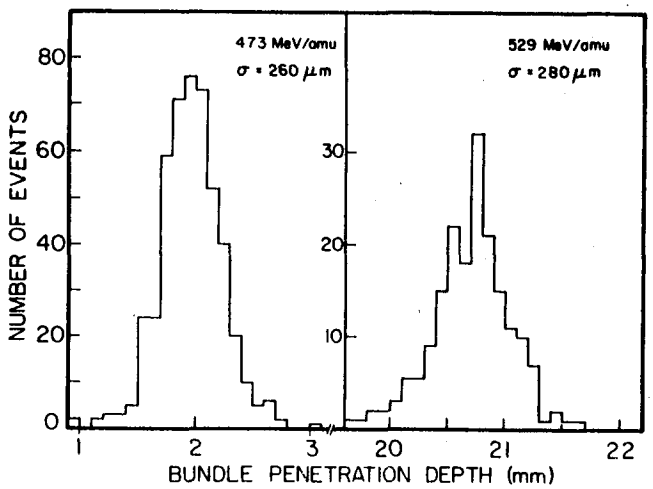

Figure 3
Range distributions for iron-56 nuclei with energies 473 and 529 MeV/amu stopping in the fiber bundle.

4. Hodoscope Results. To study the positional resolution that we could expect to obtain with a hodoscope made of scintillating fibers we have calculated, for a single track, the weighted mean position in fiber layers perpendicular to the track direction. These layers are adequately separated so that they are optically decoupled from one another. These points were then fit by a straight line as shown in Figure 4. The rms deviation of these "individual layer means" from the straight line should then give an indication of the trajectory measurement capability of this technique. Our measurements show a deviation from the best fit line of about 35 microns rms over the entire track length and 10 microns over a limited track segment. It seems clear that the larger deviation over the entire track length (about 200 fiber layers) is the result of systematic nonuniformities in the fiber bundle and that something approaching 10 microns is the true measuring precision which was obtained. This measurement precision is actually better than could be obtained if the fibers were optically decoupled from each other. (If light were detected only from the fibers through which the primary nucleus penetrates, then 100 micron fibers would give a measurement precision of 30 microns rms.) This is the result of the additional information contained in the fibers adjacent to the fibers actually traversed by the particle, thus improving our ability to estimate the "center of gravity" of the track.

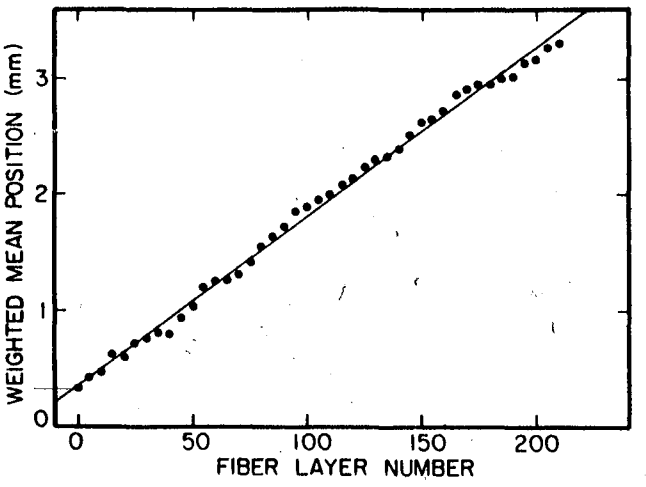

Figure 4.
Weighted mean position in the fiber bundle plotted vs. the penetration depth into the fiber bundle. Each fiber layer is 100 microns thick.

4. Conclusions. We have developed a new type of electronic detector which is capable of measuring range and trajectory to the precision required for resolving individual isotopes.

5. Acknowledgements. This work was supported in part by NASA grants NGR-26-008-001, NAGW-122, and NASA contract NAS5-27996 and in part by the McDonnell Center for the Space Sciences.

6. References

Binns, W.R., Israel, M.H., Klarmann, J. 1983a, Nucl. Inst. Meth., 216, 475.
Binns, W.R., Israel, M.H., Klarmann, J. 1983b, 18th ICRC, Vol.8, p.89.
Henke, R. P., and Benton, E. V., 1966, Nov., USNRDL-TR-1102.
Webber, W.R., and Kish, J.C., 1983, 18th ICRC, Vol.8, p.40.

THE DEVELOPMENT OF A HIGH ENERGY COSMIC RAY DETECTOR FOR SPACELAB-2*

Jacques L'Heureux, Peter Meyer+, Dietrich Müller+ and Simon P. Swordy

Enrico Fermi Institute, University of Chicago
Chicago, Illinois 60637 USA

We have constructed a large cosmic ray detector aimed at measurements of the energy spectra and of the elemental abundances of cosmic ray nuclei at very high energies, up to several TeV/nucleon. The instrument is an electronic counter telescope with a geometric factor of $5 m^2$ ster. It accomplishes measurements of the particle energies through the use of gas Cerenkov counters and of transition radiation detectors. A first space flight of this instrument is scheduled onboard Spacelab-2 in July 1985.

In this report, we shall discuss the solutions of a number of technological problems that are encountered when developing such instrumentation for Shuttle missions. The main issues that make the Space Shuttle quite different from, e.g. the balloon vehicle,, are considerations of mechanical integrity, as well as thermal control in orbit. As our instrument has to be kept in a container at atmospheric pressure, a substantial effort is required to ensure the safety of this "pressure vessel". Further, this instrument is mounted directly to the Shuttle orbiter, without the use of a pallet. The design of the support structure involves a major engineering effort.

Our instrument uses a variety of gaseous detectors. Consequently, the gas servicing under remote control represents a significant technical problem. This problem is compounded by very strict requirement on the acceptable pressure differential across the windows of the large area multiwire proportional counters ($\Delta p < 10^{-5}$ atmospheres).

The Space Shuttle can perform a variety of orbital maneuvers, subjecting the cargo bay to great extremes in solar radiation. The corresponding temperature excursions are large and we require an active thermal control system to maintain the instrument at a reasonable operating temperature.

Instrumentation for Spacelab missions must be delivered well in advance of the actual launch, and must undergo a lengthy integration procedure (one year). During this period, the instruments are essentially inaccessible to the investigator. This necessitates design for reliable operation under remote control via sophisticated electronics circuitry and data interfaces.Once in orbit, an instrument such as ours is essentially self-contained and should require little attention by the astronauts onboard. Still, a number of safety-critical instrument parameters must be processed and displayed on-board in order to permit human intervention in emergencies.

---

*Supported, in part, by NASA contract NAS8-32828.
+Also Department of Physics.

We shall discuss and illustrate these and related technical problems, and we hope to be able to describe the performance of the instrument in its first space flight.

MASS RESOLUTION OPTIMIZATION IN A LARGE ISOTOPIC COMPOSITION EXPERIMENT

J. A. Esposito*, B. S. Acharya+, V. K. Balasubrahmanyan, B. G. Mauger≠, J. F. Ormes, and R. E. Streitmatter
NASA/Goddard Space Flight Center, Greenbelt, MD 20771, U.S.A.

W. Heinrich, M. Henkel, M. Simon, and H. O. Tittel
University of Siegen, 29 Siegen, WEST GERMANY

ABSTRACT

A range-energy experiment has been built which will measure the isotopic composition of galactic cosmic rays. Recent experiments have shown an enrichment of neutron rich isotopes, ^{22}Ne and (^{25}Mg + ^{26}Mg) in particular, when compared to the solar composition. A high statistics measurement of these and other neutron-rich isotopes in the galactic flux will yield valuable information as to the source of these particles.

The 1.0 m^2-sr instrument will use a Cherenkov radiation detector (n = 1.5) to measure the particle velocity. The range of the particles will be measured by a passive nitrocellulose stack. Two scintillation counters and two gas drift chambers will be used to determine the nuclear charge and trajectory of the particles.

A computer simulation of the experiment has been used to estimate the instrument resolution. The Cherenkov detector light collection efficiency, ε_d, has been calculated. Absorption of light in the radiator has been considered in order to determine the optimum Cherenkov medium thickness, $x \cong 2.5$ cm. The computer projections also show that the Cherenkov radiator must have a uniform response to within 0.5% to achieve a mass resolution of $\delta A \leq 0.3$ amu. The experiment is expected to determine the isotopic composition for the elements neon through argon in the energy range 300-800 MeV per nucleon.

1. Introduction: Recent observations of the isotopic composition of galactic cosmic rays (1) have shown an overabundance of neutron-rich isotopes when compared with the solar composition. A discussion of the possible models which could cause this phenomena is given in Woosley and Weaver, 1981. Measurements of the galactic flux would conceivably show which processes dominate in the production of these particles.

A Large Isotopic Composition Experiment (2) (ALICE) has been designed to measure the isotopic composition of cosmic rays in the energy range 300-800 MeV per nucleon. ALICE will yield measurements for the elements Ne, Z = 10, through Ar, Z = 18.

* Physics and Astronomy Dept., Univ. of Maryland, College Park, MD 20742
+ NAS/NRC Research Associate
≠ Spacecom, P. O. Box 235, Las Cruces, NM 88004

The 1.0 m^2-sr instrument relies upon 5 active detectors to measure the particle nuclear charge, velocity and trajectory. A passive cellulose nitrate (CN) stack is used to determine the particle range. This parameter is used to determine the particle mass.

A computer simulation has been used to determine the energy losses (3) of the incident cosmic rays within the detectors for given Z and A. The energy losses are used to project the uncertainties in particle energy and range. A mass resolution of less than 0.3 amu is the design goal of the experiment.

2. Detector Complement: The experiment employs 3 distinct types of detectors for the active measurements. A schematic diagram of the instrument is shown in Figure 1.

Two gas drift chambers (4) determine the particle trajectory. The chambers are filled with a gas mixture (Ar: 90 percent, CH_4: 10 percent) and will each contain 6 groups of parallel wires. Three groups are set along the x-axis and 3 along the y-axis thus creating a cartesian coordinate system approximately 20 cm deep. The electron drift velocity, (V_d = 40.3 mm/μs), together with the difference in arrival times of the sense wire signals determines the track position. The single wire resolution of this hodoscope is ~ 200 μm.

A knowledge of the particle trajectory enables us to relate a particular event in the active chambers to the track left in the CN range stack. The particle incident angle is also found for use in cosine corrections to the path lengths through the detectors.

The remaining 3 active detectors have the same basic interior design which is shown in Figure 2. The chamber interiors are coated with a diffusely reflecting Barium Sulfate ($BaSO_4$) paint which has a reflectivity of 95 percent in the visible light region. This high reflectivity effectively reduces losses due to absorbtion by the chamber walls.

Scintillation light is produced in commercial PS-10. The 2 scintillation counters each contain a 1-cm thick sheet of PS-10 which covers the entire lower surface of the chamber interior. Sixteen equally spaced photomultiplier (PM) tubes, set 4 to a side, produce an active detection area of 2236 cm^2. Although light will be lost through absorbtion by the PS-10 and the chamber walls, a light collection efficiency, ε_d, of 49 percent is expected. A fast trigger is provided by four 2-inch PM tubes on each scintillation chamber. A coincidence between the S1 and the S2 signals trigger the instrument. This feature will collimate the particle beam, effectively minimizing the number of false events.

Pilot 425 (n = 1.5) will be used in the Cherenkov detector. Since the Cherenkov radiation is emitted primarily in the ultraviolet region, the Cherenkov material is doped with an ultraviolet-to-blue wave shifting compound to enhance the number of photons with wave lengths within the sensitivity limits of the PM tubes. The detector utilizes 24 PM tubes with an effective detection area of 3354 cm^2. The flight PM tubes have been selected for optimal resolution which we have determined corresponds to those PM tubes with the highest quantum efficiency and, hence, "gain". A sample of 86 PM tubes were tested out of which the best 24 PM tubes were selected. The Cherenkov material will have a thickness X = 2.5 cm.

The passive range stack is composed of several hundred layers of 0.03 g/cm^2 nitrocellulose sheets with a total depth of about 15 g/cm^2. After the flight, the range stack will be recovered and the sheets individually etched. Computer scanning methods will be used to produce a 3-dimensional view of the particle tracks in the range stack.

Lastly, an anti-coincidence counter is located below the range stack so that incident cosmic rays which do not stop in the stack are flagged. This feature will produce a measurement of iron secondaries in addition to the isotopic measurements.

The payload is to be elevated by balloon to an atmospheric depth of 4 g/cm^2 with a flight duration of 24 hours. A Fall 1985 launch is planned.

3. Calculated Resolution: ALICE must measure the particle mass to within 0.3 amu for the data to be useful. We may assume that the charge error, δZ, and errors associated with the trajectory, $\delta \cos \phi$, are much smaller than the uncertainties associated with the measured range and velocity, δR and $\delta \beta$, respectively.

The range of the particle is related to Z, A, and β through the equation:

$$R = \frac{A}{Z^2} f(\beta)$$

where $f(\beta)$, the velocity dependence, may be determined from proton range energy relations (3).

This relation yields a formula for the mass resolution:

$$\frac{\delta A}{A} = \{ (\frac{\delta R}{R})^2 + (\frac{1}{f(\beta)} \frac{\partial f(\beta)}{\partial \beta} \delta \beta)^2 \}^{1/2}$$

A computer simulation of the experiment has been used to estimate the instrument resolution.

Figure 3 depicts the mass error for the isotopes ^{20}Ne and ^{40}Ar, respectively. The particles are assumed to be vertically incident and the effects of delta rays and residual scintillations have not been included in this calculation. Residual scintillations are ~ 1/10 of the size of the saturated Cherenkov signal in Pilot 425. The effect of residual scintillations is similar to an increase of the index of refraction. Delta rays also mask the particle signal. The contribution of delta rays to the total Cherenkov signal has been studied (5). The combined effect of residual scintillations and delta rays is about 15% of the saturated signal. Near threshold, ~ 320 MeV/n, where the effect of delta rays is most significant, the mass error will be larger than depicted. For energies above 330 MeV/n in the Cherenkov medium, fluctuations in the delta ray signal are less than a 1σ deviation of the particle Cherenkov signal. Therefore, the mass error curves will approach those in Figure 3 at energies above 435 MeV/n and 490 MeV/n at the top of the atmosphere for ^{20}Ne and ^{40}Ar, respectively.

As of this writing, the ALICE stack has been assembled and calibration of the instrument is underway.

References

1. Mewaldt, R. A., 1981, Proc., 17th I.C.R.C., 13, 49.
2. Mauger, B. G. et al., 1983, Proc. 18th I.C.R.C., 8, 36.
3. Barkas, W. H. and Berger, M. J., 1964, NASA, SP-3013
4. Simon, M. et al., 1982, N.I.M., 192, 483-489.
5. Lezniak, J. A., 1976, N.I.M., 136, 299-306.

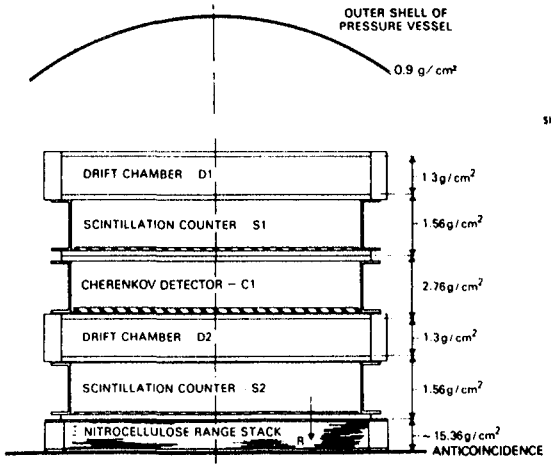

Fig. 1. ALICE schematic diagram

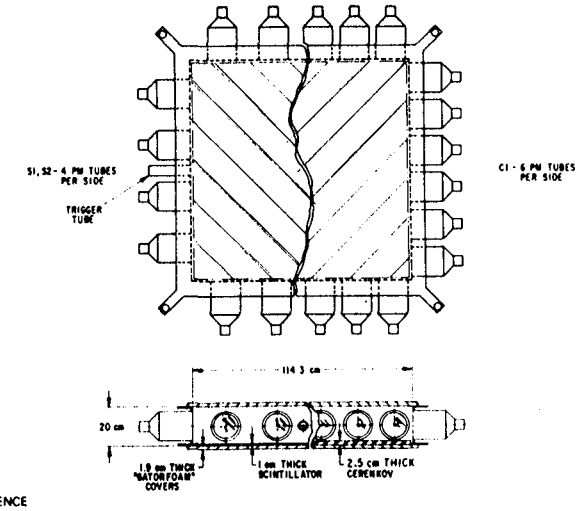

Fig. 2. Cherenkov and Scintillation Chamber Photomultiplier Tube Placement

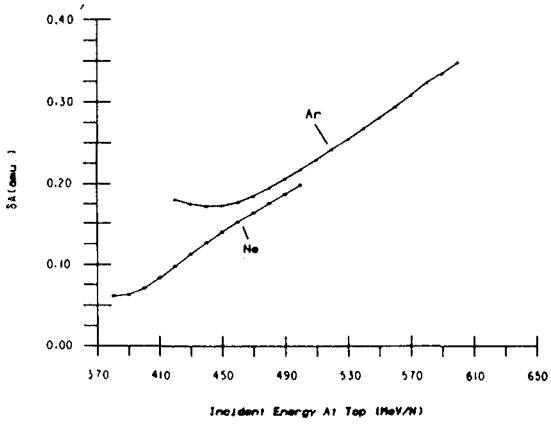

Fig. 3. Mass Uncertainties for ^{20}Ne and ^{40}Ar.

THE HEAVY IONS IN SPACE EXPERIMENT

J. H. Adams, Jr. and L. P. Beahm
E.O. Hulburt Center for Space Research
Naval Research Laboratory, Washington D.C., U.S.A.

B. Stiller
M & B Consulting Co.
Washington D.C., U.S.A.

ABSTRACT

The Heavy Ions in Space (HIIS) experiment was developed at Naval Research Laboratory and is currently in orbit onboard NASA's Long Duration Exposure Facility (LDEF). HIIS will record relativistic cosmic ray nuclei heavier than magnesium and stopping nuclei down to helium. The experiment uses plastic track detectors that have a charge resolution of 0.15 charge units at krypton (Z=36) and 0.10 charge units, or better, for nuclei lighter than cobalt (Z=27). HIIS has a collecting power of 2 square meter steradians and it has already collected more than a year's data.

1. Introduction. The Long Duration Exposure Facility (LDEF), a shuttle-launched free-flying satellite, was placed in a 28.4 degree inclination orbit at 476km on April 7, 1984. The LDEF spacecraft is a cylindrical structure, 14 feet in diameter and 30 feet long. The HIIS experiment is contained in two trays on the space-facing end of the spacecraft. LDEF will be retrieved on a later shuttle mission and returned to earth.

2. Scientific Objectives. The specific scientific objectives of this experiment are: (1) To measure the elemental composition of galactic cosmic rays. Particular emphasis will be placed on measuring individual elemental abundances for the elements zinc (Z=30) through zirconium (Z=40). These measurements will make it possible to compare the even and odd elements which have quite different nucleosynthetic origins (Cameron, 1982). (2) To measure the fluence, composition, energy spectra and arrival directions of low energy heavy ions that stop in the detector. Such ions could not have reached the LDEF orbit from outside the magnetosphere if they were fully ionized. The data collected on these ions will be examined in order to determine their origin.

3. Description of the Apparatus. The flight apparatus is shown in figure 1. Each tray contains four modules, each containing two detector stacks, a main stack and a top stack. The main stacks are sealed in a container that is filled with an atmosphere of dry breathing air. The lid of the module is an aluminum honeycomb structure with a thickness of 0.4 g/sqcm. The main stacks are 9.5 cm thick. In seven of the eight modules, the top stack is above the lid of the module, protected only by the thermal blanket. In the eighth module, this stack has been located

inside the sealed container under a specially designed lid consisting of 125 micrometer kapton film, aluminized on both sides.

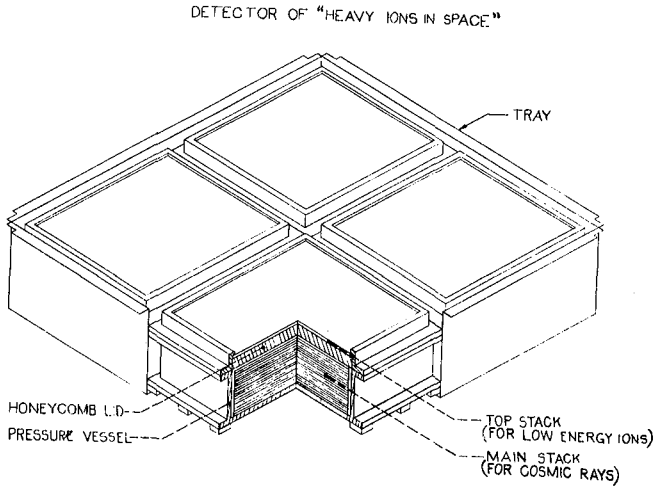

Figure 1: An LDEF tray containing four HIIS modules.

These track detector stacks will be used to measure the charge and the arrival direction of the ions that were recorded during the mission. In the case of stopping ions, the range will also be measured, and this will be used to estimate the energy of these ions.

4. Charge Resolution. The charge resolution of American Acrylics CR-39, used in HIIS, has been measured, with a 1.47 GeV/amu krypton beam at the BEVALAC. Figure 2 shows the results of the exposure. The resolution, 0.14 charge units at krypton, is adequate to resolve bromine from a much larger peak at krypton. Even a single rubidium ion, resulting from charge exchange, can be identified alongside the krypton peak. The resolution improves for lighter nuclei. We obtain 0.1 charge units resolution at iron. Similar results have been obtained for Pershore CR-39. To estimate the resolution of these detectors in a cosmic ray experiment, however, other effects must be considered.

It has been found that plastic track detectors change their response to ionizing particles with temperature at the time the particles are registered (Thompson et al. (1983)). The registration temperature effect has been investigated (Adams et al., 1984) for relativistic iron nuclei and stopping helium ions in CR-39 track detectors. These ions are more lightly ionizing than those used in the earlier work. Adams et al. found a smaller effect that had a temperature dependence opposite in sign to that observed by Thompson et al. This suggests that the registration temperature effect may not exist for ions that are somewhat more ionizing. Recently, we have measured the registration temperature effect for relativistic krypton ions. We find a very small effect of the same sign as reported earlier for relativistic iron. Our measurements show a reduction in the track-to-bulk etch rate ratio of 0.07 percent per degree centigrade between 0 and -78 degrees centigrade for CR-39.

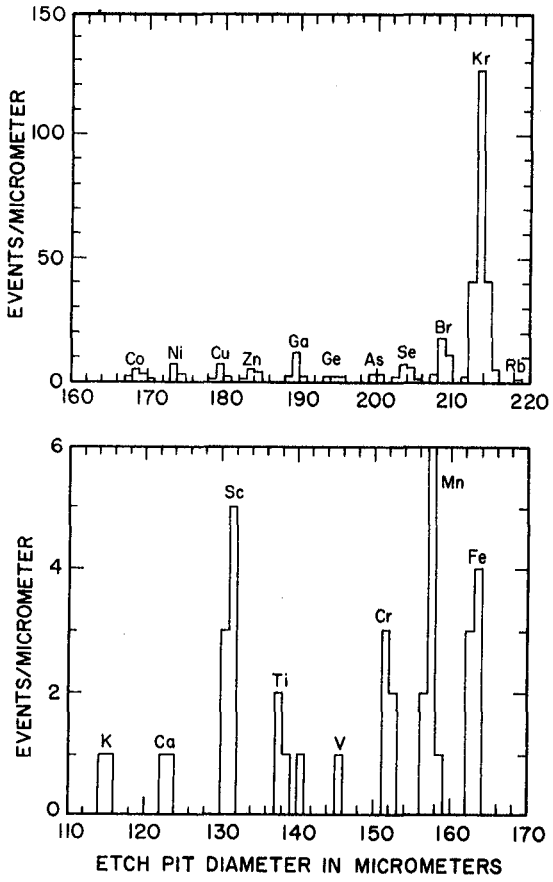

Figure 2: The distribution of average etch pit diameters for tracks from a relativistic krypton beam fragmented in a tank of water. The beam was normally incident on the detector stack. The tracks were measured in five sheets of American Acrylics CR-39 that had been etched at 70 degrees centigrade for 84 hours in 6.25N NaOH plus 0.04 percent Benax. Because of nuclear fragmentation in the detector sheets, and occasional overlapping tracks, all ten etch pits could not be measured on some tracks. Events were included in this plot if three or more etch pits had been measured on the track.

If we take this result as typical for relativistic nuclei from zinc to zirconium, the full range of temperature variation expected for the HIIS main detector stacks would only spread the individual charge peaks by +/- 0.14 charge units. The registration temperature effect is, therefore, expected to have a minor effect on the charge resolution in this part of the periodic table. A separate investigation for stopping ions from helium to silicon shows that individual charges can be resolved in this region as well.

5. Capabilities of the Experiment. The HIIS experiment has been recording ion tracks for more than a year. It should already have recorded 12,000 tracks due to cosmic rays from copper(Z=29) to zirconium. This is more than four times larger than the sample reported for the HEAO-C experiment (Binns et al., 1983). In addition to the lighter nuclei, some 49 tracks should have been recorded by cosmic rays heavier than tungsten.

The two square meter steradian collecting power of the HIIS experiment is much larger than that of the electronic charged particle telescopes which have been used to study stopping ions. HIIS will

detect stopping oxygen nuclei from 8 to 300 MeV/amu. For stopping iron, the energy range is 15 to 800 MeV/amu.

The exposure obtained, to date, on LDEF would make possible the detection of particle fluxes as low as $1.5X10^{-8}$ particles/meter sq.ster.sec. If the anomalous component ions are not fully ionized (Fisk et al., 1984), they should be found stopping in the HIIS detectors (O'Dell et al, 1977). Other sources of stopping heavy ions may be the inner radiation belt, or cosmic ray splash albedo. Chan and Price (1975) and Biswas et al. (1977) report observing stopping ions outside SKYLAB which were thought to be trapped radiation. The HIIS experiment has already accumulated more than 300 times the exposure of the SKYLAB experiment, so it may be possible to extend these earlier measurements. Humble et al. (1979) have considered the contribution from splash albedo and estimate that this effect is small, but Blanford et al. (1972) report detecting stopping heavy ions in balloon flights over Texas that they attribute to re-entrant splash albedo. This source may also contribute to the observed flux of stopping ions in the HIIS experiment.

6. Acknowledgements. The authors would like to thank Kate DeAngelis for measuring the accelerator calibrations and Andrew Gelman, John Rogers, and James Bellingham for the summers they spent preparing the HIIS experiment for launch. We would also like to thank Jim Ward for his engineering design work, and Charlie Buhler, Paul Cary, Jim Layher, and Ben Czarnaski for providing technical support during the development and testing of the the HIIS experiment. This work has been supported by the Office of Naval Research, as part of its special focus program on Spacecraft Survivablilty.

7. References

Adams, J.H., (1981), Proc of the 11th Intl. Conf. on Solid State Nuclear Track Detectors, Bristol, p 145-8.

Adams, J. H., O'Sullivan, D., and Thompson, A., (1984), Bull. Am. Phys. Soc., vol. 29, 706-7.

Binns, W. R., Grossman, D. P., Israel, M. H., Jones, M. D., Klarmann, J., Garrard, T. L., Stone, E. C., Fickle, R. K., and Waddington, C. J., (1983), Proc. 18th Intl. Cosmic Ray Conf., Bangalore, vol. 9, 106-9, 1983

Biswas, S., Durgaprasad, N., Nevatia, J., Sarkar, S., Venkatavaradan, V. S., (1977),Proc. of the 15th Intl. Cosmic Ray Conf., Plovdiv, vol. 2, 327.

Blanford, G., Friedlander, M., Klarmann, J., Pomeroy, S., Walker, R., and Wefel, J., (1972), JGR, vol. 77, 6037-6041.

Cameron, A. G. W., (1982), Astrophys. and Sp. Sci., vol. 82, 123-131.

Chan, J. H., and Price, P. B., (1975), Phys. Rev. Lett., Vol. 35, 539.

Fisk, L., Kozlovsky, B., and Ramaty, R., (1974), Ap. J. Vol. 190, L35

Humble, J. E., Smart, D. F., and Shea, M. A., (1979) Trans. Am. Gepohys. Union, vol. 60, 343.

O'Dell, F. W., Kidd, J., Seeman, N., Shapiro, M. M., Silberberg, R., and Tsao, C. H., (1977), Proc. of the 15th Cosmic Ray Conf., Plovdiv, Vol 2, 324-6.

Thompson, A., O'Sullivan, D., Adams, J. H., and Beahm, L. P., (1983), Proc. 18th Intl. Cosmic Ray Conf., Bangalore, vol. 9, 407-10.

OG9.1-12

CHERENKOV - DE/DX - RANGE MEASUREMENTS ON COSMIC RAY IRON GROUP NUCLEI

G.Sermund, G.Siegmon and W.Enge
Institut für Reine und Angewandte Kernphysik, Kiel, FR Germany
G.A.Simpson and W.R.Webber
Physics Department, University of New Hampshire, Durham, USA

KEYWORDS

Cosmic ray, Cherenkov-dE/dx-range telescope, time resolving plastic detector.

ABSTRACT

We present a balloon experiment which combined a large area plastic detector unit (4400 cm^2) with electronic dE/dx-C data.
The correlation of the electronic data with the range data of the plastic detector stack was achieved by rotating plastic detector disks which provided in this way the "passive" plastic detector with an incorporated time determination. The constant flux of cosmic ray particles with charge Z greater than 2 was used to gauge the time resolving system of the experiment.
Stopping cosmic ray iron group nuclei in the energy range 400 to 700 MeV/nuc have been identified using their electronic scintillator and Cherenkov signals and their etch conelengths and range data. The precise knowledge of the particle's trajectory proposes refined pathlength corrections to th electronic data.
This three parameter analysis provides an absolute mass scale to check whether the iron peak nuclei have the mass 56.

The Response of Ionization Chambers to Relativistic Heavy Nuclei

B.J. Newport[a], E.C. Stone[a], C.J. Waddington[b], W.R. Binns[c], D.J. Fixsen[b], T.L. Garrard[a], G. Grimm[c], M.H. Israel[c], and J. Klarmann[c].

[a]California Institute of Technology, Pasadena, California 91125, USA
[b]University of Minnesota, Minneapolis, Minnesota 55455, USA
[c]Washington University, St Louis, Missouri 63130, USA

ABSTRACT

As part of a recent calibration at the LBL Bevalac for the Heavy Nuclei Experiment on HEAO-3, we have compared the response of a set of laboratory ionization chambers to beams of $_{26}$Fe, $_{36}$Kr, $_{54}$Xe, $_{67}$Ho, and $_{79}$Au nuclei at maximum energies ranging from 1666 MeV/amu for Fe to 1049 MeV/amu for Au. The response of these chambers shows a significant deviation from the expected energy dependence, but only a slight deviation from Z^2 scaling.

1. Introduction

Gas filled ionization chambers were used on the Heavy Nuclei Experiment (HNE) on HEAO-3 (Binns et al., 1981). The response of such chambers is expected to be proportional to the energy deposited by the particle traversing them. At low energies this energy deposit is simply the ionization energy loss, while at high energies energetic knockon electrons are able to escape from the chamber, reducing the energy deposit.

To first order the ionization energy loss scales as the square of the particle charge Z, however at high Z this assumption breaks down. A more complete expression is given by Ahlen (1980, 1982), and predicts an energy loss rising slightly faster than Z^2. Such effects are important when identifying ultraheavy elements.

We have performed two calibrations of ion chambers at the LBL Bevalac using beams ranging from $_{25}$Mn to $_{79}$Au. The first, in 1982, was done with a prototype of the HNE ion chamber module which was essentially identical to that used in flight. Thus those data, reported in Garrard et al., 1983, are directly applicable to our flight experience at the energies calibrated. The second calibration, in 1984, used lab chambers which were made of thinner and more uniform materials, permitting better resolution and better knowledge of the beam energy in each ion chamber, at the cost of less direct relevance to the flight data. Figure 1 is a schematic drawing of the 1984 detector.

Particles entering the 1984 detector traversed $\sim$0.1 g cm^{-2} of mylar in the upstream window, rather than the $\sim$1 g cm^{-2} of aluminum honeycomb in the flight prototype; thus the energy loss in the window is much smaller and more uniform. Also, in the 1984 calibration the beam energy was measured with a magnetic spectrometer after being degraded to the calibration energy, rather than being calculated from an energy loss model.

The lab ion chambers had aluminized mylar electrodes (0.8 mg cm^{-2}) rather than aluminum screenwire (10 mil diameter, 62.5 mil spacing); thus the production and absorption of knockons is much more uniform. A Monte Carlo model of knockon

production correctly predicts the degradation in resolution caused by non-uniform production of knockons in the screen wire electrodes. This resolution degradation in the flight chambers tends to mask the relatively subtle deviations from Z^2 scaling.

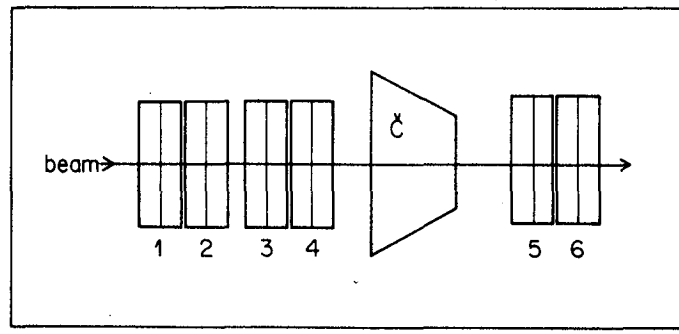

Figure 1. Schematic drawing of the 1984 detector, showing the six ion chambers.

In 1982 the ultraheavy capabilities of the Bevalac were new and we calibrated only on beams of ~1700 MeV/amu $_{25}$Mn and ~1000 MeV/amu $_{79}$Au. The 1984 calibration used beams of $_{26}$Fe, $_{36}$Kr, $_{54}$Xe, $_{67}$Ho, and $_{79}$Au at maximum energies ranging from 1666 MeV/amu for Fe to 1049 MeV/amu for Au.

2. Results of the 1984 Calibration

Figure 2 shows the response of chambers 1, 5, and 6 to $_{26}$Fe nuclei as a function of the energy at the midplane of the appropriate chamber, and compares their signals to the calculated dE/dx, arbitrarily normalized at 500 MeV/amu (requiring 27.9 eV per ion pair in the P-10 gas used (90% argon, 10% methane)). It is apparent that the signals fall below that predicted by dE/dx at energies above 700 MeV/amu. This loss of signal is somewhat surprising since at these energies we would expect knockons escaping from the exit window to be in equilibrium with those arriving from above, particularly for chambers 5 and 6 which have ~2 g cm^{-2} of upstream material. However, some of the decrease in observed signal may be due to knockons escaping from the sides of the chambers.

By interpolating to a particular energy we can construct a plot of signal versus Z at that energy. At low energies, the heaviest nuclei have an effective charge, $Z_{eff} = Z[1-\exp(-130\beta Z^{-2/3})]$, due to electron capture (Pierce and Blann, 1968). Figure 3 shows the pulse heights, scaled down by Z_{eff}^2, at four energies for Z = 26-79, using ion chambers 1, 5, and 6. The uranium data have not been included because the charge state in the magnetic spectrometer was uncertain for those beams whose energy had been degraded significantly. The straight lines represent a linear fit to the data, and it is apparent that there is a small negative non-Z^2 effect. The charge of an $_{82}$Pb nucleus would be underestimated by about 0.5 charge units at these energies, in contrast with the charge overestimate of +3 charge units observed in the calibration of the flight chambers.

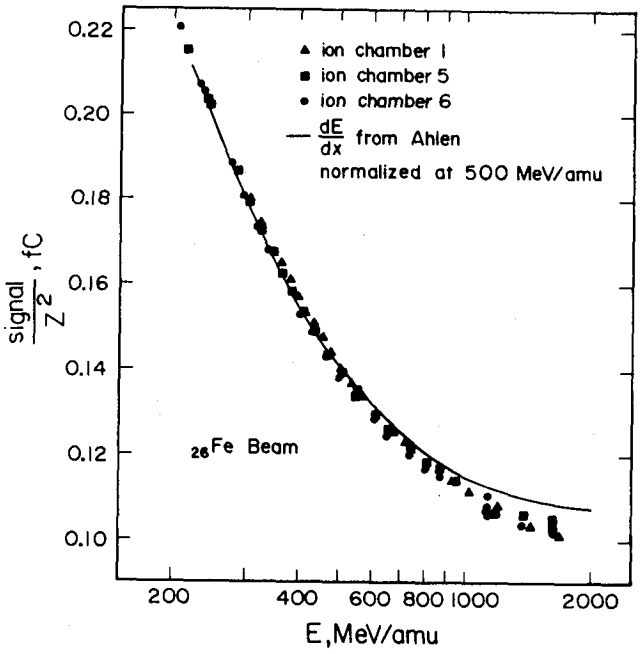

Figure 2. The response of chambers 1, 5, and 6 to $_{26}Fe$ nuclei as a function of energy.

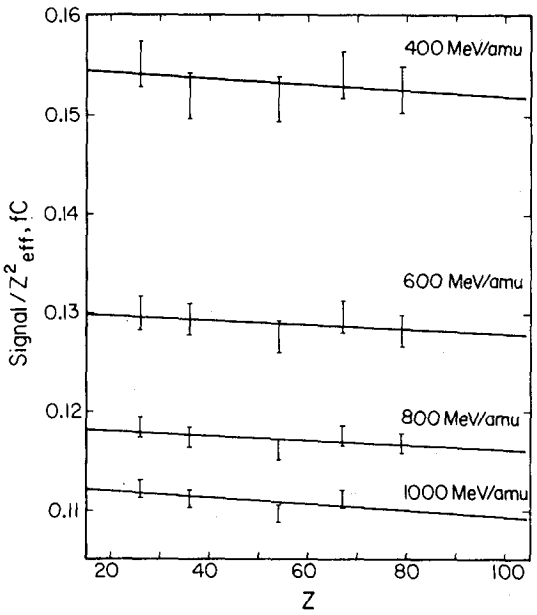

Figure 3. Response of chambers 1, 5, and 6 at four energies, scaled by Z_{eff}^2.

3. Conclusions

Although the non-Z^2 effects in these chambers differ from those observed in the prototype flight chambers, the assumption of Z^2 scaling is still not seriously in error. We also note that our published abundances above charge 50 have used primarily the Čerenkov detector to assign charges, and are unaffected by small non-Z^2 effects in the ion chambers.

Since the two calibrations differ, the ionization response to energy loss must be sensitive to details of the mass distribution above, below, and within the chambers. As a result we have used the flight data to directly determine both the energy dependence and effective non-Z^2 correction (Jones et al., (1985, OG 4.1-8) and Newport et al., (1985, OG 4.4-5)).

4. Acknowledgements

The success of this calibration was largely due to the efforts of the staff at LBL, especially Hank Crawford, Mel Flores, Peter Lindstrom, and Fred Lothrop. John Epstein provided invaluable assistance in constructing and aligning the instrument. This work was supported in part by NASA contracts NAS 8-27976, 77, 78, and grants NAG 8-498, 500, 502 and NGR 05-002-160, 24-005-050, 26-008-001.

5. References

Ahlen, S.P. 1980, *Rev. Mod. Phys.* **52,** 121
Ahlen, S.P. 1982, *Phys. Rev.* **A 25,** 1856
Binns, W.R., *et al.,* 1981, *Nucl. Inst. Meth.* **185,** 415
Garrard, T.L. *et al.,* 1983, *Proc. 18th I.C.R.C. (Bangalore),* **9,** 367
Jones, M.D. *et al.,* 1985, *Proc. 19th I.C.R.C. (San Diego),* OG 4.1-8
Newport, B.J. *et al.,* 1985, *Proc. 19th I.C.R.C. (San Diego),* OG 4.4-5
Pierce, T.E. and Blann, M. 1968, *Phys. Rev.* **173,** 390

MULTIPLE SCATTERING EFFECTS IN dE/dx-E INSTRUMENTS FOR ISOTOPIC COMPOSITION STUDIES

M.E. Wiedenbeck

Enrico Fermi Institute and Department of Physics
University of Chicago, Chicago, Illinois 60637 USA

1. Introduction. The development of cosmic ray telescopes capable of separating individual isotopes of heavy elements using the dE/dx-vs.-E technique depended critically on the incorporation of precise trajectory sensing elements into these systems. In typical implementations the particle trajectory is derived from a set of position measurements made prior to a particle's entering the first energy loss detector. The use of the trajectory obtained in this way to correct energy loss signals for the actual pathlengths through the detectors depends on the assumption that the particle trajectory is a straight line. In order to resolve iron isotopes the angle of incidence, θ, of the particle track (measured from the normal to the detector surfaces) must be known rather accurately.

When the angle of the cosmic ray's track through the ΔE detectors must be known with this high precision, the effects of multiple Coulomb scattering in the trajectory sensor, in the material between it and the ΔE detector, and in the ΔE detector itself must be taken into account. For example, when iron nuclei at 200 MeV/amu pass through a 1 g/cm^2 thick layer of silicon, multiple scattering causes a distribution of the effective angles of the particle tracks through this layer. This distribution, while centered on the angle at which the particles enter the layer, has an rms spread of approximately 0.11°. For iron particles traversing the layer at an angle of 30° this would lead to an uncertainty in the calculated mass of slightly more than 0.1 amu. These effects become increasingly more severe when one considers measurements of nuclei of lower energy, or when absorbing materials of higher atomic number are used.

In this paper we discuss an alternative approach to particle trajectory determination which can provide a significant reduction in the pathlength uncertainty in the energy loss detectors which is caused by multiple scattering. This approach involves the measurement of the locations of the points at which the particle enters and exits the detector and approximating the trajectory by a straight line between these two points, rather than by a straight line through two points along the particle's track before it entered the detector. In Section 2 the pathlength errors which result from these two approximations are compared. In Section 3 one practical implementaton of the new approach is described, and practical issues which limit its general applicability are mentioned.

2. Comparison of Pathlength Uncertainties. Figure 1 schematically shows the track of a heavy nucleus through a layer of material (such as a ΔE detector), with the scattering greatly exaggerated. Also shown are the approximations to this path which are obtained by using straight lines

through: a) points measured along the trajectory before entry into the detector, and b) the points at which the particle entered and exited the detector. Analyses by others [1] have shown that in case (a) the relative uncertainty in the path-length through the detector is given by·

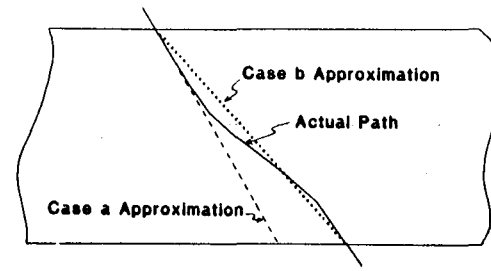

Figure 1.

$$\frac{\sigma_{\sec\theta}}{\sec\theta} = \frac{1}{\sqrt{6}} \cdot \tan\theta \cdot \sqrt{X}\ \sigma_\theta$$

where θ is the nominal angle of the particle's track (measured from the detector normal), X is the detector thickness in g/cm², and σ_θ is the rms angle of deflection over a pathlength of 1 g/cm². (Throughout this discussion we neglect the effects of particle slowing in the layer. Zumberge [2] has analyzed such effects, and the application of his approach to the cases considered here makes no qualitative changes in our results.)

For case (b) we have carried out a formal analysis in which the detector is subdivided into a large number of thin sublayers and the scatterings in each layer are treated as independent Gaussian random variables and their effects on the pathlength and on the point of exit from the detector are compounded. This analysis, carried out to first order in σ_θ, shows that the approximate trajectory (b) (see Fig. 1) agrees exactly with the true pathlength. The reason for this agreement is illustrated in Figure 2, in which we compare two paths - one involving a single scatter and the other a straight line agreeing with the first at its end points. The lenghts of the three segments shown are related by:

$$c = \sqrt{[\,a^2 + b^2 + 2ab\cdot\cos(\delta\theta)\,]}$$

which for small values of δθ reduces to:

$$c \approx a + b - \frac{1}{2}\left(\frac{ab}{a+b}\right)\cdot(\delta\theta)^2$$

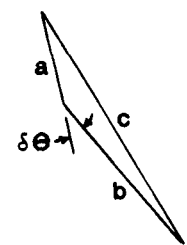

Figure 2.

That is, the difference in the two pathlengths is second order in δθ. When more than one deflection of the particle's trajectory is considered, their combined effects also produce pathlength differences, but these all involve products of the individual scattering angles and therefore again only yield second order or higher effects.

In order to carry out a quantitative comparison between the path-length errors in cases (a) and (b) we have chosen to perform Monte

Carlo calculations, rather than to extend our calculation for case (b) to second order. In addition, we have incorporated the effects of ionization energy loss in the Monte Carlo calculation, calculating the rms scattering angle in each sublayer using the actual value of the particle's velocity in that layer. In Figure 3 we compare our results for the two cases. Also shown, on the right hand abscissa, is a scale indicating the approximate contribution of these pathlength errors to the mass resolution for the measurement of iron isotopic composition. It can be seen that the determination of particle trajectories from the entry and exit points contributes negligibly to the mass resolution, while the use of a trajectory extrapolated from outside the detector leads to a mass error which, at large angles, could be the dominant source of mass uncertainty for measurements of iron isotopes.

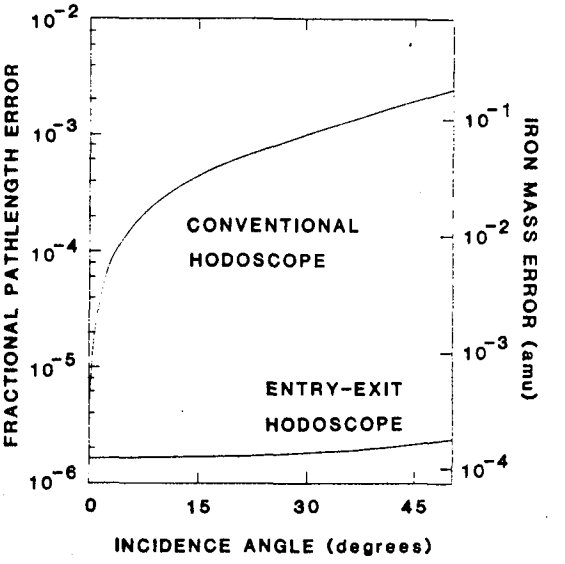

Figure 3.

An additional source of pathlength uncertainty, which occurs when the trajectory is only measured before entry into the ΔE detector stack, results from scattering in any material (such as previous ΔE detectors) between the trajectory measurement and the measurement of ΔE which is being used for mass determination. For the same amount of material, these scatterings contribute a factor $\sqrt{3}$ more to the pathlength uncertainty than do scatterings in the ΔE detector itself [1]. Normally the best mass resolution is obtained from ΔE measurements made close to a particle's end-of-range, but multiple scattering effects may significantly degrade such measurements in systems where several other thick detectors must be penetrated subsequent to the trajectory measurement. These resolution-degrading effects should become noticeable for high-Z, high-angle events in the next generation of cosmic ray composition experiments utilizing silicon solid state detectors.

3. Practical Applications. The above considerations were based on the assumption that the locations of discrete points along a particle's track can be measured exactly. Under most practical conditions the errors made in measuring the locations of these points will dominate the multiple scattering error in case (b). If two orthogonal coordinates are each measured with an uncertainty σ_x at two faces of a detector of thickness Δz, the resulting uncertainty in the pathlength between these points is:

$$\frac{\sigma_{\sec\theta}}{\sec\theta} = \frac{1}{\sqrt{2}} \cdot \sin(2\theta) \cdot \frac{\sigma_x}{\Delta z}$$

The difficulty in implementing a practical entry-and-exit trajectory system stems mostly from the fact that the ratio $\sigma_x/\Delta z$ must be $\lesssim 10^{-3}$ to

achieve the pathlength accuracy required to resolve heavy isotopes. In solid state detector telescopes one typically has $\Delta z \lesssim 5$ mm, requiring $\sigma_x \lesssim 5$ μm. While this tracking accuracy is, in principle, achievable, it is far beyond the level of presently practical systems.

Systems employing gas ionization detectors for the ΔE measurement are more amenable to the implementation of an entry-exit trajectory system because the low gas density dictates that the detectors be relatively thick. We are in the process of constructing such a system in which a ΔE detector consists of 30 cm of gas at a pressure of 10 atm (~0.5 g/cm²). We are incorporating a pair of single-wire proportional counters, one at the front of the ΔE detector and one at the back, in the same gas volume as the ΔE detector, to provide a determination of the entry and exit coordinates from combined measurements of drift time (to determine the distance of the particle track from the wire) and charge division (to determine the position along the wire). The large lever arm provided by the ΔE detector thickness (30 cm) makes it possible to derive a sufficiently accurate trajectory from position measurements made with a precision rather typical of gas-phase position sensitive detectors (~ 0.3 mm rms). While our present system uses P-10 gas (90% Ar, 10% CH_4) as the ionization medium, the entry-exit trajectory system should permit the use of heavier gases (such as Xe) to provide additional stopping power without introducing additional pathlength uncertainty. If a conventional trajectory system were used, the use of Xe instead of Ar would increase the multiple scattering induced pathlength uncertainty by a factor ~ 4, thereby severely restricting the solid angle over which satisfactory mass resolution could be attained (cf. Fig. 3).

4. Conclusions. Trajectory systems which provide the coordinates of a particle's track as it enters and exits each energy loss detector could, in principle, eliminate the contribution of multiple scattering to the mass error in dE/dx-E particle identifiers. The implementation of such systems appears most practical in systems using gaseous energy loss media. A detector system which can be used to experimentally test these results is now being developed.

5. Acknowledgements. This work was supported, in part, by the Louis Block Fund of the University of Chicago.

References

1. Particle Data Group, Rev. Mod. Phys. 56, S1 (1984) (see pp. S50-S53).
2. Zumberge, J.F., Calif. Inst. of Tech. publication SRL81-5 (unpublished Ph.D thesis) 1981.

Hexagonal Uniformly Redundant Arrays for Coded-Aperture Imaging

M. H. Finger and T. A. Prince
California Institute of Technology, Pasadena, CA 91125

1. Introduction.

Uniformly redundant arrays are used in coded-aperture imaging, a technique for forming images without mirrors or lenses. This technique is especially important for the high energy x-ray and γ-ray region above 20 keV. In this technique, a mask consisting of opaque (closed) and transparent (open) areas is placed between the photon sources to be imaged and a position sensitive detector or a detector array. Each source casts a shadow pattern of the mask or aperture onto the detector. This shadow pattern may be viewed as an encoded signal for that source direction. If each possible source code is unique, the detected composite of overlapping shadow patterns may be decoded to produce an image of the source distribution.

Figure 1 shows a mask suitable for imaging. This mask consists of an array of open (white) and closed (gray) cells arranged in a periodic pattern. The unit pattern is outlined. The mask in figure 1 is a *uniformly redundant array*[1,2] (URA). URAs have an especially desirable property: the overlap between two source codes is independent of the source directions as long as the sources are sufficiently separated. Except for periodicity, this guarantees a unique decoding of the composite shadow pattern with a maximal immunity to statistical noise.

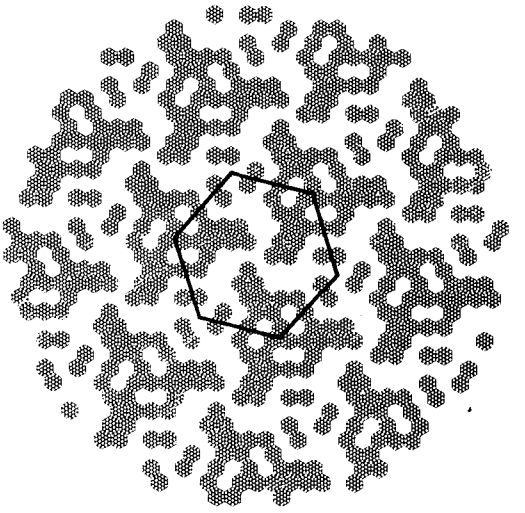

Figure 1. An HURA of order 79.

To date, most work on URAs has concentrated on those constructed on rectangular lattices. In this paper we focus on URAs constructed on hexagonal lattices, although many of the results are independent of the lattice type.

We will present complete details for the construction of a special class of URAs, the *skew-Hadamard URAs*, which have the following properties:

1) They are nearly half open and half closed.
2) They are antisymmetric (exchanging open and closed cells) upon rotation by 180° except for the central cell and its repetitions.

Some of the skew-Hadamard URAs constructed on a hexagonal lattice have additional symmetries. These special URAs that have a hexagonal unit pattern, and are antisymmetric upon rotation by 60°, we call *hexagonal uniformly redundant arrays* (HURAs). The mask in figure 1 is an HURA.

HURAs are particularly suited to our application, γ-ray imaging in high background situations. In a high background situation the best sensitivity is obtained with a half open and half closed mask. Furthermore, systematic variations of the detector background from position to position can be larger than the variations in detected flux due to sources. With a skew-Hadamard URA a simple rotation turns the mask into a near anti-mask, allowing exact position-by-position background subtraction. Also, the hexagonal symmetry of an HURA is more appropriate for a round position-sensitive detector or a close-packed array of detectors than a rectangular symmetry. This is especially true for shielded detector systems where compactness is at a premium.

2. Mathematical Structure of URAs

A URA is defined within a unit pattern which is repeated periodically. The number of cells in this unit pattern is the order v of the URA. Of these cells, k of them are closed and $v-k$ are open. The uniform redundancy property of URAs involves how frequently a given displacement between closed cells occurs. We will consider a cell within a repetition of the unit pattern as equivalent to the corresponding cell in the unit pattern, and will therefore define the difference between two cell centers as the vector displacement between them, folded back into the unit pattern. For a URA, all possible differences occur a uniform number λ times among the pairs of closed cell centers[2]. This property guarantees the uniform overlap of source codes discussed in the introduction[1,2].

The mathematical structure of a URA is that of an Abelian group difference set[3], which is specified by an Abelian (additive) group G of order v, and a set D of k elements of G with the property that any possible nonzero difference occurs exactly λ times between elements of D. For a URA the group G is the lattice translations modulo the periods of the mask pattern, and the set D contains those translations that take the central cell to a closed cell. The simplest examples of group difference sets are one-dimensional sets known as *cyclic difference sets* defined on the group of integers *mod* v. These play an important role in the construction of many URAs.

URAs in the class consided in this paper, the *skew-Hadamard URAs*, are nearly antisymmetric. That is, for any nonzero element in the group G, either it or its negative but not both, are contained in the difference set D[3]. These skew-Hadamard URAs are a subset of the *Hadamard URAs* which are nearly half open and half closed. Hadamard URAs are characterized by the parameters $v=4n-1$, $k=2n-1$, $\lambda=n-1$ for some integer n.

Johnsen[4] has proven two interesting facts about skew-Hadamard URAs :

1) All skew-Hadamard URAs have a *cyclic* group G, and therefore can be constructed from skew-Hadamard cyclic difference sets.
2) All skew-Hadamard cyclic difference sets are of prime order $v = 3$ *mod* 4 and can be generated from the quadratic residues *mod* v .

These facts allow us to present a construction for *all* antisymmetric or skew-Hadamard URAs.

3. Construction of Skew-Hadamard URAs from Quadratic Residues

We now present a simple procedure for generating any skew-Hadamard URA. An example constructed on a hexagonal lattice is shown in figure 2. The procedure consists of the following steps:

1) Choose the lattice on which the URA is to be constructed. The lattice is defined by picking two basis vectors $\vec{e}_0$ and $\vec{e}_1$. For our example we have chosen a hexagonal lattice, which has the basis vectors separated by 60° .
2) Choose as the order of the URA a prime of the form $v = 4n-1$. In our example $v = 23$.
3) Construct the order v skew-Hadamard cyclic difference set from the formula

$$D=\{1^2,2^2,...,(\frac{v-1}{2})^2\} \quad mod\ v \qquad (1)$$

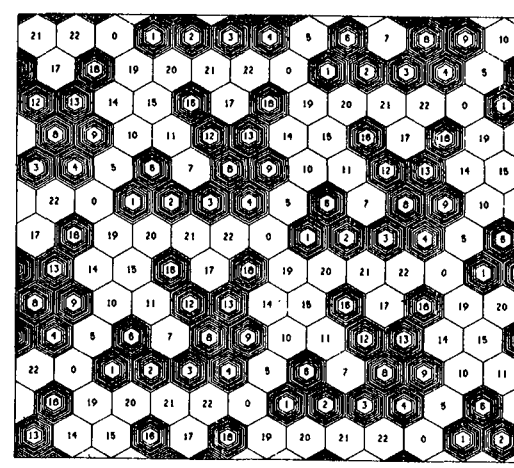

Figure 2. Construction of a skew-Hadamard URA of order 23.

4) Choose an integer r and label all the cells so that the cell centered at $i\vec{e}_0+j\vec{e}_1$ is labeled with

$$l = (i + rj)\ mod\ v \qquad (2)$$

and make all cells with labels in D closed. In our example r=5.

The heart of this procedure is the construction of the skew-Hadamard cyclic difference set in step 3. For a proof that this is a difference set see Baumert[3]. Step 4 transfers the difference set properties onto the lattice. This is done through the labeling, which transforms addition *mod v* to vector addition on the lattice modulo the resulting lattice periods.

The freedom available in this procedure rests in the choice of the lattice, the choice of the order v,and the choice of the multiplier r. The lattice type will determine what symmetries can occur. The possible orders form a rather dense set, the first few choices being v=3,7,11,19,23,31,43,47,59,67,71,79, and 83. The multiplier r determines the periods of the URA, and hence the shape of the unit pattern. Many of the v available choices result in URAs that are related by the symmetries of the lattice.

4. Hexagonal Uniformly Redundant Arrays

Of the large number of skew-Hadamard URAs, all of which can be constructed by the procedure in section 3, we wish to pick out those that have a hexagonal unit pattern when constructed on a hexagonal lattice. These we call *hexagonal uniformly redundant arrays* (HURAs)[5]. For an HURA each period when rotated by 60° is again a period. It can be shown from equation (2) that this is only possible if the multiplier r satisfies

$$r^2 = r-1 \quad mod\ v \tag{3}$$

This property has a simple geometric interpretation: a cell labeled l when rotated by 60° will have the label $rl\ mod\ v$. This feature, and the properties of quadratic residues modulo a prime, causes this restricted set of URAs to have a rotational antisymmetry upon rotation by 60° as well as 180°.

It can be shown that HURAs exist for order v=3 and any prime order of the form $12n+7$. If HURAs related by symmetry are considered equivalent, then for each of these orders there is a single HURA. The number of available HURAs is still large; figure 3 shows the number of HURAs with order v or less for v up to 10,000. In figures 4 through 8 we show examples of a few moderate order HURAs.

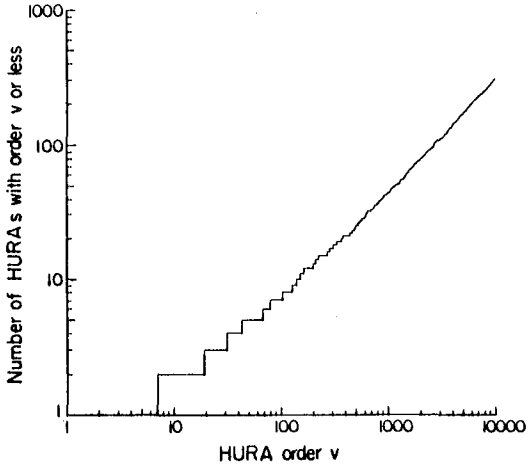

Figure 3. The number of HURAs with a given order or less.

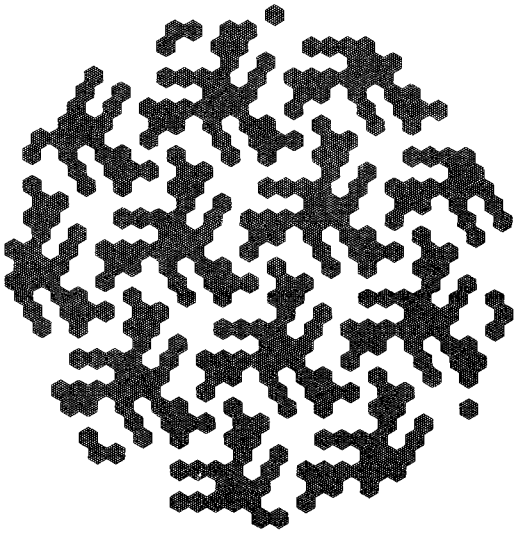

Figure 4. An HURA of order 67.

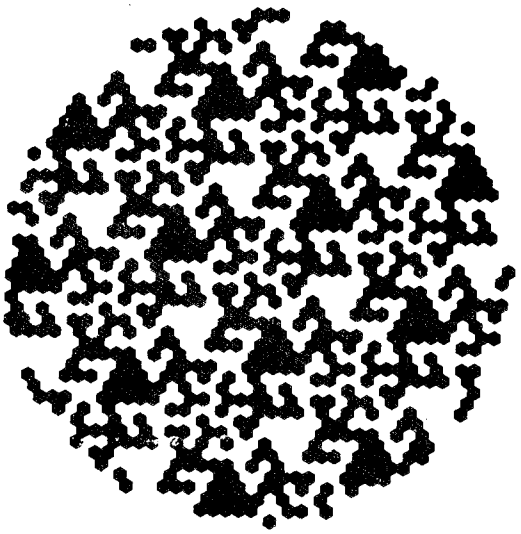

Figure 5. An HURA of order 139.

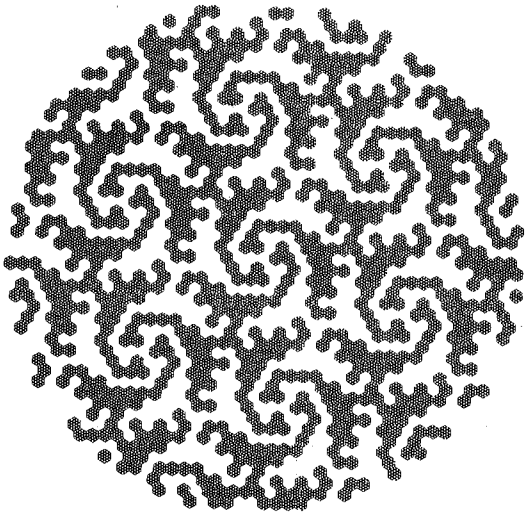

Figure 6. An HURA of order 151.

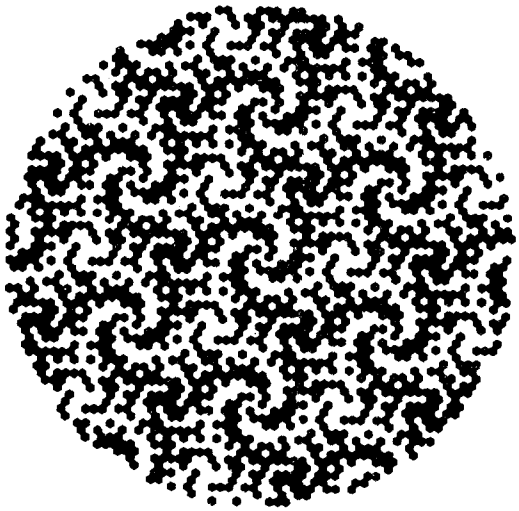

Figure 7. An HURA of order 331.

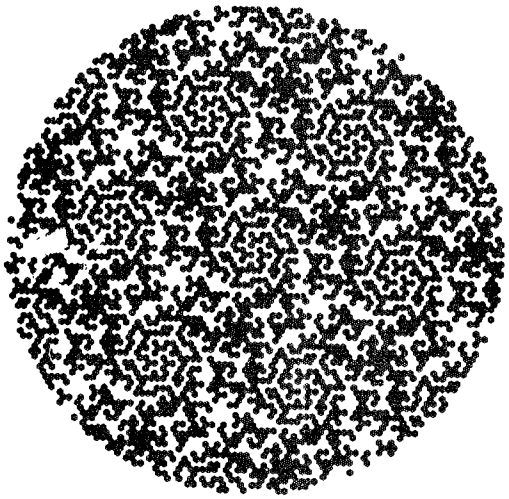

Figure 8. An HURA of order 619.

While HURAs are mathematically interesting constructs, they also have numerous attractive features for applications in astronomy instrumentation. For instance, the HURA of figure 1 is being implemented as a 115 kg lead coded-aperture mask on a Caltech imaging γ-ray telescope (see OG9.2-2).

5. Acknowledgments

We acknowledge useful discussions with W. R. Cook. This work is supported in part by NASA grant NGR 05-002-160.

References

1) Gunson and Polychronopulos,*Mon. Not. R. Astron. Soc.* **177**,485 (1976)
2) Fenimore and Cannon, *Appl. Opt.*, **17**,337 (1978)
3) Baumert, Cyclic difference sets, *Lecture Notes in Mathematics,No. 182,* Springer-Verlag (1971)
4) Johnsen, *J. Algebra,* **4**,388 (1966) [esp. Corollary 3.4 and Theorem 3.5 restricted to two cycles]
5) Cook et al., *IEEE Trans. Nucl. Sci.,* **NS-31**,771 (1984)

A Balloon-Borne Imaging Gamma-Ray Telescope

W. E. Althouse, W. R. Cook, A. C. Cummings, M. H. Finger, T. A. Prince, S. M. Schindler, C. H. Starr, and E. C. Stone

California Institute of Technology, Pasadena, CA 91125 USA

1. Introduction. This paper describes a balloon-borne coded-aperture γ-ray telescope for galactic and extragalactic astronomy observations. The instrument, called GRIP (Gamma Ray Imaging Payload), is designed for measurements in the energy range from 30 keV to 5 MeV with an angular resolution of 0.6° over a 20° field of view. Distinguishing characteristics of the telescope are a rotating hexagonal coded-aperture mask and a thick NaI scintillation camera. Rotating hexagonal coded-apertures and the development of thick scintillation cameras are discussed in *Cook et al.* [1984 and 1985, referred to as Papers I and II respectively].

2. Instrument Description. The basic elements of GRIP are shown in Figure 1. The telescope consists of a shielded detector system separated by 2.5 m from a lead coded-aperture mask. The primary detector is a position-sensitive scintillator which records the characteristic spatial pattern of photons cast by a γ-ray source through the mask.

The mask is made of lead hexagons 2 cm thick and 2.5 cm across (flat-to-flat), supported by an Al honeycomb sandwich which is transparent at γ-ray energies. The aperture contains 2000

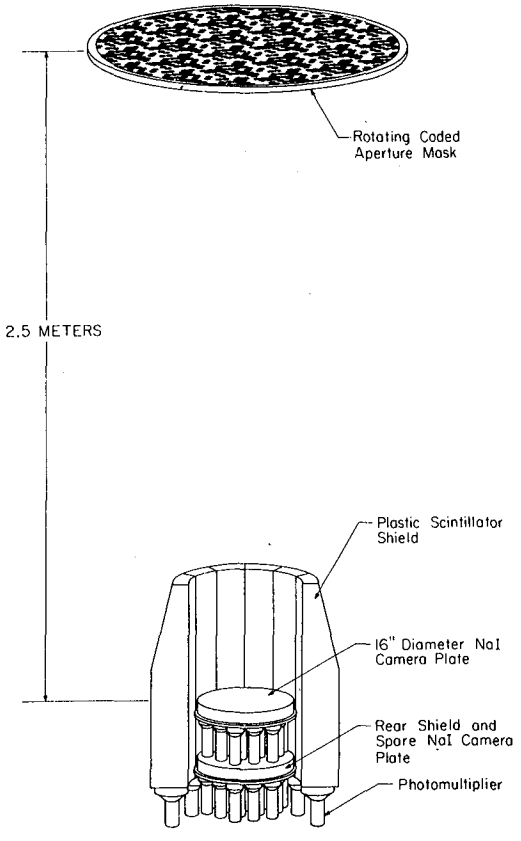

Figure 1.

Table I: **GRIP Balloon Telescope**

Primary Detector	41 cm x 5 cm NaI Anger Camera Position Resolution: < 5 mm rms (0.1-5 MeV)
Shield	Back Plate: 5 cm NaI Side: 16 cm plastic scintillator
Mask	Hexagonal URA: 2000 cells (2.5 cm) Rotation Rate: 1 rpm Spacing: 2.5 m from NaI detector Size: 1.2 m diameter x 2 cm (Pb)
Energy Range	0.03 - 5 MeV
Energy Resolution	8.3 keV FWHM @ 50 keV 70 keV FWHM @ 1 MeV
Imaging	Resolution: 0.6° (1070 pixels in 20° FOV) Angular Localization: 3 arc min (10σ source)

hexagonal cells of which half are open and half contain a lead hexagon. The cell pattern (see Figure 2) forms a hexagonal uniformly redundant array (HURA) that is optimal for coded-aperture imaging. HURA's are discussed in more detail in Paper I and in paper OG 9.2-1 in these proceedings.

Continuous mask rotation imposes an additional level of coding on the γ-ray signal. Due to the antisymmetry of the coded-aperture pattern under 60 degree rotation (open and closed cells interchange for all but the central cell) the γ-ray signal at each position on the detector is time-modulated with a 50% duty cycle. This feature allows a complete background subtraction to be performed for each detector position once every 20 seconds assuming a 1 rpm rotation rate. In addition, the continuous rotation permits extension of the field of view to 20 degrees, greatly increasing the number of pixels imaged [Paper I].

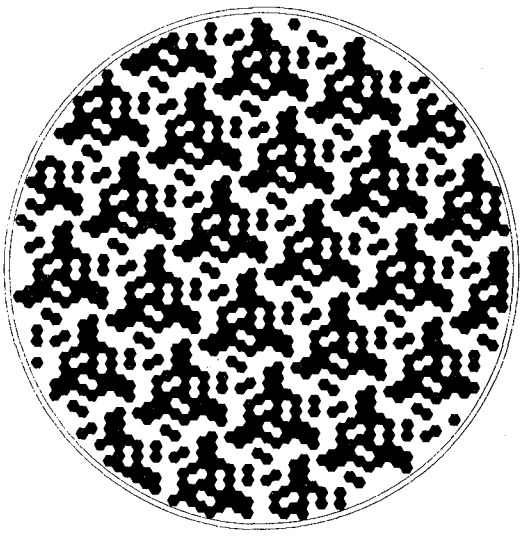

Figure 2.
GRIP coded-aperture mask pattern.

The primary detector is a NaI(Tl) camera plate 41 cm in diameter and 5 cm thick manufactured by the Harshaw Chemical Co. The NaI is viewed by nineteen 3 inch Hamamatsu R1307 photomultiplier tubes (PMT's) which are individually pulse height analyzed. The PMT gains are calibrated continuously using pulsed LED's for short term relative gain calibration and an ^{241}Am tagged γ-ray source for long term absolute gain calibration. The ^{241}Am source is situated 1 m above the coded-aperture mask and can be imaged continuously during flight, allowing a thorough checkout of the mask-detector imaging system.

Background suppression is provided by an anti-coincidence shield. On the side are 12 plastic scintillator modules which form a cylinder ~16 cm thick. Each module is viewed by a single 5 inch Hamamatsu R1416 PMT. The lower shield section is a NaI camera plate identical to the primary sensor. Further background suppression is provided by the primary scintillation camera itself. The PMT pulse heights contain information on the depth of the interaction in the crystal. Thus the lower half of the detector can be used as an effective "integral shield" for the reduction of background at low energies [Paper II].

The telescope is mounted on an elevation pointing platform suspended from an azimuthal torquing system. Azimuthal stabilization and orientation are achieved using active magnetometer feedback to the azimuthal torque motor. Elevation orientation is under command control. Two Schonstedt MND-5C-25 magnetometers provide 2-axis aspect information accurate to 1.5 arc minutes. This aspect information is recorded in the telemetry stream and allows correction of the event positions for pointing inaccuracies such as displacement and rotation of the telescope field of view.

For the initial flight of GRIP, we will record all nineteen 12 bit PMT pulse heights for each event. Event rates of up to 5×10^3/s are possible and consequently a data recording system with a 1 Mbit/s data rate is required. We have developed a 1.4 Mb/s recording system with 25 Gbyte capacity using commercial VCR's and audio digitizers. This development is described in paper OG 9.3-11 in these proceedings.

The characteristics of the instrument are summarized in Table I.

3. Instrument Performance.

Position and Energy Resolution: The GRIP scintillation camera has been designed to have ~1 cm FWHM or better position resolution over an energy range from 100 keV to 5 MeV. Figures 3a

and 3b show histograms of γ-ray event positions computed by a maximum likelihood method for beams of photons of 122 keV (^{57}Co) and 662 keV (^{137}Cs) incident on the center of the detector [Paper II]. At the lower photon energy, the 10.5mm FWHM of the distribution is dominated by photon statistics. At the higher photon energy, both Compton scattering and photon statistics contribute to the 7.0mm width of the distribution. The effect of Compton scattering is most noticeable in the extended non-Gaussian tails of the distribution.

Although the standard deviation of the distribution of computed event positions increases with energy, the FWHM of the distribution continues to narrow due to an increase in the yield of optical photons per γ-ray event [Paper II]. As a consequence, the point-source angular resolution of the GRIP telescope improves with energy. The primary effect of Compton scattering is a reduction in sensitivity due to a removal of events from the core to the tail of the position distribution.

The energy resolution of the GRIP scintillation camera is comparable to that of single PMT NaI detectors. We have measured a resolution of 7% FWHM at 662 keV.

Imaging: Figures 4a and 4b are laboratory images of 122 keV and 662 keV γ-ray sources taken with the fully configured GRIP telescope. The sources were suspended 10m from the coded-aperture mask and the imaging algorithms were adjusted to account for the finite distance to the source. The images demonstrate the ability of the telescope to locate and resolve point sources at γ-ray energies.

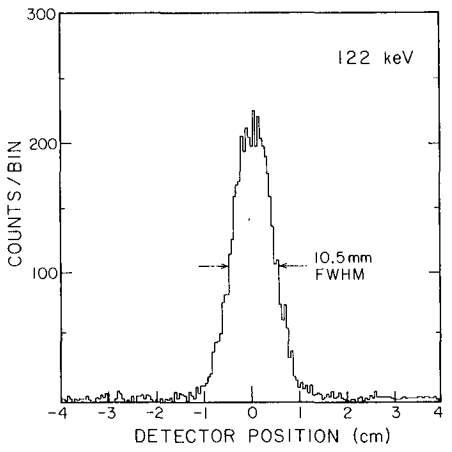

Figure 3a. Histogram of computed event positions showing position resolution at 122 keV.

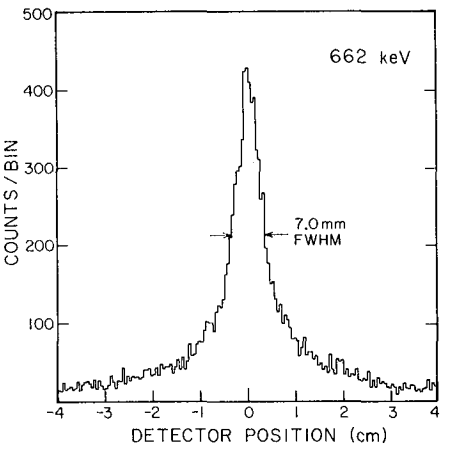

Figure 3b. Histogram showing position resolution at 662 keV.

Effective Area and Sensitivity: The geometrical imaging area of the GRIP scintillation camera is approximately 615cm^2. This area is determined by the maximum radius (~14 cm) for which good position resolution can be maintained. Additional factors determining the imaging effective area are the point-spread position determination function shown in Figure 3, the full energy detection efficiency, and the mask contrast [Paper I]. Figure 5 shows a plot of imaging effective area versus energy for the GRIP telescope.

The instrument sensitivity depends on the observed background which depends on such factors as flight location, zenith pointing angle, shielding, and instrument mass. We estimate our sensitivity to be approximately 1x10^{-5} ph/cm^2 s kev at 100 keV and 1x10^{-6} ph/cm^2 s kev at 1 MeV for a 3σ 8 hour observation from equatorial latitudes.

4. Flight Plans. The GRIP telescope is scheduled for an initial flight from Palestine, Texas in Fall 1985. Observing targets include the Cygnus region, NGC4151, and the Crab region. Future flights are anticipated from both the northern and southern hemispheres.

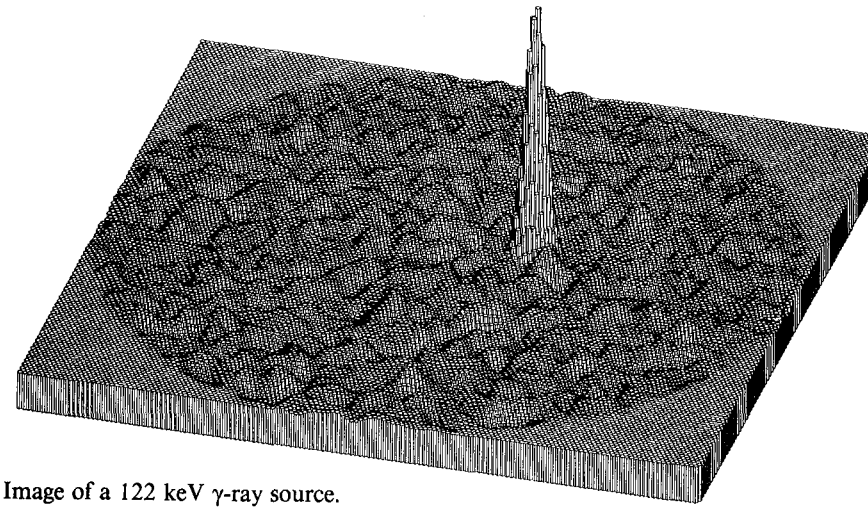

Figure 4a. Image of a 122 keV γ-ray source.

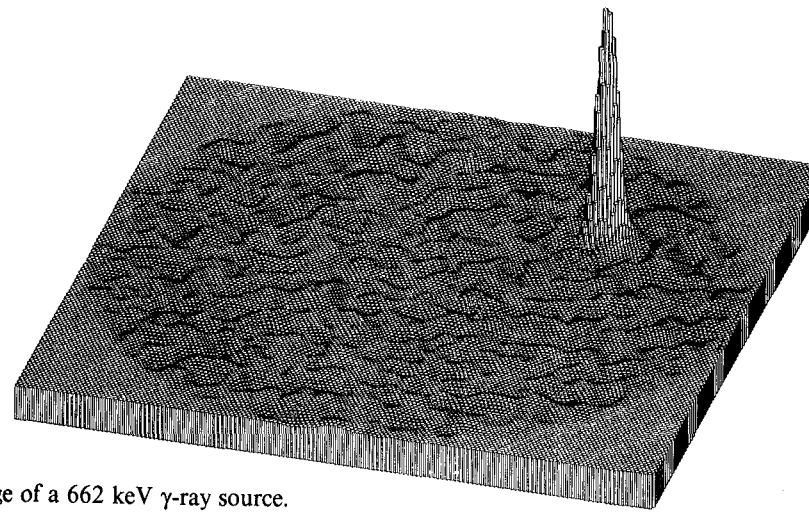

Figure 4b. Image of a 662 keV γ-ray source.

5. Acknowledgments. We thank R. E. Vogt for contributions to this project. This work is supported in part by NASA grant NGR 05-002-160.

6. References

Cook, W.R., Finger, M., Prince, T.A., and Stone E.C., *IEEE Trans. Nucl Sci.*, **NS-31**, 771(1984).

Cook, W.R., Finger, M., and Prince, T.A., *IEEE Trans. Nucl. Sci.*, **NS-32**, 129(1985).

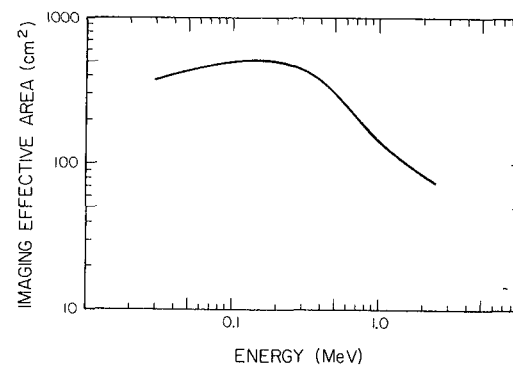

Figure 5. Effective area of the GRIP telescope taking into account position resolution, full-energy detection efficiency, and mask contrast.

A CODED APERTURE IMAGING SYSTEM OPTIMIZED FOR HARD X-RAY AND GAMMA RAY ASTRONOMY

N. Gehrels[1], T. L. Cline[1], A. F. Huters[3], M. Leventhal[2], C. J. MacCallum[3], J. D. Reber[1,4], P. D. Stang[3], B. J. Teegarden[1], and J. Tueller[1]

1. NASA/Goddard Space Flight Center, Greenbelt, MD 20771
2. AT&T Bell Laboratories, Murray Hill, NJ 07974
3. Sandia National Laboratories, Albuquerque, NM 87185
4. SUNY/Geneseo, NY 14454

ABSTRACT

A coded aperture imaging system has been designed for the Gamma-Ray Imaging Spectrometer (GRIS). The system is optimized for imaging 511-keV positron-annihilation photons. For a galactic center 511-keV source strength of 10^{-3} $cm^{-2}s^{-1}$, the source location accuracy is expected to be $\pm 0.2°$.

1. Introduction Current gamma-ray spectrometers observing in the 70 keV to 10 MeV nuclear-line energy range have poor source localization capabilities. They typically have broad fields of view (~ 10° FWHM) and no imaging systems. Recent discoveries of a number of gamma-ray sources with lines in their spectra (1,2,3) have increased interest in building spectrometers capable of mapping the source regions. An example is the positron annihilation line at 511 keV from the direction of the galactic center, whose location is known only to within ±4° (4). This large error circles several galactic-center X-ray sources in addition to the compact radio source Sgr A near the dynamic center of the galaxy. Localizing the line emission is currently one of the major goals in gamma-ray line astronomy.

The most promising technique for mapping in this energy range is coded aperture imaging using Uniformly Redundant Arrays (URAs). The basic idea is to place an array of blocking elments in the instrument aperture whose pattern is chosen such that the shadows cast on the detectors by sources at different locations in the field of view (FOV) give linearly independent sets of detector signals (5). The signals measured during an observation can then be uniquely deconvolved to give maps of the sky. Several papers have been written (6-10) discussing the application of coded aperture imaging to low-energy gamma-ray astronomy.

We are currently building a balloon-borne spectrometer to be flown in fall 1986 called the Gamma-Ray Imaging Spectrometer (GRIS) that will have a URA imaging system. In this paper we describe the imaging system and present the results of laboratory and computer simulations of its performance. A general description of the GRIS instrument is given in a companion paper (11).

2. Description of the Imaging System The Ge detectors in the GRIS instrument are located in every other cell of a 7.5 cm lattice as shown in Figure 1. The mask is a URA with a 3x5 element unit cell. It is located 1.5 m above the detectors and is arranged on a 7.5 cm grid. The

opaque elements are individual NaI blocks 6.8 cm square by 7.6 cm thick, each viewed by its own photomultiplier tube. Calculations and simulations we performed during the instrument design phase showed that it was essential for the mask to be active in order to achieve low levels for the instrumental line background at 511 keV and the continuum background over the entire spectrum.

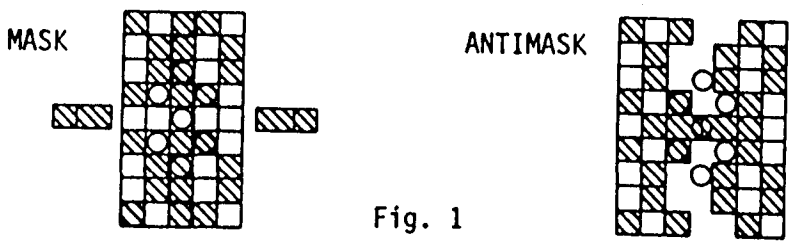

Fig. 1

Another feature of the GRIS imaging system that is essential for high-background observations is the ability to alternate between mask and antimask (see, e.g., ref. 7). The antimask is the complement of the mask, having opaque elements where the mask is open and vice versa. The incident gamma-ray flux is therefore square-wave modulated by the alternation, which is the optimum modulation for background subtraction. Normally mask-antimask systems have a separate structure for both the mask and antimask, each of which move in and out of the field of view. By a novel technique that reduces instrument weight and size, the GRIS mask is itself converted into its own antimask as illustrated in Figure 1. The mask divides into halves while two independent elements rotate into the center.

Both the mask and antimask also move as units left and right one cell so that a detector is located under each of the 15 elements in the mask unit cell at least once. In this way the 7-detector GRIS array is made to act like a 15-detector array in terms of its imaging capability. To produce a map, the mask system moves through 6 positions (3 mask, 3 antimask).

The maps produced by the imaging system have 15 sky bins arranged in a 3x5 matrix. The bins are each 3° square as determined by the mask cell size and the detector-mask separation. The region mapped is therefore 9°x15°. As will be shown below, this bin size and mapping region are a good match for the hard X-ray source distribution in the galactic center direction.

3. Imaging Sensitivity and Resolution There is a decrease in sensitivity that all imaging systems suffer compared with non-imaging wide FOV systems which occurs when a source is not in the center of a sky bin. This is due to the fact that the source signal in the detectors is not fully modulated. The effect can be as large as a factor of 2.2 in sensitivity if the source is at the corner of four bins. To reduce this variation in sensitivity across the map and also increase the number of effective pixels in the final map, we will use an offset pointing technique. The basic idea is that the pointing direction of the instrument is changed between imaging cycles so that a given source appears at

different locations in the different sky maps. By changing the pointing 1° at a time in a 3x3 grid, the 3° sky bins are divided into 1° pixels. The final map then has an approximately uniform sensitivity that turns out for a single point source to be ~1.4 times poorer than a wide FOV instrument. The 3° bin size combined with the finite detector size gives the imaging system a point-spread function FWHM of ~4°.

The localization accuracy of the centroid of a point source image depends on the source strength and the number of sources in the field, but is in general much better than the 4° beam width. For the GRIS mask and detector arrangement operated in the offset pointing mode, the accuracy to which the position of a point source of strength S (photons $cm^{-2}s^{-1}$) can be determined is given by

$$\text{source location accuracy } (1\sigma) \approx 1.4 \quad \theta \frac{\sigma_s}{S} \qquad (1)$$

where θ is the bin size of the mask (3°), and σ_s is the uncertainty in the flux measurement that would occur for a wide FOV observation. For a galactic center 511-keV line flux of 10^{-3} ph $cm^{-2}s^{-1}$ observed by GRIS for 8 hours at 3.5 g cm^{-2} atmosphere depth from Alice Springs, Australia, the value of σ_s/S is better than 1/20. Hence, GRIS will be able to localize the source position to within ±0.2°, which will be more than an order of magnitude improvement over the present best position (4).

4. Laboratory Tests and Computer Simulations A special laboratory test setup of the GRIS imaging system was assembled using NaI detectors in place of the Ge array and Fe and Al mask elements in place of the NaI elements. The detector and mask geometries were similar to those of GRIS except that the laboratory detector-mask separation was 45 cm instead of 1.5 m. This gives 9° sky bins, and was done to reduce the effects of the nonparallel gamma-ray beam produced by the radioactive source used in the laboratory. An ^{241}Am source was located 10 m from the detectors on a large, precise x-y positioning system. Figure 2 shows a map generated in the laboratory of a single on-axis source. The 9 offset pointing maps were combined into a final map with 3° pixel size (three times GRIS). The laboratory data were taken with very high statistical significance (~.1%) and then noise was added to the detector signals by computer. The noise level was chosen such that each unblocked detector signal was a 1.7σ measurement. This corresponds to a measurement of total significance $\sigma_s/S = 0.06$ in Equation (1).

To better understand the mapping capabilities of the GRIS imaging system, a computer simulation of the galactic center was performed. The computer simulation assumed a full 8-hour observation with GRIS of the 20-80 keV X-ray range from Alice Springs. Included in the galactic center direction were the 3 strongest sources (GX1+4, GCX-1, and GX5-1), with intensities assumed to be those measured by HEAO A4. In order to make the simulation as realistic as possible the data were "taken" using offset pointing, rotation of the image in the FOV, different length mask-antimask intervals during transit, and the expected instrumental background (12). Figure 3 shows the results, with the three sources clearly resolved.

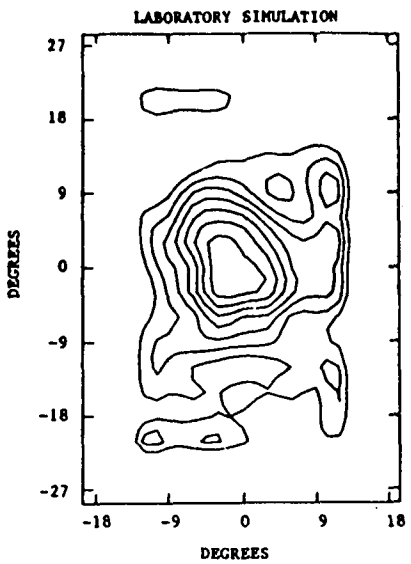

Fig. 2

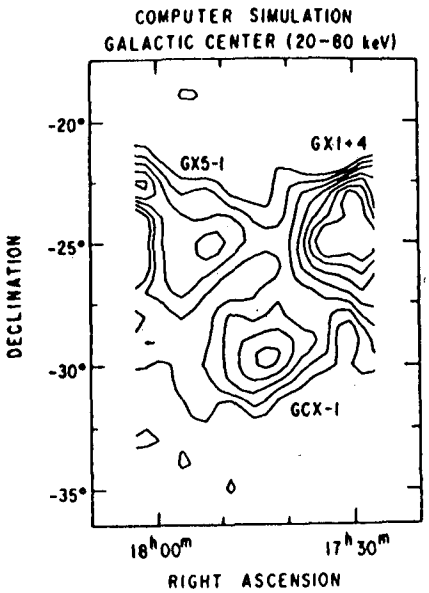

Fig. 3

References

1. M. Leventhal, et al., Ap. J. 225, L11, 1978.
2. R. C. Lamb, et al., Nature 305, 37, 1983.
3. W. A. Mahoney, et al., Ap. J. 286, 578, 1984.
4. G. R. Riegler, et al., Ap. J. 248, L13, 1981.
5. E. E. Fenimore and T. M. Cannon, Applied Optics 17, 337, 1978.
6. G. Di Cocco, et al., IEEE Trans. Nucl. Sci. NS-31, No. 1, 771, 1984.
7. M. L. McConnell, et al., IEEE Trans. on Nucl. Sci NS-29, No. 1, 155, 1982.
8. R. Kroeger and D. Muller, 18th ICRC, Vol. T, 1, 1983.
9. J.-P. Roques and G. Debousy, 14th Inter. Symp. on Space Tech. and Sci., Tokyo, p. 1523, 1984.
10. W. R. Cook, et al., IEEE Trans. Nucl. Sci. NS-31, No. 1, 771, 1984.
11. B. J. Teegarden, et al., 19th ICRC, 1985.
12. N. Gehrels, to be published in Nucl. Inst. Meth., 1985.

THE GAMMA-RAY IMAGING SPECTROMETER (GRIS): A NEW BALLOON-BORNE EXPERIMENT FOR GAMMA-RAY LINE ASTRONOMY

B. J. Teegarden, T. L. Cline, N. Gehrels,
G. Porreca, J. Tueller
NASA/Goddard Space Flight Center
Greenbelt, MD 20771

Marvin Leventhal
ATT/Bell Laboratories

A. F. Huters, C. J. MacCallum and P. D. Stang
Sandia National Laboratories

1. INTRODUCTION High resolution gamma-ray spectroscopy is a relatively new field that holds great promise for further understanding of high energy astrophysical processes. Preliminary results such as the annihilation radiation from the galactic center (Leventhal et al. 1978; Riegler et al. 1981), the ^{26}Al line from the galactic plane (Mahoney et al. 1984) and cyclotron lines from neutron stars (see e.g. Trumper et al. 1978) may well be just the initial discoveries of a rich and as yet undeveloped field. When the high resolution gamma-ray spectrometer (GRSE) was removed from the GRO payload NASA decided to initiate a balloon program to permit continued development and improvement of instrumentation in this field, as well as continued scientific observations. The Gamma-Ray Imaging Spectrometer (GRIS) is one of the experiments selected as part of this program. The instrument contains a number of new and innovative features that are expected to produce a significant improvement in source location accuracy and sensitivity over previous balloon and satellite experiments.

2. EXPERIMENT DESCRIPTION The basic instrument consists of an array of seven coaxial n-type germanium detectors surrounded by a thick active NaI shield/collimator. Located above this assembly is an active NaI coded-aperture mask for imaging and precise source location. The instrument performance is summarized in Table 1, and the central (pointed) section shown in Figure 1. The seven germanium detectors are each enclosed in individual cryostats. This design (rather than a single large multi-detector cryostat) was chosen for two principal reasons: 1) minimization of internally produced background (to be discussed in more detail later) and 2) ease of replacement of individual detectors, as well as upgrades and modifications.

A new concept has been introduced in the design of the germanium detectors wherein the cathode (outer surface layer) is divided into segments. The active germanium volume is therefore effectively divided into a stack of pancake-shaped detectors each ~1 cm thick. This takes advantage of the fact that over most of the relevant energy range the majority of photons undergo more than one interaction before they deposit all of their energy in the germanium crystal. Furthermore, the great majority of the background events over this same energy range are single point interactions. The resultant background suppression and improvement in sensitivity will be discussed later in more quantitative terms.

TABLE 1.

SUMMARY OF EXPERIMENT CHARACTERISTICS

Energy Range	0.02 to 10 MeV
Detector Size	6.5 cm dia. x 6.5 cm length nominal (Up to 7.5 cm detectors can be accomodated if available.)
Total Detector Area	232 cm^2 (309 cm^2 for 7.5 cm detectors)
3 Sigma Narrow Line Sensitivity	4.6×10^{-5} cm^{-2}-sec^{-1} at 60 keV 1.4×10^{-4} cm^{-2}-sec^{-1} at 511 keV 4.8×10^{-5} cm^{-2}-sec^{-1} at 2 MeV
Fields-of-view	20° FWHM coarse 3° x 3° FWHM fine 9° x 15° imaging
Imaging Pt. Spread Function (FWHM)	4°
Source Location Accuracy	± 0.2° for f = 10^{-3} cm^2-sec^{-1} at 511 keV
Pointing Accuracy and Stability	± 0.1°
Experiment Power	233 W
Experiment Weight	1500 kg
Telemetry Rate	56 K bits/sec

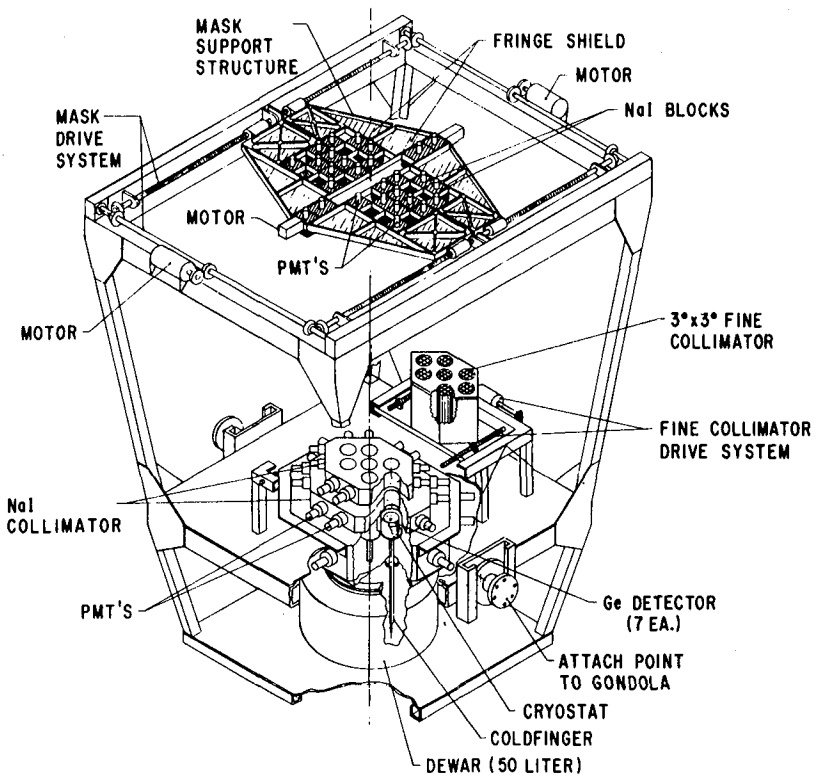

Fig. 1. GRIS pointed section.

The germanium detector array is cooled conventionally by a LN_2 dewar located beneath the detectors. NaI polyscin was chosen for the shield because of a) its relatively low cost, b) its high light output which allows a low threshold to be set and c) its fast response time which results in a lower overall shield dead time.

An active, uniformly-redundant mask system is used to generate sky maps

Fig. 1. GRIS pointed section.
over a $9^0 x 15^0$ field-of view. A detailed descripion if the GRIS imaging system is presented elsewhere in these proceedings (Gehrels et al. 1985). The mask is constructed from blocks of NaI scintillator since a passive mask would result in an unacceptably high 511-keV background. We have chosen a mask/antimask configuration for this experiment since it provides a direct unambiguous determination of the instrument background. We have discovered a unique method whereby the mask can be converted into its own antimask by a simple motion of components. This reduces the total amount of scintillators required by approximately a factor of two. The system is designed such that the mask can be completely removed from the 20^0 FOV defined by the NaI collimator. In this configuration the instrument will operate in the usual on-source/off-source mode. This mode will be used in observations where the ultimate instrument sensitivity is required as well as for observing the diffuse galactic plane emission.

A passive fine collimator has been included for observing single isolated hard X-ray sources. Its primary purpose is to reduce the diffuse x-ray contribution to the overall background. It can be moved in and out of the field-of-view during the flight to allow maximum flexibility of the observing program. When it is in place the mask is moved out of the FOV.

A conventional azimuth-over-elevation pointing system with a momentum wheel for azimuth control will be used. Coarse pointing control will use the earth's magnetic field as a reference. A CID camera will be used to image star fields and the sun to obtain an independent and more accurate measure of the absolute pointing direction. The system is expected to have an overall accuracy and stability of $\sim \pm 0.1^0$.

3. INSTRUMENT BACKGROUND AND SENSITIVITY Extensive modelling of the GRIS instrumental background has been performed (Gehrels 1985). The primary sources of this background are:

Continuum

1) Diffuse X-ray and atmospheric background photons entering through the experiment aperture.
2) Elastic collisions of secondary neutrons with Ge nuclei.
3) Beta-decay from cosmic-ray induced radioactivity in the Ge detectors.
4) Leakage of high energy atmospheric background photons through the shield.

Lines

1) De-excitation of nuclei in the Ge detectors that have been excited by primary cosmic rays and secondary neutrons.
2) $Beta^+$-decay of excited nuclei in the passive material surrounding the Ge detectors.
3) Pair-production due to high-energy atmospheric background photons interacting in the passive material surrounding the Ge detectors.

The effect of atmospheric gamma rays has been modelled using a Monte

Carlo program. A complete analysis of the effect of all possible cosmic-ray interactions has been carried out. This has involved examining ~ 2000 different interaction channels. These calculations have led to a number of key results that have had a profound effect on the design of the GRIS experiment. These are summarized as follows:

1) Nearly all of the important beta-decays go into the ground state. This means that there is no accompanying gamma-ray and that the energy deposition in the Ge is localized. Rejection of single-point interactions will therefore produce a significant supression of the continuum background.

2) Passive material inside the shield and in the FOV is a significant contributor to the background. This has led to the choice of an active mask and to a minimal-mass cryostat design.

3) The shield thickness and threshold are critical. This has lead to the choice of NaI for the shield.

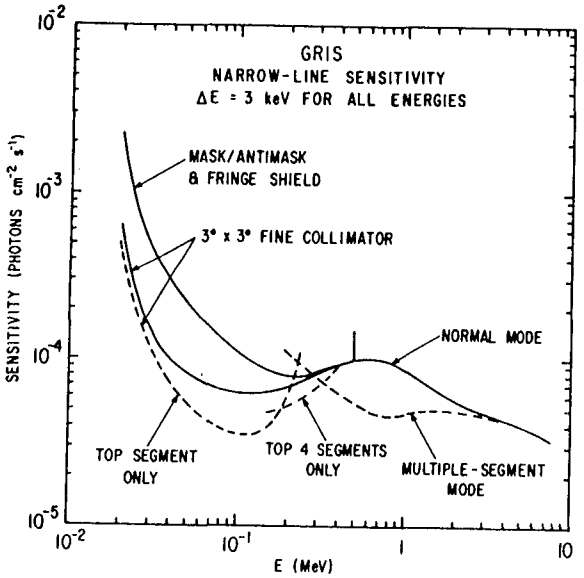

The results of these calculations have been compared with previous balloon results and found to be in excellent agreement. The resultant sensitivities are plotted in Fig 2. and represent typically a factor of ~5 improvement over the best previous balloon and satellite measurements.

Fig. 2. GRIS narrow line sensitivity. Cases for different segment requirements are shown.

4. REFERENCES

1. Gehrels N. 1985, Nuclear Instruments and Methods,
2. Gehrels, N., Cline, T. L. Reber, J. D., Teegarden, B. J., Tueller, J., Leventhal, M., Huters, A., MacCallum, C., and Stang, P. D. 1985, these proceedings.
3. Leventhal, M., MacCallum, C. J. and Stang, P. D. 1978, Ap J., 225, L11.
4. Mahoney, W. A., Ling, J. C., Wheaton, W. A. and Jacobson, A. S. 1984, Ap. J., 286, 578.
5. Riegler, G. R., et al., 1981, Ap. J., 248, L13.
6. Trumper, J., Pietsch, W., Reppin, C., Voges, W., Staubert, R. and Kendziorra, E. 1978, Ap. J., 219, L105.

MODELING A HIGH ENERGY GAMMA-RAY TELESCOPE

T.L. Jenkins, G.M. Frye, Jr., C.J. Hall, A. Owens, G.N. Pendleton
Case Western Reserve University
Cleveland, Ohio 44106, U.S.A.

J.N. Carter, D. Ramsden
Department of Physics
Southampton University
Southampton SO9 5NH, United Kingdom

B. Agrinier
Service d'Astrophysique
C.E.N. Saclay, 91191 Gif-sur-Yvette, France

1. Introduction. We have developed a Monte Carlo program to simulate a high energy gamma-ray telescope using a coded aperture mask (CAMTRAC). The ultimate purpose of the calculation will be to determine the optimum design parameters for such an instrument. The model can also used to ascertain under what conditions CAMTRAC performance is superior to that of conventional telescopes which employ electron-positron pair direction as the sole means of determining gamma ray direction.

2. Procedure. The CAMTRAC telescope is assumed to consist of a coded aperture mask below which is located a position sensitive gamma-ray detector. It is assumed that an energy measurement is made for each converted photon. The model telescope is characterized by the following parameters:

an energy dependent gamma-ray conversion efficiency,

an energy dependent point spread function (PSF) for the determination of the gamma-ray direction from the pair direction,

an energy dependent PSF for the measurement of the gamma-ray conversion point in the detector plane,

a mask pattern, cell size and distance of the mask from the detector plane,

an energy dependent transmission for the opaque cells in the mask,

a resolution function for the energy measurement made on individual converted photons.

The source of photons is characterized by:

the integrated number of photons incident on the detector from a point source,

the integrated number of photons per unit solid angle incident on the detector from a uniform background,

an energy spectrum for both point source and background photons which varies as E^{-2}.

A computational run consists of generating a set of data and then analyzing it to determine whether or not a point source is apparent in the data set and, if so, to determine its position. The analysis method used is an adaptation of the maximum likelihood method used by A.M.T. Pollock, et al.(1) to search for extragalactic point sources in the COS-B data. In our application of this method, the likelihood function,

$$W(\underline{r},X) = \sum_i \ln[S(\underline{r} - \underline{R}_i;E_i)T(E_i)X + (1-X)/\Omega\ ]$$

is formed for each of several hundred points in a selected region of the sky about seven degrees in diameter. The summation is made over all events in the data set. $\underline{r}$ is the angular position of the point on the celestial sphere where the function is being evaluated, $\underline{R}_i$ is the point on the sphere to which the gamma ray pair direction is pointing for event i, E_i is the measured energy of the photon, and $S(\underline{r}-\underline{R}_i;E_i)$ is the normalized angular PSF. $T(E_i)$ is the mask transmission if the event in question lies in the shadow of an opaque portion of the mask for a photon coming from position $\underline{r}$ in the sky, otherwise it is 1. X is the fraction of the set of events in the data that originate from a point source as opposed to background. Ω is the solid angle subtended by that portion of the sky from which the data set is drawn. The argument of the logarithm in the summation is the probability of observing the event i if there is a point source at position $\underline{r}$, from which a fraction X of the events originate. At each point, $\underline{r}$, the maximum in $W(\underline{r},X)$ is determined in the range $0 < x < 1$. The difference between this maximum and $W(\underline{r},0)$, called λ in reference 1, is the quantity whose maximum is sought in the region of the sky searched. The position of this maximum could be considered to be the point that has a maximum probability of containing a source.

To compare the CAMTRAC system to a conventional telescope, the same calculation can be performed without a mask. In this case, the procedure used for calculating the point source position is exactly the same as that used for the CAMTRAC case except that the factor $T(E_i)$ is replaced by 1 in the expression for $W(\underline{r},X)$. The CAMTRAC telescope will detect fewer photons for a given incident flux because of absorption by the mask. In addition, the decoding process implicit in any algorithm that searches for the mask shadow in the distribution of conversion points introduces noise in the likelihood function, $W(\underline{r},X)$. This noise is worse when the number of point source photons is small.

2. Results. The table below shows the source location accuracy, expressed as r.m.s. error in source location, for two different levels of background and four point source intensities. The intensities are expressed as the total number of photons incident on the telescope above 10 MeV. As can be seen, the CAMTRAC detector has a source location accuracy superior to the conventional telescope by a factor of three in those cases where the point source intensity is most intense. The maximum point source intensity given in the table corresponds to a source of approximately the intensity of the Crab exposed to a detector one square meter in area for four hours. The greater of the two background levels corresponds approximately to the background that one would experience from the diffuse galactic radiation in the anti-center region under the same conditions of exposure. The statistical error in the computed values shown in the table is 15 to 25%.

R.M.S. SOURCE LOCATION ACCURACY, MINUTES OF ARC

	CAMTRAC		CONVENTIONAL	
Background (ph/sr) = Source (ph)	1.2×10^5	0.6×10^5	1.2×10^5	0.6×10^5
5000	1.4	1.7	4.3	5.2
2500	5.6	4.4	7.0	8.9
1250	32.6	48.0	19.2	14.8
625	85.0	90.8	64.9	63.1

4. Conclusions. A simple model is used in this simulation and the variables of the CAMTRAC system have not been optimized. However, the results show that the coded aperture mask system holds the promise of greatly improving the accuracy of locating point sources of gamma rays. In addition, it can be expected to improve the resolution of structure in extended sources of gamma rays.

5. Acknowledgements. This work was supported by grant NAGW-451 from the U.S. National Aeronautics and Space Administration.

(1) A.M.T. Pollock, G.F. Bignami, W. Hermsen, G. Kanbach, G.G. Lichti, J.L. Masnou, B.N. Swanenburg, and R.D. Wills, (1981) Astron. Astrophys. 94, 116

SECONDARY GAMMA-RAY PRODUCTION IN A CODED APERTURE MASK.

A. Owens, G.M. Frye, Jr., C.J. Hall, T.L. Jenkins, G.N. Pendleton.
Case Western Reserve University, Cleveland Ohio 44106, U.S.A.

J.N. Carter, D. Ramsden,
Southampton University, Southampton SO9 5NH, U.K.

B. Agrinier, E. Bonfand, C. Gouiffes, A. Tabary,
Section d'Astrophysique, Centre d'Etudes Nucleâires de Saclay, France.

1. Introduction. The application of the coded aperture mask to high energy γ-ray astronomy will provide the capability of locating a cosmic γ-ray point source with a precision of a few arc-minutes above 20 MeV (1). Recent tests using a mask in conjunction with drift chamber detectors have shown that the expected point spread function is achieved over an acceptance cone of 25^0 (2). A telescope employing this technique differs from a conventional telescope only in that the presence of the mask modifies the radiation field in the vicinity of the detection plane. In addition to reducing the primary photon flux incident on the detector by absorption in the mask elements, the mask will also be a secondary radiator of γ-rays. In this paper we consider the various background components in a CAMTRAC (Coded Aperture Mask Track Chamber) telescope and compare Monte-Carlo calculations with recent measurements obtained using a prototype instrument in a tagged photon beam line. This instrument is described elsewhere in this conference (3).

2. Secondary Background Production in a Mask. There are several mechanisims by which photons may be generated in a mask. Charged particles may generate γ-rays via bremsstralung, π^0-production or spallation in the mask material. By using veto counters, in front of and behind the mask, it is estimated that the contribution due to these components will be $< 10^{-5}$ γ's per incident particle, and therefore they can be neglected. Neutron interactions in the mask may produce secondary γ's through neutron capture or inelastic scattering. Butler et al. (4) have shown that this component is negligible, being $< 10^{-6}$ γ's per incident neutron for photon energies above 10 MeV. Gamma-rays incident on a mask may Compton scatter, or produce pairs within the mask material, that generate secondary photons by bremsstralung of the first generation electron(s), or (if an electromagnetic cascade is induced) by the secondary electrons. This component is potentially the most troublesome since in some of these

interactions none of the electrons will reach the veto counters.

3. Monte-Carlo Calculations. Monte-Carlo calculations have been carried out using the EGS electron-photon transport code of Ford and Nelson (5). Mono-energetic photons were allowed to fall normally on lead slabs of various thicknesses and the secondary photon and electron energy and radial distributions recorded. These distributions were found to agree, within statistical uncertainty, with those derived using the calculations of Messel and Crawford (6) and the experimental data of Darriulat et al. (7) In Fig. 1 we consider the various components that emerged from a 2.73 RL tungsten slab as a function of incident photon energy. A secondary photon threshold of 12.5 MeV was assumed in the calculations, this value being representative of the lower limit of our telescope. The various contributions arise as follows; F_1 is the transmitted component (i.e. $F_1 = e^{-\mu(E)t}$ where $\mu(E)$ is the linear attenuation coefficient of the mask material and t is the mask thickness), F_2 is the fraction of incident photons that generated secondary γ-rays, F_3 is the fraction of incident photons in which secondary γ-rays were also accompanied by an electron with a kinetic energy > 1 MeV, and F_4 is the fraction of incident photons that produced secondary γ-rays and no electron > 1 MeV that left the slab. Therefore $F_2 = F_3 + F_4$. A scintillation counter placed immediately behind the slab will veto component F_3, and thus F_4 represents the intrinsic secondary background due to the mask. The energy spectrum of the unvetoed secondary component, integrated over 2π steradians, was found to be well represented by the empirical function;

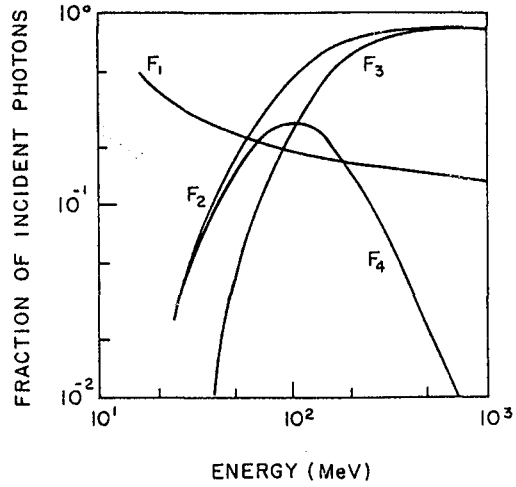

Fig. 1 The fraction of the various classes of events emitted from a 2.73 RL tungsten slab as a function of incident photon energy. Refer to the text for the definition of the symbols used.

$$dN(E,\bar{E}) = 3.79 \times 10^{-2}\, E^{0.96}\, \bar{E}^{-a}\, \exp(-1.054 \times 10^{-2} E) \times \exp(-47.17\, \bar{E}\, E^{-1.55})\, d\bar{E} \quad \gamma\text{'s / incident photon MeV} \qquad (1)$$

where $a = \begin{cases} 0.843 + 3.6 \times 10^{-3} E - 6.3 \times 10^{-6} E^2, & 20 \leq E \leq 400 \text{ MeV} \\ 1.29, & E > 400 \text{ MeV} \end{cases}$

and E and $\bar{E}$ are the incident and secondary γ-ray energies respectively. By comparison with Monte-Carlo data it is estimated that the average error in $dN(E,\bar{E})$, determined by Eq. 1, is < 10% over the incident energy range 20 to 600 MeV and secondary energies $1 < \bar{E} < E$.

In Fig. 2 we consider the case for a spectrum varying as E^{-2} normally incident on a mask consisting of equal open and opaque elements. The various components are shown separately integrated over 2π steradians. The band in the Fig. encompasses single and multiple secondary photon emission. For any detection system placed immediately behind the mask the true detector background would lie within these bounds. It can be seen from Fig. 2 that the unvetoed secondary component constitutes < 5% of the incident γ-rays. Further, since this component drops more rapidly than the incident flux ($\sim E^{-3}$ as opposed to E^{-2}) it can be neglected for energies > 200 MeV. It should be noted that for a practical telescope with a mask and a detection area of 1 m^2, separated by 1 m, the measured unvetoed background will be approximately a factor of 1.2 lower than that shown at energies < 20 MeV due to the angular distribution of the secondary γ-rays. The median of this distribution ranges from about 15° to 3° for secondary energies 10 MeV to 200 MeV. Since this is much greater than the angular size of the unit mask cell at the detection plane, the secondary γ-rays will not reproduce the mask pattern, and will therefore constitute an almost uniform background level.

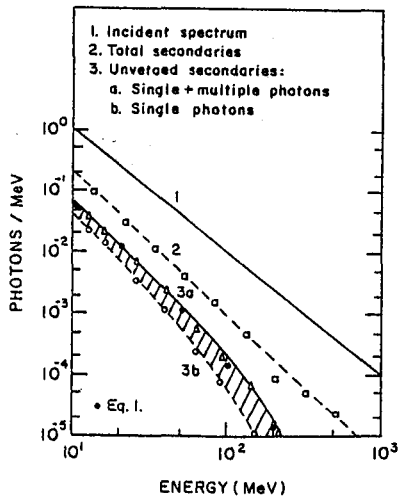

Fig. 2 The various contributions to a detector counting rate for an E^{-2} spectrum normally incident on a tunsten mask of thickness 2.73 RL.

4. Experimental. It can be seen from Fig. 1 that the most efficient production of unvetoed secondary photons occurs for incident γ-ray energies of $\sim$100 MeV. For this reason secondary γ-ray spectra have been measured at a range of incident photon energies ranging from 23 to 400 MeV using a CAMTRAC telescope at the tagged photon facility at CEN Saclay,

France. Here we report preliminary results for normally incident γ-rays of energies 27, 48, 90 and 108 MeV. The mask used during these runs was a 2.73 RL tungsten checkerboard of unit cell size 6.3 mm. A counter in front of the mask vetoed charged particle induced events, while a counter behind the mask tagged those events in which a secondary γ-ray was also accompanied by a charged particle that did not trigger the detector anti-coincidence. A calorimeter located behind the track chamber measured the photon energy with a typical energy resolution of 57% FWHM at 100 MeV. Fig. 3 shows the total secondary spectra measured at various incident energies. These were determined by comparing runs with and without the mask in place. For comparison the results of Monte-Carlo calculations are also shown from which it can be seen there is reasonable agreement. Also shown in Fig. 3 is the spectrum of events for which a charged particle (> 1 MeV) was also detected in the counter behind the mask, from which we conclude that the unvetoed secondary component produced in the mask comprises at worst $\sim 10^{-3}$ γ's per incident photon per MeV.

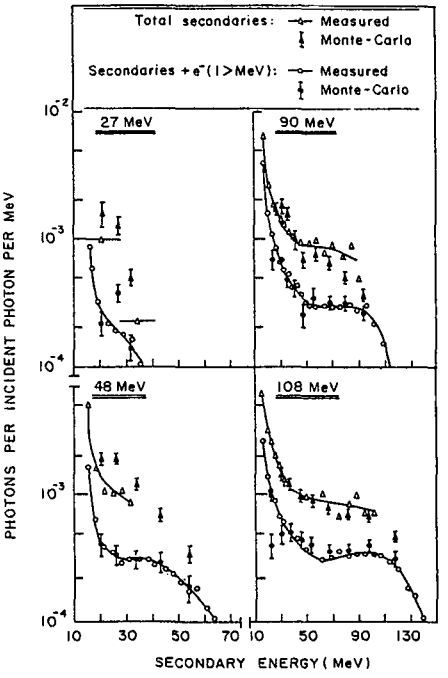

Fig. 3 Experimental and Monte-Carlo secondary γ-ray spectra at various incident γ-ray energies.

5. Acknowledgements. This work was supported by NASA grant NAGW-451 and grants from the SERC.

References

1. Carter, J.N. et al; Mon. Not. R. Astr. Soc., 198 (1982) 33.
2. Frye, G.M., Jr., et al; to be published in the Proc. of the Workshop on the Space Station, LSU (1984).
3. Jenkins, T.L. et al; this conference, paper OG 9.2-7.
4. Butler, R.C. et al; Nucl. Instr. and Meth., 221 (1984) 41.
5. Ford, R.L. and Nelson, W.R.; The EGS code system, SLAC-210 (1978).
6. Messel, H. and Crawford, D.F.; Electron-Photon Shower Distribution Function Tables for Lead, Copper and Air absorbers, Pergamon Press New York (1970).
7. Darriulat, P. et al; Nucl. Instr. and Meth., 129 (1975) 105.

OPERATING CHARACTERISTICS OF A PROTOTYPE HIGH ENERGY GAMMA-RAY TELESCOPE

T.L. Jenkins, G.M. Frye, Jr., C.J. Hall, A. Owens, G.N. Pendleton
Physics Dept., Case Western Reserve University
Cleveland, Ohio 44106, U.S.A.

J.N. Carter, D. Ramsden
Department of Physics, Southampton University
Southampton SO9 5NH, United Kingdom

B. Agrinier, E. Bonfand, A. Refloch, A. Tabary
Service d'Astrophysique, C.E.N. Saclay
91191 Gif-sur-Yvette, France

1. Introduction. The field of gamma-ray astronomy in the energy range from ten to several hundred MeV is severely limited by the angular resolution that can be achieved by present instruments. The identification of some of the point sources found by the COS-B mission and the resolution of detailed structure existing in those sources may depend on the development of a new class of instrument (1). The coded aperture mask telescope, used successfully at X-ray energies (2), holds the promise of being such an instrument. We have operated a prototype coded aperture telescope in a tagged photon beam ranging in energy from 23 to 123 MeV. The purpose of the experiment was to demonstrate the feasibility of operating a coded aperture mask telescope in this energy region. This paper reports some preliminary results and conclusions drawn from some of the data resulting from this experiment.

2. Apparatus and Procedure. The apparatus is illustrated in figure 1. The incident beam passed through a mask, an anticoincidence counter, a position sensitive gamma-ray detector, a time-of-flight (TOF) counter, and a scintillation calorimeter. For the runs reported here, the mask consisted of an array of tungsten blocks, 6.3 millimeters square, arranged in a checkerboard pattern. The blocks were 2.7 radiation lengths thick and produced a spatial modulation of the beam that passed through the mask. The position-sensitive detector consisted of a stack of three drift-chamber modules.

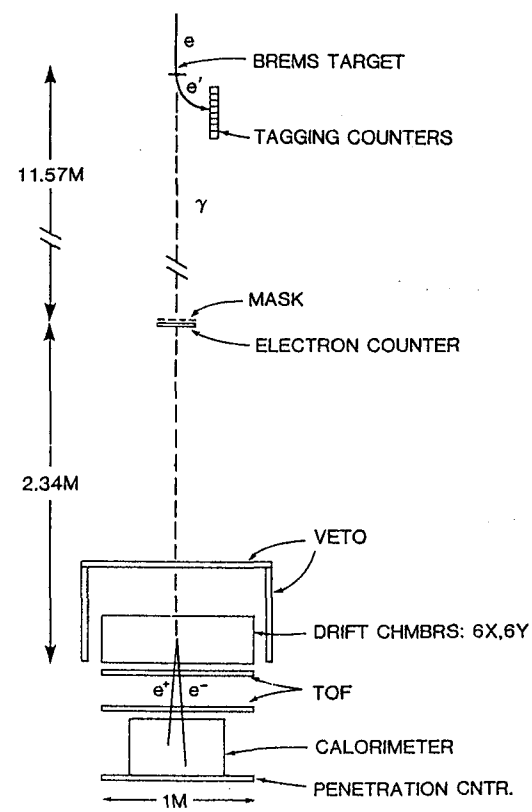

Fig. 1. Diagram of the apparatus.

Each module contained four drift chambers, two for measuring each of the two coordinates orthogonal to the beam. Photons converting in the drift-chamber array produced electron-positron pairs which passed through the remainder of the chambers and into the time-of-flight detector and the calorimeter. Readout of the chambers and calorimeter was initiated by a coincidence of a tagging count and the time-of-flight counters in the absence of a signal from the anticoincidence counter.

The experiment was operated in the low energy hall of the electron linac of the C.E.N. Saclay laboratory. A tagged bremsstrahlung beam was used as the source of photons. Eight tagging channels provided energy identification of individual photons from 52% to 68% of the full electron energy. A signal from one of these tagging channels was required for readout of the experiment. Photon energy bands of 94-119, 78-99, 42-53, and 23-30 MeV were used. The assembly of chambers and associated scintillation counters and calorimeters could be rotated to permit data-taking at angles of incidence up to 40 degrees from the normal. The mask was rotated by the same amount during these runs.

The chambers had active areas of 85 by 85 centimeters. They had 9 millimeter gaps and 4 centimeter drift distances. No provision was made within the individual chambers to resolve the left-right ambiguity but chambers within one module were arranged in a staggered pattern so that the ambiguity could be resolved when observing reasonably straight tracks. The drift field was established by field planes which consisted of printed circuit boards each 1% of a radiation length in thickness on which the field-shaping electrodes had been etched. They were operated on an argon-isobutane mixture with a drift field of 1 kilovolt per centimeter. Pulses from groups of chamber sense wires were discriminated and sent to a set of fast flip-flops which routed the logic pulses alternately to two time-to-digital converter (TDC) channels for each group. This permitted the recording of double hits on a sense wire as might be caused by the passage of a pair of tracks through the chambers. Pulse pair resolution was about 1 millimeter. The TDC's were operated in a CAMAC system which was controlled by a PDP-11/24 computer. TDC data for each reporting sense wire were recorded on magnetic tape along with the tagging channel, and pulse heights from the TOF scintillators and calorimeter.

Prior to the operation of the experiment at the electron linac it was determined that the chambers suffered from a loss of efficiency in the 25% of the drift space farthest from the sense wires. Using cosmic ray muons, it was found that individual track positions had a root-mean-square uncertainty of approximately 1 millimeter.

Following the data taking runs, the TDC data from the events were processed by a pattern recognition and track fitting program. From this came a list of positions of the conversion vertices of individual gamma rays. Approximately 25% of the triggers resulted in a conversion vertex appearing in the fiducial volume of the chamber array. The two-dimensional distribution of vertices could be matched to the checkerboard pattern of the mask. Vertex positions relative to the mask pattern were determined and aggregated to produce a plot of vertex density as a

function of distance across the shadows of the opaque and transmitting mask elements. Figure 2 shows such a plot.

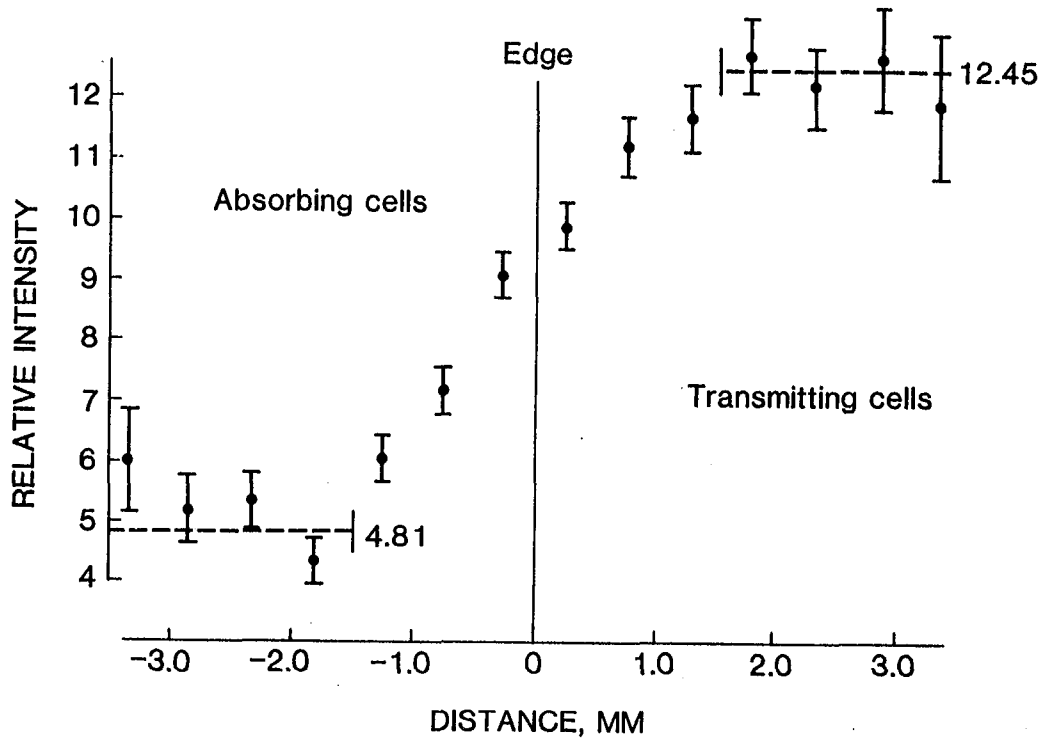

Fig. 2 Vertex density as a function of position within the shadows of opaque (left) and transparent (right) mask elements. The case shown is for 106 MeV photons at normal incidence.

3. Results. We refer to the ratio of vertex density behind the opaque mask elements to that behind the transmitting elements as the modulation ratio. This ratio should be simply the known transmission of the tungsten elements at the photon energy in question. Except under the most favorable conditions, this did not turn out to be the case. The table below shows the modulation ratio for several of the runs and the theoretical ratio.

The increase of the modulation ratio above the theoretical value could be viewed as the result of the addition of a uniform background of events which are not modulated by the mask. We attribute this uniform background predominantly to a population of events that failed to be properly recognized and fitted by the reconstruction program. The unexpectedly low efficiency of the chambers and track error made it difficult, even with manual scanning, to identify the track origins and trajectories with certainty. This problem was exacerbated at low energies where scattering of the tracks was greater. Supporting this supposition, a calculation in which the chamber data were simulated by Monte Carlo methods shows that, as chamber efficiency is diminished and track accuracy decreased, the track recognition and fitting program fails to calculate the vertex

positions to about the degree observed. Furthermore, placing more stringent requirements on the quality of the fit to the experimental data produced a smaller sample of vertex positions but one which showed considerably less of this uniform background. In the table, cases marked with * were those to which this more stringent requirement was applied. Approximately half the events met the requirement.

PHOTON ENERGY (MeV)	INCIDENT ANGLE (Degrees)	MEASURED RATIO	THEORET. RATIO	PHOTON ENERGY (MeV)	INCIDENT ANGLE (Degrees)	MEASURED RATIO	THEORET. RATIO
106	* 0	.287	.225	88	20	.632	.244
106	0	.405	.225	47	0	.598	.276
106	13	.557	.231	47	10	.718	.280
106	* 26	.536	.251	47	20	.751	.293
106	26	.653	.251	26	0	.737	.333
88	0	.474	.229	26	10	.669	.338
88	10	.614	.233				

The error in vertex location for events that were properly recognized can be estimated from the width of the transition region between the shadows of the opaque and transmitting regions. In the case shown in figure 2, the vertex density makes the transition from 25% to 75% of full height over a distance of 1.5 millimeters. If one were to model the vertex position point spread function by a gaussian, this would imply an r.m.s. uncertainty in vertex location of 1.1 millimeters. The table below shows the vertex location accuracy and modulation ratio other energies and angles.

4. Conclusions. We have demonstrated the feasibility of using a coded aperture mask telescope at photon energies higher than used heretofore. In this experiment, the reliability and accuracy of recognizing and fitting tracks was not as great as would be needed for an astronomical instrument. This condition could be improved by increasing the number of chambers used and by improving the efficiency of the chambers.

5. Acknowledgements. We wish to thank A. Veyssiere and the staff of the A.L.S. low energy beam facility for their assistance and cooperation in making these measurements. This work was supported by grant NAGW-451 from the U.S. National Aeronautics and Space Administration and grants from the U.K. Science and Engineering Research Council.

(1) J.N. Carter, D. Ramsden, G.M. Frye, Jr., T.L. Jenkins, R. Koga, (1982) Mon. Not. R. astr. Soc., 198, 33

(2) R.J. Proctor, G.K. Skinner, A.P. Wilmore, (1978) Mon. Not. R. astro. Soc., 185, 745 and D. Cardini, et al., (1983) Astron. Astrophys., 127, 169

AN EXPERIMENTAL ASSESSMENT OF THE IMAGING QUALITY OF THE LOW ENERGY GAMMA-RAY TELESCOPE ZEBRA.

Butler,R.C., Caroli,E., Di Cocco,G., Natalucci,L.
Spada,G., Spizzichino,A. and Stephen,J.B.
Istituto TESRE - CNR, Via De' Castagnoli 1,
40126 Bologna, ITALY.

Carter,J.N., Charalambous,P.M., Dean, A.J., Graeme,G.,
Maggioli,P., Young,N.G.S. and Younis,F.
Physics Department, Southampton University,
Highfield, Southampton, UK.

Boella,G., Perotti,F. and Villa,G.
Istituto di Fisica Cosmica, Milan, ITALY.

La Padula,C., Ubertini,P.
Istituto Astrofisica Spaziali, Frascati, ITALY.

ABSTRACT

One gamma-ray detection plane of the ZEBRA telescope, consisting of nine position sensitive scintillation crystal bars designed to operate over the spectral range 0.2 to 10 MeV, has been constructed in the laboratory. A series of experimental images has been generated using a scaled down flight pattern mask in conjunction with a diverging gamma-ray beam. Point and extended sources have been imaged in order to assess quantitatively the performance of the system.

1. INTRODUCTION. The balloon-borne low energy gamma-ray imaging telescope ZEBRA is designed to operate in the spectral range 0.2 - 10 MeV. A detailed description of the telescope configuration may be found elsewhere (1). It consists of two independent detection modules mounted on either side of a three axis gimbal system. Each module comprises a position sensitive detection plane (PSD) of 9 Sodium Iodide scintillation bars, each of dimensions 5.8cm x 5.0cm x 55cm, with 13 similarly sized non position sensitive bars for anticoincidence purposes. At a distance of 3.5 metres in front of this plane is situated a coded aperture mask, constructed out of Tungsten alloy elements arranged in a 2 x 2 mosaic of a 9 x 7 Uniformly Redundant Array (URA) pattern (2). The intrinsic angular resolution of the device is governed by the angle subtended by a mask element at the detection plane. For the ZEBRA telescope this amounts to

$\sim 1^{\circ} \times \sim 1^{\circ}$. The point source location accuracy, however, is determined by the positional resolution of the detection plane and the strength of the detected source. For this reason, the bars in either detection module are mounted orthogonally in order to symmetrise and optimise this parameter.

The position sensitive detection bars have been studied carefully in the laboratory environment in order to fully assess their imaging capabilities. The initial tests were performed on single bar imaging systems (3), extending later to experimental systems of several bars operating in conjunction to provide two dimensional data.

In the last few months, a full ZEBRA PSD of nine bar units has been assembled in the laboratory and a series of experimental images has been generated. The arrangement consisted of the 9 bar plane in front of which, at a distance of 2.5 metres, a half-size 9 x 7 pattern mask was aligned so as to be perfectly parallel. This configuration naturally leads to the imaging system being 'focussed' on a source plane a further 2.5 metres from the PSD. Signals from the 18 photomultiplier tubes were digitised by two ADC's and stored on magnetic tape via a PDP 11/24 computer, subsequent analysis being performed on an HP 1000 computing system.

Two types of source distribution were studied: point sources, both single and multiple, and extended sources artificially contrived by continuously moving a point source during the integration period. For these laboratory experiments a preliminary calibration of the detection plane was performed by means of a collimated source (Cs.137 ~662 keV) placed very close to each bar in succession at three well determined positions along the length. An energy look-up table was also calculated for each bar in order to provide a uniform spectral response both down the length of the bars and between the entire set.

2. EXPERIMENTAL IMAGES.

a) Point Sources. A 100μC Cs 137 source was employed as the object to be imaged. At a distance of ~5 metres the counting rate was found to be ~15% of the integerated background event rate. The source was placed in over 80 well defined positions across the object plane and images accumulated for 10**5 events (i.e. about 1.5 x 10**4 source counts). For the purposes of analysis, an energy window around 662 keV was established such that only events under the Cs energy loss photopeak were accepted.

The data were binned in 128 energy bins of which 112 corresponded to the active region of the bars (the central 49cm), thus the shadow of one mask element covered 16 pixels. A straightforward correlation analysis (4) of the 9

x 112 data set and the 9 x 7 mask pattern allowed reconstruction of the source distribution. A typical example of the many images obtained is shown in Figure 1.

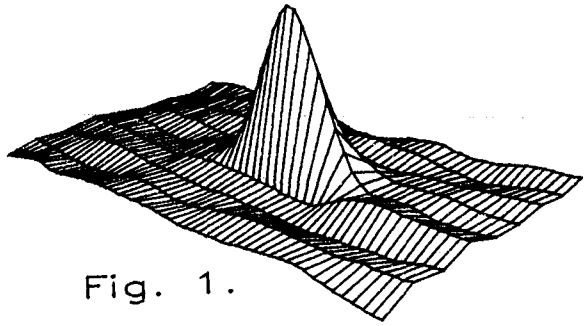

Fig. 1.

The triangular point spread function intrinsic to this decoding method is readily apparent. In this image there are ~5 x 10**4 source counts and ~3 x 10**4 background events. The full width at half maximum of the peak is 16.45 +/- 0.13 channels in comparison to the theoretical minimum of 16. The larger figure is due to the finite positional resolution of the detection plane and mechanical errors in setting up the experiment.

Figure 2. shows the reconstructed peak positions obtained from 6 images in comparison to the true source positions, the data being expressed in arcminutes from the centre of the field of view. The line is a weighted least sqares fit to the experimental data. The error bars are 1 sigma, and it can be seen that the two sets of data are in excellent agreement.

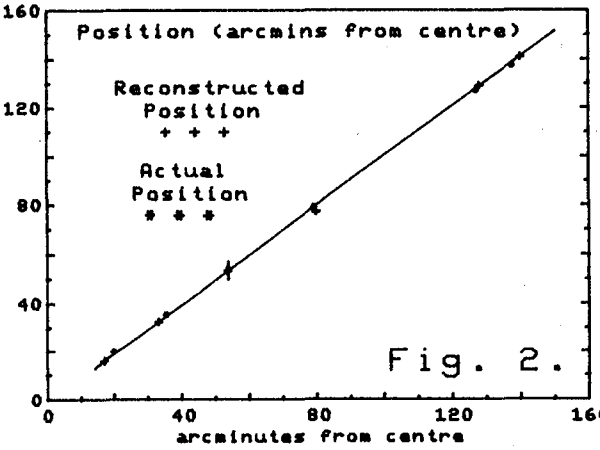

Fig. 2.

A slight magnification mismatch is evident, probably due to difficulties in employing a diverging gamma-ray beam and the subsequent need to measure mask/source and mask/PSD distances very accurately. The reconstructed intensity at each position is shown in Figure 3. Some very slight reduction in intensity for more off-axis sources is apparent. This is due to a combination of the cosine effect, self vignetting by the body of the mask and the reduced apparent integral thickness of the detection plane (5,6).

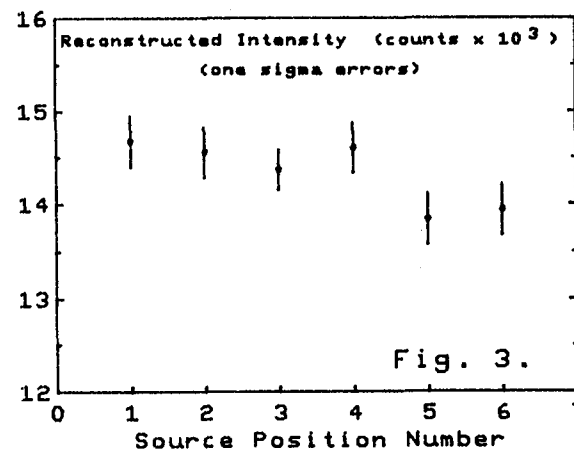

Fig. 3.

The point source location accuracy as a function of signal to noise ratio (SNR) is depicted in Figure 4. The two scales on the X-axis reflect the different values which

may be attributed to the variance of the background, either with or without accounting for systematic structure.

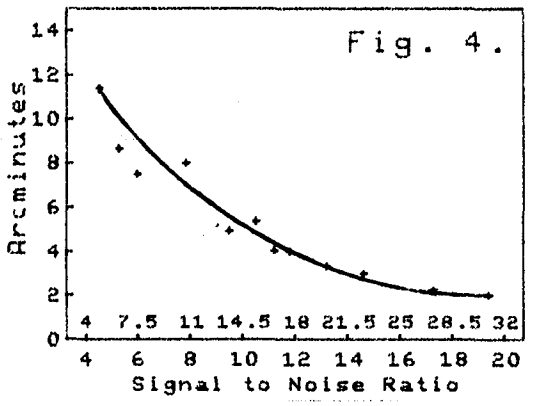

Fig. 4.

b) Extended Sources. In order to simulate an extended source, a point source was made to rotate within the field of view. Several images were accumulated for different radii. Figure five depicts such a source with a radius of 20 cm (~2°). The centre of the distribution falls to the background level as expected. Analysis of the extended source distributions is continuing.

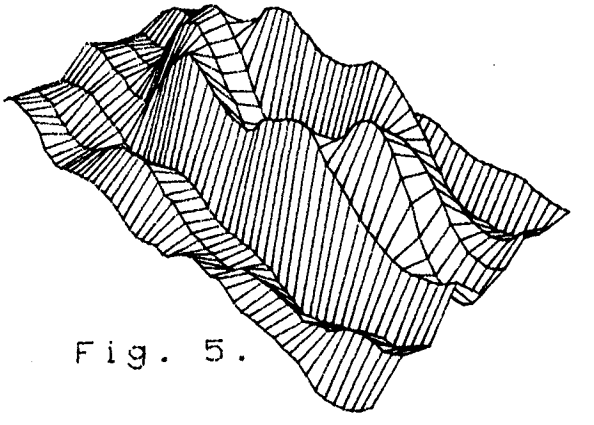
Fig. 5.

3. CONCLUSIONS This paper presents the first two dimensional images to be obtained using one full ZEBRA detection PSD. Using only preliminary laboratory calibration procedures, and making no allowance for non-uniformities in the background event rate (such as background subtraction) it has been demonstrated that high quality images may be obtained. The point source location accuracy is at the arc minute level.

REFERENCES

1. Baker, R.E. et al Proceedings 18th ICRC, Bangalore (1983)
2. MacWilliams, F.J. and Sloane, N.J.A. Proc. IEEE 64 1715 (1976)
3. Charalambous, P.M. et al Nucl. Instr. and Meths. in Phys. Res. 221 183 (1984)
4. Fenimore, E.E. and Cannon, T.M. Appl. Opt. 17 337 (1978)
5. Butler, R.C. et al Nucl. Instr. and Meths. in Phys. Res. 221 41 (1984)
6. Charalambous, P.M. et al Appl. Opt. 23 4118 (1984)

ADVANCED TECHNIQUES FOR HIGH RESOLUTION SPECTROSCOPIC OBSERVATIONS OF COSMIC GAMMA-RAY SOURCES

J.L. Matteson, M.R. Pelling and L.E. Peterson
Center for Astrophysics and Space Sciences
University of California, San Diego
La Jolla, CA 92093 USA

R.P. Lin and K.A. Anderson
Space Sciences Laboratory,
University of California, Berkeley
Berkeley, CA 94720 USA

R.H. Pehl
Lawrence Berkeley Laboratory
University of California, Berkeley
Berkeley, CA 94720 USA

K.C. Hurley, G. Vedrenne and M. Niel
Centre d'Etude Spatiale des Rayonnements
31029 Toulouse, Cedex, France

Ph. Durouchoux
Service d'Astrophysique
Centre d'Etudes Nucleaires de Saclay
91190 Gif-Sur-Yvette Cedex, France

ABSTRACT

We describe an advanced gamma-ray spectrometer that is currently in development. It will obtain a sensitivity of $< 10^{-4}$ph/cm^2-sec in a 6 hour balloon observation and uses innovative techniques for background reduction and source imaging.

1. Introduction. Over the past decade gamma-ray spectrometers have achieved sensitivities of 10^{-4} to 10^{-3}ph/cm^2-sec to steady sources. This has lead to the discovery of gamma-ray line emission and narrow band continuum structure in the spectra of a wide variety of objects and phenomena [1], e.g. the galactic center, X-ray pulsators, the Crab pulsar, gamma-ray bursts and transients, and solar flares, the interstellar medium [2] and SS433 [3]. In spite of the impressive observational progress, it is generally true that line emission has been detected from only the brightest sources. The discovery of fainter sources and detailed study of the brighter ones requires factors of 10 to 100 sensitivity gain [4]. This is only practical with much lower background instruments than are available today. The goal of the collaborative program described here is to develop an instrument that has much lower background per unit area and is an order of magnitude more sensitive per unit observing time than present instruments. This will be used for observations of isolated sources and complex source fields from balloons at a sensitivity of $< 10^{-4}$ph/cm^2-sec, and its techniques will be applicable to future instruments carried in space, where $< 10^{-5}$ph/cm^2-sec could be achieved.

Instrumentation. The instrument, shown in Figure 1, contains an aray of twelve 5.5 x 5.5 cm, coaxial, n-type Ge detectors. These have an energy resolution of 1.4 (<0.6) keV at 511 (<100) keV, a total area of ~ 300 cm^2 and operate from 10 keV to 10 MeV. They are contained in a single cryostat that has very high thermal efficiency, allowing 80 hours of operation with a 10 liter LN_2 Dewar. This is surrounded by anticoincidence shield made of 5 cm thick BGO at the sides and rear and 10 cm thick CsI at the front. Apertures in the latter define a 19° FWHM field of view. The instrument has 3 operating modes, or configurations, which result from the use of additional collimation components. (a) The "Source Mode" uses a 3° FWHM passive collimator which is optimized for observations of discrete sources at known positions. (b) The "Image Mode" uses an optimum coded modulator to observe complex source regions by imaging a 12° FWHM field with 2.5° angular resolution (c) In the "Diffuse Mode" the 19° FWHM aperture is left clear in order to maximize the sensitivity to diffuse sources. The instrument mass is 450 kg.

The detectors use dual electrical segments and pulse shape discrimination to distinguished between Compton scattered gamma-rays, which are multiple site interactions, and β-decays which are essentially single site [5]. The latter are the dominant background component from a few hundred keV to > 1 MeV in heavily shielded Ge instruments [6,7,8] and represent a fundamental obstacle to sensitivity improvements. Their elimination is a major goal of this program. Gamma-rays $\leq$ 200 keV are mostly detected in the 1.5 cm thick front segment. Higher energy gamma-rays are mostly detected as a coincidence between the two segments or a multiple site event in the rear, 4.0 cm thick, segment. The latter is possible because the detector's finite charge drift velocity results in a sharp (broad) charge pulse for single (multiple) site events which is sensed by a pulse shape discriminator. This rejects > 95 percent of the single site events while accepting >80 percent of the multiple site events.

Imaging is achieved through the use of the optimum coded modulator. This produces temporal aperture modulation that is mathematically equivalent to the better known spatial aperture modulations [9]. It consists of 63 opaque and transparent moving elements which are located ~ 200 cm above the detectors and modulate the flux from gamma-ray sources. The resulting moving shadowgram produces temporally modulated counting rates in the detectors, from which a 2-dimensional, sidelobe-free gamma-ray image is deconvolved. The modulator elements, made of BGO with PIN photodiodes, operate in anticoincidence with the detectors.

The anticoincidence shield is primarily made of BGO, which offers greater attenuation per unit shield mass than CsI or NaI and also results in a more compact shield due to its high density, 2 times that of NaI. However, the low light output of BGO necessitates good PMT light collection in order to achieve a low anticoincidence threshold, < 100 keV. Therefore the shield will use ~ 50 separate BGO elements, based on a nominal 5 x 7 x 21 cm size, each with its own PMT.

3. Background and Sensitivity. The background is shown in Figure 2 and the sensitivity for a 6 hour balloon observation is shown in Figure 3. At 1 MeV the background is 0.14 and the detector volume is 11.5 times that of the

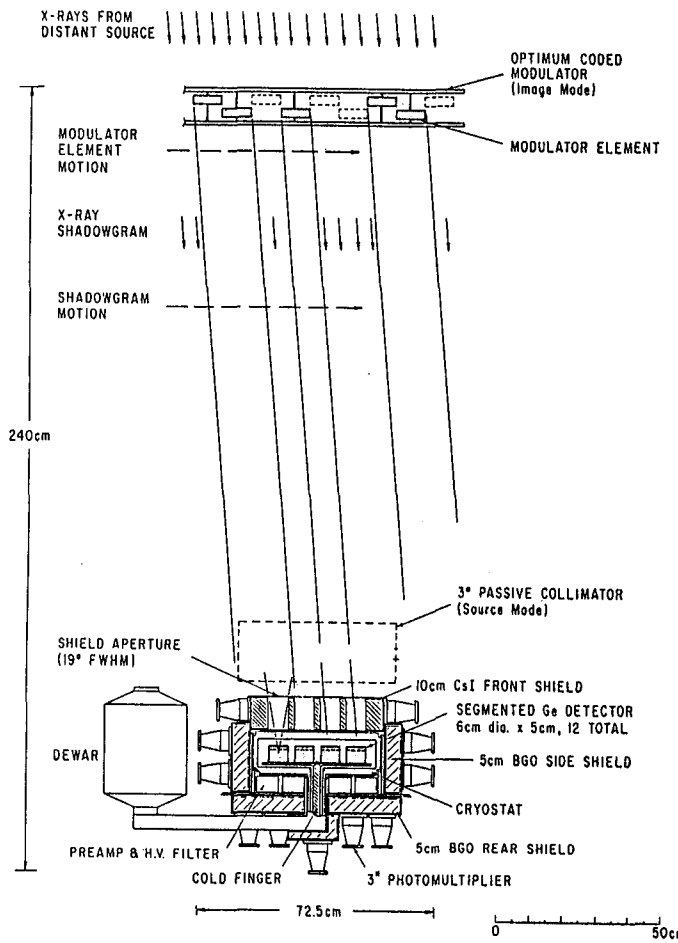

Figure 1. The high reduction gamma-ray spectrometer contains an array of 12 coaxial Ge detectors surrounded by a BGO and CsI anticoincidence shield. A cross section is shown of the optimum coded modulator, which is located 200 cm above the detector and used for imaging observations.

most sensitive contemporary instrument [10,11] resulting in a sensitivity improvement per unit observing time that is a factor of 9 (= 11.5/0.14). The detectors' superior energy resolution results in an additional sensitivity gain of a factor of ~ 1.5 below ~ 500 keV.

4. Program Status and Plans. The detector, shield and modulator concepts have been proven in extensive laboratory tests. In the fall of 1985 a test balloon flight of a single, heavily shielded detector will be performed. The 8 cm thick CsI shield will reduce the gamma-ray leakage to a point where rejection of detector radioactivity can be clearly seen. It is planned to conduct the first scientific observations with the complete instrument in the fall of 1987.

5. Acknowledgement This work is supported at the University of California by NASA Grant, NAGW-449.

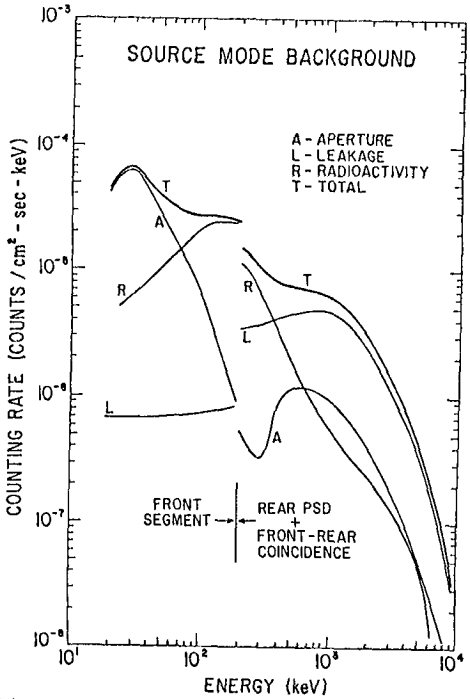

Figure 2. The Source Mode background components are shown for the different gamma-ray acceptance modes of the detectors. The 3° collimator results in a small aperture flux which is ~ 20 times greater below 300 keV in the Image Mode. A 98 percent rejection of detector radioactivity at 1 MeV is assumed. Such a reduction would allow a 10 times further reduction in the total background of future instruments through the use of a thicker anticoincidence shield.

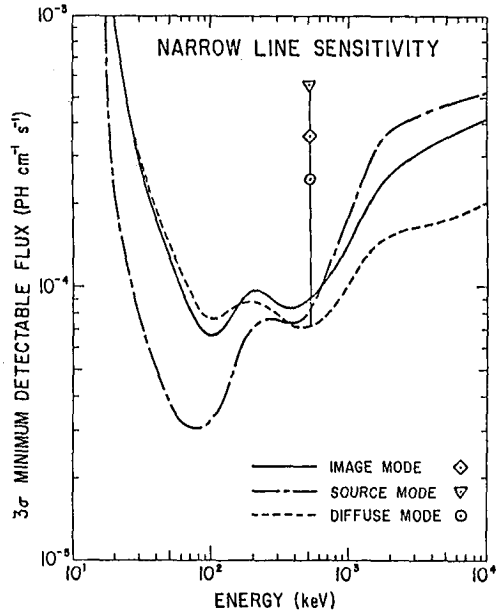

Figure 3. The sensitivity to narrow lines is shown for a 6 hour balloon observation. The increase below ~ 50 keV is primarily due to decreasing atmospheric transmission. Differences among the observing modes are due to different backgrounds and source modulation efficiencies. Carried in space with a 10 cm BGO shield, this instrument could achieve an Image Mode sensitivity of 10^{-5}ph/cm^2-sec over most of its energy range in a 7-day observation.

References

1. Matteson, J.L., (1983), Adv. Space Res., 3, 135.
2. Mahoney, W.A., et al., (1984) Ap.J. 286, 578.
3. Lamb, R.C., et al., (1983), Nature 305, 37.
4. Matteson, J.L., (1981), in X-Ray Astronomy in the 1980's, Holt, S.S., ed., NASA TM 83848, p. 549.
5. Roth, J., et al., (1984), IEEE Transactions on Nuclear Science, NS-31, 367.
6. Matteson, J.L., et al., (1982), UCSD proposal-9006, High Resolution Gamma-Ray Spectroscopy of Cosmic Sources.
7. Gehrels, N., et al., (1984), IEEE Transactions on Nuclear Science, NS-31, 307.
8. Gehrels, N., (1985), NASA TM 86162.
9. Proctor, R.J., (1981), in X-Ray Astronomy in the 1980's, Holt, S.S., ed., NASA TM 83848, p. 335.
10. Leventhal, M., et al., (1977), Ap.J., 216, 491.
11. Leventhal, M., et al., (1977), Ap.J. (Letters, 225, L11.

THE GAMMA-RAY TELESCOPE GAMMA-1

- Akimov,V.V., Nesterov,V.E., Kalinkin,L.F., Balibanov,V.M., Prilutsky,O.F., Rodin,V.G., Leikov,N.G., Bielaoussov,A.S., Dobrian,L.B. Poluektov,V.P., Gerassimov,I.A., Koslov V.D.
  Institute for Cosmic Research, Moscow (IKI)

- Voronov,S.A., Galper,A.M., Kirrilov-Ugriumov,V.G., Oserov,Y.V., Grigoriev,V.A., Iaurkine,Y.T., Popov,A.V.
  Moscow Institute of Physics (MIFI)

- Kurnosova,L.V., Fradkin,M.N.
  Physical Institute of the Academy of Sciences, Moscow (FIAN)

- Tsuikin,E.I.
  Leningrad Physical and Technical Institute (LFTI)

- Leray,J.P., Gros,M., Parlier,B., Soroka,F., Masse,P.
  S.A.P. / D.P.h, Centre d'Etudes Nucléaires, Saclay (France)

- Bazer-Bachi,A.R., Lavigne,J.M.
  Centre d'Etudes Spatiales des Rayonnements, Toulouse (France)

ABSTRACT

French and Soviet specialists have designed and built the gamma-ray telescope GAMMA-1 to detect cosmic gamma rays above 50 MeV. The sensitive area of the detector is 1400 cm^2, energy resolution is 30% at 300 MeV, and angular resolution 1.2° at 300 MeV (and less than 20'arc when a coded aperture mask is used).Results on calibration of the qualification model and Monte-Carlo calculations are presented.

1. Introduction. SAS.II, then the long-lived COS-B, have shown the interest of high-energy gamma ray astronomy. Numerous point sources have been found, but identification with physical objects has been possible for only a few of them. The first objective of the GAMMA-1 experiment was to increase the sensitive area, and lower the angular resolution of a gamma ray detector. A wide gap spark chamber, tested at DESY in 1976 (1,2), showed that it was possible to obtain better than 2° angular resolution with this technique.

However, in order to still increase this resolution, a model of coded aperture mask was developped (3). In a spark chamber, image deconvolution is performed not only by position detectors,but also by taking into account the rough (<3°) arrival direction information. The addition of this mask, and the complexity of the experiment itself, resulted in some delay over the initial launch date.

2. The experiment. The Gamma-1 telescope is illustrated on Fig.1. The main detector is a 50X50 cm ,12-layered wide gap spark chamber. It is shielded with lateral and upper anticoincidence,inside and outside the satellite skin. A time of flight (SV + SN) can veto upgoing particles,

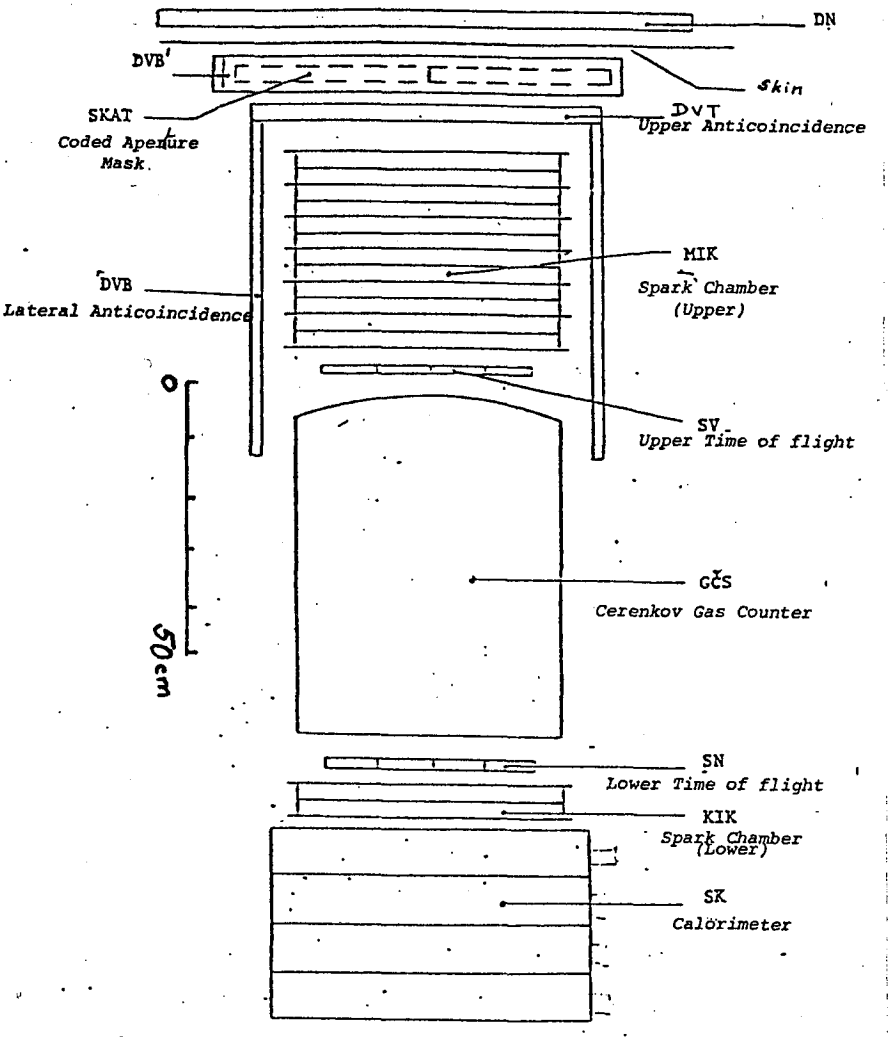

Fig. 1

THE GAMMA - 1 EXPERIMENT

in redudance with a Cerenkov gas counter. A two layered spark chamber below the SN counter is helpful when the very high energy electron-positron pair cannot be separated in the upper chamber.

To measure the energy, scattering is used from 50 to 200 MeV, and a four-layered-calorimeter is used above 100 MeV.

The spark images are viewed through an optical system by two orthogonal vidicon cameras and digitised before storage on a recorder. The 50 cm width of the chamber is divided in4096 points (localisation accuracy 0.125 mm). For each spark, there are three lines of sweep, separated by 17 mm; the width of each digitised spark is also recorded.

The dead time of the high voltage (24 KV) generator is less than 0.5 sec. Data from the vidicons, and from all counters, along with housekeeping informations, are dumped to the telemetry station twice a day.

The coded mask is made of two orthogonal one-dimensionnal arrays of 1cm-thick tungsten bar,each one covering half of the field of view, which can slide on or off the field of view of the experiment. The experiment can be put in many different modes by telecommands(for instance, recording of proton tracks to check linearity of the imaging system.) while the satellite is above the station.

3. Calibration. The qualification model has been extensively calibrated in the tagged gamma ray beam of the accelerator "Pakhra", near Moscow. The set-up of the beam has been described elsewhere (4), but Fig. 2 shows arrival directions of 1000 gamma rays on top of the chamber, on axis (bin size 1cm). FWHM is about 4cm.The energy resolution, from 30 to 700 MeV, is about 30 MeV, and the openning of the beam 2.5 mrad.

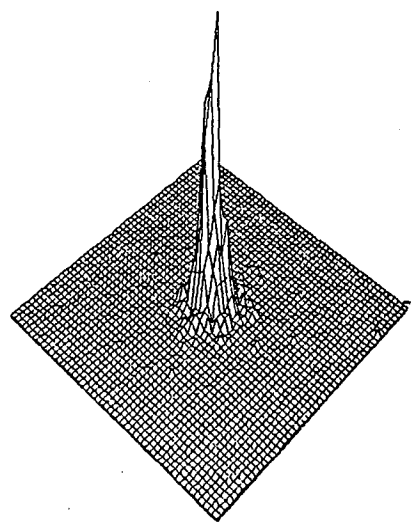

Fig.2

In parallel, Monte-Carlo calculations were performed, to check the actual response up to 700 MeV, and to be used as calibration above.

Figures 3 and 4 show the efficiency and angular resolution of the detector,without the coded mask. Energy resolution (as measured by the calorimeter), decreases from 95% at 50 MeV to 30% at 500 MeV.

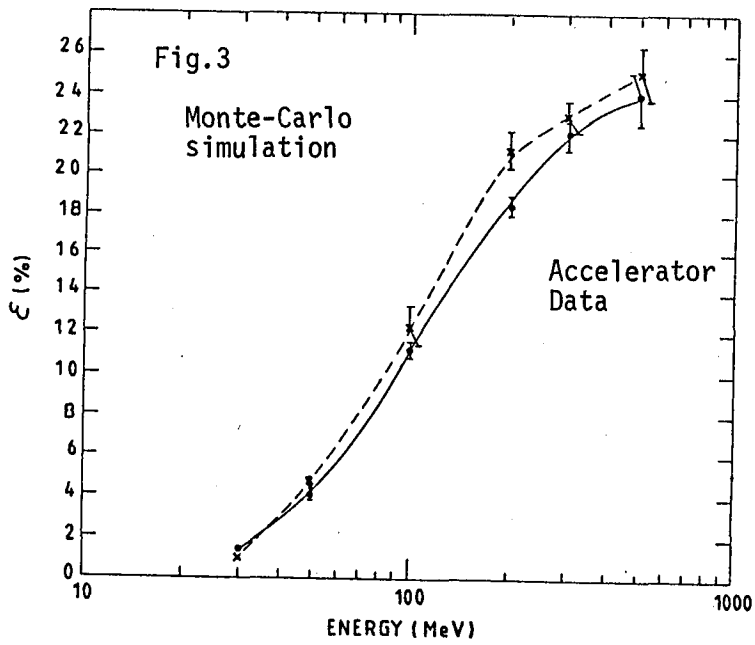

Calibrations have also been performed using the mask. An exemple of correlation function at 300 M eV is given in Fig. 5. Bin size is 5' arc. The actual position of the beam was at -15'. Reconstructed direction is $(-10 \pm 5)'$ arc, with a FWHM of 28'.

Such a figure may seem high, but when one takes into account the angular width of the beam itself, the FWHM is less than 15' of arc.

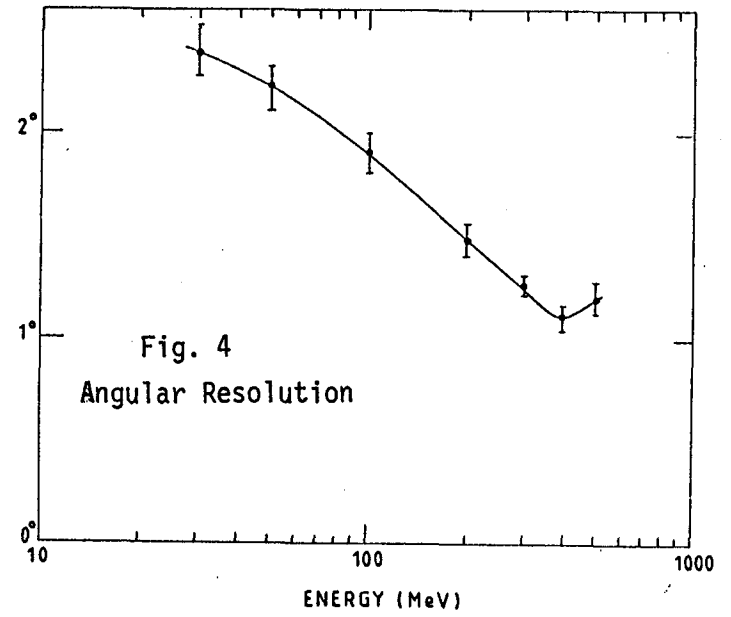

Fig. 4
Angular Resolution

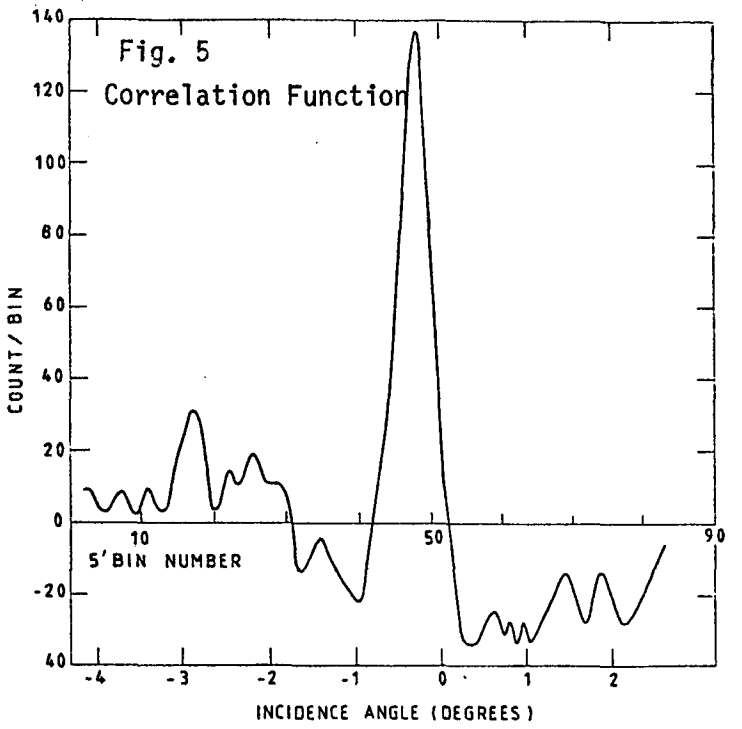

Fig. 5
Correlation Function

4. Conclusions. The calibrations performed on the qualification model of the Gamma-1 experiment , as well as calculations, have shown its potential in reconstructing gamma-rays directions. The use of a coded mask can give images with 15' arc resolution. Absolute celestial coordinates are obtained with the help of a stellar sensor with 5' arc accuracy.

Without the mask, upper flux limits of 10^{-7} should be detected within two weeks of exposure, using a sensitive area of 1400 CM^2 , and gamma rays within 10° of the axis.

Calibration of the flight model will be performed at the end of 1985, on a reduced program. Then, it will be integrated in a Salyut-type, 3-axes stabilised, satellite, to be launched in late 86 on a low-altitude orbit.

References. 1- Akimov, V.V. et al, Nuclear Inst. & Met., 147, 329 (1977)
2.- Bazer-Bachi, A.R., et al, Proc 12th Eslab Symposium, Frascati(1977)
3.- Prilutsky, O.F., Proc XXII COSPAR Meeting, Bangalore (1979)
4.- Zverev,V.G., et al, Atomizdat 1980, p45 (Moscow)

THE FIGARO EXPERIMENT FOR THE OBSERVATION OF TIME MARKED SOURCES IN THE LOW ENERGY GAMMA-RAY RANGE

G. Agnetta (1), B. Agrinier (2), J.P. Chabaud (3), E. Costa (4), R. Di Raffaele (1), P. Frabel (3), G. Gerardi (1), C. Gouiffes (2), M.F. Landrea (5), P. Mandrou (3), J.L. Masnou (5), E. Massaro (6), M. Niel (3), G. Rouaix (3), B. Sacco (1), M. Salvati (4), L. Scarsi (1), A. Tabary (2), G. Vedrenne (3)

(1) Istituto di Fisica Cosmica e Informatica, CNR - Palermo, Italy
(2) Service d' Astrophysique, CEN Saclay, France
(3) CESR, Université P. Sabatier, Toulouse, France
(4) Istituto di Astrofisica Spaziale, CNR - Frascati, Italy
(5) Observatoire de Meudon, Meudon, France
(6) Istituto Astronomico, Università "La Sapienza", Roma, Italy

1. INTRODUCTION. The only two firmly identified galactic γ-ray sources in the second COS B catalogue (1) are the pulsars PSR 0531+21 (Crab) and PSR 0833-45 (Vela). Their spectra are rather similar in the medium energy γ-ray band, but differ drastically at lower frequencies. In the region between 100 keV and 10 MeV the detailed shape of the emission is particularly important, since one expects a turn-off which is related to the geometry of the source (2). A marginal evidence of such a turn-off just below 1 MeV has been reported for the Vela pulsar by Tümer et al. (3).

In order to study sources with a well marked time signature in this energy band, we have specifically designed the FIGARO - French Italian GAmma Ray Observatory - experiment (4), whose first version was launched in November 1983 from the Sao Manuel base (Brazil), and was destroyed in a free fall following a balloon burst at an altitude of 50 mbar. The available portion of the growth curve and the calibration data demonstrate that the effective area and the noise figure (extrapolated to the float altitude) were in accordance with the project goals, and indicate that the required level of sensitivity can indeed be reached (5).

In this contribution we give a brief description of the new improved version of the experiment, FIGARO II, which is nearly completed and whose launch is scheduled before summer 1986.

2. DESCRIPTION OF THE EXPERIMENT. FIGARO II is a wide angle γ-ray detector with a total geometric area of 3600 cm^2

of NaI(Tl), 50 mm thick. It is actively shielded from the atmospheric background by a lateral wall of NaI(Tl) tiles (25 cm high, 70 mm thick), and by a lower array of plastic scintillator blocks having a grammage of 50 g cm^{-2}. At variance with the first version, the main detector is square instead of rectangular, providing a more favourable ratio area vs weight; the lateral wall is higher by 5 cm; and the photo multiplier tubes of the nine detector elements are reversed, embedded within the bottom plastic, so as to have a field of view free of passive material, and to extend to lower energies the accessible spectral band.

The reduction of the geometrical area by about 13% does not affect appreciably the sensitivity of the experiment: in fact, it is very nearly compensated by the increased efficiency achieved with the PM's reversal, and by the lower noise contributed by the calibration source. In the new version, the gains of the individual detector elements are monitored with 511-keV photons from a very weak positron source (Na^{22} of about 40 nCi of activity), tagged by the companion photons emitted in the opposite direction, and detected on a small BGO crystal. An upper plastic shield 5 mm thick is used to anticoincide low energy charged particles. A schematic view of the complete payload (but not the BGO detector of the tagged source) is shown in Fig. 1.

Data from the nine detector elements are analyzed by a single 8 bit A/D converter, if there are no veto signals from the various anticoincidence sets. The anticoincidence window depends on the pulse height, and can be varied by telecommand. Qualified events are transmitted individually with a time resolution better than 0.05 ms; they are also cumulated onboard into 10 counters, and transmitted on a different telemetry channel every 2 ms. Signals which are tagged by a coincidence with the BGO crystal are sent separately, and analyzed in order to monitor continuously the gains of the individual amplifiers; these are corrected and equalized by telecommand, so that only one channel of A/D conversion is needed.

3. EFFECTIVE AREA AND SENSITIVITY. With respect to FIGARO I, this second version can be flown profitably at lower altitudes, with a safer heavy-load balloon, because of the improved performance at the lower end of the spectral window; furthermore, the spectral capabilities have been significantly increased with the adoption of the A/D converter. Both changes have been warranted by the low counting rate demonstrated by the Brazil flight.

On the other hand, the most critical experimental solutions have remained unchanged, so that we feel confident in modelling FIGARO II with the Monte Carlo code used successfully so far. Fig. 2 shows the total (▲) and photopeak (▼) effective area at a float altitude of 5 g cm^{-2} of residual pressure. The estimated sensitivity to a pulsed continuum, attainable in a five hour pass during a transmediterranean flight is reported in Fig. 3 for the same residual pressure; the numerical modelling of the γ-ray atmospheric background used in this computations has been described in detail elsewhere (6).

Apart pulsars, which remain our main target, all time-marked sources in this energy band such as hard-tail X-ray pulsators, solar flares and γ-ray bursts can be observed with a very high sensitivity by this experiment. For the γ-bursts, in particular, it will be very interesting the search for decaying periodicities during the event.

References

1. Swanenburg, B.N. et al., (1981), Astrophys. J. Letters, 243, L69
2. Salvati, M., (1983), Space Sci. Rev., 36, 145
3. Tümer, O.T. et al., (1984), Nature, 310, 214
4. Agnetta, G. et al., (1983), Adv. Space Res., 3, 113
5. Gouiffes, C., Thesis, Université Curie, Paris, (1985)
6. Costa, E. et al., (1984), Astrophys. Space Sci., 100, 165

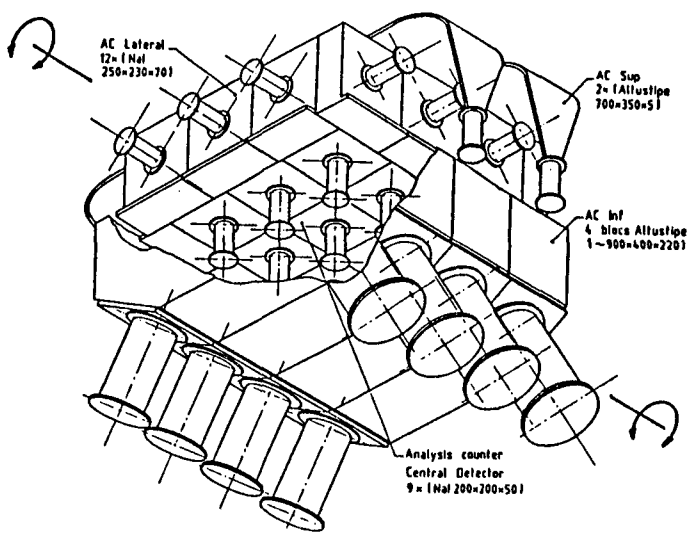

FIG.1

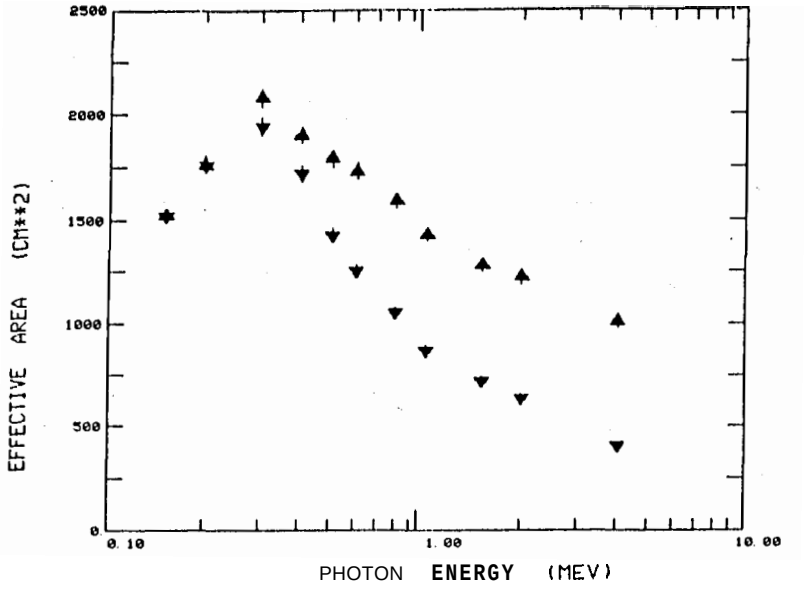
EFFECTIVE AREA (CM**2)
2500
2000
1500
1000
500
0
0.10
1.00
10.00
PHOTON ENERGY (MEV)

Fig. 2

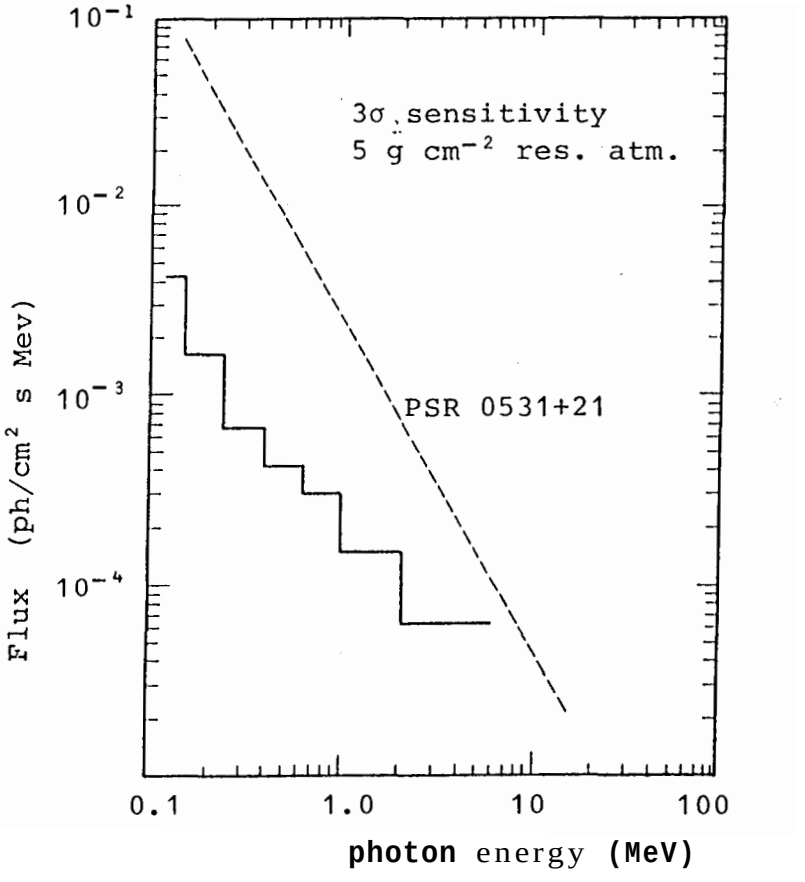
Flux (ph/cm² s Mev)
10⁻¹
10⁻²
10⁻³
10⁻⁴
3σ sensitivity
5 g cm⁻² res. atm.
PSR 0531+21
0.1
1.0
10
100
photon energy (MeV)

Fig. 3

HIGH ENERGY GAMMA RAY BALLOON INSTRUMENT

D.J. Thompson, R.G. Baker, D.L. Bertsch, J.R. Chesney,
S.M. Derdeyn, C.H. Ehrmann, C.E. Fichtel, S.D. Hunter,
J.S. Jacques, N.A. Laubenthal, R.W. Ross
Code 662, NASA/Goddard Space Flight Center
Greenbelt, Maryland 20771 U.S.A

1. Introduction. The High Energy Gamma Ray Balloon Instrument was built in part to verify certain subsystems' performance for the Energetic Gamma Ray Experiment Telescope (EGRET) instrument, the high energy telescope to be carried on the Gamma Ray Observatory (1). This paper describes the instrument, the performance of some subsystems, and some relevant results.

2. Instrument Description. The instrument is similar in size to EGRET and has the basic elements of a conventional high energy γ-ray telescope. However, being a test vehicle and constrained by the weight and cost limitations of a balloon program, it is much more austere than EGRET. It has, for example, only 12 spark chamber modules (Figure 1), compared to the 36 on EGRET. A γ-ray entering from above produces no signal in the anticoincidence scintillator "A", but may convert to an electron-positron pair in one of the plates interleaved with the upper 10 spark chamber modules. The electron and positron trigger the coincidence system consisting of scintillators "B", "C", and "D" with the proper time of flight signature between "B" and "C". The inclusion of the "D" signal was optional and commandable. The coincidence signal is used to initiate the high voltage pulse to the spark chambers and the readout of the γ-ray event. The basic information about the γ-ray, arrival direction and estimated energy, is derived from the reconstructed picture of the electron and positron trajectories in the spark chamber. Each of the eight pair production plates is a sheet of 0.08 radiation length lead, supported on a grid of stretched high-strength steel wires. The spark chambers have an active area of 81 cm by 81 cm, are of the wire grid design with magnetic core readout and are essentially identical to those being used on the EGRET instrument.

The anticoincidence counter consists of three pieces of scintillator which form a five sided box around the upper spark chamber assembly. The placement of the anti-coincidence system inside the pressure vessel reduces weight and is far less costly than the machined and polished dome surrounding the entire upper portion of the EGRET instrument. The shorter, modular design of the balloon anticoincidence is not as effective as the monolithic dome and it therefore

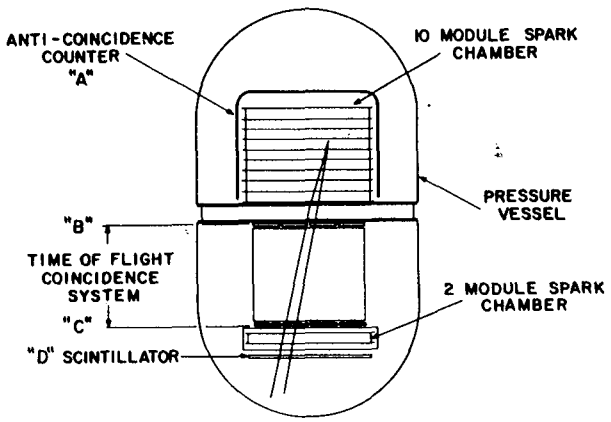

Figure 1 -- Schematic diagram of the High Energy Gamma Ray Balloon Instrument

represents a more severe test of its ability to screen out unwanted events.

The "B" and "C" parts of the triggering system each consist of an array of 16 scintillator tiles in a 4 by 4 pattern. Each tile has its own light pipe and phototube. This coincidence system serves two purposes: (1) The allowed combinations of "B" and "C" tiles define the instrument aperture. (2) These scintillator planes are operated in a time-of-flight arrangement which requires that the particles pass through the "B" plane before the "C" plane, i.e., they must be downward moving. The performance of this coincidence system is discussed in Section 3. The EGRET coincidence system uses the same 4 by 4 scintillator arrays and an almost identical time-of-flight electronics system. The "D" detector is a single unit of plastic scintillator which may be used to verify that at least one of the particles penetrates the entire detector.

The active detectors are contained in a pressure vessel made of aluminum honeycomb with Kevlar face sheets. This composite vessel is lightweight and low density (area density less than 0.5 g cm^{-2}) yet capable of being evacuated to remove contaminants. The upper portion of the vessel and the lower spark chamber area are filled with a spark chamber gas mixture (98.5% neon, 0.75% ethane, 0.75% argon), while the region containing the coincidence scintillator, phototubes, and electronics is filled with air. The active area is approximately 6560 cm^2 with an area efficiency factor of about 1800 cm^2 (E> 400 MeV) The instrument size is 3 m by 1.6 m diameter. With its gondola, it weighs 1300 kg. Balloon flights which provide the results reported here were launched from Palestine, Texas.

3. Relevant Subsystems.

a. Spark Chamber. The individual modules have 992 wires in each plane, giving a positional resolution of about 0.4 mm for spark location. The modules are made entirely of low-outgassing materials with the beams themselves being made of Macor. An extensive effort was made in developing techniques for stacking, holding, and determining the alignment of the spark chambers, so that the absolute pointing direction of the assembly could be determined with high precision. The use of a set of optical refererences allowed the absolute pointing direction to be determined to an arcmin. The techniques which have been used in the EGRET development are a direct successor. The performance of the spark chambers is seen in Fig. 2, which shows the electron-positron pair resulting from a high energy γ ray interaction. The vertical scale has been compressed in the figure by a factor of 4.7.

b. Time-of-flight coincidence system. The time-of-flight measurement is an important discriminator against unwanted triggers. Each of the 32 tile signals from the "B" and "C" arrays is sent to a constant fraction discriminator. The discriminator signals are summed for each array (with propagation times matched). The time difference between the total "B" signal and the total "C" signal is then digitized using a circuit similar to previous experiments (2). With a 75 cm separation, the time difference between upward-moving and downward-moving particles is 5

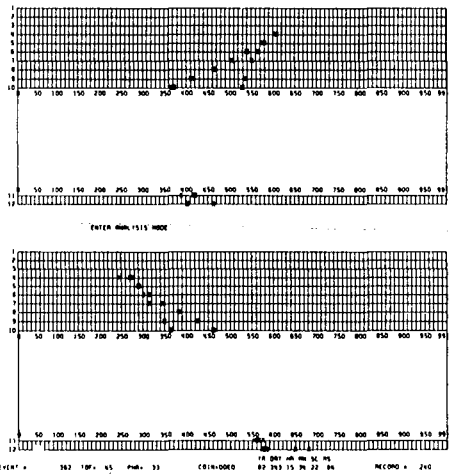

Figure 2 - Orthogonal views of a γ-ray pair production event in the spark chamber.

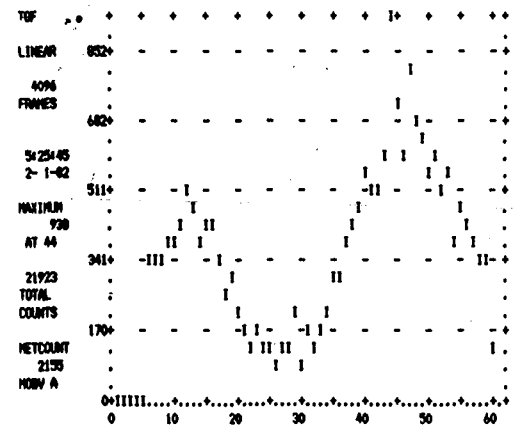

Figure 3 - Time of flight histogram for neutral events during one balloon flight.

nsec. The acceptance threshold for the time difference is adjustable by command. The discrimination, summation, digitization, and comparison is completed in about 400 nsec and is included in the trigger signal to the spark chamber. A histogram of the time-of-flight measurements is accumulated in the data system and regularly telemetered to the ground station. A sample histogram for neutral events, taken directly from the Ground Support Equipment display, is shown in Figure 3. The peak to the right represents downward-moving γ rays and is well separated from the upward-moving peak to the left.

c. Anticoincidence System. As noted in Section 2, the anticoincidence scintillator on the High Energy Gamma Ray Balloon Instrument does not surround the upper layer of the time-of-flight coincidence system, in contrast to other instruments such as SAS-2, COS-B, and EGRET. This short anticoincidence system was recognized as a negative design aspect, because horizontal or even partially downward moving particles could interact above the upper layer of the coincidence system and produce a downward moving particle within the instrument aperture.

An approximate model of predicted event rates was developed from the data of SAS-2 and tested on previous balloon instruments. When applied to the geometry and material factors of this instrument, this model gave the predicted rates which are shown in Table 1, which also shows the observed event rates during a balloon flight. The model did not take into account the different characteristics of this anticoincidence system from all the others.

The overall agreement between the predicted and observed event rate is an indication that the short anticoincidence system was not a major limitation of the instrument. The differences in the types of events seen is probably in large part the result of the anticoincidence configuration, for which no correction was made in the model. The fraction of events which are recognizable γ rays is also high compared

Table I

Type of Event	Predicted Events/s	Observed Events/s
Gamma Ray pairs (1)	1.1	0.9
Upper Wall Events (2)	0.9	0.6
Scattered single tracks (3)	0.8	0.8
Other (4)	0.6	1.0

(1) Recognizable pairs. The prediction includes atmospheric γ rays and γ rays produced in the outer instrument shell.
(2) Tracks originating in the walls of the upper chamber.
(3) This number is generally consistent with the expected number of low energy Compton γ-rays plus pair production γ-rays for which one track is too short to meet the acceptance criteria.
(4) This category includes short single tracks, multiple single tracks, and events with little information.

to earlier balloon instruments. This favorable rate of useful events was predicted by the model based on the better active volume to wall ratio and to the improved directional recognition of the time-of-flight system. The similarity of this balloon instrument to the EGRET instrument and the known superior aspects of EGRET strongly suggest that EGRET will also have a high fraction of useful events.

d. Automatic Data Processing. The majority of the data for a high energy γ-ray telescope are the spark chamber pictures. A set of programs, originally developed for the SAS-2 instrument and since refined, analyze the event pictures by pattern recognition. These programs efficiently screen out pictures which do not contain useful information and identify the track structure of potential γ-ray events, such as the one shown in Fig. 2. Even though the information content of this instrument is low compared to other γ-ray telescopes, the results of the automatic analysis showed that this program works very well even here, both in selecting desired events and structuring them correctly.

4. Summary. The High Energy Gamma Ray Balloon Instrument has provided a flight test of an austere version of the EGRET telescope. The results have proven the instrument subsystems and approaches and have assisted in the development of assembly procedures used for EGRET.

5. Acknowledgements. We thank George Simpson and Bill Cruickshank for their valuable assistance in the early stages of the program. Our thanks go also to the National Scientific Balloon Facility, Palestine, Texas, for their flight support.

6. References

1. Fichtel, C.E., et al. 1983, ICRC, Paper T1-10, p. 19.
2. Ross, R.W., and Chesney, J.R., 1979, IEEE Trans. Nuc. Sci, NS-27, p.370.

MEASURED PERFORMANCE OF THE NEW UNIVERSITY OF CALIFORNIA GAMMA RAY TELESCOPE

A. D. Zych, T. O'Neill, W. Sweeney, J. Simone*, O. T. Tümer and R. S. White

IGPP, University of California, Riverside, CA 92521

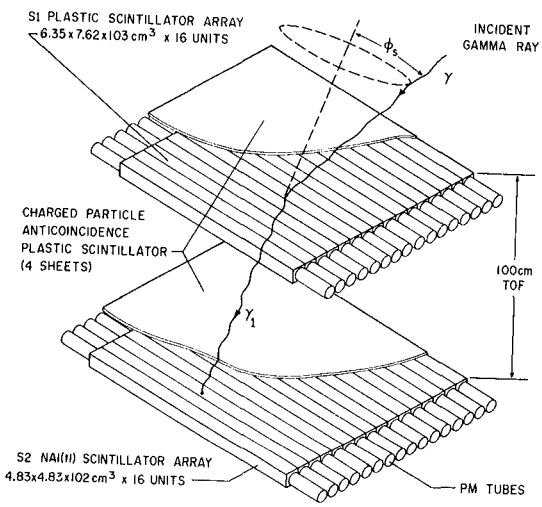

Figure 1

The design and expected performance of the new University of California medium energy balloon-borne gamma ray telescope shown in Figure 1 have been previously described (1,2). This telescope is sensitive to 1-30 MeV gamma rays. In this presentation the results of our initial calibration will be fully described. This will include the position and energy resolutions of 32 plastic and NaI(Tℓ) scintillator bars, each 100 cm long. The telescope's measured angular and energy resolutions as a function of incident angle will be compared with detailed Monte Carlo calculations at 1.37, 2.75 and 6.13 MeV. The expected resolutions are 5° FHWM and 8% at 2.75 MeV. The expected area-efficiency is 250 cm.

The telescope is now being prepared for a balloon flight in September, 1985.

1. A. D. Zych et al. (1983), Proc. 18th Int. Cosmic Ray Conf. 9, 343-346.
2. J. Simone, et al. (1985), IEEE, Trans. Nuc. Sci. NS-32, 124-128.

---

*Calif. State University, Los Angeles, CA 90032

BURST AND TRANSIENT SOURCE EXPERIMENT (BATSE) FOR THE GAMMA RAY OBSERVATORY (GRO)

G.J. Fishman, C.A. Meegan, T.A. Parnell, and R.B. Wilson
Space Science Laboratory
NASA/Marshall Space Flight Center
Huntsville, Alabama 35812

W. Paciesas
Physics Department
University of Alabama in Huntsville
Huntsville, Alabama 35899

J.L. Matteson
Center for Astrophysics and Space Sciences
University of California, San Diego
La Jolla, California 92093

T. Cline and B. Teegarden
Laboratory for High Energy Astrophysics
NASA/Goddard Space Flight Center
Greenbelt, Maryland 20771

1. Introduction. The Burst and Transient Source Experiment (BATSE) on the Gamma Ray Observatory (GRO) is expected to provide new and better observational data on bursts to test current and future models of burst sources. These data will include: (1) the celestial distribution of hundreds of burst sources over the life of the mission, (2) burst locations within several degrees, within 2 days after their occurrence, (3) observations of weaker bursts and better observations of short timescale fluctuations and spectral variations, (4) observations by a single experiment over a much larger energy range than previously available, and (5) more sensitive measurements of the spectral features which have been observed in many bursts. This paper briefly describes the GRO mission, the BATSE instrumentation and the burst observational capabilities. More comprehensive descriptions have previously been presented [1,2]. Two associated papers in this conference describe in more detail the capabilities for spectral observations of gamma-ray bursts [3] and capabilities for observations of other types of discrete sources [4].

2. Instrumentation. BATSE is one of four experiments on the GRO (Figure 1), a major shuttle-launched, free-flying observatory (to be launched in 1988). The spacecraft, one of the heaviest to be launched by the shuttle, has a self-contained propulsion system to enable the spacecraft to maintain a low altitude (between 350 km and450 km) for an extended period. The capability to refuel the GRO from the shuttle can allow mission durations considerably longer than the 2-year

nominal mission. The spacecraft is stabilized in three axes and the primary instrument axis can point anywhere in the sky with 0.5° accuracy and with 2 arcmin aspect. The complete space-craft weighs over 15,000 kg and will occupy about one-half of the shuttle payload bay.

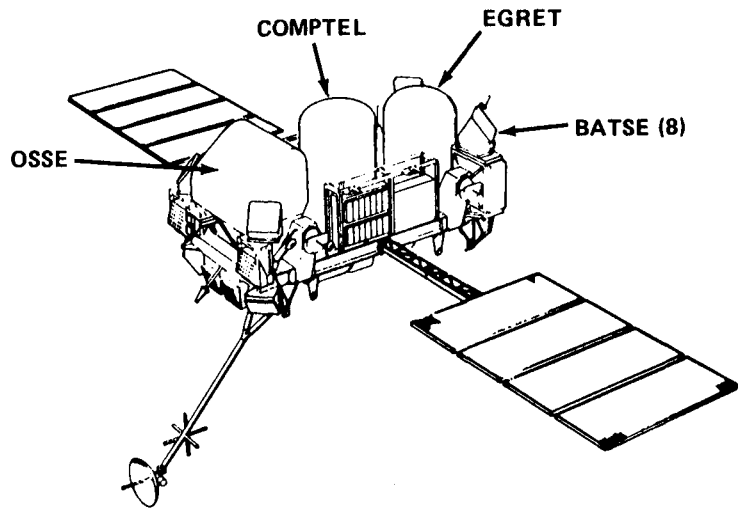

GAMMA RAY OBSERVATORY (GRO)

Figure 1

The BATSE experiment is an all-sky gamma-ray monitoring experiment designed primarily for the detection and detailed study of gamma-ray bursts and other transient high-energy sources in the energy range from 20 keV to 10 MeV. Eight uncollimated detector modules are positioned around the spacecraft to provide an unobstructed view of the sky (see Figure 1). A large-area, flat crystal scintillation detector provides a high sensitivity for weak bursts and fine time structure studies within stronger bursts. A spectroscopy scintillation detector is included in each detector module. This detector is

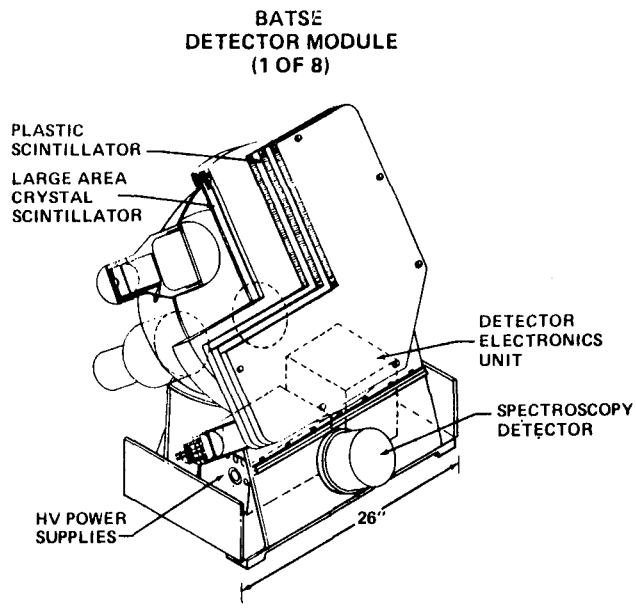

Figure 2

optimized to obtain better energy resolution and to cover a wider energy range than the large-area detectors. Figure 2 shows a cut-away view of one of the detector modules. Figures 3 and 4 show the effective area and resolution of the BATSE detectors. For sufficiently strong bursts, temporal fluctuations down to several microseconds may be detectable as well as coarse spectral variations on timescales as short as 10 ms. The location of gamma-ray bursts to within several degrees may be determined using the relative responses of the BATSE large area detectors (2).

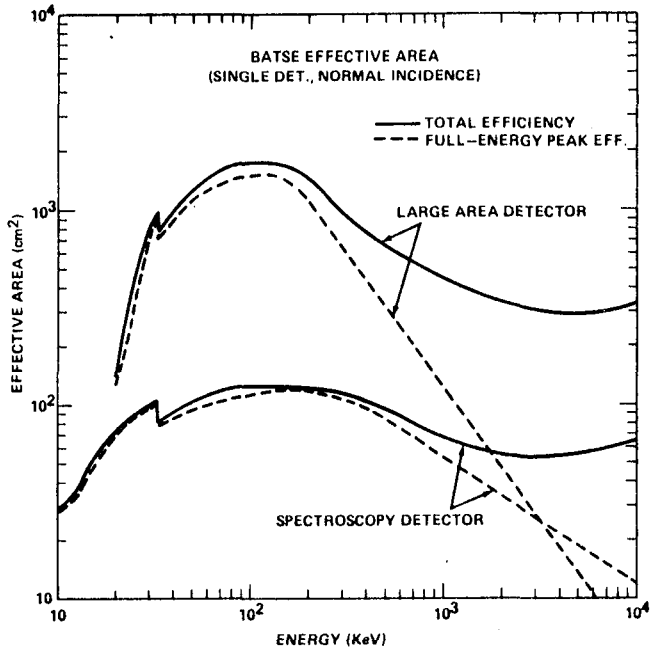

Figure 3

Scintillation pulses from the detectors are processed by two means in each module. An array of four fast discriminators can provide count rates up to about 10^6 cps with negligible dead-time. A pulse height-to- time converter simultaneously provides spectral data on each pulse. A gated baseline restoration circuit greatly reduces gain variations for counting rates up to $\sim 2 \times 10^5$ cps. All high voltage power supplies for the PMT's are independent and are programmable with 8-bit resolution.

Data from all sixteen detectors (eight large-area and eight spectroscopy) are routed to a central electronics unit for digital processing by special-purpose data boards

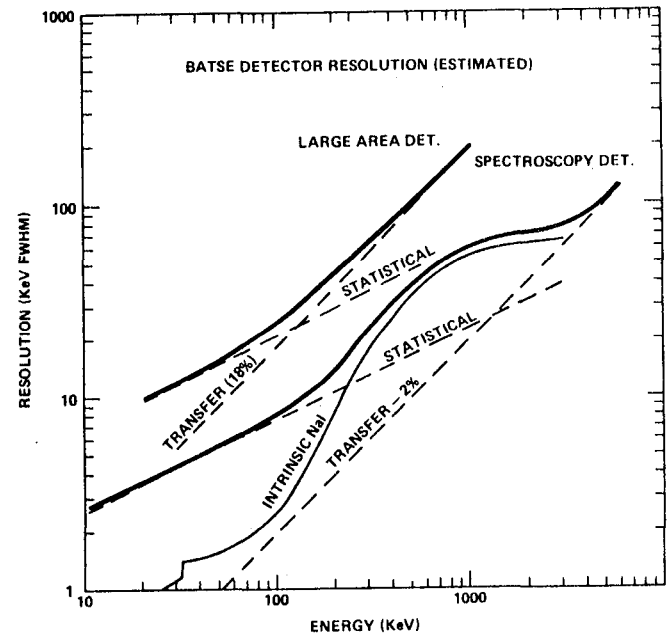

Figure 4

under the control of a microprocessor. Spectral 4 data are accumulated into 128 channels for the large-area detectors and 256 channels for the spectroscopy detectors. Twelve data types are available with different, programmable parameters to specify energy channel widths and temporal resolution [1,2]. The data system also contains a burst trigger system to detect and rapidly accumulate a large amount of data (~500 kB) for later playback through the GRO telemetry system. The burst trigger signal is sent to the other three instruments on the GRO, which also have capabilities for burst observations with their scintillation detectors.

The BATSE large area detectors, in addition to providing better single-spacecraft locations of gamma bursts than has been thus far possible, will permit observations of weaker gamma-bursts. An accurate Log N-Log S distribution can be measured over four decades in S (from ~ 10^{-7} to 10^{-3} ergs/cm^2) during the GRO mission, as well as the celestial distribution of hundreds of bursts. Prior difficulties in the measurement and interpretation of Log N-Log S data[5] should be overcome by BATSE. The BATSE/ GRO experiment will also become an important component of the interplanetary burst timing network. The unprecedented sensitiv- ity of the BATSE detectors may also uncover new, unexpected characteristics of bursts and other transient high-energy objects.

References

1. G.J. Fishman, C.A. Meegan, T.A. Parnell, and R.B. Wilson, in Gamma-Ray Transients and Related Astrophysical Phenomena, AIP Conf. Proc. No. 77, pp. 443-451 (1982).

2. G.J. Fishman, C.A. Meegan, T.A. Parnell, R.B. Wilson, and W. Paciesas, in High Energy Transients in Astrophysics, AIP Conf. Proc. No. 115, pp. 651-664 (1984).

3. J. L. Matteson, G.J. Fishman, C.A. Meegan, T.A. Parnell, R.B. Wilson, W. Paciesas, T. Cline, and B. Teegarden, paper OG 9.2-15, these proceedings.

4. W. Paciesas, R.B. Wilson, G.J. Fishman and C.A. Meegan, paper OG 9.2-16, these proceedings.

5. C.A. Meegan, G.J. Fishman, and R.B. Wilson, Ap. J., 291, pp 479-485 (1985).

GAMMA-RAY BURST SPECTROSCOPY CAPABILITIES OF THE BATSE/GRO EXPERIMENT

J. L. Matteson
Center for Astrophysics and Space Sciences
University of California, San Diego
La Jolla, California 92093 USA

G.J. Fishman, C.A. Meegan, T.A. Parnell and R.B. Wilson
Space Science Laboratory
NASA/Marshall Space Flight Center
Huntsville, Alabama 35812 USA

W. Paciesas
Physics Department
University of Alabama in Huntsville
Huntsville, Alabama 35899

T. Cline and B. Teegarden
Laboratory for High Energy Astrophysics
NASA/Goddard Space Flight Center
Greenbelt, Maryland 20771 USA

ABSTRACT

A scintillation spectrometer is included in each of the eight BATSE/GRO detector modules, resulting in all-sky coverage for gamma-ray bursts. The scientific motivation, design and capabilities of these spectrometers for performing spectral observations over a wide range of gamma-ray energies and burst intensities are described.

1. Introduction. In the past five years it has become clear on both observational [1,2] and theoretical [3] grounds that the spectra of gamma-ray bursts are rich sources of information which is crucial to determining the nature of the burst phenomenon. The observations have revealed various spectral components, most of which must arise in separate regions. A long-lived component in the x-ray band may be the afterglow of the cooling burst plasma [4]. A gamma-ray component from tens to hundreds of keV, the classical burst emission, has an exponential form [5,6] and appears to be due to some thermal process with a temperature of $\sim 10^9$ K. Above ~500 keV a high energy gamma-ray component often extends to at least 6 MeV with an approximate power law form [7] and has been observed up to 30 MeV in one case [8]. In the 25-70 keV band unresolved absorption lines have been observed in ~30 percent of the bursts and a few emission lines have also been observed [5,6,9]. These have been interpreted as due to cyclotron processes in terragauss fields, i.e. near a neutron star. At ~400 keV, broad, marginally resolved emission lines with ~200 keV width have been observed in ~5 percent of the bursts [5,6] and are interpreted as red-shifted pair annihilation radiation. All these lines' narrow widths require a cool, $T<2\times10^8$K, region for their formaton. A narrow, ~40 keV wide, emission line observed in one burst at ~740 keV is consistent with a redshifted gamma-ray from the first excited state of ^{56}Fe [10] and implies a temperature of ~ 2×10^9K. All of the components vary on time scales

shorter than the observations' integration times, which range from 0.25 sec to 5 seconds. In general, correlations among the components' variations have not been established. However, the annihilation line appears to be correlated with intensity on a 0.25 sec time scale in one well observed burst [11].

It is apparent that each region has its particular spectral signature which, in principle, can be independently followed with time-resolved spectroscopy over a broad energy band during a burst. Such observations would result in a new level of understanding of the evolution of the physical conditions of the various emission regions, their causal relationships, and their relationships to the underlying energy source of the burst. This is the primary motivation for the BATSE Spectroscopy Detectors, which are the subject of this paper. The very short cooling time scales near a neutron star, $<10^{-6}$ sec, imply that the spectral components are expected vary on the same time scale as the intensity. Thus sensitive spectral observations are required on short time scales, typically 0.1-1 sec, often as short as 10 msec and in one case, 5 March 1979, <0.2 msec.

2. Instrumentation. An overall description of the BATSE experiment is presented in an accompanying paper [12]. Each of the eight BATSE modules contains a 12.70 cm x 5.62 cm NaI(Tl) Spectroscopy Detector, which has an energy resolution of 7 percent at 662 keV and a Be window that extends its energy range down to 7 keV. (The effective area versus energy is shown in the accompanying paper.) The set of detectors has all-sky coverage and burst data are taken taken from the four detectors which most directly view a burst, resulting in an average sensitive detector area of ~ 500 cm^2. 14 keV to 10 MeV energy losses are analyzed into 2752 linear channels and then data compressed into 256 channels, preserving the detectors' energy resolution. An average event conversion cycle requires ~ 6μs, allowing a throughput of ~ $2x10^5$/sec-det, which corresponds to a burst flux of ~ $2x10^{-4}$erg/cm^2-sec. Discriminators at 7 keV, 20 MeV and 40 MeV provide data in the 7-14 keV, 10-20 MeV, 20-40 MeV and > 40 MeV bands. Linear operation at high counting rates is assured by 1) high current PMT bleeder strings which are zener diode regulated and 2) a gated baseline restorer in the analog electronics. It is planned to calibrate the nonlinear light output of the NaI(Tl) scintillators below 100 keV with the monochromatic x-ray beam at the Stanford Synchrotron Radiation Laboratory. Additional calibrations up to ~ 10 MeV will use radioactive sources and neutron capture gamma-rays.

The data are simultaneously stored in memories in two modes which are enabled by the BATSE burst trigger and preserve the detector IDs. In the HER (high energy resolution) mode, 192 spectra, including discriminator counts, are stored with a time resolution based on a time-to-spill algorithm that allows integrations as short as 64 msec at times of high rates and provides up to ~ 100 seconds of coverage with an average integration time of ~ 1 sec. Higher time resolution, for a subset of a burst's gamma-rays, is provided by the TTE (time-tagged events) mode, which stores 65,536 pulse heights, each time tagged to 128 μs precision. These data will provide a statistically significant spectrum measurement for each ~ 200 counts during source limited observations, e.g. each msec at a burst flux of ~ $5x10^{-5}$erg/cm^2-sec. Part of the TTE memory acts as a

pre-trigger buffer and will capture the leading edge of a burst that preceeds the the burst trigger.

3. Background and Sensitivity. Since the detectors are unshielded, their background is dominated by gamma-rays of cosmic, spacecraft and atmospheric origin. Lines at 511 keV and several other energies due to detector radioactivity will not significantly affect the sensitivity and the 511 keV line will be used for energy calibration. The background rate above 20 keV will be ~ 2000 sec^{-1}. A burst with <E> = 100 keV and a flux of $2x10^{-6}$ erg/cm^2-sec would produce the same rate.

In order to estimate sensitivity, we assume a 5 second burst with the spectrum, $dN/dE = 1/E\ exp(-E/250\ keV)$ plus an extension above 300 keV as an E^{-2} power law. Line strengths are expressed in units of fractional equivalent width, i.e. the usual equivalent width (keV) divided by the line centroid energy (keV). Figure 1a shows the sensitivity to unresolved lines. Data from various line observations [5,9,10] are plotted. These all have large equivalent widths and much weaker lines could be detected in the more intense bursts. The time required to detect a typical, 20 percent width line is shown in Figure 1b. During the most intense flux periods it

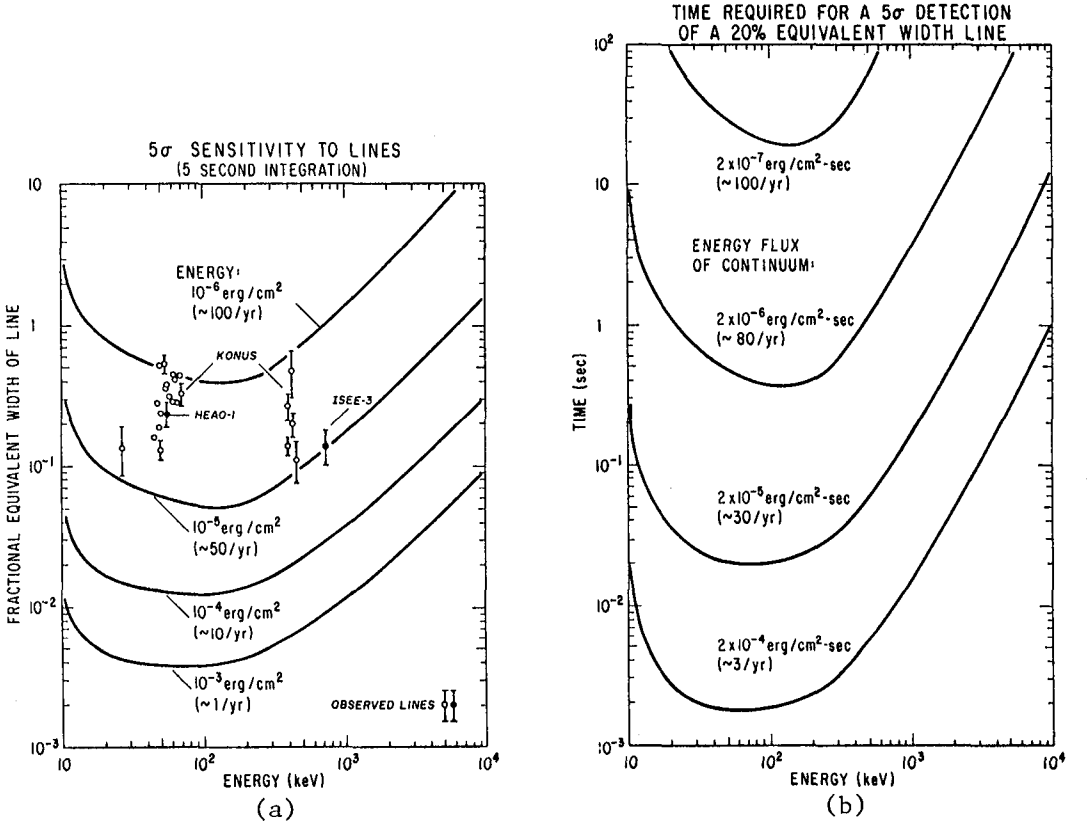

Figure 1. (a) - Sensitivity to spectral lines. (b) - Integration times required for line detection. The observations will be background limited at fluences (fluxes) below 10^{-5} erg/cm^2 ($2x10^{-6}$ erg/cm^2-sec). The anticipated observed frequency of bursts above the indicated strength is given in parenthesis.

will be possible to obtain cyclotron and annihilation line measurements with few msec time resolution, while at low fluxes, i.e. ~ 10^{-6}erg/cm^2-sec, ~ 1 sec time resolution will be possible. The search for nuclear lines in the ~ 1-10 MeV region will require longer integration times, from ~ 0.01 to 1 sec in the more intense bursts. Assuming 6 logarithmic energy channels per decade, 5σ measurements of the continuum spectrum would require half of the time indicated in Figure 1b.

4. Conclusion. The BATSE Spectroscopy Detectors have a powerful combination of energy band, sensitivity, and energy and time resolution, which represents a one to two orders of magnitude improvement over previous instruments. We can anticipate an equally large increase in our knowledge of gamma-ray bursts late in the decade when these detectors' observations become available.

5. Acknowledgements. This work is supported at the University of California, San Diego by NASA Contracts NAS8-35012 and NAS8-36081.

References

1. Teegarden, B.J., (1982), in Gamma Ray Transients and Related Astrophysical Phenomena, Lingenfelter, R.E., Hudson, H.S., and Worrall, D.M., eds. Am. Inst. of Physics, N.Y., p. 123.
2. Teegarden, B.J., (1984), in High Energy Transients in Astrophysics, Woosley, S.E., ed., Am. Inst. of Physics, NY, p. 352.
3. Lamb, D.Q., (1982), in High Energy Transients in Astrophysics, Woosley, S.E., ed., Am. Inst. of Physics, NY, p. 512.
4. Laros, J.G., et al., (1984), Ap.J., 286, 681.
5. Mazets, E.P., et al., (1981), Nature, 290,378.
6. Mazets, E.P., et al., (1983), in Positron-Electron Pairs in Astrophysics, Burns, M.L., Harding, A.K., and Ramaty, R., eds., Am. Inst. of Physics, N.Y., p. 36.
7. Matz, S.M., et al., (1985), Ap.J. (Letters), 288, L37.
8. Rieger, E. et al., (1982), in Accreting Neutron Stars, Brinkman W. and Trumper, J., eds., Max-Planck Institute, Garching, p. 229.
9. Hueter, G.J., et al., (1984), in High Energy Transients in Astrophysics, Woosley, S.E., ed., Am. Inst. of Physics, NY, p. 373.
10. Teegarden, B.J., and Cline, T.L., (1980), Ap.J. (Letters) 236, L67.
11. Barat, C., et al., (1984), Ap.J. (Letters), 286, L11.
12. Fishman, G.J., et al., (1985), paper OG9.2-14, these proceedings.

CAPABILITIES OF THE GRO/BATSE FOR MONITORING OF DISCRETE SOURCES

W. S. Paciesas
Department of Physics, University of Alabama in Huntsville
Huntsville AL 35899
USA

R. B. Wilson, G. J. Fishman, and C. A. Meegan
Space Science Laboratory, NASA Marshall Space Flight Center
Huntsville AL 35812
USA

ABSTRACT

Although the Burst and Transient Source Experiment (BATSE) to be flown on the Gamma Ray Observatory has as its primary objective the detection of gamma ray bursts, its uncollimated design will enable it to serve a unique function as an all-sky monitor for bright hard x-ray and low-energy gamma ray sources. Pulsating sources may be detected by conventional techniques such as summed-epoch and Fourier analyses. The BATSE will, in addition, be able to use earth occultation in an unprecedented way to monitor sufficiently bright sources as often as several times per day over ~85% of the sky. We present estimates of the expected BATSE sensitivity using both of these techniques.

I. INTRODUCTION

Various details of the design and expected performance of the BATSE have been presented in previous papers [1-3]. Although the prime scientific objective of this instrument is to detect and characterize gamma ray bursts, the observation of other types of sources constitutes an important secondary objective. The ability to act as a near-all-sky monitor for persistent and longer-lived transient sources (by using earth occultation) and for long-period pulsating sources (by the standard techniques such as epoch-folding, Fourier analysis, etc.) is inherent in the instrument as designed for its prime objective. The capability to detect short-period pulsars has been incorporated by adding electronics hardware and software which performs on-board epoch-folding. We report here the results of calculations of the estimated BATSE sensitivity for observations using the epoch-folding and earth-occultation techniques. These results apply only to the BATSE large area detectors. Similar analyses of data from the spectroscopy detectors may significantly improve the sensitivity in specific cases where a wider energy range and/or finer energy resolution are of interest.

II. DETECTOR EFFICIENCY AND BACKGROUND ESTIMATES

The accuracy of the calculated sensitivity depends upon the reliability of the estimates of a detector's efficiency and its expected background properties. Estimates of the efficiency of a BATSE large area detector which we used for this calculation have been derived analytically and are presented in an accompanying paper at this conference [3]. The expected background in orbit is the sum of three principal components: the diffuse gamma ray sky background, the earth's atmospheric gamma ray albedo, and the

interactions of charged particles in the detector and surrounding material. We have calculated the first component by convolving the diffuse background spectrum with the estimated detector efficiency. The sum of the second and third components was taken to be equal to the background of the detectors in MSFC's balloon-borne instrument [4], which can be considered design prototypes of the BATSE large area detectors.

III. SENSITIVITY USING THE OCCULTATION TECHNIQUE

Approximately 85% of the sky is occulted at some time during each GRO orbit; the orbital precession of 7° per day ensures that any point in the sky may be monitored at least once every two months with the occultation technique. A sufficiently long-lived source will produce one or more steps in the overall detector count rate corresponding to immersion into and/or emersion from occultation by the earth. This is of interest not only for monitoring the variability of persistent sources and long-lived transients, but also for detecting transients on timescales of a few minutes to a few days which are too long-lived and/or too weak to trigger the on-board burst detection system. Although a few such events have been observed previously [e. g., ref. 5], very little is known of their nature.

The time of occurrence of the occultation steps provides information on the location of a transient. The accuracy of the source location will depend somewhat on its intensity and its elevation above the orbit plane; preliminary estimates indicate that an accuracy of ~0.5° should be typical.

Because of the wide field of view of the BATSE detectors, the variation in background due to the difference in surface brightness between earth and sky will occur on a much longer timescale than the occultation steps (which last about 8 s for a source in the plane of the orbit). It is assumed that other systematic background variations will also be negligible on the occultation timescale, and that improvement of sensitivity by summation of the occultation steps over many orbits will be feasible.

The sensitivity estimates were derived by assuming that the source intensity at each step may be determined by taking the difference of two 60 s integrations, one while the source was unocculted and the other while it was occulted. Table I shows the estimated sensitivity (relative to the intensity of the Crab nebula) at 99.9% confidence for several different energy ranges. The improvement obtained by multi-orbit summation is evident. The practical upper limit to the number of orbits which may be combined is presently unknown.

Table I. BATSE Occultation Sensitivity

Energy Range (keV)	99.9% confidence sensitivity (Crab units)		
	1 orbit (90 min.)	16 orbits (1 day)	224 orbits (2 weeks)
20-50	0.1	0.03	0.007
50-100	0.2	0.04	0.01
20-100	0.07	0.02	0.005
100-500	0.3	0.08	0.02

The most sensitive sky survey performed thus far at these energies used the UCSD/MIT A-4 instrument on HEAO-1 [6]. This instrument scanned the entire sky once every six months using fan-shaped fields of view, so that a given source was typically observable for several weeks at a time at six month intervals. In Table II we list the number of sources in the A-4 catalog which would be detected by BATSE in the 40-80 keV energy band for various timescales. It is interesting to note that the limiting sensitivity of the A-4 survey in this range is approximately the same as the BATSE sensitivity for a two-week orbit sum. Thus, the BATSE will be able to monitor all 40-80 keV sources in the A-4 catalog with two-week time resolution.

Table II. BATSE Sensitivity to HEAO A-4 Catalog Sources

40-80 keV (99.9% confidence)

Time Resolution	BATSE sensitivity (Crab units)	Number of HEAO A-4 sources
1 orbit (90 minutes)	0.1	5
16 orbits (1 day)	0.03	17
224 orbits (2 weeks)	0.009	46

IV. SENSITIVITY TO PULSATING SOURCES

Pulsating sources fall into two categories in the BATSE data, according to their pulse period. The first type have periods longer than ~10 s, so that the continuous readout of rates with 1.024 s or 2.048 s resolution may be used to search for both known and unknown periodicities. All-sky coverage is implicit, except during earth occultation. The second type, with shorter periods (down to a few ms), requires on-board folding and thus is possible only for known periodicities. The hardware limits on-board folding to two periods at a time, one using data from selected large area detectors and the other from selected spectroscopy detectors.

It has been assumed for the purpose of estimating sensitivity that pulsating sources will be detected by using the conventional epoch-folding technique. In addition to its dependence upon predicted detector efficiency and background, the time required to observe pulsations of a particular statistical significance using this method is dependent upon the shape of the pulse light curve. Table III shows the estimated sensitivity (99.9% confidence) relative to the pulsed flux of the Crab pulsar (assumed to be 0.027 ph/cm^2-s in the 30-100 keV range) for several values of the integration time and for three cases of pulse light curve: a sine-wave, the hard x-ray light curve of the Crab pulsar, and a rectangular pulse with 10% duty cycle.

Table III. BATSE Pulsar Sensitivity (30-100 keV)

	99.9% confidence pulsed sensitivity (Crab pulsar units)		
Integration length	Sine shape	Crab shape	Rectangular shape
1 orbit (90 minutes)	0.2	0.1	0.04
16 orbits (1 day)	0.04	0.02	0.01
224 orbits (2 weeks)	0.01	0.007	0.003

V. SUMMARY

Sensitivities attainable with the BATSE in observing non-burst sources have been estimated using assumptions appropriate to searches for known or suspected sources and presented in this paper. Except in the case of short-period pulsars (where on-board folding requires a priori knowledge of the approximate pulse period), it will also be possible to examine the BATSE data for previously unsuspected sources. In this latter case, efficient search procedures will most likely make use of other techniques such as Fourier analysis which have not been explicitly considered in our sensitivity estimates. Therefore, these estimates should be treated with some caution in applying them to generalized searches.

Finally, we show in Table IV the time required for BATSE to achieve 99.9% confidence measurements of typical high energy sources using the occultation technique and, where applicable, epoch-folding. It is clear that the successful application of these and similar techniques to the BATSE data will provide unprecedented and valuable sensitivity for near all-sky monitoring of low energy gamma ray sources.

Table IV. BATSE Sensitivity (30-100 keV) -- Selected Sources

	Pulse	Time required (99.9% conf. detection)	
	Period	Total emission	Pulsed component
Source name	(s)	(occultation)	(summed epoch)
A0535+26 (max.)	104	single step	single pulse
Centaurus A	N/A	single step	N/A
Crab pulsar	.033	single step *	1 minute
Vela X-1	283	single step	single pulse
Hercules X-1	1.24	6 hours	20 minutes
NGC 4151	N/A	1/2 day	N/A
3C273	N/A	2 days	N/A
A0535+26 (min.)	104	3 days	2 hours
MKN 509	N/A	2 weeks	N/A

* nebula plus pulsar

REFERENCES

1. G. J. Fishman et al., in Gamma-Ray Transients and Related Astrophysical Phenomena, AIP Conf. Proc. No. 77, pp. 443-451 (1982).

2. G. J. Fishman et al., in High Energy Transients in Astrophysics, AIP Conf. Proc. No. 115, pp. 651-664 (1984).

3. G. J. Fishman et al., paper OG9.2-14, these proceedings.

4. R. B. Wilson et al., in Gamma-Ray Transients and Related Astrophysical Phenomena, AIP Conf. Proc. No. 77, pp. 67-78 (1982).

5. Carol Armbruster and Kent S. Wood, in High Energy Transients in Astrophysics, AIP Conf. Proc. No. 115, pp. 73-76 (1984).

6. A. M. Levine et al., Astrophys. J. Suppl., 54, 581 (1984).

LAPEX: A PHOSWICH BALLOON EXPERIMENT FOR HARD X-RAY ASTRONOMY

F. Frontera, A. Basili, D. Dal Fiume, T. Franceschini, G. Landini, E. Morelli, J.M. Poulsen, A. Rubini, and S. Silvestri

Istituto Tecnologie e Studio Radiazioni Extraterrestri, Consiglio Nazionale Ricerche, Via Castagnoli, 1 - 40126 Bologna, Italy.

E. Costa, D. Cardini, and A. Emanuele

Istituto di Astrofisica Spaziale, Consiglio Nazionale Ricerche, 00044 Frascati, Italy.

1. Introduction. Satellite and balloon observations have shown that several classes of celestial objects are hard ($\geq$ 15 keV) X-ray emitters. A complete sky survey in the 15-180 keV energy band with a sensitivity of ~ 10 mCrab has been performed with the UCSD/MIT instrument (A4) on board the HEAO 1 satellite (1). About 70 X-ray sources were detected, including galactic and extragalactic objects. Hard X-ray emission has been detected in the Galaxy from X-ray pulsars, black hole candidates, transient X-ray sources, burst sources. Extragalactic sources of hard X-ray emission include clusters of galaxies, QSOs, BL Lac objects, Seyfert galaxies.

While the few brightest hard X-ray sources are well studied, much additional observational work is required to obtain spectral and temporal information in the 20-200 keV band from sources with flux levels in the range 1-10 mCrab (10^{-6} - 10^{-5} photons/cm^{2}s keV).

Another open issue is the identification of the hard X-ray sources with objects known at lower X-ray energies or at optical wavelengths. As the HEAO 1-A4 sky survey results have shown, the central galactic plane region ($|b^{II}| < 10°$, $260 \leq l^{II} \leq 50°$) is crowded with many hard X-ray sources, which were not resolved with the 1.5° x 20° crossed collimators of the HEAO 1-A4 detectors. These crowded sky fields require observations with better angular resolution.

Future satellite missions like SAX (Italy) and XTE (U.S.A.), which have as primary objectives the observation of hard (15-200 keV) X-ray sources at sensitivity levels of about one order of magnitude better than the A4 experiment, are yet at their early study phases. Their field of view of 1° FWHM will not make it possible to resolve all of the crowded fields. Therefore selected sky fields can be profitably studied with balloon observations that have limiting sensitivities of about 1 mCrab in the 20-200 keV energy band and angular resolutions better than 1°.

In this framework, we are developing a Large Area Phoswich Experiment (LAPEX), which meets the above-mentioned requirements. It has:

i. a broad energy band of operation (20-300 keV);
ii. a 3 σ sensitivity of about 1 mCrab in 10^4 s of live observing time;
iii. imaging capabilities with an angular resolution of about 20'.

The first balloon flight of the LAPEX is scheduled for 1986.

2. Experiment Description. We report here the essential characteristics of the experiment. A detailed technical description of the entire payload has already been given (2) and an experiment summary is found in Table 1. The detection plane is an array of 16 scintillator detectors. Each detector is made of a 145 x 145 mm^2 NaI(Tl) crystal 6 mm thick, which is sandwiched with a CsI(Na) crystal having the same frontal surface and a thickness of 50 mm. The scintillations of both crystals are viewed by a photomultiplier tube (PMT) of diameter 5" through a light guide of lead glass 15 mm thick. Each group of 4 detection units is surrounded by a NE110 plastic scintillator, exclusive of the aperture. A passive graded shield (Pb, Sn, Cu) is inserted between the crystals and the lateral plastic scintillator. A bank of four passive collimators is mounted above each group of four detection units. The collimators are made of electroformed hexagonal tubes of lead (0.1 mm) surrounded by Tin (0.25 mm) and Copper (.08 mm) on both sides. The collimators cause a 9% reduction of the total geometric area. Each collimator bank is mounted so as to obtain a triangular response with a flat top of 20'. Each collimator bank can rock by 8°, indipendently of the other three, at a desired frequency.

Table 1
Experiment summary

Energy range of operation	20-300 keV
Total geometric area	3400 cm^2
Energy resolution ($\Delta E/E$) at 60 keV	17% (FWHM)
Field of view	3° (FWHM)
Angular resolution	20' (FWHM)
Time resolution	100 μs
Spectral bin width	~ 1 keV
Telescope mounting	alt-azimuthal
Post-facto attitude reconstruction	3'
Guiding system	automatic, from ground station

Above the rocking collimators one can mount a set of 16 rotating modulation collimators (RMC), one for each detection unit, in a configuration that makes the instrument a true imaging device. Through a proper choice of the distance between the grid planes of each RMC it is possible to image a sky field with an angular resolution that depends on the minimun pitch-angle (angular distance between planes of maximum transmission). A description of this multi-pitch rotation modulation collimator (MPMC) can be found in refs. 2 and 3. For our experiment we have chosen 8 different distances between grid planes, a minimum pitch-angle of 40', grid planes made of tungsten strips with 1.5 x 1.5 mm^2 square section, and a rotation period of 100 s. The MPMC will operate in the 20-200 keV band.

An active gain control system will allow a continuous monitoring of the instrument gain and, if required, to adjust it to a preselected value. The gain control is based on the use of ^{241}Am sources deposited into plastic scintillators placed at the bottom of the rocking collimators.

The α particles associated with the ^{241}Am X-rays give a signal in the plastic which allows to tag the X-ray events, therefore to measure the detector gain at 60 keV and, if required, to change the PMT high voltage.

An absolute calibration of the detection plane is also available and this is based on the use of ^{139}Ce sources which scan the field of view every 2000 s.

3. Observation strategy and expected performances. The instrument will operate with either the rocking collimators or the MPMC. In the first case the observation strategy of the celestial objects is to point in turn two banks of collimators in the source direction and the other two towards an empty field. The banks are swopped between ON and OFF positions at a selected frequency. We have carefully evaluated various systematic errors in the background subtraction due to this rocking technique, e.g. background variations due to variations of exposed area, atmospheric thickness and telescope zenith angle. We have found that the systematic errors can be controlled within 0.3%. As a consequence, we expect to be able to measure source fluxes as low as 1% of the background at a significance level of 3 σ. The expected background count rate is based on an in-flight test (4). Figure 1 shows the expected spectrum determination sensitivity of the instrument when it will operate with the rocking collimators. We plan to use rocking collimators to study isolated sources.

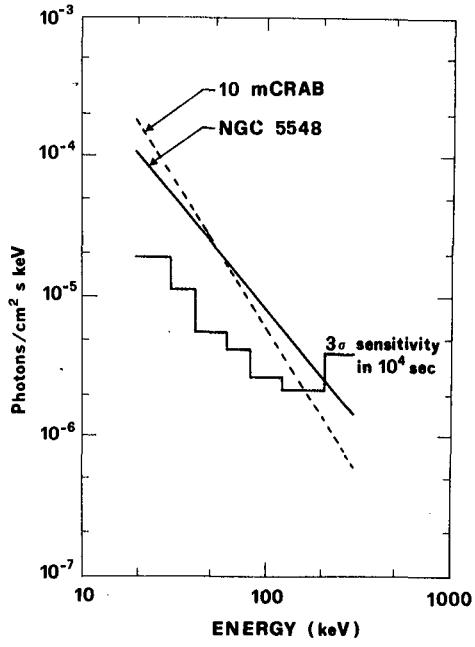

Fig. 1. – Spectrum determination sensitivity of the instrument with the rocking collimators

The MPMC will be mounted to resolve complex fields. When the instrument is used in this configuration the flux sensitivity will be lower (by a factor of ~ 3), but the angular resolution will be at least 20' FWHM. As an example, Fig. 2 shows the expected image in the 20-200 keV band of two X-ray sources 1° apart, one 0.5 Crab and the other 0.3 Crab, for an observing time of 100 s. Computer simulations have shown that the multi-pitch approach is superior to the classical RMC configuration, specially in case of crowded fields.

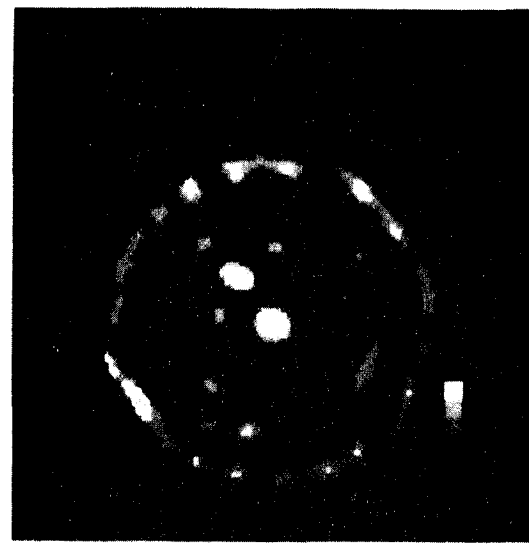

Fig. 2. – Imaging capability of the instrument with the MPMC. This image was obtained simulating a field with two X-ray sources 1° apart of comparable intensity (see text).

References

1. Levine, A.M. et al. 1984, Ap. J. Suppl. 54, 581.
2. Frontera, F. et al. 1984, Nuovo Cimento 7C, 656.
3. Makishima, K. et al. 1978, Space Astronomy XX, 277.
4. Frontera, F. et al. 1985, Nucl. Instr. and Meth. A235, 573.

AN IMPROVED TIME OF FLIGHT GAMMA-RAY TELESCOPE TO MONITOR DIFFUSE GAMMA-RAY IN THE ENERGY RANGE 5 MeV - 50 MeV

Da Costa Fereira Neri A., Bui-Van A., Lavigne, J.M., Sabaud C., Vedrenne G., CESR, Toulouse

Agrinier B., Gouiffes C., Service d'Astrophysique, Saclay

Abstract

A time of flight measuring device is the basic triggering system of most of the medium and high energy gamma-ray telescopes. A simple gamma-ray telescope has been built in order to check in flight conditions the functionning of an advanced time of flight system. The technical ratings of the system will be described. This telescope has been flown twice with stratospheric balloons, its axis being oriented at various zenital directions. The results of these flights for what concern : diffuse gamma-rays, atmospheric secondaries, and various causes of noise in the 5 MeV-50 MeV energy range will be presented.

1. Introduction and motivation. Gamma ray telescopes for energies in excess of 10 MeV are mostly built around a track chamber in which photons are materialized by pair effect. Coordinates of track of an event is read if the veto counter above and on the sides of the chamber have not been triggered and if downward moving particles (supposed to be electrons) issuing from the bottom trigger a set of thin counters in coïncidence see (1) (2). This last set of two counters is usually named "time of flight" measurement since its purpose is to measure sense and duration of travel of the electrons across it and also to give a limit to the angular aperture of the telescope.

Nevertheless once looking at the tracks visually or with the help of some track identifying software one is left with only a few percent of "good events" among the initial trigger rate of the chamber. This fact leading to a waste of telemetry bit rate.

A second fact is the large number of upward moving events giving tracks stopping in the chamber or reflected backward and simulating pairs /1/. These events if not properly removed by the time of flight counters (T.O.F.) can plague the data. In order to improve the characteristics of a gamma-ray telescope designed for the energy range 5 MeV-50 MeV (3) (AGATHE experiment) we have undertaken to built a T.O.F. telescope with the double objective to improve its capabilities on a short T.O.F. path (57.5cm) but with realistic lateral dimensions (80x40cm) keeping in view to reduce the total dimensions of the telescope. In a second step we included this T.O.F. in a very simple gamma ray telescope and had it flown with a stratospheric balloon in order to monitor and try to explain various counting rate observed in balloon borne gamma ray experiments.

2. Description. The experimental set-up used in flight is shown fig. 1. It includes from the top :

1. An anticoïncidence counter plastic scintillator NE 102A with dimensions 85x45x1 cm.

2. A Tantalum target 0.03 cm thick the same thickness used in the Agathe telescope spark-chamber.
3. T.O.F. counters made of two sheets of NE 102A plastic scintillators with dimensions 80x40x0.5 cm placed at 57.5 cm separation.
4. We had at the bottom a 10 cm thick plastic scintillator calorimeter (85x45x10cm) made of Altustipe blue 155 manufactured by Altutor. This scintillator was used in various electrons beam for other purposes and proved to be linear far electrons up to 24 MeV for the 10 cm thickness. Photomultipliers were XP2020 for the AC and T.O.F., and XP 2041 for the calorimeter.

NIM electronic units were used for the fast electronics and ADC, and home made electronic circuits for housekeeping informations and interfacing with telemetry . The whole telescope could be rotated in flight at various zenit angles and stabilized in azimut. Basic events were defined by $\overline{AC}$+S1+S2 and T.O.F. value in a 50nsec window. The functionning of the T.O.F. measurement is based on the comparison with a Time to Amplitude Converter of the mean arrival time in S1 (upper T.O.F. counter) and S2 (lower T.O.F. counter). These mean arrival times on each counter were obtained by sending left and right signals in a very performing "Time Pick-off"circuit made by Schlumberger-Enertec and then both signals from the T.P.O. output in a "mean-timer" Lecroy.
The informations sent by telemetry were
- T.O.F. observed in the 50 nsec window, with 256 channels accuracy. The width of the window and the delay in S2 allowing to display upward and downward moving particles.
- Amplitudes in T.O.F. counter S1 and S2 obtained by mixing dynodes signal from left and right PM tubes and digitized in 256 channel ADC.
- Amplitude read in the calorimeter digitized in 256 channel the muon peak beeing in the channel 118.

3. Results. Fig.2 shows the T.O.F. spectra obtained at ceiling (4mb) for O° zenit direction in AC ON and AC OFF configuration.
- T.O.F. spectrum : The first and second peak being respectively upward and downward moving events are very clearly separated when using particles see AC OFF at celing Fig. 2 a small displacement of the peaks toward greater time difference at ceiling can be explained by a much larger isotropy of arrival direction. When looking at gamma-ray T.O.F. (AC ON configuration) the separation is not so good and is probably due to the fact that pair of particles are reaching the lower T.O.F. counter at spatial distances not so negligible for the mean-timer compensation to be efficient. Nevertheless distinction between the two senses of travel is still very good and can be made of the order of 10^{-3} at the expense of a small loss of good events. Another noticeable fact that can be observed on the T.O.F. distribution AC ON is the great number of upward moving events a fact also noted with Double Compton Telescope although using very different thickness of material and neutral events selection. (5)
- Calorimeter. The spectra obtained for gamma-ray events (AC ON) at various zenit angle have been used with the efficiency curve for gamma-ray obtained by Monte Carlo computation to derive the atmospheric gamma-ray spectrum above 5MeV in these directions.

Preliminary result at 180° inclination which are useful in particular for satellite experiments (fig. 3) agree well with other experiment at same latitude but higher energies (4).

4. Conclusion. These preliminary results will be refined by making use of the full informations from the amplitudes and T.O.F.; and also given for other zenital direction monitored during the flights. A first explanation for what concern the discrepancy between trigger-rate and acceptable pictures from track chamber seems to be the large acceptance angle of the counter telescope for low energy gamma-ray. A way to improve this situation could be to locate the particles in the two T.O.F. counters in order to derive an estimate of the incoming direction. More or less sophisticated use of the amplitudes from left and right PM tube on each T.O.F. counter can bring very sensitive improvement (6), it could be used on our telescope at a very moderate cost.

References

1. Lavigne, J.M. et al. Nucl. Instr. & Meth. 199 (1982) 585
2. Ross R.W., Chesney J.R., IEEE Trans on Nucl. Science Vol N 527 n°1 Feb. 1980
3. Lavigne J.M. et al. Ap. J. vol. 261, 720, 1982, October 15
4. Thompson D.J. J.G.R. vol. 79, N°10, p.1309, April 1, 1974
5. Schonfelder V, et al. Ap. J. vol. 240, 350 Aug. 15, 1980
6. D'Agostini et al. Nuclear Inst. & Meth. 185 (1981) 49

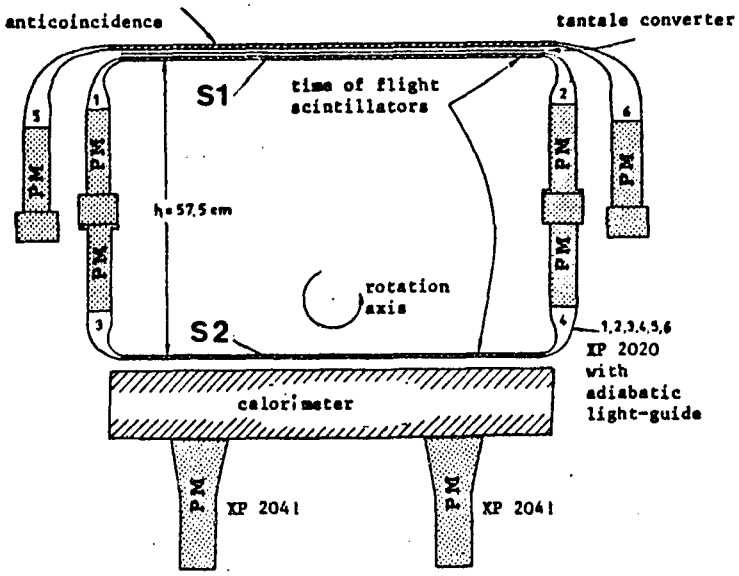

FIG 1

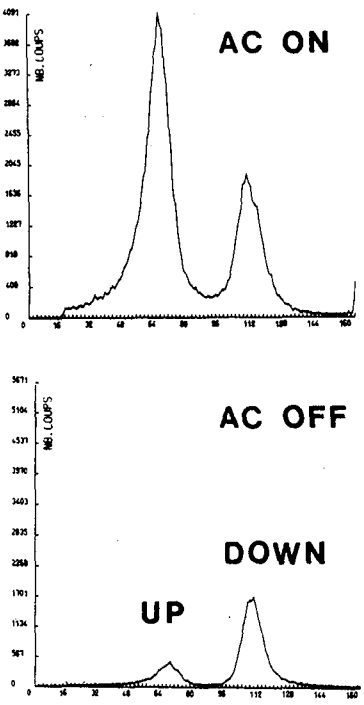

FIG 2

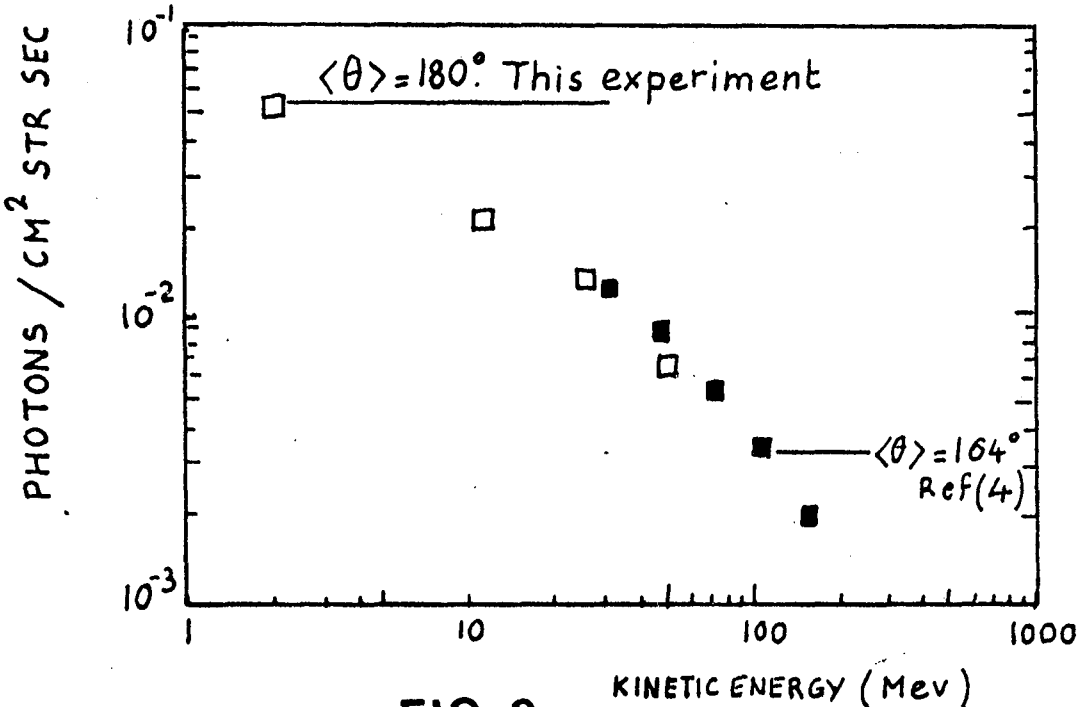

FIG 3

Results of a Study to Build a Gamma-Ray Telescope in an External Tank

David Koch
Smithsonian Astrophysical Observatory
60 Garden Street
Cambridge, MA 02138 USA

Abstract

In response to the ever-present need for a very large gamma-ray detector for energies greater than 100 MeV, a concept to build a telescope of 250,000 cm^2 sensitive area using a Space Shuttle External Tank (ET) is presented. In the Space Station era, for the first time, large detectors can be constructed on-orbit which would otherwise be limited in size by the launch vehicle. The ET will serve both as the spacecraft and the Cherenkov pressure vessel. The significant feature is that the sensitive area will be forty times that of the high energy detector on GRO and will be able to locate even the faintest sources from the GRO survey to a few arc minutes. The detection technique is based upon that originally proposed by Greisen.(1)

1. Introduction

The results to date in high energy gamma-ray astronomy are based primarily upon measurements with instruments of only about 600 cm^2 sensitive area. The next generation high energy detector, EGRET, on the Gamma Ray Observatory (GRO) will have a sensitive area of about an order of magnitude greater. The survey resulting from GRO, in particular from EGRET, should produce a list of sources with the same log N/log S distribution as in previous astronomical surveys. That is, the bulk of the sources should be at the limiting sensitivity of EGRET and due to the detection technique, be of maximum positional uncertainty. Spark chambers have been the workhorse in high energy gamma-ray astronomy since they provide simultaneously a large field of view and positional information which is needed to carry out the survey work. However, spark chambers become impractical if they are substantially larger than EGRET due to complexity and deadtime. In addition, when carrying out discrete source studies, the large field of view is of no advantage. Although GRO does not strain the limits of the Shuttle, a substantial increase in size (more than an order of magnitude) cannot be accommodated as a conventional payload. Therefore new directions must be sought to circumvent the launch capability within the current Shuttle system and a detection technique must be used which can easily be extended to very large areas without also multiplying the complexity.

2. Unconventional Solution

With the advent of the Space Station, unconventional approaches are possible for the construction of large cosmic-ray detectors. The gas-Cherenkov telescope originally conceived by Greisen and proven on several balloon flights(2,3,4) can provide the next advance in high energy gamma-ray detection. It is based upon the principle of imaging the Cherenkov light produced by the created electron pair. The gamma-ray imaging telescope system (GRITS) has 40 times the sensitive area of GRO, thus provid-

ing among other attendant improvements, measurements of variability one-fortieth as small. An angular resolution of a few arcminutes approaches the ultimate limit imposed by the physics of the pair-production mechanism. The key to this concept is the Space Station, and the availability on-orbit of the currently disposed of external tank (ET). The ET is ideal for this application since it is a large, clean, rigid, thin-walled, insulated, light-tight, gas-tight pressure vessel.

3. Gas Cherenkov Detection Technique

The combination of signatures and constraints utilized in this instrument result in a straightforward detection of gamma rays and inherently excellent non-gamma-ray background rejection. For the energies of concern, greater than 100 MeV, photons interact exclusively to produce an electron-positron pair. Figure 1 illustrates how the ET is to be instrumented. At the top of the telescope a thin converter is tightly sandwiched between two plastic scintillators to form the trigger module. The scintillator on the incident side is used as a veto to reject all singly-charged particles. The one on the exit side is used to detect the two charged particles resulting from the conversion of the neutral gamma ray.

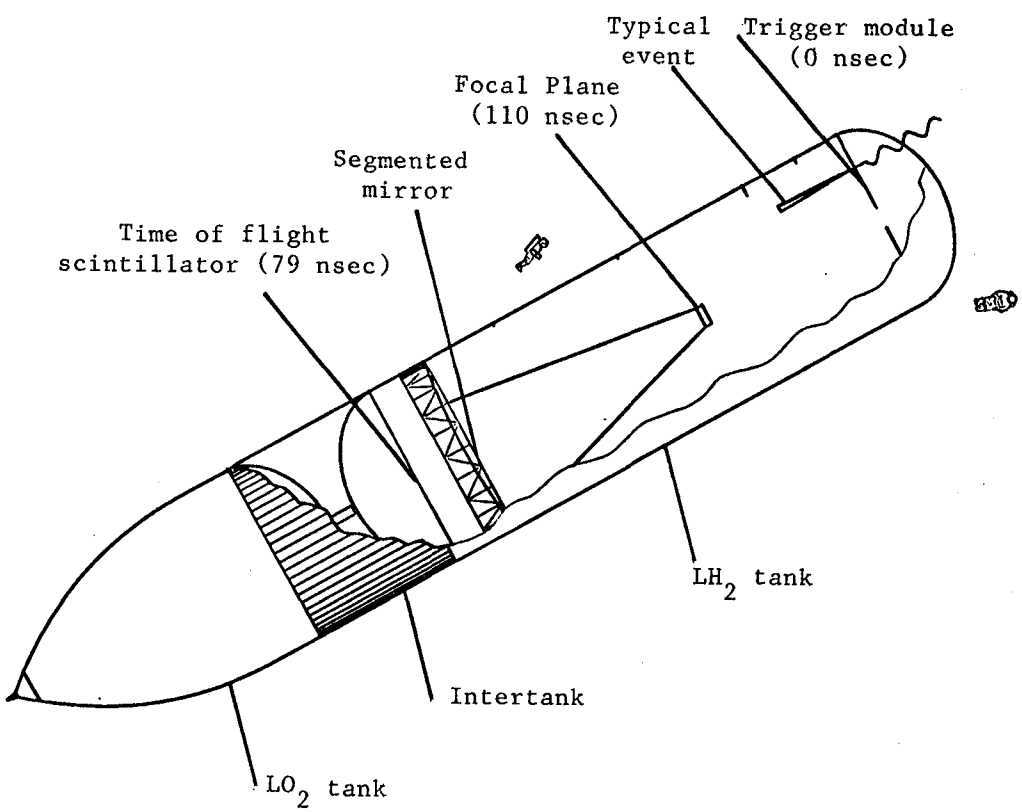

Figure 1. Major elements of the gamma-ray imaging telescope. The numbers indicate the elapsed time in nanoseconds for each signal composing the threefold time-delayed coincidence. In addition, there is a charged particle veto at t = 0. The overall length of the ET is 46.5 meters.

The energetic pair then travels the length of the telescope producing Cherenkov light in the gas-filled ET. For the index of refraction selected, 1.0000726 (air at 1/4 atm), the cone angle of emitted light is 1.4 deg, 5.8 visible light photons are produced per particle per meter of path length and the threshold for emission is at a Lorentz factor of 83. The two cones of light are imaged by a mirror at the far end of the ET onto an array of 127 photomultiplier tubes or a multineedle detector.(5) At the focus the two rings (not filled circles) of light arrive 110 nanosec after the pair creation. Data from the focal plane array are used to determine that the image and the amplitude of light corresponds to two rings of light. A time of flight (TOF) scintillator is placed behind the mirror to detect the passage of the charged pair 79 nanosec after the conversion of the gamma ray.

The electronic signature of an event is a threefold time-delayed coincidence of a pulse from the trigger module with no commensurate veto, 79 nanosec later a pulse in the TOF scintillator and 110 nanosec after the trigger, a pulse at the focal plane. During data reduction, the pulse height data from the light in the focal plane are not only used to validate the detection of two particles, but the location of the rings in the focal plane is used in the determination of the incident direction of the gamma ray. The combination of signatures and constraints make this detection technique naturally immune to all forms of non-gamma-ray background. Table 1 lists various types of background and the method the instrument uses to reject them.

For the converter material, active scintillators are used rather than a passive material such as lead. Measurement of the pulse height in the converter will determine the thickness of material through which the electron pair underwent multiple Coulomb scattering. Non-uniformimities in the light collecting efficiency which would otherwise make the pulse height measurements meaningless can be removed by making the same pulse height measurements in the thin trigger scintillator which will be of the same geometry and mounted directly under the converter scintillator. The amount of scattering in the trigger scintillator and the Cherenkov gas is both constant and smaller than that in the converter. Having determined the amount of scattering to expect in the converter will improve the uncertainties involved in determining the total amount of Coulomb scattering for each event. Knowing the scattering and having measured the angular separation of the particles in the focal plane will determine the energy of the incident gamma ray.

4. Angular Resolution and Sensitivity

Due to implementation constraints, only about half of the cross section of the ET can contain unobstructed trigger modules for a sensitive area of 250,000 cm^2. For converter thicknesses resulting in multiple Coulomb scattering commensurate with the emission angle, the sensitivity is roughly independent of the converter efficiency. To first order a resolution element is proportional to the square root of the converter thickness. Hence, a converter of 0.036 radiation lengths has been chosen to provide the optimum angular resolution with very little loss in sensitivity. This results in an RMS cell size of 1.1 degrees for energies greater than 300 MeV. (The emission angle at 300 MeV is 0.6 degrees.) Since the centroid uncertainty is about one-tenth of the cell size (and

is roughly inversely proportional to energy), the error radius for all point sources seen with a signal to noise of ten is 7 arc minutes. Using only events of energy greater than 1 GeV with no loss in sensitivity gives a position to 2 arc minutes. The counting rates for various sources at energies greater than 300 MeV are:

R(Vela) = 70 counts/hour
R(Crab) = 9.8 counts/hour
R(Bkgd) = 0.8 counts/hour/cell (near the Crab and Vela).

Thus a signal to noise of 10 can be reached in 1.4 hours for Vela and in 11 hours for the Crab.

TABLE 1
Methods Of Rejection Of Non-Gamma-Ray Background

EFFECT	REJECTION METHOD
Singly charged primary	Amplitude and shape of light indicative of two rings and veto directly above converter with two-particle trigger directly below
Hadrons	Same as above and require Lorentz factor greater than 83
Chance coincidences	Amplitude and shape of light indicative of two rings and threefold time-delayed coincidence
Backward going events	Same as chance coincidences and not trigger veto
Decaying muons	Amplitude and shape of light indicative of two rings and Lorentz factor greater than 83
Off-axis events	Mirror and focal-plane geometry

References

1. Greisen, K.I. 1966, Perspectives in Modern Physics, ed. R. Marshak (New York: Interscience Publishers), p. 355.
2. Koch, D.G. et al. 1973, Performance of a Gas-Cherenkov Gamma-Ray Telescope, Nuclear Inst. & Meth., 108, 349.
3. McBreen, B. et al. 1973, Pulsed High Energy Gamma-Rays from the Crab Nebula, Ap. J., 183, 571.
4. Greisen, K. et al. 1975, Change in the High-Energy Radiation from the Crab, Ap. J., 197, 471.
5. Comby, G. et al. 1982, Detector for U.V. Cerenkov Imaging Device, IEEE Trans. Nucl. Sci. NS-29, 328.

GeV GAMMA-RAY ASTRONOMY TELESCOPES WITH HIGH ANGULAR RESOLUTION

B. McBreen,
Physics Department,
University College,
Dublin 4, Ireland.

ABSTRACT

It is shown that a major improvement in angular resolution for the detection of gamma-rays in the GeV region can be obtained with a single crystal as converter. The electron produced by a gamma-ray incident at a small angle to a major crystal axis or plane is captured into channeling and radiates gamma rays. The channeling radiation and the electron-positron pair can be detected and yield point source locations with a precision of 5 arcseconds at 10 GeV. This is an improvement of three orders of magnitude on the angular precision of telescopes sensitive to gamma-rays above 50 MeV flown on satellites.

1. Introduction. During the past two decades observational gamma-ray astronomy been established as an important branch of astrophysical research. Gamma-ray telescopes flown from high altitude balloons provided the initial detection of the Crab Nebula pulsar. Similar but smaller telescopes were flown aboard the SAS-2 and COS-B satellites. These experiments (1,2) explored the galactic plane emission initially discovered by OSO-3 (3). The SAS-2 and COS-B experiments have detected 26 sources with COS-B making the major contribution (4,5). The identification of the gamma-ray sources with known objects at other frequencies has in all but four cases been unsuccessful. The poor angular resolution of the gamma-ray telescopes flown on satellites, with typical error boxes of a few square degrees, accounts for the failure to identify counterparts for the majority of the gamma-ray sources. The present observational situation emphasises an urgent requirement for telescopes with a major improvement in angular resolution.

2 Pair Production. The most probable opening angle of an electron or positron in pair production is $\theta = 0.8/E_\gamma$ where E_γ is the gamma-ray energy in MeV (6). The limitation results from the scattering in the pair production process due the unobserved momentum of the recoil nucleus. The most probable opening angle of an electron from a 2 GeV gamma-ray is 1.4 arcminutes assuming equipartion of energy between the electron-position pair. For a 100 GeV gamma-ray the opening angle of 1.6 arcseconds is comparable with the resolution of ground based optical telescopes. The cross-section for pair production by gamma-rays incident at small angles to crystal planes and axes has been predicted (7) and verified in experiments at accelerators (8). The cross-section depends on the polarisation of the gamma-rays. The variation of the cross-section above 1 GeV is large and may be used to measure the polarisation of the gamma-rays from cosmic sources.

A new pair creation process has been predicted (9) for high energy gamma-rays aligned with major crystal axes and planes. The crystal assisted cross-section along the <111> axes of heavy elements in equal to the Bethe-Heitler value at 10 GeV and exceeds it by an order of magnitude at 30 GeV. The directional pair creation process, if verified by experiment, predicts a higher efficiency for the detection of gamma-rays incident along major crystal axes and planes.

3 Channeling Radiation. Relativistic electrons and positrons, entering the crystal at a small angle to a major axis or plane and captured into channeling, radiate a characteristic spectrum of x-ray and gamma-rays. The theory of channeling radiation has been experimentally confirmed in experiments at accelerators using single crystals of diamond and silicon (10). The channeling radiation intensity from relativistic electrons is far greater than coherent bremsstrahlung and the bremsstrahlung from electrons travelling at random directions in the crystal. In gamma-ray pair production in a lead crystal the electron-positron pairs are produced near an atomic nucleus except for a small fraction that pair produce in the field of atomic electrons. In a model (11) for axial channeling in high Z materials, like lead, the atomic string is replaced by a tube of charge spread continuously with constant density inside a cylinder whose axis coincides with that of the atomic string. The radius R of the tube is determined by the amplitude of the thermal vibrations of the nucleii. The distance R in high Z materials is comparable with the electron screening radius and small in comparison with the distance d between neighbouring atoms in the string. Electrons with energy $E = \gamma\ mc^2$ will move inside the tube with angular frequency

$$\omega = \frac{e}{R}\left(\frac{2Z}{md\gamma}\right)^{\frac{1}{2}} \qquad (1)$$

where γ is the Lorentz factor. The positrons, unlike the electrons, will not be channeled as no significant bound states exist. The critical angle for electron capture into channeling is

$$\theta_A = \left(\frac{2Ze^2}{dE}\right)^{\frac{1}{2}} \qquad (2)$$

The values of θ_A, in arcminutes, for the <100>, <110> and <111> axes of lead are 2.4, 2.8 and 3.8 for 1 GeV electron. The electron will be channeled because the opening angle in pair production is smaller than the critical angle. At higher gamma-ray energies the electron will be channeled since θ and θ_A decrease as E^{-1} and $E^{-\frac{1}{2}}$ respectively. The electron may be dechanneled by a single Coulomb scattering through an angle greater than θ_A or by the accumulation of a large number of random scatterings. In lead the length ℓ in which half the electrons will be dechanneled is $\ell = 4\times10^{-7}\gamma$cm.

In the model adopted for crystal planes, the planes are replaced with layers of positive charge of constant density and thickness 2R. The critical angle for electron capture into the layer is

$$\theta_p = \left(\frac{2\pi RZe^2}{Ed^2}\right)^{\frac{1}{2}} \qquad (3)$$

The angle θ_p refers only to the angle perpendicular to the plane since

the angle in the plane can take any value. The angle θ_p is typically three times smaller for planes than axes resulting in a higher gamma-ray threshold for electron capture and channeling. The opening angle of an electron with half the gamma-ray energy and the capture angle into the (100) plane of lead are equal to 0.4 arcminutes for gamma-ray energies of 8 GeV.

The transverse oscillations of the channeled particles generate electromagnetic radiation which has been studies for electrons and positrons entering the crystal. The electron energy loss in lead is typically $10^{-1}\ \gamma^2$ MeV cm^{-1} for the major axes and $10^{-3}\ \gamma^2$ MeV cm^{-1} for the major planes (11). In the GeV energy range the channeling radiation is far greater than the bremsstrahlung radiation from electrons travelling at random directions in the crystal. The channeling radiation and bremsstrahlung have different spectral and angular properties providing additional discrimination against the bremsstrahlung background from nonchanneled electrons and positrons. The maximum frequency of the channeling radiation is given by $\omega_m = \omega\ \gamma^2$ (12). The radiation from the channeled relativistic electrons is in the x-ray and gamma-ray regions and the maximum frequency increases as $\gamma^{3/2}$. For the <111> axis of lead the maximum energy of the radiated photons from 2 GeV electrons is about 100 MeV. For very high energy electrons the transverse motion of the electron is relativistic and the maximum frequency increases as $\gamma^{1/2}$. In channeling radiation the crystal governs the motion of the electron and therefore the halfwidth of the angular distribution is not due to multiple scattering but is determined by the radiation and beamed into an angle $1/\gamma$ where γ is the Lorentz factor of the radiating electron. The bremsstrahlung radiation is beamed into a much larger angle which is determined by the multiple scattering of the electron and positron in the crystal converter.

4 Gamma-Ray Telescopes. In almost all detectors sensitive to gamma-rays about 50 MeV flown on balloons and satellites, the direction of the gamma-ray was deduced from the directions of the electron-positron pair produced in a lead converter with an unspecified polycrystalline structure and recorded in a spark chamber (13,14,15,16). Two major changes in the traditional design of gamma-ray telescopes are required to utilise channeling radiation. [1] The converter should be replaced with a single crystal or a mosaic of aligned single crystals to cover the typical telescope areas of 0.1 to 1 m^2. [2] The drift or spark chambers for the detection of the electron-position pair require additional converters for the pair production and detection of the channeled radiation. In addition since this telescope can operate in both survey and pointed modes, the telescope requires a stabilised platform for pointed observations of selected sources.

A telescope of this type would have the following features: [1] As in conventional gamma-ray telescopes, operating in a survey mode with a large field of view, the directions of the electron and positron can be used to establish the incident direction of the gamma-ray to a precision of about 0.5°. [2] The requirement that the opening angle of the electron in pair production be equal to the capture angle into channeling determines the threshold energy of the detector. The gamma-ray threshold energy in lead for axial and planar channeling is about 2

GeV and 8 GeV. The channeled electron will typically radiate a burst of five or more gamma-rays into an angle of halfwidth $1/\gamma$. The number of bremsstrahlung photons radiated by an electron in a random direction in the crystal is

$$N = \frac{4x}{3t} \ln \left(\frac{\omega_2}{\omega_1}\right) \quad (4)$$

where x is the path length, t is the radiation length and ω_2 and ω_1 are the maximum and minimum frequencies of the detected photons. In a typical gamma-ray astronomy telescope, with x = 0.2 radiation lengths, N will be less than one for the electron and positron. [3] The capture angle of the electron into channeling determines the angular resolution of the telescope. The beamwidths of the axial and planar channels are different. The planar channel beamwidth is determined perpendicular to the crystal plane but in the crystal plane can take any value. The axial and planar channels may be used in point mode operation to map selected sources. The point source location precision will be about one-fifth of the beamwidth or 5 arcseconds at 10 GeV for planar channeling. [4] The gamma-rays from the channeled electron along with the electron-positron pair must be recorded in a spark or drift chamber which includes additional converters for the gamma-rays.

5 Conclusions. It has been shown that a major increase in the angular resolution of gamma-ray astronomy telescopes can be obtained with a crystalline converter. The characteristic signature of a gamma-ray incident at a small angle to a major crystal axis or plane arises from the radiation from the channeled electron that is beamed into an angle $1/\gamma$. The detection of the electron-positron pair and the gamma radiation from the channeled electron can yield point source locations with a precision of 5 arcseconds at 10 GeV.

6. References.

(1) Fichtel, C.E., et al., Astrophys. J. 198, 163 (1975).
(2) Bignami, G.F., et al., Annu. Rev. Astron. Astrophys. 21, 67(1983).
(3) Kraushaar, W.L., et al., Astrophys. J. 177, 341 (1972).
(4) Swanenberg, B.N., et al., Astrophys. J. 243, L69 (1981).
(5) Hartman, R.C., et al., Astrophys. J. 230, 597 (1979).
(6) Olsen, H., Phys. Rev. 131, 406 (1963).
(7) Uberall, H., Phys. Rev. 103, 1055 (1956).
(8) Palazzi, G.D., Rev. Mod. Phys. 40, 611 (1968).
(9) Kimball, J.C., et al., Nucl. Instrum. Methods, B2,25,1984.
(10) Beloshitsky, V.V., et al., Phys. Reports 93, No. 3, 117 (1982).
(11) Bonch-Osmolovskii, A.G., et al., Yad. Fiz. 29, 432 (1979), Sov. J. Nucl. Phys., 29, 216 (1979).
(12) Kumakhov, M.A., Phys. Status Solidii (b), 84, 41 (1977).
(13) Albats, P., et al., , Proceed. 12th ESLAB Symposium, ESA SP-124, 287 (1977).
(14) McKechnie, S.P., et al., Space Science Instrumentation, (5), 81 (1979)
(15) Parlier, B., et al., Nucl. Instrum. Methods, 148, 483 1978.
(16) Share, G.H., et al., Proceed. of 12th ESLAB Symposium, ESA SP-124, 107 (1977).

OG 9.3-5

AN APPROACH OF REDUCING THE BACKGROUND INDUCED BY NEUTRONS

Shen Changquan
Gu Yidong
Sun Yangfang
Ma Yuqian
Dai Changjiang
Fan Zhenzi

Institute of High Energy Physics,Academia Sinica
P.O.Box 918 Beijing,China

1.Introduction

The background induced by interactions of neutrons with detector material (and shield material) is difficult to be rejected.It is one of the most important factors to affect the sensitivity of a balloon-borne gamma-ray astronomical telescope.

The main component of neutron flux at the major detector of the telescope is incident neutrons,that consists of atmospheric neutrons and neutrons locally produced in the balloon platform. Therefore,shielding the detector from incident neutrons is a possible way to reduce the background. NaI (Tl) crystal is very widely used in gamma-ray astronomical telescope. Our balloon-borne experiment have shown that ^{6}LiF shield is effective to reduce the background in NaI crystal.

2.Methods

The energy range of neutrons which can produce important background effects in gamma-ray telescope goes from thermal energies to several hundred MeV (1,2). For our perpose,the ideal neutron shield is an effective absorber or moderator with little gamma-ray production. The isotope ^{6}Li has large (n,α) cross section,which is 942 barns for thermal neutrons and inversely proportional to the square root of neutron energy. Also both ^{6}Li and F nuclei have very little gamma-ray production in neutron flux. Therefore we use ^{6}LiF as the neutron shield.

We built a balloon payload with two identical 75 mm dia. by 75 mm thick NaI (Tl) crystals. It was launched two times, in June of 1983 and in June of 1984. The block diagram of the experiment is shown in Fig 1. The apparatus consists of two identical parts: A and B. The only difference between them is that crystal A is surrounded by a passive neutron

shield but crystal B is naked. For the first flight,the shield was 0.4 $g.cm^{-2}$ thick ^{6}LiF covered by 6.5 cm thick polythene. For the second flight it was o.6 $g.cm^{-2}$ thick ^{6}LiF only. The powdery ^{6}LiF was sticked between two layer of 2 mm thick polythene with silica gel,then this sandwich was shaped as a 12 cm dia.by 16 cm deep cylinder and crystal A was placed in it.

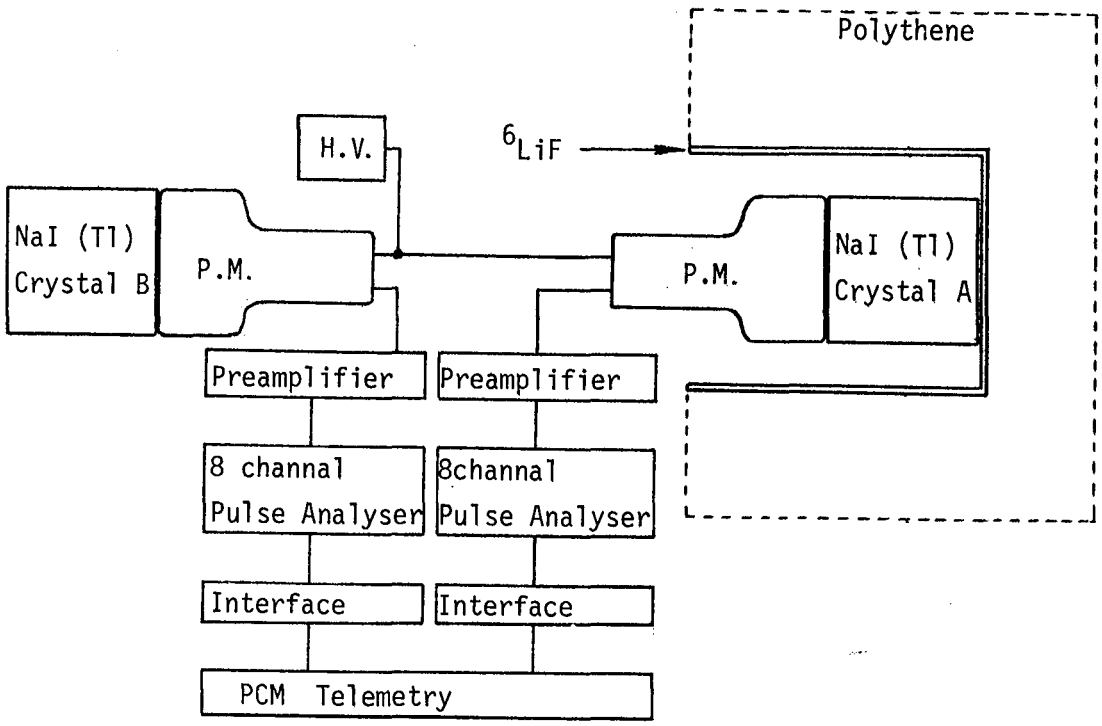

Fig 1. The block diagram of the on board experiment.

3. Result

During the first flight, the background spectra measured by the two detectors with/without neutron shield respectively are different, but they have similar integral background rate in 0.06-2 MeV range.

For the second flight, the integral background rate of the shielded detector in 0.06-2 MeV is about 12% lower than that of the naked one at the altitute 17±1 km where the background rate has its maximum. This value is in excess of 21 times of its standard deviation. The integrated spectra measured there for both detector A and B is shown in Fig 2. In the spectra all counts with energy higher than 2 MeV have been taken off since most of them are contributed by cosmic rays. At other altutute,

similar results were recorded.

4.Discussion

Neutrons arriving at a NaI detector may interact by several mechanisms that lead to background counts which have the appearance of the desired gamma-rays events.Firstly,they may undergo radiation capture at either the ^{127}I or ^{23}Na nuclei of the NaI crystal. The ^{127}I has a much larger cross section for neutron absorption than ^{23}Na.

Radiative absorption of ^{127}I leads to a variety of possible prompt gamma-rays via the reaction ^{127}I (n,r)^{128}I. Over an energy range from 60 keV up to about 6.7 MeV,184 different energies were recorded by Archer et al (3).There is also a delayed effect from each neutron absorption on ^{127}I by the beta decay of the product ^{128}I with a half-life of 25 minutes. It makes a continuous spectrum in the energy range less than 2.2 MeV and some gamma-rays e.g. 443 keV gamma-ray.

^{127}I has a resonance region over 15 eV to 1.0 keV in which approximately 75% of absorption events originate,and the strongest resonance region is over 20 eV to 50 eV. Whereas ^{6}LiF can effectively absorbs neutrons in these energy range,for example 0.6 $g.cm^{-2}$ thick LiF layer can absorbs 44% of 15 eV neutrons, 25% of 50 eV neutrons and 7% 1 keV neutrons.This is the reason why ^{6}LiF shield reduces the background.

The second important neutron interaction mecanisms is the inelastic acattering of neutrons at an ^{127}I nucleus. Some energy levels of ^{127}I to be excited by this effect can contribute to the background by emission of gamma-rays at certain energies among which the 58 and 203 keV is the strongest two. Some calculations (2) show that the overall effect of inelastic scattering of the same order as that from prompt effects of neutron absorption and the energy loss spectrum for this mechanisms is roughly a power low of order -1.5 in the energy range 0.2-12 MeV. The background contributed by this mechanisms has not been reduced since we have not found any effective absorber or moderator with little gamma-ray production for fast neutrons.

In our first flight, 6.5 cm thick polythene was used as a moderator. It could slow down some neutrons and make them easier to be absorbed by ^{6}LiF,so that it seems to reduce the background further. But the result is negative, it is similar to Leventhals experiment (4). It indicates

that there is some effects in this moderator which increase the background and off set advantage of ^{6}LiF. It seems that it should be careful to add lots of material surround the major detector, since all material could be a background source in the space environment.

In our experiment,since there is no active shield surrounding the NaI (Tl) detectors,the atmospheric gamma-rays are dominant component in background. In this case the value 12% is a significant part of the neutron induced background. Therefore the results are interesting if you also consider 0.6 mm thick ^{6}LiF is neither heavy nor expensive.

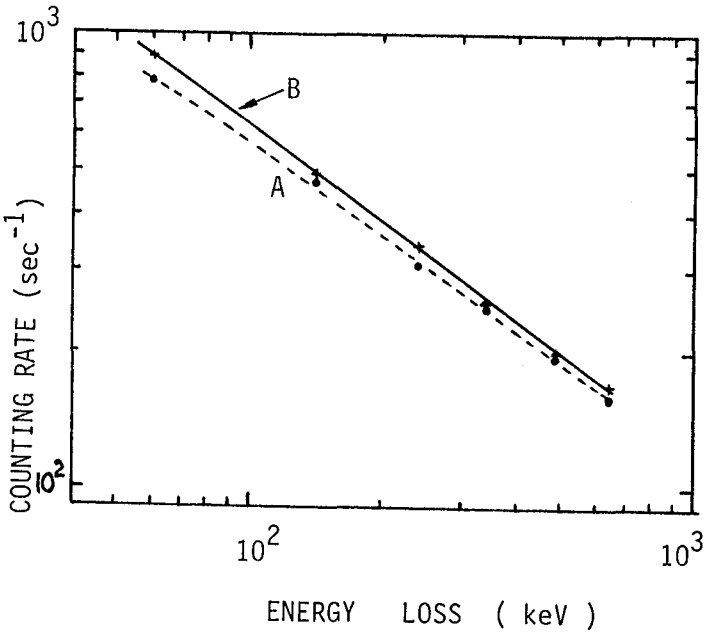

Fig.2.
The energy loss spectrum integrated up to 2 MeV at the altitude 17 km for naked detector B (line) and detector A (dot line) shielded by ^{6}LiF.

References

(1) Chupp E.L., "Gamma-ray Astronomy",Published by D.Reidel Publishing Company (1976),p218

(2) Charalambous P.M. et al.,Nucl.Instr.and Meths (1985),(in Press)

(3) Archer N.P. et al., Nucl. Phys. 83,241 (1966).

(4) Leventhal M.et al.,Ap.J. 240, 338 (1980)

NEUTRON-INDUCED 2.2 MEV BACKGROUND IN GAMMA RAY TELESCOPES

E. M. Zanrosso*, J. L. Long**, A. D. Zych and R. S. White
IGPP, University of California, Riverside, CA 92521
*Xerox Corporation, 125 N. Vinedo Ave., Pasadena, CA 91107
**Hughes Aircraft, P.O. Box 92426, Bldg. R8/2240, Los Angeles, CA 90009

1. Introduction. Neutron-induced gamma ray production is an important source of background in Compton scatter gamma ray telescopes where organic scintillator material is used. Most important is deuteron formation when atmospheric albedo and locally produced neutrons are thermalized and subsequently absorbed in the hydrogenous material. The resulting 2.2 MeV gamma ray line radiation essentially represents a continuous isotropic source within the scintillator itself. Interestingly, using a scintillator material with a high hydrogen-to-carbon ratio to minimize the neutron-induced 4.4 MeV carbon line favors the np reaction.

The full problem of neutron-induced background in Compton scatter telescopes has been previously discussed (1). In this paper we will present results of observations with the University of California balloon-borne Compton scatter telescope (2,3) where the 2.2 MeV induced line emission is prominently seen.

2. Observations. The neutron-induced 2.2 MeV line feature has consistently been present in the background gamma ray spectra measured with the University of California Compton scatter telescope. Figure 1a shows a typical energy spectrum accumulated over a period of 34 hours during a balloon flight from Palestine, Texas in September, 1978. The cutout (Fig. 1b) shows a 1/2 hour accumulation of the line feature at 2.13 MeV with a 0.98 MeV FWHM with the continuum background subtracted. In addition to an expected shift downward in the mean energy from 2.23 MeV due to some loss in event energy from the second scintillator, there was a systematic drift (3.3% or 70 keV) in the mean energy of this 2.2 MeV line feature over the duration of the balloon flight.

Each of the telescope's 56 scintillator cells was calibrated prior to the flight with gamma ray reference sources. During the flight LED light sources in each cell are used to normalize the photomultiplier gains to the pre-flight calibration. The systematic drift referred to above was due to the temperature related drift of the telescope's LED-pulser system which wasn't compensated.

The observed count rates for the 2.2 MeV gamma rays are given in Table 1 for two different geomagnetic vertical cutoff rigidities. With the University of California telescope, the 2.2 MeV line feature is also observed in the upward-moving background spectrum. The upward-moving line feature is approximately four times as intense as the downward moving but is effectively separated from the latter with time-of-flight.

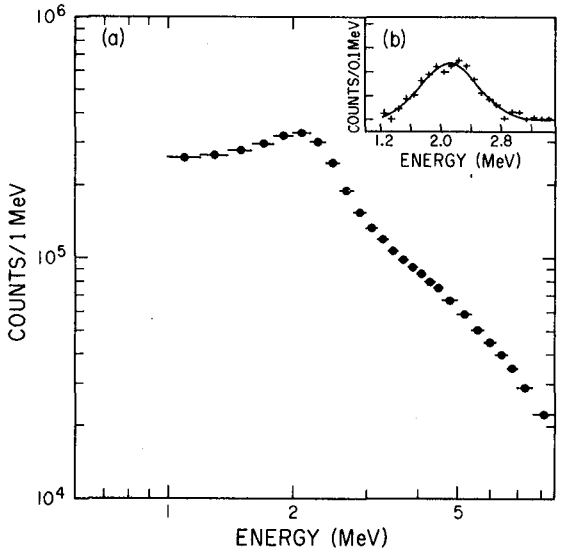

Fig. 1(a) Count rate spectrum of downward moving gamma rays at 4 g/cm^2. (b) Line feature at 2.13 MeV mean energy with continuum background subtracted.

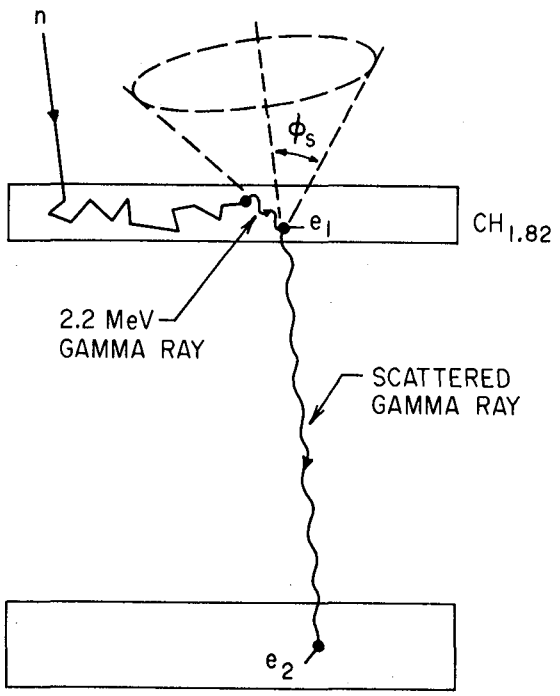

Fig. 2 Typical neutron thermalization and absorption to produce background 2.2 MeV events.

Table 1. Measured Count Rate of 2.2 MeV Induced Gamma Rays

Vertical Cutoff (GV)	Photons/sec
4.5 GV (Palestine, Texas)	2.1
9.0 GV (Alice Springs, Australia)	1.4

3. Calculations. The basic process for detecting a neutron-induced 2.2 MeV photon and misidentifying its direction of origin with a celestial source within the field-of-view of the telescope is shown in Figure 2. First, atmospheric neutrons incident on the large 100 x 100 x 12.5 cm^3 upper scintillator array filled with a mineral oil-based liquid scintillator (H/C = 1.82) are moderated by the hydrogen and carbon until they either escape the boundaries of the array or are absorbed by the hydrogen. Most of the absorbed neutrons are thermalized first ($E_n \approx 0.025$ eV).

The fraction of incident isotropic neutrons which actually are absorbed has been calculated with a Monte Carlo code. These results are

summarized in Table 2. Typically, about 20% of the incident neutrons are absorbed; they have an exponential absorption time distribution with a mean time of about 140 μsec.

Table 2. Thermalization and Absorption of Isotropic Neutrons Incident on a 100 x 100 x 12.5 cm^3 Scintillator (H/C=1.82)

E_n(MeV)	Percent Thermalized	Percent Absorbed
10	25	14
1	43	23
0.1	42	22
0.01	40	20

Near the top of the earth's atmosphere the cosmic ray albedo neutron flux is relatively insensitive to float altitude changes typical of balloons. Thus the 2.2 MeV gamma ray production rate in the large scintillator array is constant. Using a value of 0.1 neutron/cm^2-sec for this flux (4) at 9 GV, the production rate is approximately 250/sec for the upper scintillator array. At 4.5 GV this rate should be larger by a factor of 2.1. It is primarily neutrons above 10 keV that produce this flux due to the flatness of the albedo spectrum below this energy.

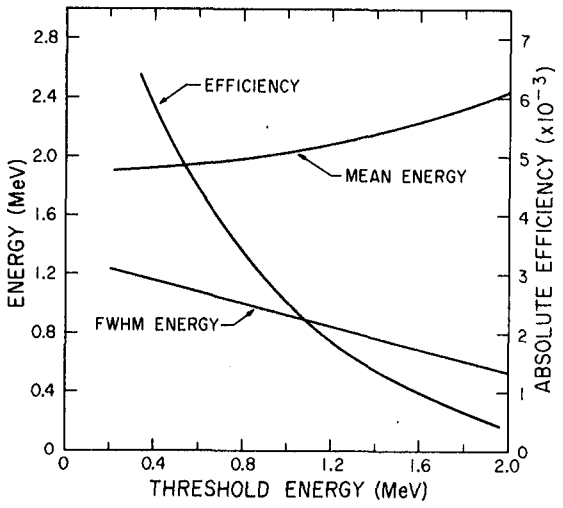

Fig. 3 2.2 MeV gamma ray detection efficiency as a function of energy threshold. Also shown are the variations in mean energy and FWHM.

The actual counting rate for the induced 2.2 MeV γs depends on the double scatter efficiency of the telescope which, in turn, is very sensitive to the energy thresholds in the two scintillator arrays. We have used our gamma ray Monte Carlo transport code to calculate this efficiency for 2.2 MeV photons distributed uniformly throughout the upper scintillator array with an isotropic angular distribution. These results are shown in Figure 3 as a function of the summed energy threshold for the upper and lower scintillator arrays. For a 1 MeV threshold the expected rate is 0.6/sec compared with the observed rate of 1.4/sec at 9 GV. In the above calculation we have neglected the non-negligible downward neutron flux due to the atmosphere remaining above the balloon and any locally produced neutrons in the telescope itself.

The efficiency and, therefore, the count rate is a very sensitive function of the threshold. Also affected by the threshold are the mean energy assigned to the 2.2 MeV peak and the FWHM of the line feature. This is because the threshold energy is comparable both to 2.2 MeV and the energy resolution of the telescope.

Since the production rate of induced 2.2 MeV γs is constant the telescope count rate of these events is a sensitive function of the photomultiplier tube gains. For example, a gain increase of 10%, which is effectively an energy threshold reduction by the same amount, will account for a count rate increase of 16% while the mean energy of the line changes by 7.8% or 160 keV.

The induced 2.2 MeV line emission poses a limitation for observing this same line feature from celestial gamma ray sources. The importance of this line emission in astrophysical processes is illustrated by its dominance in the Sun's solar flare gamma ray emission. Based on our measured count rate of this line feature, our minimum detectable flux for 2.2 MeV line emission is $2.2 \times 10^{-4} \gamma/cm^2$-sec at the 4 sigma level for six hours of observation at 9 GV.

4. Conclusions. The sensitivity for observing 2.2 MeV line emission from celestial sources will be limited by the neutron-induced background at this energy. This will be especially true of gamma ray telescopes which use substantial amounts of organic scintillator materials. This source of background cannot be removed with pulse shape discrimination techniques in the organic scintillator because of the relatively long time delay between the initial neutron scatter and its absorption by hydrogen. Any positive detection of 2.2 MeV line emission will be in addition to the ever-present induced emission.

Gamma ray telescopes which do not use organic scintillator as their primary detection element but do use large quantities for charged particle shields will also see this background unless precautions are taken. Compton scatter telescopes with improved angular resolution will have somewhat improved sensitivity because valid event circles can be better correlated with known source directions.

The 2.2 MeV background line feature, however, can be used for energy calibration purposes if needed or, which is preferred, used for verification that the calibration and gain-control methods are stable with respect to long term drift.

5. Acknowledgments. We wish to acknowledge NASA grant NGR-05-008-022 for support of this research.

References

1. R. S. White and V. Schönfelder, (1977), Astrophys. and Spc. Sci. 38, 19.
2. Herzo, D., et al., (1975), Nuc. Instr. and Meth. 123, 583.
3. Zych, A. D., et al., (1975), IEEE Trans. Nuc. Sci., NS-22, 605.
4. Jenkins, R. W., et al. (1970), Journ. Geophys. Res., 75, 4197.

A COMPARISON OF CALCULATED AND MEASURED BACKGROUND NOISE RATES IN HARD X-RAY TELESCOPES AT BALLOON ALTITUDE

A.J.Dean[1], N.A.Dipper[1], R.A.Lewis[1], F.Perotti[2]

1. Department of Physics, University of Southampton, Southampton, UK
2. Istituto di Fisica Cosmica, Milano, Italy.

ABSTRACT

An actively shielded hard X-ray astronomical telescope has been flown on stratospheric balloons. In this paper we compare the measured spectral distribution of the background noise counting rates over the energy loss range 20-300keV with the contributions estimated from a series of Monte Carlo and other computations. The relative contributions of individual particle interactions are assessed.

1. Introduction. The sensitivity of hard X-ray telescopes is dependent to a first approximation upon a number of desirable characteristics: a large sensitive area, long observation periods, high photon detection efficiency and a low background noise level. The first two factors are very dependent upon the platform from which the telescope must operate, whilst the effective suppression of background noise requires a detailed analysis of the physical processes involved. We present in this paper the background levels observed in an actively shielded collimated telescope during a balloon flight from Palestine, Texas in 1982. The experimental results are compared with theoretical and computer predictions of the background counting rates.

2. Configuration of the Hard X-ray Telescope. The telescope was composed of 8 NaI(Tl) scintillation crystals (200x200x6mm) shielded over the lower 2π steradians by a 5cm thick NaI(Tl) crystal of the same area. A thin plastic scintillator designed to reject events due to charged particles covered a large fraction of the upper 2π steradians. The aperture of the detectors was restricted to 3 degrees FWHM by a copper collimator. A passive graded shield also surrounded the collimators and the sides of the crystals. A schematic diagram of the telescope is shown in Fig.1. In addition a Sodium Iodide detection crystal, identical to the primary crystal in the telescope, was flown in a completely unshielded configuration in order to determine the efficiency of the

shielding system. The telescope and unshielded crystal were flown on the same stratospheric balloon gondola from Palestine, Texas.

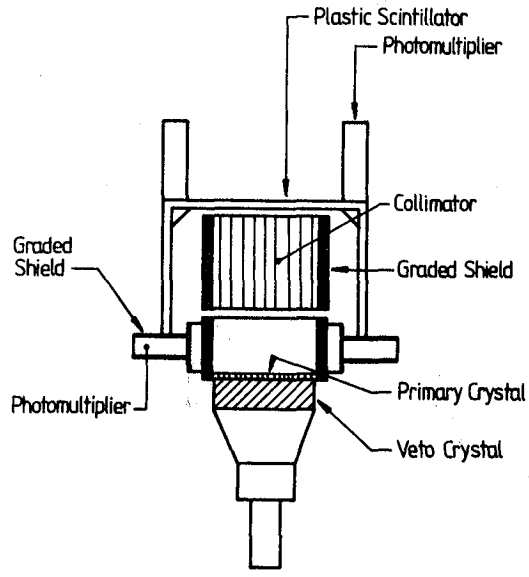

Fig.1. A schematic view of the X-ray telescope detector units

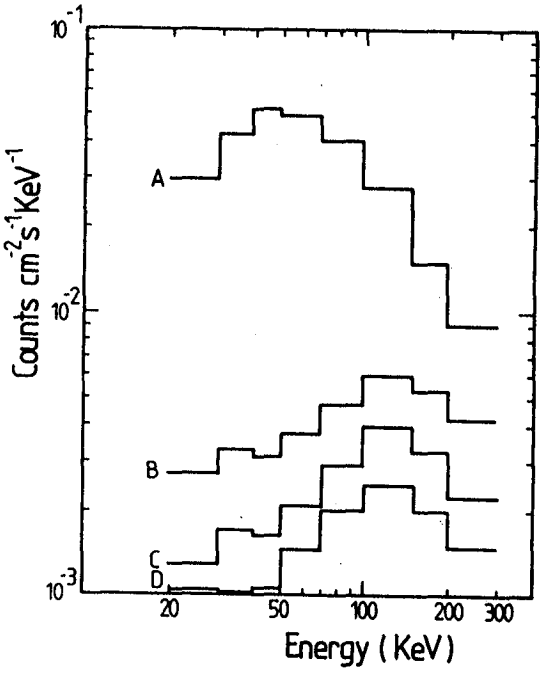

Fig.2. The counting rate in the MIFRASO NaI(Tl) detectors at 4.1mbs residual pressure for four different shielding configurations;
a) counting rate in unshielded det.
b) counting rate in unshielded det. with all active anticoincidence off.
c) counting rate in shielded det. with NaI(Tl) active shield on but with plastic anticoincidence off.
d) counting rate in primary det. with all shielding systems functioning.

Figure 2 demonstrates the effectiveness of each type of shield by showing the counting rates at balloon altitudes for different shielding configurations. It clearly demonstrates that the majority of the reduction

in background counting rate is achieved by the passive shield with both sets of active anticoincidence causing roughly similar further reductions in the unwanted background noise.

3. Comparison of measured and calculated background levels. The predicted background counting rate in the detectors of the MIFRASO telescope was computed by a combination of theoretical and Monte Carlo techniques. The photon induced background was determined from the results of an extensive Monte Carlo model of the entire detection system. The program modelled the processes of photoelectric absorption and Compton scattering, but neglected electron transport due to the fact that the path lengths involved for the energy range under consideration are generally small compared to the dimensions of the elements of the telescope. The angular and energy distribution of the gamma-ray fluxes incident over the detector could be varied to suit the particular physical processes under investigation. In each case the energy deposits in all the elements of the telescope were recorded in order to provide an insight into the efficiency of the various shielding systems.

Neutrons arriving at the primary crystal may generate background noise by a variety of mechanisms but the most important are (n,γ) radiative capture and inelastic scattering by the 127_I nuclei. Radiative capture by 127_I leads to a variety of possible prompt gamma-rays by the reaction $127_I(n,\gamma)128_I$. The various gamma-ray energies are very extensive and extend from 60 keV up to 6.7 MeV. There is also a delayed effect from the decay of 128 which has a half life of 25 min. The two lowest levels to be excited by inelastic scattering at a 127_I nucleus lead to the emission of gamma-rays at energies of 58 and 203 keV.

The neutron flux incident upon the detectors is made up of two components, atmospheric neutrons and those produced within the payload by "boil off" from cosmic ray interactions. The modified neutron flux will depend upon the exact geometry and mass of the payload but may be estimated as described by Charalambous et al (1985) by assuming a uniform distribution of mass and integrating over the volume of the payload. This neutron flux was folded with the cross sections for radiative capture and inelastic scattering to yield an estimate for the background counting rate of neutron induced events. The contribution from charged particles has been estimated from the effect of the plastic scintillator shield. If

the shield is assumed to be 100% efficient over the solid angle that it covers, it is possible by considering the effect of switching on and off the shield, to estimate the number of events caused by particles that enter through the solid angle that is not shielded.

High energy cosmic ray protons which are incident upon the material of the detection plane give rise to background events which are derived from the radioactive spallation products produced in the interaction. In general, the veto pulse may be made as long as possible to suppress a number of these types of events. However, since the timescales associated with many of the decay schemes are considerably longer than practicable veto pulse lengths the active shield does not eliminate this type of noise. Calculations of spallation involved background are extremely complex and subject to considerable error so that a reliable estimate of this source of noise is best obtained by experiment. Results of such tests have been reported in the literature (Baker et al 1979) and have been used to yield an estimate for the MIFRASO detectors.

The results of the various calculations are shown in Fig.3. The agreement between calculation and experiment is quite good being within a factor of two and having the same spectral distribution. The similarity in spectral shapes is an encouraging sign that the relative contributions of the various effects as determined by calculation are correct

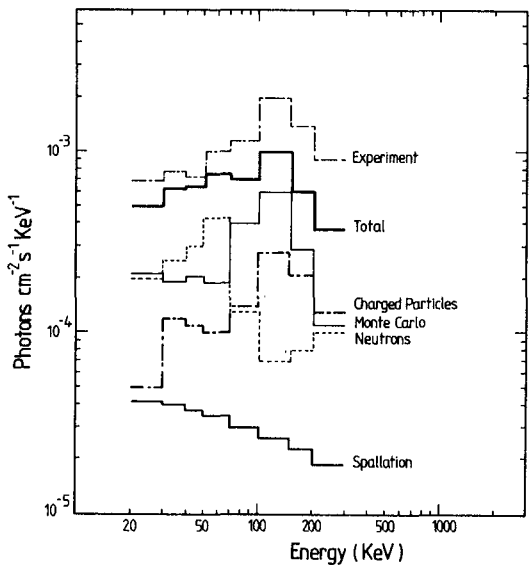

Fig.3. A comparison between observed and calculated background noise events.

References

1. Baker R.E.et al.NIMS, 158. (1979) 595.

2. Charalambous,P.C.et al. NIMS (in press

3. Dean,A.J. and Dipper,N.A. MNRAS (1981), 194, 219.

OG 9.3-8

THE FINAL COS-B DATABASE - NOW PUBLICLY AVAILABLE

H.A. Mayer-Hasselwander[4], K. Bennett[6], G.F. Bignami[2], J.B.G.M. Bloemen[1a], R. Buccheri[3], P.A. Caraveo[2], W. Hermsen[1], G. Kanbach[4], F. Lebrun[5], J.A. Paul[5], B. Sacco[3], A.W. Strong[4]

The 'Caravane' Collaboration for the COS-B satellite:
[1]Laboratory for Space Research Leiden, Leiden, The Netherlands
[2]Istituto di Fisica Cosmica del CNR, Milano, Italy
[3]Istituto di Fisica Cosmica e Informatica del CNR, Palermo, Italy
[4]Max Planck Institut für Physik und Astrophysik, Institut für Extraterrestrische Physik, Garching bei München, Germany
[5]Service d'Astrophysique, Centre d'Etudes Nucléaires de Saclay, France
[6]Space Science Departement of the European Space Agency, ESTEC, Noordwijk, The Netherlands
[a]Sterrewacht Leiden, Huygens Laboratorium, Leiden, The Netherlands

ABSTRACT

The data obtained by the gamma-ray satellite COS-B have been processed, condensed and integrated together with the relevant mission and experiment parameters into the 'Final COS-B Database'. The database contents and the access programs available with the database are outlined. The final sky coverage and a presentation of the large-scale distribution of the observed Milky-Way emission are given. The database is anounced to be available through the European Space Agency.

1. Introduction: Gamma-ray astronomy in the energy range from about 50 MeV up to several GeV is based at present on the data obtained by only two successful satellite experiments, both using the sparkchamber technique: the first flown in 1972-1973 on the SAS-2 satellite of NASA, the second flown on the ESA satellite COS-B. SAS-2 operated ≈7 months and aquired about 8,000 gamma-ray events (1), COS-B was in successful operation from August 1975 until April 1982 and recorded about 210,000 gamma photons. A presentation of part of the COS-B database was given by Mayer-Hasselwander et al. (2).

The two datasets differ in the following respects: a) The low orbit of SAS-2 was well shielded by the earth's magnetic field against the cosmic-ray flux, ensuring a very low instrumental background level; the highly eccentric orbit (due to practical constraints) of COS-B exposed the satellite to the full cosmic-ray intensity, inducing a comparatively high instrumental background level, which is variable with the solar 11-year cycle. b) The COS-B experiment was supplemented by an energy calorimeter, providing good energy information for each recorded photon. c) Due to the differences in experiment configuration the low-energy threshold of SAS-2 was somewhat lower (≈30 MeV), than for COS-B (≈50 MeV). d) The COS-B experiment achieved a complete coverage of the galactic ridge. Its long lifetime, allowing for repeated observations in regions of special interest, enabled detailed analyses of the spatial distribution and of possible time variations of the observed emission.

The databases of SAS-2 (3) and of COS-B will remain for several years the only available gamma-ray survey data, and after the forthcoming experiments GAMMA-1 and EGRET, these databases will remain of interest e.g. in the search for possible secular and periodic time variations of celestial gamma-ray objects. Although considerable analysis effort already has been invested to

exploit the data, certainly much more can be done by applying new methods or by using the data together with upcoming new results in other ranges of the electromagnetic spectrum. So it appeared to be mandatory to establish and to make available the COS-B database in a way which will make possible future analysis also by scientists not familiar with the experiment.

2. The COS-B experiment and mission: The European Space Agency's satellite COS-B was dedicated to gamma-ray astronomy in the energy range 50 MeV to 5 GeV and carried a single experiment: a sparkchamber telescope (4), developed in collaboration by six European institutes. The experiment became operational on August 17, 1975 and was switched of on April 25, 1982, when onboard resources were exhausted. During this timespan 65 observations, mostly of a month duration, were performed. The satellite was spin stabilized, with the telescope axis along the spin axis and circular sky regions of about 40 degree diameter were covered in each observation. The majority of the pointings were distributed along the galactic equator, 15 observations were devoted to regions at high ($\geq 20°$) galactic latitudes. Several regions of specific interest were repeatedly observed. The overall coverage of the sky is illustrated by Figure 1.

The highly eccentric polar orbit of COS-B with an apogee around 90,000 km, chosen to maximize useful observation time while allowing real-time data transmission, exposed the experiment to the solar modulated interplanetary cosmic-ray flux. The unexpectedly long operational life of the experiment, specifically of the sparkchamber, was acompanied by a long-term degradation and by short-term disturbances of its performance and consequently of the experiment sensitivity. The instrumental background and its variation and the changes in instruments sensitivity were thoroughly investigated. The corrections finally adopted and incorporated in the final database were derived by the method described in a subsequent paper (5). The possible impact of their statistical and systematic uncertainties must be considered in any type of analysis. It is emphasized that the corrections are averages over complete periods.

3. The database content and organisation: The database consists of several parts: A) the observation period, basic dataset, and individual gamma-ray event information, B) the experiment sensitivity, energy dispersion and pointspread functions as derived by accelerator and inflight calibrations, C) programs for easy and efficient access of the database, which produce event lists and skymaps for selected data parameters and time intervals, D) binned skymaps of the galactic disc.

Part A) consists of 3 files: the first one contains a list of the parameters of the 65 observations, including background and sensitivity corrections for each period; the second provides similar information for the 5,943 datasets which correspond to the uninterrupted time intervals during original data recording; the third contains 209,537 entries, one for each accepted gamma-ray event.

Part B) contains the instrument response functions. The sensitivity, energy-dispersion and pointspread-function files are derived from prelaunch calibration; the latter is also based on analysis of the brightest gamma-ray source, the Vela pulsar.

In part C) a collection of Fortran-77 programs is provided, which should allow for easy handling and efficient access of the database. Included are programs to move the database between tape and disc, to make event selections on event parameters and time intervals, and to produce binned skymaps of intensities, counts and exposures. Since these programs access the files in direct access mode, the database has to reside on disc, requiring about 25 Mb of disc space. The system was developed and used under various IBM operating systems (360/OS, MVT, MVS; VM/370, CMS), but also after moderate adaption,

has been successfully used on a VAX computer.

Part D) contains an atlas in several energy bands of the Milky Way.

Figure 2 gives as an illustration a map of the galactic disc emission (150 MeV), produced by a maximum entropy algorithm (7) using the database.

A more detailed description of the gamma-ray data and instrument response functions is in preparation (6). In view of the complexity of the data it is recommended to consult or to collaborate with members of the 'Caravane' collaboration when detailed analysis of the data is undertaken. It is hoped, that the release of this unique database will promote the full exploitation of the data, which appears mandatory in view of the enormous efforts in acquiring it.

The database is available on tape from the COS-B project scientist, Dr.K. Bennett, at the Space Science Department of ESA.

References:

1. Fichtel, C.E. et al.: 1975, Astrophys. J. **198**,163
2. Mayer-Hasselwander, H.A. et al.: 1982, Astron. Astrophys. **105**,164
3. Fichtel, C.E. et al.: 1978, NASA Technical Memorandum 79650
4. Bignami, G.F. et al.: 1975, Space Science Instrum. **1**,245
5. Strong, A.W. et al.: 1985, Proc. XIX ICRC, La Jolla
6. Mayer-Hasselwander, H.A. et al.: in prep. for Astron. Astrophys. Suppl.
7. Skilling, J. et al.: 1979, Mon. Not. Roy. Astr. Soc. **187**,145

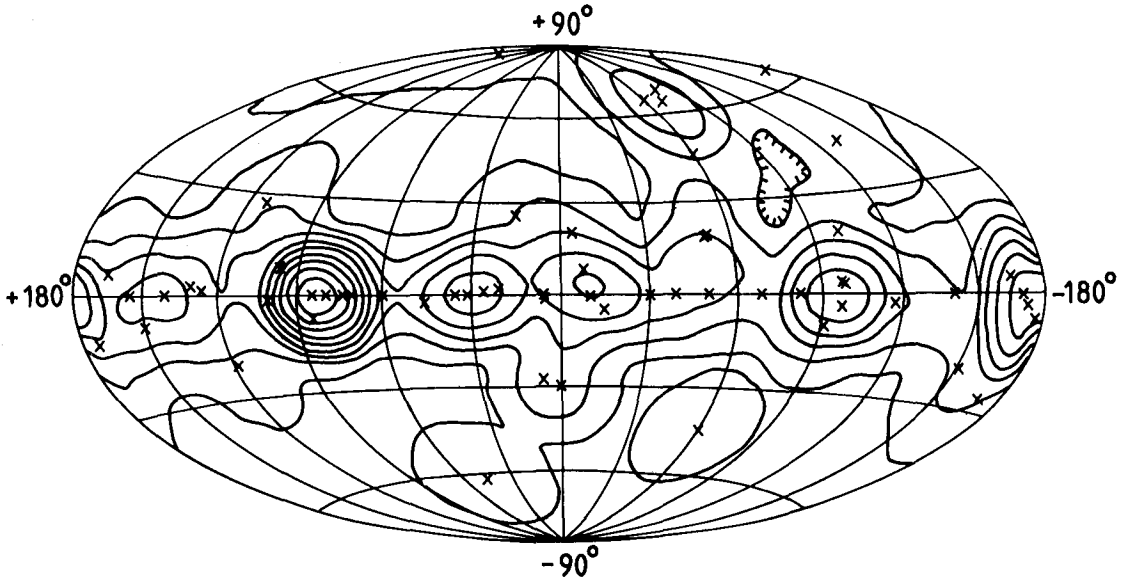

Figure 1: Approximate sky exposure achieved by the COS-B experiment. The contour levels are in 32 d steps, the lowest being 8 d (the exposure time is weighted with the inclination dependance of the sensitivity). The crosses indicate the pointing directions of the 65 observation periods.

Figure 2: Preliminary 'maximum entropy' deconvolved map of the galactic disk, indicating the structure in the emission seen in the energy range 150 MeV to 5 GeV, derived from the database described in this paper. An approximately logarithmic intensity scale was chosen to allow the display of structure in both intense and weak emission regions. This presentation does not give accurate absolute intensities.

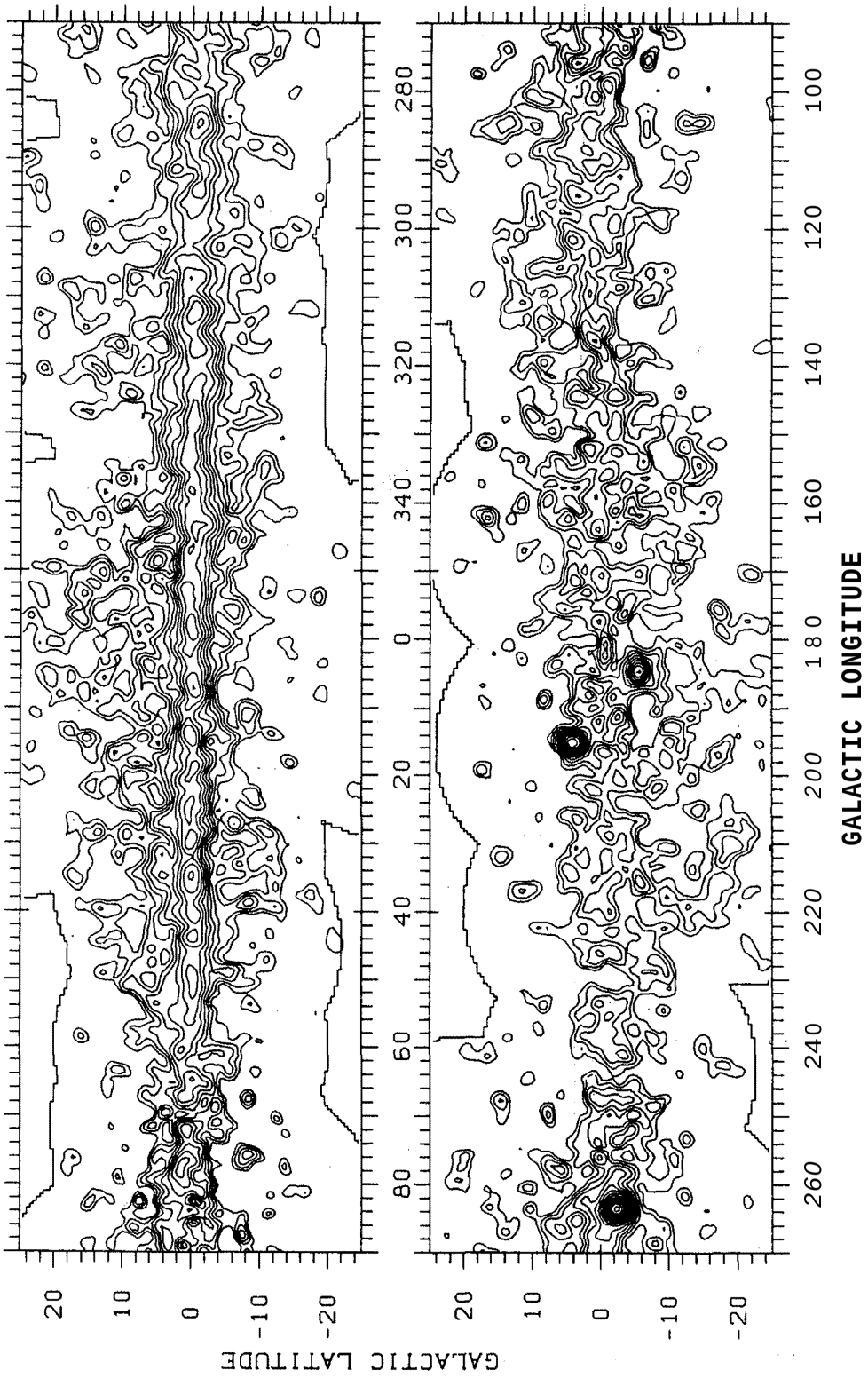
GALACTIC LATITUDE
20
10
0
-10
-20
80
60
40
20
0
340
320
300
280
260
240
220
200
180
160
140
120
100
GALACTIC LONGITUDE

THE FINAL COS-B DATABASE: IN-FLIGHT CALIBRATION OF INSTRUMENTAL PARAMETERS

A.W. Strong[4], *J.B.G.M. Bloemen*[1a], *R. Buccheri*[3], *W. Hermsen*[1], *F. Lebrun*[5], *H.A. Mayer – Haßelwander*[4]

The Caravane Collaboration for the COS-B satellite:

1. Laboratory for Space Research, Leiden, The Netherlands
2. Istituto di Fisica Cosmica del CNR, Milano, Italy
3. Istituto di Fisica Cosmica e Informatica del CNR, Palermo, Italy
4. Max-Planck Institut für Physik und Astrophysik, Institute für Extraterrestrische Physik, Garching-bei-München, Germany
5. Service d'Astrophysique, Centre d'Etudes Nucleaires de Saclay, France
6. Space Science Department of the European Space Agency, ESTEC, Noordwijk, The Netherlands

a Sterrewacht Leiden, Huygens Laboratorium, Leiden, The Netherlands

ABSTRACT

A method for the determination of the temporal variation of sensitivity and instrumental background of the COS-B experiment is described, and representative results are presented.

1. INTRODUCTION

The COS-B experiment operated for 6.7 years during which appreciable variations in sensitivity and background occurred. Effective use of these data for scientific analysis requires the determination of the variations and this involves the intercalibration of overlapping observations of the same regions of sky made at different epochs. The final database (described in Mayer-Hasselwander et al. 1985 and this confererence, OG9.3-8) provides ample coverage for such a determination, but owing to the large amount of data involved the problem is not trivial.

Three types of temporal response variation can be distinguished:

(i) long term variations in sensitivity due to degradation in spark- chamber performance

(ii) shorter term period-to-period variations in effective sensitivity due to fluctuations in spark-chamber performance or to the manual editing process

(iii) long-term variations in instrumental background arising from variations in the ambient cosmic-ray intensity.

A method of determination of the variations which uses a non-linear optimisation technique has been successfully applied. The general principle is to use the Galactic diffuse emission as a stable 'calibration source'to compare the response of the instrument at different epochs. The main problem is that observations far apart on the sky are effectively decoupled and this method can give no information on the relative detector response; however the instrument pointing directions were fairly randomly distributed in time so that there should be no correlation between sensitivity and pointing direction, and this can be used as a strong constraint on the solution.

The method is designed to find a set of parameters which lead to maximum consistency between the intensities derived from different observation periods. This will be briefly described and the resulting sensitivity and background variations presented.

2. METHOD

The gamma-ray sky (latitudes $|b| < 30^o$) is divided into *subcells* of 1^o square, and the field of view of each observation period (20^o radius) is divided into *cells* of 100^o square by raster scans 1^o wide along increasing longitude. For each period i the predicted number of gamma-ray events in subcell j based on the total observations is

$$n_{ij} = f_i e_{ij} \frac{\sum_k (n^o_{kj} - f_k e_{kj} \Delta I_{Bk})}{\sum_k f_k e_{kj}} + f_i e_{ij} \Delta I_{Bi}$$

where the sum is over all periods in which the subcell was observed and

n^o_{kj}= number of events observed in subcell j in period k

f_i= sensitivity relative to the first period ($i = 0$), e_{ij}= nominal exposure (in $cm^2 s$) to subcell j in period i (uncorrected for temporal variations), ΔI_{Bi}= change in background in period i relative to period 0 .

We define

$$\chi^2 = \sum_i \sum_m \frac{r^2_{im}}{N_{im}}$$

where $N_{im} = \sum_{j \subset cell\ m} n_{ij}$, $N^o_{im} = \sum_{j \subset cell\ m} n^o_{ij}$, and $r_{im} = N^o_{im} - N_{im}$.

The background variation was found from independent studies to correlate with the solar-modulated cosmic ray intensity. This confirmed the expectation that the background is due to γ-rays produced by cosmic-ray interactions with the material in front of the telescope. On this basis the *background variation* was assumed to have the form $\Delta I_{Bi} = b \Delta S_3$ where ΔS_3 is the change in rate of a scaler sensitive to the total charged particle intensity in the detector. The constant b was determined in the analysis along with the sensitivities.

In order to avoid any correlation of sensitivity with position on the sky (see Sec.1), a *fluctuation parameter* S is defined by $S = \sum_i (1 - \frac{f_i}{f^o})^2$, where f^o is chosen to fit the temporal smooth long-term trend. The technique then consists of minimizing χ^2 subject to the constraint of constant S. Suitable values of S were found empirically and adopted in the final determination of the sensitivity and background parameters. Although the method involves about 60 free parameters the number of constraints is much larger than this and the minimization can be performed by suitable conjugate gradient methods (see Strong et al. 1985 for details).

3. RESULTS

Fig 1 shows the variation of sensitivity based on application of the method to data in the range 70 - 5000 MeV. Most evident is the long term variation which causes a 50% reduction over the full time span of the experiment. The method was also applied to the separate energy ranges 70-150, 150-300 and 300-5000 MeV to obtain three independent estimates. The results are consistent with those from the total energy range and show that the period-to-period variations are significant and, further, that the sensitivities are determined with an accuracy which is usually better than 10%. In addition the results in the 3 ranges give an indication of the accuracy of the sensitivity determination in individual periods.

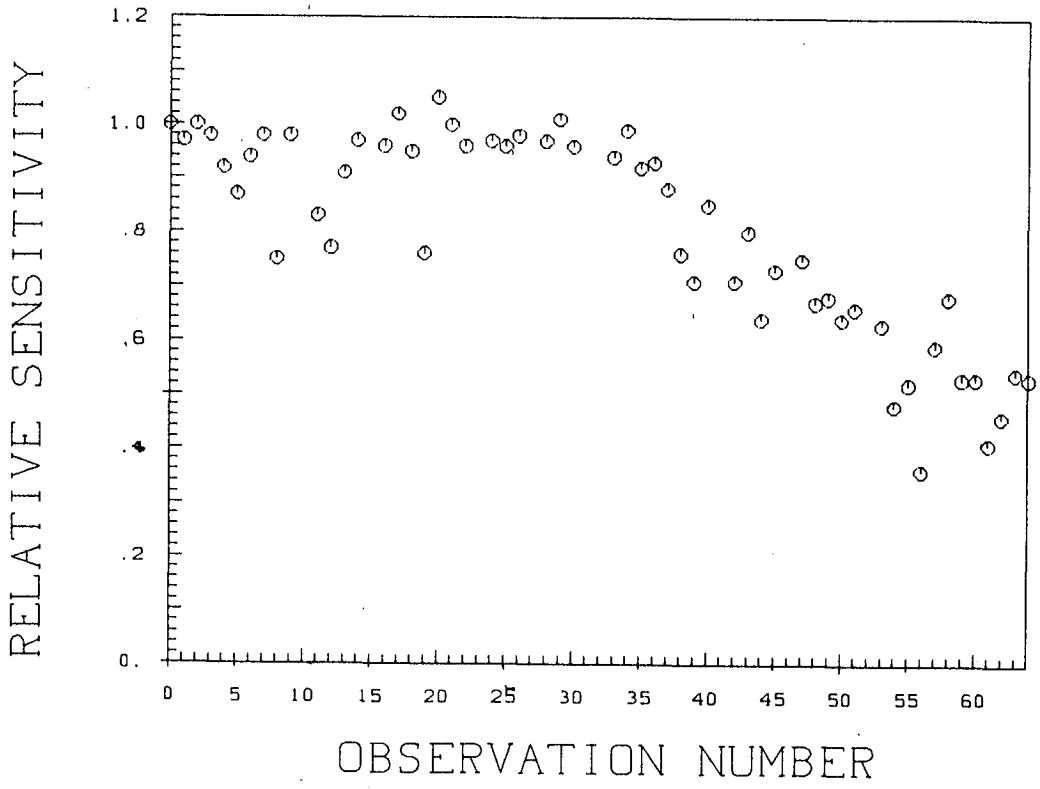

FIG 1. *Relative sensitivity as function of observation period determined for the 70-5000 MeV energy range using the method described in the text. The sensitivity of the first period (Period 0) is taken as 1.0. Periods pointed at high latitudes with insufficient overlap are not displayed.*

There is no trend visible when the sensitivities are plotted as a function of Galactic longitude, demonstrating the success of the technique described above. The larger fluctuations in sensitivity can be identified as originating in known effects such as instrumental malfunctions, and where an independent estimate of the size of the effect can be made the agreement is satisfactory.

Fig 2 shows as an example the background variation in the energy range 300-5000 MeV. The total variation amounts to about 30% of the average absolute background level.

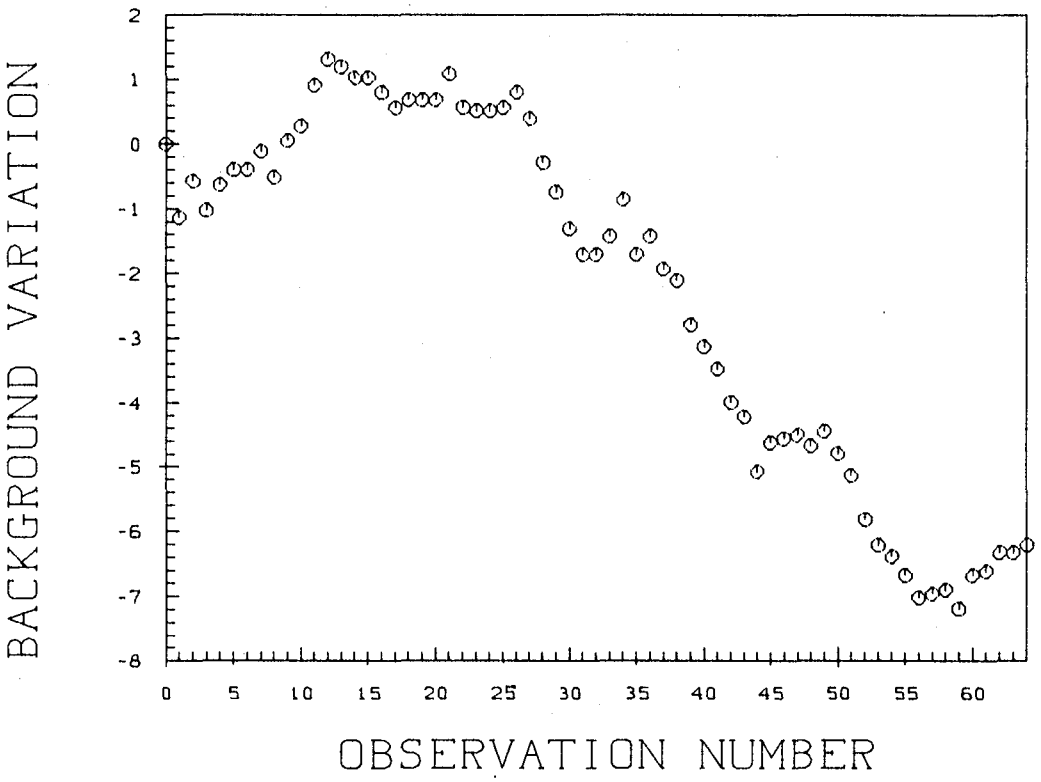

FIG 2. *Variation of background level relative to first period for the 300-5000 MeV energy range. Units:* 10^{-6} *ph* $cm^{-2}sr^{-1}s^{-1}$. *The variation is assumed proportional to the rate in a charged particle scaler, with a constant of proportionality determined from the overlap analysis.*

A complete description of the method and results will be given in Strong et al. (1985).

REFERENCES

Mayer-Hasselwander H A et al. (1985) *in preparation*

Strong A W et al. (1985) *in preparation*

069.3-10

A STAR CAMERA ASPECT SYSTEM SUITABLE FOR USE ON BALLOON EXPERIMENTS

S.D. Hunter, R.G. Baker
Code 662, NASA/Goddard Space Flight Center
Greenbelt, Maryland 20771 U.S.A.

1. Introduction. We have designed, built and flown, on a balloon borne experiment, a star camera aspect system. This system was designed to provide offset corrections to the magnetometer and inclinometer readings used to control an azimuth and elevation pointed experiment. The solid state camera used is a General Electric TN2500 CID camera with a Nikkon Noct-Nikkor 58mm f/1.2 lens. The camera is controlled by a Texas Instrument TMS 9995 microprocessor, including commandable exposure and noise rejection threshold, as well as formatting the data for telemetry to the ground. As a background program, the TMS 9995 runs the aspect program to analyze a fraction of the pictures taken so that aspect information and offset corrections are available to the experiment in near real time. The analysis consists of pattern recognition of the star field with a star catalog in ROM memory and a least-squares calculation. The hardware, software and star catalog which make up this system are fully described in reference 1. This paper describes the performance of this system in ground based tests and as part of the NASA/GSFC High Energy Gamma-Ray Balloon Instrument (2).

2. Ground Tests. Ground based tests were performed during 1983 and early 1984 to check the operation of the star camera and aspect program. The TN2500 camera provides an 8 bit digital output, in addition to a standard analog output, which made the camera easy to interface to the microprocessor and provided a convenient measure of star intensities. In the following, ADC counts or counts refers to the digitized output of the pixel or pixels illuminatd by a star.

The intensity of several observed stars in ADC counts for a five second exposure (integration time) as a function of visual magnitude is shown in Figure 1. Each data point represents a lower bound to the intensity because some of the light from a star can fall on the inactive area of the CID chip between the pixels. Stars of magnitude fainter than about 3 illuminate single pixels whereas brighter stars illuminate several pixels. Their intensity is the sum of the response of all the pixels comprising the star image. The observed intensity of brighter stars was fairly constant except for atmospheric effects. The intensity of dimmer stars varied much more dramatically as the star image partially or completely fell on the inactive area between pixels.

For the ground tests, the CID chip was cooled to about 5°C with a thermo-electric cooler. This reduced the thermal noise by a factor of two to between 5 and 8 counts. Thus, from Figure 1, it can be seen that, for a five second exposure, stars of magnitude six were detected with a signal-to-noise ratio of about one. A signal-to-noise ratio of one and the inclusion of a few noise pixels, which are indistinguishable from star images, does not affect the operation of the aspect program other than to slow down the calculation. The aspect program, when provided with the approximate altitude and elevation of the camera, was able to calculate the aspect information for the observations.

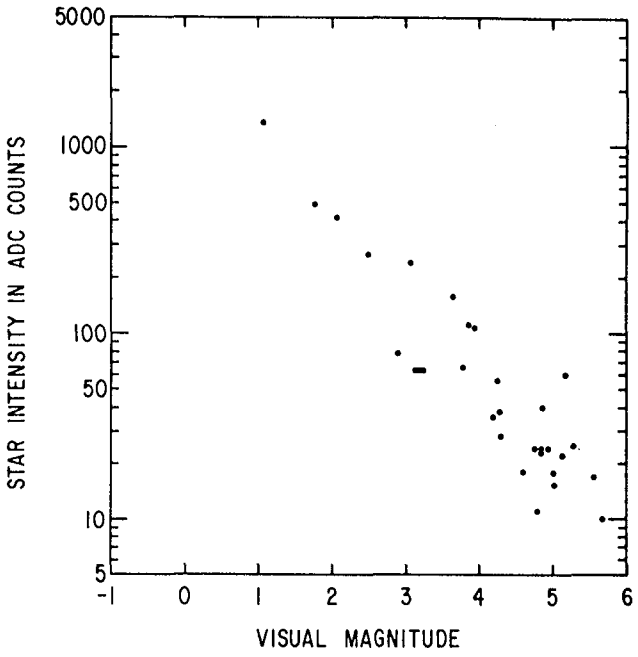

Figure 1 -- CID camera star intensity as a function of visual magnitude for a five second exposure.

3. Balloon Flights. The first balloon borne experiment to use this camera aspect system was flown on May 9, 1984. The first two hours of the flight were dedicated to tests of the aspect system. Three regions of the sky were observed in the constellations of Hercules, Ursa Major and Aquila. During the Aquila observation, 78 pictures were taken. The star Altair (53-x Aqu., Mv = 0.77) was seen in all the pictures. It was so bright that all the pixels which formed the star image were saturated. The star 50-γ Aqu, Mv = 2.7 was seen in almost all the pictures. Its single pixel intensity varied between 25 and 70 counts. The star 60-β Aqu., Mv = 3.7 was seen in only three pictures. The observed intensity was 10, 22 and 33 counts. The only dimmer star observed was 75-Her., Mv = 4.2, which had an average observed intensity of about 8 counts. The signal to noise ratio for these observations was about one although the thermo-electric cooler was not needed due to the low temperature at balloon altitudes.

The azimuth-elevation pointing system of the balloon experiment held the desired azimuth pointing direction within a 0.5° deadband. The elevation drive was powered off during the camera tests. Within the azimuth deadband the experiment moved with an azimuthal velocity between 0.08 and 0.1 degrees per second at all times. This azimuth velocity produced an effective exposure of about 0.5 second per pixel since the star images were smeared over several pixels. Taking into account this effective exposure, the above intensities are consistent with the ground based results shown in Figure 1 if scaled by a factor of ten to correct for the difference between the 0.5 second effective exposure and the 5 second ground based exposure.

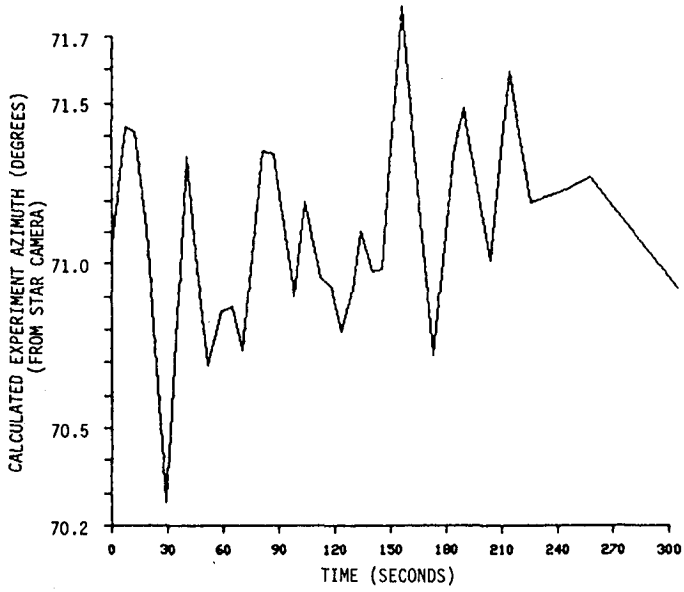

Figure 2 -- The azimuth angle calculated for the experiment by the aspect program.

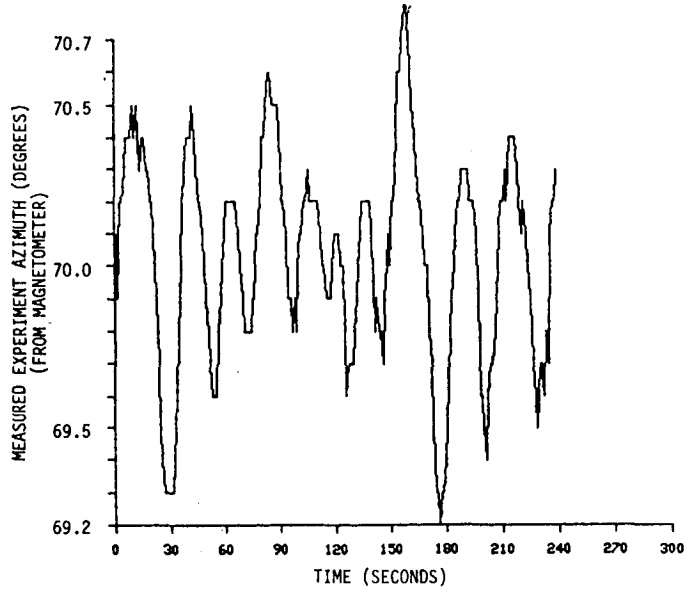

Figure 3 -- The azimuth angle measured for the experiment by the magnetometer.

During the balloon flight the aspect program was not able to analyze any of the pictures because only one in about twenty pictures is processed by the program, although all pictures are telemetered to the ground. For a picture to be processed by the aspect program, it must contain at least three stars, real or noise. To complete the analysis and determine the aspect information, the picture must contain at least three real stars. Noise pixels are treated as stars without a match in the star catalog and are ignored by the program.

During post flight analysis of all the pictures the aspect program was able to analyze the pictures that contained three real stars. The aspect program was modified to complete the analysis if only two real stars were found. The aspect information determined by this analysis is not as accurate as in the case when three or more stars are observed.

Part of the results of this modified analysis, the calculated azimuth of the experiment, is shown in Figure 2. The exposure time for the observations used for Figure 2 was five seconds for the period labeled 0 to 170 seconds and ten seconds afterward. Figure 3 shows the azimuth of the experiment as measured by the pointing system megnetometer for the same time period as shown in Figure 2. It can be seen, by comparing these two figures, that the azimuth calculated by the aspect system shows the same time variations as the azimuth measured with the magnetometer except for a discrepancy of about one degree. This discrepancy between the measured azimuth and the azimuth calculated with respect to the inertial star frame provides the offset correction needed to account for uncertainties in the latitude and longitude of the balloon, the alignment of the magnetometer and the deviation angle of the magnetic field. Similar analysis of th elevation angle would provide the offset correction for the inclinometer

4. Summary. We have shown that our aspect system can provide accurate near real time aspect information for balloon experiments if a factor of two to five improvement in the stability of the balloon experiment can be made to reduce smearing of the star images. In addition, if the calculated offset correction is averaged over several analyzed pictures, the offset correction can be determined with an accuracy of at least 0.1°.

5. Acknowledgements. S. D. Hunter also held a National Research Council Associateship at NASA/Goddard Space Flight Center and was affiliated with the University of Maryland during the period of this work. We thank the National Scientific Balloon Facility, Palestine, Texas, for their flight support.

6. References.

1. A Star Camera and Aspect Determination System for Balloon Borne Payloads, R.G. Baker and S.D. Hunter, NASA X Document, in preparation.
2. High Energy Gamma Ray Balloon Instrument, D.J. Thompson, et al., paper OG9.2-15, these proceedings.

Balloon-Borne Video Cassette Recorders For Digital Data Storage

W.E. Althouse and **W.R. Cook**

California Institute of Technology, Pasadena, CA. 91125, U.S.A.

1. Introduction

A high-speed, high-capacity digital data storage system has been developed for a new balloon-borne γ-ray telescope (see paper OG9.2-2). The system incorporates sophisticated, yet easy to use and economical consumer products: the portable video cassette recorder (VCR) and a relatively newer item - the "digital audio processor". The in-flight recording system employs eight VCRs and will provide a continuous data storage rate of 1.4 megabits/sec throughout a 40 hour balloon flight. Data storage capacity is 25 gigabytes and power consumption is only 10 watts.

2. The Digital Audio Processor

The key to rapid development of a VCR based digital data storage system was the availability of the digital audio processor, a consumer product intended to allow the use of a home VCR as a digital audio tape recorder. A simplified block diagram of such a processor, the Sony PCM-701ES is shown in Figure 1. In normal stereo recording operation the incoming left and right audio signals are each digitized with 16 bit resolution at a rate of 44 kHz. The digital data are multiplexed onto a single serial line and input to the "record data processor" at a rate of 1.4 megabits/sec. The processor adds error detecting and correcting codes, interleaves the data, and finally generates a video signal in standard NTSC television format suitable for recording on any home VCR. On playback the digital data are unscrambled, corrected for errors, and sent to 16 bit DACs which reconstruct the original audio waveforms. The powerful "cross interleaved" error correction scheme [1,2] virtually eliminates errors due to dropouts on the VCR tape, as is required for noise-free audio reproduction.

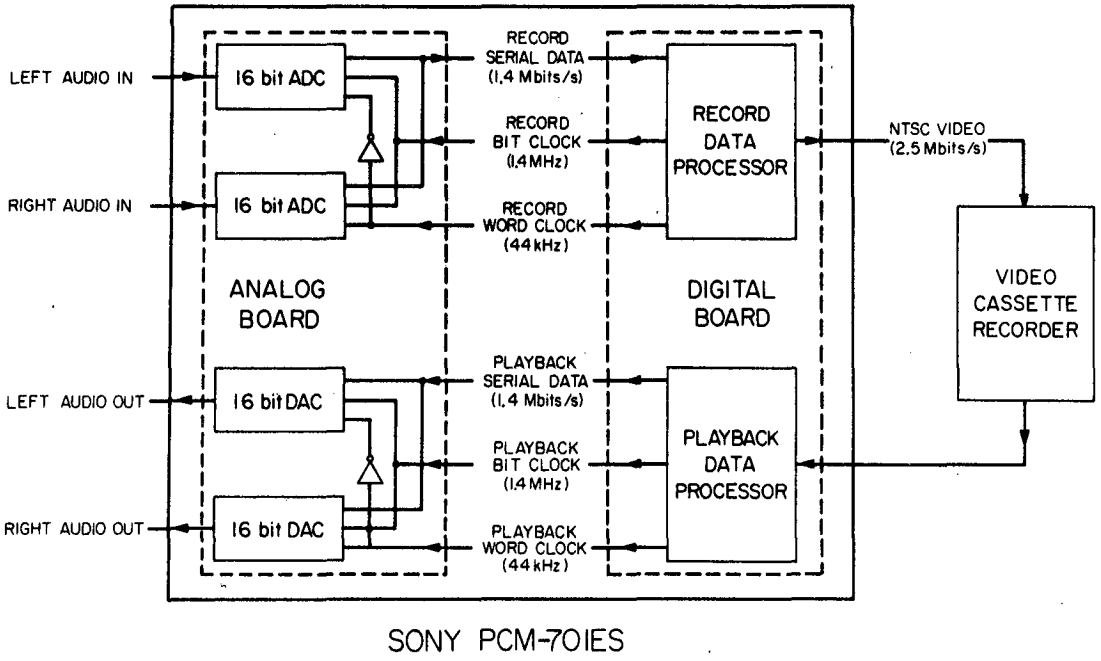

Figure 1. Simplified block diagram of the Sony PCM-701ES Digital Audio Processor.

As shown in Figure 1, the circuitry within the Sony PCM-701ES is conveniently divided into two main printed circuit boards - an analog board and a digital board. For our purpose only the digital board is required. It has been incorporated in our flight recording system (Figure 2) and as part of a record/playback computer peripheral (Figure 3). The digital board is very easy to use. It operates from a single 5 volt supply, is TTL compatible and provides standard 75 ohm video input and output. Power consumption is 3 watts.

The Sony PCM-701ES may be operated in either a 14 or 16 bit mode. In the 16 bit mode the full resolution of the 16 bit ADCs and DACs are used, but fewer error correcting bits are encoded. In the 14 bit mode tape dropouts of up to 32 horizontal television scan lines can be perfectly corrected, while in the 16 bit mode error correction is guaranteed only for dropouts of up to 16 lines [3]. Nonetheless, for the convenience of a simple 16 bit word-aligned format we have used the 16 bit mode. As discused below, the error rate is quite low when high-quality tape is used.

3. Application

In our balloon flight application, γ-ray event data are written into a 2K byte buffer memory while a second buffer memory is read into the PCM-701ES digital board in the format described below. Each buffer can hold 63 events, and buffers are switched synchronously every 11.7 msec, slaved to the PCM-701ES data clock. Thus, ~5400 events per second can be recorded with no deadtime, while the PCM-701ES is supplied with a continuous data stream of 1.4 megabits/sec. The NTSC video signal is fed to eight Sony SL2000 portable VCRs, which are operated sequentially with a capacity of 5 hours recording time for each VCR. Data capacities are summarized in Table I.

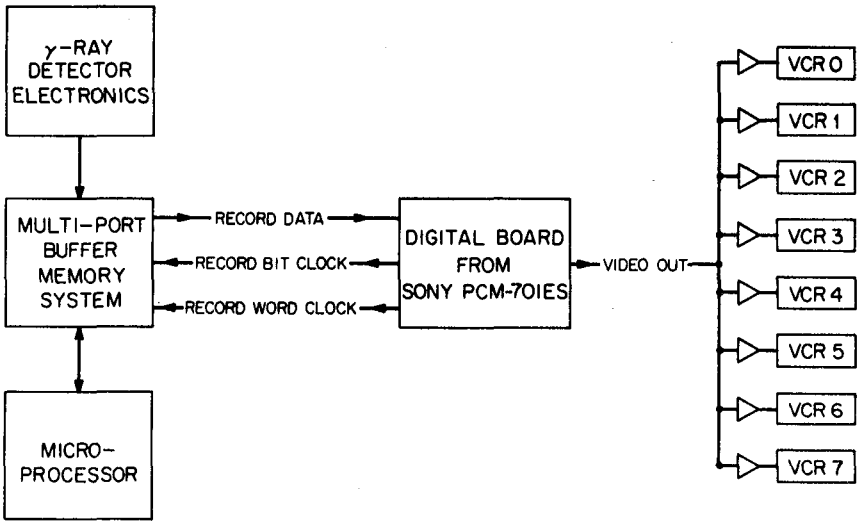

Figure 2. Block diagram illustrating the use of the Sony PCM-701ES digital board in a balloon-borne data recording system.

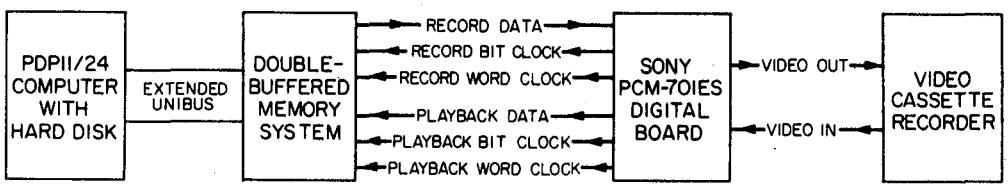

Figure 3. Block diagram showing the Sony PCM-701ES digital board as part of a mass storage computer peripheral.

Table 1. Balloon-Borne γ-ray Telescope Data Storage System	
Data Rate	1.4×10^6 bits/sec 175,000 bytes/sec 5400 events/sec
Recording Time (per tape) (total)	 5 hrs 40 hrs (8 VCRs)
Data Capacity (per tape) (total)	 2.5×10^{10} bits 3.2×10^9 bytes 9.7×10^7 events 2×10^{11} bits 2.5×10^{10} bytes 7.8×10^8 events
Power Consumption Digital board Portable VCR (total)	 3 watts 7 watts 10 watts

We have measured the error rate using Sony L750 Ultra High Grade tape recorded at "βIII" speed on Sony SL2000 portable VCRs. In initial tests approximately 1.5 million 2K byte data blocks were recorded on each of seven video cassettes using seven different VCRs (21 gigabytes total). Each data block contained a 32 bit start code, a 32 bit block count, approximately 1000 psuedo-random 16 bit numbers, a 32 bit stop code and a 16 bit cyclic redundancy check (CRC) code. The tapes were played back on a single VCR and each data block was checked for an accurate start and stop code, CRC error, and sequential block count. Of the 10.5 million blocks checked ~300 were missing (due to "playback muting", where the PCM-701ES simply replaced long stretches of uncorrectable data with a fixed data word), and 19 CRC errors were detected (due to "playback interpolation" where the PCM-701ES replaced isolated uncorrectable data words with the average of adjacent words). The fraction of blocks discarded due to detected errors was $\sim 3 \times 10^{-5}$, a negligible data loss rate for most data acquisition applications. A sample of 600,000 "good" blocks were checked 100% for undetected errors and none were found. Thus the undetected block error rate was less than 2×10^{-6}, acceptable for our present application.

The VCR data systems discussed here were used to record and playback data for the formation of the γ-ray images presented in paper OG9.2-2. In this process 56 megabytes of data were recovered without a single detected error.

This work was supported in part by NASA grant NGR 05-002-160.

4. References

[1] Doi, T.T., Odaka, K., Fukuda, G., Furukawa, S., "Cross Interleave Code for Error Correction of Digital Audio Systems", Audio Engineering Society Preprint, 1979.

[2] Doi, T.T., Tsuchiya, Y., and Iga, A., "On Several Standards for Converting PCM Signals into Video Signals", *J. Audio Eng. Soc.*, **26-9**, pp. 641-649, 1978.

[3] Sony PCM-701ES Operating Instructions, 1983.

A POSITION SENSITIVE PHOSWICH HARD X-RAY DETECTOR SYSTEM

A.J.Dean, C.G.Hanson, C.J.Hopkins, R.A.Lewis, J.Fraser-Mitchell
Department of Physics, University of Southampton, Southampton UK

ABSTRACT

A prototype position sensitive phoswich hard X-ray detector, designed for eventual astronomical usage, has been tested in the laboratory. The scintillation crystal geometry was designed on the basis of a Monte Carlo simulation of the internal optics and includes a 3mm thick NaI(Tl) primary X-ray detector which is actively shielded by a 20mm thick CsI(Tl) scintillation crystal. This phoswich arrangement is viewed by a number of two inch photomultipliers. Measured values of the positional and spectral resolution of incident X-ray photons are compared with calculation.

1. Introduction. The use of the coded aperture mask is rapidly becoming a well established technique for the imaging of high energy X/gamma-ray photons (10 keV $\lesssim E_\gamma \lesssim$ 1 GeV) [1,2]. The successful application of this technique and the imaging quality of the final telescope system are related to the development of a suitable position sensitive photon detection plane. The performance of this element must be optimised with respect to a number of factors in order that a high quality astronomical telescope can be constructed. First and foremost, the detection plane must have the best possible positional resolution for the incoming photons so that high definition images can be made. However, to ensure that sophisticated astrophysical information may be extracted from the imaging data it is also important that the detector has good spectral resolution for the detector photons and that the background noise level is reduced to a minimum level in order to maximise the sensitivity of the overall system.

A number of position sensitive detector systems are currently under development for astronomical use in the hard X/gamma-ray region of the electromagnetic spectrum ranging from the thick inorganic scintillators for gamma-ray photons to xenon gas proportional counters at the lower end ($E_\gamma \lesssim$ 100 keV) of this spectral range [3,4,5,6]. At the present time the most effective detection system to cover the hard X-ray spectral range $\sim$15-300 keV comprises a thin (few mm) NaI crystal which is actively shielded. The phoswich/collimator arrangement has been extensively used to accumulate hard X-ray astronomical information. Here we describe the development of a prototype position sensitive phoswich system. Apart from eventual use as an imaging syystem such a device has the additional advantage of potential operation as an X-ray polarimeter.

2. The Detector System and Associated Tests. A prototype NaI(Tl)/CsI(Tl) phoswich system was constructed as shown in Fig.1. The dimensions of the assembly were 262mm x 62mm x 33mm. The NaI(Tl) and CsI(Tl) crystals were 3mm and 20mm thick respectively. A thin aluminium entrance window enabled the system to be studied with X-ray photons down to $\sim$15 keV. The 'bottom' face of the arrangement was covered in glass to enable the scintillation light to be detected by a suitable array of photomultiplier tubes which were optically coupled by means

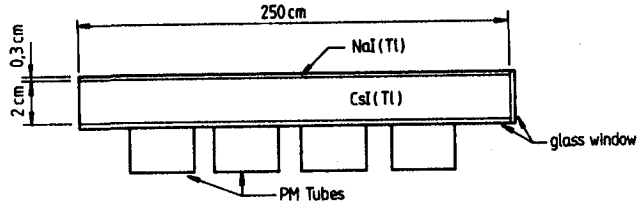

Fig.1. A prototype NaI(Tl)/CsI(Tl) position sensitive phoswich system.

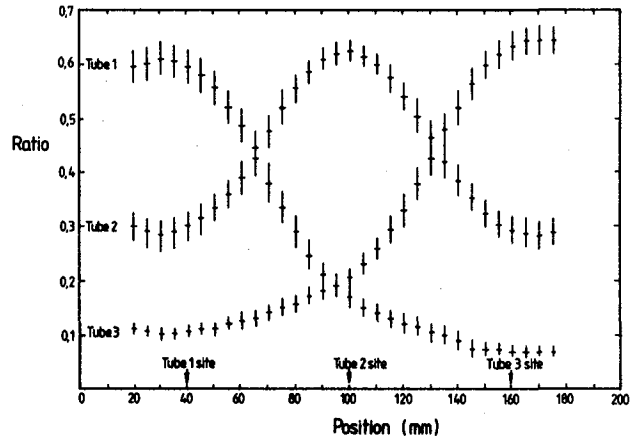

Fig.2. The ratio of individual photomultiplier signals to the total signal as a function of position along the length of the detector.

of a highly transparent silicon grease. The photomultiplier signals were processed by a Harshaw NC25A pulse shape discrimination unit and in conjunction with a CAMAC/PDP-11 computer system in order to select genuine X-ray events and record the various signal amplitudes for individual X-ray events. A highly collimated Am 241 source was used to irradiate a well defined (<2mm) position on the surface of the NaI crystal.

Figure 2 shows the ratio of individual photomultiplier signals to the total signal, as a function of position along the length of the detector. The measurements were taken at 5mm intervals on a line which joins the centres of the phototubes. Approximately 10^4 events were recorded for each position. The positions of the photomultiplier tubes are indicated on the X-axis. The shape of

the curves was found to be in excellent agreement with the prediction of a Monte Carlo simulation of the scintillation light collection efficiency for various X-ray interaction positions over the surface area of the detector system.

An appropriate event location algorithm was constructed on the basis of the above experimental data and subsequently used to calculate the position of interaction of incident X-rays. Figure 3 shows a graph of positional resolution versus position along the line joining the centres of the photomultiplier tubes. It can be

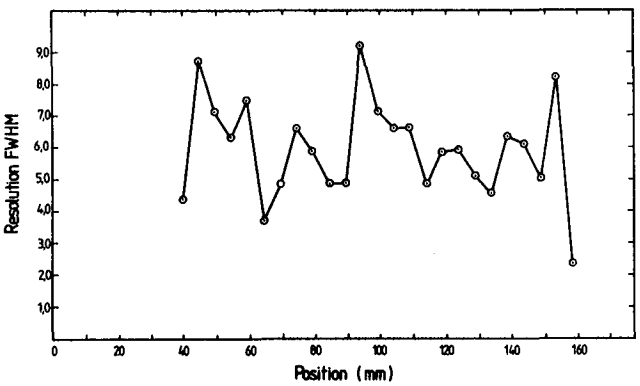

Fig.3. Positional resolution (FWHM) as a function of position using data from Fig.2.

seen for such a 'linear' case that the best positional resolution occurs in the region between the photomultiplier tubes where the gradients of the signal ratio versus position are at a maximum. The relatively poor resolution above the centres of the photocathodes leads to a 'spikey' response which is undesirable for coded aperture imaging.

Figure 4 demonstrates the improvement which may be gained by sampling the scintillation light over a two dimensional sample. In this case the photomultiplier signals (lighter lines) and positional resolution (heavy line) are taken along a line of symmetry between two rows of PM tubes. The positions of the individual photomultipliers are indicated along the X-axis. The great improvement in the uniformity of the positional resolution clearly demonstrates that a two dimensional must be employed as in the traditional gamma-camera.

The spectral resolution of the system was found to be competitive the best scintillation devices.

3. Conclusions. The above preliminary tests have demonstrated that a position sensitive phoswich detector can be made to operate in the hard X-ray region of the electromagnetic spectrum with a positional resolution of a few millimetres. For historical reasons the original attempt has been to develop a one-dimensional position sensitive counter. It was found that this device had an extremely non-uniform positional resolution function which is not suitable for the production of good quality coded aperture images. When operated as a two-dimensional device, in a similar manner to the gamma-camera, it was found that

a phoswich device could be made to operate with good spectral and positional resolutions for the incident hard X-rays.

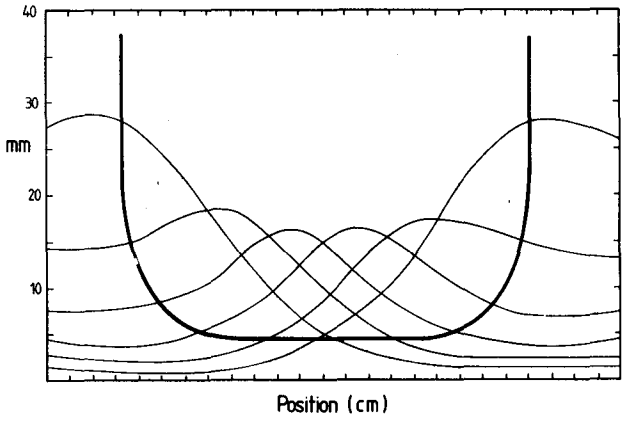

Fig.4. Ratio of individual photomultiplier signals as a function of position along a line equidistant between two rows of photomultipliers (light curves) and arbitrary units). Calculated positional resolution along this line (heavy curve)

References

1. G.K.Skinner, NIMS in Phys.Res.(1969), 221, 33
2. A.J.Dean, NIMS in PHys.Res.(1984), 221, 183
3. P.M.Charalambous et al. NIMS in Phys.Res. (1984) 221, 183
4. A.P.Willmore et al. NIMS in Phys.Res. (1984) 221, 284
5. P. Mandrou. Adv. Space Res. (1984), 3, 525
6. W.R.Cook et al (1983), IEEE Nuclear Science Symp. SRL 83-27

A Cerenkov Imaging Telescope for High Energy Gamma Rays

P. Ferrando and P. Goret
CEN / Saclay - France

Abstract

A large area gamma ray telescope based on the gas Cerenkov imaging technique is presented. The performances of the instrument for the observation of high energy gamma ray point sources are discussed.

1 - Introduction

A new field in high energy astrophysics was opened with the discovery by SAS-2 and COS-B of some 25 gamma ray sources above 30 MeV (see /1/ for a review). After the publication of the COS-B catalog the situation is as follows: (i) sources are located with error radii of a fraction of a degree at best, (ii) detailed energy spectra up to a few GeV could be extracted for only a few sources (Crab, Vela and Geminga), (iii) reliable data on periodicity are available only for the Crab and Vela pulsars. The main limitation in these experiments was the restricted sensitive area of the telescopes which prevented from accumulating a sufficient statistics of photons to provide detailed results for the fainter sources.

On the upper energy side air shower arrays were also successful at identifying gamma ray sources from a few hundreds of GeV up to 10^{16} eV (a review is given in /2/). Hampered by a copious cosmic proton background these experiments typically locate gamma ray sources within a few degrees.

More accurate data will be collected by the GRO /3/ and GAMMA-1 /4/ instruments with sensitive areas of 2000cm² and 500 cm² respectively. However it is anticipated that the range 1-100 GeV, where the best angular resolution can be reached, will remain essentially unexplored calling for still larger instruments able to bridge the gap between orbiting telescopes and ground based detectors.

A promising technique to reach this goal is to use the Cerenkov light radiated in a gas by the pair electrons. The idea, originally developed by K. Greisen, led to the design of a large balloon borne telescope which was first to detect the Crab pulsar at several hundreds MeV /5/. More recently the concept was revived with two proposals for a gas Cerenkov gamma ray telescope for the Space Station /6/,/7/. In this paper we discuss in more details the expected performances of the large area Cerenkov imaging telescope for high energy gamma rays as proposed in /7/.

2 - The Gamma Ray Imaging Telescope (GRIMTEL)

A preliminary description of a gas Cerenkov imaging telescope was given in /7/ and a more detailed account was presented in /8/. A sketch of the telescope is shown in Figure 1. Briefly the incident gamma ray is converted into a e+/e- pair in the lead target. Both electrons emit Cerenkov light in the radiator gas at a well defined angle to the particle's trajectories. After being reflected by the mirror the Cerenkov photons are detected by a 2-dimensional position sensitive detector at the focal plane. The image pattern consists of 2 circles with fixed radius whose centers give the

direction of propagation of each electron in the gas. The incident gamma ray direction is approximated from the bissector of the two electron directions. The physical characteristics of the envisioned GRIMTEL instrument are summarized in Table 1. The electronic signature of a gamma ray is the 4-fold coincidence S1 x S2 x S3 x F with S3 and F being delayed compared to S2 by 16ns and 33 ns respectively. The directionality and high energy threshold of the Cerenkov effect makes the telescope naturally immune to cosmic ray induced background. The difference between the present proposal and the one described by D. Koch in /6/ lies in the granularity of the focal detector. The latter instrument detects individual Cerenkov photons with an angular uncertainty of 0.21 degree compared to 0.017 for the GRIMTEL. We believe that the improved angular resolution will result in a more reliable gamma ray signature and a better angular resolution to individual gamma rays. In addition it opens the possibility to estimate the energy by the amount of Coulomb scattering in the radiator gas. In the next section we present the expected performances of the GRIMTEL instrument.

3 - Performances of the GRIMTEL

The physical effects ultimately shaping the Cerenkov images of high energy gamma rays are as follows:

- the angle at which converted electrons are emitted
- the Coulomb scattering in the remaining target material
- the Coulomb scattering in the radiator gas
- the chromatic dispersion of the Cerenkov effect

Since we are using a thick target (0.5 r.l.) the 1st effect may be neglected compared to the 2nd one. The 4th effect is minute compared to the 3rd one and may also be ignored.

A Monte-Carlo simulation was performed to evaluate the performances of the instrument. Images of gamma ray events are first generated with the above mentioned 2nd and 3rd effects taken into account. We assume that each electron gives 15 Cerenkov photoelectrons on average in the 5 meters long radiator. In a second step each image are searched for 2 Cerenkov circles whose center coordinates are determined. A typical image of a 2 GeV gamma ray is shown in figure 2 together with the fitted circles. In some cases, especially at very high energy, the circles are so close they cannot be disentangled. For those events the gamma ray signature is a number of photoelectrons along a single circle being twice that for singly charged particles. The effective sensitive area of the GRIMTEL as a function of the aspect of the source to the telescope axis is shown in figure 3. It is seen that a figure of 28000 cm^2 at 0° above 1GeV is reached i.e. 14 times larger than in the GRO instrument. The GRIMTEL with a field of view of about 5° is best suited to the observation of gamma ray point sources. The r.m.s. angular resolution to individual gamma rays is estimated as 0.45° at 2 GeV, 0.18° at 5 GeV and 0.10° at 10 GeV. The improvement brought up by the GRIMTEL over the GRO experiment is not with the intrinsic angular resolution which is similar for both instruments. Rather it is that the larger area enables statistically significant observations to be performed at higher energies where the angular accuracy is significantly better.

The energy measurement could be best achieved with using a shower calorimeter. However if restrictions on weight would rule out this possibility an estimate of the energy could still be obtained from a measurement of the Coulomb scattering in the radiator gas. Investigations of the energy resolution attainable with this method are in progress.

4 - Final comments

The feasability of the proposed experiment depends critically on the availability of a photon detector with fine spatial resolution and sensitive areas of several thousands of cm^2. In addition the device should deliver a fast linear response to Cerenkov light in order to take part in the trigger generation. The latter requirement is essential for minimizing the telescope dead time so that the readout of the focal detector, with its large number of cells, be triggered only on those events with an appropriate number of Cerenkov photoelectrons. Gaseous detectors sensitive to VUV light have been used successfully to record the Cerenkov rings of charged particles in accelerator beams (see /9/ for a review). An experiment, using a multineedle detector to record the Cerenkov images of 500 MeV gamma rays, is in preparation at Saclay. Development of multianode photomultipliers with a 3x3 mm^2 pixel size are also currently in progress at Saclay. With these devices a new generation of very large gamma ray telescopes can be envisioned for long exposures on the Space Station. These instruments, with a sensitivity higher by more than one order of magnitude over present day experiments, will undoubtedly increase our present knowledge of the astrophysics associated with celestial gamma ray sources.

References

/1/ G.F. Bignami and W. Hermsen
Ann. Rev. Astron. Astroph. 1983 Vol21 p.67

/2/ R.C. Lamb
Proc. of the Workshop on Cosmic Ray Experiments for the Space Station Era - Baton Rouge 1984

/3/ E.B. Hughes et al.
IEEE Trans. Nucl. Sci. 1980 Vol NS-27

/4/ R. Bazer-Bachi et al.
Proc. 12th ESLAB Symposium - Frascati 1977

/5/ D. Koch et al.
Nucl. Instr. Meth. 1973 Vol 108 p. 349

/6/ D. Koch
' A large area gamma ray imaging telescope system
SAO Report 1983

/7/ P. Goret
' A large area gamma ray telescope for point source studies above 1 GeV ' - idem ref. /2/

/8/ P. Ferrando et al.
' A Cerenkov imaging detector for very high energy gamma rays'
6th Symposium on X and Gamma Ray Sources and Applications
Ann Arbor - 1985 - to be published in Nucl. Instr. Meth.

/9/ G.B. Coutrakon
IEEE Trans. Nucl. Sci. 1984 Vol NS-31 p.27

/10/G. Comby et al.
IEEE Trans. Nucl. Sci. 1982 Vol NS-29 p.328

Converter:
0.5 r.l. lead
Mirror:
spherical f/1.7
Ø = 3 meters
f = 5 meters
Radiator gas:
N2 at STP
Cerenkov angle = 1.5°
Focal detector:
Ø = 60 cm
cell size = 3x3 mm²
# of cells = 31,400

Table 1 - Physical characteristics of the GRIMTEL.

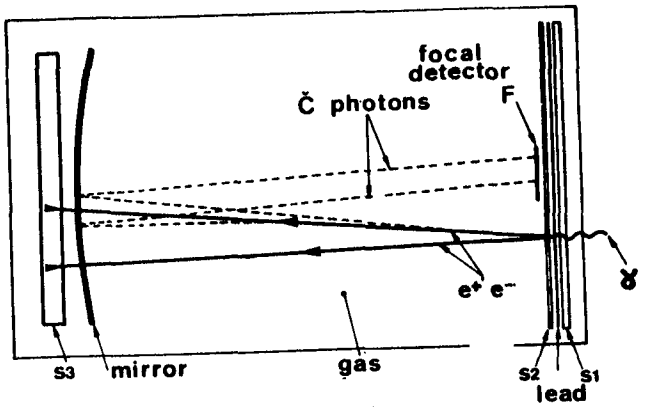

Figure 1 - Sketch of the GRIMTEL.

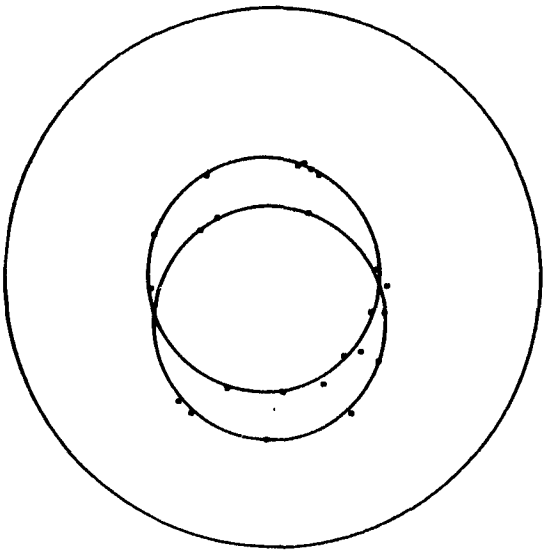

Figure 2 - A simulated Cerenkov image of a 2 GeV gamma ray with fitted circles. Each dot represents a cell lit up by a Cerenkov photon.

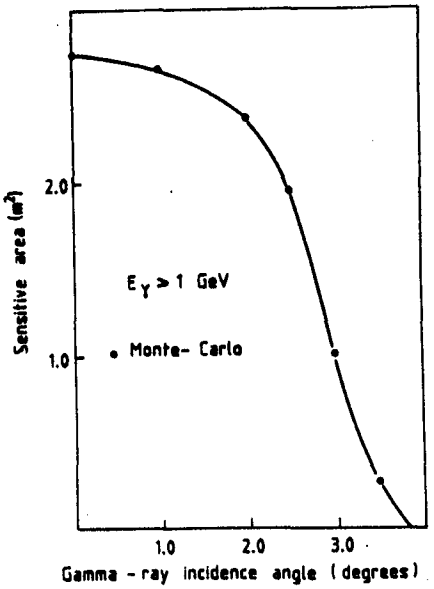

Figure 3 -The effective area of the GRIMTEL as a function of the aspect of the source to the telescope axis.

THE UNIVERSITY OF DURHAM MARK III VERY HIGH ENERGY GAMMA RAY TELESCOPE

P.M.Chadwick, N.A.Dipper, J.C.Dowthwaite, I.W.Kirkman,
T.J.L.McComb, K.J.Orford and K.E.Turver
Department of Physics,University of Durham,
South Road, Durham DH1 3LE, UK.

ABSTRACT

A new very high energy gamma-ray telescope employing the atmospheric Cerenkov light technique and currently nearing completion is described. The telescope is designed to have capability as both a wide angle instrument (4 degree field of view) for sky survey work and as a narrow field of view instrument (1.35 degrees) for conventional drift-scanning and tracking modes of operation. The telescope consists of two 10 sq. m. mirrors operated in fast coincidence with multiple phototube assemblies at the prime focus of each mirror. The design philosophy of the instrument is discussed and comparisons of its performance with our previous telescopes are made.

1. INTRODUCTION

During the period 1981 - 1984 we operated a very high energy gamma-ray (> 1000 GeV) facility at Dugway, Utah, U.S.A [1]. This facility initially comprised an array of four telescopes, each consisting of three 1.5 m diameter searchlight mirrors focussed onto three phototubes. Each set of phototubes was operated in fast coincidence, which enabled us to maintain a high gain and singles counting rate (~ 30 kHz) but have a negligible accidental (noise) coincidence rate.

In an attempt to overcome the restrictive optics enforced by the use of f(0.4) searchlight mirrors and to optimise the mirror design for VHE gamma-ray astronomy, in 1983 one of the telescopes was remirrored with purpose-built mirrors. Mirrors of focal length 2.2 m were employed which gave a 1.25 degree field of view using 2" phototubes, compared with the original field of view of 1.75 degrees. Operation of the modified (Mark II) system along side the original (Mark I) system has shown that the narrowing of the field of view has achieved its design objective in improving the ratio of detected gamma-rays to background cosmic ray events for discrete objects. We believe that the geometrical aperture of the Mark II telescope is near optimum, eliminating a maximum number of off-source protons but allowing detection of all gamma-rays from a point source in the centre of the field of view.

The Dugway facility has proved successful during its four years of operation. Numerous sources of VHE gamma rays have been discovered or confirmed. The strongest source detected to date (4U0115 +63,[2]) required observation for 25 hours to give a detection significant at the 4.4 σ level, with proportionally longer periods required for weaker sources. When available observing time is taken into account, this limits the number of thorough examinations of source candidates to 3-4 per year with the original telescopes. Clearly, to fully exploit this energy range of the electromagnetic spectrum, a much more sensitive telescope is required.

2.TELESCOPE DESIGN The Mark III telescope will be capable of operating in three distinct modes:-

(a) Sky survey work where a large solid angle (for reasonable sky coverage), combined with good gamma ray/proton ratio, is required.

(b) Tracking of possible pulsed sources where a small telescope opening angle is desirable giving mimimum acceptance of background cosmic rays.

(c) Drift scan mode where a moderate opening angle is required to enable the source to be within the field of view for a reasonable time.

The design philosophy adopted is one of having a ring of six off-axis detector channels surrounding the on-axis one to satisfy requirement (a). Such an arrangement enables seven adjacent areas of sky to be viewed when in sky survey mode with the advantages of background reduction achievable with a narrow angle system. When operating in tracking mode, such an arrangement of seven channels enables six simultaneous off-source measurements to be made, allowing a continuous monitor of the nearby background conditions. The telescope design allows for the addition of a second ring of twelve phototubes, thus allowing a trebling of the area surveyed in a given time. The telescope has been designed so that photomultiplier packages can be easily changed. For example, in drift scan mode of operation we have the option of employing larger phototubes, thus increasing the aperture.

The Mark III telescope comprises a light collector of 20 sq. m. deployed as two 10 sq. m. dishes. A third smaller mirror of 3 sq. m. located between these two allows 3-fold fast coincidence to further reduce accidental noise counts.

A number of different techniques of mirror construction have been investigated. The goal has been to produce mirrors with physical characteristics well suited to the observation of Cerenkov light, which are both light, cheap and easy to produce. Our starting point was the mirrors successfully used on the Mark II telescope which were 0.6 m diameter and machined out of solid aluminium plate and polished. We have investigated pressing and spinning thin aluminium sheet, thermo-forming perspex, bonding thin aluminium sheet to a solid former and pressing thin glass mirrors. The method of manufacture adopted is the bonding of aluminium honeycomb to high reflectivity anodised aluminium sheet after stretching over a former. The method produces mirrors with spot size less than 0.1 degree. The telescope comprises 112 0.6 m diameter mirrors giving 2x10 sq m flux collectors with focal lengths of 2.5 m.

The telescope is mounted on an alt-azimuth mount and is steered under computer control by two DC electric servomotors. Direction sensing is by two absolute digital shaft encoders, giving position resolution of 0.1 degrees.

The main requirement for photomultipliers used in Cerenkov light work is unusual. We require a tube with a low noise performance under conditions of high photocathode illumination. In Figure 1 we show the noise performance of a number of tubes under conditions of photocathode illumination typical of a night sky Cerenkov experiment. The very rapid increase of noise counts with photomultiplier gain noted for the 5" tube (RCA 4522) mitigates against its use although this tube has been extensively used to date. We have selected fast 3" tubes (EMI 9821) as our prime tube when operating in tracking mode.

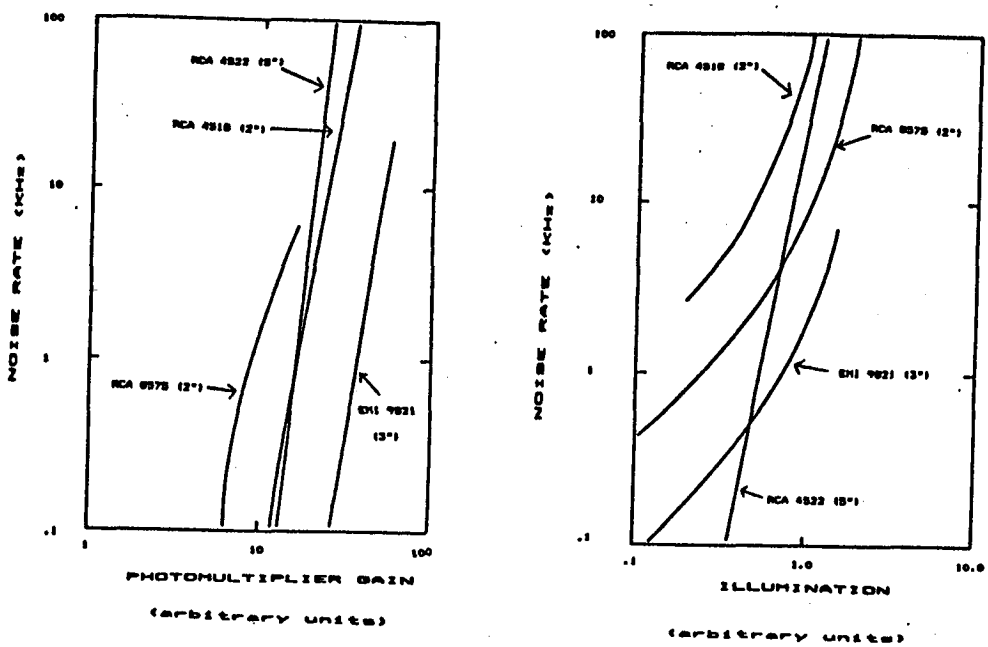

Figure 1. The variation of noise count rate (for a discrimination level typical of our experimental conditions) with phototube gain for constant illumination (a) and illumination level for constant gain (b) for a number of fast photomultipliers. In Fig. 1(b), the RCA 4522 is run at a lower gain than the other tubes.

Our experience with the Mark II telescope and our calculations of Cerenkov emission by gamma-ray showers [3] lead to a best choice of 1.35 degrees for the opening angle of the new telescope. With 3" diameter photomultipliers, this implies a mirror focal length of 2.5 m and an f-number of ~1 for our deployed area. Scaling from the count rates achieved with the Mark I and II telescopes and using our measurements of phototube characteristics leads to an estimation of a counting rate of >200 per minute per phototube pair with a single telescope. This should enable sources of comparable strength to those already established to be detected at the 3σ level in one night's observing time. In addition a useful search for unknown periodicity in e.g. Cygnus X-3 would become feasible.

3.ELECTRONICS

With 15 channels of analogue information to be recorded when operating in survey mode (and the possibility of increasing to ~40 at a later date), the use of CAMAC with its high channel density and high speed as the data recording standard becomes neccessary. Each PMT signal is amplified and discriminated, and fast concidences between the signals from the two mirror units are generated. On each coincidence, the pulse heights are digitized using a fast ADC, and the time of occurrence of the event is recorded. The heart of the data logging system is a purpose built MC 68000-based microprocessor system. In order to have a system dead-time of less than 0.5 ms to avoid possible data loss, it is neccessary to employ a true 16-bit processor to run the CAMAC bus as close to its maximum rate as possible. Total dead-time with this system is 0.3 ms per event.

The data from each event, along with house-keeping information every minute is recorded on a 3M cartridge drive system with a capacity of 68 Mbyte per tape. We have incorporated a system of recording minimum information (event time only) for events occurring within the system dead time to enable recording of very intense short term bursts of events.

We control the telescope with six microcomputers running on a local area network and communicating with the 68000 data logger. One of these computers is responsible for the steering of the telescope, a second acts as master controller for the experiment and the others are responsible for analysing and displaying the status of the experiment on a continuous basis.

ACKNOWLEDGEMENTS

We are grateful to the Science and Engineering Research Council for funding this work, Durham University Microprocessor Centre for the design and construction of the data logging computer, and the staff of the Workshops in the Department of Physics for the construction of the telescope.

REFERENCES

(1) Gibson A.I. et al, (1982), Nature, 296,833.
(2) Dowthwaite, J.C. et al (1985), submitted to Astron. Astrophys. (1985).
(3) Macrae, H. and K.E.Turver (1982) unpublished.

A New Ultra High Energy Gamma Ray Telescope at Ōhya Mine

Aoki T., Higashi S.[o], Kamiya Y.[n], Kitamura T., Matsuno S., Mizutani K.[s], Mitsui K., Muraki Y., Okada A., Ohashi Y., Sato T.[o], Suwada T.[o], Shibata S.[n], and Takahashi T.[o]

Inst. for Cosmic Rays, Univ. of Tokyo, Tanashi, Tokyo
o) Dep. of Physics, Osaka City Univ., Sumiyoshi, Osaka
n) Dep. of Physics, Nagoya Univ., Chikusa, Nagoya
s) Dep. of Physics, Saitama Univ., Urawa

1. Introduction

Search for the ultra high energy gamma rays coming from point sources is one of the main experimental aims of Ōhya project (Fig. 1)[1]. A fast air shower timing system has been constructed at ICRR for the study of the angular resolution of the system and operated approximately half a year. This paper describes the characteristics of the surface array of Ohya "air shower telescope".

2. Detail of the System

The array of the 24 channel scintillation counters situated at the campus of ICRR (Tanashi, Tokyo) is shown in Fig. 2. Each scintillator has an area of 0.25 m^2 and a thickness of 5 cm. The scintillation light is observed by the phtomultipliers located at 50 cm above the scintillator. Photomultipliers HAMAMATSU H1161 (R329) are used under a typical high voltage condition $\sim$1.4 KV. The output signal from the photomultiplier is sent to the preamplifire Le Croy 612A (gain x 10) via 100 m cable (71B/U). The output pulse height for the single particle is $\sim$30 mV and is discriminated by Le Croy 623B. The discriminator out-put signal is then sent to a coincidence circuit 380A. The delay time of the signal from the input of the preamplifire to the out-put of the coincidence circuit is 35 ns.

The out-put of the coincidence circuit is used for the start signal of the TDC 2228A. Meanwhile one of the out-

put signals of each discriminator is delayed by 20 m cable and is used for the stop signal of the time digitizer. The start pulse arrives ∿15 ns before the stop signal. The time digitizer has a time resolution of 250 ps. The pulse height distribution is also recorded by ADC 2249W. The circuit diagram is shown in Fig. 3.

The liniarity of the phtomultiplier out-put and the time jittering was investigated by the photo-diode. As shown in Fig. 4, in the 3 decades of the pulse height range (from 3 mV to 3 V), the linearity is seen. Typical time jittering of the photomultiplier is given in Fig. 5. For the number of particles $N_e \geq 10$, time jittering becomes ∿1ns (catalogue value is 0.9 ns). The jittering of the electronics is less than 250 ps.

3. Angular Resolution of the Telescope

The trigger pulse is created when the air shower hits more than any 6 scintillation counters. The number of the fired scintillator is presented by the histogram of Fig. 6. The dotted line represents the data in which(digitizer)point deviates less than 3 standard deviation from the least-square fitting plane.

The air shower front is simply approximated by a plane: $Z = a X + b Y + C$. For the vertical shower a and b take zero : a=b=0. The shower with zenith angle less than 15° is only used for the present data analysis. The plane determined by the least-square fitting is obtained by :

Define $\chi^2 = \frac{1}{\sigma^2}\Sigma(Z_i - aX_i - bY_i - c)^2$ and differentiate χ^2 by a,b,c. Then we get:

$$\Sigma X_i Z_i = a\cdot\Sigma X_i^2 + b\cdot\Sigma X_i Y_i + c\cdot\Sigma X_i$$
$$\Sigma Y_i Z_i = a\cdot\Sigma X_i Y_i + b\cdot\Sigma Y_i^2 + c\cdot\Sigma Y_i$$
$$\Sigma Z_i = a\cdot\Sigma X_i + b\cdot\Sigma Y_i + c\cdot N \ .$$

Parameters a,b and c are determined by

$$a = |A|/\Delta \ , \quad b = |B|/\Delta \ , \quad c = |C|/\Delta \quad \text{and} \quad \Delta = \begin{vmatrix} \Sigma X_i^2 & \Sigma X_i Y_i & \Sigma X_i \\ \Sigma X_i Y_i & \Sigma Y_i^2 & \Sigma Y_i \\ \Sigma X_i & \Sigma Y_i & N \end{vmatrix} .$$

The statistical deviations in a,b and c σ_a , σ_b, and σ_c are given by

$\sigma_a^2 = \sigma^2[N\Sigma Y_i^2 - (\Sigma Y_i)^2]/\Delta$, $\sigma_b^2 = \sigma^2[N\Sigma x_i^2 - (\Sigma X_i)^2]/\Delta$.

The angular resolution of the system $\sqrt{\sigma_\theta^2}$ is defined by $\sqrt{\sigma_a^2 + \sigma_b^2}$.

Fig. 7 indicates the distribution of $\Delta Z_i = Z_i - (aX_i + bY_i + c)$ from the least-square fitting for the data of each scintillator. Fig. 7 shows the fluctuation of shower front σ_z is ± 2.5 m.

Figs. 8 and 9 represent the distribution of the angular resolution σ_θ of each shower. Each curve shows when we take the data with $Z_i \geq 3$, 5 , and the number of total fired scintillators is greater than $\geq$ 6, 10, 15 respectively. From these figures we conclude that our telescope has an angular resolution of 0.5° (at 1σ).

It is interesting to compare present result with the former measurement by Kiel group[2] with the use of 1 m^2 scntillators. Their data show on the angular resolution 1°. The data analysis is still continuing for the direction of the Cyg. X-3. The data will be presented at the conference.

References

1) Ōhya group : This conference proceeding, HE 5.1-7.
2) Kiel group : Proceed. of 12th ICRC,3,1038(1971).

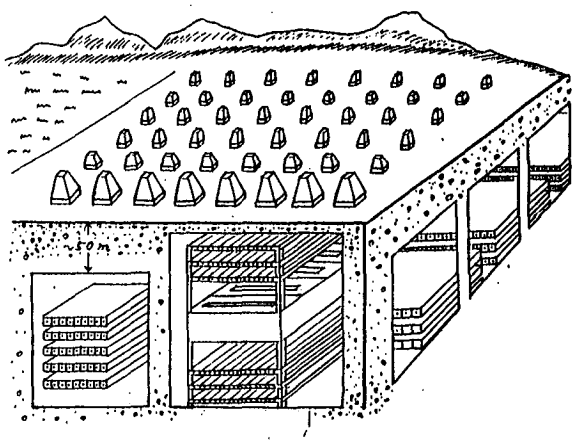

Fig. 1

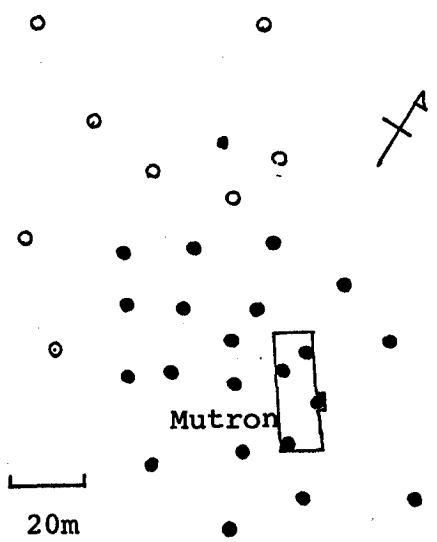

Fig. 2

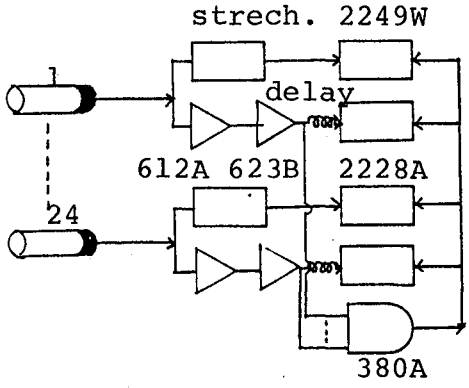

Fig. 3

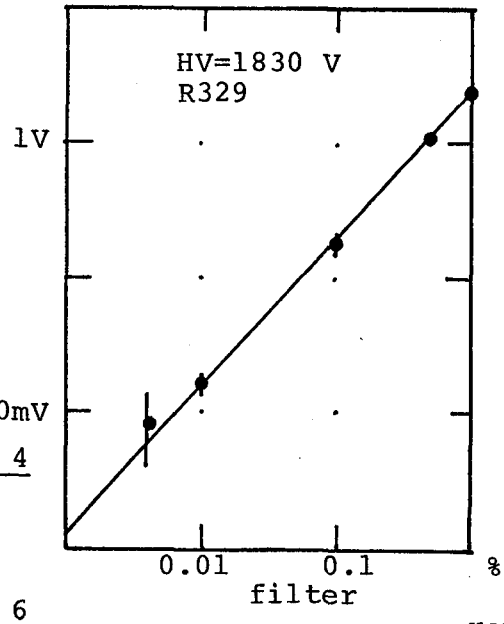

Fig. 4

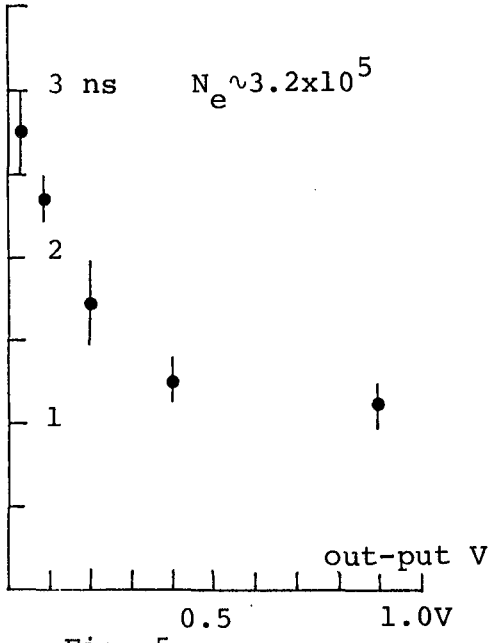

Fig. 5

Fig. 6

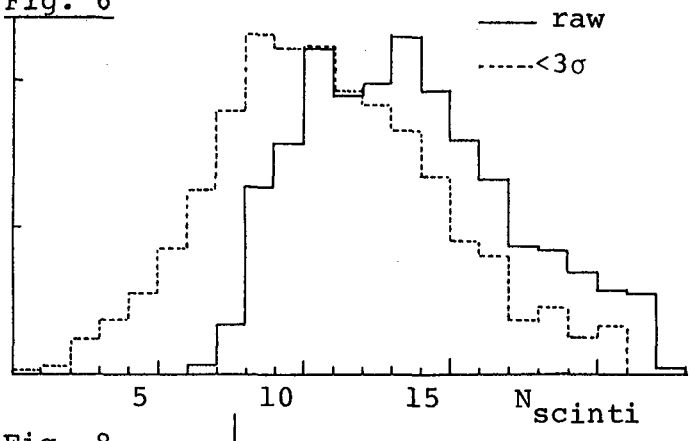

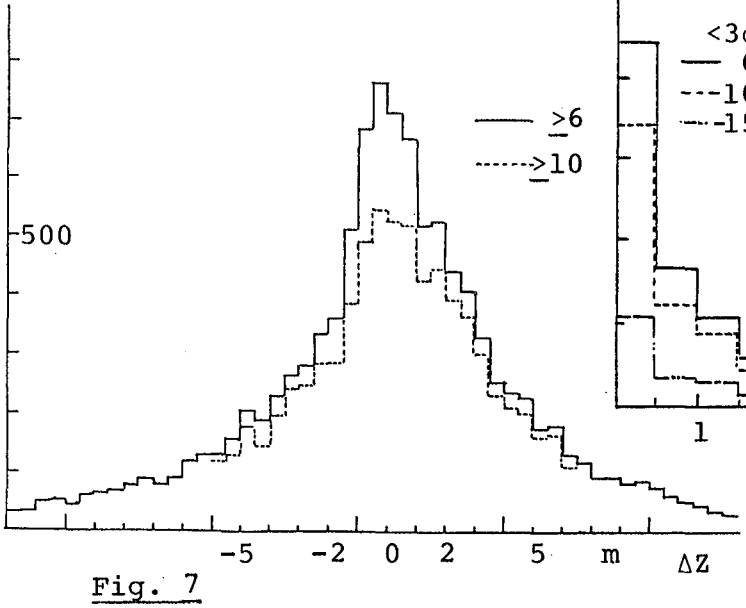

Fig. 7

Fig. 8

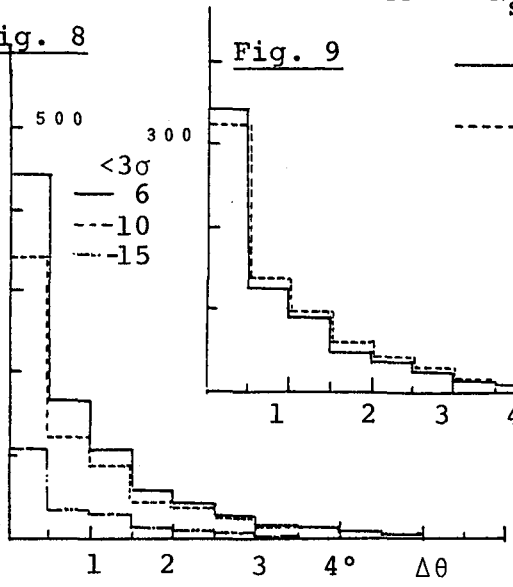

Fig. 9

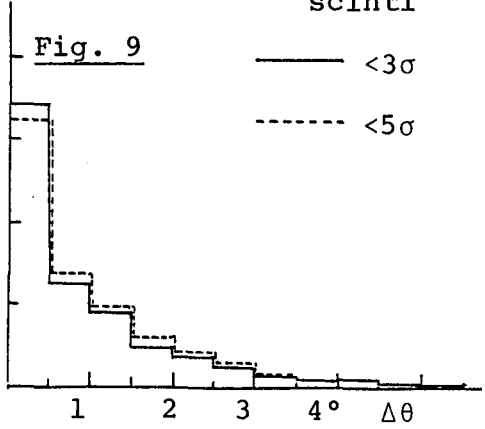

THE BUCKLAND PARK AIR SHOWER ARRAY

R.W. Clay, C.L. Corani, J.R. Patterson, B.R. Dawson, P.G. Edwards, A.G. Gregory, J.R. Prescott, S.D. Elton, and D. Ciampa.

Physics Department, University of Adelaide, Adelaide, South Australia. 5000.

ABSTRACT

The new Buckland Park Air Shower Array has been producing analysed shower data since July 1984. The array is described and some preliminary performance figures are presented.

1. Introduction. The Buckland Park array has recently been upgraded with the addition of new scintillators with the result that its shower size response has been extended to ~ 10^4 particles at threshold. The array now detects events at a mean rate of ~ 1/10s. The main purposes of the new array are to continue the study of point sources of ultra high energy gamma rays[1,2] in the southern hemisphere and the properties of cosmic ray air showers with sizes less than 10^5 particles.

2. Array Description. The design considerations and predictions are given in ref. 4. Briefly, the major considerations in optimizing the rates of detection of small air showers were the need to increase the ground area covered by closely-spaced detectors and to increase the individual detector areas so as to minimize sampling fluctuations.

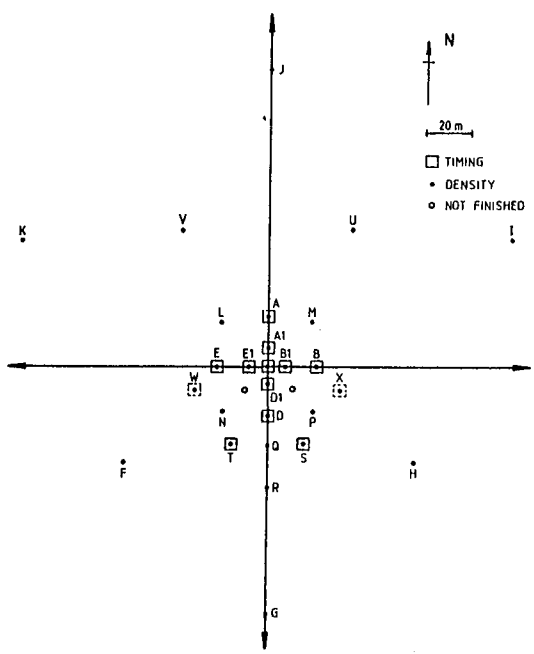

Fig. 1 Array layout

The array consists of 27 scintillators arranged as shown in figure 1. New scintillators have been added to the old array[3] to increase the density of detectors near the centre where eight detectors A1, B1, C, D1, E1, D, S and T have also been increased in size from 1 m^2 to 2.25 m^2.

The detectors are scintillators of 50 mm thickness housed in pyramidal enclosures[4] which are then housed in thermally insulated galvanised iron huts. All detectors contain a particle density measuring photomultiplier (RCA 8055 general purpose 120 mm tube or

equivalent) which feeds a pre-amplifier at the detector before signal transmission to the central laboratory. Saturation occurs at ~ 300 particle level Eleven of the detectors have, in addition, a fast timing photo-multiplier (Philips XP2040) which directly drives 50 ohm cable (RG8) to the central laboratory. Fast timing detectors were added at sites S and T to enable directions to be found for small showers falling nearby and to improve the angular accuracy in the north-south plane for medium and larger showers falling near the centre. Two further slow detectors will soon be added as indicated in figure 1 and fast timing introduced in X and W detectors to improve directional measurement of showers in the east-west plane.

An event is recognized when any two of the 19 inner amplitude measuring detectors trigger at the threshold of 2 particles, (each of which has an individual rate ~ 0.5 Hz) and any two of the fast timing detectors also trigger. (Their individual rates are ~ 100Hz). The slow system thresholds are set well above those in the fast system to ensure that, in most cases, the fast detectors trigger as closely as possible to the start of the photomultiplier pulse and reduce timing uncertainties associated with the fast system rise time (σ_t ~ 5ns). A further result is that except for the smallest of showers, there are normally many more than two fast detectors triggered and directions can be found with timing redundancy. The final trigger rate is ~ 8000 events day^{-1}.

The density measuring channels have final pulse shapes which are quite long (rise ~ 100ns, fall ~ 5μs) and these pulses are fed to CAMAC Peak-sensing ADCs (LeCroy 2259A) which are gated by the array trigger. The array data is calibrated and partly analyzed (for angles of incidence) by a Nova mini-computer system. Output is presently recorded on magnetic tape for later analysis and one 2400 foot tape lasts about five days. The resolved single particle peaks of all detectors are monitored regularly, normally when each tape is changed.

The relative times of arrival of the fast timing pulses are measured with ~ 1 ns bit resolution using a CAMAC Time to Digital Convertor (LeCroy 2228A). Our previous practice had been to start the TDC off using a discriminator output from the central detector, the others being delayed a fixed amount to act as stops. With our more loose coincidence system we now do not specify any particular fast channel to be the TDC start channel. Instead the fast coincidence output triggers the TDC start. In order to ensure that all pulses will be within the range of the TDC, there is a further monostable delay of ~ 200 ns in each channel after the discriminator and before the TDC stop. These delays appear to be inherently quite stable and do not suffer from any bandwidth limitations of delay cable.

Any combination of fast timing detectors may trigger on a given event. We need to find one timing detector which has been triggered and calculate all usable (non-collinear) time differences after subtraction of the known delays. It is then straightforward to calculate the zenith and azimuth angles for the shower axis. At the same time, right ascension, declination and Julian time are calculated for the event. The chi-square fitting parameter for a planar shower front is consistent

with a directional accuracy ~ 2.5/cos θ degrees where most detectors are triggered. The worst cases will be for small showers triggering only our inner 2.25 m^2 detectors. In these cases, we have a detector spacing of only 8m and directions are expected to have uncertainties $\gtrsim 10°$.

3 Preliminary Results. The array detects showers with analysed sizes down to 10^4 particles and with our present preliminary shower analysis we have a median shower size ~ 0.9×10^5 particles. Figure 2 shows a preliminary graph of the size distribution for analysed showers over the whole array and compares it to the performance of the old array. We are beginning to develop our directional analysis system and Table 1 shows a sky map with the accumulation of events for several sidereal days in which only showers with at least five measured times are used. The map shows the extent of sky coverage available from Buckland Park.

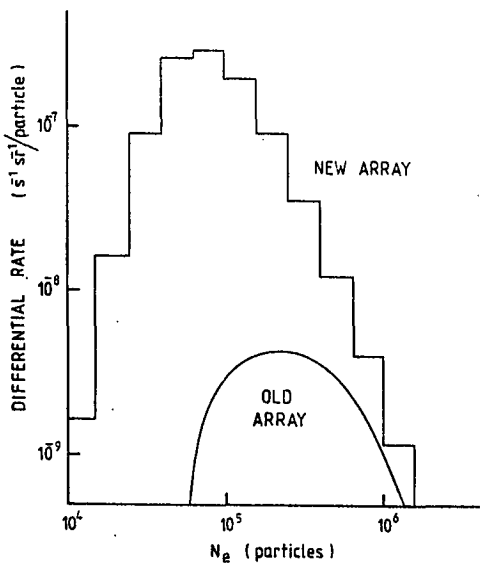

Fig. 2 Size Distribution for all events accepted by whole array. The events are analysed using the NKG function and MINUIT[5] program package.

References

1. Protheroe, R.J., Clay, R.W. and Gerhardy, P.R., 1984, Ap. J. (Lett.) 280, L47.
2. Protheroe, R.J. and Clay, R.W., (1985) Nature (in the press)
3. Crouch, P.C., Gerhardy, P.R., Patterson, J.R., Clay, R.W. and Gregory, A.G. (1981) Nucl. Inst. Meth., 179, 467.
4. Clay, R.W., Corani, C.L., Dawson, B.R., Gregory, A.G., Patterson, J.R., and Prescott, J.R., (1983) Proc. 18th Int. C.R.C. (Bangalore), 6, 257.
5. James, F. and Roos, M., 1975, Computer Phys. Comm. 10, 343.

0	0	3	5	14	38	43	103	141	187	235	272	257	268	240	197	151	100	66	24	10	7	8	1	0	0	1	1
0.5	0	0	10	16	23	70	109	144	178	231	245	308	237	235	181	152	93	70	33	14	5	3	1	0	0	0	0
1.0	0	2	4	15	29	56	100	136	186	218	270	295	269	256	197	139	102	66	37	26	7	6	2	1	0	0	0
1.5	0	2	4	20	31	67	96	143	203	230	259	265	257	256	199	153	91	61	37	19	9	2	0	1	0	0	0
2.0	0	1	12	8	31	39	102	150	182	239	250	274	255	266	200	137	98	68	24	17	7	4	2	1	0	0	0
2.5	0	3	5	8	26	55	115	153	174	173	253	285	279	237	216	140	113	57	37	18	9	2	0	1	0	0	0
3.0	0	2	5	9	25	68	106	143	177	246	261	272	246	218	205	136	104	57	20	8	0	1	1	1	0	1	0
3.5	0	1	8	16	36	62	87	149	197	237	239	285	250	250	186	143	80	67	25	16	6	2	1	1	0	0	0
4.0	0	1	6	20	36	42	80	144	187	210	258	265	262	259	183	162	99	69	29	13	8	2	0	0	1	0	0
4.5	0	0	5	17	26	50	101	131	194	228	283	248	234	238	184	160	98	53	52	17	8	4	1	0	0	0	0
5.0	1	2	7	18	35	51	95	140	205	253	254	264	294	245	182	156	104	57	29	22	10	3	1	1	0	0	0
5.5	1	4	5	12	25	67	88	141	193	258	246	261	269	229	191	148	88	63	29	14	4	2	1	2	0	0	0
6.0	0	1	2	15	39	48	95	137	210	240	276	291	278	244	181	144	98	59	37	8	11	4	1	0	1	2	0
6.5	0	2	3	14	26	77	81	141	180	254	245	269	258	228	215	145	98	68	27	12	6	1	2	1	0	0	1
7.0	0	3	6	12	39	55	87	153	209	220	272	264	255	258	212	159	84	61	36	13	6	5	1	1	0	0	1
7.5	1	3	3	18	25	50	102	146	198	263	268	261	259	239	191	155	108	54	37	12	8	5	1	0	0	0	0
8.0	0	2	6	16	32	58	102	129	190	249	275	278	248	244	182	158	96	55	30	15	12	1	1	0	0	0	0
8.5	0	1	8	10	28	63	96	119	202	222	274	295	281	230	211	147	100	78	40	18	12	2	1	0	0	1	0
9.0	0	2	2	18	25	65	87	128	192	227	263	265	277	242	216	159	96	63	30	16	6	0	0	2	0	1	0
9.5	0	2	3	18	28	50	100	122	161	228	255	314	266	243	199	145	82	57	29	12	4	5	1	1	0	0	0
10.0	1	3	5	10	34	56	109	159	202	230	263	257	260	250	192	161	94	64	26	12	5	2	0	0	0	0	0
10.5	0	2	4	13	26	57	97	144	191	227	271	282	280	244	213	138	105	52	37	13	3	3	2	1	1	0	0
11.0	0	1	1	18	22	66	106	154	200	225	261	263	280	260	191	148	90	65	48	18	7	3	0	0	1	0	0
11.5	0	5	2	10	29	64	100	146	185	208	260	276	284	265	217	156	98	43	31	14	3	1	0	1	0	0	2
12.0	0	3	3	12	29	46	97	153	174	233	275	249	259	228	194	145	103	41	26	24	5	2	1	0	1	0	0
12.5	0	2	6	13	37	60	92	134	194	238	255	253	308	225	196	178	104	59	25	15	3	4	0	1	0	1	1
13.0	0	2	4	16	30	58	93	144	180	190	269	283	260	218	193	139	106	58	38	17	5	3	2	2	0	0	0
13.5	0	0	4	17	39	45	108	144	192	241	274	288	281	230	199	131	101	52	34	15	7	3	1	0	1	0	0
14.0	0	2	6	12	26	62	74	132	185	229	266	280	272	255	210	134	107	53	28	20	6	3	1	1	0	0	1
14.5	0	2	6	12	24	62	102	151	191	219	244	287	249	246	202	150	92	58	37	16	6	3	1	0	0	1	0
15.0	0	1	2	22	39	58	90	133	207	259	273	264	282	253	210	146	114	64	34	19	3	2	0	0	1	1	0
15.5	0	0	7	15	30	51	104	142	187	205	293	276	262	237	195	144	103	54	31	11	7	6	2	0	0	0	0
16.0	0	1	11	22	29	69	108	139	207	234	233	269	293	246	182	157	100	64	23	18	5	5	3	1	0	0	0
16.5	0	0	5	16	24	55	96	147	205	235	252	267	264	246	199	145	98	80	33	12	1	3	1	0	0	0	0
17.0	0	0	7	10	32	50	103	149	185	231	277	276	254	228	217	167	108	63	36	30	4	3	2	0	1	0	0
17.5	2	3	7	15	24	55	90	133	203	233	282	282	248	237	210	144	98	70	31	18	8	5	1	1	0	0	0
18.0	0	2	4	14	28	63	100	134	176	212	271	263	257	227	180	149	91	68	37	19	3	4	2	0	0	0	0
18.5	0	2	6	8	31	48	93	156	183	226	268	289	280	227	188	154	92	60	35	18	7	1	2	0	0	0	0
19.0	0	2	3	17	36	70	84	136	198	233	237	282	280	253	198	154	107	60	40	15	8	7	0	0	0	0	0
19.5	0	1	7	9	29	63	102	141	180	248	267	279	265	241	200	161	109	65	33	12	6	3	1	0	1	0	0
20.0	1	2	6	12	31	58	96	145	170	216	250	310	291	238	201	141	95	64	22	9	7	2	1	0	0	0	0
20.5	0	2	7	13	24	51	90	129	165	237	249	267	259	249	206	150	110	69	29	14	5	5	2	0	0	0	0
21.0	2	0	6	17	28	53	83	149	193	216	281	279	272	237	197	148	101	59	24	19	5	4	0	0	0	0	0
21.5	1	1	2	14	26	66	105	120	186	233	252	271	251	233	194	161	106	72	37	19	5	4	5	1	0	0	0
22.0	0	3	7	15	31	54	97	147	194	238	280	269	271	221	188	147	113	44	40	22	4	7	0	0	0	1	0
22.5	0	5	7	12	28	61	110	137	188	242	262	269	232	221	219	158	115	57	31	20	4	2	0	1	0	0	0
23.0	2	1	3	19	39	50	108	138	199	212	259	244	289	261	205	145	92	61	28	12	7	2	1	0	0	1	0
23.5	0	1	6	15	27	62	99	125	196	205	248	301	283	247	193	151	104	50	21	18	7	3	2	0	0	0	0
	-90	-85	-80	-75	-70	-65	-60	-55	-50	-45	-40	-35	-30	-25	-20	-15	-10	-5	0	5	10	15	20	25	30	35	40

RIGHT ASCENSION (HOURS)

DECLINATION (DEGREES)

TABLE 1

Sky map showing typical coverage of the southern sky. The median shower size is 0.9×10^5 particles.

AN EAS EXPERIMENT AT MOUNTAIN ALTITUDE FOR THE DETECTION OF GAMMA-RAY SOURCES

O.C. Allkofer, M. Samorski and W. Stamm

Institut für Reine und Angewandte Kernphysik,
University of Kiel, Olshausenstr. 40-60, D-2300 Kiel,
West Germany

ABSTRACT.

The plan of an extensive air shower experiment 2.200 m above sea level for the detection of 10^{14} - 10^{17} eV gamma-rays from sources in the declination band 0° to +60° is described.

I. INTRODUCTION. Gamma-ray emission beyond 10^{14} eV has been reported of the sources Cygnus X-3 (Samorski and Stamm 1983a, 1983b, Lloyd-Evans et al. 1983, Baltrusaitis et al. 1985a, Bhat et al. 1985), Vela X-1 (Protheroe et al. 1984), LMC X-4 (Protheroe and Clay 1985), Hercules X-1 (Baltrusaitis et al. 1985b), and the Crab nebula (Dzikowski et al. 1981, Boone et al. 1984). For gamma-ray astronomy in this energy range new EAS experiments are needed meeting special requirements, as for example an improved angular resolution to allow better discrimination against the background of normal showers and larger effective detection areas especially for the lower energy range of showers to be detected.

The Kiel group plans to set up a new experiment dedicated to the detection of gamma-ray sources in the energy region 10^{14} - 10^{17} eV, to be run at mountain altitude at a site far south from Kiel.

II. SITE OF THE EXPERIMENT. A suitable site for the new experiment seems to be the Astronomical Observatory on top of the Roque de los Muchachos at the Canary island La Palma, where a relatively plane area of 200 x 200 m^2 is available and the electrical power supply requirements are fulfilled. The geographical position is 28.8° north and 17.9° west, at an elevation of 2.200 m above sea level (x = 780 g/cm^2).

At the latitude of this site Cygnus X-3 and Hercules X-1 can be detected under better condition than at Kiel (latitude 54.4°), and in addition three further candidate sources are in the observation field of the experiment, the Crab nebula, Geminga (2 CG 195 + 05) and the 1.5 ms pulsar PSR 1937 + 21, all three known as gamma-ray emitters around 10^{12} eV.

Since showers of same primary energy contain more particles at mountain altitude than at sea level, the energy range at this mountain site can be extended to energies below 10^{15} eV.

III. DETECTOR ARRAY. A plan of the detector array is presented in Fig. 1. In total 56 scintillation counters of 1 m^2 each (scintillators NE 102 A, 5 cm thick) will be distributed over an area of 200 x 200 m^2 and will be equipped with one photomultiplier VALVO XP 2050 each for particle density measurements. In order to cover the large dynamical range required for EAS particle density measurements the signals will be picked up at three different points of successively decreasing gain on the resistor chain of the photomultipliers, giving 3 x 56 = 168

analog informations per shower handled by the same number of analog to digital converters (ADCs).

Fast timing measurements will be performed with the quadratic grid of 6 x 6 scintillation counters in the centre of the array (grid width 10 m). Each of these 36 detectors will be equipped with an additional fast photomultiplier VALVO XP 2041. Since timing modules containing 8 time to digital converters (TDCs) each with common start and individual stops will be used, the 4 x 4 central counters of the 6 x 6 array will provide common start signals for the respective 8 adjacent counters, so that 16 x 8 = 128 time differences will be available for each event. The high redundancy of fast timing channels will ensure reliable operation over long periods.

From the central section of the 6 x 6 counters 25 hard-wired 4-fold coincidences between each 4 adjacent detectors will be formed. Any of the 25 possible 4-fold coincidence signals will trigger the array.

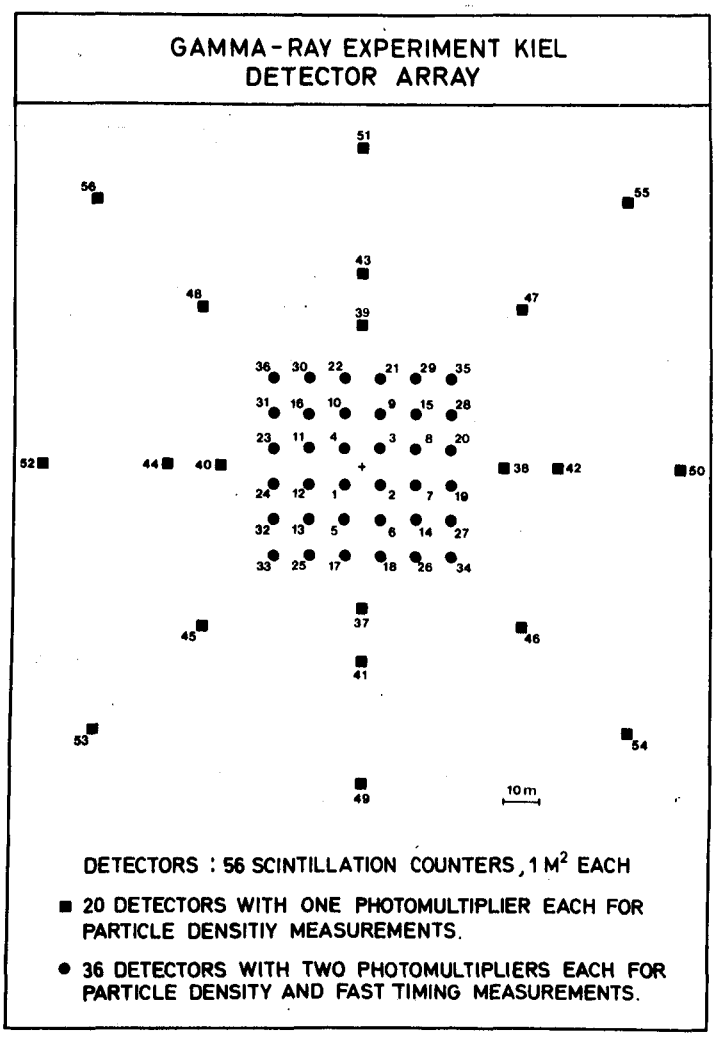

Figure 1. Plan of the EAS detector array for gamma ray observations.

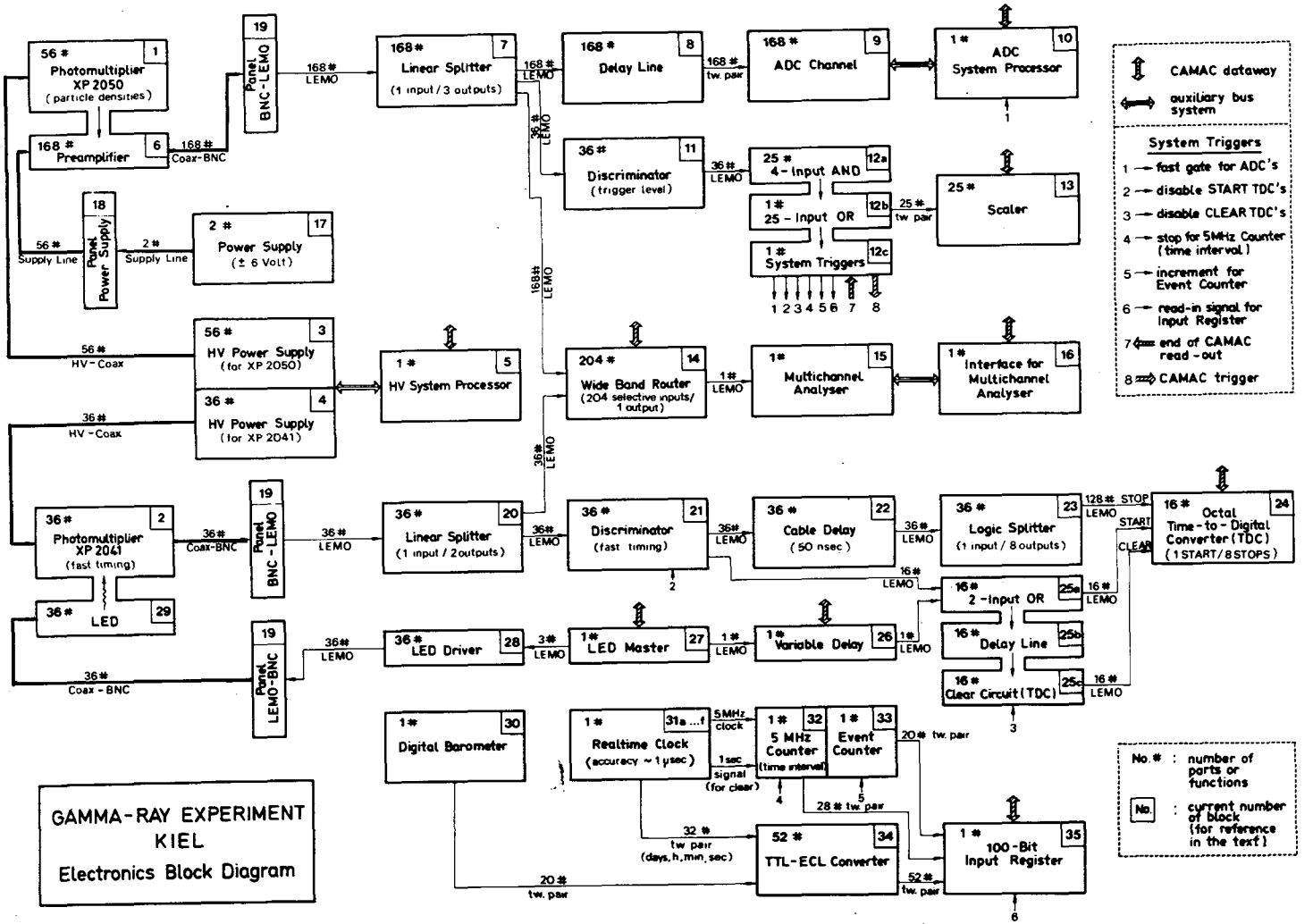

Figure 2. Block diagram of the electronic layout.

According to the relatively small grid width of the detectors in the centre (10 m) and the selected triggering condition all showers of primary energy above 10^{14} eV will be detected, when the core will hit a central area of about 70 x 70 m^2, with an angular resolution of the order of 1 degree at a rate of about 20 events per minute. For primary energies above 10^{15} eV an angular resolution better than 1 degree is expected, at an effective area larger than 100 x 100 m^2.

IV. ELECTRONIC LAYOUT. A detailed block diagram of the electronics is shown in Fig. 2. In all essential parts only reliable commercial micro-electronic systems will be employed. The whole system will be managed and controlled by a PDP 11/24 processor with 256 kB MOS memory and two magnetic disk drives of 28 MB each. The readout and control will be based on standard CAMAC technique. The arrival times of the showers will be determined by means of a high precision real time clock controlled by a Standard Time receiver to allow phase measurements of gamma-rays from pulsars.

Without interrupting or disturbing the air shower measurements the processor will in turn connect via a multiplexer each photomultiplier output to a multichannel analyser, controlling the position of the one-particle-peak and adjusting the PM high voltage, if necessary.

A few times per day the processor will interrupt the measurements at given times for a few seconds for checking the fast timing channels. For this purpose simultaneous test signals will be produced in each fast timing phototube by triggering light emitting diodes (LEDs). By introducing computer regulated time delays between the start and stop signals of all TDCs, the zero point and the linearity of each of the 128 timing channels will be controlled. The various test functions and monitoring of the performance of the experimental equipment will enable a running of the array with a minimum of maintainance.

The authors are gratefully acknowledging the cooperation of Prof. Dr. E. Bagge in the planning phase of this experiment and wish to thank Mr. Ing. K. Sauerland for his engaged support in the electronic design.

REFERENCES.

Baltrusaitis, R.M., et al. 1985a, 1985b, preprints, University of Utah.
Bhat, C.L., et al. 1985, paper submitted to Ap. J. (February 1985).
Boone, J., et al. 1984, Ap. J., 285, 264.
Dzikowski, T., et al. 1981, 17th ICRC (Paris), 1, 8.
Lloyd-Evans, J., et al. 1983, Nature (Letters), 305, 784.
Protheroe, R.J., et al. 1984, Ap. J. (Letters), 280, L47.
Protheroe, R.J., and Clay, R.W. 1985, Nature (Letters), 315, 205.
Samorski, M., and Stamm, W. 1983a, Ap. J. (Letters), 268, L17.
Samorski, M., and Stamm, W. 1983b, 18th ICRC (Bangalore), 1, 135.

AN OBSERVATORY TO STUDY 10^{10} TO 10^{17} EV GAMMA RAYS

Trevor C. Weekes
Whipple Observatory, Harvard-Smithsonian Center
for Astrophysics

Abstract

A facility is described which incorporates many of the best features of existing gamma ray telescopes at a single site. In addition to reducing the flux sensitivity in some energy ranges, it permits the measurement of the energy spectrum over seven decades of energy.

1. Introduction. Ground-based gamma-ray astronomy has matured from a discipline with a small number of detections requiring confirmation to one in which there are several sources that are well-established (Cyg X-3, the Crab, Her X-1) but which now demand more detailed observations before the emission mechanisms can be understood. In at least one source, Cyg X-3, there is some question concerning the nature of the observed particles. All of the sources show evidence for time variability. Since many techniques, whose absolute sensitivities are poorly understood, have been employed and since many of the detections do not have large statistical significance, it is difficult to derive an energy spectrum that can be compared with source models. The energy spectrum in the range 10^{14} - 10^{16} eV is particularly interesting since there is the possibility of detecting the absorption dip caused by pair production on the 3o K microwave background.

A single facility which combines the best features of the many techniques used to cover the energy range from 10^{10} to 10^{18} eV would eliminate the ambiguity arising from the use of different techniques at different epochs. Below we describe in qualitative terms a Very High Energy Gamma Ray Observatory and then list its advantages for each decade of the energy range covered.

2. Physical Description. The observatory will consist of a combination of pointed atmospheric Cherenkov telescopes and all-sky particle detector arrays. It will be located on a mountain plateau at an altitude of about 3.0 km. The array will cover an area of approximately 1.8×10^8 m^2 which must be reasonably flat for ease of construction and access. A central control room will house the recording electronics, the on-line computer, the atomic clocks and the operators.

(a) Atmospheric Cherenkov detectors. This array will consist of a central large reflector (with aperture in the range 15-20m) surrounded by six reflectors of 10m aperture on the corners of a hexagon and at a distance of 75m from the center (figure 1). These atmospheric Cherenkov telescopes will be modeled on the Whipple Observatory 10m

Optical Reflector. Each will be composed of tessellated segments but the f number will be larger to give a greater depth of focus. Variable focal length segments will be used to improve the optical figure and reduce the light path difference across the reflector. The reflectors will be protected by domes to preserve the mirror coatings and also to permit the reflectors to operate as air Cherenkov muon telescopes under cloudy or brightmoon conditions. Each reflector will be equipped as an imaging device with an array of phototubes at its focus. The number and size of phototubes will be chosen so as to have a pixel diameter of 0.25° and a field of view of 3.4° (e.g. 169 tubes of diameter 4 cm). The telescopes will operate in parallel and will track the position of a suspected source.

The particle detector array will consist of $1m^2$ scintillators with fast timing, arranged in a hexagonal 25m grid spacing as shown in figure 2. The inner seven detectors will be clusters of five scintillators; the total number of scintillators will be 65. When any three adjacent detectors exceed a two particle level, a readout command will be generated. The read out will include the pulse size, the relative time of arrival at each detector and the absolute time.

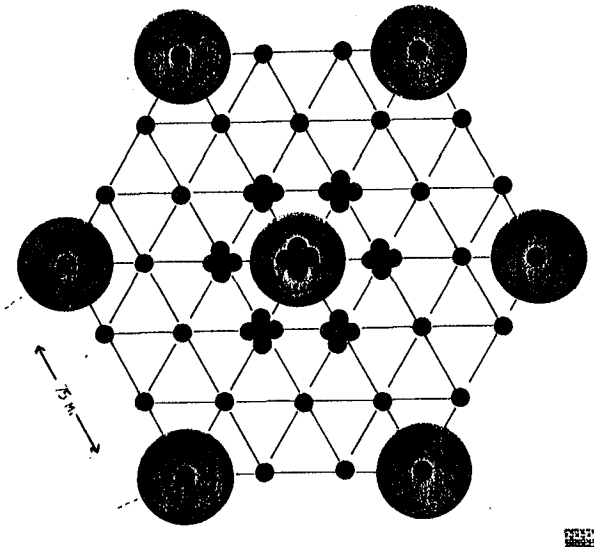

Figure 1. Seven large reflectors with spacing of 75 m.

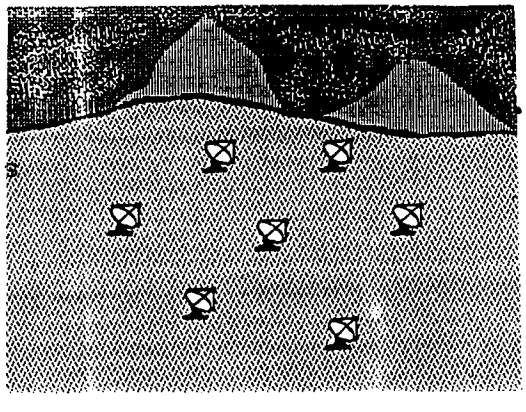

Figure 2. Layout of full array. Large circles are large reflectors; small circles are scintillators. Grid spacing is 25m.

3. Operating Mode. The facility will actually consist of five separate gamma-ray telescopes, which will operate in overlapping energy ranges with the advantage that cross-calibration will be straightforward. The ranges covered are shown in figure 3 and the telescopes are described below.

(a) Low energy atmospheric Cherenkov telescope; (LEACT) in this mode the central light detector will be operated in coincidence with one or more of the outer light detectors at a very low threshold to detect the minimum energy gamma-ray showers. Using fast electronics, small pixels and large mirror areas, it will be possible to achieve an energy threshold close to 10 GeV. This will have two important advantages: (a) it will overlap with the upper end of the coverage available with EGRET on the GRO (b) it opens up a new, and previously unexplored, region of the electromagnetic spectrum in which the background contributions from Cherenkov light deficient proton-initiated air showers will be small (Turver and Weekes, 1978). The light levels will be too low for energies below 100 GeV to permit full use to be made of the imaging technique but the reduced proton background will compensate for the loss of angular resolution.

(b) Imaging Telescope (IT); this will operate on the same principle as the existing telescope at the Whipple Observatory in the energy range 10^{11} to 10^{13} eV. However each shower will be seen by at least three telescopes so that both the angular resolution and collection area will be improved: a factor of ten improvement in minimum flux sensitivity is estimated. Recent Monte Carlo simulations (Hillas, this conference OG 9.5-3) indicate that, for showers that are well sampled, it will be possible to differentiate the primary (electromagnetic or hadronic). High energy (10^{13} - 10^{14} eV) events will saturate the central pixels but their shapes and energies can be determined from the outer pixels.

(c) Wide angle Cherenkov detector (WACD); the centroid of the Cherenkov light image for a gamma ray initiated shower of primary energy 10^{12} eV, with impact parameter 100m from the detector axis, falls 1^{o} from the center of the field. The lateral distribution of Cherenkov light falls off beyond 100m. However a sensitive detector will have a large collection area for showers of energy 10^{13} eV whose impact parameters are in the range 100-250m; the centroid of their light distribution will fall in the ring of phototubes 1.5^{o} from the axis. By triggering on signals in the outer pixels of the adjacent detectors the collection area for air showers is in the range 10^{13} to 10^{15} eV will be $\sim 10^{5}$ m^2. This large collection area (a hundred times greater than a small particle array detector) will compensate for the small duty cycle (<10%) of the atmospheric Cherenkov detector.

(d) Gas Cherenkov Muon Telescope (GCMT); the small duty cycle of the atmospheric detectors can be increased by

having the reflectors housed in light-tight domes (which can be opened for night-sky use). Under dark conditions, the imaging reflectors can easily detect the Cherenkov light ring from single particles (muons) within the dome. If the dome is large enough to permit the reflectors to track sidereally, then sources can be tracked under cloudy or moonlit conditions (or even during the day if the dome is sufficiently light-tight). The collection area for muons is essentially that of the optical collector $75m^2$ This mode would only be justified if it is shown that the directional anisotropies detected in the direction of Cygnus X-3 result from showers with a high component of muons (Samorski and Stamm (1983); Marshak et al. (1985)).

(e) Particle Air Shower Array (PASA); at mountain altitude this conventional array of particle detectors will have an energy threshold close to 10^{14} eV and a high energy cut-off dictated by exposure time and flux levels. Using state-of-the-art fast phototubes and electronics, the angular resolutions will be $\sim 1^{o}$. There will be considerable overlap with the atmospheric Cherenkov detectors although the particle array will act as an all-sky monitor and the light-detectors will track specific sources.

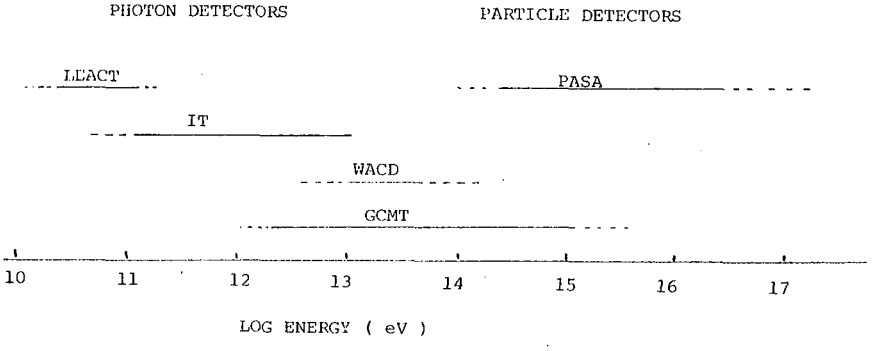

Figure 3. Distribution with energy.

4. Discussion. The facility described above involves no new technology; rather it requires a duplication and concentration of existing telescopes at an optimum site. It also requires an investment on a scale not normally associated with ground-based cosmic ray experiments.

References.

Marshak, M.L., et al. (1985), preprint.
Samorski, M., Stamm, W., (1983), 18th ICRC. 11, 244.
Turver, K.E., Weekes, T.C. (1978), Nouvo Cimento. 45B, 99.

A NEW ARRAY FOR THE STUDY OF ULTRA HIGH ENERGY GAMMA-RAY SOURCES

Brooke G, Lambert A, Ogden P A, Patel M, Perrett J C,
Reid R J O, Watson A A and West A A.

Physics Department, University of Leeds, Leeds LS2 9JT, UK.

ABSTRACT

This paper describes the design and operation of a $32 \times 1\,m^2$ array of scintillation detectors for the detection of 10^{15} eV cosmic rays with an expected angular resolution of $<1^o$, thus improving the present signal/background ratio for γ-ray sources. Data are recorded on a hybrid CAMAC and 'in-house' system which uses a laser and Pockel-Cell arrangement to routinely calibrate the timing stability of the detectors.

1. Introduction. The charged nature of the majority of cosmic ray primaries means that it is not possible to identify their source regions from measurements of the direction of the shower axis and thus most air shower groups have settled for a directional resolution of $\lesssim 5^o$ which is adequate for estimation of primary energy. With the recent discovery of pulsed gamma-rays from Cygnus X-3 (Samorski and Stamm 1983, Lloyd-Evans et al 1983), possible only because of its known periodicity, precise angular resolution assumes a new significance. It is to be expected that other sources, less luminous than Cygnus X-3, will be detected when arrays of enhanced sensitivity have been developed; improvement of angular resolution will be one of the key factors here and is especially important as some of the other signatures of the neutral primaries have now been questioned (Marshak et al 1985).

The array now under construction at Haverah Park, GREX, has been designed to trigger on showers with a shower size $N > 10^4$ particles; the full array becoming sensitive at $\sim 3 \times 10^4$.

2. The detector. A Philips 2312B photomultiplier tube (PMT) with a risetime of 2.5 ns and a gain of 3×10^7 at 2 kV, looks up at a $1\,m^2 \times 10$ cm block of NE102 plastic scintillator (Figure 1). The inside of the detector box is painted black to minimize the amount of reflected light reaching the PMT , thus improving the light pulse risetime. This is at the cost of a reduction in the amount of light reaching the tube. We do however use a sheet of aluminized foil above the scintillator to add substantially to the light yield without materially affecting the risetime. With this arrangement a single vertical particle passing through the scintillator produces > 50 photoelectrons in the PMT.

3. Description of the array. The array consists of 32 detectors of $1\,m^2 \times 10$ cm NE102 plastic scintillator positioned on 30 and 50 m grids (Figure 2). The centre of the array is coincident with the 50, 150 and 500 water-Cerenkov array run at Haverah Park by the Leeds University group. Signals from the anode of the photomultiplier (PMT) are transmitted along high bandwidth cable (Aerialite 363) to the recording electronics situated at the centre of the array. The array records a shower coincidence when any three detectors trigger at $> 1\,m^{-2}$ inside a 1 μs window. Fast timing, for arrival direction, is started at 1/3

particle per detector. The contours of log(N) in Figure 2 show the sensitivity of the array to showers of different sizes.

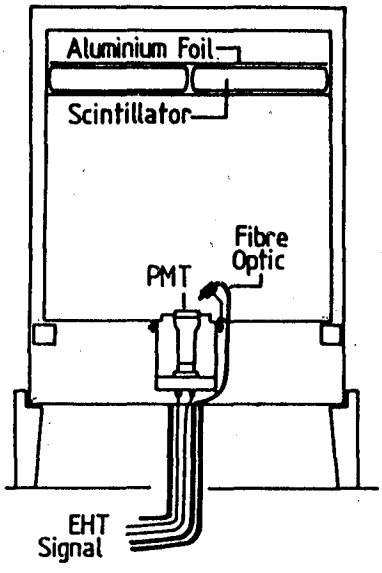

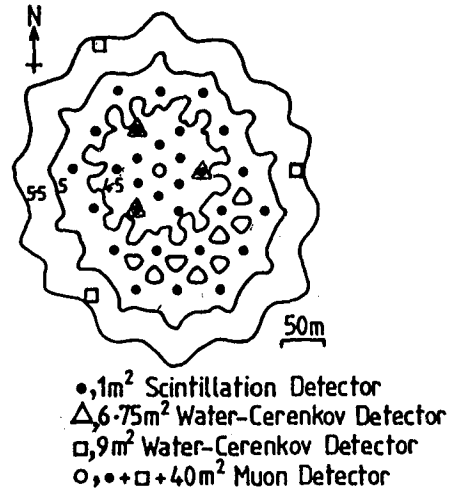

Figure 1: The GREX scintillation detector showing the arrangement of the PMT, scintillator and Fibre Optic cable.

Figure 2: Disposition of the GREX scintillation detectors in relation to the 50 and 150 m water-Cerenkov detectors and the 40 m^2 muon detector. The contours show the sensitive area of the array to showers of log(N) > 4.5, 5.0 and 5.5.

The GREX array transmits event triggers to various external arrays:- Nottingham University's 40 m^2 detector and the 50 and 150 m water-Cerenkov arrays. Every two hours a Timing Stability Pulse (TSP) is applied to monitor the gain and timing stability of the detectors. Figure 3 shows the set-up that is used to do this. The output from a 2 mW HeNe laser is modulated by a Pöckel-cell driven by an externally triggered step generator. The resulting light pulse has a 10 ns FWHM with a 1.5 ns rise-time. This is transmitted to all the detectors via 50/125 graded index fibre optic cable. The detectors trigger on this light pulse and the resulting signals are treated just as if a 32 fold coincidence was recorded.

The GREX system will be capable of supervising 32 detectors each working at a D1 trigger rate of 200 - 300 s^{-1} with only $\sim$1 - 3% deadtime (allowing 2 µs deadtime per background pulse). When the full system is in operation the main contribution to deadtime will be the event processing time or to be more precise the readout time via the slow, but cheap, CAMAC/GPIB interface. The readout time is very software-dependent and for that reason the code will be written in the C-language. The GPIB interfaces to an S100 based machine (North Star Horizon microcomputer) via an IEEE - S100 interface. GREX data will be merged with data from the 50 and 150 m water-Cerenkov arrays and then recorded on magnetic tape. The expected recording rate is $\sim$16 Mb of data per week corresponding to

$\sim$ 10 events min^{-1}. To help merge GREX data with muon data from the Nottingham University group the event time ($\pm$ 1 ms) will be transmitted to their recording system after every event.

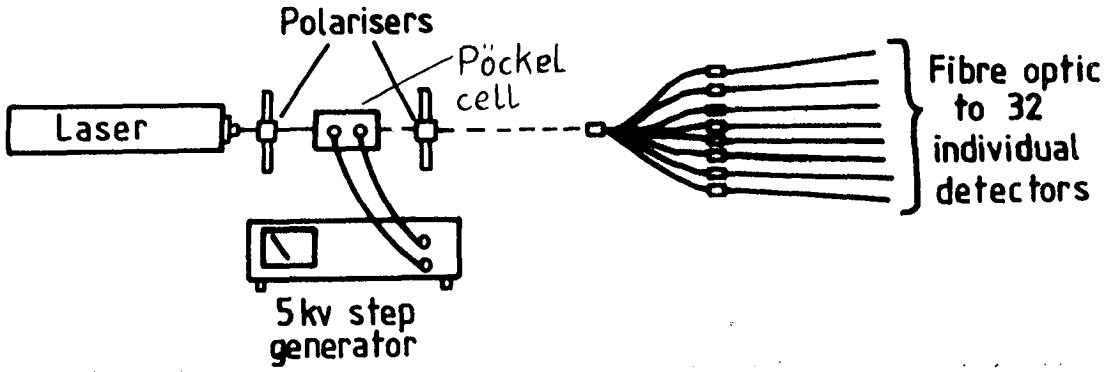

Figure 3: The timing calibration set-up. The Pöckel-cell chops a 10 ns wide light pulse with 1.5 ns risetime. The resulting light pulse is transmitted to all 32 detectors.

4. Recording electronics. The recording electronics in the new Haverah Park gamma-ray experiment, GREX, is a hybrid of commercial LeCroy modules (CAMAC based) and 'in-house' electronics. Figure 4 shows how the various systems are integrated. Signals from the detectors are transmitted to a discriminator board which incorporates the LeCroy MVL407 (quad ultrafast voltage comparator). The signal is split three ways:- one is integrated and input to a LeCroy ADC (4300), while the others are input into two quarters of the MVL407, referred to as the D1 and the D2 discriminators. If the D1 discriminator, set at $\sim$ 1/3 particle threshold, triggers, and if the D1 gate is open the LeCroy TDC (4208) connected to that channel starts counting at 1 GHz. The low D1 threshold is used to keep timing fluctuations to a minimum. If the D2 discriminator triggers, (threshold > 1 m^{-2}) a 1 µs coincidence window pulse is produced. If the D2 gate is open then the coincidence window pulse is transmitted to the majority logic board.

The majority logic board adds all the coincidence window pulses from the 32 possible D2 discriminators and then discriminates at three times the D2 level giving the 3-fold coincidence and producing a majority logic output pulse. This pulse is transmitted to the coincidence logic board and the event time board which latches the event time to a resolution of 1 ms.

When any TDC triggers the ADC input gate is opened and a fast clear pulse is generated after a 1 µs delay. The fast clear pulse will be 'gated out' if a coincidence is recorded by the majority logic board. If there has not been an event within 1 µs of the first TDC triggering then the fast clear pulse is allowed to clear the 4 TCDs and 2 ADCs. It takes 1 µs to clear all the LeCroy modules; thus there will be 2 µs deadtime per background pulse from any of the 32 detectors.

When a shower coincidence is recorded within 1 µs after the first TDC has triggered (time allowed for the shower to traverse the array) a common pulse is sent to all TDCs. At the end of the 1 µs the CAMAC 'look at me'

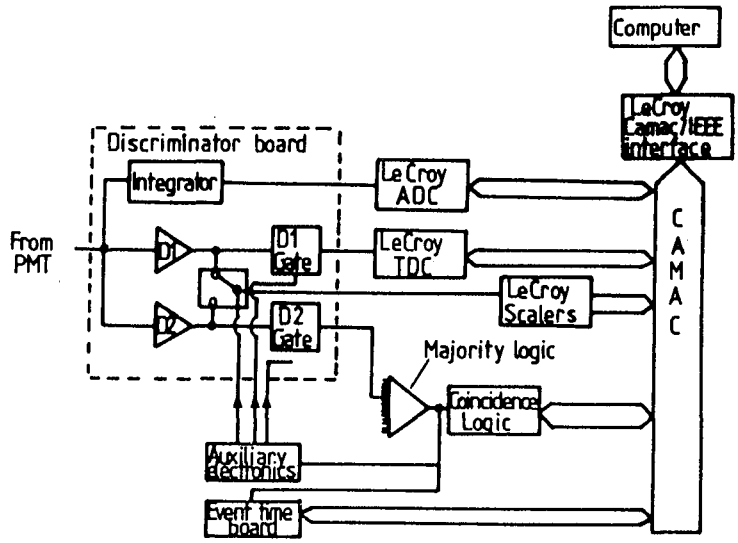

Figure 4: Schematic block diagram of the GREX recording electronics. The ADC, TDC, scalers and the GPIB interface are commercial LeCroy modules. The remaining electronics were built 'in-house'.

(LAM) flag is set. The TDCs are capable of recording positive and negative times, i.e. when a TDC triggers before or after the common start/stop pulse. In our system the three detectors that formed the coincidence will have negative times and the remaining detectors which have recorded particles associated with the shower will have positive times. The relative arrival times are recorded to a resolution of 1 ns. The LAM flag is tested by the controlling computer and when detected instructs the 8901 GPIB-CAMAC crate controller to read the data from all the LeCroy modules, event time-board, digital thermometer and barometer. When the event has been processed the TDCs, ADCs and auxiliary electronics are reset; thus the whole system becomes active at the same time.

5. Auxiliary functions. Fast clear pulses are generated on every background pulse, i.e. every time D1 triggers and thus a single noisy detector could result in a large deadtime. Monitoring of detector performance is achieved by recording the D1 and D2 rates. This is achieved with extra electronics, referred to as the auxiliary electronics in Figure 4, which switches the input to the LeCroy scalers (4434) alternately between D1 and D2 pulses. If a detector should become 'noisy' then its contribution to the system can be negated by closing the D1 and D2 gates.

Acknowledgements. We would like to thank the Science and Engineering Research Council for their continued support.

References

†A Lambert and J Lloyd-Evans - this conference, OG-9.5-2.
J Lloyd-Evans et al 1983 Nature 305, 784.
M L Marshak et al 1985 Phys Rev Lett 54, 2079.
M Samorski and N Stamm 1983 Ap J Lett 268, L17.

Akeno 20km^2 Air Shower Array (Akeno Branch)

M.Teshima*, H.Ohoka, Y.Matsubara*, T.Hara, Y.Hatano, N.Hayashida, C.X.He**, M.Honda, F.Ishikawa, K.Kamata, T.Kifune, M.Mori*, M.Nagano, K.Nishijima***, Y.Ohno and G.Tanahashi

Institute for Cosmic Ray Research, University of Tokyo, Tokyo, 188 Japan
*Department of Physics, Kyoto University, Kyoto, 606 Japan
**Institute of High Energy Physics, Academia Sinica, Beijing, China
***The Graduate School of Science and Technology,Kobe University,Kobe,657

As the first stage of the future huge array we have expanded the Akeno air shower array to about 20km^2 by adding 19 scintillation detectors of 2.25m^2 area outside the present 1km^2 Akeno array with a new data collection system. These detectors are spaced about 1km from each other and connected by two optical fiber cables. This array has been in partial operation from 8th, Sep. 1984 and full operation from 20th, Dec. 1984. 20m^2 muon stations are planned to be set with 2km separation and one of them is now under construction.

1. Introduction

The origin of the highest energy cosmic rays is an interesting problem. We have a chance to connect their sources with the astronomical objects, because their propagation becomes simpler than that of lower energies and the possible sources may be limited to some kinds of active astronomical objects. The observation of giant air shower (GAS) produced by cosmic rays above 10^{19} eV have been made at Volcano Ranch[1], Haverah Park[2], Narabrai[3] and Yakutsuk[4]. But there still remain the discrepancies among experiments not only in their energy spectrum but also in their arrival direction distribution.

In order to clarify the present ambiguities on the experiments and to extend the observation to higher energy, a plan of huge surface array of area over 100km^2 is currently under discussion in Japan. In this report we describe about the "Akeno Branch" which is just constructed at Akeno with the intention of being a part of the huge array.

2. Array of "Akeno Branch"

The detector arrangement of the "Akeno Branch" is shown in fig.1. The open circles are the scintillation detectors of 2.25m^2 each, located at about 1km separation. The closed circles are scintillation counters of 1m^2 area of the

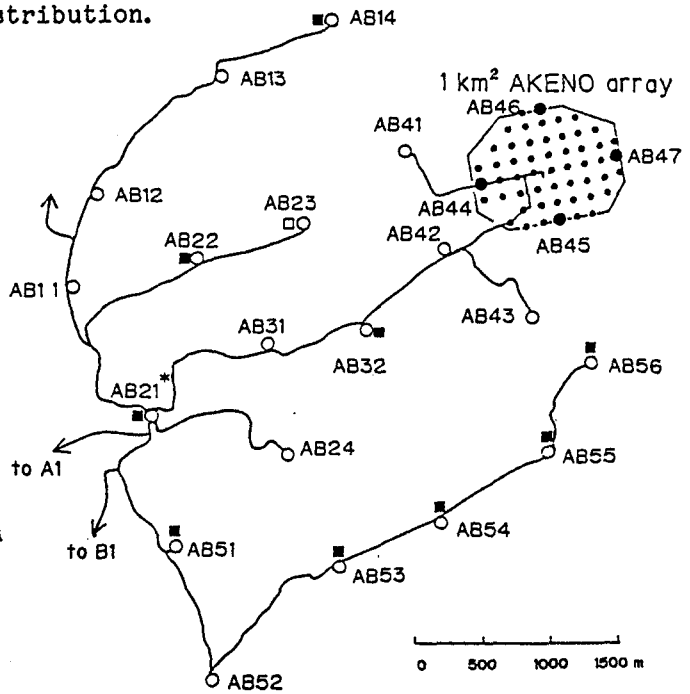

Fig.1 The detector arrangement of the "Akeno Branch".

existing "1km^2 Akeno array"[5]. The four large ones are also connected to the present new recording system. The open square is a muon detectors of 20m^2 area under construction and the closed ones will be arranged within a few years. Each detector is connected to the next one with two optical fiber cables successively on a string as shown by a solid line. One cable is used for sending the control commands to each module of the detector from the center, and the other is for data transmission.

Inside the 1km^2 array, there are unshielded detectors of total area of 169m^2, shielded detectors of 225m^2 (1GeV for vertical traversing muons) and 75m^2 (0.5GeV), and 53 fast timing channels of 10nsec resolution. These are effective to measure the properties of the large showers at far from the core.

3. Data acquisition system

In each station there is a module called Detector Control Unit (DCU) which is designed with one board micro computer(Z-80A). DCU consists of 3 major parts; communication part, data processing part and detector monitor and control part. Several DCU's are tied to a common string which consists of two directional optical fibers. One fiber of outgoing direction from the center is used to send commands, clock pulses for the timer of DCU and timer frame (clear pulse for the timer). Another one is used to accept the status information of each detector for the trigger conditions and to collect shower data and monitor data from DCU's at the center. The communication data rates on strings are 625kb/s.

Every DCU has a timer which synchronizes to that of the center with 20nsec accuracy. All signals from the detector are digitized and stored in the ring-image-memory of DCU with the incident time of 20nsec accuracy. Each DCU sends the information to the center in every 3.2 μsec period whether the detector is hit by a particle or not. With this status information, coincidence requirements can be set at the center. 6 folds coincidence of neighbouring detectors is required for the trigger. When GAS hits over the array, central unit recognizes coincidence of signals from many detectors and knows its occurence time. Then the central unit issues a command for all DCU's to search for the GAS data in the ring memory with the time information of coincidence. Each DCU which has accepted this command, stops data acquisition and searches for the all corresponding data recorded within 100 μsec before and after the coincidence. Central unit commands DCU's to send the picked out data one by one. These data are sent to micro-computer(NEC 16bit PC9801) at Akeno central laboratory through RS232C line of optical fiber and stored in the 10MB Hard Disk.

With this system not only the air shower data and monitor data are acquired but also detector conditions can be controlled at the center. Supplied voltage to the phototube, temperature, counting rate and pulse height distribution of detectors are monitored periodically. The discrimination level of the amplifier and the high voltage to the phototube can be controlled on request from the center. These functions enable us to maintain the detectors stable for long term and make data reliable. The details of this system are described in Ohoka and Teshima[6].

4. Array response

The response of the present array was examined by analyzing the artificial showers which were simulated by the Monte Carlo method. The

fluctuations of electron density and the shower front structure at core distances between 500m and 3000m of 10^{18}-10^{19}eV EAS observed at $4km^2/20km^2$ array[7] were used for the present simulation.

The threshold energy of detectable air shower is found to be about $10^{17.5}$eV and the recording efficiency reaches 100% at $10^{18.5}$eV as shown in fig.2. The histograms show the response and effective area for the showers hit inside the array. The broken line shows the area for all events including outside the array. The sensitivity for shower size and arrival direction in case of showers hit inside the array are shown in fig.3(a),(b) respectively. We can determine the electron size with 30% accuracy, arrival direction with 3 degree and core position with 80m. However for the showers outside the array, these are 150%, 9 degree and 150m, we need much caution to use the outer showers for the discussion of primary energy spectrum and their arrival directions.

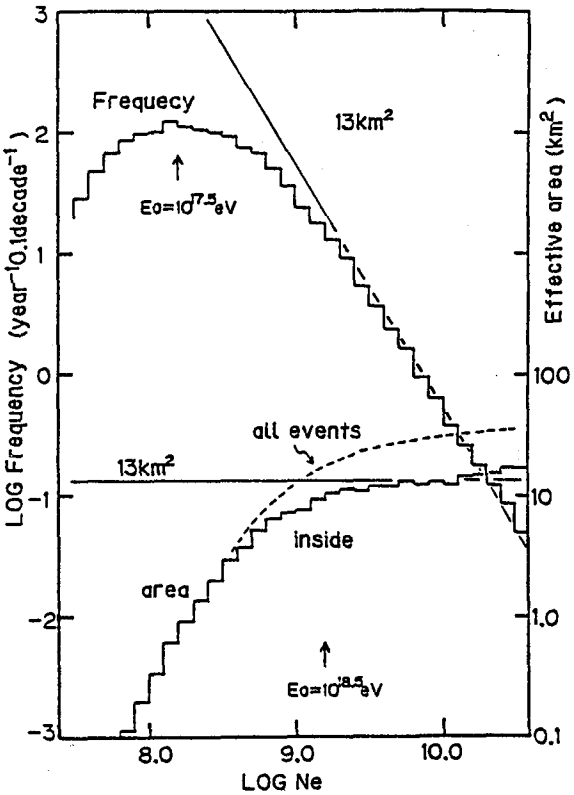

Fig.2 The detection efficiency of EAS with "Akeno Branch".

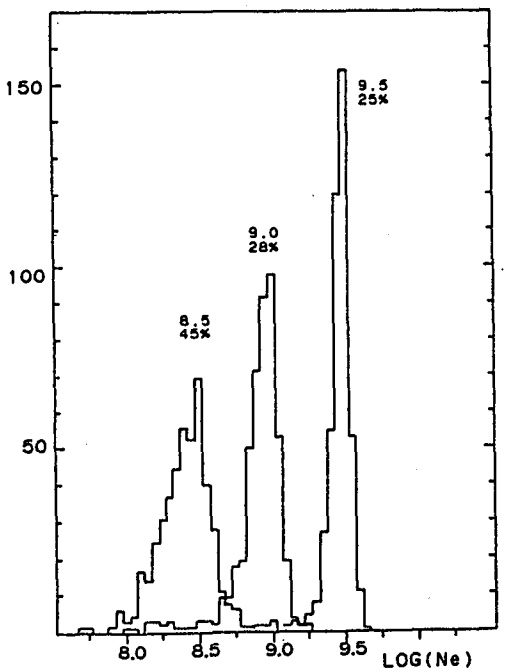

(a)

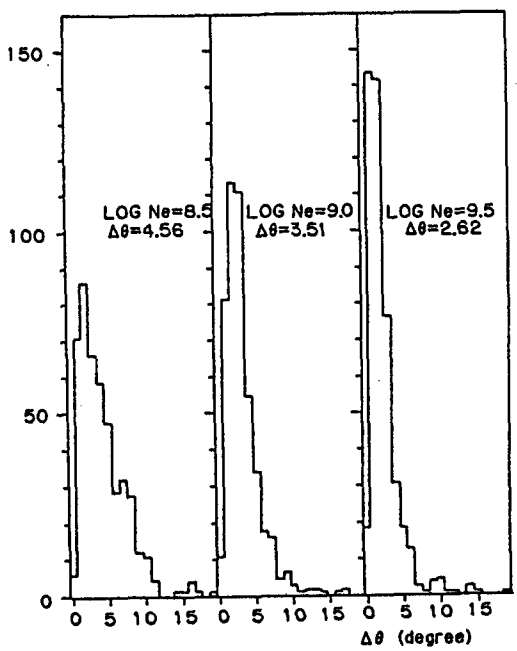

(b)

Fig.3 The sensitivity for shower size(a) and arrival direction(b) in the case of showers whose core hit inside of array.

5. Conclusion and future plan

The observation of ultra high energy cosmic rays has started at Akeno. In order to determine their origin, the expansion of array to 100km^2 is under planning. The technical problems for expansion is already solved through the experience under the construction of Akeno Branch.

The schematic diagram of recording system of the future array is shown in fig.4. The whole array is divided into several Branches. Each Branch is managed by BCU(Branch Control Unit) which is connected successively to the next one with two optical fiber cables "String". This structure is exactly the same as that inside Branch. The commands from the center and data from the Branch are put on this "String". The clock pulse is supplied from the central unit SCU(System Control Unit) to each DCU(Detector Control Unit) via BCU (Branch Control Unit). Since the timer of every DCU synchronizes to the central timer, we can manage the GAS hit in the boundary gap between branches, in the same way as ones hit inside a Branch.

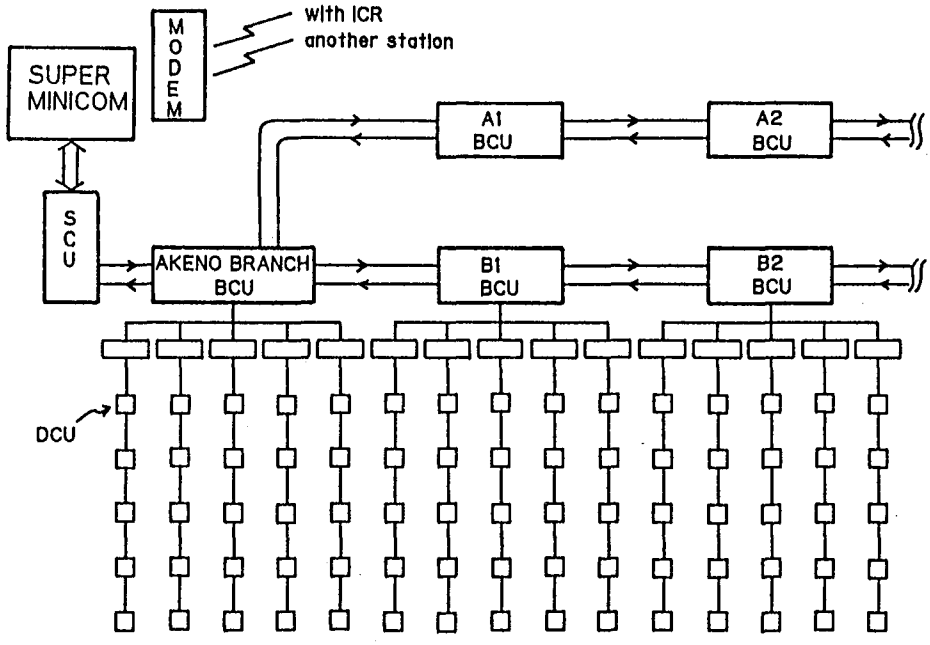

Fig.4 The data acquisition system of future surface array.

Acknowledgements

The authors wish to thank the participants of GAS workshops held in Japan for their fruitful discussions. The simulation was carried out with FACOM M380 at the computer room of Institute for Nuclear Study, University of Tokyo.

Reference

[1] J.Linsley, Proc. 8th ICRC, Jaipur 4 (1963) 295.
[2] D.M.Edge et al., J. Phys. A 6 (1973) 1612.
[3] C.J. Bell et al., J. Phys. A 7 (1974) 990.
[4] O.S. Diminstein et al., Proc. 15th ICRC, Plovdiv 8 (1977) 154.
[5] T.Hara et al., Proc. 16th ICRC, Kyoto 8 (1979) 135.
[6] H.Ohoka and M.Teshima, to be appeared.
[7] M.Teshima et al., This conf. HE 4.7-3

MINI AND SUPER MINI ARRAYS FOR THE STUDY OF HIGHEST ENERGY COSMIC RAYS

John Linsley
Department of Physics and Astronomy
University of New Mexico, Albuquerque, NM 87131
USA

ABSTRACT

The chief difficulty in studying the highest energy cosmic rays is the extremely low intensity, only $\sim$ 5 particles per km^2 sr century above 10^{20} eV. Instead of attacking the problem by assembling all of the available resources in one place, as has been done in the past, I suggest a way that the task can be performed at much less cost per unit sensitive area, by using numerous inexpensive mini arrays operating independently of each other. In addition to the quantities usually observed, each mini array will record shower particle arrival time distributions. At 10^{20} eV the saving in cost per primary particle is estimated to be a factor of 10 or better, compared to methods now in use, even for mini arrays newly built from scratch for just this purpose.

Clearly, however, all of the existing air shower arrays can be made to serve as mini arrays, without interfering with their other functions, by simply adding transient recorders to the existing instrumentation. Giant arrays such as the one at Haverah Park can be made to function as clusters of mini arrays. The new array-telescopes being planned and built for UHE γ-ray astronomy will add further to the number of these installations.

The main difficulty which can be forseen is in determining shower directions accurately. Ideally one would like to be able to identify nearly horizontal but upward moving showers produced by $> 10^{19}$ eV neutrinos, and one would like to obtain information on shower profiles for measuring the interaction mean free path of the primary particles. Compact installations with which it may be possible eventually to carry out these difficult tasks, called 'super-mini arrays', will also be described.

1. Introduction. In the 1950's the empirical upper limit of the cosmic ray energy spectrum was quickly raised from 10^{17} to 10^{19} eV (more than one joule) by using arrays of simple counters to detect extensive air showers. In the 1960's these arrays attained giant size (tens of km^2) and the limit was pushed to 10^{20} eV. Since then detailed studies have shown that the primaries are nuclei mostly as light as hydrogen or helium. Above 10^{19} eV the arrival directions are markedly anisotropic and the energy spectrum has an interesting flattening or bump. But returns are diminishing; in order to make further progress one needs a 100-fold increase in collecting area without a proportionate increase in cost. Methods relying on radio and acoustic signals have their advocates, but they have not yet produced worthwhile results. The Fly's Eye atmospheric fluorescence detector has proven to be useful for studying the structure of very large showers, but it is not cost-competitive for areas as

large as are needed. Mini arrays are low cost counter systems designed to make fuller use of the information carried by air shower secondary particles, especially those with large impact parameters (1-2 km). They can operate practically anywhere--in cities, for example. Super-mini's are an advanced form capable of determining the profile of a shower as well as its energy and direction.

2. Using arrival time spread to measure core distance. My suggestion depends on a well known property of air showers, whose utility has been somehow overlooked, the fact that the longitudinal thickness of the particle swarm increases rapidly with increasing distance from the shower axis, from 1 or 2 m at r < 10 m to hundreds of m beyond 1 km.[1,2] This is shown by data on arrival time distributions using as a measure of width the dispersion defined by $\sigma_t = [\int (t-\langle t\rangle)^2 p(t)dt]^{\frac{1}{2}}$, where p(t) is the probability of a particle arriving in dt, and <t> is the mean arrival time. In Fig. 1 the points are for single particle distributions built up from observations of individual particles belonging to showers of energies $\sim 10^{17}$ eV and various zenith angles < 45°.[2] The curve represents an empirical formula,

$$\sigma_t = 2.6(1 + r/30)^b \qquad (1)$$

with b = 1.5, where σ_t is in ns and r is in m, which fits these results and those for smaller r.[3-6] Can this be used *in individual events*, to determine r from measurements of σ_t? It can, within accuracy limits that depend on 1) the sensitivity of the parameters to primary energy and zenith angle, and 2) the effect on the parameters of hidden variables such as starting depth, primary mass and so forth.

To investigate these limits, and at the same time simulate use of the proposed method, I made use of the original records (oscilloscope photographs) of the Volcano Ranch experiment. Only those for the final year of operation (1962-63) still exist, but in that year 16 showers were recorded which satisfied the condition ($E > 10^{19}$ eV) for inclusion in the *Catalogue of Highest Energy Cosmic Rays*.[7] These are enough for the present purpose. The *Catalogue* lists the observed values of r and particle density S for each detector of the array as well as the size, energy, zenith angle and so forth of the event as a whole. For events such as these most of the 19 detectors were struck by one or more particles. The first step was to select in an unbiased manner one pulse per event. It should not be too small because of statistical errors nor too large because of a technical problem (particle densities > 10 m^{-2} were encoded in such a manner that pulse duration information was lost). The one chosen in each case is the one with greatest S such that S < 7 m^{-2}. Tracings of the selected pulses are shown in Fig. 2, together with tracings of a bandwidth limited (BWL) test pulse and a typical train of 1 MHz timing pulses. The number of particles contributing to the various pulses (n = AScosθ

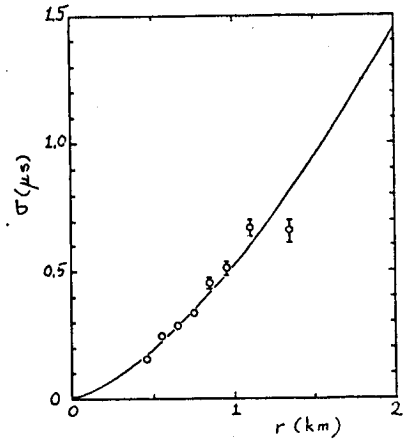

Fig. 1. Dispersion vs distance from AS core. Points from single particle delay distributions (Linsley and Scarsi 1962), curve from (1).

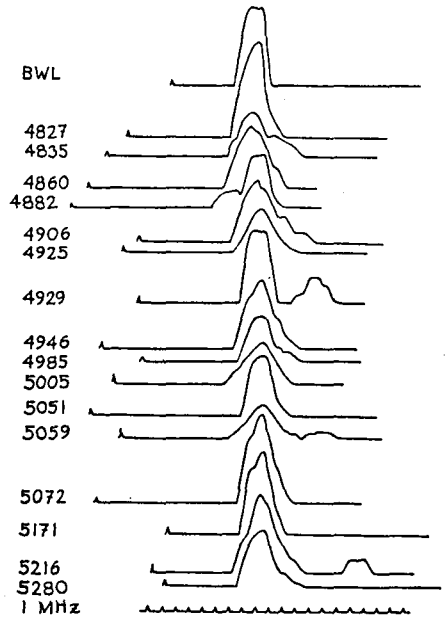

Fig. 2. Selected pulses for 16 AS with E > 10^{19} eV, identified by event No., with a typical bandwidth limited test pulse (BWL) and typical train of 1 MHz timing pulses.

where A is the detector area, 3.26 m^2) ranges from 6 to 22, averaging 12, and the values of r range from 0.9 to 2.0 km, averaging 1.4 km. The average energy of the showers is $3 \cdot 10^{19}$ eV; the zenith angles range from 7° to 55°.

The scintillator pulses and a number of test pulses were digitized and the dispersions were calculated. The dispersion of the input signal was estimated using the relation $\sigma^2_{in} \sim \sigma^2_{obs} - \sigma^2_{BWL}$. In earlier work with scintillators it had been found that arrival time distributions are θ dependent, but no energy dependence had been found.[2] In this case, setting the exponent in (1) equal to $b_1 + b_2 \sec\theta + b_3 \log(E/10^{17}\text{eV})$, it was found from the high energy sample that b_1=1.94 ±.08, b_2= -0.39±.06. By comparison with the lower energy data of Fig. 1 it was found that b_3=0±.06. This is consistent with the amount of energy dependence found by Barrett *et al.* using water Cerenkov detectors.[8] Fig. 3 shows the agreement between results of Ref. 2, results for the 16 events from the *Catalogue* (normalized to b = 1.5), and results for another previously published large event (normalized the same way).[1] Core distances denoted by r' were then calculated for the *Catalogue* events, using (1) with θ-dependent b, and compared to the values of r found previously in the usual way.[7] The dispersion of r'/r was found to be 30%.

3. Determining the energy. The final step in this simulation was to find new energy estimates. I used the Volcano Ranch method, but the Yakutsk method could just as well have been used.[9] Either relies on empirical studies of the way particle density varies with core distance and zenith angle. Letting E' be the energy required to procuce the observed density at r', and E the energy found previously, I found that as expected the systematic difference was negligible (10%). Because the structure function is very steep at large distances it was expected that the random errors would be quite large. The

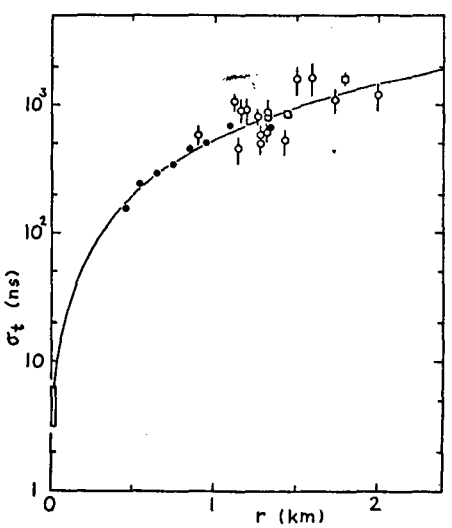

Fig. 3. Dispersion vs core distance. Filled circles and curve as in Fig. 1, open circles for individual events of Fig. 2, squares for event No. 2533 (Linsley Scarsi and Rossi 1961).

rms deviation from the mean of log(E'/E) was, indeed, 0.3, corresponding to a factor of 2 in the ratio. The largest deviations were a factor of 5 over and a factor of 4 under.

This is not far from being acceptable. In order to provide a sensitive area of 10 km^2 per mini array at 10^{20} eV one must measure r out to 1.8 km. At that range S = 6 m^{-2}, so with 4 m^2 of scintillator, n = 20 particles as compared to 12, the average for these 16 events. Thus the simple statistical errors in σ_t and S would be less even in the extreme case. For a *median* 10^{20} eV event ($r \sim 1.8/\sqrt{2}$ km) I find n = 70, so the improvement would be substantial. One should begin, of course, with mini arrays located at the existing giant arrays (Haverah Park, Yakutsk) so as to calibrate the new method.[10] Work of this kind will lead to refinements in (1) so that more accurate corrections can be made for systematic variations with E and θ. With such improvements and modern instrumentation I am confident that the random error in r can be reduced to 10%, leading to a random error in E of a factor 1.5. This would be entirely adequate for studies of the primary cosmic ray spectrum and anisotropy above 10^{19} eV, which now are limited by inadequate sensitive area, especially in locations where the southern sky is visible.[6]

4. Super mini arrays. The successful operation of the Utah Fly's Eye proves that with the information carried by air shower *photons* one can find shower energies, trajectories and profiles, out to distances of order 10 km. However such an instrument is expensive to build and operate, it must be located in a remote area with a favorable climate, and it can be turned on only 5-10% of the time. The underlying idea of a mini array is making more efficient use of the information carried by shower *particles* at large core distances. Why not go further? The number of particles is adequate even at 1.8 km, about 50 in 10 m^2, half of them muons. Suppose one could record both the direction (within 1 or 2 degrees) and the arrival time (within 10 ns) of each particle. The muons will arrive first; suppose they are separated from the electrons by shielding. Neglecting scattering and geomagnetic deflection, *the muon directions will all lie in the shower-detector plane. Within this plane the muon directions will be distributed in a manner that corresponds exactly to the longitudinal profile of the muon sources.* In the same approximation, assuming v = c as well, the arrival times will be perfectly correlated with the directions. It can be shown, still in this approximation, that *data giving the arrival direction and relative arrival time of just 3 particles are sufficient to determine the shower trajectory: the impact parameter and the direction in space,* albeit the data must be rather precise. Will the advantage of having 25 or more particles rather than 3 be enough to compensate for imperfections of the model and the measurements?[11]

References. [1]LINSLEY *et al.* 1961, Phys. Rev. Lett. 6, 485; [2]LINSLEY and SCARSI 1962, Phys. Rev. 128, 2384; [3]BASSI *et al.* 1953, Phys. Rev. 92, 441; [4]WOIDNECK and BÖHM 1975, J. Phys. A 8, 997; [5]McDONALD *et al.* 1977, Proc. 15th ICRC 8, 228; [6] CLAY and DAWSON 1984, Aust. J. Phys. 37, 309; [7]LINSLEY 1980, in *Catalogue of Highest Energy Cosmic Rays*, ed. M. Wada (Inst. Phys. and Chem. Res.: Tokyo) 1, 3; [8]BARRETT *et al.* 1977, Proc. 15th ICRC 8, 172; [9]BOWER *et al.* 1983, J. Phys. G 9, L53 and Proc. 18th ICRC 9, 207; [10]BROOKE *et al.* 1983, Proc. 18th ICRC 9, 420; [11]LINSLEY 1983, Univ. New Mexico Res. Report UNML-9/26/83.

DETECTION OF 10^{10} GEV COSMIC NEUTRINOS WITH A SPACE STATION

John Linsley
Department of Physics and Astronomy
University of New Mexico, Albuquerque, NM 87131
USA

ABSTRACT

Studies carried out by the author and a colleague in 1980-83 showed the potential value of SOCRAS (Space Observatory of Cosmic Ray Air Showers) for studying the highest energy cosmic rays, including the neutrinos produced in collisions of cosmic ray protons with photons of the 3° background radiation. This instrument would look down at the atmosphere from a space station orbiting the earth at an altitude of 500-600 km. During the night portion of each orbit, air showers would be imaged in the fluorescent light they produce. Progress toward the eventual realization of this scheme is described, including a suggestion by Torii for improving the vertical resolution, measurements of the terrestrial background light by Halverson, and especially an application of the LPM effect, expected to increase the sensitivity for upward moving neutrinos by several orders of magnitude.

1. Introduction. This is a status report on an idea suggested to me by, I believe, Hugh Hudson, at a meeting of a High Energy Astrophysics Advisory Panel at Caltech in September, 1979. I learned later that independently, at nearly the same time, a similar idea for detecting very large air showers with a "Satellite Fly's Eye", was described by S. Torii at a monthly meeting of the Air Shower Division of the Tokyo University Institute for Cosmic Ray Research.

It is well known, of course, that a proposal for detecting air showers from an aircraft by means of atmospheric Cerenkov light reflected from snow was made much earlier, by Chudakov (1972), and showers have in fact been detected using reflected Cerenkov light from a snow field at Plateau Rosa by Castagnoli *et al.* (1981).

Following the meeting at Caltech, on the basis of some crude calculations, I submitted the following in response to a request by the Panel, for 'Projects and Ideas for the 1980's':

Title. Study of 10^{20} eV Cosmic Rays by Observing Air Showers from a Platform in Space.

Description. Record real-time development of air showers produced in earth's atmosphere by cosmic rays, using mirror of very large size but low optical quality (mylar?) with array of fast photoelectric detectors, to sense air scintillation. Mirror pointed downward from satellite in low orbit. Data obtained during half-orbits when sun is hidden.

Purpose. To determine cosmic-ray energy spectrum and arrival direction distribution in the range 10^{18} to $> 10^{20}$ eV with greatly improved statistical accuracy and notable freedom from systematic errors, compared to alternative methods. It is probable that individual primary particles could be sorted according to approximate mass.

Justification. Goals are the same as those of the Univ. of Utah Fly's Eye project and those of large projects in U.K. and U.S.S.R.--to derive information relevant to astrophysics from a distinct cosmic ray component that appears to be extragalactic in origin.[1]

2. Progress 1980-1983. During the next year I discussed the idea with colleagues, and at length one of them, R. Benson, agreed to help in choosing tentative design parameters and making improved performance estimates. These were reported at an AAS meeting and at the Paris ICRC.[2,3] As indicated above, the plan was to use a single mirror. In order to view what we regarded as a large enough target (100 km diameter circle) with adequate image quality we were constrained to a fairly high orbit (500-600 km). For good enough image quality over such a large field of view the number of sensing elements (photomultipliers) would have to be large, $\sim$ 5000. We estimated that in order to achieve a good enough signal to noise ratio for energies down to 10^{10} GeV we would need a mirror $\sim$ 30 m in diameter.

We concluded that the primary advantage of the method we proposed is that *uniformity of response over a very large sensitive area is achieved using a single compact instrument*. Compared to counter arrays it would have equal angular resolution and possibly better energy resolution. It would observe the entire sky, pole to pole, and the counting rate for highest energy cosmic rays would be 50-100 times greater than the combined rate of all ground based arrays then in existence. Compared to a ground based fluorescence detector the counting rate would again be much greater (100 times as great as the Utah Fly's Eye). Moreover, the sensitive area would be *inherently energy independent*, whereas the sensitive area of a ground based Fly's Eye depends strongly on the primary energy, *in a manner that varies with atmospheric conditions*.

In Paris we learned about the work of Torii, whose optical design called for wide angle optics (solid angle $\sim \pi$) appropriate to a lower orbit (200-300 km). He called our attention to the importance of reflected Cerenkov light in this application. This light, strongly collimated in the forward direction, will be diffusely reflected by the earth's surface in the vicinity of the core location, yielding an intensity at our receiver comparable to the maximum intensity of the fluorescent light, *but separated in time and space*. In case of a shower whose fluorescent light had effectively died out before the shower reached earth, this additional component would produce an isolated dot (at a time consistent with $v = c$) so that the composite image would resemble an exclamation point. More often the Cerenkov component would simply add to the intensity from the final image pixel. The additional information from the Cerenkov light will be very helpful in fixing the location of shower trajectories along the line of sight to the detector. This is important for estimating the primary mass, and for accuracy in determining the primary energy.[4]

The initial estimates of SOCRAS sensitivity paralleled the initial estimates made for ground based detectors, estimates which had often proven to be overoptimistic. A painstaking study was made of past shortcomings to locate any weakness or possible oversights that would account for this. It was found that the uncertainty in the initial SOCRAS estimate was large enough to be critical, and some possible errors were identified. It was concluded that it is essential to base further planning on

the actual performance of ground based complete systems, especially the Utah Fly's Eye, which at that time was just beginning full operation.[7]

3. Neutrino Astronomy. Two circumstances combine to make SOCRAS attractive for neutrino astronomy. One is the very large mass of atmosphere that can be viewed (10^{11} tons); the other is a feature of the energy spectrum of cosmic neutrinos: there is a shoulder due to photopion production in collisions of cosmic ray protons with photons of the 3° background radiation, making energies $\sim 10^{10}$ GeV relatively favorable for detecting such neutrinos. Consequently the capability of SOCRAS as a neutrino detector was made the subject of a special study.

Three detection modes were envisioned. In all cases the neutrino must interact with a nucleus to produce one or more secondaries capable of initiating an air shower. If its energy is very high ($\sim 10^{10}$ GeV) the shower can be detected by means of air fluorescence in the usual way (mode I). For much lower energies ($\sim 10^{4}$ GeV) the shower could be detected by means of Cerenkov light, provided that the neutrino penetrated the earth, emerging within the target area, and then interacted in the atmosphere (mode II). For intermediate energies ($\sim 10^{6}$ GeV) the neutrino (in this case ν_μ or $\bar{\nu}_\mu$), travelling upward, would have to interact beneath the surface, producing a very high energy muon (mode III). The muon would be detected by means of atmospheric Cerenkov radiation produced by showers from pairs or bremsstrahlung photons.

It was concluded, however, that for modes II and III there would not be a clear enough signature, so that without great difficulty the signals could not be separated from noise. In addition, because the detection solid angle is very small in these modes, the counting rates would not be as great as for an undersea detector (DUMAND) of comparable complexity. In case of Mode I, the signature of a neutrino is a shower propagating in such a direction, and at such a depth, that the primary particle must have penetrated a very large amount of local material (say more than 1000 g/cm^2 of atmosphere or crust) before interacting. Identification would be no problem. However the predicted rate was disappointingly low.[5,6]

4. Progress since 1983. Regarding sensitivity estimates, the continued improvements in over-all performance of the Utah Fly's Eye are very encouraging. A student of Bowen at the University of Arizona has made tests indicating that the intensity of background light for a downward viewing fluorescence detector is several times less than for upward viewing, and he plans a ground based experiment exploiting this result (Halverson 1984). In tests carried out by the Utah group, optical filters were found to improve the signal to noise ratio of atmospheric fluorescence detectors by a factor of 4 (Cady *et al.* 1983). Similar filters have been tried out in work at Srinagar (Bhat *et al.* 1985). An alternative optical system suggested by Garipov (1982), using crossed cylindrical mirrors, might be easier to construct in space and have other advantages.

The most notable new development, however, relates to neutrino detection. Sokolsky (1983) pointed out that because of the LPM (Landau-Migdal-Pomeranchuk) effect, showers initiated in the earth by upward moving neutrinos will emerge with most of their energy intact, for ν_e-rock collisions within several hundred meters of the surface. The result

is an increase of effective target mass by 3 or 4 orders of magnitude (Cady *et al.* 1983b). Even with this much increase, the 10^{10} GeV neutrinos from photopion production may still go undetected by the Utah device. At best the counting rate will be so low that hardly anything can be learned from the neutrino arrival directions (which of course point directly to the site of the initial proton-photon collision) or the zenith angle distribution (from which in principle $\sigma_{\nu h}$ can be learned). The 100-fold greater sensitivity of SOCRAS will result in a counting rate of 2-20 neutrino events per year. For > 10^{10} GeV nuclei the counting rate will be several thousand per year. This is still more than 50 times as great as all existing ground based detectors combined.[8,9]

4. Bibliography

1) LINSLEY, J. 1979, "Study of 10^{20} eV Cosmic Rays by observing Air Showers from a Platform in Space", response to Call for Projects and Ideas in High Energy Astrophysics for the 1980's, Astronomy Survey Committee (Field Committee).

2) BENSON, R. and LINSLEY, J. 1980, "Satellite Observation of Cosmic Ray Air Showers", Bull. Amer. Astron. Soc. 12, 818 (abstract).

3) BENSON, R. and LINSLEY, J. 1981, "Satellite Observation of Cosmic Ray Air Showers", Proc. 17th ICRC (Paris) 8, 145-148.

4) BENSON, R. and LINSLEY, J. 1981, "Astronomical Applications of Large, Aberration-Limited Reflectors on Earth and in Space", Proc. Southwest Regional Conference for Astronomy and Astrophysics, eds. P.S. Riherd and P.F. Gott (Texas Tech Univ.: Lubbock, Texas) 7, 161-168.

5) LINSLEY, J. 1981, "Neutrino Astronomy using SOCRAS, a Satellite Observatory for Cosmic Ray Air Showers", *ibid.*, pp. 169-178.

6) LINSLEY, J. 1981, "Detection of High Energy Cosmic Neutrinos by means of Atmospheric Fluorescence", Bull. Amer. Astron. Soc. 13, 883 (abstract).

7) LINSLEY, J. 1982, "Air Shower Measurements from Space", Proc. Workshop on Very High Energy Interactions in Cosmic Rays, eds. M.L. Cherry *et al.* (Univ. of Pennsylvania: Philadelphia) 476-491.

9) LINSLEY, J. 1983, "Possibilities and Prospects for learning Behavior of Interactions from Extensive Air Shower Data (10^{16}-10^{20} eV Region)", Univ. New Mexico Research Report UNML-9/26/83 (14 pp). See also rapporteur paper, Proc. 18th ICRC (Bangalore) 12, 135.

References. BHAT *et al.* 1985, "Spectral Differentiation of Atmospheric Fluorescent Events from Background Cerenkov Emission", preprint; CASTAGNOLI *et al.* 1981, Proc. 17th ICRC (Paris) 6, 103; CADY *et al.* 1983, Proc. 18th ICRC (Bangalore) 9, 351; 1983b, *ibid.* 11, 485; CHUDAKOV 1972, Proc. Symposium on Cosmic Rays, Yakutsk; GARIPOV 1982, Izv. Akad. Nauk SSSR, Ser. Fiz. 46, 1839; HALVERSON 1984, "Terrestrial Background for Air Fluorescence Detection", Workshop on Cosmic Ray and High Energy Gamma Ray Experiments for the Space Station Era, Louisiana State Univ., talk; SOKOLSKY 1983, Proc. Utah Cosmic Ray Workshop, ed. T.K. Gaisser (Bartol Foundation: Newark NJ) p. 153; TORII 1981, private communication.

The Longitudinal Thickness of Air Shower Fronts

R.W. Clay, R.J.V. Brissenden, S.D Elton, N.R. Wild
Physics Department
University of Adelaide
Adelaide South Australia 5000.

1. Introduction Linsley (1983) has proposed a technique for the detection and analysis of air showers at large distances from the shower axis based on a measurement of the shower front thickness and the assumption that this thickness is closely related to the core distance. We have been investigating (Clay and Dawson 1984) some of the problems involved with realising such a technique and report here some related observations. We have been particularly interested in the practical problems of how consistent the measurements of the shower front would be, how one would use the measurement, and how the rate of triggered events would depend on the minimum pulse width required.

2. Apparatus We have used two of the 2.25 m^2 detectors (Prescott et al. 1983) of the Buckland Park array (separation ~ 11m) and recorded the pulse shapes from each detector when one of them produced a pulse greater than some specified width (~ 100ns). Any structure related to shower development ought to be reflected by agreement between the observed pulse shapes.

Oscilloscope recording was based on the digitising of an event by a Tektronix 7912 (500ns at 1ns intervals) and photography of a Tektronix 7834 at 50ns/division. Figure 1 includes an example of the single particle response of the 7912. The 7834 system had a rather similar impulse response, limited by the detector impulse response. The 7834 channel was used to trigger the recording system. Recording was triggered by the output of a pulse width discriminator (a coincidence between a prompt and a delayed sample of the waveform) at an amplitude a little below the single particle level. Thus the system triggered when either a broad pulse or a series of pulses was detected. The system also triggered on very large narrow pulses whose reponse at the one particle level still extended to 100ns. These triggers were easily recognisable.

3. Results The system was run first to see to what extent pulses from relatively close-by detectors agreed in terms of their width or pulse shape. 51 events were obtained with signals from both detectors and some of these are shown in figure 1.

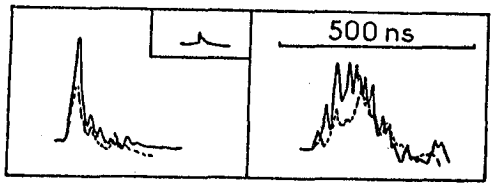

Fig. 1. Examples of pulses triggering the recording system. The outputs of two detectors closeby are shown for two events together with (insert) a single particle impulse response.

If Linsley's expression for the shower thickness against core distance

is correct then these events are from showers at core distances of at least 200m and the detector spacing of 11m is rather small in comparison.

Firstly, we make the general observation that the pulses detected by the 7912 system (but triggered by a wide pulse in the other detector) all have widths at the single particle level which are $\gtrsim$ 100ns except for 8 events which showed no signal at all on the 7912 system. The latter events were for small numbers of particles in the triggering detector and we can probably say that these events simply had density fluctuations such that no particles passed through the second detector. In other words, broad pulses in one detector were always associated with broad pulses in a close-by detector.

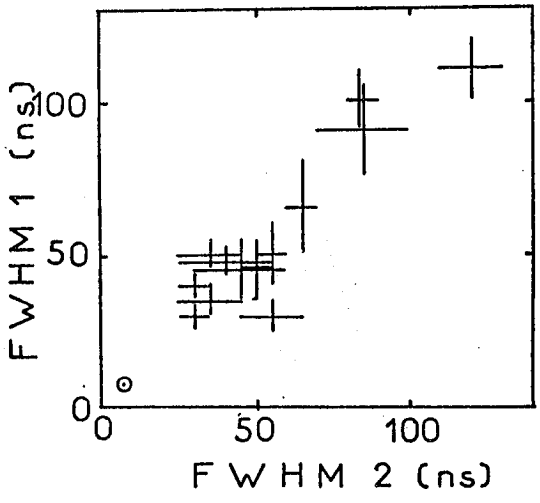

Fig. 2. The relationship between shower front thickness measured by two closeby detectors. The system impulse response is shown by a circle.

Figure 2 shows the relationship found between the full width at half maximum (FWHM) of the signals in the two channels in the cases for which such a parameter could be adequately defined (cases where, for instance, the leading edge of pulses were lost could not be used for this purpose). It would appear that there is a clear and well correlated relationship between measurements made in the two channels so that one can conclude that measurements can be made for such showers ($E_p \gtrsim 10^{17}$ eV, $r \gtrsim 200$m) which truly represent the local shower width. Alternatively one might say that a measurement of the FWHM using a 2.25m^2 detector appears to make a physically reproducible measurement of shower longitudinal structure, at least over distances of the order of 11m. It does not, of course, indicate necessarily that the shower is not lumpy in its longitudinal distribution over larger distance intervals.

4. Effects of the Pulse Width Discrimination The pulse width discriminator reduces the number of triggers accepted from a scintillator by a very great deal, typically from 2×10^4Hz to $\sim 10^{-4}$Hz. Our system simply checks to see whether or not there is a pulse above the discrimination threshold at a given time after the first trigger. This can be simulated by very high density events due to shower cores falling on a detector which has a low level in its impulse response extending to 100ns. These can easily be eliminated by inspection or probably better by the use of a coincidence system.

If Linsley's expression for width versus core distance is roughly correct, we can determine our collecting area vs energy and using the known energy spectrum we can predict the number of events we expect to detect. This is of the order of 1 event hr^{-1} and such an event rate is found in practice although this depends substantially on the threshold chosen when only a single detector is used.

5. Further Work in Progress A pilot array using the technique is currently under design and construction at Buckland Park. It is expected to consist of five, $2m^2$ water Cerenkov detectors with a typical spacing of ~ 500m. Each site will be self-contained in terms of pulse shape discrimination, digitisation, and data storage in non-volatile memory but, in this particular case, fast timing will be used for direction finding with signals carried by cable to a central site. One site will be operated independently of the local mains power supply with solar panels as the power source as a pilot experiment for a major array of stand-alone detectors.

Digitisation is expected to be carried out at a sample rate of ~ 80MHz for up to 4 μs after the detection of each event by a pulse width discriminator. We have investigated a number of digitising systems and are building a pilot system based on LeCroy MVV200 charge coupled cell analog shift registers. The pilot system will be operational by mid 1986.

Acknowledgement This work is supported by the Australian Research Grants Scheme.

References

Clay, R.W. and Dawson, B.R. (1984) Aust. J. Phys., 37, 309.

Prescott, J.R., Clay, R.W., Corani, C.L., Dawson, B.R., Gregory, A.G., and Patterson, J.R., (1983) Proc. 18th Int. C.R.C. (Bangalore), 6, 257.

Linsley, J. (1983) Rapporteur 18th Int. C.R.C. (Bangalore) 12, 135.

CERENKOV LIGHT IMAGES OF EAS PRODUCED BY PRIMARY GAMMA RAYS AND BY NUCLEI

A. M. Hillas
Physics Department
University of Leeds, Leeds LS2 9JT, UK.

ABSTRACT

It is shown that it should be possible to distinguish very effectively between background hadronic showers and TeV gamma-ray showers from a point source on the basis of the width, length and orientation of the Cerenkov light images of the shower, seen in the focal plane of a focusing mirror, even with a relatively coarse pixel size such as employed in the Mt. Hopkins detector.

1. Detection of point sources of cosmic rays

Certain X-ray binaries, pulsars and active galaxies appear to be point sources of TeV cosmic rays — presumed to be gamma-rays. The sources have been detected by observing flashes of Cerenkov radiation from small showers in the upper atmosphere, but these do not stand out clearly against the intense isotropic background of ordinary proton (or nuclear) showers. If the appearance of the Cerenkov flashes differs for the two classes of shower, much of the background might be rejected. In another paper, Cawley et al. (1) describe the modification of the 10m reflector at the Whipple Observatory (Mt. Hopkins, Arizona) to record details of each Cerenkov image on a 0.5° grid, using 37 photomultipliers in the focal plane of the focusing mirror. (A central photomultiplier is surrounded by a ring of 6 others, then by a further ring of 12, and another of 18 — the whole forming a hexagonal grid pattern.) Predictions of the response of this system to air showers will be presented. Even though the r.m.s. widths of shower images are less than 0.5°, the image dimensions should be measured well enough to provide discrimination between types of shower, though the alignment of the short image with the source will be much less clear than with finer angular resolution.

2. Simulation of Cerenkov image patterns

A 3-dimensional Monte-Carlo calculation is used to simulate shower development. The computer program has been used previously for other investigations (2) and is much more detailed than is necessary for calculating Cerenkov processes, following particles down to an energy 0.05 MeV (far below the Cerenkov threshold), although "thin sampling" (3) is used to follow particles below 1/4000 of the primary energy to reduce computing time. The model atmosphere is not isothermal. Hadronic collisions have been simulated both by a radial scaling model with rising cross-sections and by a model with increased production of low-energy secondaries (relative to scaling) at high primary energies (though a less drastic change than proposed by Wdowczyk and Wolfendale, for example, as the important particles in the fragmentation region — high x — are largely retained). However, at TeV energies, there is little difference between the models, being constrained by accelerator data, so the simulation results have been combined together in the presentations below.

Although some loss of Cerenkov light by Rayleigh and aerosol scattering is allowed for (2), scattered light is assumed not to contribute to the spread of the image (size $<1^{\circ}$) in a clear mountain atmosphere. The

light is assumed to be received by a collector of 10m diameter (taken as 2/3 efficient) on the ground, and the directions of arrival of the rays recorded. The rays are traced to see whether they would reach a particular photomultiplier of the 37-tube array as used on Mt. Hopkins, assuming the mirror forms perfect images of stars. (About 50% of the light is lost in gaps between the tubes.) Fluctuations in conversion of photons were incorporated, but not the fluctuations in the electron multiplication process. The altitude (2300m) and geomagnetic field were taken to be the values appropriate for Mt. Hopkins.

All gamma-ray showers were taken to come from the direction of a source in the centre of the field of view, and were sampled from a spectrum $E^{-2.25}dE$ from 0.25 TeV upwards, and impact points were sampled randomly over an area of 250m radius. Showers for analysis had to give signals of at least 40 photoelectrons in at least 2 of the innermost 19 tubes. The proton background showers were sampled from a spectrum $E^{-2.65}dE$, and the images were displaced randomly over a sky area large enough to cover the field of view, to simulate an isotropic background. Some showers initiated by oxygen nuclei were also simulated, using a simplified nuclear breakup representation. As these are easier to distinguish from gamma showers, and as for a given intensity of flash a higher threshold energy is needed than for a proton shower, not so much attention was paid to such showers generated by heavy nuclei.

3. Parameters used to describe Cerenkov images of showers

A typical simulated image is shown alongside in Figure 1. The figures give numbers of photoelectrons in each photomultiplier. (2 TeV gamma-ray from source in centre of field. Impact parameter 60m, zenith angle 30°.) The image axis (dashed line) is determined: this line minimises the signal-weighted sum of squares of perpendicular angular distance of the detectors. (As small distant noise signals can distort the small r.m.s. dimensions, *any individual signal below 1% of the total in all 37 tubes is ignored.*)

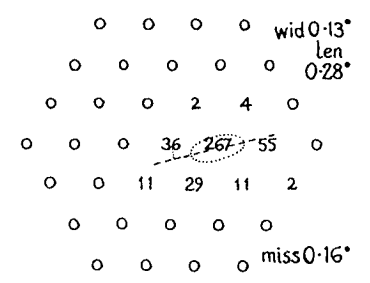

Figure 1.

The r.m.s. spread of light in directions parallel and perpendicular to this axis are referred to as the *LENGTH* and *WIDTH* of the image. *FRAC(2)* (following a suggestion by Weekes) measures the general concentration of light: it is the fraction of light collected by all 37 tubes that is contained in the 2 largest signals. The orientation of the image relative to the (central) source is described by (a) *MISS*, the perpendicular distance of the centre of the field (the source) from the image axis, (b) the *AZIMUTHAL-WIDTH*, the r.m.s. image width relative to a new axis which joins the source to the centroid of the image, and (c) the *DISTANCE* (distance of image centroid from source), to be compared with the distance of the brightest point (tube with largest signal) from the source – thus related to the orientation of the skew images.

Showers aimed directly at the observer will not have distinctive shapes. (The maximum signal will occur in the central photomultiplier – referred to as *ZONE 0*.) Showers having impact parameters at some distance away are viewed partly from the side, and the width and length of the image reflect largely the width and length of the particle cascade. The geometry depends on the impact parameter, so it is important to classify separately shower images having the largest signal in one of the tubes in

the inner ring of 6 surrounding the centre (these are *ZONE 1* showers), showers with maximum signal in the next ring of 12 tubes (*ZONE 2*), etc.: the latter correspond to somewhat higher energies or impact parameters.

It is found that hadronic showers have longer and more fluctuating images (leading particle effect), and are wider (due largely to emission angles of pions), and are not systematically aligned with the source (if isotropic) — larger *MISS* and *AZIMUTHAL-WIDTH*, smaller *DISTANCE* of centroid for a given *ZONE* (position of peak signal).

4. Comparison of image parameters for different kinds of shower

Figure 2, below, shows the distribution of the widths, lengths, and other parameters of background proton showers, and for showers from oxygen

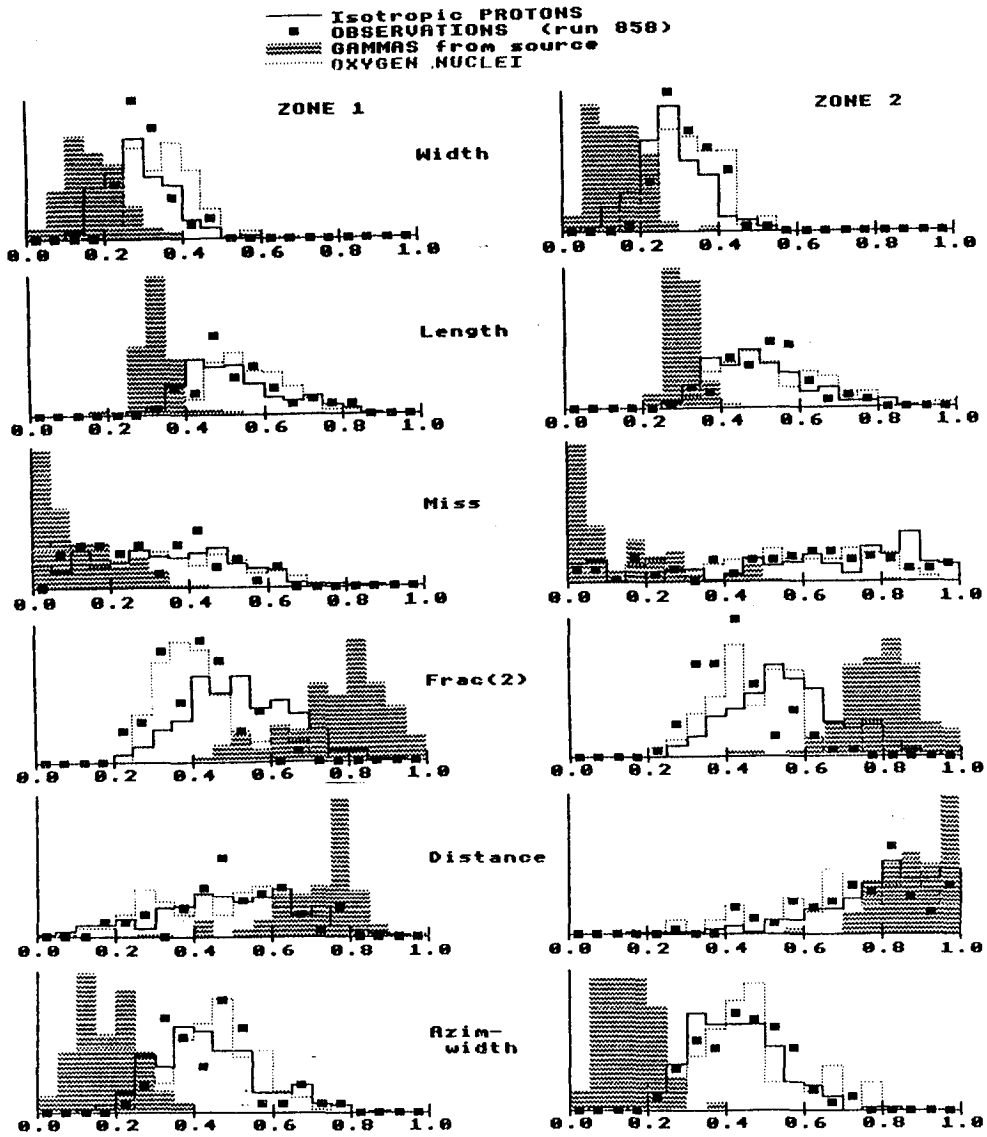

Figure 2: histograms of image characteristics. (vertical showers)

nuclei, compared with those for gamma-ray showers (shaded histogram) from a source placed in the centre of the field of view. Units: degrees — except for *FRAC(2)*, which is dimensionless. The triggering requirement is

as given above (2/19 at least 40 p.e.). Showers having the brightest signal on the inner ring of 6 tubes (zone 1) or the next ring of 12 (zone 2) are shown in the left and right column. The histograms demonstrate the more concentrated images of the gamma showers. Some real background showers observed in the zenith have been analysed in the same way (using data supplied by M.F.Cawley, D.J.Fegan and N.A.Porter). It seems that the simulations agree well with most features of the observed images, though some additional image spreading may be present in reality. Tests of the predicted image characteristics for gamma showers are not yet available.

5. Selection of gamma-ray showers from the general background

One can define, for each of the 6 image parameters, a boundary marking off the "gamma domain", containing most gamma images, but not many protons. If one then requires that 4 out of 6 parameters lie in the gamma domain, it is possible, in the case of the simulated images, to accept 60-70% of gamma showers, but only 1-2% of proton background showers. One would like to have the precise ranges of these parameters verified by experiment, but based on the simulations one might require, where $x=\sec\phi - 1$, ϕ being the zenith angle,

WIDTH < 0.21-0.17x, LENGTH < 0.35-0.13x, MISS < 0.17, FRAC(2) > 0.72+0.28x, DISTANCE > 0.65, AZIMWIDTH < 0.21-0.11x ... for Zone 1 showers, and Width < 0.19-0.2x, Length < 0.33-0.13x, Miss < 0.22, Frac(2) > 0.72+0.31x, Distance > 0.83+0.04x, Azimwidth < 0.20-0.11x ... for Zone 2 showers.

6. Miscellaneous features

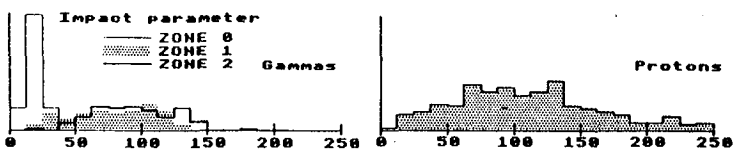

Figure 3: distribution of impact parameter.

Figure 3 shows the distance to the shower axis when showers are selected by the (2/19) triggering criterion, and the images are classified into zones (by peak signal position). Gamma showers (from a point source) peaking in the central tube have much smaller impact parameters than do other showers.

Energies and fluxes for vertical showers. With the above triggering requirement (and 10m diameter mirror, 2300m altitude, etc.), the effective threshold for gamma showers that peak in zone 1 (or 2) is 0.4 (0.7) TeV,* and the rate of showers in zone 1 (or 2) is equal to the flux of primary gammas above 0.4 (0.7) TeV within a radius of 88m (117m). A total of 550 (or 390) photoelectrons in all 37 tubes corresponds to $E_\gamma = 1$ TeV.

* (Median energy 0.7 (1.3) TeV)

7. Higher energies

Angular distance of image centroid from source as seen in ideal detector — i.e. large field of view and good resolution — is given quite well (for gamma showers) by the expression $\theta = 1.5\times10^{-5}\,(r + r_o)^2$ degrees, where at 1 TeV, $r_o = 150$m, at 40 TeV, $r_o = 195$m and at 1000 TeV $r_o = 230$m. This shows that at much higher energies the shower images are further from the source: at 40 TeV and typical impact parameter 110m the centroid would be at 1.5^o — but the image would still have only 0.5^o lengthways spread about this, so a bigger field of view would be needed: detection would be harder.

References

(1) Cawley, M.F., et al., paper OG 9..
(2) Hillas, A.M. (1982) J. Phys. G 8, 1475-92; 8, 1461-73.
(3) Hillas, A.M. (1981) 17th Int. Cosmic Ray Conf., Paris, 9, 193-6.

OG-9.5-2

SHOWER DISC SAMPLING AND THE ANGULAR RESOLUTION OF γ-RAY SHOWER DETECTORS

A. Lambert and J. Lloyd-Evans†

Department of Physics, University of Leeds, LEEDS 2, UK.

† Now at NASA/Goddard Space Flight Centre, USA.

ABSTRACT

As part of our design study for the new UHE γ-ray detector being constructed at Haverah Park (1), we have undertaken a series of experiments using scintillators operated side-by-side in $> 10^{15}$ eV air showers. Investigation of the rms sampling fluctuations in the shower disc arrival time yields an upper limit to the intrinsic sampling uncertainty, $\sigma_{rms} = (1.1 \pm 0.1)$ns, implying an angular resolution capability $< 1^{o}$ for an inter-detector spacing of ~ 25 m.

1. Introduction. That an angular resolution of $1.5^{o} - 2.0^{o}$ can be achieved by extensive air shower arrays was shown conclusively by the identification of Cyg X-3 as a source of UHE ($> 10^{15}$ eV) γ-rays (2). Subsequent confirmation (3) and reports of detections of Vela X-1 (4) and LMC X-4 (5) have highlighted the need for a new generation of arrays with a much improved detection signal to noise ratio.

The prospects for detecting a source improve with increasing collecting area, exposure time, or knowledge of source periodicity, but most acutely with improved directional resolution, especially in view of the fact that periodic γ-ray sources are likely to be time variable and lack a constant phase maximum (e.g. (6)), thereby precluding extended observations.

Here we concentrate on an experimental determination of the angular resolution achievable by the new γ-ray detection system in construction at Haverah Park (1).

2. Description of the detectors and the recording system. We have studied the extensive air shower disc at energies $10^{15} - 10^{16}$ eV using two $1\ m^2$ plastic scintillation detectors in conjunction with a 50 m water-Cerenkov array. Because this work formed the initial stages of the design study for the new array, the scintillation detectors were not identical in construction. The 'start' detector consisted of $1\ m^2$ type NE102A 7.6 cm thick scintillator, viewed from below at a distance 61 cm by a Philips 2312B 3"ϕ PMT, risetime < 3 s. The 'stop' detector consisted of $1\ m^2$ type (see (7)) 9 cm thick scintillator viewed from above at a distance 38 cm by an EMI 9821B 3"ϕ PMT, risetime < 3 s. We found it essential to blacken the entire detector interior to eliminate multiple reflections ensuring that the PMT views only the direct light from the scintillator.

The scintillators were situated at the centre of the 50 m water-Cerenkov array used to provide the EAS trigger, and, in subsequent analysis, the shower arrival direction, size, and core position. A block diagram of the arrangement is shown in Figure 1.

A variety of detector configurations, shown schematically in Figure 2 were used to investigate the timing response in EAS and also for a loose

trigger condition (termed "single particles") in which both detectors were required only to exceed the $^1/_3$ particle discrimination level.

3. Detector and recording system limitations. The combined limitation of the detectors and recording electronics was investigated using both the loose trigger and vertical showers at small core distances, experiments (4) and (1) of Figure 2 respectively. A rapid increase in the standard deviation of the time delay, $\sigma(\Delta t)$, at smaller densities was found, due partly to the leading-edge type of discrimination employed and also some electronic cross-talk at low voltage levels which has since been eradicated. For densities>1.6 particles m^{-2} the intrinsic timing resolution of the detector and recording electronics was constant at $\sigma(\Delta t) = 0.89 \pm 0.09$ ns. The identical detector configuration, in response to 50 m shower triggers with zenith angles, $\theta < 10^o$, core distances, $r < 25$ m, and both scintillator densities $> 1.6\ m^{-2}$ gave $\sigma(\Delta t) = 0.92 \pm 0.11$ ns, which is not significantly different to the intrinsic resolution. A density threshold of 1.6 particles m^{-2} has consequently been imposed for the remaining analysis.

4. Scintillator timing response in 10^{15} eV showers. Two independent samples of the shower front at the same core distance were obtained with side-by-side detectors (Figure 2, experiment (3)). Separating the detectors by 3 m (experiment (2)) allowed for the effect of small core distance differences to be investigated. Even when side-by-side, the time delay between detectors, Δt, must be corrected to allow for the transit time of the shower disc through the detector centres. The 50 m water-Cerenkov array determines the shower direction to an accuracy of $\lesssim 5^o$, which is quite adequate for this correction to be made. Figure 3A shows the mean time delay $\overline{\Delta t}$, before and after correction, for a sample of showers in four azimuth angles defined in Figure 3. After correction the $\overline{\Delta t}$ are consistent with expectation.

5. Time structure of the particle disc. The standard deviation of the time delay distribution, $\sigma(\Delta t)$, is directly attributable to rms fluctuations of the distance into the shower front at which the detectors trigger. We expect $\sigma(\Delta t)$ to increase at larger core distances due to the decreasing particle density and increasing shower front thickness. Figure 4 shows $\sigma(\Delta t)$ as a function of core distance; superposed are lines representing angular resolutions of $\pm 1^o$ and $\pm 0.5^o$. The results indicate that an angular resolution of $< 1^o$ may be achieved. This is in good agreement with the predicted angular resolution obtained from an empirical relationship derived by Linsley (8). Figure 4 also shows that the angular resolution is practically independent of core distance, at least out to 75 m, the improved baseline compensates completely for the effect of a rising $\sigma(\Delta t)$.

6. Discussion. Little, albeit careful, previous work has been done on the sampling of the EAS disc. Bassi, Clark and Rossi (9) obtained thickness ~ 2-3 m for core distances < 60 m and shower sizes $10^5 - 10^6$. More recent work, by the Kiel group (10,11) aimed to measure the longitudinal profile and curvature of the disc in small air showers. They reported a radius of curvature of 600 m for the electron disc with respect to the muon disc at energies $\sim 10^{15}$ eV (10). The limitation of the present work is that although $\sigma(\Delta t)$ reveals the magnitude of the timing

fluctuations, we cannot determine the presence of a systematic curvature of the disc. We emphasise this since it is of paramount importance in assessing the attainable angular resolution; the effect of neglecting a curvature of 600 m is to increase the angular uncertainty by $\sim 3^{o}$. An accurate correction for curvature in individual showers requires many detectors surrounding the shower core. Of the 32 detectors in the new Haverah Park array (1), 14 are located inside a radius of 50 m on a 25 m grid spacing, providing a powerful facility for the future investigation of curvature.

We note that the results discussed are for nucleon-induced showers. The expected absence of a prompt muon front in γ-ray initiated showers may worsen the attainable resolution.

7. Conclusions. We have shown that the scintillation detectors designed for use in the new Haverah Park array (1) have a timing resolution of better than 1 ns. An investigation of their performance in small air showers leads us to expect an angular resolution of $< 1^{o}$ for this array.

Figure 1

BLOCK DIAGRAM OF SETUP

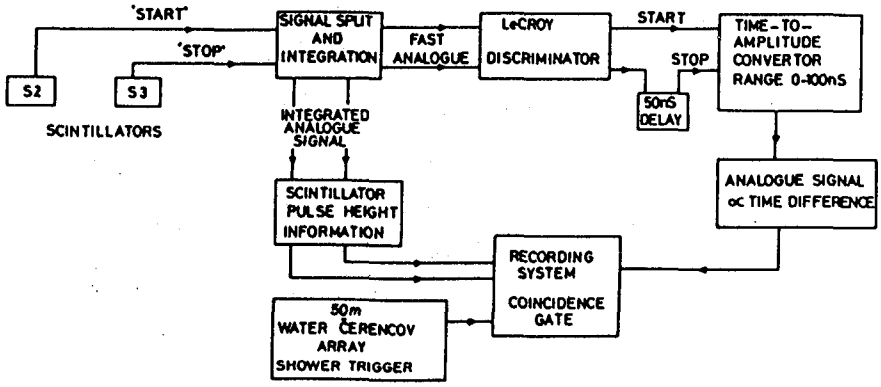

TIME-TO-AMPLITUDE CONVERTER : EG&G ORTEC MODEL TH200A/N

LeCROY DISCRIMINATOR : MVL 407 TB QUAD

Discriminator threshold $\sim {}^{1}/_{3}$ particle m^{-2}.

8. Acknowledgements. We thank Andy West for his valued assistance. The Science and Engineering Research Council (UK) are thanked by AL for the provision of a studentship.

Figure 2

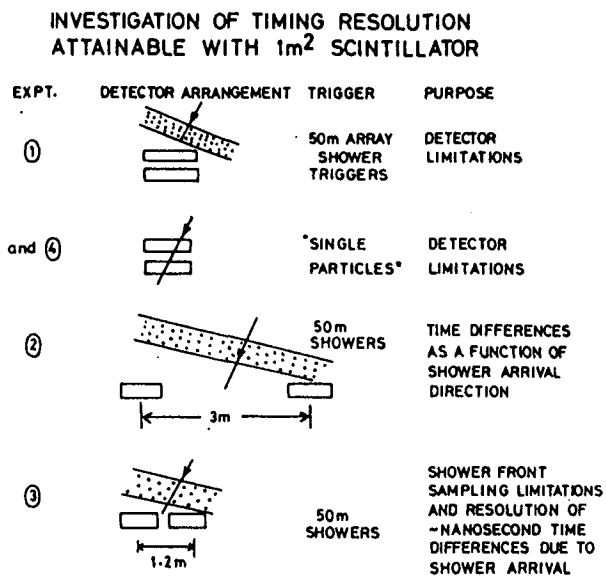

Figure 3

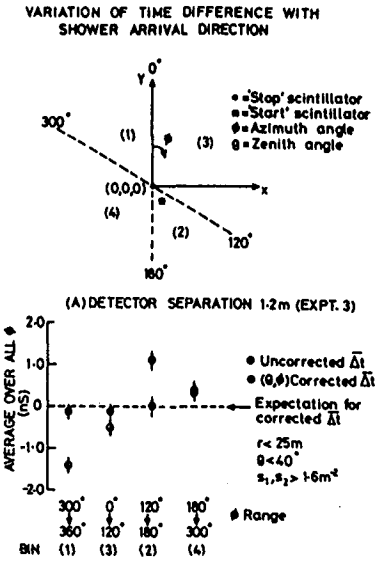

References

(1) Brooke G B et al, this Conf. OG-9.4-7
(2) Samorski M and Stamm W 1983 Ap J Lett. 268, L17
(3) Lloyd-Evans J et al 1983 Nature 305, 784
(4) Protheroe R J et al 1984 Ap J Lett. 280, L47
(5) Protheroe R J and Clay R W 1985 Nature 315, 205
(6) Lambert A et al, this Conf. OG-2.1-6
(7) Clark G 1957 Rev. Sci. Instrum. 28, 6, 433
(8) Linsley J 1984 Research Note UNML-7/6/84 University of New Mexico
(9) Bassi P, Clark G and Rossi B 1953 Phys Rev 92, 441
(10) Woidneck C P et al 1971 12th ICCR (Hobart) 3, 1038
(11) Woidneck C P and Bohm E 1975 J Phys A: Math Gen: 8, 6, 997

Figure 4

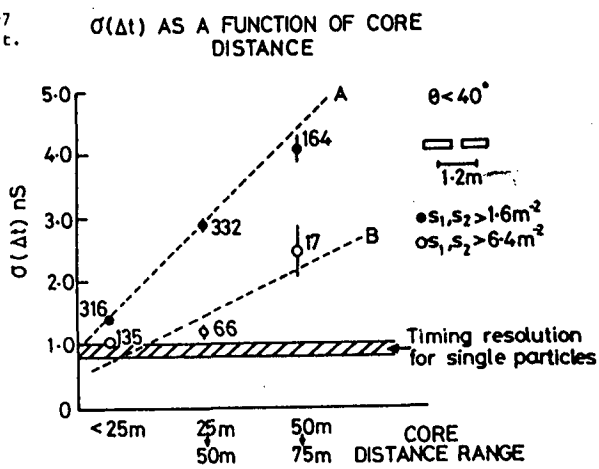

The region below the dotted line represents the timing resolution resulting in an angular error: A±1°, B±0·5°

APPLICATION OF IMAGING TO THE ATMOSPHERIC CHERENKOV TECHNIQUE

M.F. Cawley[1], D.J. Fegan[1], K. Gibbs[2], P.W. Gorham[3], A.M. Hillas[6], R.C. Lamb[4], D.F. Liebing[4], P.K. MacKeown[5], N.A. Porter[1], V.J. Stenger[3], and T.C. Weekes[2].

1. Physics Department, University College, Dublin.
2. Harvard-Smithsonian Center for Astrophysics.
3. Physics Department, University of Hawaii.
4. Physics Department, Iowa State University.
5. Physics Department, University of Hong Kong.
6. Physics Department, University of Leeds.

1. Introduction. Turver and Weekes (1977) proposed using a system of phototubes in the focal plane of a large reflector to give an air Cherenkov camera for gamma ray astronomy. A more detailed description of a detector based on the 10m Optical Reflector at the Whipple Observatory was given by Weekes (1981) and Fegan et al. (1983). Preliminary results with a 19 element camera have been reported previously (Cawley et al. 1983). In 1983 the camera was increased to 37 pixels; it has now been routinely operated for two years and some results are presented at this conference (OG 2.3-1, 2.1-11, 2.2-9, 2.7-3, and 2.4-4). In this paper we present a brief physical description of the camera, its mode of operation, and the data reduction procedures; the Monte Carlo simulations on which these are based are also reviewed.

2. The Camera. Each of the 37 camera pixels is a 5cm diameter RCA phototube, 6342A (S11 photocathode). The phototube layout is shown in figure 1; to allow space for the magnetic shields the spacing between centers is 6.25cm. The focal plane scale is 1^{o} per 12.5cm; the useful area of each photocathode is equivalent to 0.36^{o} so that the useful coverage of the full 3.5^{o} diameter field is approximately 50%.

A typical integral pulse height spectrum for a single camera pixel is shown in figure 2 and the trigger level, corresponding to 45 ± 12 photoelectrons, indicated. The absolute gain of each pixel was determined at monthly intervals using an Americium light source which had been previously calibrated against a muon Cherenkov telescope. The relative gain correction was determined by uniformly illuminating all pixels with a pulsed N_2 light source; this was done at the beginning and end of each night's observation.

3. Operating Mode. Observations were only attempted when sky conditions were excellent. Each set of observations consisted of a pair of tracking scans over the same range of azimuth and elevation angles. In one of these, the ON run,

the reflector was directed at the suspected source. The OFF run was offset by 30 minutes of Right Ascension. The order of ON and OFF runs was interchanged to reduce the possibility of systematic errors.

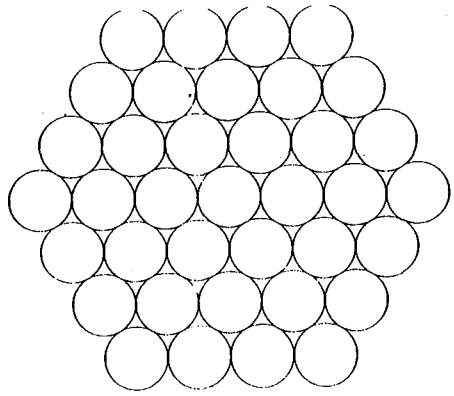

FIG. 1 Phototube Layout

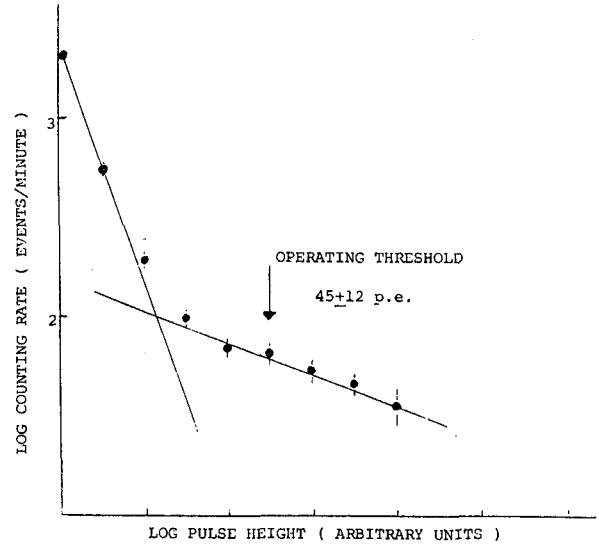

FIG. 2 Integral Pulse Height Spectrum

4. Simulations. The original concept of the camera (Weekes 1981) was based on the Monte Carlo simulations of Rieke (1969) which gave the average features of 250 gamma-ray initiated showers. Realistic estimates of the performance of the camera required that fluctuations be taken into account as well as the geomagnetic field. To optimise the selection of gamma rays, hadron-initiated showers must also be simulated.

Three sets of simulations of shower images measured by the Whipple Observatory camera are discussed below; because the conditions assumed are somewhat different, it is not possible to compare these quantitatively. Some large qualitative differences are apparent and are unexplained.

(a) Durham simulations. The Durham Monte Carlo program, which was previously used to evaluate the performance of the 10m reflector in a single detector mode (Browning and Turver 1975), was used to simulate the response of the camera to 300 and 1000 GeV gamma-ray initiated showers (Turver, private communication, 1983). The results were quite different from those expected, with fluctuations dominating the shape and orientation of the shower images. The angular width of the shower was smaller than that of the background events measured by the camera (MacKeown et al. 1983); the orientation of the shower major axis showed little correlation with the position of the shower relative to the optic axis and thus suggested that

detailed processing of the shower images would be of limited value.

(b) Altai simulations. Plyasheshnikov and Bignami (1984) have used a compressed Monte Carlo method to evaluate the effectiveness of imaging in improving the sensitivity of the atmospheric Cherenkov technique. They simulated the response of a 10m reflector to both gamma-ray and proton initiated showers for energies from 0.1 to 2.0 TeV. They concluded that there was no difference between the average size of two kinds of images but the orientation i.e. radiating out from the center, would permit the preferential selection of gamma-ray initiated showers. This conclusion is in obvious disagreement with (a). They also suggest that the greater fluctuations along the major axis in proton-initiated showers could be used statistically to discriminate against the proton background.

(c) Leeds simulations. Hillas (this conference OG9.5-3) has simulated the response of the 10m reflector to both photon and proton-initiated air showers taking into account the optical parameters of the 10m reflector. He has simulated the expected response of the system to a proton--initiated background using typical operating parameters. The agreement between the simulated and measured background is good and suggest that the experimental parameters have been realistically accounted for.

Significant differences are found between the gamma-ray and proton shower images; in particular the angular size of the gamma-ray shower is almost a factor of two smaller than that of the proton image. In addition the gamma rays originating from a point source on axis are radially distributed as predicted in (b). Because the angular size of the images is comparable to the pixel size, this radial distribution is difficult to measure with the Whipple Observatory camera.

5. Data Reduction Procedures. All data is reduced off-line using a variety of selection algorithms designed to optimise the detection of a gamma ray signal. Because there is some disagreement between the simulations it is not possible to isolate a single algorithm that will maximise the selection efficiency. Instead the development of an algorithm is an iterative process with the selection criteria initially based on the simulations and modified after feedback from tests on actual data suspected to contain a gamma-ray source that can be regarded as a standard candle.

After calibration, data is sorted according to the following general criterion: (a) all data, (b) data sorted according to total brightness (shower energy), (c) data sorted by size and/or shape, (d) data sorted by orientation, (e) some combination of the above.

An early selection, suggested by the Durham gamma-ray

simulations, was the use of the parameter, ι to select compact (small angular size) showers as candidate gamma rays. $r = (p_1+p_2)/\text{total}$, the fraction of the light intercepted by the camera that is contained in the two highest pixels). This is confirmed by the Leeds simulations which show that the greater angular size of proton showers arises from greater width along the major axis caused by the greater penetration of the proton shower and along the minor axis caused by hadron interactions in the proton shower.

Following the Plyasheshnikov and Bignami (1984) the effectiveness of a selection procedure is the improved signal-to-noise ratio

$$h = \frac{A'_\gamma}{A_\gamma}\left(\frac{A'_h}{A_h}\right)^{-1/2}$$

where A_γ and A_h refer to the collection areas for gamma-ray and proton showers without selection and the dashed values are the post-selection values. h can be evaluated from the simulations where the source and background spectrum must be taken into account. The factor (A'_h/A_h) can be evaluated empirically since it is the ratio of event rate after and before selection. At the zenith this is 0.016. Using the Durham simulations A'_γ/A_γ is 0.5; the Leeds simulations indicate a higher value, so that h >4 at the zenith. It falls off with zenith angle becoming ineffective for z > 30°. As discussed in Hillas (1985) the combination of r with other measured parameters can be expected to significantly improve the value of h.

Using the method described in Weekes (1976) and the Durham simulations, we derive the effective energy threshold, E = 200 GeV and the gamma-ray collection area ($A'_\gamma = 9.4\times10^3 m^2$).

6. Acknowledgements. This work was supported by the U.S. Department of Energy, the Smithsonian Scholarly Studies Fund and National Board of Science and Technology of Ireland.

References.

Browning, R, Turver, K.E. (1975), Nouvo Cimento, 38A,223.
Cawley, M.F. et al. (1983), 18th ICRC, 1, 118.
Fegan, D.J. et al. (1983) Nucl. Inst. & Meth. 211, 179.
Plyasheshnikov, A.V. and Bignami, G.F., (1984), preprint.
Rieke, G.H. (1969), 11th ICRC, 3, 601.
Turver, K.E., Weekes, T.C. (1978), Nuovo Cimento, 45B, 99.
Weekes, T.C. (1981). 17th ICRC, 8, 34.

A METHOD TO IMPROVE OBSERVATIONS OF GAMMA RAY SOURCES NEAR 10^{15} eV

Sommers, P. and Elbert, J.W.

Physics Department, University of Utah, Salt Lake City, UT 84112 USA

ABSTRACT

Now that sources of gamma rays near 10^{15} eV have been identified, there is a need for "telescopes" which can study in detail the high energy gamma ray emissions from these sources. We analyze the capabilities of a Cerenkov detector which can track a source at large zenith angle (small elevation angle). Because the observed showers must then develop far from the detector, the effective detection area is very large. During a single half-hour hot phase of Cygnus X-3, for example, it may be possible to detect 45 signal showers compared with 10 background showers. Time structure within the hot phase may then be discernible. The precise capabilities of the detector depend on its mirror size, angular acceptance, electronic speed, coincidence properties, etc. We present calculations for one feasible design using mirrors of an improved Fly's Eye type.

For observing distant air showers, the effective detection area of a Cerenkov detector is determined by its angular aperture according to the formula

$$A = \pi(D \cdot \tan\phi)^2 \qquad (1)$$

where ϕ is the 1/2-aperture angle and D is the distance from the detector to the position of Cerenkov light emission. The relevant geometry is indicated in figure 1. A very large detection area can be attained at large zenith angle because the large atmospheric slant depth causes the showers to develop far from the detector. Relatively high primary energies are required in order to yield a detectable photon density at the detector. Our calculations concern showers of 1 PeV ($=10^{15}$ eV) or greater energy. Table 1 shows how the detection area increases with zenith angle for ϕ = 1.7 degrees. The distance D is the distance from a slant depth of 600 gm/cm^2 (depth of maximum for PeV showers) to a vertical depth of 862 gm/cm^2 (corresponding to the Fly's Eye altitude). The distances are computed using the U.S. Standard Atmosphere and incorporating the (small) effects of the earth's curvature.[1] For quick calculations it is helpful to have an analytic formula which yields approximately correct values. If atmospheric depth is given by $x = 1030 \exp(-h/7)$ gm/cm^2, with h the vertical altitude above sea level in km, then one gets

$$D \approx \frac{1}{\cos\theta} \left\{ -7 \ln \left(\frac{600 \cos\theta}{1030} \right) - h_0 \right\} \qquad (2)$$

where θ is the zenith angle and h_0 is the detector's altitude in km above sea level.

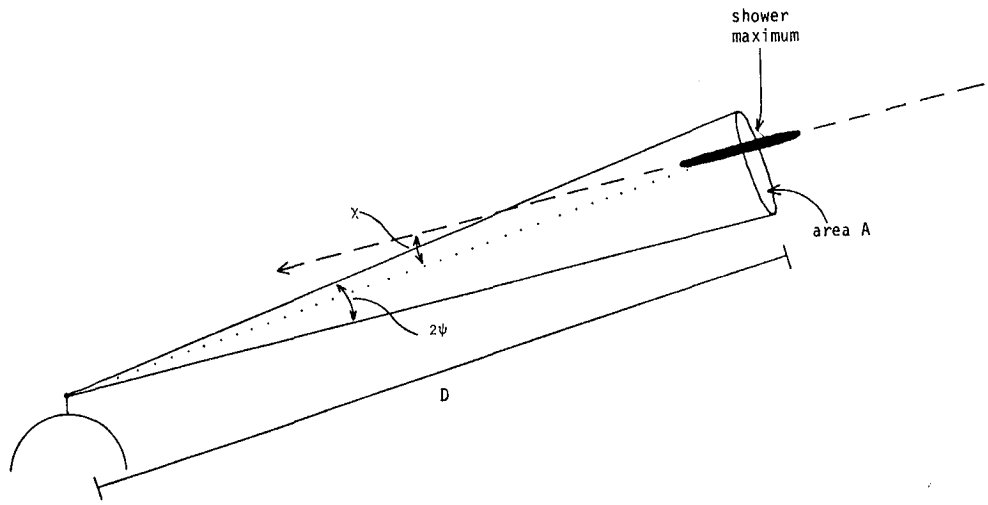

Figure 1

Using numerical simulations of Cerenkov light emission[2] and atmospheric propagation,[3] we have studied the dependence of the detector amplitude on zenith angle and the viewing angle χ (between the shower core and the detector's line of sight to shower maximum). For mirrors of 96 inches diameter (as proposed for an improved Fly's Eye), with 70% reflectivity and for phototube cathodes of the S-11 type with extended UV response, we find the number of photoelectrons to be given approximately by

$$PE \approx 1.3\times10^{7}\ E\ D^{-2.5} \times \begin{cases} e^{\chi_c-\chi} & (\chi>\chi_c) \\ 1 & (\chi<\chi_c) \end{cases} \qquad (3)$$

where E is the primary γ-ray energy in PeV, D is the distance as in table 1, χ is measured in degrees, and χ_c is a zenith-angle-dependent critical angle (see table 1). The PE values in table 1 are obtained from this formula with $\chi < \chi_c$. A factor of 1.5 should be applied to the right side of equation 3 for an approximate conversion to photons/meter^2. The formula applies to γ-ray showers; hadronic showers yield an amplitude smaller by a factor of 0.73.

Table 1

Zenith Angle (deg)	D (km)	A [ψ=1.7°] (km^2)	PE (photoelectrons)	χ_c (deg)
60	16	.71	13000	.8
65	21	1.2	6400	.8
70	30	2.5	2600	.7
75	46	5.9	910	.6
80	84	20.	200	.5

For a fixed amplitude threshold and fixed zenith angle, there is a maximum viewing angle at which a shower can be detected. Suppose the threshold is set at the PE value given in table 1 for a 1 PeV shower. The maximum viewing angle for γ-ray showers is then (from eqn 3)

$$\chi^{\gamma}_{max}(E) = \begin{cases} \chi_c + \ln E & E>1 \\ 0 & E<1. \end{cases} \qquad (4)$$

Since this angle is energy dependent, the 1/2-aperture ϕ which optimizes the signal-to-noise ratio depends on the source's spectral index. (In principle, the signal's dependence on ϕ can be used to determine the spectral index.) Table 2 presents some expected results for Cyg X-3 based on the Kiel data (differential spectral index of 2.1 with a cutoff at 20 PeV). The signal rate is computed by

$$\text{signal rate} = \int_1^{20} \frac{dS}{dE} \cdot \text{area}(E)\, dE \qquad (5)$$

where $\frac{dS}{dE}$ is the differential flux from Cyg X-3 (taken as a typical hot phase flux of 10 times the time-averaged flux). The area(E) is given by equation (1) with ϕ replaced by $\chi^{\gamma}_{max}(E)$ if $\chi^{\gamma}_{max}(E)$ is less than ϕ. For the background rate we use

$$\text{background rate} = A \int_{1/.73}^{\infty} \frac{dN}{dE}\, \Omega(E) dE. \qquad (6)$$

Here A is the area from table 1, $\frac{dN}{dE}$ is the cosmic ray flux (with the spectral index taken to be 2.8) and $\Omega(E)=2\pi(1-\cos \chi^{H}_{max}(E))$, where the maximum viewing angle for hadronic showers is $\chi^{H}_{max}(E) = \chi^{\gamma}_{max}(.73E)$. The last 3 columns of table 2 give the numbers of showers and signal-to-noise ratio from a single Cyg X-3 observation for 1720 seconds (.1 period).

Because of the strong dependence of rates on zenith angle in this range, careful monitoring of background rates is essential for identification of the signal from a source. Moreover, it may be necessary to operate two or more separated detectors in coincidence in order to reject spurious triggers from stray muons and background light fluctuations. Nevertheless, it appears feasible to detect a source like Cyg X-3 in a single short observation and to see some detail in the light curve. If a neutron star rotation period is modulating the PeV emissions from Cyg X-3, that period should be discoverable using this method.

TABLE 2

Zenith Angle (deg)	Optimal ψ (deg)	Signal rate (s^{-1})	Background rate (s^{-1})	Signal/noise coefficient ($s^{-1/2}$)	Signal at 1720s (showers)	Background at 1720s (showers)	Signal/Noise at 1720s
60	1.75	.0082	.0019	.19	14	3.2	7.8
65	1.75	.014	.0033	.25	24	5.6	10
70	1.7	.026	.0056	.34	44	9.7	14
75	1.65	.054	.011	.51	92	19	21
80	1.6	.16	.031	.90	270	53	37

Acknowledgement.
This research was supported by the United States National Science Foundation under grant number PHY8415294.

Notes.
1. Based on tables in "An Analysis of the Nuclear Interaction of High Energy Cosmic Rays," Osborne, J.L., Ph.D. thesis, University of Durham (1966).

2. Based on shower properties given in Hillas, A.M., J. Phys. G 8, 1461 (1982).

3. Based on tables in Elterman, L. & Toolin, R.B., Handbook of Geophysics and Space Environments, (Bedford, Mass.: U.S.A.F. Cambridge Research Laboratories), Chapter 7 (1965).

ANGULAR RESOLUTION OF AIR SHOWER ARRAY-TELESCOPES

John Linsley
Department of Physics and Astronomy
University of New Mexico, Albuquerque, NM 87131
USA

ABSTRACT

A fundamental limit on the angular resolution of air shower array-telescopes is set by the finite number of shower particles coupled with the finite thickness of the particle swarm. Consequently the angular resolution which can be achieved in practice depends in a determinate manner on the size and number of detectors in an array-telescope, as well as on the detector separation and the timing resolution. It is also necessary to examine the meaning of 'particle density' in whatever type of detector is used. Results are given which can be used to predict the angular resolution of a given instrument for showers of various sizes, and to compare different instruments.

1. Introduction. Counter arrays for studying air showers are usually multi-purpose installations whose design represents a compromise between many requirements, including limits on construction and operation costs. Ordinarily the requirement for accuracy in measuring shower directions is not very stringent: angular resolving power of a few degrees is adequate. It is a fact of experience that resolving power of this order is achieved almost as a matter of course by applying the 'fast-timing' method of Bassi *et al.* (1953). Arrays which are physically small (diameter < 100 m) need to have 1-10 ns timing resolution, but this is not very difficult to achieve using scintillators. For giant arrays (diameter > 1 km) it might be difficult, but in this case the counter separations (the baselines for time of flight triangulation) are much greater, so the timing doesn't need to be as fast. The angular resolution characteristics of existing arrays have been studied with great care (see for example Clark *et al.* 1961, Linsley and Scarsi 1962, Lloyd-Evans 1982), but this seems always to have been done case by case, after the fact, so when I was asked recently, "What is the limiting precision of determining EAS directions? Is it possible, on a 300 m basis, to see the front within ± 1 ns, so as to achieve an angular resolution of 1 mrad?" (Cocconi 1984), I was unable to find a ready made answer. The question relates to a timely application: observing point sources of > 10^{15} eV γ-rays, in which the signal to noise ratio of an air shower array-telescope depends critically on the angular resolution $\Delta\theta$, being proportional to $(\Delta\theta)^2$.

2. Error in arrival time. For an isolated detector the error in the apparent arrival time will include the instrumental error and the effect of fluctuations due to the finite number of particles producing the signal. The contribution of fluctuations is given by $\delta t = \sigma_t/\sqrt{n}$, where n is the number of independent contributions to the signal and σ_t is the arrival time dispersion. This relation assumes that the fiducial time is the *average* arrival time. In practice it may be more convenient to use

instead $t_{\frac{1}{2}}$, the median time, or t_j, the time of the j-th particle, but this makes only a small difference (a factor of order 1) which I will neglect. For vertical showers on a thin scintillator of area A, n = mSA, where S is the 'particle density' as it usually is expressed, in units of the signal made by a relativistic muon. The factor m takes into account evidence that the average-size contribution to shower signals may be less than one muon (McDonald *et al.* 1977). For S I will use the NKG formula, $S = (N/r_o^2)C(r/r_o)^{s-2}(r/r_o + 1)^{s-4.5}$, where N is the shower size, s is the age, r_o is the Moliére length, and $C = \Gamma(4.5-s)/[2\pi\Gamma(s)\Gamma(4.5-2s)]$. I find empirically that

$$\sigma_t = \sigma_{to}(r/r_t + 1)^b \qquad (1)$$

with typical values σ_{to} = 2.6 ns, r_t = 30 m and b = 1.5.* Substituting in the formula for δt I obtain

$$\delta t = \frac{\sigma_{to} r_o}{\sqrt{CmNA}} (r/r_o)^{1-\frac{1}{2}s}(r/r_o+1)^{2\frac{1}{4}-\frac{1}{2}s}(r/r_t+1)^b \ . \qquad (2)$$

This tells us that one method of improving the angular resolution is to increase the size of the detectors. For primary energies not too great it will also help to increase the altitude, because $\sqrt{N}$ will increase faster than $\sigma_{to}r_o$. To look at typical numbers I assume s = 1, which gives me C ≅ 0.4. Then I take r_o = 100 m, A = 1 m^2, N = 10^5 and m = 1. I obtain

$$\delta t = (1.3 \text{ ns})(r/100)^{0.5}(r/100+1)^{1.75}(r/30+1)^{1.5}$$

and find these values:

r (m) =	10	20	50	100	200
δt (ns) =	0.8	1.7	8.1	39	267

Thus in order to locate a shower front within, say, 1 ns at greater and greater core distances one must use scintillators of rapidly increasing size. (In this example, whereas 3 m^2 detectors would be adequate up to 20 m, at 50 m the detector area would have to be 65 m^2.)

3. Angular resolution. The exact angular resolution of an array-telescope will depend on details of the layout and the data processing, but if the system is well designed the result will be approximately

$$\Delta\theta = c\delta t(R)/R \ , \qquad (3)$$

where the 'effective baseline' R is such that $\delta t(R)$ equals the instrumental timing error, which I will call Δt. The idea is that in a 'well designed' system the separation of the detectors will be small enough in relation to r_o, A, and shower sizes of interest, so that typical useful events will produce several signals with δt approximately equal to Δt. These signals will dominate the usual least-squares fitting procedure for computing the shower direction. Signals with $\delta t \ll \Delta t$ will have little weight because the corresponding baselines will be $\ll$ R; signals with δt

---

* See conference paper HE4.7-14 for experimental results on $b(E,\theta)$ for $10^{17}<E<10^{20}$ eV, and more references. In that experiment, as in most others, the energy dependence was found to be too small to detect. Parameter b controls the large core distance behavior of σ_t, which is not the main issue here. Measurements near the core are more difficult to make and to interpret; more data are needed. The results of Woidneck and Böhm (1975) favor a smaller value for σ_{to}, around 1.6 ns. See also Clay and Dawson (1984) and McDonald *et al.* (1977).

>> Δt will have little weight in spite of having baselines > R, because δt is such a rapidly increasing function for large core distances.

Moving the radical $\sqrt{mNA}$ to the left hand side of (2), one sees that the right hand side depends only on certain constants and r. Solving for r (graphically or numerically), representing the result as $r = f(\sqrt{mNA} \cdot \delta t)$, and then letting r = R so that δt can be replaced by Δt, one obtains the desired result:

$$\Delta\theta = c\Delta t / f(\sqrt{mNA} \cdot \Delta t) \qquad (4)$$

4. Discussion. Taking the Kiel array as an example (Bagge *et al.* 1979), Δt = 1 ns and A = 1 m^2, so for $mN = 10^5$ the effective baseline R is 13 m (by interpolation in the table above), and the angular resolution is predicted to be 23 mrad. This prediction is in good agreement with what is claimed by the Kiel group: $\Delta\theta$ better than 1° for $N = 10^5$-10^7. I have tested the predictions in other cases (MIT Agassiz, MIT Volcano Ranch, and Haverah Park arrays), each time finding satisfactory agreement.

Fig. 1 shows curves of constant angular resolution in coordinates log(Δt) vs log(mNA), calculated in the way I have explained, using (4). In region A the performance of an array-telescope is *particle statistics limited*. In this region, improving the instrumental time resolution does little to improve $\Delta\theta$. In region B the performance is limited instead by characteristics of the detectors and recording system, so there is room for improvement in $\Delta\theta$ by improving these characteristics.

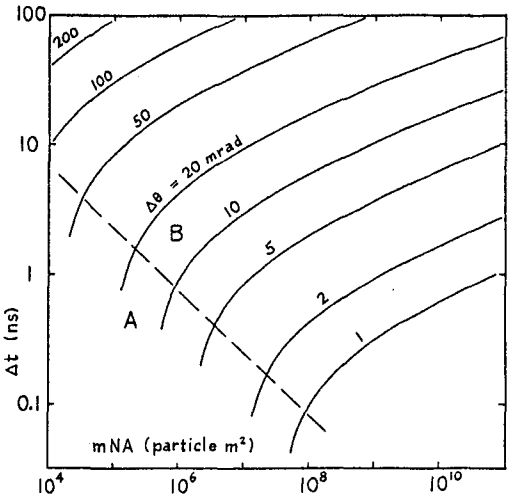

Fig. 1. Curves of constant angular resolution ($\Delta\theta$, mrad) for an array-telescope with given timing error Δt and area per detector A, for showers of size N. See text for explanation of m, and of regions A & B.

For E = 10^{15} eV (N = 10^5 at sea level, systems like the one at Kiel are already in region A. The most practical way to improve their performance is by greatly increasing the size (or density) of the detectors, or by moving to a higher altitude. A goal of 5 mrad angular resolution within the next decade seems to be realistic. This can be achieved with scintillation counters, without improving Δt. The improvement in signal to noise ratio for point sources of γ-rays, a factor of $(20/5)^2$, will be substantial.

Improving still further so as to attain $\Delta\theta$ = 1-2 mrad at this energy seems to require a radical change, from scintillators to some other kind of device with an intrinsically much faster response. Workers at SLAC have constructed planar spark counters (PSC's) with dimensions of 10 x 300 cm, and these have been tested at PEP giving on-line timing resolution better than 200 ps, as well as position resolution smaller than 4 mm

(Atwood *et al.* 1983, Ogawa *et al.* 1984). The timing resolution of similar 30 x 30 cm units constructed at Novosibirsk is reported to be as small as 24 ps (Fedotovich *et al.* 1982).

References.

Atwood, W.B., Bowden, G.B., Bonneaud, G.R., Klem, D.E., Ogawa, A., Pestov, Yu.N., Pitthan, R. and Sugahara, R. 1983, Nucl. Instrum. and Methods 206, 99.

Bagge, E.R., Samorski, M. and Stamm, W. 1979, Proc. 16th ICRC (Kyoto) 13, 260.

Bassi, P., Clark, G. and Rossi, B. 1953, Phys. Rev. 92, 441.

Clark, G., Earl, J., Kraushaar, W., Linsley, J., Rossi, B. and Scherb, F. 1961, Phys. Rev. 122, 637.

Clay, R.W. and Dawson, B.R. 1984, Aust. J. Phys. 37, 309.

Cocconi, G. 1984, private communication.

Fedotovich, G.V., Pestov, Yu.N. and Putilin, K.N. 1982, Proc. International Conference on Instrumentation for Colliding Beam Physics, SLAC-Report 250 (Stanford University, Stanford CA) p. 127.

Linsley, J. and Scarsi, L. 1962, Phys. Rev. 128, 2384.

Lloyd-Evans, J. 1982, Thesis, University of Leeds.

McDonald, D.M., Clay, R.W. and Prescott, J.R. 1977, Proc. 15th ICRC (Plovdiv) 8, 228.

Ogawa, A., Atwood, W.B., Fujiwara, N., Pestov, Yu.N., and Sugahara, R. 1984, IEEE Transactions on Nuclear Science NS-31, 121.

Woidneck, C.P. and Böhm, E. 1975, J. Phys. A 8, 997.

ASTROPHYSICAL APPLICATIONS OF HIGH ANGULAR RESOLUTION ARRAY-TELESCOPES

John Linsley
Department of Physics and Astronomy
University of New Mexico, Albuquerque, NM 87131
USA

ABSTRACT

The air shower array-telescopes which are currently being used to search for and study point sources of UHE γ-rays have angular resolution ∿ 1°, limited by either the small total area of particle detectors or poor timing resolution. As the signal to noise ratio depends sensitively on the angular resolution, it seems certain that this figure will quickly be surpassed when second generation instruments come into operation. Since the trajectories of galactic cosmic rays with $E > 10^5$ GeV are practically straight lines on scales of 1 A.U. or less, these new instruments will be able to observe a shadow cast by the moon (angular diameter 0.5°). Although the angular diameter of the sun is practically the same, its 'shadow' will be more complex because of its magnetic field. Thus, high angular resolution observations of the sun afford a means of investigating the solar magnetic field, and also the charge composition of cosmic rays, including the ratio of antiprotons to protons.

1. Introduction. The first search for point sources of air shower primaries using fast timing to measure the individual arrival directions was made by Clark, using an array of four 0.13 m^2 scintillators located on the roof of the physics building at MIT. In reporting the results of this search he commented, "The sun and moon must cast a 'shadow' in the flux of high energy primary cosmic rays, and observations of this shadow effect might give new information about the magnetic fields of these bodies." (Clark 1957) With detectors of this size, and the best available electronics, the angular resolution (resolution in zenith angle, θ) was 4°; with a sample of 2660 events no statistically significant evidence of point sources was found. Studies made in the past 3 decades have shown that the sun's large scale magnetic field is weaker than it was thought to be in 1957, and have shown that it is not a simple dipole field. Nevertheless, there is no doubt that the shadow of the sun will show effects of the kind that Clark anticipated. It is known now that the moon has no magnetic field. Therefore the shadow of the moon predicted by Clark will be simply a geometrical shadow.

Regarding the sun, it is still not possible to predict quantitatively, with certainty, what effects will be observed. On the one hand, there is uncertainty about the magnetic field of the sun. "At the present time, very little is known about the actual magnetic field configuration and its changes", according to Zirker, writing in 1981. On the other hand, there is uncertainty about the charge composition of the cosmic rays that produce air showers. One would prefer to address these uncertainties one at a time, but having to deal simultaneously with two interlocking problems is common enough in cosmic ray studies. Despite the complexity some preliminary estimates will be made.

2. The method. The essential variables are:

1) The deficit in counting rate, which determines the statistical errors. This depends on the area A of the array-telescope and the energy E of the cosmic rays. (This is in a regime where E and cp are indistinguishable.)

2) The angular resolution of the array-telescope, and

3) The magnetic deflection.

Regardless of magnetic effects, the counting rate deficit due to particles intercepted by the sun or moon will equal $JA\Omega$, where J is the intensity and $\Omega = 5 \cdot 10^{-7}$ steradian is the solid angle subtended by either of these bodies (Liouville's theorem). I will assume $A = 10^4$ m^2 for second generation array-telescopes. Then using the observed all particle cosmic ray energy spectrum, for primary energy 10^4, 10^5, 10^6 GeV the rate in question amounts to 80,000, 1,500, and 30 counts per year, respectively.

From an analysis of the statistical limitations on the angular resolution of array-telescopes it seems that an accuracy of 5 mrad at 10^6 GeV will be attained in the next few years by second generation instruments. The corresponding practical limits at 10^4 and 10^5 GeV are estimated to be 20 and 10 mrad, respectively. Achieving further improvement will have to await development of large area detectors capable of a much faster response than scintillators (conference paper OG9.6-5). For comparison, the accuracy of direction measurements in a proposed space station magnetic spectrometer facility will be 0.02 mrad (Müller 1985). Thus one can be fairly certain of detecting the shadow of the moon at 10^5 and 10^6 GeV with second generation resolution, but detection at 10^4 GeV seems doubtful, even with the more favorable counting rate.

The arrival direction of cosmic rays affected by the solar magnetic field will also be affected by the interplanetary magnetic field and the geomagnetic field. The latter fields will modify the arrival direction of cosmic rays grazing the moon. To estimate these effects I will use the relation

$$\theta = \frac{300Z}{E} \int B_{\perp} d\ell \ , \qquad (1)$$

where θ is the angular deflection (radian) in a given plane, produced by the perpendicular magnetic field $B_{\perp}$ (gauss) in a region covered by the integration, acting on a cosmic ray with charge number Z and energy E (eV). This holds when θ is not too large. In case of the earth one can use Störmer theory. Here I will use a Störmer-theory calculation of equatorial-plane orbits for illustrating approximately how cosmic ray orbits will be affected by the large-scale solar magnetic field. The illustration is valid to the extent that the heliomagnetic field varies as $1/R^3$ over a sufficient range of distances from the sun.

3. The geomagnetic effect. In this case the field integral is approximately $6 \cdot 10^7$ gauss cm (= 0.1 gauss x $R_{\oplus}$). It is noteworthy that this is nearly 2 orders of magnitude greater than for the spectrometer mentioned above. Substituting in (1), one finds that the deflection will be undetectable using array-telescopes except possibly for Fe nuclei at 10^4 GeV.

4. The effect of the interplanetary magnetic field. Assuming $B_{\perp} = 5 \cdot 10^{-6}$ gauss (Ness 1965), one finds that in case of travel from the moon the

effect will be completely negligible. For travel from the sun, the magnetic field integral will be $\sim 10^8$ gauss cm, so as in the geomagnetic case, the effect will be negligible except for 10^4 GeV Fe nuclei.

5. The heliomagnetic effect. The heliomagnetic field consists of a hierarchy of structures, the largest of which are called active regions. Typical data, given in Table 1, imply values of the magnetic field integral of order $1\text{-}2 \cdot 10^{11}$ gauss cm over regions with a size of order $R_\odot$, so by a simple scaling argument, comparing the sun with the earth, one expects sizable effects up to proton energies of 10^5-10^6 GeV, and correspondingly higher energies for Fe nuclei. Table 1 shows that above large active regions the field strength decreases with increasing distance about as $1/R^3$, so to at least a crude approximation the field can be modeled as a dipole. Fig. 1 shows trajectories of 20 GeV protons in the equatorial plane of the earth (Hillas 1972). The apparent location of the occulting object for an observer at infinity using protons or antiprotons is also shown. According to Störmer theory the same picture applies to the sun, when its field is approximated by a dipole, provided that the particle energy is scaled upward by a factor $(M_\odot/M_\oplus)^{\frac{1}{2}}$, where M denotes magnetic dipole moment. Choosing $M_\odot = 3 \cdot 10^{32}$ gauss cm, so that the equatorial surface field will be about 1 gauss, the scale factor comes out 2000. Hence Fig. 1 also illustrates the behavior of $4 \cdot 10^4$ GeV protons, or 10^6 GeV Fe nuclei, in the vicinity of the sun. Again using Störmer theory, the same picture can be applied to higher energy particles by drawing larger circles to represent the limb of the occulting sphere, the radius being proportional to $\sqrt{E}$. It appears by inspection of the figure that the proton and antiproton images will be separated adequately up to about 10^5 GeV.

Table 1. Magnetic field strength (gauss) vs height (solar radii) above active regions (Dulk and McLean 1978).

height	B
1.02	300
1.1	10
2	0.5
5	0.05

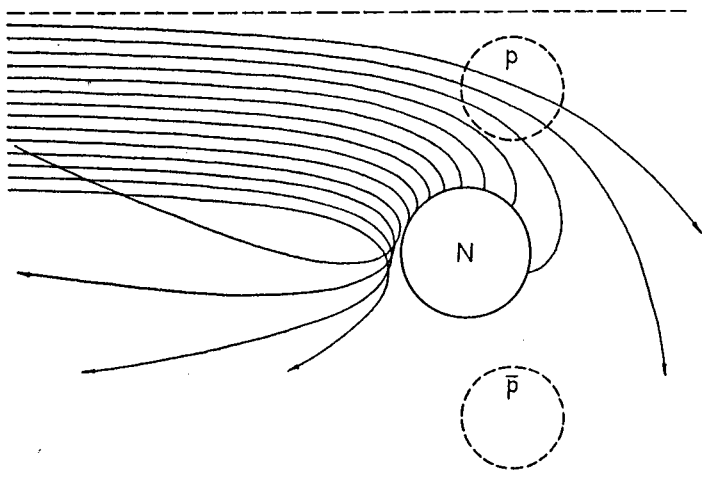

Fig. 1. Trajectories of charged particles in the equatorial plane of the earth's field, with asymptotic direction indicated by the dashed line, and equally spaced impact parameters (Hillas 1972). The solid circle represents the real location of the equator; the dashed circles, the apparent location of the occulting object for protons (p) and antiprotons ($\bar{p}$) at infinity.

6. Conclusions. Using second generation array-telescopes which I assume will have resolving power of 10 mrad at 10^5 GeV and 5 mrad at 10^6 GeV, it appears that the following can be done:

1) Detect the cosmic ray shadow of the moon. This will be a simple geometrical shadow, undisplaced and undistorted. The detailed character of the shadow will provide an independent test of the instrumental resolution of whatever array is used.

2) Detect the cosmic ray shadow of the sun. This shadow will be complex, made up of partial shadows corresponding to primary charges Z = 1, 2, ... The partial shadows will be displaced from the true direction of the sun through angles proportional to Z/E. The larger the angular displacement, the more these partial shadows will be enlarged and distorted. Hence, partial shadows will only be discernable when they are near the true sun; otherwise they will blend into the background.

3) *identify the partial shadows belonging to primary protons, alpha particles, and principal charge groups through Fe, and thus measure the cosmic ray charge spectrum for a fixed rigidity of about 10^5 GeV/c.* The identification can be done in an empirical manner, with only crude information about the strength and character of the heliomagnetic field. At an energy a factor 2-3 lower than pictured in Fig. 1 (and all still lower energies) there will be no discernable shadow, because even the proton shadow will blend with the background. As one goes to higher energies, *the first shadow to appear will be the proton shadow.* As E is increased further, the proton shadow will move inward until it lies in the direction of the true sun. As this happens the shadows belonging to Z = 2 and more will successively, for the appropriate value of E, occupy the position where the proton shadow lies in Fig. 2.

4) measure the antiproton abundance up to $\sim 10^6$, where according to some models the fraction of antiprotons is nearly 0.5 (Stecker and Wolfendale 1984).

Acknowledgement. The stimulus for giving attention to the solar-lunar shadows at this time came from Alan Watson, to whom the idea had occurred independently. (I had forgotten about Clark's early comment until I stumbled across it again a short time ago.) I am grateful to Jeremy Lloyd-Evans for discussions and an opportunity to compare my conclusions with some of his, derived from independent work he has been doing on this problem recently.

References.

Clark, G.W. 1957, Phys. Rev. 108, 450.
Dulk, G.A. and McLean, F.B. 1978, Solar Phys. 57, 279.
Hillas, A.M. 1972, in *Cosmic Rays* (Pergamon Press: Oxford) p. 17.
Müller, D. 1985, *A Magnet Spectrometer Facility: Rationale and Science Themes*, preprint.
Ness, N.F. 1965, Proc. 9th ICRC (London) 1, 14.
Stecker, F. and Wolfendale, A.W. 1984, Nature 309, 37.
Zirker, J. 1981, in *The Sun as a Star*, ed. S. Jordan (NASA publication SP-450) p. 135.

ANGULAR RESOLUTION OF AN EAS ARRAY FOR GAMMA RAY ASTRONOMY AT ENERGIES $> 5 \times 10^{13}$ eV

Apte, A.R., Gopalakrishnan, N.V., Tonwar, S.C., and Uma, V.

Tata Institute of Fundamental Research
Homi Bhabha Marg, Colaba, Bombay-400 005
India

ABSTRACT

A 24 detector extensive air shower array is being operated at Ootacamund (2300 m altitude, 11.4°N latitude) in southern India for a study of arrival directions of showers of energies greater than 5×10^{13} eV. Various configurations of the array of detectors have been used to estimate the accuracy in determination of arrival angle of showers with such an array. These studies show that it is possible to achieve an angular resolution of better than 2° with the Ooty array for search for point sources of Cosmic gamma rays at energies above 5×10^{13} eV.

1. INTRODUCTION

Interstellar magnetic field causes charged particle trajectories to be tortuous and uncertain for all but the most energetic particles. Therefore information on the highest energy processes occurring in astrophysics can be obtained only from studies of high energy gamma ray photons which travel unscattered and practically unabso -rbed through great lengths of galactic and intergalactic space. Observa -tions at energies less than about 10^{10} eV have been carried out with satellite borne instruments which can discriminate efficiently between photons from a source and the isotropic charged particle background. However, studies of photons of energies above 10^{11} eV require very large effective collection areas which are possible with only ground based techniques. Atmospheric Cerenkov radiation technique has been successful for energies above 10^{11} eV and studies of extensive air showers have been carried out to detect sources of very high energy photons of energi -es above 10^{14} eV. Since most of the Cerenkov photons are produced in the atmosphere near the cascade maximum and suffer negligible scattering before arriving at the detectors placed at sea level or mountain altitude relative timing techniques using detectors spaced few tens of meters apart enable the determination of arrival direction of individual showers to an accuracy[1] of better than about 0.5°. Such good angular resolution of an atmospheric Cerenkov radiation (ACR) telescope allows observation of a small angular region around the suspected source of high energy photons enabling achievement of a large value for the signal to backgrou -nd (S/B) ratio. Studies of extensive air showers (EAS), on the other hand, involve detection of electrons which suffer considerable scattering in the atmosphere. It is therefore expected that angular resolution of an EAS telescope would be much poorer compared to an ACR telescope. However no detailed and systematic studies exist on the possible angular

resolution that can be achieved with an air shower array at various energies above 10^{14} eV. In fact, various angular size bins have been used in different experiments[2,3,4] based on approximate estimates of angular resolution of respective arrays, which leads to widely varying values of the S/B ratio causing uncertainities in the estimates of flux of high energy photons from a suspected source.

Since June '84, we have operated an EAS array at Ootacamund (Ooty for short, 2200 m altitude, 11.4° N latitude) in southern India for study of sources of high energy Cosmic ray photons. With data from this experiment we have studied in various ways the time resolution of air shower detectors and the angular resolution achievable with this array. In the next section are presented the details of the array, shower selection and recording system. The observed time resolution of EAS detectors is discussed in section 3 and in section 4 are presented the results on angular resolution achieved with Ooty array for showers of energies $> 5 \times 10^{13}$ eV. The conclusions drawn from this study are given in the last section.

2. EXPERIMENTAL SYSTEM

The EAS array at Ooty consists of 24 scintillation detect-ors of various sizes spread over an area of radius of about 40 meters. 20 detectors are plastic scintillators, each 5 cm thick and the other four called N,E,W, and S,are liquid scintillators using 10 cm thick column of mineral oil. These four scintillation detectors are only used for selection of showers through a 4-fold coincidence called NEWS. These four detectors are located at the corners of an approximate square around the centre of side length of about 10 m (see figure 1 of paper OG 2.6-8). All the scintillators are viewed by 5 cm diameter fast photomultipliers (RCA 8575) placed some distance above the scintillator giving about 10% uniformity in signal over the area of the scintillator. Showers are first selected with a four fold coincidence of 100 ns wide pulses obtained from discriminators (LRS 623B) for N,E,W, andS. The thresholds for the discriminators have been set at 30 mV while the mean pulse amplitude for near vertical muons is about 100 mV for these detectors. However, this selection with an observed shower rate of about 30 per minute selects many very small size showers which do not trigger many of the other 20 detectors. Since the angular resolution is expected to depend on the number of detectors available for determinat-ion of shower arrival direction, showers which trigger only few detectors are not considered to be useful for studies of Cosmic gamma ray sources. In an attempt to optimise the selection of showers which trigger a large number of detectors but at the same time keeping the shower size threshold lower, an additional requirement of at least 3 particles in one of the four selection detectors is included in the final shower trigger. Observed shower rate with this final trigger is about 7 per minute. Each such trigger causes the digitization of the charge collected at the anode for each photomultiplier using fast ADC's (LRS 2248A) and the digitization of the relative delay between the trigger and the output from discriminators for each detector with an accuracy of 0.25 ns by using fast TDC's (LRS 2228A). Pulses from the photomultipliers going to the discriminators are amplified with gain 10 (LRS 612A) to keep the effective threshold low while obtaining a good

charge measurement for single particles with the ADC's. For each shower information from all the ADC and TDC channels is transferred to a memory buffer preceding a magnetic tape recording system such that the system can record all the details of showers coming as close as 1.5 ms relative to each other. Real time information is read for each shower from a clock running on a crystal with stability of about 1 part in 10^9 per day which is corrected periodically with ATA time signals broadcast from New Delhi. Data collected on magtape at Ooty are then analysed at Bombay using the CYBER 170/730 computer system at the Tata Institute.

3. TIME RESOLUTION OF EAS DETECTORS

The inherent time resolution of particle detection system used in the present experiment is contributed by the rise time and time jitter in the photomultiplier, amplifier, discriminator and the TDC apart from the scintillator and photon reflections inthe hood on which the photomultiplier is mounted. This resolution has been measured experimentally by mounting two photomultipliers on the same scintillator. The relative time measured between these two channels for showers has a distribution with standard deviation (σ) of about 1 ns which seems to depend only weakly on the particle density over the detector. However the distribution of the relative time between two detectors (N and 6) which are located within 2 m of each other is much broader reflecting the thickness of the shower disk. It is this distribution which is relevant for estimating the accuracy in the determination of arrival angle of showers. The standard deviation for this distribution is 5.2 ns for particle densities of less than 5 particles m^{-2} and 3.8 ns for larger densities. Correcting for the angular distribution of showers and the distance between these two detectors, it is clear that the minimum uncertainity in time measurement by individual detectors, at least for low size showers is about 3 ns. Therefore an EAS array with largest distance span of about 20 m between timing detectors, for example the EAS array at Kiel[2], can hardly achieve an angular resolution better than about 3° for small size showers.

4. ANGULAR RESOLUTION OF OOTY EAS ARRAY

Sine timing information from 24 detectors is available for getting a best fit to a plane shower front passing through all these detectors, it is possible to reduce the effect of timing fluctuations discussed above and achieve a better abgular resolution. In an attempt to estimate the angular resolution of the array, data have been analysed using different sets of detectors and the values of right ascension and declination are compared. In the first instance, the array is split into two arrays, one with odd numbered detectors and the other with even numbered detectors. RA and δ are computed independently with the two arrays. The distribution of the differences between the two RA values as well as the distribution of the differences between the two δ values, show a broad symmetric distribution with σ of about 3°. This suggests a value for σ of about 2° for each sub-array. Another study has been made by comparing the RA and δ values for two arrays, one with all the 20 detectors (excluding the timing selection and reference detectors N,E,W,and S) and the other with only inner 9 detectors. The value of σ for the distribution of the difference in RA values as well as the distribution of the difference in δ values is about 2°. This result suggests that the angular resolution for the array using all the 20

detectors is much better, assuming that the array with only inner 9 detectors has a resolution of about 2°.

These results have been obtained using only those showers which have triggered all the 24 detectors, evidently a sample of some what larger size showers. However similar results have been obtained using showers which have triggered only inner 15 detectors. It should also be noted that showers selected in the manner discussed earlier have on the average 20 out of 24 detectors triggered and nearly 80% of the showers have timing information available from at least 15 out of the 20 detectors, ignoring the selection detectors. The energy threshold for showers triggering at least 15 out of 20 detectors is estimated to be about 5×10^{13} eV.

4. CONCLUSIONS

Ooty air shower array with 24 scintillation detectors, has been used to measure the arrival angles of showers using the relative timing technique. From the computed differences in the values of the right ascension and the declination for showers for various configura -tions of detectors used for calculation of arrival directions, it is estimated that the angular resolution of Ooty array is better than about 2° for showers of energies greater than about 5×10^{13} eV. Results from the search for sources of very high energy gamma rays using data collected with the Ooty array since June '84 is reported elsewhere (OG 2.6-8) in this Conference using the values of angular resolution obtained here.

ACKNOWLEDGEMENTS

It is a pleasure to thank Prof. B.V. Sreekantan for his encouragement and fruitful discussions.

References:

1. Gupta, S.K. et al., preprint (1985).
2. Samorski, M. and Stamm, W., Astrophys. J.(Letters) 268, L17(1983)
3. Lloyd-Evans, J., et al.,Nature 305, 784 (1983)
4. Morello, M.et al.,in 18th International Cosmic Ray Conference, Conference Papers, Bangalore, 1983, Vol.1, p.127

NOTE ON THE DETECTION OF HIGH ENERGY PRIMARY COSMIC GAMMA RAYS BY AIR SHOWER OBSERVATION

KASAHARA,K., TORII,S.*, AND YUDA,T.

Institute for Cosmic-Ray Research, University of Tokyo, Tanashi, Tokyo
**Kanagawa University, Rokkakubashi, Kanagawa*

Basic materials are given which are indispensable to searching for point sources of gamma rays in the PeV energy region by observing air showers. Advantage of a mountain level observation is stressed. The possibility that all the existing Cygnus X3 data for > PeV are of gamma ray origin seems not so high.

1. Introduction A mountain altitude experiment is being planned at Mt. Norikura ($735 g/cm^2$, latitude 36°) in a form capable of searching for point sources of astrophysical high energy gamma rays in the PeV energy region.

As well known, several groups[1] have reported observations of air showers exceeding PeV ($=10^{15}$ eV) energy that are supposed to be originated by particles coming from Cyg X3. Similar results[2] have also reported on Vela X1 and Crab pulsar. Gamma rays would be the only reasonable candidate which arrives at earth without being deflected from such objects and is detectable by air shower. Should they be other exotic particles, it is rather difficult to conceive such ones without abundant gamma rays.

However, the observations so far seem not to show the characteristics of air showers by gamma rays: for example, showers of the Kiel group contain as many muons as hadronic origin and a shower selection condition of s (age) > 1.1 does not put a substantial weight on gamma primaries. Akeno group selelcted muon poor showers but s is $\sim$ 1 which is, as gamma showers, so young that one may afraid of showers induced by protons penetrating deep in the atmosphere; the number of such showers might not be negligible as the angular resolution is $\Delta\theta \sim 10°$.

In confirming the existence of PeV energy gamma primaries from Cyg X3, in knowing their intensity and spectrum, and in searching for other similar point sources, mountain level observations have advantage. By assuming an observation at Mt. Norikura, we shall show it in many respects by using Monte-Carlo showers.

2. Characteristics of air showers in the PeV energy region Figure 1 shows a superposition of the transition of the number of electrons (size, N_e) of 1000 simulated air showers, each of which is generated by a 10^{15} eV gamma ray. The effective depths for zenith angles 0, 20, 30, and 45

degrees at observation depths 735 g/cm^2 (Mt. Norikura) and 927 g/cm^2 (say, Akeno) are indicated in the figure. It is to be noted that the fluctuation of the size is minimum at mountain levels.

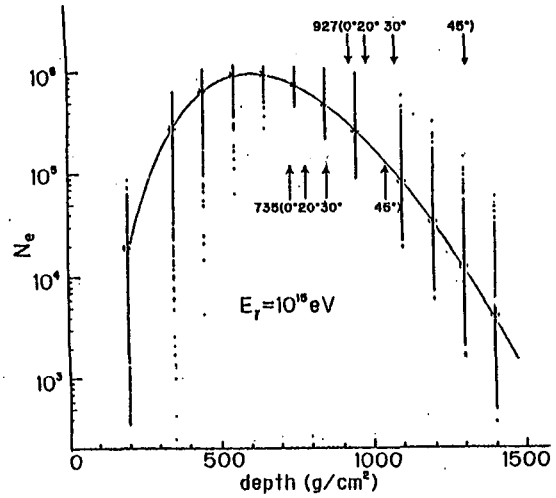

Fig.1 Transition of N_e by 10^{15}eV gamma primary in the atmosphere. 1000 showers are superposed. Effective depths for zenith angles 0,20,30,45^0 at 735 and 927 g/cm^2 are indicated.

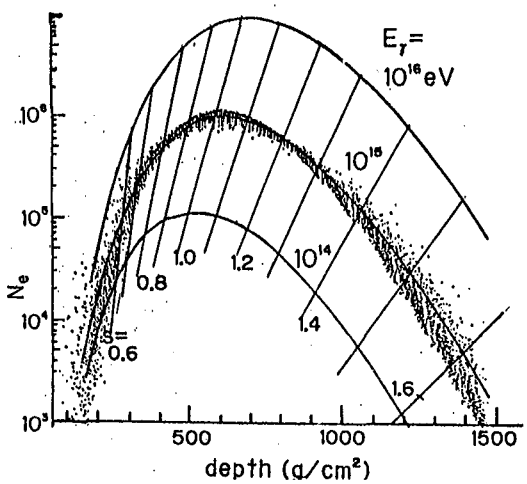

Fig.2 Showers in Fig.1 are superposed by reference to their centre of gravity. Solid lines show analytical result for average N_e and age s.

The apparent large fluctuation is reduced if the showers are shifted and superposed by reference to their centre of gravity (of which the average is 650 g/cm^2) as shown in Fig.2, i.e., each shower has almost the same shape very close to the simple average in Fig.1. The average transition of N_e and age parameter s under approximation B (analytical calculation) is also inlaid. The figure tells that there is almost a unique relation among the primary energy E_0 , N_e and s.

Figure 3 shows the distribution of s in the integral form. Note that the fitting of a lateral distribution by NKG function will result in a younger age than here. (see Ref.3). The distribution of the size can well be approximated by log-Gauss form at depth Z=600 to 1500 g/cm^2 and the dispersion is given by $\sigma=\Delta N_e/N_e \sim \sigma_0(Z\sec\theta-735)+\sigma_1$ (%) where $\sigma_0=-0.01\log_{10}(E_0/\mathrm{PeV})+0.04$ $g^{-1}cm^2$, $\sigma_1=-4\log_{10}(E_0/\mathrm{PeV})+10$ and θ is the zenith angle.

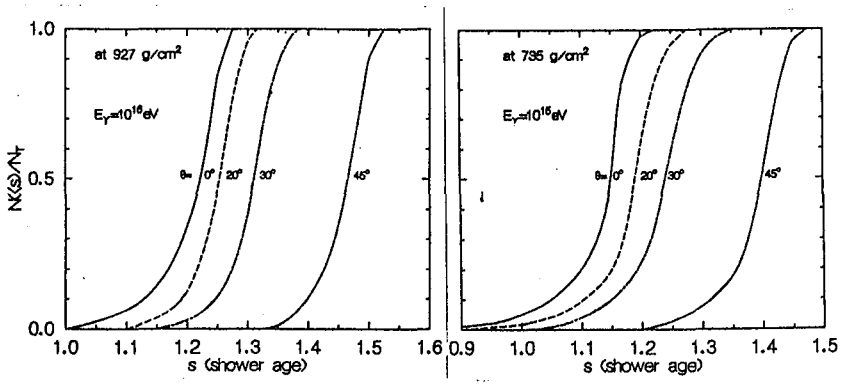

Fig.3 Normalized integral distribution of shower age s. 10^{16} eV primary (at 927 g/cm^2, left). and 10^{15}eV primary (at 735 g/cm^2, right). Parameters are the zenith angle.

To see characteristics of background showers, 1000 proton initiated showers at 10^{15} eV are superposed in Fig.4 as in Fig.1. The hadronic cases give lower maxima than the gamma case (denoted by dash in this fig.) by $\sim 1/1.5$, while at deeper depths they have larger values than the gamma. This means that the background intensity at mountain levels is $(\sim 1/1.5)^2 \sim$ 1/2 of the one at the near-sea-level depth.

3. Fast timing efficiency To know the arrival direction of air showers by fast timing (FT) technique within, say, $\Delta\theta \sim 1^\circ$ with time resolution of $\Delta t = 1 \sim 4$ ns, a certain number of electrons must fall in a detector at $r = 10 \sim 40$ m from the air shower centre. We require this number to be more than 30 at $r = 10$ m and 10 at $r = 20, 30, 40$ m. In figure 5 is shown the percentage of the showers that fill such conditions for a primary energy of 10^{15} eV and a 1 m^2 detector. The assumed lateral distribution is the one obtained by our Monte-Carlo calculation and is consistent with Ref. 3.

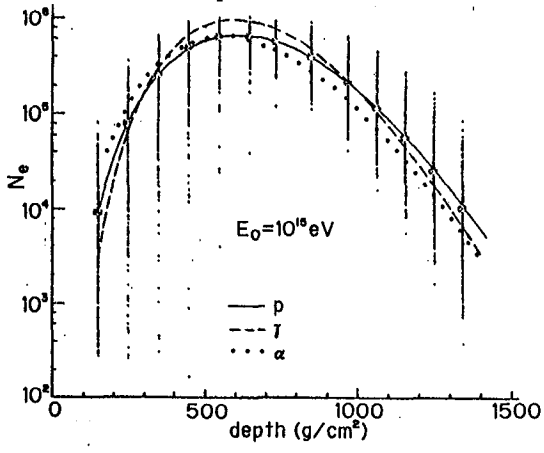

Fig.4 Transition of Ne by 10^{15} eV protons. 1000 showers are superposed. Solid line is average. Average curve by gamma and alfa of the same energy is shown by dash and dot, respectively.

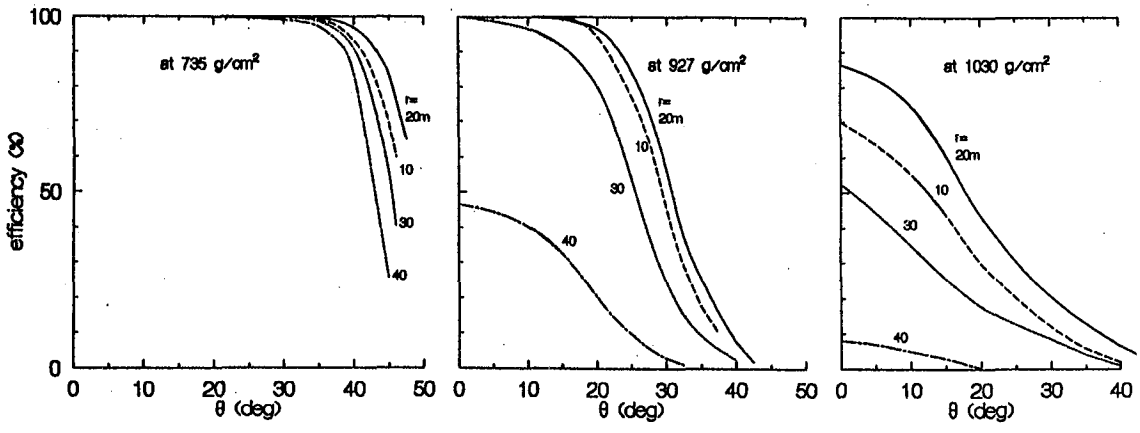

Fig.5 Percentage of showers that satisfy $N_e/m^2 > 30$ at r=10 m from the air shower core, or $N_e/m^2 > 10$ at r=20, 30, or 40 m as a function of zenith angle for primary of 10^{15}eV.

The threshold energy as seen from FT is about 0.3, 1, 3 PeV for depths 735, 930, 1030 g/cm^2, respectively. An energy three times higher than this would be needed for high quality data at the respective depth.

4. Background showers Assuming an appropriate primary cosmic ray spectra above 70 TeV with compositions ranging from protons to irons, background showers of hadronic origin are computed and the size distribution is shown in Fig.6 where the angular resolution is assumed to

be $\Delta\theta=1^\circ$ ($=2\sigma$). No cut by muon number or age is imposed here. For reference, the size distribution by primary gamma rays with an energy spectrum $E^{-\beta-1}*(1+E/E_c)^{\beta-\gamma}dE$ is also shown, where $\beta=1, \gamma=2, E_c=10^{16}$ eV and the intensity is adjusted to be compatible with the Cyg X3 observation so far. Cut by the age would not be effective for reducing the background; muon number cut will be needed for further reduction.

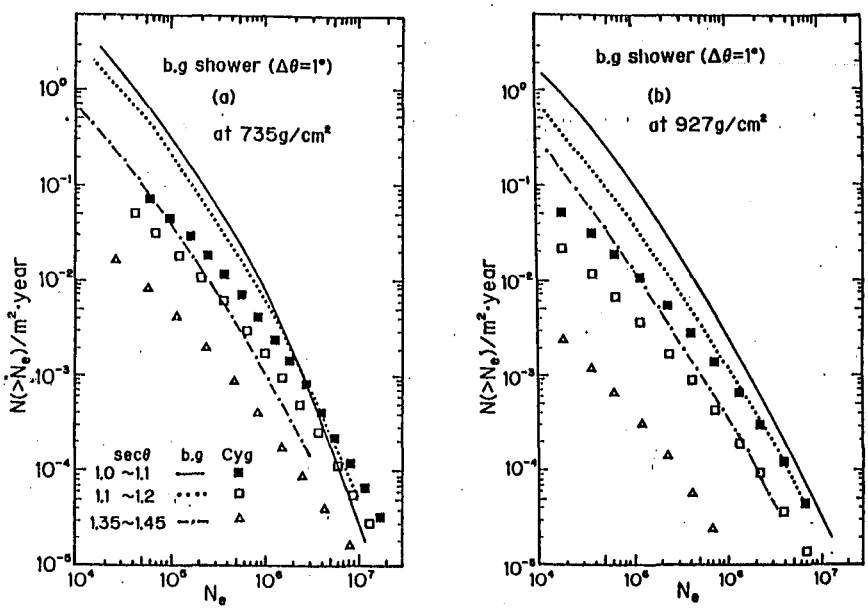

Fig.6 Integral shower size distribution by background hadrons. Solid line for secθ=1~1.1, dot 1.1~1.2, dot-dash 1.35~1.45. $\Delta\theta=1^\circ$ is assumed. At 735 g/cm^2 (left) and 927 g/cm^2 (right). For reference, a model of signals from Cyg X3 is also shown by symbols in respective range of θ.

5. On the determination of energy and intensity. To determine the primary energy at a near-sea-level, we need accurate age which, however, cannot be obtained easily in the experiment. In this sense, mountain level observation has advantage because of small size fluctuation for a given primary energy. If a size is determined, it's primary energy is estimated by $\langle E_0\rangle\sim 0.14\exp((Z/735+\sec\theta-2)/0.27)\times(N_e/10^5)^{0.84}$ (PeV) with an error, $\sigma=\Delta E/E\sim 9\exp((Z/735+\sec\theta-2)/0.46)\times(E/\mathrm{PeV})^{-0.15}$ (%) A special care must be paid to deriving the primary intensity because the detection efficiency changes from 0 to 100 % in a narrow range of primary energy around PeV, if the detection threshold is set by a constant value of the size (say, $10^5\sim 5\times 10^5$).

FACOM M380 of INS was used for the present simulation.

References

1. M.Samorsky and W.Stamm, Ap.J.,268,L17(1983).
J.Lloyd-Evans etal Nature, 305, 784(1983).
T.Kifune etal, this conference.
2. J.Boon etal, 18th ICRC, Bangalore, XG 57(1983).
R.J.Protherore and P.R.Gerhardy, Ap.J.,Lett., 280,L47(1984).
3. M.Hillas and J.Lapikens, 15th ICRC, Plovdiv, 8,460(1977).
A.A.Lagutin etal, 16th ICRC, Kyoto, 7,18(1979).

ON THE STATISTICAL SIGNIFICANCE OF EXCESS EVENTS - REMARKS OF CAUTION AND THE NEED FOR A STANDARD METHOD OF CALCULATION

R. Staubert
Astronomisches Institut der Universität Tübingen, Tübingen, Germany

ABSTRACT

Methods for calculating the statistical significance of excess events and the interpretation of the formally derived values are discussed. It is argued that a simple formula for a conservative estimate should generally be used in order to provide a common understanding of quoted values.

1. Introduction. Substantial nonuniformity exists in the cosmic ray literature with respect to how the statistical significance of features or excess events is being calculated (e.g. point sources, spectral lines, light curves). Consequently, there is no mutual understanding about what the confidence in some result might really be when a number of 'standard deviations' are being quoted. Some of the proposed procedures for calculation need to be taken with caution. On the other hand, there is a clear need for the adoption of a standard method to allow the reliable intercomparison of quoted results and create a common understanding of the associated confidence.

A number of methods and formulae have been proposed together with sometimes extended mathematical derivation or justification (Ref. 1-4). It has become clear however, that some of these methods need to be taken with caution. On the other hand there is a very simple formula which is being widely used by X-ray astronomers providing a common understanding.

2. Statistical Significance. An example for the statistical situation which we like to discuss is given in Figure 1.

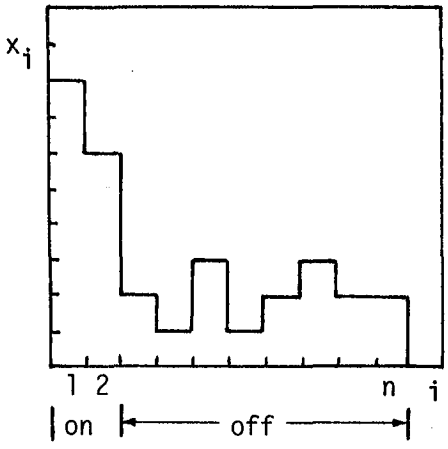

Fig. 1. Statistical example.

Numbers of events x_i are plotted versus bin number $i = 1....n$, corresponding to intervals of some physical variable (e.g. energy, phase, electric charge, time, ...). In the example given there seem to be 'excess events' in bins 1 and 2 as compared to the 'background' defined by the other bins. The excess is

$$\text{ON} - \alpha\,\text{OFF},$$

when ON and OFF are the integrated counts in channels 1 to 2 and in channels 3 to n, respectively and α is the ratio of the corresponding number of bins, here $2/(n-2)$.

The general questions then are:
1. Does the excess correspond to the presence of a physical signal?
2. What is the 'significance of the signal'?

It is important to distinguish between these two questions. They correspond to the assumption that one out of two alternative hypothesis is true:
- the null hypothesis H0 is, that there really is only background,
- the hypothesis H1 is, that a true signal exists in addition to background.
When a statement is made about a statistical situation, it should be clear under which hypothesis this statement holds.

The first of the two questions may be answered by giving the probability for a chance occurance of the observed excess by a statistical fluctuation (under H0). It is of course necessary to use the proper statistic (e.g. binomial statistic for small numbers of events). If a low probability for the chance occurance of 'excess events' is found, it is then usually concluded that the presence of a 'physical signal' is likely. From there on hypothesis one is advocated and all statements made should refer to H1.

Only under H1 the term significance should be used. In particular the often used formula $(ON - \alpha OFF)/\alpha\sqrt{OFF}$ is useless (as are a number of other formulae, see e.g. (4)). Also the probability which answers the first question should not be converted into a significance (as is sometimes done by using the integrated Gaussian distribution, even in cases where the Gaussian statistic does not apply).

In answering the second question then the presence of a signal is assumed (H1). The 'significance of the signal' k can be defined as the ratio of the best estimate of the signal to its uncertainty. In the case of Poissonian counting statistic for which the variance is equal to the mean a straightforward error propagation leads to the well known formula (in terms of the above defined variables):

$$\text{'significance'} \quad k = \frac{ON - \alpha OFF}{\sqrt{ON + \alpha^2 OFF}} \qquad [1]$$

in units of standard deviations σ (see Ref. (3,5,6,7); note that in (3) this formula is interpreted incorrectly). Formula [1] may be also derived by using the more complicated maximum likelyhood ratio (6).

A general criticism of the work of (3) and to some extent of (1) and (2) is given in (6). While it is very important, not to overestimate statistical significance, Ref. (3) does too much, leading to an underestimate.

More recently, (5) has contributed significantly to the confusion by trying to show that formula [1] is incorrect and should be replaced by another complicated formula. The main argument is that the new formula fits much better to Monte Carlo simulations than formula [1] does. The whole discussion is misleading and suffers from the fact that no distinction between H1 and H0 is made: while formula [1] refers to H1 the Monte Carlo simulations as well as the new formula refer to H0, so their distributions are necessarily different.

For the example given in Fig. 1 (with a unit of 1 for the scale of counts x_i) the two questions can be answered as follows:

1. The probability (under H0) for a chance occurance of 14 events in bins 1 and 2 whith an average rate of 6 in two bins is $\lesssim 10^{-3}$, using binomial statistic (note that Poissonian statistic gives the somewhat larger probability of 3.6×10^{-3}).
2. If one feels that the probability of 10^{-3} is low enough to postulate the existence of a physical signal (H1), then the significance of this signal is

$$k = \frac{14 - (2/10)\ 16}{\sqrt{14 + (2/10)^2\ 16}} = 2.6 \text{ standard deviations.}$$

To put it in other words again we consider Figure 2.

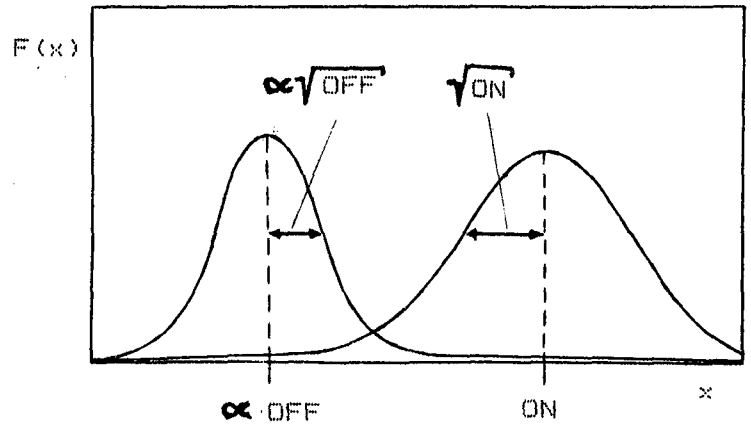

Figure 2. Representation of event number distributions.

If the signal ON - α OFF is compared to the standard deviation of the background $\alpha\sqrt{OFF}$, one gets an estimate for the chance occurance under the null hypothesis H0.
If, on the other hand, ON - α OFF is compared to both the standard deviations of the background and the signal, as is done by formula [1] under H1, one gets a different estimate. This is related to the probability that a second measurement (under identical conditions) will lead to a null result (ON $\leqslant \alpha$ OFF). It is this estimate that should be called 'significance of the detected signal'.

3. Final remarks

Values of significances in units of standard deviations are usually quoted when the detection of some signal is claimed. Consequently, a formula refering to H1 (existence of a signal) should be used.

Formula [1] has been widely adopted by X-ray astronomers and has as such served successfully as a standard allowing the reliable intercomparison of stated values of significance. It is up to the individual from what level of significance onward one starts to 'believe' in some reported result. Our personal view is that using formula [1] a minimum significance of 3 standard deviations (better yet 5) should be reached.

References

1. Hearn, D. 1969, Nucl.Instr.Methods 79, 200
2. O'Mongain, E. 1973, Nature 241, 376
3. Cherry, M.L. et al. 1980, Ap.J. 242, 1257
4. Li, T.P. and Ma, Y.Q. 1983, Ap.J. 272, 317
5. Li, T.P. and Ma, Y.Q. 1983, Proc.18th Int.Cosmic Ray Conf., Bangalore, XG 3-7, p.76
6. Nolan, P.L. 1982, preprint UCSD SP-82-15
7. Peterson, L. 1975, ARAA 13, 423

A NEW APPROACH TO EVALUATE GAMMA-RAY MEASUREMENTS

De Jager O.C., J.W.H. Swanepoel*, B.C. Raubenheimer and D.J. van der Walt.

PU-CSIR Cosmic ray Research Unit; PU for CHE; 2520 Potchefstroom; SOUTH AFRICA

* Dept of Statistics; PU for CHE; 2520 Potchefstroom; SOUTH AFRICA

ABSTRACT: Misunderstanding about the term "random samples" and its implications may easily arise. Conditions under which the phases, obtained from arrival times, do not form a random sample and the dangers involved are discussed. Watson's U^2 test for uniformity is recommended for light curves with duty cycles larger than 10%. Under certain conditions, non-parametric density estimation may be used to determine estimates of the true light curve and its parameters.

1. INTRODUCTION: Consider a series of arrival times t_i $i=1,...,N$, of γ-rays from a certain source direction. The case is studied where the data contains a periodic component of strength p (pulsed counts/total counts) and period T. In the case of detectors with low count rates, the obvious requirement is to determine the significance of p as being due to a periodic source against the possibility that it is only a statistical fluctuation from the uniform background. The deduction of a possible light curve is also important. In this paper the following points are covered: (1) the problem of "random samples", (2) tests for uniformity, (3) non-parametric density estimators of the true periodic light curve and (4) the determination of the light curve parameters from the non-parametric density estimator.

2. THE PROBLEM OF "RANDOM SAMPLES": The measured data are the arrival times with the property $t_i > t_{i-1}$ $(i=2,...,N)$. Assume this process, apart from the periodic component in the data, to be time independent. It is desirable to estimate the true light curve from the arrival times. This is done by folding the t_i's modulo 2π, with respect to a known period T. This results in the "sample" $(\theta_1,...,\theta_N)$, with θ_i the so called phases which are calculated as

$$\theta_i = \frac{2\pi t_i}{T} \pmod{2\pi} = 2\pi\left|\frac{t_i}{T} - k\right|, \quad i = 1, \ldots, N, \; k \in \mathbb{N}^+ \qquad (1)$$

The choice of 2π is to allow the application of trigonometric functions on the phases. This sample has mostly been treated as being random. This sample would be random if and only if (a) all the θ_i's are identically djstributed and (b) if they are statistically independent. If the phases do not form a random sample, then no conclusions about the "true underlying light curve" can be made. The fact is that the phases do not form a random sample! This can be seen as follows:

From eq. (1) the probability density functions (p.d.f) of θ_i and t_i are related by the following wrapping process (Mardia, 1972):

$$f_{\theta_i}(\theta) = \frac{T}{2\pi} \sum_{k=0}^{\infty} f_{t_i}\left(\frac{\theta T}{2\pi} + Tk\right) \qquad (2)$$

Since $t_i > t_{i-1}$, it follows that $f_{\theta_i}(\theta) \neq f_{\theta_j}(\theta)$ for every θ and all $i \neq j$, thus proving that the θ_i's are not identically distributed. Furthermore $t_i = t_{i-1} + (t_i - t_{i-1})$, which implies that t_i is a function of t_{i-1}. Since θ_i is a function of t_i, it follows that θ_i is also a function of θ_{i-1}. This shows that the phases are not independently distributed. It should however be noted that if the time differences $v_i = t_i - t_{i-1}$ are used, a random sample would result by folding the v_i's.

From simulations of arrival times the following seems evident (let $b = E(t_i - t_{i-1}) \equiv 1/\text{count rate}$): The distributions become approximately identical when $T < b$. If $T \approx b$, then it suffices to add a constant large time to each t_i, so that $t_1 >> 0$. This will ensure almost identically distributed random phases. If the period T equals the whole period of observation ($T >> b$), then

$$\theta_i = \frac{2\pi t_i}{T} \quad \text{and} \quad f_{\theta_i}(0) = \frac{T}{2\pi} f_{t_i}(0) \qquad (3)$$

so that the phases are not identically distributed. The "runs-test" (Lindgren, 1976) was used to determine whether the phases are independently distributed: For $T < b$, the phases seem to be independent random variables and for $T >> b$ there was strong evidence for dependency, which is also clear from eq. (3). Independency can with a 10% uncertainty be accepted for $T < 3b$. This result seems to be independent of the pulsed fraction.

Thus, for T>3b, the true light curve cannot be estimated. In γ-ray astronomy this problem amounts to the case of astrophysical objects with periods that is large in comparison with b.

3. TESTS FOR UNIFORMITY: Let θ be a random variable with p.d.f. f(θ), which is assumed to be unknown. An appropriate test in this case would be some non-parametric test:

$$H_o: f(\theta) = U(\theta) = 1/2\pi \text{ against } H_1: f(\theta) \neq U(\theta) \qquad (4)$$

The alternative hypothesis H_1 only suggests that the unknown p.d.f. is different from uniformity. In order to compare tests, the following general form of f(θ), which covers most cases in γ-ray astronomy, was assumed:

$$f(\theta) = p_1 S(\theta;\ \mu_1,\ \delta_1) + p_2 S(\theta;\ \mu_2,\ \delta_2) + \frac{1-p_1-p_2}{2\pi} \qquad (5)$$

The pulsed fraction and phase (mean position) of each peak are denoted for i=1,2 by p_i and μ_i respectively, while δ_i refers to the FWHM of each peak, divided by the period T.

The two most commonly used tests for uniformity in γ-ray astronomy are:

1) χ^2-test: The advantage of this test is that it is a non-parametric test, but its drawback is the choice of the number of bins K (=degrees of freedom+1) and their positions on the phasogram. The best choice for K is $1/\hat{\delta}$, where $\hat{\delta}$ is some estimate of δ. From simulations it was evident that the sensitivity of this test increases with decreasing duty cycles.

2) Rayleigh test (Mardia, 1972): The motivation for the use of this test is its independence of bins. It is however a parametric test that was derived for von Mises alternatives. This corresponds to $p_1=1$, $p_2=0$ and $S(\theta;\mu_1,\delta_1)$ the von Mises distribution $M(\theta;\mu,\kappa)$. In the case of bimodal data (as with certain pulsars), the phase difference is ≈0,42 and the value of the test statistic $\bar{R}$ is small when $p_1 \approx p_2$. This is the result of two nearly opposing vectors, cancelling each other, when the test statistic

$$\bar{R} = \sqrt{(\bar{C}^2 + \bar{S}^2)} \quad \text{with } \bar{C} = \frac{1}{N}\sum_{i=1}^{N} \cos\theta_i;\ \bar{S} = \frac{1}{N}\sum_{i=1}^{N} \sin\theta_i \qquad (6)$$

is computed. Consequently bimodal data may be interpreted by this test as being uniform and real sources could then be discarded.

Two somewhat neglected non-parametric tests in this area of research are Kuiper's V_N test and Watson's U^2 test. Their distributions under H_o with the corresponding critical values are discussed by Mardia (1972). A brief outline of each test's algorithm is as follows:

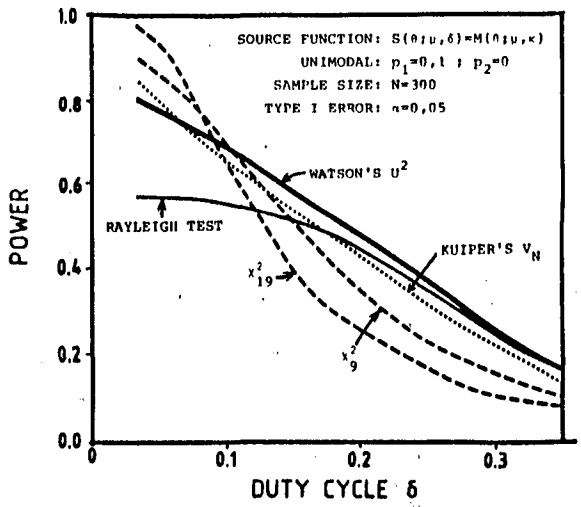

Figure 1 Power curves of the four different tests for uniformity. The light curve is assumed to be unimodal. The subscripts for the χ^2-test refer to the degrees of freedom.

3) Kuiper's V_N test: Let $\theta_{(1)},\ldots,\theta_{(N)}$ be the ordered phases. With $U_i=\theta_{(i)}/2\pi$, the test statistic is computed by

$$V_N = \max_i\left(U_i - \frac{i}{N}\right) - \min_i\left(U_i - \frac{i}{N}\right) + \frac{1}{N} \qquad (7)$$

so that only the minimum and maximum deviations from the uniform distribution are taken into account. It can intuitively be seen that this test will be sensitive to light curves with narrow duty cycles, but insensitive to those with broad duty cycles.

4) Watson's U^2 test: With U_i as above, the statistic is computed as follows:

$$U^2 = \sum_{i=1}^{N}\left[U_i - \bar{U} - \{(2i-1)/(2N)\} + \tfrac{1}{2}\right]^2 + {}^1/_{12N} \qquad (8)$$

This is a type of a mean square error with respect to the uniform distribution, so that the information of each phase is taken directly into account in the calculation of U^2.

The procedure to determine which of these four tests is the best test, would be to find the test with the largest power. Since these tests are non-parametric, (except the Rayleigh test), one cannot expect to find a single test with the largest power for all choices of parameters in eq. (5). An indication of the relative performances of these tests are given in Figure 1, which was obtained through simulations of unimodal data. It can be seen that Watson's test is the best test for duty cycles larger than 10% and the χ^2-test is best for duty cycles less than 10%. In the latter case it can be seen that the power of the χ^2-test increases if the number of bins is increased. A good choice is $K \approx 1/\delta$. At small duty cycles it can be seen that the Rayleigh test performs badly relative to any other test. These conclusions remain independent of the pulsed fraction p_1.

The question obviously arises whether one may use these tests for uniformity when the phases are not random. The answer is yes, but it applies only to those kind of tests where the distribution of the test statistic is insensitive (robust) with respect to deviations from randomness. This has been investigated for the four discussed tests by looking for a change in the critical values as T increases with respect to b. Fortunately these values did not change, so that these tests may be used for any relation between T and b.

4. NON-PARAMETRIC DENSITY ESTIMATION OF LIGHT CURVES: Although a test for uniformity is a first step in identifying a source, the additional estimation of a light curve is very important. The usual method to display a light curve in γ-ray astronomy, is to bin the data into a histogram. The disadvantage of this method is that it is dependent on bin positions and their sizes. A more correct way to display an estimate of the true unknown p.d.f., is through the use of a non-parametric density estimator. This method assumes that the data is random. Since the light curve is a periodic one, a good estimator would be a truncated Fourier series. This estimate and its standard error can easily be computed. The application to estimation on a circle is as follows: Let the random sample be $D=(\theta_1,\ldots,\theta_N)$ with unknown p.d.f. $f(\theta)$. The characteristic function (c.f.) of $f(\theta)$ and its corresponding estimator are

$$\phi_p = \int_0^{2\pi} e^{ip\theta} f(\theta)d\theta = \alpha_p + i\beta_p \text{ and } \hat{\phi}_p = \hat{\alpha}_p + i\hat{\beta}_p = \left(\frac{1}{N}\sum_{i=1}^{N} \cos p\theta_i\right) + i\left(\frac{1}{N}\sum_{i=1}^{N} \sin p\theta_i\right) \qquad (8)$$

Using the inversion formula (Mardia, 1972) we obtain

$$f(\theta) = \frac{1}{2\pi}(1 + 2\sum_{p=1}^{\infty}(\alpha_p \cos p\theta + \beta_p \sin p\theta))$$

The following asymptotically unbiased estimator of $f(\theta)$ is proposed:

$$\hat{f}(\theta;\ D,\ m) = \frac{1}{2\pi}\left(1 + 2\sum_{p=1}^{m}\left(\hat{\alpha}_p \cos p\theta + \hat{\beta}_p \sin p\theta\right)\right) \qquad (9)$$

where m is some "smoothing parameter". Using the method of cross-validation (Bowman, 1984), m can be estimated by $\hat{m}$, where $\hat{m}$ is that value of m which minimizes

$$\sum_{i=1}^{N}\left[\frac{1}{N}\int_0^{2\pi} \hat{f}^2_{N-1}(\theta;D_i,m)d\theta - \frac{2}{N}\hat{f}_{N-1}(\theta;D_i,m)\right] \text{ with } D_i=(\theta_1,\ldots,\theta_{i-1},\theta_{i+1},\ldots,\theta_N) \qquad (10)$$

The approximate confidence band of $f(\theta)$ is

$$\hat{f}(\theta;\ D,\ \hat{m}) \pm S\sqrt{(\text{var } \hat{f})} \qquad (11)$$

with s=1.96 being the quantity determining the 95% confidence limit. The probability that the true p.d.f will be within the band, will be approximately 95%. Figure 2 displays an example of these bands. One can thus use these bands, in their own fashion, to determine the significance of periodic emission. For $\delta << 1$, one may encounter the problem of oversmoothing. Tabulated values of $\hat{m}$ for such cases will be presented by the authors.

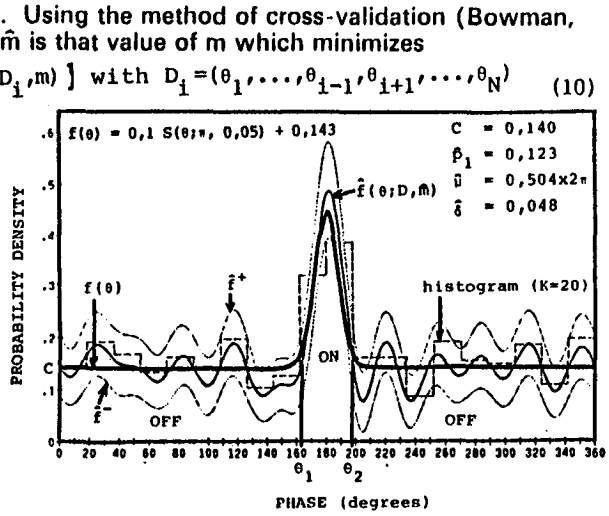

Figure 1 The density estimator $\hat{f}(\theta;D,\hat{m})$ of $f(\theta)$. The 95% confidence band is indicated by $\hat{f}^{\pm}$. The ON- and OFF-source regions are also indicated.

5. LIGHT CURVE PARAMETERS FROM THE DENSITY ESTIMATOR: Even if one does not have any knowledge of the true p.d.f $f(\theta)$, it is still desirable to know the light curve parameters. Since the estimator is asymptotically unbiased, one may estimate the desired

parameters as follows:: Determine the pulsed region θ_1 and θ_2 roughly. Then determine the uniform background level c:

$$c = \left[\int_0^{\theta_1} f(\theta)d\theta + \int_{\theta_2}^{2\pi} f(\theta)d\theta \right] / \left[2\pi - \theta_2 + \theta_1 \right] \qquad (13)$$

Using this line of height c, determine a better estimate of the pulsed region. This may lead to a small improvement of c. Obtain the light curve parameters:

$$p = \int_{\theta_1}^{\theta_2} (\hat{f}(\theta)-c)d\theta \quad \text{and} \quad \mu = \int_{\theta_1}^{\theta_2} \theta(\hat{f}(\theta)-c)d\theta \; / \; p \qquad (14)$$

The duty cycle (FWHM) can be obtained graphically or numerically from the peak of the light curve. The latter can only be done when a specific source function $S(\theta;\mu,\delta)$ is assumed:

$$\sigma^2(\delta) = \int_{\theta_1}^{\theta_2} \theta^2 (\hat{f}(\theta)-c)d\theta \; / \; p - \mu^2 \qquad (15)$$

From these parameters one can obtain the significance of periodic emission in terms of the usual number of standard deviations NSIG from the uniform background. Using a normal distribution for $S(\theta;\mu,\delta)$ and the interval $\mu \pm 1.96\sigma$ (95% area under the normal curve for this interval) for the pulsed region, NSIG was computed for unimodal light curves with a 10% periodic signal. The results are presented in Figure 3. The latter can be used to determine the total number of events that is required to obtain a certain level of significance. From Figure 3 it can be seen that the smaller the duty cycle, the easier it is to identify a source. This method can also be applied to bimodal light curves.

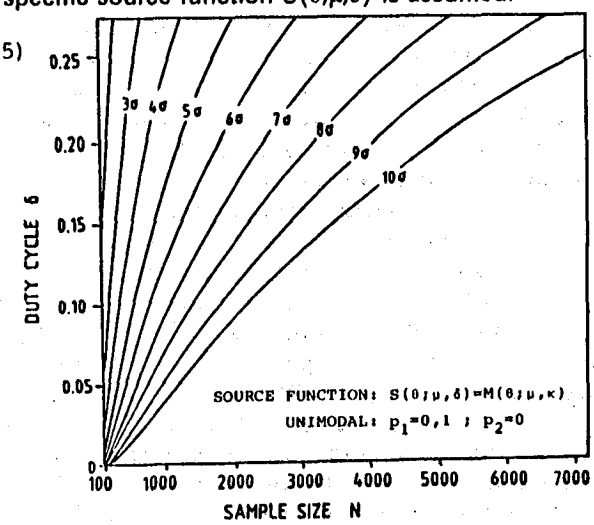

FIGURE 3 Contours of significance of periodic emission as function of the pulse-duty cycle and sample size.

6. CONCLUSIONS: When the phases are formed from the arrival times, great care should be taken if the periodic light curve and the corresponding parameters are to be estimated from the sample. In the first place analysis should be restricted to time independent processes (i.e. the form of the light curve should not change during the observation time). The next step would be to perform a test for the independency of the sample. The null-hypothesis of independency will usually be accepted for $T<3b$. This condition will usually also ensure that the sample variables (phases) are identically distributed if one let $t_1>>0$. Under these conditions the sample will be random and the p.d.f. with its corresponding parameters can be estimated. Certain tests for uniformity, like those discussed in section 3, may be used whether the sample is random or not. Watson's test seems to be the best test of those discussed for unimodal light curves with duty cycles larger than 10%, while the χ^2-test performs better at smaller duty cycles. The best choice for the number of bins in the χ^2-test is approximately $1/\delta$. The Rayleigh test is not a very dependable test since it is a parametric test that was derived for a very limited form of the light curve.

Likelihood ratio tests for uniformity are presently being investigated by the authors. This will result in the best test for light curves of the form of eq. (5). Such an analysis would automatically present the light curve parameters with their corresponding standard errors.

ACKNOWLEDGEMENTS: J.W.H. Swanepoel wishes to thank the South African CSIR for financial support.

REFERENCES:

1. Mardia, K.V. (1972). Statistics of Directional Data.
2. Lindgren, B.W. (1976). Statistical Theory, 3rd ed., p. 498.
3. Bowman, A.W. (1984). Biometrika V71, no 2, pp 353-360

A NEW STATISTIC FOR THE ANALYSIS OF CIRCULAR DATA IN GAMMA-RAY ASTRONOMY

R.J. Protheroe
Department of Physics, University of Adelaide
Adelaide, South Australia 5001.

1. INTRODUCTION The analysis of directional data (see e.g., Mardia, 1972) is important in many fields of science. In particular, circular data, where each datum may be represented by a point on the circumference of a circle, often occur in astronomy. For example, the arrival of high energy photons from a pulsar recorded as a function of time may be plotted as a function of the pulsar phase and represented by points on the circumference of a circle if the period of the pulsar is known. In this case one would wish to test for evidence of pulsed emission of high energy photons. This would often be done by binning the data into a linear histogram and using conventional statistical tests such as the χ^2 test, etc., although this procedure has disadvantages for circular data. Alternatively, one may use statistical tests designed specifically for directional data. The latter include the Rayleigh test (see e.g. Mardia, 1972), Kuiper's Kolmogorov-Smirnov type test (Kuiper, 1960), Watson's Cramer-von Mises type test (Watson, 1961) and the Hodges-Ajne's test (Hodges, 1955; Ajne, 1968).

The Rayleigh test and the Hodges-Ajne's test are useful where a sinusoidal component is expected or when the excess events are expected to be concentrated over half the cycle (Ajne, 1968). Unfortunately, however, these tests are not powerful for detecting narrow peaked pulses in the presence of a uniform background. Tests for such a situation are highly desirable for testing, for example, for evidence of ultra-high energy γ-ray emission from neutron star binary X-ray sources where the duration of the γ-ray pulses is observed to be a small fraction of the orbital period (~0.007 in the case of Cygnus X-3 [Samorski and Stamm, 1983], ~0.02 in the case of Vela X-1 [Protheroe et al., 1984] and ~0.05 in the case of LMC X-4 [Protheroe and Clay, 1985]). I have recently proposed a new statistic which meets these requirements (Protheroe, 1985). Here, the test based on this statistic is outlined and its power compared with other tests.

2. PREVIOUS TESTS Leahy et al. (1983) have already shown that the Rayleigh test is not as powerful a test for the presence of narrow pulses as the χ^2 test after binning the data. In binning the data however, two decisions have to be made: (a) where to start binning (i.e. at what phase or direction); (b) how many bins to have (or what is the bin size). The optimum bin size will depend on how wide the pulse is, while ideally the bin origin should be chosen such that the pulse lies in the middle of a bin. This information is however usually not known **a priori** and O'Mongain (1973) has pointed out that re-binning the data would reduce one's confidence in any effect subsequently found. For example, Hillas (1975) has shown that if the bin origin is chosen to maximise the number of events in one bin then the significance of a high count is much less than if the bin origin had been chosen beforehand. An 'educated guess' is

usually made as to how narrow a pulse could be. No guess can be made about the best bin origin however. This is clearly unsatisfactory and a statistic which requires no binning of the data but still provides a powerful test for narrow pulses will be proposed.

3. THE PROPOSED STATISTIC The requirements of the new statistic are: (i) it should be sensitive to the distance between pairs of points on the circle, having a high value if more points are closer together than expected; (ii) it should be sensitive to grouping of several points in the same region; (iii) the sensitivity to a very small distance between an individual pair of points should not be so great that an "accidentally" close pair dominates the statistic. I will define the distance between two observations x_i and x_j as

$$\Delta_{ij} = 0.5 - |\{|(x_i - x_j)| - 0.5\}|. \qquad (1)$$

Averaging $1/\Delta$ over adjacent pairs would satisfy (i), averaging over all pairs would satisfy (ii) and averaging $(\Delta + 1/n)^{-1}$ over all pairs would satisfy (iii). I have therefore proposed the following statistic:

$$T_n = \frac{2}{n(n-1)} \sum_{i=1}^{n-1} \sum_{j=i+1}^{n} (\Delta_{ij} + 1/n)^{-1} \qquad (2)$$

Its null distribution has been computed using Monte Carlo methods for n ranging from 2 to 200. Crictical values for $\alpha = 0.1$, 0.05, 0.01 and 0.005 are given in Table 1 for several values of n. Coefficients of a 4th order polynomial in $\ell n(n)$ are given in Table 2 to facilitate interpolation for other values of n in this range.

The power function (e.g. Hoel, 1971) of the test for n=50 and α=0.05 has been calculated by the Monte Carlo method for the alternatives to a uniform distribution in the form of a uniform distribution plus a von Mises distribution (e.g. Mardia, 1972).

$$f(x) = (1-b) + b \exp[\kappa \cos 2\pi(x-x_0))]/I_0(\kappa) \qquad (3)$$

where

$$I_0(\kappa) = \sum_{r=0}^{\infty} \frac{1}{r!^2} (\kappa/2)^{2r}, \qquad (4)$$

κ is the concentration parameter and b is the fraction of all events which are not uniformly distributed. The resulting contours of constant power are plotted in Fig 1. The 99% contour for the Rayleigh test has been added to Fig. 1 for comparison. Also shown are 99% contours for tests using Kuiper's V_n and Watson's U^2 statistics and the test based on the statistic Z_2^2 used by Buccheri et al. (1983) in their search for γ-ray emission from radio pulsars. Note that all the tests have very similar powers for broad pulses but that T_n is considerably more powerful than the others for narrow pulses.

4. CONCLUSION I have proposed a new statistic for the analysis of circular data. The test based on this statistic has recently been used in a search for ultra-high energy γ-ray from neutron star binary X-ray sources (Protheroe and Clay, 1985). The statistic is designed

n	α = .10	.05	.01	.005
2	1.82	1.90	1.98	1.99
3	2.24	2.40	2.68	2.78
4	2.60	2.78	3.15	3.28
5	2.91	3.09	3.49	3.65
6	3.17	3.36	3.77	3.94
7	3.40	3.59	4.01	4.18
8	3.61	3.80	4.21	4.38
9	3.80	3.98	4.39	4.56
10	3.97	4.15	4.55	4.72
12	4.27	4.44	4.82	5.00
14	4.53	4.69	5.06	5.23
16	4.75	4.92	5.27	5.44
18	4.96	5.11	5.45	5.62
20	5.14	5.29	5.62	5.78
30	5.86	5.99	6.28	6.42
40	6.38	6.50	6.76	6.89
50	6.79	6.90	7.14	7.26
60	7.12	7.23	7.46	7.57
70	7.41	7.51	7.73	7.83
80	7.66	7.75	7.96	8.05
90	7.88	7.97	8.16	8.25
100	8.07	8.16	8.35	8.43
120	8.42	8.50	8.66	8.74
130	8.57	8.64	8.80	8.88
140	8.71	8.78	8.92	9.00
160	8.96	9.03	9.15	9.22
180	9.19	9.25	9.34	9.41
200	9.39	9.44	9.51	9.58

Table 1. Critical values $T_{n,\alpha}$ for the proposed test of uniformity with the test statistic T_n (equation 2). $Pr(T_n > T_{n,\alpha}) = \alpha$. (Reproduced from Protheroe, 1985).

α	0.1	0.05	0.01	0.005
A_0	1.368	1.214	0.5523	0.3170
A_1	0.3467	0.8400	2.3416	2.807
A_2	0.4862	0.2436	-0.4819	-0.6597
A_3	-0.07407	-0.02658	0.1155	0.1418
A_4	0.004515	0.001132	-0.009005	-0.01038

Table 2. Polynomial Coefficients for interpolating $T_{n,\alpha}$. The 4th order polynomial $T_{n,\alpha} = \sum_{i=0}^{4} A_i [\ell n(n)]^i$ is valid for $2 < n < 200$. . (Reproduced from Protheroe, 1985).

specifically for situations where one requires a test of uniformity which is powerful against alternatives in which a small fraction of the observations are grouped in a small range of directions, or phases.

ACKNOWLEDGEMENTS This work has been supported in part by provision of a Queen Elizabeth II Fellowship and by a grant from the Australian Research Grants Scheme.

REFERENCES

Ajne, B., 1968: Biometrika, **55**, 343-354.
Buccheri, R. et al., 1983: Astron. Astrophysics, **128**, 245-251.
Hillas, A.M., 1975: Proc. 14th Int. Cosmic Ray Conf. (Munich), **9** 3439-3443.
Hodges, J.L., 1955: Ann. Math. Statist., **26**, 523-527.
Hoel, P.G. 1971: "Intoduction to Mathematical Statistics" 4th Edition (New York: J. Wiley and Sons).
Kuiper, N.H. 1960: Ned. Akad. Wet. Proc., **A63**, 38-47.
Leahy, D.A. et al., 1983: Astrophys. J., **272**, 256-258.
Lloyd-Evans, J. et al., 1983: Nature, **305**, 784-786.
Mardia, K.V. 1972: "Statistics of Directional Data" (London: Academic Press).
O'Mongain, E. 1973: Nature, **241**, 376-379.
Protheroe, R.J., et al. 1984: Ap.J. (Lett.), 280, L47-L50.
Protheroe, R.J. 1985: Astron. Expr. (submitted).
Protheroe, R.J. and Clay, R.W. 1985: Nature, in the press; see also these proceedings, paper OG 2.6-10.
Samorski, M. and Stamm, W. 1983a: Proc. 18th Int. Cosmic Ray Conf. (Bangalore), **1**, 135-138.
Watson, G.S. 1961: Biometrika, **48**, 109-114.

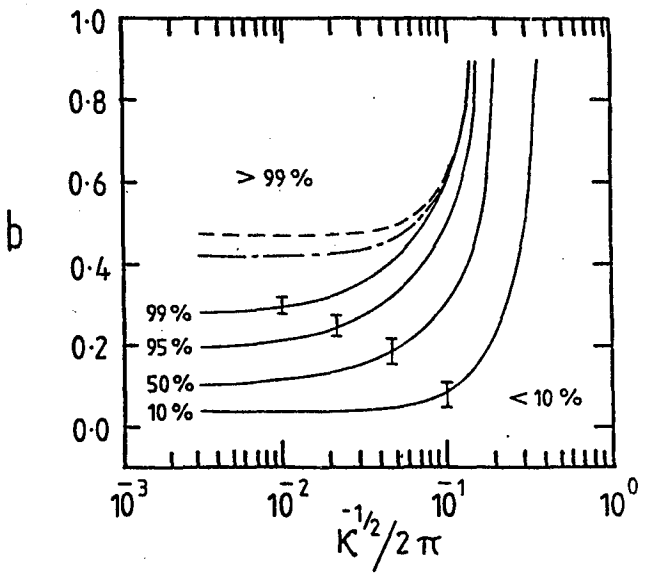

Figure 1. Contour map of the power function P(b, κ) for $\alpha = 0.05$ for the test based on the statistic T_n. 99% contours for the Rayleigh test (dashed line) and Kuiper's test (chain line) are also given for comparison. (The 99% contours for the Z_2^2 test and for Watson's test are indistinguishable from that for Kuiper's test).

THE ANGULAR RESOLUTION OF AIR SHOWER GAMMA RAY TELESCOPES

C.Morello, G.Navarra (*), L.Periale and P.Vallania

Istituto di Comogeofisica del CNR and
(*) Istituto di Fisica Generale dell'Università di Torino, Italia

A crucial characteristic of air shower arrays in the field of high energy gamma-ray Astronomy is their angular resolving power, the arrival directions being obtained by the time of flight measurements. An approach to the optimization of "air shower array-telescopes" has been recently discussed by J.Linsley (1). By using the small installation operating at the Plateau Rosà station (3500 m a.s.l.) we have studied the resolution in the definition of the shower front as a function of the shower size.

The apparatus (2) consists of four liquid scintillator detectors positioned at the corners of a rhombus (7 x 14 m diagonals, 8 m side). The detectors dimensions are 100 x 100 x 30 cm^3, each of them is viewed by two photomultipliers placed at two opposite corners.
The traversal of a particle is defined by the coincidence of the two photomultipliers and its arrival time by the mean of the two detection times (the discrimination is done in leading edge mode, at a 0.25 particle level).An EAS is defined by a four-fold coincidence.
The timing resolution is obtained by measuring $\Delta T = T_1 - T_2$ (δT = 50 ps step), where T_1 and T_2 are the time of flights between the detectors placed at the vertex of two parallel sides.
Different shower sizes are selected by measuring the particle density on a central plastic scintillator (0.5 m^2 area, 15 cm thick), see Fig. 1. For given thresholds in the number of particles (N) on the central detector: the mean number $\bar{n}$ of particles on each 1 m^2 detector, the mean distance $\bar{r}$ from the shower core, and the mean primary energy $\bar{E}_o$, are calculated on the hypotesis of pure electromagnetic cascades.
Due to the tails in the timing distributions we have defined our errors as the half widths of the distributions at half maxima (HWHM). The measured HWHM of the response of an isolated detector to the trasversal of a single particle is S_{id} = 1.25 ns and that of the sole electronic system (including the rise time fluctuations of the PM s) is S_{ie} = 0.59 ns. Since we don't expect the temporal response of the detector being constant as a function of the number of particles on it, we have used for the instrumental uncertainties (S_i) the two extreme values S_{id} and S_{ie}. After subtracting from the HWHM ($\bar{S}$) of the distribution of $T_1 - T_2$

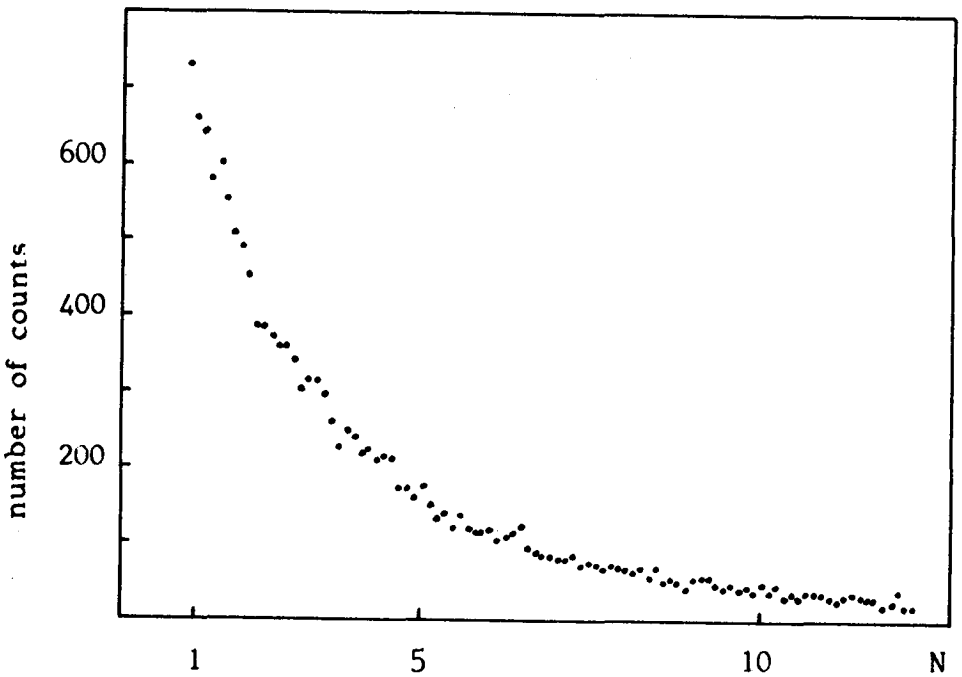

Fig.1: Pulse height spectrum of the central detector triggered by the fourfold coincidence. The cut on the left side is due to the ADC threshold.

such instrumental resolution, we obtain the physical limit to the accuracy in the definition of the shower front as a function of N. Fig. 2 shows such accuracies:

a) measured ($\sqrt{(S_N/2)^2 - S_i^2}$);

b) deduced from the resolution measured at the 1 particle level, scaling by $1/\sqrt{n}$ ($S_V/\sqrt{n}$, $S_V = \sqrt{2\,(S_o/2)^2 - S_i^2}$);

c) obtained by using the Linsley's formula ($2.6\,(\bar{r}/30 + 1)^{1.5}/\sqrt{n}$ ns, $\bar{r}$ in m)
against N, $\bar{n}$, $\bar{r}$, $\bar{E}_o$.

It can be seen that the trend of the measured resolutions as $1/\sqrt{n}$ is verified inside the uncertainty of the instrumental dispersion and also the absolute values do not move much away from those obtained by using the Linsley's formula.

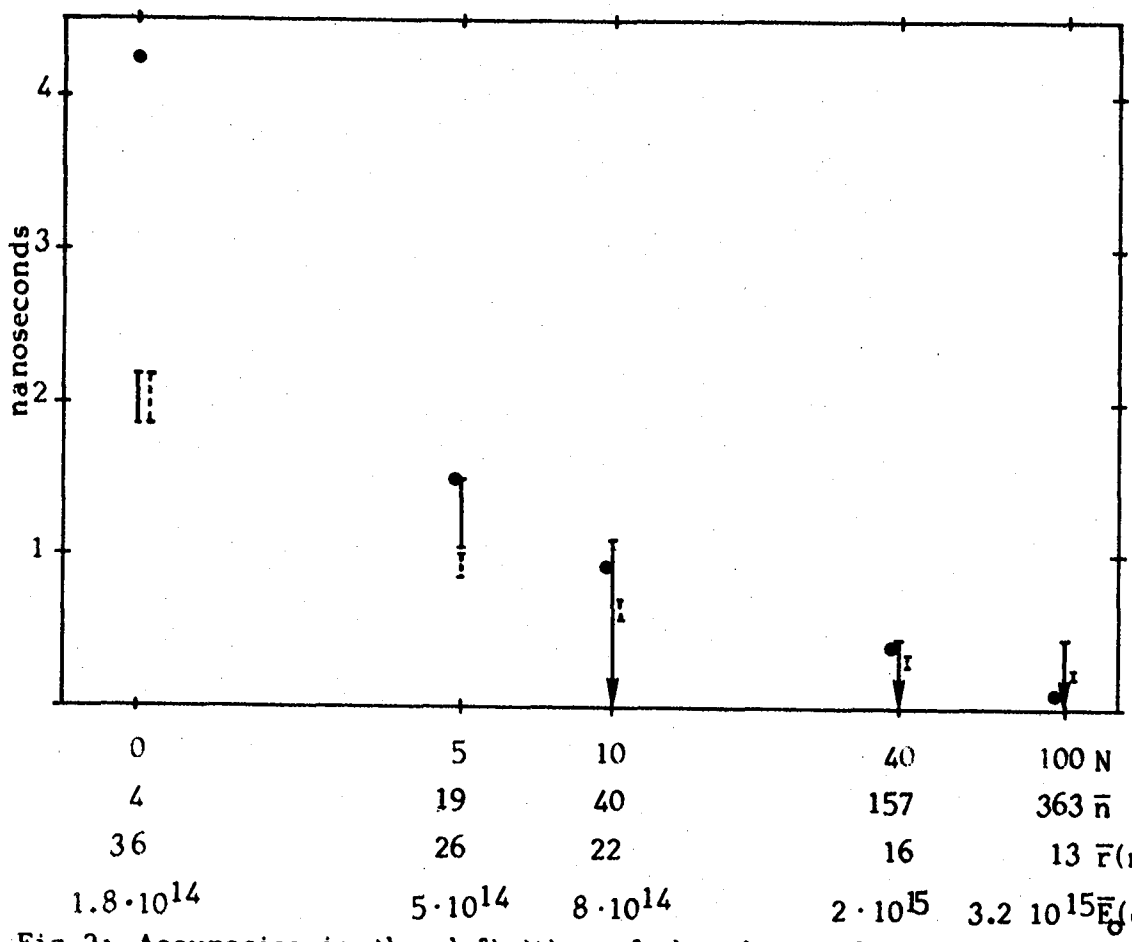

Fig.2: Accuracies in the definition of the shower front: a- continuous line; b- dotted line; c- full dots (see text).

At our atmosperic depth and by using detectors of 1 m^2 area an accuracy in the definition of the shower front St < 0.5 ns can be reached at primary energies $\bar{E}_o \sim 2.10^{15}$ eV at a typical core distance $\bar{r}$ = 16 m.

References

1. Linsley J. (1984), Research Note UNML - 7/6/84, University of New Mexico, Albunquerque.

2. Morello C. and Navarra G., (1981), N.I.M., 187,533

AUTHOR INDEX

BIBLIOGRAPHIC DATA SHEET

1. Report No.	2. Government Accession No.	3. Recipient's Catalog No.
NASA CP-2376 Volume 3		

4. Title and Subtitle	5. Report Date
19th International Cosmic Ray Conference Conference Papers	August 1985
	6. Performing Organization Code 665
7. Author(s) Frank C. Jones, compiler	8. Performing Organization Report No.
9. Performing Organization Name and Address Laboratory for High Energy Astrophysics Goddard Space Flight Center Greenbelt, MD 20771	10. Work Unit No. 11. Contract or Grant No.
12. Sponsoring Agency Name and Address National Aeronautics and Space Administration Washington, D. C. 20546	13. Type of Report and Period Covered Conference Publication 14. Sponsoring Agency Code

15. Supplementary Notes

16. Abstract

These volumes contain papers submitted for presentation at the 19th International Cosmic Ray Conference, held on the campus of the University of California, San Diego, in La Jolla, CA., August 11-23, 1985. The conference is held every other year. The present volume contains papers with Paper Codes OG 7.1 through OG 9.5 and deals with cosmic-ray sources, acceleration and propagation through the galaxy. This volume also contains papers on the various experimental techniques used in detecting.

17. Key Words (Selected by Author(s))	18. Distribution Statement
cosmic-ray sources, cosmic-ray acceleration, cosmic-ray propagation, shock acceleration, cosmic-ray instruments, gamma-ray telescopes, air-shower arrays	Unclassified - Unlimited Subject Category - 93

19. Security Classif. (of this report)	20. Security Classif. (of this page)	21. No. of Pages	22. Price*
Unclassified	Unclassified		

*For sale by the National Technical Information Service, Springfield, Virginia 22161

NASA
National Aeronautics and
Space Administration

Goddard Space Flight Center
Greenbelt, Maryland 20771